PHOTOGRAPH THIS SHEET

DTIC ACCESSION NUMBER: ADA087513

LEVEL: III

INVENTORY

Denver Research Inst, Col.
Labs. for Applied Mechanics

Proceedings of the International Pyrotechnics
Seminar (5th) Held at Vail, Colorado, 12-16 July 1976,

DOCUMENT IDENTIFICATION

Blunt, R.M. ; 7 May 1976

DISTRIBUTION STATEMENT A

Approved for public release
Distribution Unlimited

DISTRIBUTION STATEMENT

ACCESSION FOR	
NTIS GRA&I	☒
DTIC TAB	☐
UNANNOUNCED	☐
JUSTIFICATION	

BY

DISTRIBUTION /
AVAILABILITY CODES

DIST	AVAIL AND/OR SPECIAL	
A		

DISTRIBUTION STAMP

DTIC
ELECTE
AUG 6 1980
S D
D
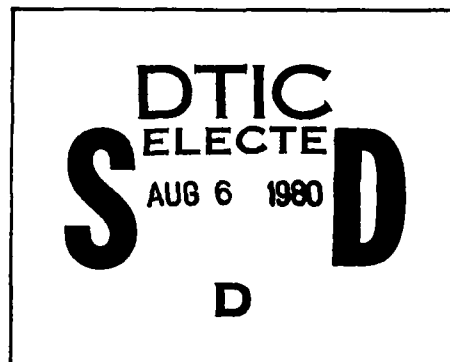
DATE ACCESSIONED

See also AD-A057599, dtd. 17 Jun. '74

80 8 1 001

DATE RECEIVED IN DTIC

PHOTOGRAPH THIS SHEET AND RETURN TO DTIC-DDA-2

DTIC FORM OCT 79 70A

DOCUMENT PROCESSING SHEET

ADA087513

Approved for Public Release;
Distribution Unlimited

The Proceedings of ~~four~~ *five* earlier seminars in
this series can be obtained from:
NATIONAL TECHNICAL INFORMATION SERVICE
U.S. DEPARTMENT OF COMMERCE
5285 PORT ROYAL ROAD
SPRINGFIELD, VA 22161

Their Ordering Identification is:
First -- AD 679971
Second -- AD 913407
Third -- AD 913408
Fourth -- AD-A057599
Sixth -- AD-A063797

**PROCEEDINGS
OF THE
FIFTH INTERNATIONAL PYROTECHNICS SEMINAR**

12-16 JULY 1976

Approved for Public Release;
Distribution Unlimited

Chairman
R.M. Blunt, Laboratories for Applied Mechanics

Denver Research Institute
University of Denver
Denver, Colorado
80210

The Proceedings of ~~four~~ five earlier seminars in
this series can be obtained from:
NATIONAL TECHNICAL INFORMATION SERVICE
U.S. DEPARTMENT OF COMMERCE
5285 PORT ROYAL ROAD
SPRINGFIELD, VA 22161

Their Ordering Identification is:
First   -- AD 679911
Second -- AD 913407
Third   -- AD 913408
Fourth -- AD-A057599
Sixth   -- AD-A063797

FIFTH SEMINAR PROCEEDINGS

INTRODUCTION

This seminar is the child--or perhaps the grandchild--of an idea that was discussed at length in 1967 by Jim Kottenstette, Ralph Williams, Bill Cronk, Bernie Douda and me. The idea as it was debated among us was concerned with the need for formal course work to provide an educational grounding in Ordnance Science and Engineering similar to the existing courses in other engineering fields of specialization. Unfortunately, this idea never came to be a reality, but it did form the kernel around which the first Seminar in Estes Park was built, with great help and encouragement from Bill Cronk and Bernie Douda.

I sincerely hope that this Fifth Seminar will be as rewarding to the participants as the previous four appear to have been. It seems somehow appropriate that it should be held in Colorado's Centennial Year and our nation's Bicentennial Year.

Once again, thanks to all of you whose reports on your research programs have justified the publication of these Proceedings and provided the basis for holding this Seminar. As the "old-timers" know, these Seminars are totally self-justifying and self-supporting. There is no monetary support from any organization, although the Naval Weapons Support Center, Crane and the Naval Air Systems Command provide moral support. My special thanks to Dr. B.E. Douda and the Chemical Sciences Branch, NWSC for their help.

R.M. Blunt
Chairman

May 7, 1976
Denver, Colorado

TABLE OF CONTENTS

PYROTECHNIC REACTION MECHANISMS

Edward J. Bair

Chemistry Department, Indiana University

Bloomington, Indiana 47401

ABSTRACT

The object of the research is to explore ways to produce bright, selective, gas phase, infrared emitters from reactions which produce vibrationally excited molecules directly, as opposed to indirect thermal excitation. The experiments consist of time resolved spectroscopic measurements following flash initiated reactions in which the vibrational energy distributions of the reaction intermediates are observed.

The research thus far suggests that recombination is a promising way to obtain a level of infrared emission which compares favorably with the energy dissipated as heat. There is experimental evidence that a major fraction of the energy of a combination reaction can appear as infrared emission at specific wavelengths. The long range objectives of the research are to convert this fact into a practical principle for producing selective infrared radiation from a variety of chemical reactions. The results show that the vibrational disequilibrium in real systems ranges from vibrational energy poor to vibrational energy rich.

I. INTRODUCTION

A pyrotechnic flare for the visible and near infrared region
of the spectrum requires an energetic reaction to create a high
temperature medium, and additives with spectral transitions at
the desired wavelengths. It is usually not necessary to consider
the mechanism by which the emitters are excited. If the reacting
gases are hot enough, the emitters are certain to be excited. Once
the upper state of an allowed electronic transition is excited, its
radiative lifetime is so short that there is little probability of
any outcome of the excitation other than loss of energy by radiation,
even when the radiation is absorbed and re-emitted by radiative
transfer.

Gaseous systems which radiate at longer wavelengths in the infrared
appear more complicated because of their relatively long radiative
lifetime. There may be thousands of collisions during the radiative
lifetime of an excited infrared emitter, and many processes compete
with radiation to dissipate or redistribute the energy. The following
requirements are placed on the systems we have studied. First, the
reactions must produce vibrationally excited molecules. Secondly, the
vibrational energy distributions must be observable by methods at our
disposal. Finally, the reaction system must be one in which the major
elements of the mechanism are known, or can be determined.

The following processes affect vibrational energy distributions.

$$\text{translation} \rightarrow \text{vibration}$$
$$\text{exothermic reaction} \rightarrow \text{vibration}$$
$$\text{recombination} \rightarrow \text{vibration}$$
$$\text{vibration} \rightarrow \text{vibration}$$
$$\text{vibration} \rightarrow \text{reaction}$$
$$\text{vibration} \rightarrow \text{translation}$$
$$\text{vibration} \rightarrow \text{radiation}$$

The first three create vibrational excitation. The next two redistribute
it, or form products which can regenerate it. The final two dissipate
energy, either as heat, or as the desired radiation. The object is to

choose reactions which generate as much vibrational excitation as possible in a system which sustains the excitation as long as possible in order that its ultimate fate will be radiation, rather than dissipation as heat.

Recombination is an exothermic reaction which deserves special mention. All reactions of this class produce vibrationally excited products in their highest levels of vibration. In considering recombination as a source of vibrational excitation, it is also natural to consider the advantage of polyatomic molecules over diatomics as emitters. Rates of recombination are typically 2-3 orders of magnitude faster for triatomic, than for diatomic products. At flame temperatures the number of thermally populated vibrational states is an order of magnitude, or more, greater for triatomic molecules. Because of this, a major fraction of triatomic molecules in a flame would be vibrationally excited, but most of the diatomic molecules would not.

II. EXPERIMENTAL RESULTS

Two of the systems which have been studied, taken together, illustrate vibrational excitation as it might occur in a flame. The experiment consists of ozone absorbance measurements at a sequence of times before, during, and after a photolysis flash in ozone and ozone-oxygen mixtures. The experiment is repeated at different spectral frequencies to give a matrix of absorbances as a function of time and spectral frequency.

It should be noted that a time dependent, flash initiated reaction is analogous to the same reactions in a steady state flame as a function of position. The transformation between the time coordinate of the time dependent system and position coordinates in the flame would be fairly direct, if lateral diffusion within the flame could be neglected. The 3-dimensionality of flames makes reaction mechanisms in flames more complex than the analogous processes in time-dependent homogeneous systems.

In the first system to be described, spontaneous decomposition of ozone is initiated by flash photolyzing a small fraction of the initial sample. The resulting time evolution of the ozone spectrum is shown in

Fig. 1. The progressive variation in spectral distribution is related to the vibrational excitation, as will be explained further. The sequence of spectra in this time range are somewhat analogous to the reactions in the premix and inner cone regions of a flame. Decomposition of a small amount of ozone by the flash release enough reactive products and energy to propagate spontaneous decomposition throughout the next 100 µsec, or so. At the end of the observed process, most of the ozone has been decomposed, energy has been released causing the sytem to be hot, and the system still contains a moderately high concentration of atomic dissociation products. In the absence of fuel (ozone) with which the atoms can react, their fate is to recombine with oxygen molecules. This is a much slower process, such as that which would occur in the outer cone of a flame.

To accelerate the recombination, and accentuate the vibrational energy changes which accompany them, they are studied in a different system containing ozone mixed with a large excess of oxygen. These results are shown in Fig. 2. In this case, the photolysis flash decomposes most of the ozone directly, leaving a system containing oxygen atoms, as before. This system has a much lower kinetic temperature than the first system, because of the excess oxygen, but since the recombination reaction rate is not greatly temperature dependent the main effect of the added oxygen is to increase the rate of recombination, and at the same time, minimize competition from thermal decomposition.

In thermal decomposition the sequence is from top-to-bottom. The system with the highest vibrational excitation has the smallest concentration. In recombination, the sequence is from bottom-to-top, starting with a small amount of freshly recombined ozone having the largest amount of vibrational excitation, and progressing toward fully recombined ozone in which the excitation has been lost by radiation and thermal dissipation. The vibrational distribution of the hot, thermally dissociated ozone is similar to that of the freshly recombined cold ozone.

III. ANALYSIS OF THE REACTION MECHANISM

The first step in interpreting the results is to reconcile the observed ozone concentrations and vibrational excitation with the known features of the reaction mechanism.[1] The kinetic parameters of the reactions are known well enough to construct a mathematical model of the reaction at moderate temperatures which satisfactorily predicts the chemistry which occurs under a wide range of initial conditions when the system remains at moderate temperature. The principal reactions involved in the flash initiated, thermal decomposition of ozone are the following.

$$O_3 + h\nu \rightarrow O(^1D)\ O_2(^1\Delta) \tag{1}$$

$$O(^1D) + O_3 \rightarrow 2\ O(^3P) + O_2(^3\Sigma) \tag{2}$$

$$O(^1D) + O_3 \rightarrow 2\ O_2(^3\Sigma) \tag{3}$$

$$O(^1D) + M \rightarrow O(^3P) + M \tag{4}$$

$$O(^1D) + O_2 \rightarrow O_2(^1\Sigma) + O(^3P) \tag{5}$$

$$O(^3P) + O_3 \rightarrow 2\ O_2(^3\Sigma) \tag{6}$$

$$O(^3P) + O_2(^3\Sigma) + M \rightarrow O_3 + M \tag{7}$$

$$O_2(^1\Delta) + O_3 \rightarrow O(^3P) + 2\ O_2(^3\Sigma) \tag{8}$$

$$O_2(^1\Sigma) + O_3 \rightarrow O(^3P) + 2\ O_2(^3\Sigma) \tag{9}$$

$$O_3 + M \rightarrow O(^3P) + O_2(^3\Sigma) + M \tag{10}$$
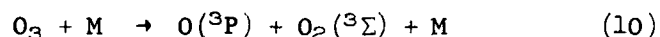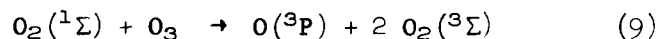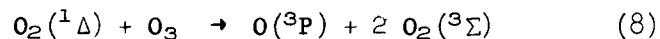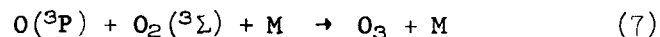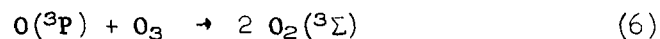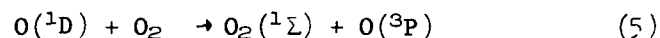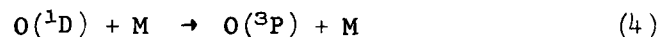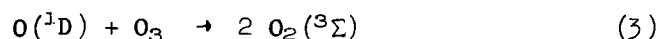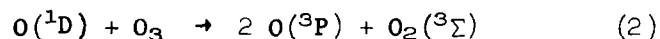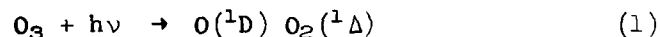
When the reactions are fast enough to cause energy distributions which depart substantially from thermal equilibrium, this is not necessarily true. One of the purposes of the research is to account for these departures from normal equilibrium kinetics.

The information to be extracted from the ozone spectral measurements is the ozone concentration and the vibrational temperature as a function of time. Regardless of spectral variations caused by vibrational excitation, the ozone concentration is proportional to the integrated absorbance as a function of spectral frequency. The absorbance is

measured at a discrete set of frequencies. To obtain the integrated absorbance, the spectrum is converted to a continuous function of frequency, using a LaGrange interpolation polynomial, then integrated numerically.

For a simple description of the vibrational distribution of ozone, we characterize if by the temperature at which a system of ozone at thermal equilibrium would have the same total energy in its excited vibrational states as that which is observed. To determine the vibrational temperature from the spectra, the spectrum at any time t, during a reaction, is compared with a spectrum taken at 195°K, at which temperature vibrational excitation is negligible.

The first step is to calculate the average absorption frequencies $\langle \nu_t \rangle$ and $\langle \nu_c \rangle$, for the spectrum at time t and the cold spectrum, respectively. This is given by

$$\langle \nu_t \rangle = \frac{\Sigma A_t(\nu_j) \, \nu_j}{\Sigma A_t(\nu_j)} \tag{1}$$

The vibrational energy of ozone in cm^{-1} is given in terms of the vibrational quantum numbers by[2]

$$G_{ijk}'' = 1103.2 \, v_1 + 701.4 \, v_2 + 1042.1 \, v_3 + 2.0 \, v_1(v_1-1)$$
$$- 1.0 \, v_2(v_2-1) - 15.0 \, v_3(v_3-1) - 11.0 \, v_1 v_2$$
$$- 39.0 \, v_1 v_3 - 21.0 \, v_2 v_3 \tag{2}$$

where i,j,k refer to the quantum numbers v_1, v_2, v_3. The relative population of each vibrational state at equilibrium is given, in terms of the vibrational energy by

$$P_{ijk}(T) = \frac{\exp(-\, hcG_{ijk}''/kT)}{\displaystyle\sum_{i,j,k} \exp(-\, hcG_{ijk}''/kT)} = \frac{\exp(-\, hcG_{ijk}''/kT)}{Q_{vib}} \tag{3}$$

where the sum is taken over all states below the dissociation energy.

Whether or not the vibrational distribution of a particular system of hot ozone is an equilibrium distribution, the spectrum is the sum of the overlapping contributions from each state that is excited. The origin of each excited component is displaced toward lower frequency from the ground state component by the magnitude of the excited state vibrational frequency. The integrated absorbance of each component is proportional to the relative population of the state which causes it. The average vibrational energy given by equation (4) is readily determined from the experimental data. The shift in the average frequency at time t from that of the spectrum of cold ozone can be equated with the average vibrational excitation of the system in wavenumbers.

$$\langle E_{vib} \rangle = | \langle \nu_c \rangle - \langle \nu_t \rangle | \tag{4}$$

This assumes that the integrated strength of each component is symmetric about the center of the component. This assumption is valid for the lower states but becomes less certain at higher levels of excitation. To obtain the vibrational temperature as a function of the energy shift, the energy shift is calculated for a representative set of temperatures, and the numerical results are used to express the vibrational temperature as a function of the energy shift.

$$T_{vib} = 260.2 + 1.309 \, \omega - .001060 \, \omega^2 + 4.818 \times 10^{-7} \, \omega^3 \tag{5}$$

where $\omega = \langle E_{vib} \rangle$ is the observed frequency shift in cm^{-1}.

The concentrations and vibrational temperatures observed during the flash initiated decomposition of pure ozone are compared with the equilibrium kinetic model in Fig. 3 and Fig. 4. The rate of ozone decomposition is significantly faster than that predicted by the equilibrium model. The adiabatic temperature predicted by the model is much higher than the observed ozone vibrational temperature, but since thermal dissociation is highly endothermic, the real adiabatic temperature could be in reasonable agreement, if thermal discociation is, in fact, the

process responsible for the enhanced rate of reaction. The enhanced rate is tentatively assigned to an enhanced rate of vibrational excitation of ozone by the sequence

$$O(^3P) + O_3 \rightarrow 2\ O_2\dagger$$

$$O_2\dagger + O_3 \rightarrow O_2 + O_3\dagger$$
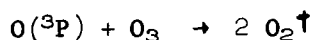
The concentrations and vibrational temperatures of the recombining ozone are compared with the equilibrium model in Fig. 5 and Fig. 6. In this case, the adiabatic temperature is held close to the initial room temperature by the large excess of oxygen in the initial reaction mixture. The relatively significant vibrational excitation is due entirely to the vibrational disequilibrium which results from the rapid rate of recombination. The rate of recombination is slower than that predicted by the accepted "best value" for the recombination rate, but not remarkably slower. If there is a real discrepancy, it is tentatively interpreted as competition by thermal dissociation at the observed ozone vibrational temperature.

IV. ANALYSIS OF THE VIBRATIONAL ENERGY DISTRIBUTION

A difficulty in studying the total vibrational excitation in polyatomic molecules is the large number of vibrational states which must be considered when the excitation is significant. This section describes the contribution of different vibrational levels v_{ijk} to the shape of the spectrum of a triatomic molecule for an electronic transition from a bound lower electronic state to a continuous upper state. It shows why the symmetric stretching mode is dominant in determining the shape of the spectrum component from any specific vibrational state. The spectral absorption coefficient may be written

$$k_\nu = \frac{8\pi^3 \nu}{3hc}\ R^2 \tag{7}$$

The transition moment integral R may be factored into a constant term R_e, representing the motions of the electrons, and a matrix element for each vibrational state ijk.

$$R = \frac{R_e}{n} \sum_{ijk} n_{ijk} \langle \varphi_i(Q_1) \, \varphi_j(Q_2) \, \varphi_k(Q_3) \mid E'(Q_1,Q_2,Q_3) \rangle \tag{8}$$

The $\varphi_n(Q_n)$ are vibrational wavefunctions of the lower state as a function of the corresponding normal coordinates. $E'(Q_1,Q_2,Q_3)$ represents the continuum wavefunction of the upper state at an energy difference corresponding to the absorption frequency ν as a function of the same normal coordinates. To a good approximation $E''(Q_1,Q_2,Q_3)$ can be replaced by a δ function having the value $\delta = 1$ where the coordinates correspond to a position on classical potential surface, and a value $\delta = 0$ elsewhere.

The symmetric stretching wavefunction and the symmetric stretching cross section of the potential energy surface are related to the vibrational components of the spectrum as shown in Fig. 7. The amplitude of the absorption coefficient at frequency ν is porportional to the amplitude of the vibrational wavefunction at the corresponding Q_1, except for the normalizing factor $dQ_1/d\nu$ which corrects for the effect of the curvature of the potential function on the relative interval in Q_1 and ν. The shape of the spectrum component as a function of ν is roughly a reflection of the shape of the vibrational wavefunction as a function of displacement Q_1. The central frequency of successively higher vibrational state components shifts toward successively lower frequency corresponding to the difference in energy of the upper and lower states.

The contribution of the asymmetric stretching mode to the shape of the spectrum is quite different, as can be shown on the 3-dimensional potential energy surfaces in Fig. 8. The symmetric stretching mode is normal to the potential energy trough (along the front-to-back diagonal in the drawing), and intersects the upper potential surface at the energy which corresponds to the frequency of the transition. The asymmetric stretching mode, on the other hand, follows the minimum in the potential energy and is parallel to both the upper and lower surface. A normal

mode can influence the shape of the spectrum components only if it intersects the upper state potential surface, since the upper state wavefunction exists only at the potential energy surface. The asymmetric stretch does not intersect the surface except by coupling with the symmetric stretching mode. The centers of spectral components having various asymmetric stretching quantum numbers are shifted according to the energy difference of the transition. The shape of the spectrum component is determined by the symmetric stretching quantum number alone.

The contribution of the bending mode to the shape of the spectrum is accounted for in somewhat similar fashion. Since the nascent excited molecule has an energy in excess of the dissociation limit, the bending force constant of the upper state is much smaller than for the ground state. The classical turning points of the upper state bending potential function tend to lie beyond the limits of the bending wavefunction in the ground electronic state. Therefore the shape of a given vibrational component is independent of both the bending and asymmetric stretching quantum numbers. Equation (2) therefore reduces, in practice, to

$$R = \frac{R_e}{n} \sum_{ijk} n_{ijk} \langle \varphi_i(Q_1) \mid E'(Q_1) \rangle \tag{9}$$

since the overlap integral involving $\varphi_j(Q_2)$ and $\varphi_k(Q_3)$ vanishes except where it coincides with $\varphi_i(Q_1)$.

The principles outlined above are obviously qualitative, but their applicability can be examined by comparing the spectrum of ozone at 195°K, where the vibrations are essentially unexcited, with that the 333°K, where each of the three normal modes have small, but observable excited state populations, as given below.

T	P_{000}	P_{010}	P_{001}	P_{100}
195	.993	.0058	.0005	.0003
333	.933	.0451	.0104	.0080

The spectrum of ozone at 195°K is shown in Fig. 9. The changes which occur when the ozone is heated to 333°K are small, and can best be shown by difference. The spectrum in Fig. 10 is obtained by multiplying the cold spectrum by 0.933 and subtracting it from the hot spectrum. The difference is therefore the vibrationally excited component. The detailed band structure results from the fact that the upper state is bound with respect to the symmetric stretching and bending modes. It is quite different in the hot and cold spectra, and the changes are accentuated in the difference spectrum. The solid smooth curve indicates the position of the cold spectrum. The dotted curve is obtained by moving the solid curve toward lower frequency by the weighted average vibrational excitation. Since the bending and asymmetric stretching components are dominant, the agreement between the dotted curve and the observed difference spectrum is expected.

To obtain the spectra in Fig. 11 the spectrum of the vibrationally excited components is first smoothed by a process equivalent to narrowing the spectral band pass. Next the smooth curve corresponding to the cold spectrum is multiplied by .0451, the fraction of molecules in the excited bending mode, moved 701 wavenumbers toward lower, frequency, and subtracted from the spectrum of the hot components. The difference spectrum now consists of components due to symmetric and asymmetric stretching. The asymetric stretching component is subtracted by multiplying the cold spectrum by .0104, shifting 1042 wavenumbers toward lower frequency, and subtracting. Now the resultant spectrum is primarily the component due to symmetric stretching. The subtraction process leaves the difference spectrum with all of the residual band structure, and since it represents only 0.8 percent of the original, it has considerable fluctuation. Nevertheless, the observed component has the bimodal character which is predicted.[3]

The general procedure for analyzing the vibrational energy distributions in systems such as those represented by Fig. 1 and Fig. 2 is now somewhat clearer, although the actual analysis is still in progress at this time. That procedure is to use the observed spectra to find the upper state potential energy and the lower state vibrational wavefunctions in best agreement with

the data, then use those parameters to extrapolate to higher vibrational levels. Fig. 12 illustrates a start toward the application of that process. The upper state potential energy is first determined, ad indicated in Fig. 7, by comparing the observed cold spectrum with a harmonic oscillator ground state function. The potential energy that is found in this way can be written

$$E' = 39316 - 3718. \, Q_1 + 369.7 \, Q_1^2 - 137.3 \, Q_1^3 + 27.37 \, Q_1^4 \qquad (10)$$

where Q_1 is expressed in dimensionless, mass weighted units, and the polynomial is valid over the region 30,000 to 48,000 cm^{-1}. Next the harmonic oscillator wavefunction for the first excited symmetric stretching level is compared with data points for the observed spectrum. This comparison is shown by the dotted curve, and the data points in Fig. 12. Although the harmonic oscillator approximation is reasonable, an adjustment of the anharmonicity brings the observed and calculated spectrum components into agreement within experimental error.

With the intensive research that has surrounded ozone for the past decade, its reaction mechanisms at thermal equilibrium are better understood that the mechanism of most energetic systems of simple gas molecules. When the reaction occur in systems which are only marginally isothermal, it is not uncommon to find discrepancies in reaction rates which might be attributable to vibrational nonequilibrium.[4] These discrepancies may well be resolvable by further measurements in systems where the vibrational temperature of the reactant is well characterized, even though it is a disequilibrium temperature.

V. SUMMARY

A quantitative account of the apparent vibrational features in the spectra of Fig. 1 and Fig. 2 has not yet been accomplished, although the procedure which has been outlined holds promise for doing this. The highest degree of vibrational excitation gives the same spectral features, whether the excitation is caused by thermal excitation or by recombination.

Qualitatively the features resemble those which might be expected, with the main central peak from the v_{oxx} components lying at lower frequency under conditions of maximum excitation, and shifting toward higher frequency when the excitation becomes smaller. The hypothesis that recombination is a useful strategy for sustaining vibrational excitation is supported by the results. The important function of the reactions in Fig. 1 are not to produce a high temperature, but to use the energy of the reaction to produce a maximum amount of products which can recombine. When this phase of the reaction is complete, the products will recombine, producing vibrationally excited products as they do. If the system is hot enough to cause thermal decomposition during this period, this simply serves as a mechanism for sustaining the excitation.

Since this research was started, Von Rosenberg and Trainor[5] have described experiments in which they observe the infrared radiation associated with the ozone recombination reaction.[5] Their experiments tend to confirm the suggestion that recombination is an efficient process for converting energy of reaction to infrared radiation.

References

[1]R. F. Hampson and D. Garvin, Technical Note 866, National Bureau of Standards, June 1975. A critical evaluation of several hundred papers aimed at producing an accurate model of the chemistry of the atmosphere, including many reactions of interest in combusion.

[2]D. J. McCaa and J. H. Shaw, J. Mol. Spectrosc. 25, 374 (1968).

[3]G. Herzberg, Infrared and Raman Spectra, Von Nostrand, Inc. (1945).

[4]V. D. Baiamonte, L. G. Hartshorn, and E. J. Bair, J. Chem. Phys. 55, 3617, (1971); W. M. Jones and N. Davidson, J. Am. Chem. Soc., 84, 2868, (1962); P. L. T. Bevan and G. R. A. Johnson, Trans. Farad. Soc., 69, 216 (1973).

[5]C. W. Von Rosenberg, Jr., and D. W. Trainor, J. Chem. Phys., 61, 2442 (1974); 63, 5348 (1975).
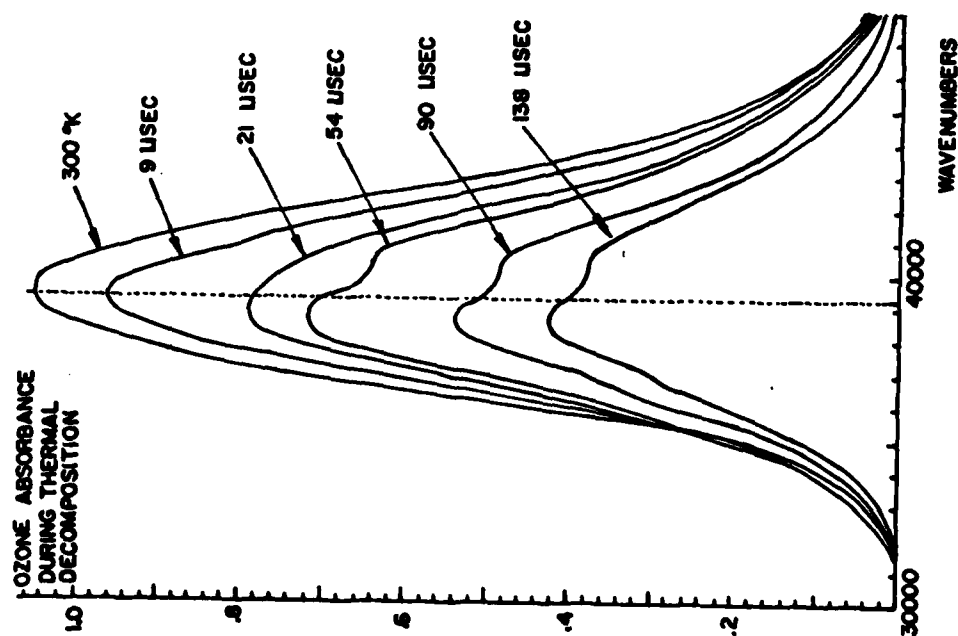
Fig. 1 Ozone disappearance during flash
initiated thermal decomposition.

Fig. 2 Ozone reappearance as a result of
$O(^3P) + O_2$ recombination.

The irregularities in both spectra at intermediate times is the result of varying degrees of
vibrational excitation, as explained in the text.
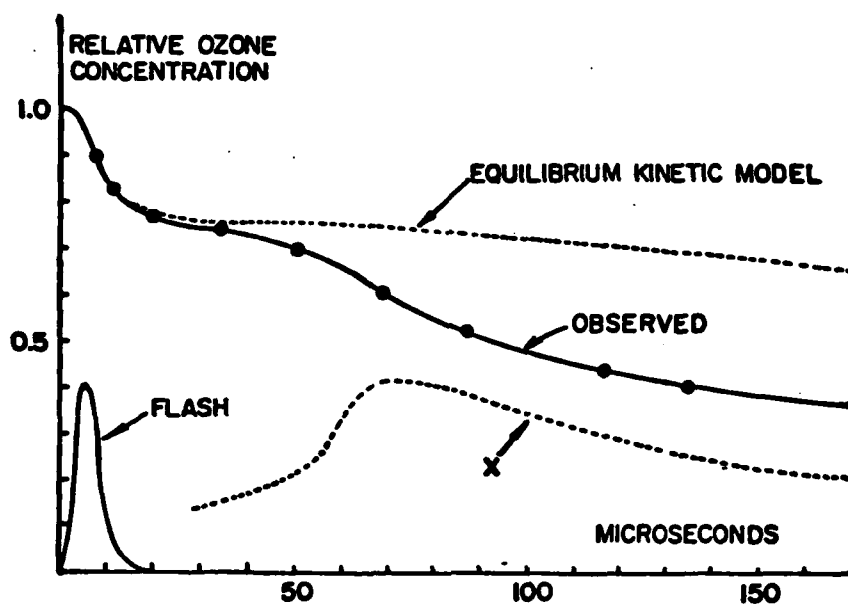
Fig. 3 Ozone disappearance during flash initiated thermal
decomposition compared with thermal equilibrium model.
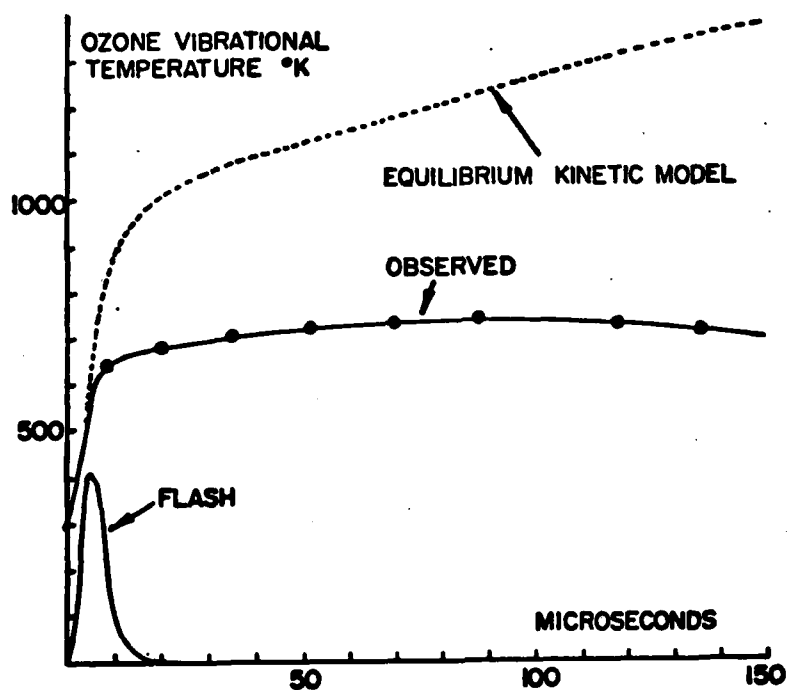
Fig. 4 Observed ozone vibrational temerature in comparison with
calculated adiabatic temperature during flash initiated thermal
decomposition.
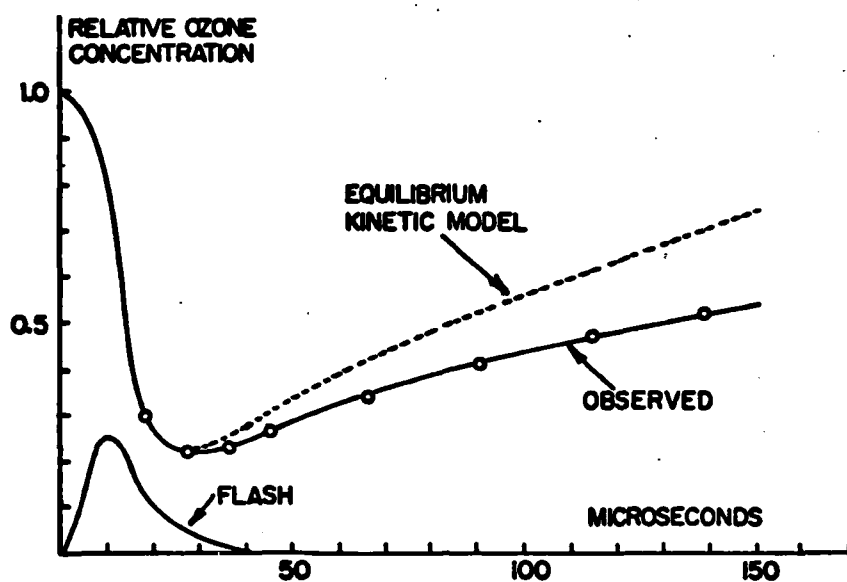
Fig. 5 Ozone concentration during recombination compared with thermal equilibrium model.
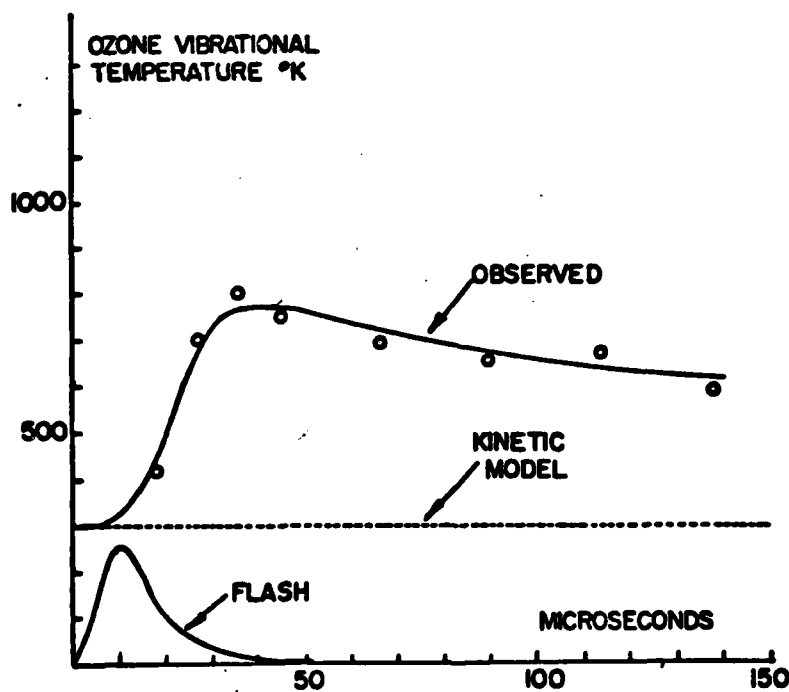
Fig. 6 Observed ozone vibrational temperature in comparison with the calculated adiabatic temperature during recombination.

18

ENERGY KCAL

197

142

80
69
59
45
24

0

O('D) + 2 O(³P)

3 O(³P)

O('D) + O₂('Δ)
O('D) + O₂(³Σ_g⁻)
O(³P) + O₂('Σ_g⁺)
O(³P) + O₂('Δ_g)
O(³P) + O₂(³Σ_g⁻)

O₃

R O₂—O
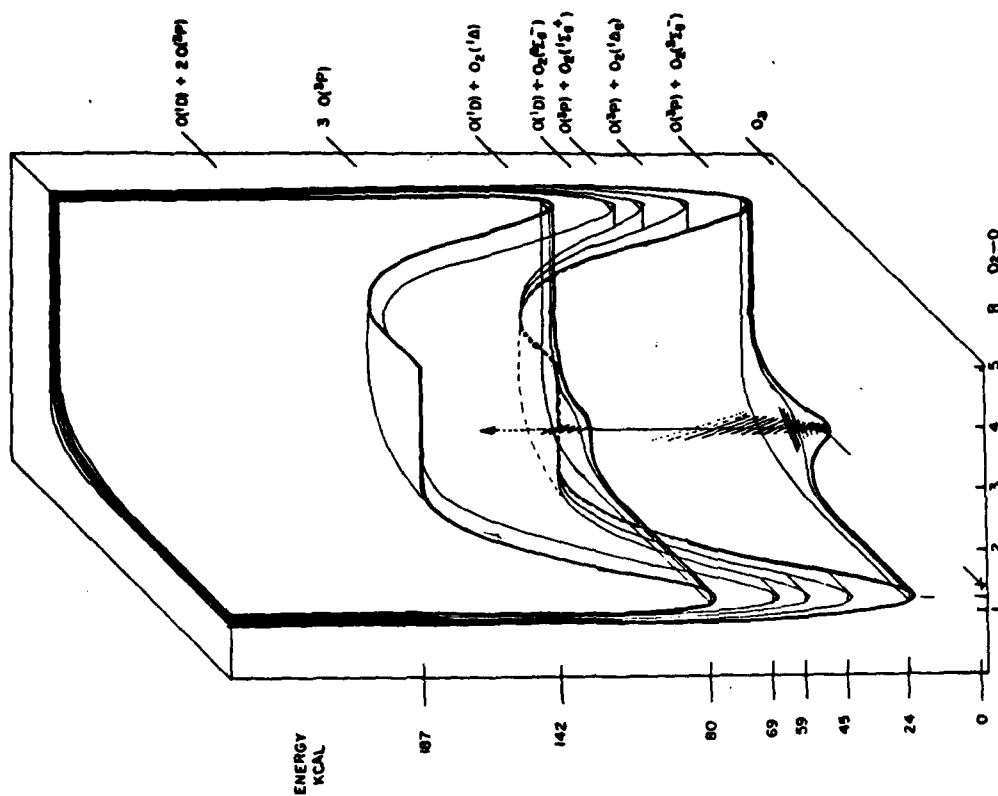
Fig. 8 3-dimensional view of the potential
energy surfaces for ozone.

CM⁻¹

40000

30000

20000

10000
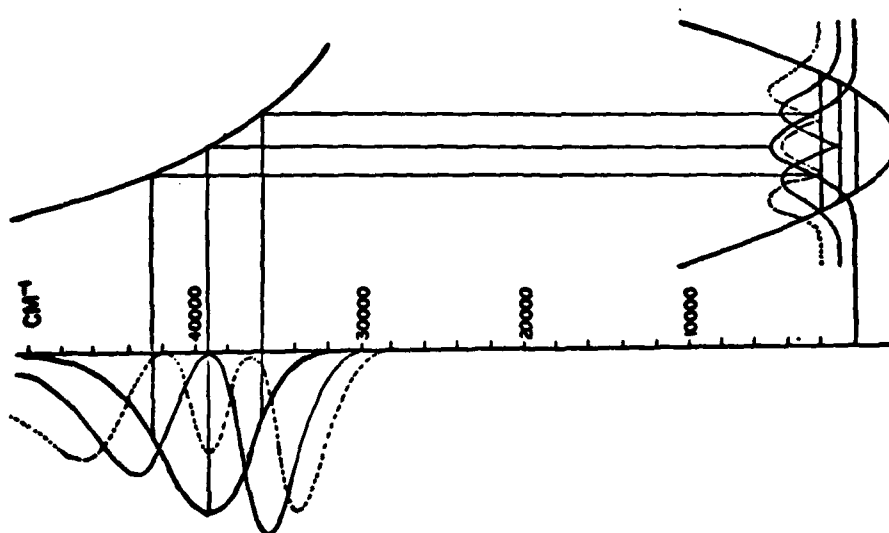
Fig. 7 Relation bewteen the ultraviolet spectrum
components and the symmetric stretching cross
section of the potential energy surface.
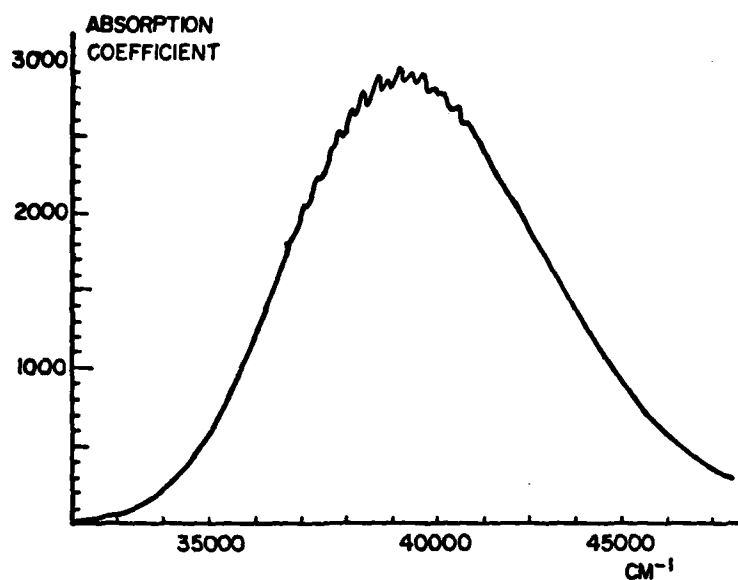
Fig. 9 Spectrum of ozone at 195°K where excited vibrational states are virtually unpopulated.
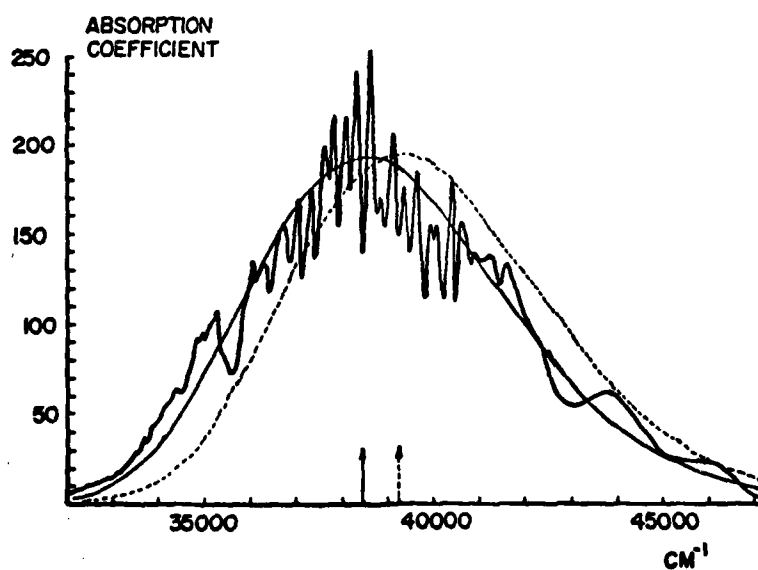
Fig. 10 Vibrationally excited component of the ozone spectrum at 333°K obtained by subtracting the normalized cold spectrum from the hot spectrum.

ABSORPTION COEFFICIENT
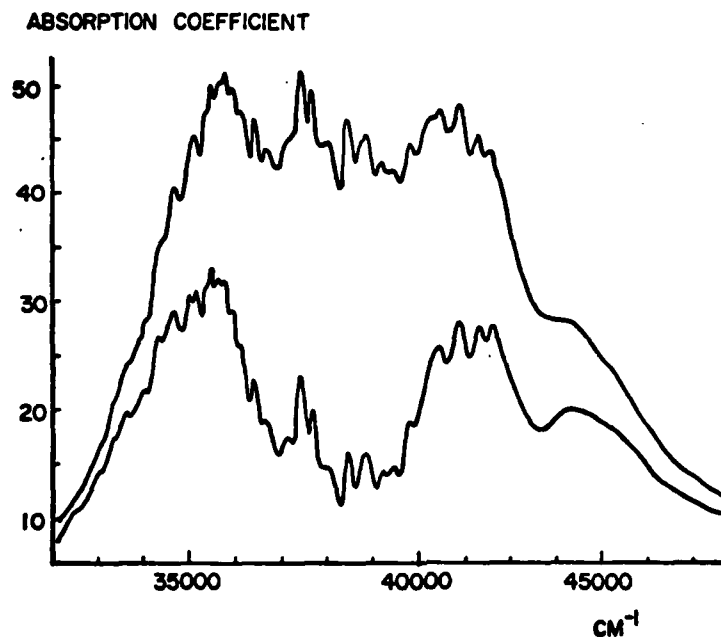
Fig. 11 Vibrationally excited component minus contributions from
bending (top curve) and asymmetric stretching (bottom curve). The
bottom curve is therefore the symmetric stretching component.
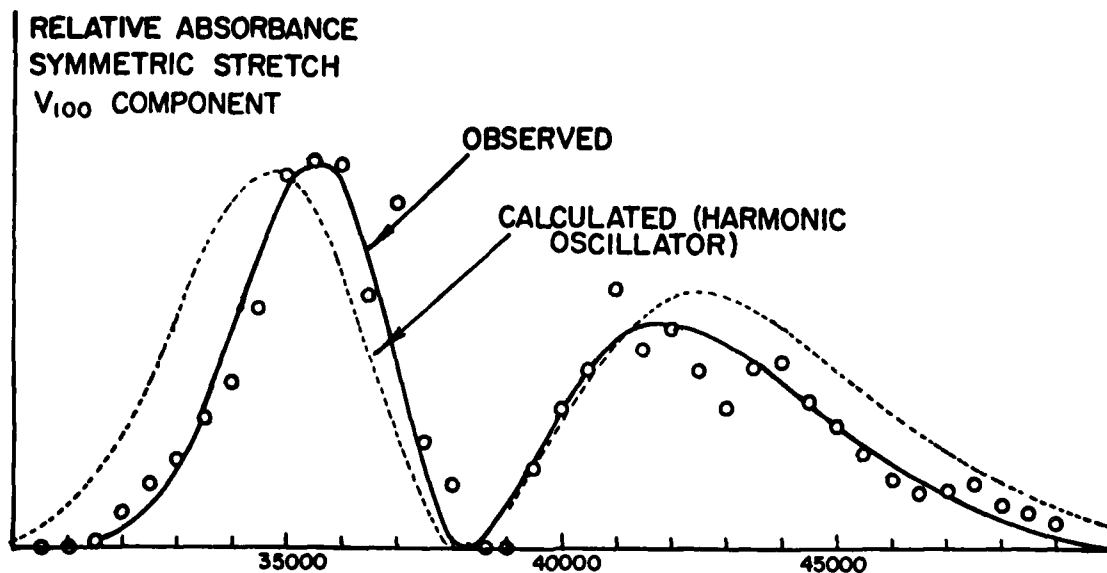
Fig. 12 Comparison between the observed bending component (solid line
and experimental points) and the bending component calculated using a
harmonic oscillator wave function (dotted curve).

CHEMICAL NEUTRALIZATION OF LAND MINES

BY

T. C. Beveridge and D. C. Heberlein
US Army Mobility Equipment R&D Command
Fort Belvoir, VA 22060

and

A. J. Tulis, J. N. Keith and W. K. Sumida
IIT Research Institute
10 West 35th Street
Chicago, Illinois   60616

INTRODUCTION

Even though chemical procedures exist for the destruction of stabilized explosives, these procedures require both long lengths of time and large quantities of reagents. These properties of the destruction processes make them poor candidates for the neutralization of armed explosive devices. The objective of this program has been to establish techniques for the rapid non-explosive neutralization of military mines using a minimum amount of reagents. The primary emphasis in the present program has been to establish an approach that leads to a rapid and safe neutralization of the main charge explosive in land mines.

Two different chemical approaches were considered for the rapid neutralization of land mines: (1) hypergolic ignition of the main charge explosive; and, (2) chemical reaction of the main charge with a solvent/amine combination. The use of hypergols for igniting explosives was reported at the Fourth International Pyrotechnics Seminar in 1974. Although hypergolic ignition leads to the rapid autocatalytic decomposition of the entire main explosive charge, the process can lead to detonation in certain circumstances. Previous work on the use of solvent/ amine combinations to neutralize explosives had been conducted primarily under adiabatic conditions.   Ignition of the main charge explosive could also be attained under adiabatic conditions for certain solvent/amine ratios.

The principle difficulty in allowing adiabatic conditions
for the neutralization of explosives in land mines is the
fact that the process, once initiated, cannot be easily controlled.
Isothermal conditions, on the other hand, are compatible
with control of the chemical process. The work presented
here was directed at establishing an isothermal process that
would lead to the rapid, complete, and safe degradation of
the main charge explosive. To this end, the present program
addressed the following four different aspects of using a
solvent/amine combination under isothermal conditions:

a. Calorimetry experiments to determine enthalpic
changes and reaction half-lives of acetonitrile-
isopropylamine and acetone-isopropylamine combinations
with trinitrotoluene.

b. Development of an unreacted core model to define
dissolution/reaction rates for cast TNT.

c. Determination of the chemical compatibility of
primary and booster type explosives with the
solvent/amine systems.

d. Investigation of dynamic delivery techniques for the
rapid penetration of soil cover, mine casing material,
and explosive fracture and erosion.

As a result of these investigations, two prototypes have been
constructed and tested that operate at nearly isothermal
conditions. A discussion of these prototypes together with
a short film depicting their use will be presented in the
final section.

CALORIMETRY EXPERIMENTS

A thorough literature search gave no thermodynamic or kinetic
data on the reactions of trinitrotoluene with amines or similar
nucleophiles. Kinetic rate constants and equilibrium constants
are available for a large number of Meisenheimer and Janovsky
complexes of trinitrobenzene and similar nitroaromatics.
These data are principally derived from spectroscopic and

relaxation measurements. The only data presently available on the secondary degradative reactions has been given by Fendler et al[1] on the Meinseheimer complexes of trinitroanisole with alkoxides.

For this investigation a series of titration and solution thermograms were obtained for various concentrations of solvent/amine with trinitrotoluene. A Tronac Model 450 Adiabatic Titration Calorimeter was used with a water bath set at 15.8°C.

Trinitrotoluene-Isopropylamine Reaction in Acetone: The reaction enthalpies measured are given in Figure 1. Surprisingly the heat of reaction is found to be essentially independent of the trinitrotoluene concentration, but directly proportional to the isopropylamine concentration. The obvious interpretation of this result is that the enthalpies represent not a reaction of trinitrotoluene with amine, but rather a reaction between the amine and acetone which may be catalyzed by trinitrotoluene or one of its complexes.

If it is assumed that the reaction parameter is proportional to the enthalpy liberated, kinetic data can be obtained from the thermograms. The reaction half-lives as calculated from the thermograms are shown in Figure 2. The best results were obtained by plotting $t_{1/2}$ versus $TNT^{-1}IPA^{-1}$. The thermochemical data imply that the exotherm in the thermogram is produced by a reaction between the amine and acetone and not between the amine and the trinitrotoluene. In this interpretation, the kinetic data suggests that the solvent/amine reaction is catalyzed by trinitrotoluene or by one of the trinitrotoluene complexes. One possibility is that the trinitrotoluene stabilizes the enamine of isopropylamine and acetone in the form of the Janovsky complex. This complex undergoes further reaction with the ketone, releasing the trinitrotoluene for further reaction.
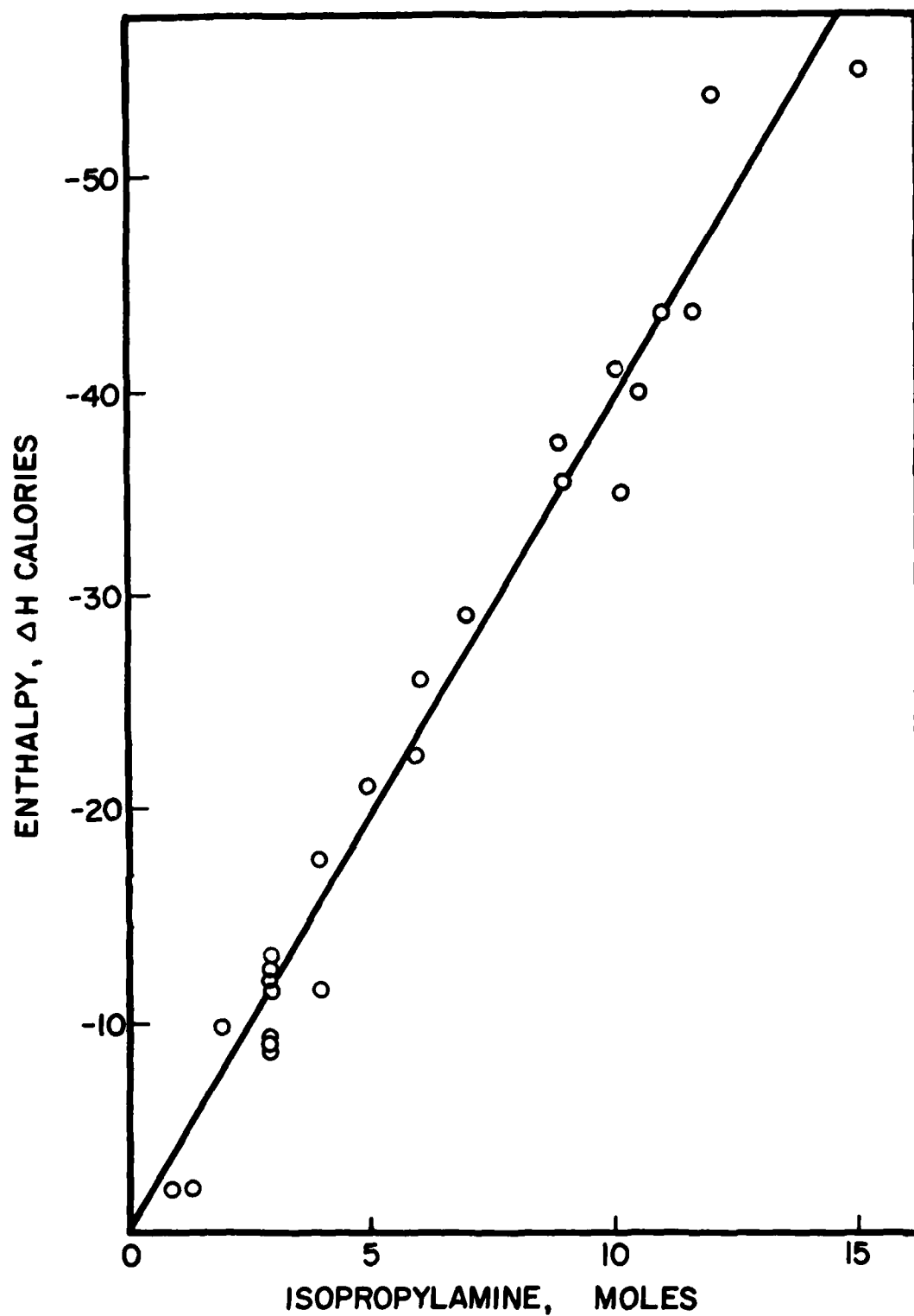
Figure 1: Trinitrotoluene-Isopropylamine Reaction Enthalpies in Acetone
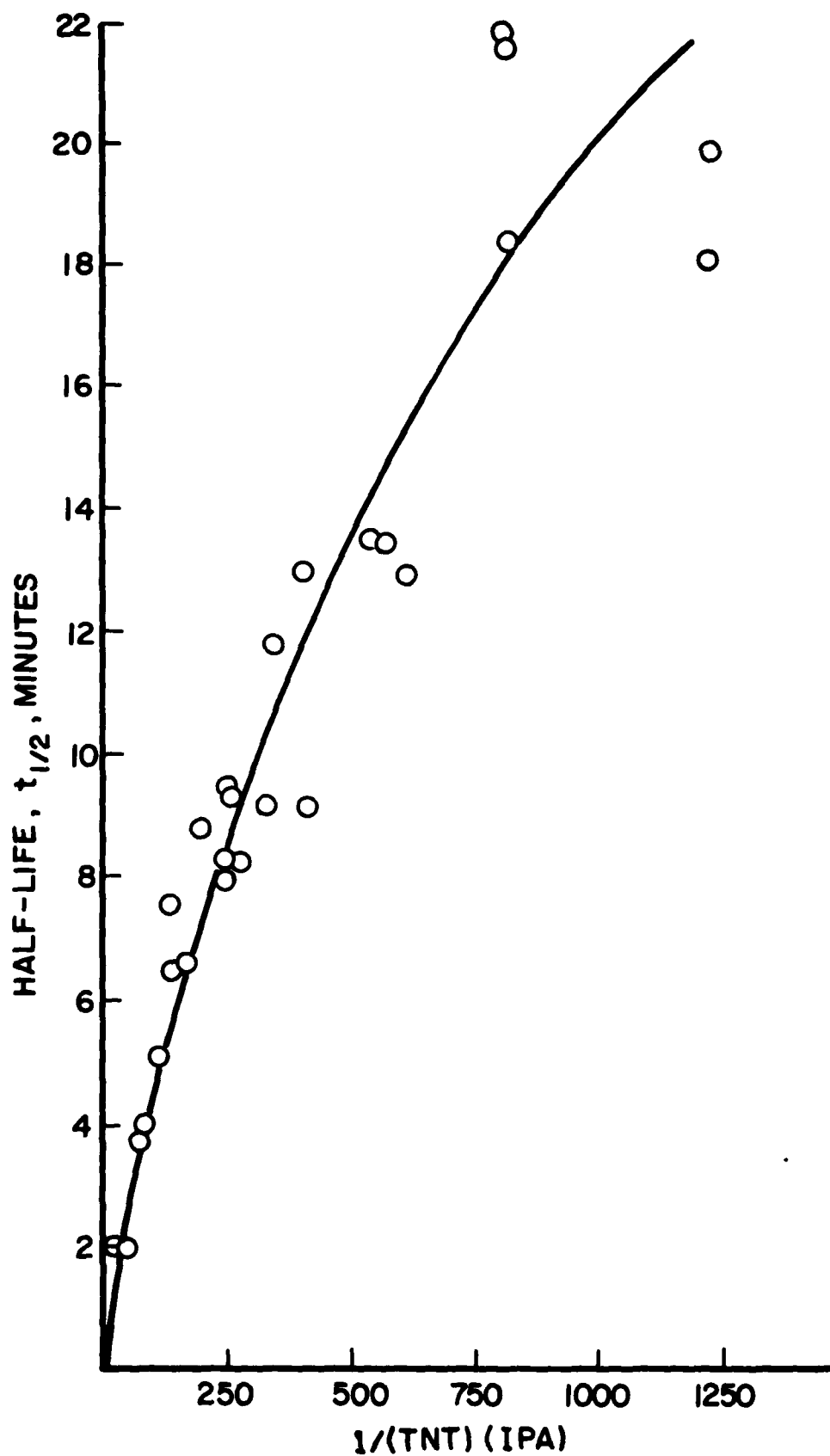
Figure 2: Half-Life of Trinitrotoluene-Isopropylamine Reaction in Acetone

Trinitrotoluene-Isopropylamine Reaction in Acetonitrile:

The results of these experiments are shown in Figure 3. The value of the first exotherm is strictly proportional to the trinitrotoluene concentration at constant amine concentration, but it is also approximately proportional to the amine concentration. The most obvious cause for such behavior is the existence of an equilibrium step. However, the variation over a 2.4 fold range of isopropylamine concentrations is too great to estimate the amine dependence accurately. The half-lives, determined in the same manner as for the acetone data, indicate that the half-life is inversely proportional to the product of the trinitrotoluene and the isopropylamine concentration. These results are shown in Figure 4.

The calorimetric data reveal a fundamental difference between the reaction of trinitrotoluene with isopropylamine in acetone and in acetonitrile. The half-lives of both reactions are inversely proportional to the product of the trinitrotoluene and isopropylamine concentrations, but the reaction in acetonitrile is several orders of magnitude slower under similar conditions. These results have important implications for the use of the two chemical systems.

Initially, it would seem that the faster rate of reaction in acetone would give a steeply increasing exothermic reaction as the solubility of the trinitrotoluene increased with rising temperatures. However, the exothermic heat in the acetone reaction is proportional only to the amine concentration, and an endothermic heat must be added to this as the trinitrotoluene dissolves. An equimolar reaction of trinitrotoluene with isopropylamine in acetone will be accompanied by an overall heat of only -0.18 kcal/mole. Initially the temperature rise is rapid because heat is produced by the amine and acetone already in solution. However, as more trinitrotoluene dissolves, much of the exothermic heat obtained from the reaction is consumed in dissolving the trinitrotoluene such that the reacting solution will begin to cool.
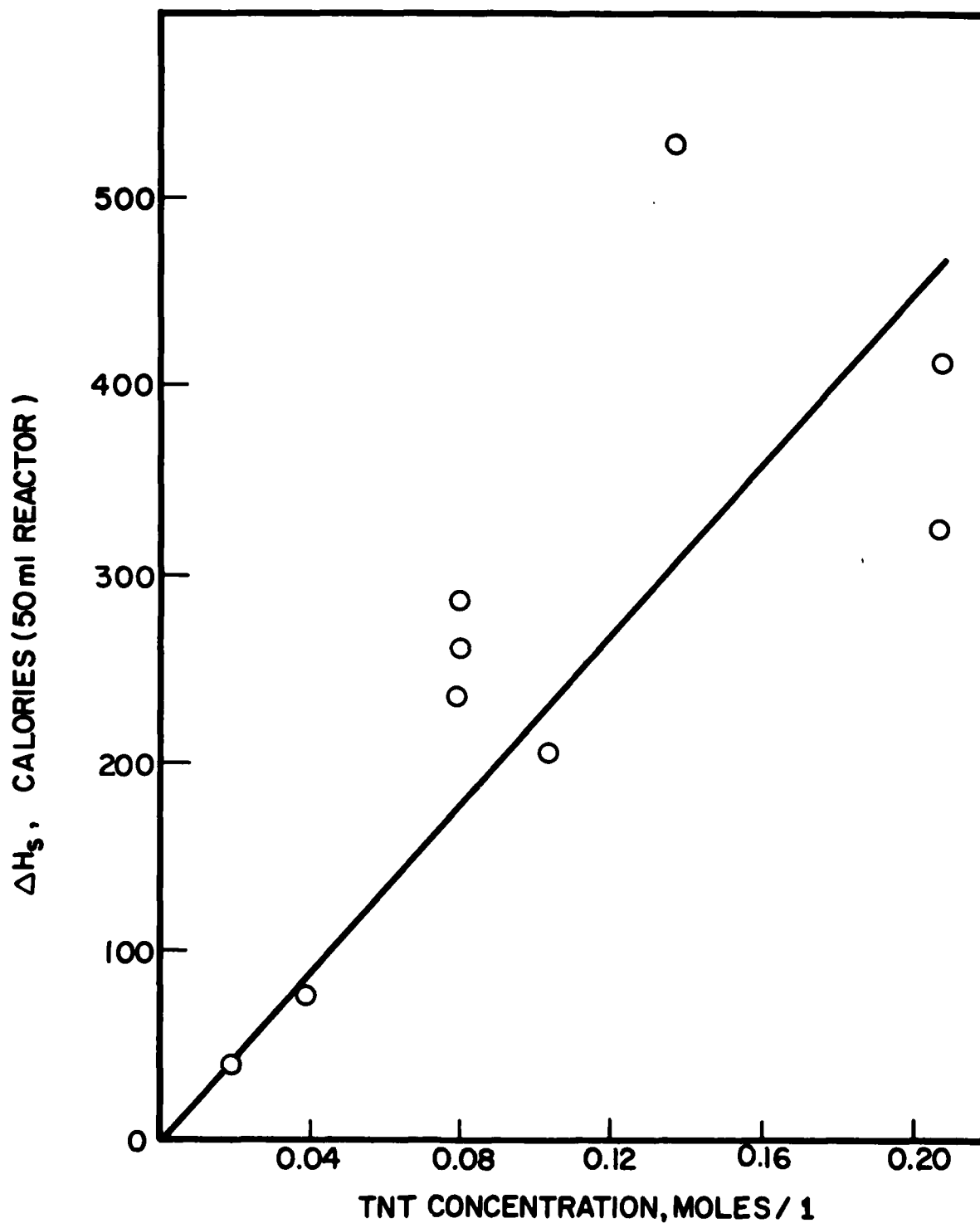
Figure 3: Second Exotherm Heat of Reaction of Trinitrotoluene in Acetonitrile-Isopropylamine
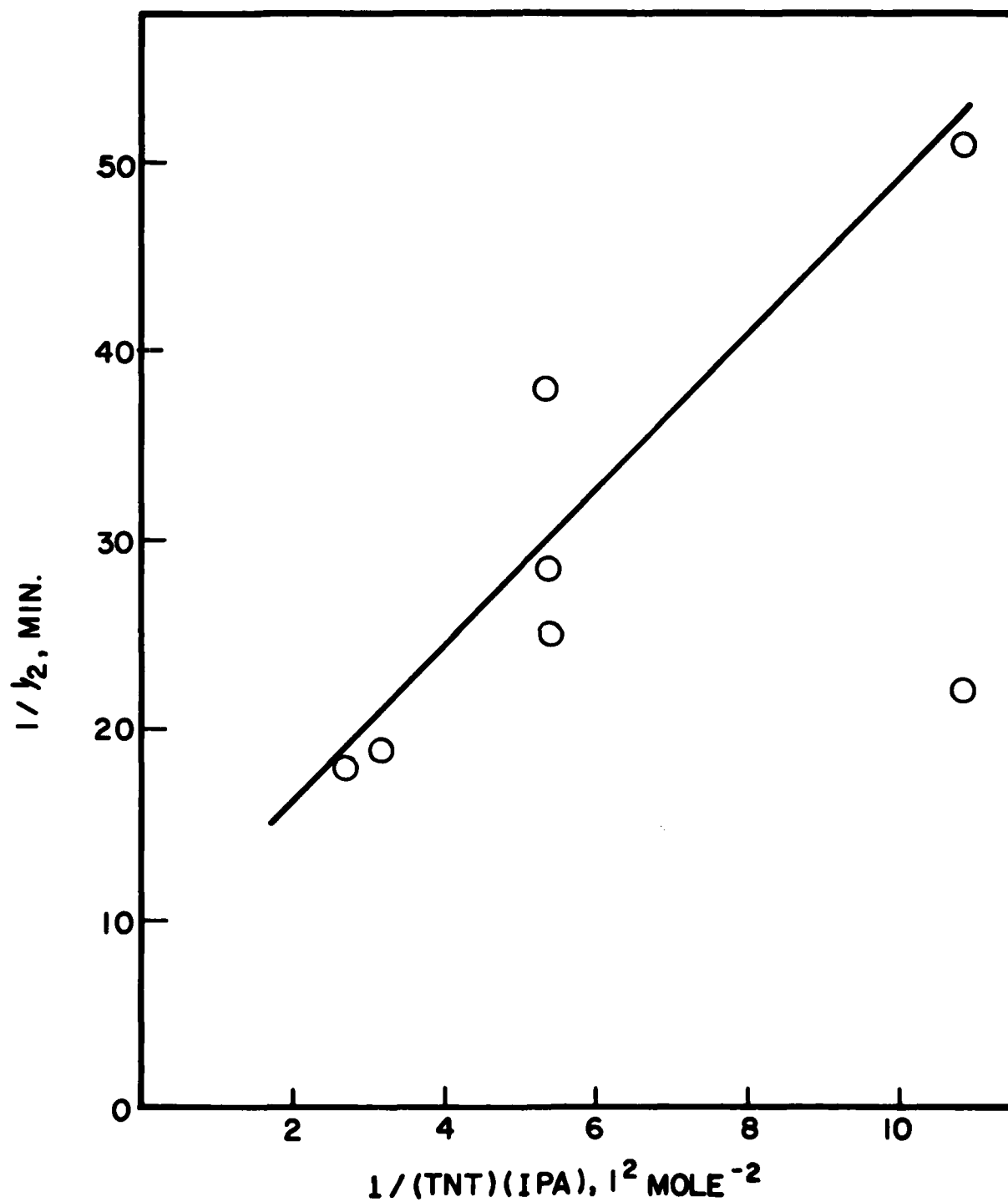
Figure 4: Kinetic Results for Calorimetric Experiments with Trinitrotoluene in Acetonitrile-Isopropylamine

Reaction of trinitrotoluene with isopropylamine in aceto-
nitrile is accompanied by an exotherm of -15 kcal/mole of
trinitrotoluene, more than enough to offset the 4.43 kcal/mole
heat of solution. This occurs within seconds of dissolution.
A slow exotherm follows, about -40 kcal/mole of trinitrotoluene
and the rate of reaction is accelerated by the dissolution
of more trinitrotoluene. The results, even at low solvent/
trinitrotoluene ratios, is a steeply rising temperature which,
if sufficient mass is present to compensate for radiant heat
loss, will eventually become high enough to boil off the solvent
and ignite the product. This result anticipates the need to
use an isothermal process for delivering the acetonitrile/
isopropylamine system to fully armed explosive devices.

THE UNREACTED EXPLOSIVE CORE

Dissolution experiments were conducted with one-inch
diameter spherical TNT castings which were prepared by casting
one-inch diameter hemispheres and then gluing the two halves
together. The experiments were conducted isothermally and
with an excessive amount of fluid. Turbulent flow with a
random flow pattern was achieved with baffles and an air-
driven mechanical stirrer. Experiments were conducted with
acetone, acetonitrile, isopropylamine, and mixtures of acetone-
isopropylamine and acetonitrile-isopropylamine. Figure 5
gives the unreacted core dissolution data-temperature
correlation for TNT spheres in pure solvents and isopropylamine.
The dissolution rate per unit area is plotted in the Arrhenius
manner, i.e., as log of dissolution rate versus the inverse
of absolute temperature. Figure 6 depicts the unreacted core
dissolution correlation of calculated and experimental data
for a 40/60 isopropylamine/acetone solution with solid TNT.
The experimental and calculated curves are shown separately.
Figure 7 shows the correlation of the calculated and experi-
mental data for a 40/60 isopropylamine/acetonitrile solution
with solid TNT. The specifics of the theoretical model have
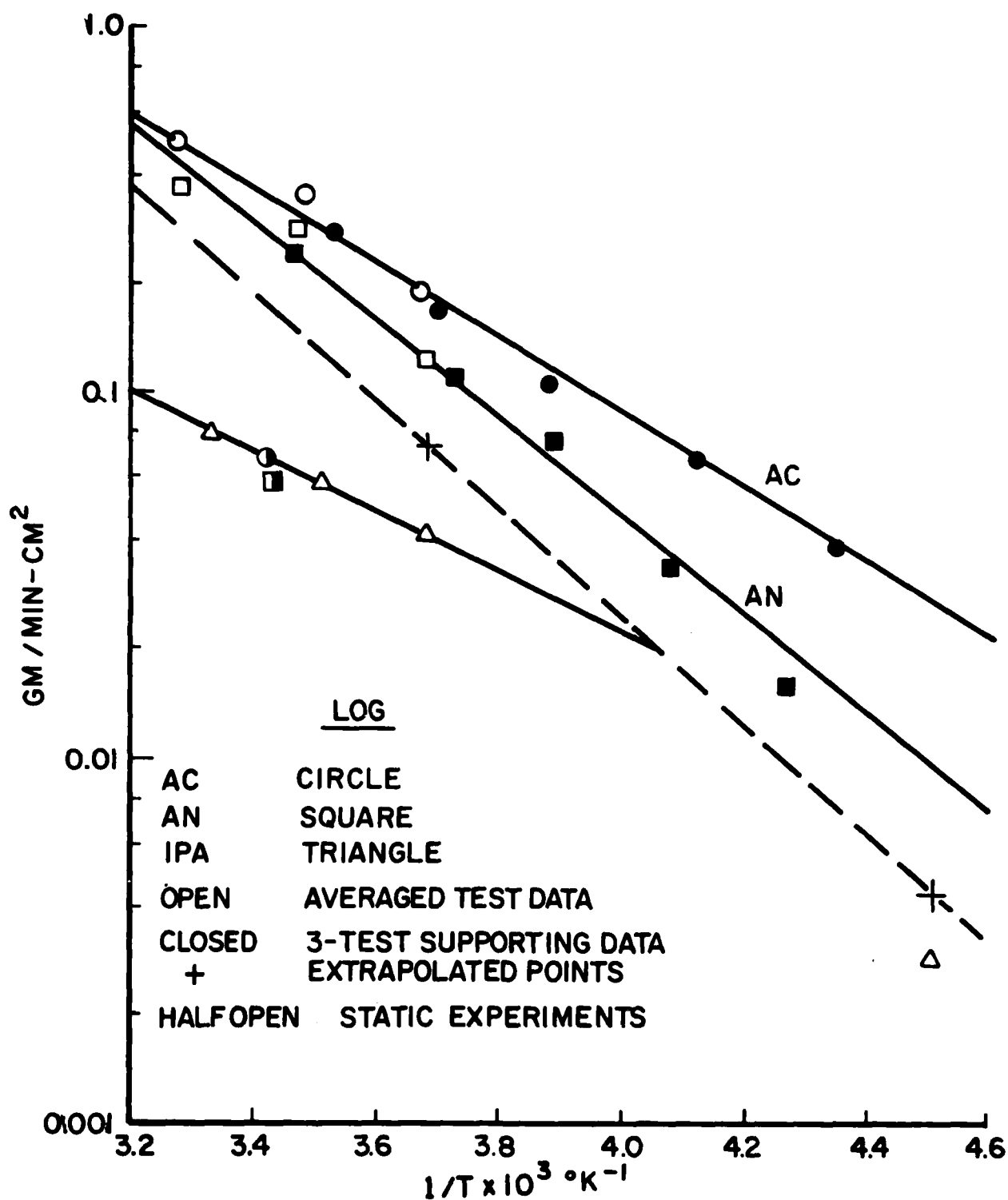
Figure 5: Unreacted-Core Dissolution Data Temperature Correlation for Trinitrotoluene in Pure Solvents and Amine
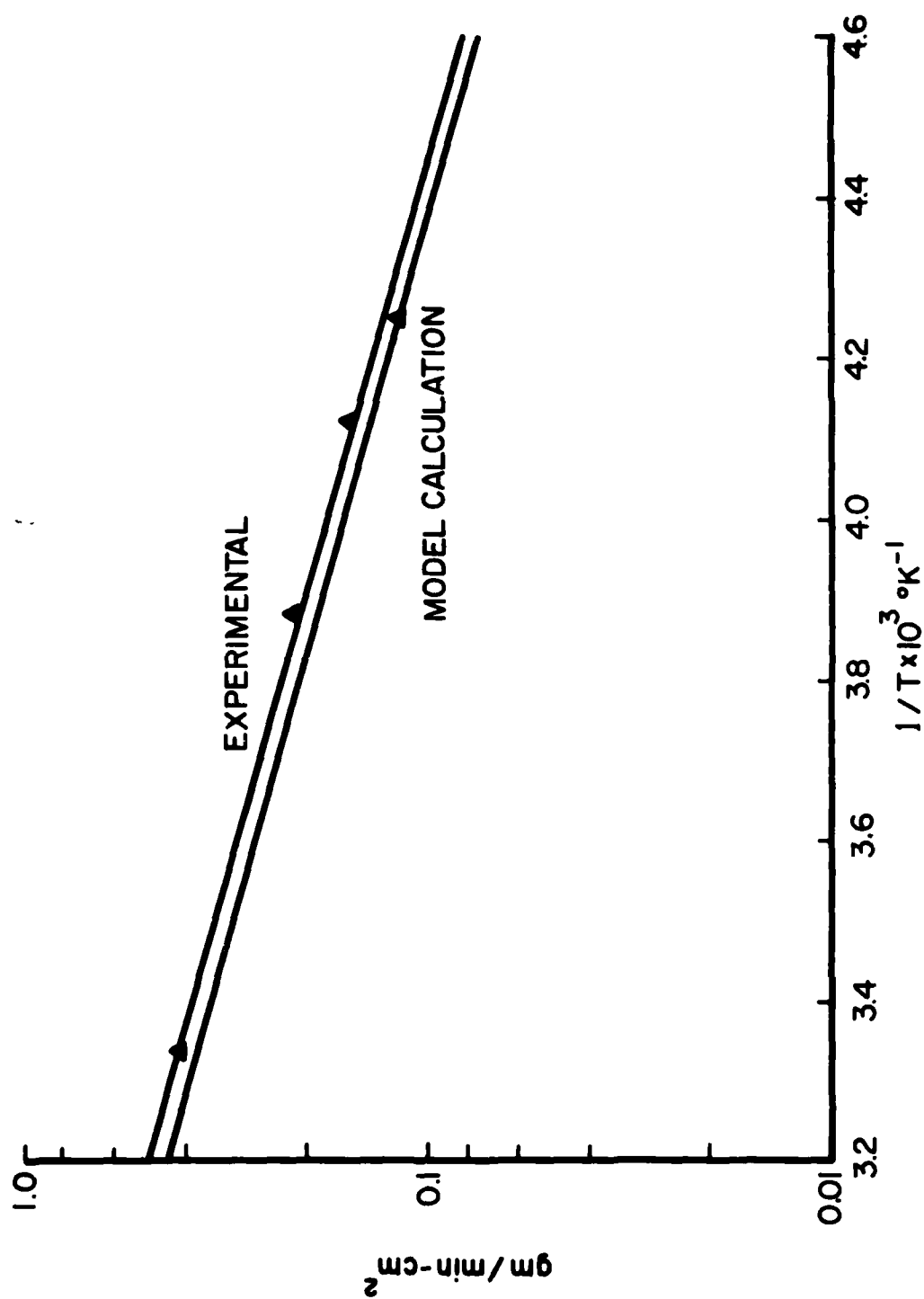
Figure 6: Unreacted-Core Dissolution Correlation of Calculated and Experimental Data for 40/60 Isopropylamine/Acetone and Solid Trinitrotoluene
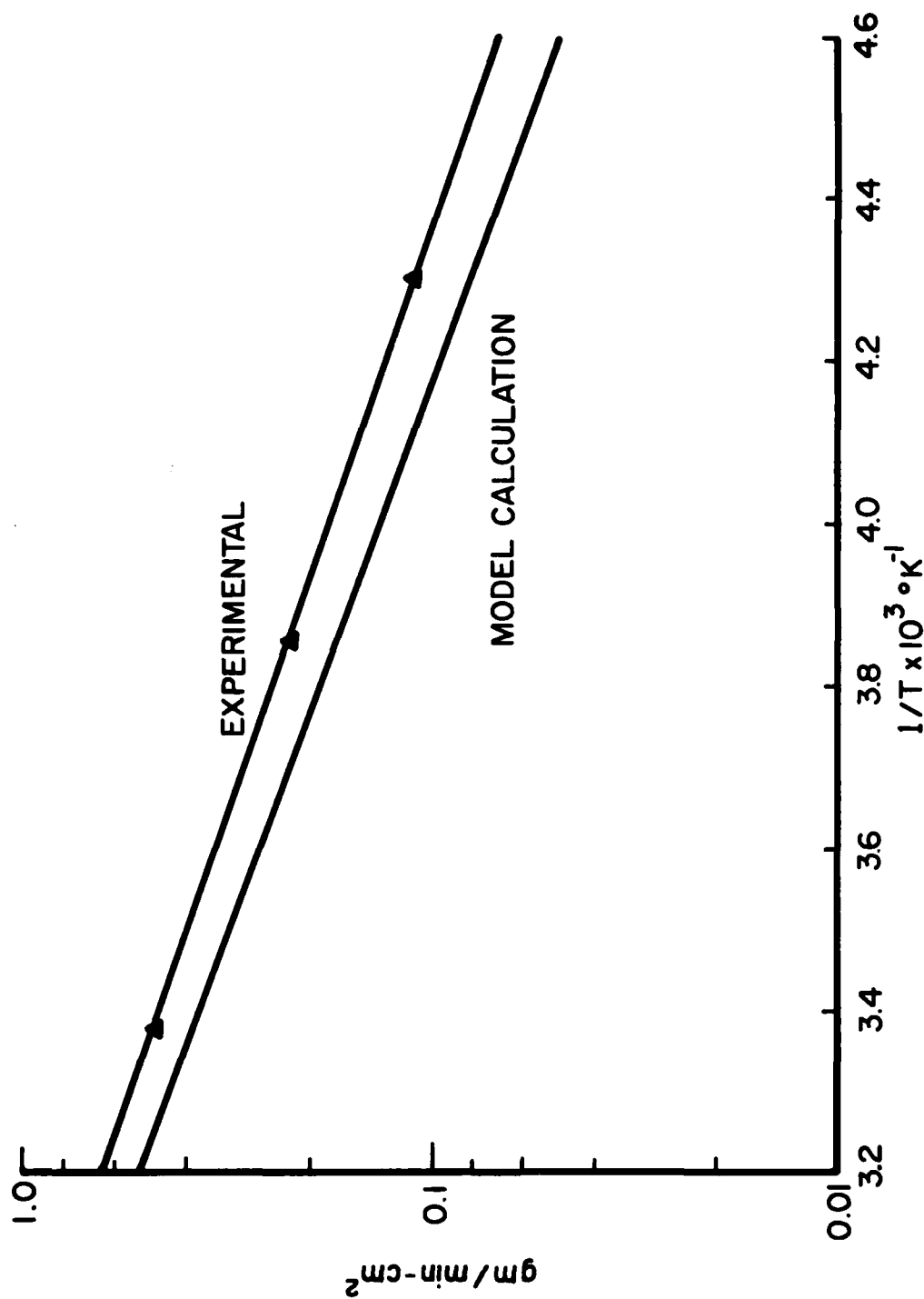
Figure 7: Unreacted-Core Dissolution Correlation of Calculated
and Experimental Data for 40/60 Isopropylamine/
Acetonitrile and Solid Trinitrotoluene

been presented elsewhere[2]. The evolution of the theoretical
model in terms of experimental data was necessary for the
stipulation of system requirements against a variety of
land mine types. The model places restrictions on minimum
neutralization times, minimal amount of reagents ,and optimal
solvent/amine ratios.

CHEMICAL COMPATIBILITY WITH BOOSTER EXPLOSIVES

Although the primary goal of the chemical neutralization
process was the destruction of the main charge explosive, the
reactivity of amines with booster type explosives such as PETN
and tetryl had to be determine. Thermograms of PETN
displayed a sharp melting endotherm at 140°C which was followed
by a decomposition exotherm which went off scale at 190°C.
Thermograms of tetryl exhibited a sharp melting endotherm at
125°C and a large decomposition exotherm near 210°C.

PETN was treated with isopropylamine in both acetone
and acetonitrile solutions at concentrations up to 40 percent.
No color change of other evidence of reaction was observed.
On evaporation of the solutions, white crystalline residues
were recovered and subjected to Differential Thermal Analysis
(DTA). All resultant thermograms were essentially the same
as those of PETN, indicating no reaction. A typical product
thermogram is compared with that of PETN in Figure 8.

Tetryl reacted immediately in a mixture of isopropylamine
and acetone. A red color evolved immediately, turning
to near black with continued reaction. No precipitation
occurred on dilution with water. A thermogram of this residue
is given in Figure 9 together with that for the unreacted
tetryl.

It is concluded that the PETN can be dissolved and dis-
persed in the solvent/amine systems, but no reaction occurs
with the isopropylamine. Tetryl is completely transformed

34

HEATING RATE: 10°C/MIN
THERMOCOUPLE: CHROMEL/ALUMEL
REFERENCE: 100mg Al_2O_3
SAMPLE: (A) 75mg Al_2O_3 +
25mg DRY
RECRYSTALLIZED
PETN

(B) 75mg Al_2O_3 +
25mg PETN-IPA
REACTION
PRODUCT
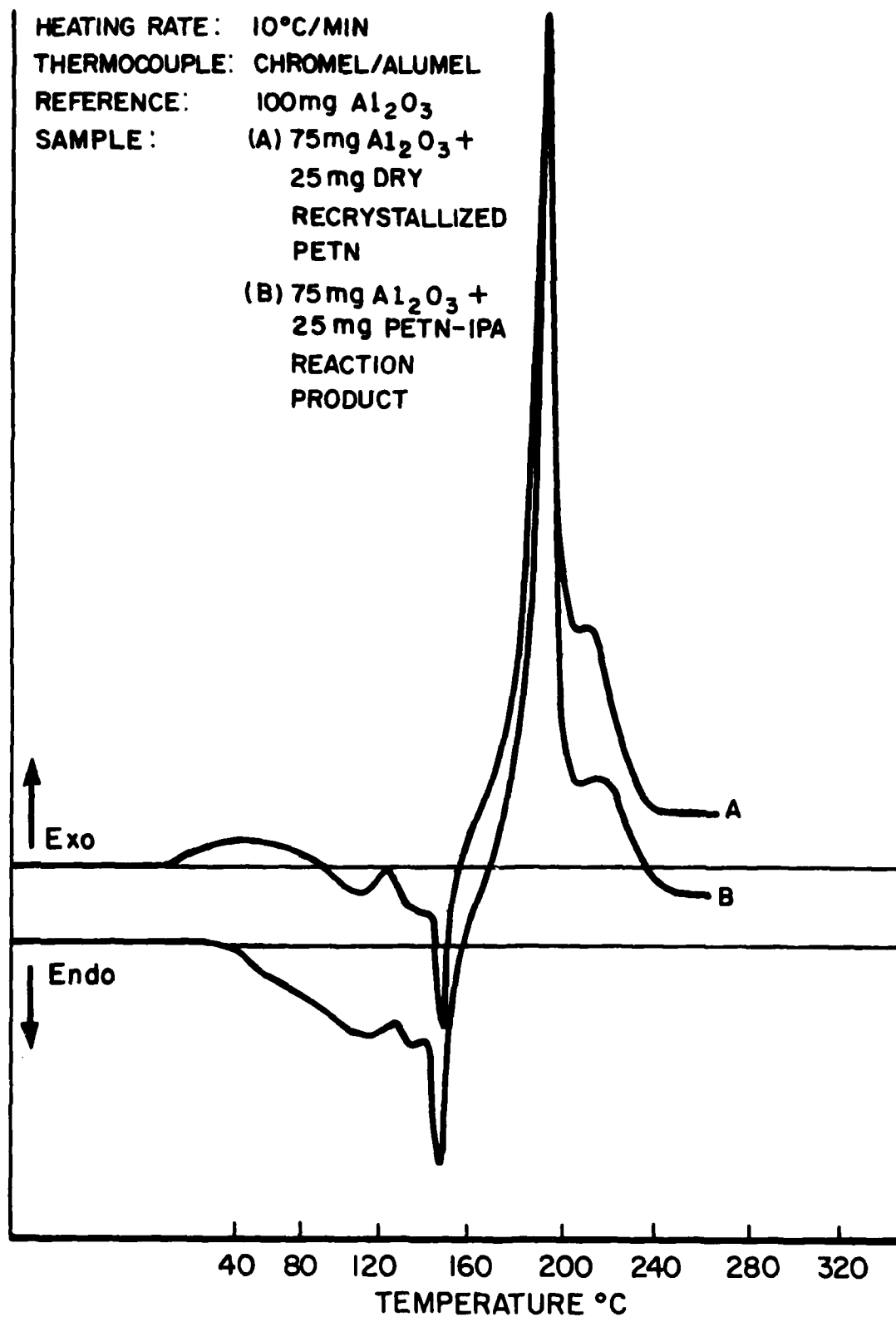
Figure 8: Comparison of DTA Thermograms of PETN-Isopropylamine Product with pure PETN

HEATING RATE: 10 °C/min

THERMOCOUPLE: CHROMEL/ALUMEL

REFERENCE: 100 mg Al_2O_3

SAMPLE (A) 50 mg Al_2O_3 +
50 mg TETRYL

(B) 30 mg Al_2O_3 +
90 mg TETRYL-
IPA REACTION
PRODUCT, ONE DAY OLD

Exo

Endo

A

B

TEMPERATURE °C
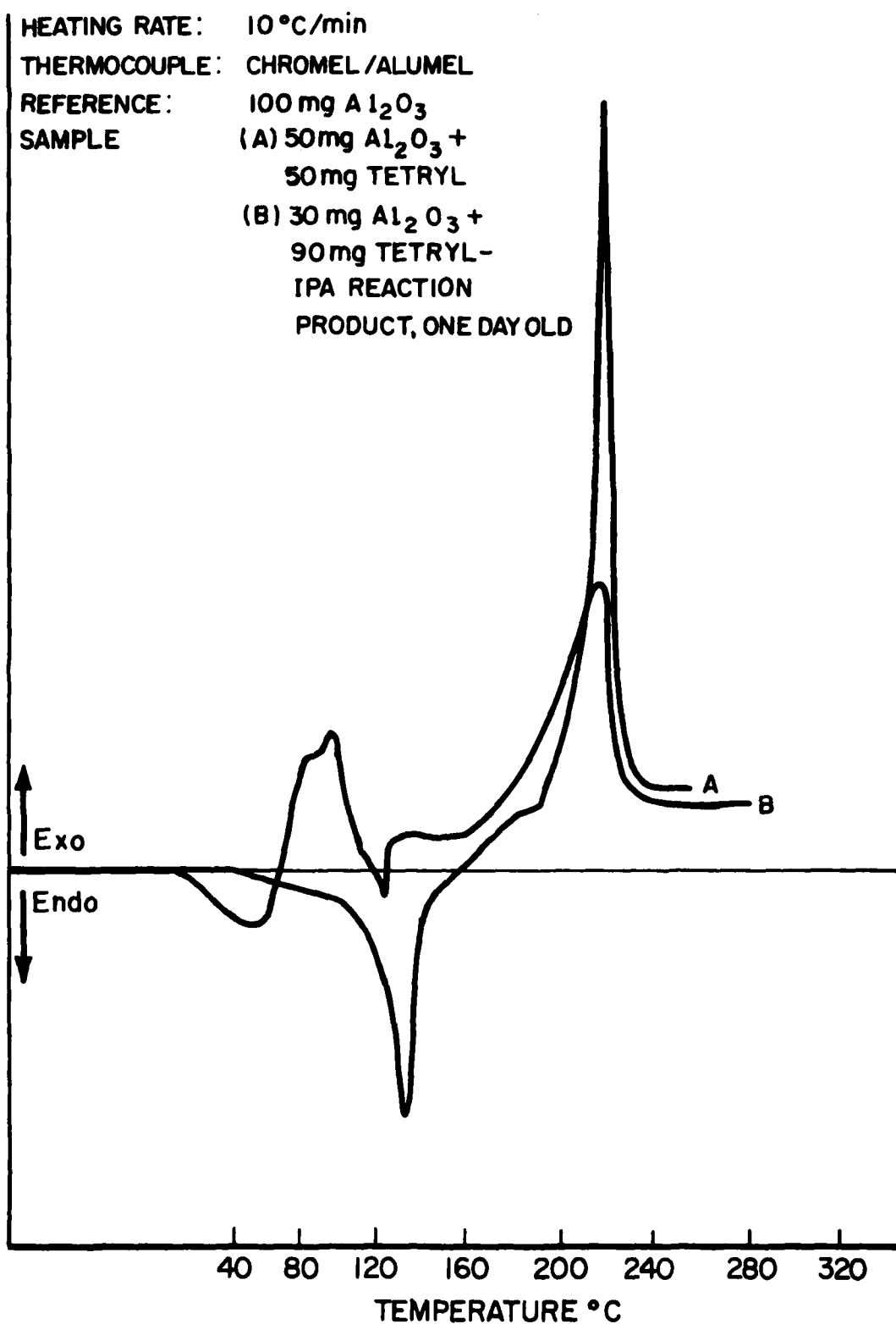
Figure 9: Comparison of DTA Thermograms of One Day Old
Tetryl-Isopropylamine Product with Pure Tetryl

in a reaction with isopropylamine in either acetone or
acetonitrile. The difference in the thermograms indicates
that the reacted tetryl has been transformed into a non-
sensitive compound.

DYNAMIC DELIVERY TECHNIQUES

Acetone-isopropylamine and acetonitrile-isopropylamine
systems have been extensively field tested against cast
trinitrotoluene in simulated armed mines. The reaction is
complete and irreversible, leading to a non-sensitive residue.
The reaction is fairly rapid, requiring approximately 1 to
2 minutes to neutralize small antipersonnel mines and from
10 to 12 minutes to react large antitank mines. To minimize
the time necessary for the neutralization of each mine or
explosive device, the chemicals are accelerated to high
speeds through a high pressure intensifier. The reagents
themselves are thereby used to perforate soil cover and mine
casings. After the high pressure penetration of the explosive
device, additional chemicals are fed at a lower pressure into
the explosive at pressures of approximately 200 psi. The
process is best understood through viewing this short film,
a narrative description of which follows.

The mine chosen for this demonstration is a simulated
Soviet antipersonnel wood mine utilizing 1/2 pound of cast
trinitrotoluene. A high pressure fluid jet, typically
generating short pressure pulses from 30,000 to 60,000 psi,
is used to penetrate the soil overburden and the mine casing.
This high pressure burst is followed by a lower pressure
delivery of the chemicals into the mine. The deep purple
color of the liquid visible in the film is a positive indica-
tion that the trinitrotoluene is being reacted. Because the
process is rapid, a much larger amount of chemicals was
used in this demonstration to allow adequate photographic
coverage of the process. The reaction is complete and leaves
no unreacted trinitrotoluene.

The second half of this film shows a backpack system
in which the chemicals are delivered to the mine via a long
standoff tube. Eventually, the pressure intensifier shown
previously will be replaced by a small propellant charge
that will accelerate the chemicals toward the mine
through the long standoff tube. In this demonstration, a
hole was cut in one end of the mine into which the far end
of the standoff tube was injected. Tiny holes drilled radially
in the far arm of the standoff tube dispersed the chemicals
into the mine at a delivery pressure of approximately
180 psi. The entire process takes less than two minutes.
The process is safe, quiet and does not lead to smoke evolution.

The two prototype systems just described operate at
very nearly isothermal conditions. The temperature of the
reacting vessel, i.e., the mine, are determined by the
temperature of the delivered chemicals. The reacted explosive
is dispersed out of the mine and any heat evolution from
continued reaction occurs outside of the mine.

FUTURE EXPERIMENTS AND APPLICATIONS

Experiments to determine methods for chemically neutralizing
RDX are presently underway. These new data together with the
data presented here for trinitrotoluene, PETN and tetryl
cover the major explosive types most likely to be found in
US and foreign land mines. Significantly, the process is
rapid for a chemical process. The process looks particularly
attractive for in situ neutralization of most types of explosive
devices with applicability ranging from the countermine
approach described here to clearance of airfields of unexpended
munitions, neutralization of explosive devices in urban
warfare without effecting collateral damage, to the increasing
problem of desensitizing clandestinely deployed explosive
devices in public buildings.

REFERENCES

1. E. G. Fendler et al, J. Organic Chemistry 35, No. 2, February 1970, pg. 287.

2. A. J. Tulis et al, Proceedings, VI Interamerican Congress on Chemical Engineering, 13 July, 1975.

IGNITION CHARACTERISTICS OF BORON/CALCIUM CHROMATE*

by

N. E. Brown, 2516
P. K. Morenus, 2516
Explosive Materials Division
Sandia Laboratories
Albuquerque, New Mexico 87115

ABSTRACT

A series of boron/calcium chromate compositions (10/90 to 25/75 weight percent) have been tested to determine the influence of composition and blending procedure on ignition sensitivity, ignition time and function time. Resistance after fire (RAF) measurements were made during the firing test and on the compacted residue after testing. A 12.5% boron/87.5% calcium chromate composition has been found to have optimum properties with respect to ignition sensitivity and high resistance after fire.

INTRODUCTION

A miniature pyrotechnic igniter[1] was developed which uses 4.5 mg of 20/80 boron-calcium chromate[2] mixture as the ignition charge and 5.0 mg of 41/59 titanium-potassium perchlorate for the output charge. This igniter has been reliable from both an ignition and a functional standpoint. The resistance-after-fire (RAF) must be greater than 1.0 ohms for 200 ms after the igniter functions. A high reliability is required to pass the RAF requirement. A RAF failure rate of about one unit in twenty is experienced with the present 20/80 compositions. This report documents studies which have been conducted at Unidynamics-Phoenix to investigate the effect of composition on ignition sensitivity, function time and RAF. Compositions which contained from 10 to 25% boron were evaluated. Resistance measurements were also made on the compacted residue in the igniter cavity to give more basic information about the influence of composition on the conductivity of the ash.

MATERIALS

The boron used in these pyrotechnic blends was a standard 90 to 92% purity amorphous powder purchased from Trona Chemicals. The average particle size was 1.0 um. The calcium chromate used was Baker and Adamson (Allied Chemical) Code 1526 powder, 95% minimum, with an average particle size of 2 um. Prior to blending, the calcium chromate was calcined at 963°K for six hours. The weight loss after calcining was 1.8% or less. Additional powder requirements are listed in Table I.

TABLE I

Boron

Water soluble boron	0.5%	Maximum
Insoluble in hydrogen peroxide	1.0%	"
Total magnesium	4-6%	
Moisture	0.5%	Maximum

Calcium Chromate

$CaCrO_3$ + $Ca(OH)_2$	4.0%	Maximum
Al_2O_3	0.8%	"
Na_2O	0.1%	"
Si	0.1%	"
S	0.5%	"
Cl	0.05%	"

BLENDING

Various procedures were used for blending the formulations due to differences in lot sizes and changes to improve homogeneity. In general, the process involves screening the individual ingredients through a U.S. Standard No. 325 sieve. Weighed quantities of the boron and calcium chromate are blended in a roll mill and then the dry ingredients are screened through a U.S. Standard No. 60 sieve from two to five times. Sufficient isopropyl alcohol (0.481/kg) was added to the mixture to form a thick paste and the mix was allowed to air dry with intermittent stirring for two hours and four more hours without stirring. The damp blend was subdivided into 50 gram sublots and dried in a vacuum oven at room temperature for 16 hours with a vacuum of 10×10^3 Pa. The pyrotechnic was heated to $343 \pm 2°K$ for four hours at atmospheric pressure. A final screening through a U.S. Standard No. 30 sieve was used to break up the large agglomerates. This procedure does not break up all the calcium chromate agglomerates which are detected in a smear test of the final blend.

Alternate procedures using an Eppenbach Homo-Mill are being investigated. More isopropyl alcohol is used and the agglomerates are broken up by the strong whipping action of the blender. This method, however, suffers from segregation during the drying procedure. The density of the boron and calcium chromate are significantly different and segregation is possible. However, preliminary information has shown the resulting mixture to be more homogeneous based on a physical and microscopic examination and test fire data.

EXPERIMENTAL RESULTS

Figure 1 shows the design of the miniature igniter which was used as a test vehicle to evaluate the various pyrotechnic blends. The header was cleaned and polished and then bridged with annealed Tophet A wire which had a diameter of 30.5 μm and a resistance of 451 ± 4 ohms/foot. The resulting unit had a resistance tolerance of 0.900 to 1.027 ohms. The header was loaded and tested a maximum of two times. The ignition charge of boron-calcium chromate (4.5 ± 0.5 mg) was consolidated at 103 MPa. A 51 μm mica barrier with two 380 um flash holes was installed over the ignition charge. The output charge of 5.0 mg Ti/KClO$_4$ was consolidated at 103 MPa. A Kapton closure disk was installed and a thin layer of Dow Corning 3140 silastic was applied and air cured for 24 hours. The bridgewire resistance was checked and the units were x-rayed.

BORON/CALCIUM CHROMATE (4.5 mg.)
(20) (80)

TITANIUM / POTASSIUM PERCHLORATE (5mg.)
(41) (59)

TOPHET A (30.5 μm DIA.) BRIDGE (1 OHM)

MICA DISK

POLYIMIDE DISK

DC3140 SILASTIC

KOVAR PIN

METALLIZED & BRAZED (Cu/Ag)

ALUMINA

KOVAR

4.6 mm

TEFLON

KOVAR
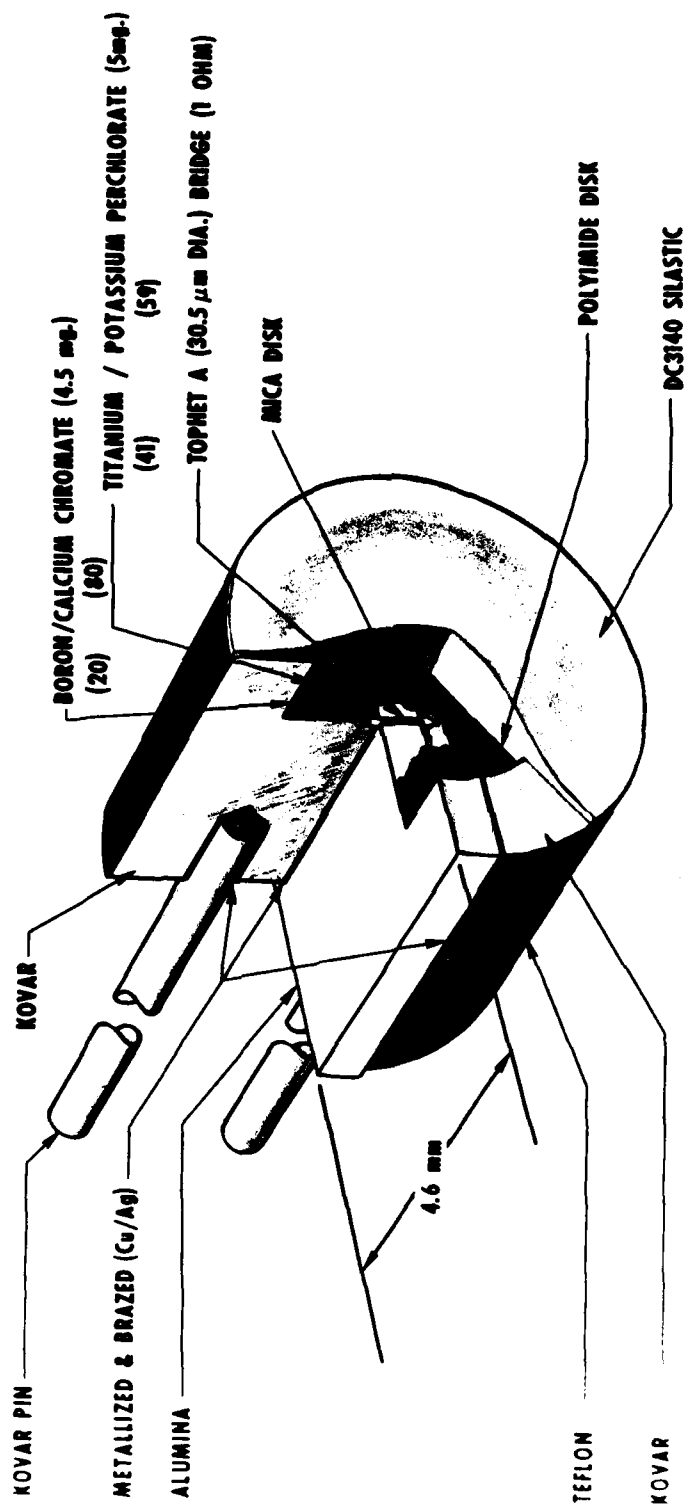
Figure 1 - Miniature Igniter

IGNITION SENSITIVITY

Four groups (20 units) of boron-calcium chromate mixes were each sub-
divided into two subgroups of ten units. Half of the units were conditioned
at 344°K and subjected to a 3.5 ampere current for 200 milliseconds from a
UN-333-E tester. Go-no go results, ignition time, function time and RAF were
determined. Ignition time was read from the current-time trace and corre-
sponded to the bridgewire burnout time. Function time was measured from
application of the fire pulse and sensed by an ion probe mounted in front of
the unit. RAF was calculated from the current and voltage traces for the
duration of the 200 ms pulse.

The second ten units of each blend were heated to 344°K and subjected
to an 8.0 mJ, 2.5 us pulse from a UN-334-E tester. Average current and volt-
age levels were 57 amperes and 57 volts, respectively. Function time and go-
no go data were the only measurements made.

Figure 2 shows the variation in function time from a 10/90 to 25/75
boron-calcium chromate. Six failures were noted in the 10/90 formulation
and were not included in the average function times.

After functional testing, each fired unit was examined microscopically
and the pin-to-pin resistance was measured using either a VOMatic 360 cir-
cuit tester or an Alinco Model 101-5B igniter circuit tester. The residue
resistance was measured before and after consolidation of 103 MPa.

TABLE II

Composition	Resistance at 200 ms	Before Consolidation	After Consolidation
10/90	8 > 1000 Ω	14 > 1.5 x 10^7 Ω	14 > 1.5 x 10^7 Ω
15/85	25, 40, 750 Ω 7 > 1000 Ω	350, 400 Ω 18 > 1000 Ω	850, 400, 330, 250 Ω 16 > 1000 Ω
20/80	10 > 1000 Ω	27, 73, 350, 280, 750 Ω 15 > 1000 Ω	1.8 to 17.4 Ω
25/75	1.8, 1.2 Ω 6 > 1000 Ω	13.8, 54, 1.0, 1.5, 8.8, 420 Ω 14 > 1000 Ω	1.4 to 9.0 Ω

These data indicate that the RAF problem with the 20-80 mixture is due
to a residue which is quite conductive. The variability is probably depend-
ent upon the position of the residue in the cavity; high RAF is observed if
the residue does not bridge the insulator between the two halfs of the
header and low RAF if the residue bridges the gap.

Another test series was conducted to gain statistical information on
12.5/87.5 and 15/85 boron-calcium chromate. Slight changes were made in the
wet mixing, drying and screening procedures for better process definition
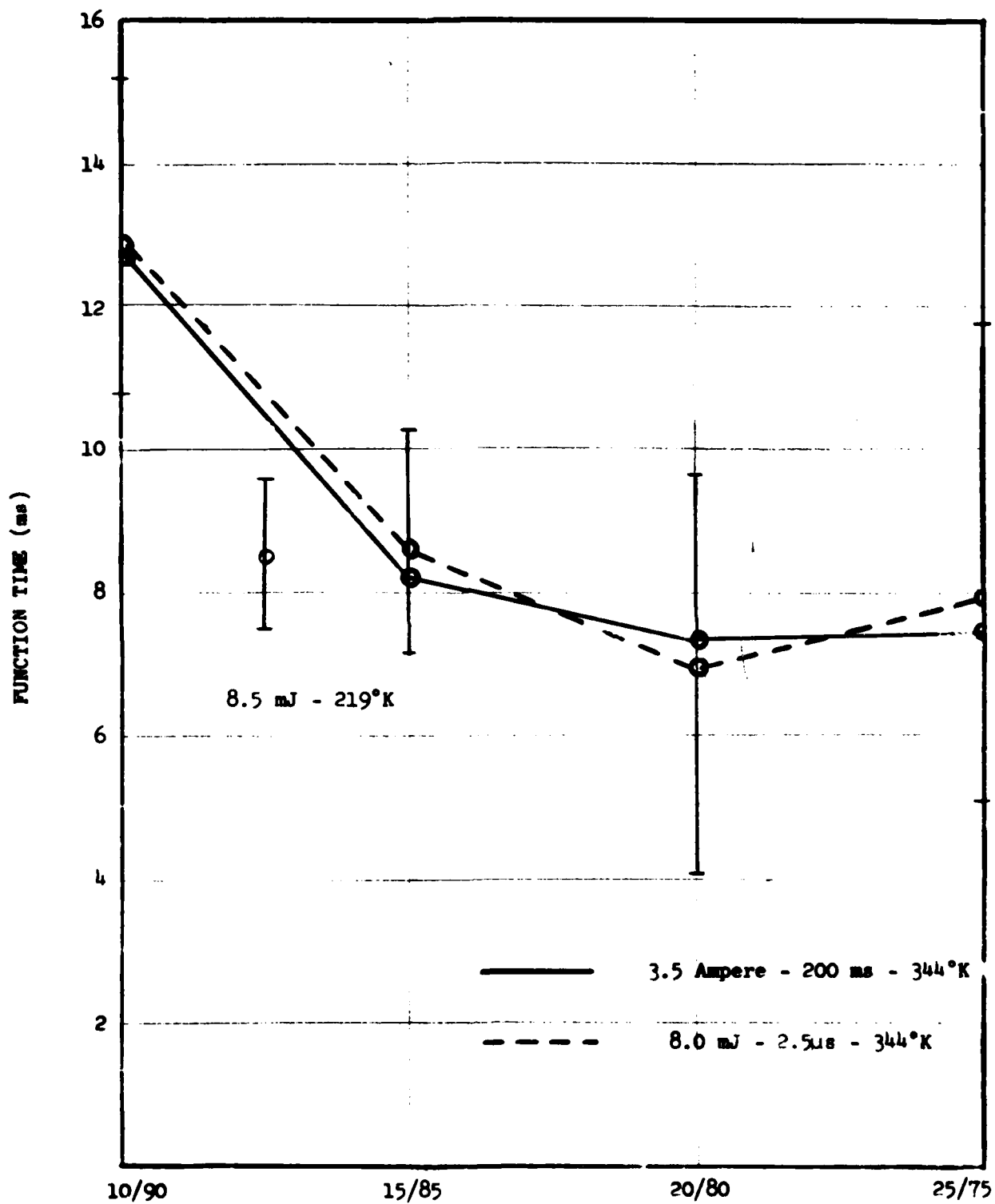
FIGURE 2 - FUNCTION TIME VS. B/CaCrO₄ COMPOSITION

and to increase the homogeneity of the blend. Bruceton testing on the Sandia UN-344 tester was conducted at room temperature with a 2.5 μs pulse. Table III is a summary of the Bruceton test data:

TABLE III

% Boron	n	$\bar{x}$ (mJ)	σ (mJ)	All Fire (mJ) .999 at 95% Confidence
12.5	34	7.84	0.39	9.81
5	30	6.79	0.70	10.9

All fire testing was conducted on the Sandia UN-334 tester at 219°K with a fire pulse of 10 mJ for 2.5 μs. Twenty-five successful tests were completed on the 12.5/87.5 composition and one failure in 25 tests was noted with 15/85 composition. This failure was consistent with the all fire level of 10.9 mJ.

RAF measurements on the units from 0 to 200 ms, on the cooled residue and on the compacted residue in the igniter header are shown in Table IV. The 12.5/87.5 formulation shows a dramatic improvement over the 20/80 boron-calcium chromate formulation.

TABLE IV

% Boron	Resistance at 200 ms	Ash	Ash Consolidated
12.5	23/24 > 300 Ω	31/31 > 1000Ω	1 @ 300 Ω 30/31 > 1000 Ω
15	20/25 > 300 Ω	31/33 > 1000Ω 3.2	9 @ 35 to 900 Ω 26/35 > 1000 Ω

The dramatic improvement of ash resistivity of the 12.5/87.5 boron-calcium chromate is to be noted. A large proportion of the units have resistance over 1 x 10^8 ohms. However, the variable nature of RAF is demonstrated by the one unit which had a compacted resistance of only 300 ohms. This particular unit exhibited a relatively low RAF in dynamic testing and a high RAF (> 10^8 ohms) before compaction.

Photomicrographs were taken of the fired units. The main difference was a change in the slag color from blackish-green for the 10/90 to a blackish-brown residue at 20/80 boron-calcium chromate. A limited program was conducted to look for chromium metal and none was found. Further work is needed to characterize the chemical species which are present in the residue.

The photographs show that the slag-like residue fills the cavity after firing and is in contact with the walls of the igniter. Thus, substantial improvements in RAF could be made by coating the inside of the charge cavity with an insulator, changing the header design or by decreasing the conductivity of the ash. The latter approach was investigated due to the

relative ease of preparing and testing new formulations. The 12.5/87.5 and 15/85 boron-calcium chromate were selected for further evaluation.

The final test series involved testing 350 igniters with a 12.5/87.5 boron-calcium chromate pyrotechnic formulation. A standard 40 shot Bruceton test was performed at 219°K using the UN-334-E pulse generator. Units were tested at six current levels with the 2.5 us pulse to give variable energy. Voltage and current were recorded to allow calculation of the energy levels. The mean ignition energy was 7.63 mJ with a standard deviation of 0.47 mJ. The all fire energy for 0.999 reliability at 97.5% confidence is 9.935 mJ.

An additional 103 igniters were used to conduct a dual high level current attribute test to verify the validity of the previous data. The first 59 units were tested at 8.5 mJ with the standard fire pulse. One failure was recorded and the remaining 44 units were tested at 9.5 mJ with no failures to function.

The results of this series were combined with the Bruceton data, statistically grouped, averaged and analyzed in a computer program. The mean firing energy was 7.587 mJ with a standard deviation of 0.569 mJ. An all fire energy (.999 response at 97.5% confidence level) is calculated to be 9.774 mJ which is in good agreement with 9.935 mJ determined in the Bruceton test.

RAF was measured on 100 units which were tested at 344°K. Sixty of the units exhibited high RAF, reaching resistance levels in excess of 10^4 ohms within 200 ms. The resistance of 12 units were below 500 ohms after this time period which is acceptable. However, four units were less than 25 ohms including one unit with an indicated resistance of essentially 0 ohms.

DISCUSSION AND CONCLUSIONS

The data in Table V summarize the most important Bruceton ignition sensitivity data.

TABLE V

% Boron	n	$\bar{x}$ (mJ)	σ (mJ)	All Fire (mJ) .999 at 95%	Comments
20	40	4.97	0.79	9.05	
12.5	30	7.84	0.39	9.81	
15	30	6.79	0.70	10.9	1/90 failed
12.5	40	7.63	0.47	9.93	.999 at 97.5%
12.5	139	7.59	0.57	9.77	1/59 failed 8.5 mJ 0/44 failed 9.5 mJ

These data show the decrease in sensitivity as the boron content is decreased from 20 to 12.5%. The decrease in standard deviation due to improved blending procedures allows the 10 mJ all fire requirement to be fulfilled in spite of decreased sensitivity. Attribute testing of the igniters close to the all-fire level indicates that ignition sensitivity is approximated by a normal distribution.

The ash resistance in Table II is seen to be extremely variable based on RAF, cold resistance and resistance after compaction at 103 MPa. With a large electrode surface such as present in the miniature igniter, a high resistance residue is probably necessary to assure a high RAF. However, it is evident that RAF is very complex and is certainly dependent on the insulator disk and the titanium-potassium perchlorate output charge. High boron compositions such as the 25/75 mixture are relatively conductive and may allow development of a component with low RAF if such a characteristic is desired.

FUTURE STUDIES

New sources of calcium chromate will be evaluated to establish a qualified powder to replace the Allied calcium chromate which is not available. All insoluble hexavalent chromium compounds have been declared a carcinogen by the National Institute of Occupational Safety and Health (NIOSH). The evaluation studies will determine the effect of calcining on parameters such as particle size, surface area and ignition sensitivity.

The time and temperature at which the $CaCrO_4$ is calcined affects the performance of the pyrotechnic. Studies would evaluate the effects that the calcining parameters have on particle size, surface area and ignition sensitivity.

Improved methods of blending boron and calcium chromate will be evaluated. The present blending liquid, isopropyl alcohol, may be undesirable because it can react with $CaCrO_4$. A non-reactive liquid may be more desirable. The Homo mill was a great improvement over earlier roll mill blending, yet it may not be the final answer to a homogeneous blend.

REFERENCES

1. Craig, J. R. and Villa, F. J., "Miniature Igniter," U.S. Patent 3,906,858, September 23, 1975.

2. Ellern, H., *Military and Civilian Pyrotechnics*, Chemical Publishing Co., Inc. (1968), pp. 282-284.

ACKNOWLEDGMENTS

PYROTECHNIC CHARACTERISTICS AND ANALYSIS OF
REACTION PRODUCTS FOR THE TiH_x-$KClO_4$ SYSTEM

C. H. H. Chong, J. W. Reed, J. E. Glaub,
and R. L. Yauger, Mound Laboratory*

ABSTRACT

Pyrotechnic mixtures consisting of TiH_x-$KClO_4$ in various ratios
were fired in a system capable of measuring time-pressure-
temperature characteristics and of collecting gas generated for
mass spectrometer analysis.

Fourteen firings of various mix ratios were conducted and appro-
priate data were collected. Presence of moisture, solid compound
formation, and variation of gas composition of the various mixed
ratios were observed.

Analyses of gaseous products by mass spectrometry and of solids
by x-ray diffraction, along with transient temperature and pressure
measurements, were conducted in conjunction with theoretical
thermodynamic equilibrium computations to study the pyrotechnic
reaction.

INTRODUCTION

Pyrotechnic investigations, generally, are concerned with such
critical attributes as: 1) determining the ignitability of various
compositions from bridgewire systems utilizing numerous ignition
modes, or 2) measuring the degree of safety in terms of their
static sensitivity to such standard tests as impact, friction,
or electrostatic spark conditions. Other pertinent data relative
to any particular pyrotechnic system of interest being considered
would naturally include its thermal stability, the various fuel
to oxidant ratios and their respective calorific output, and other
related pieces of information.

Until recently, very little investigation has been done in the
pyrotechnic area regarding the characteristics and analysis of
reaction products. It is the intent of this paper to present these
features for a particular pyrotechnic system, namely, TiH_x-$KClO_4$,
in a confined system. The work involved the use of various fuel-
to-oxidant ratios to study the time-temperature-pressure phenomena
that occurred after ignition, the analysis of the gaseous combustion
products obtained, and the resultant solid products formed.

The experimental work involved taking a given quantity of the
pyrotechnic charge and initiating it directly with the bridgewire.
The method of ignition was the hot-wire technique in which the
wire is heated by the instantaneous discharge of a charged capacitor.
The pyrotechnic was confined in a closed evacuated system to which
were affixed various sensing devices. After a particular pyrotechnic
mix was fired, the gaseous and solid products of the system were
analyzed.

Again, let us emphasize, it is not the purpose of this paper to present those atypical characteristics of the pyrotechnic itself since this has been done by others but rather to discuss the findings encountered when the pyrotechnic was subjected to a set of conditions in a limited (confined) geometry. Thus, one is dealing primarily with a possible application of the pyrotechnic and not merely behavioral characteristics of the material.

EXPERIMENTAL

Equipment

A stainless steel reactor-receiver system was used in the pyrotechnic firing studies (Figure 1). The after portion of the system consisted of a threaded hole for inserting a loaded bridgewire unit 0.62 in. (1.57 cm) in length with 0.562 - 18 threads. The loaded bridgewire configuration is shown in Figure 2.

The bridgewire assembly consists basically of an original cavity 0.236 in. (0.600 cm) in diameter and 0.420 in. (1.067 cm) deep. A ceramic (Al_2O_3) bridgewire unit and charge holder sleeve are inserted within this cavity and are glued together with epoxy. The pyrotechnic charge is pressed in the sleeve which contains a volume of 0.042 cm³ [0.150 in. (0.381 cm) i.d. x 0.146 in. (0.371 cm) long] using ~10 kpsi of pressure; the bridgewire is 1.7 mil nickel-chromel (Tophet-C) wire; resistance of the wire varies from 0.9525 to 1.0936 ohms. The preparation of these assemblies, i.e., insertion and gluing of the ceramic components as well as the loading of the charge mix, was performed by personnel familiar with these operations.

The upper end of the reactor-receiver was sealed with a Neoprene O-ring using a 2 in. (5.1 cm) diameter flange to insure positive

seating of the gasket and flange and compressed by tightening 6-1/4 in.-20 screws. Attached to this flange was a Nupro bellow valve part number 4BW-SW and a brass tapered male sample port. Within the body of this cylindrical system was a free volume of ~10 cm³. The exact volume was determined using P-V-T methods. This chamber consisted of a narrow opening which in turn opened into a larger chamber ending with a 10 μm, nominal stainless steel frit leading into the valve region.

The firing was monitored by a multi-point recording of time-temperature and pressure. The recorder was a Minneapolis Honeywell Model 1508 Visicorder Recording Oscillograph. The pressure transducer was a 4-313 Bell and Howell (Consolidated Electrodynamics) bridge type with a 0-750 psia (0-5.2 MPa) range. Chromel-alumel thermocouples, type ISA-K, were used. A high pressure Panametrics probe Model 2000 hydrometer, was inserted into the combustion chamber whenever the measurement of moisture level was required. The low voltage fire set which functioned by charging a capacitor (arming) then discharging (firing) the electrical charge through the loaded bridgewire, was fabricated at our laboratory (Figure 3). The set was designed to ignite very low impedance bridgewires.

Material

The pyrotechnic material used throughout this study was TiH_x-$KClO_4$. The procurement, synthesis techniques, fabrication, analysis, etc. will be described by Sandia and other Mound personnel at this session. Suffice to say, the fuel (TiH_x) and oxidizer ($KClO_4$) were combined in various weight percent ratios. The combination of TiH_x-$KClO_4$ used in our studies is listed as follows:

Experiment Number	x Value	TiH_x-$KClO_4$ (wt. % ratio)
1	1.93	33/67
2	1.53	33/67
3	0.9	33/67
4	0.69	33/67
5	0.69	33/67
6	0.66	31/69
7	0.66	31/69
8	0.69	33/67
9	0.69	33/67
10	0.66	31/69
11	0.66	31/69
12	0.66	45/55
13	0.66	45/55
14	0.19	33/67

The densities of the charge compacts were calculated to be approximately 1.90 g/cm^3. This value was obtained from the weight of charge mix used and from volume calculations, i.e., 80 mg pyrotechnic charge and calculated volume of 0.042 cm^3.

Firing Procedure

Firing experiments utilizing the TiH_x-$KClO_4$ pyrotechnic system were conducted as follows: A weight quantity of the charge, usually 80 mg, was pressed into the bridgewire housing chamber and then threaded into place. The charged reactor was then sealed, the accessory components were attached, and the entire system was evacuated to $\gtrsim$ 10 torr. These experiments were thus conducted in vacuum.

Firing of the pyrotechnic was performed behind protective shielding. The necessary connections, i.e., transducer, thermocouple, and firing leads, were made and the appropriate valve was closed just prior to firing.

Immediately following combustion, the system was checked for possible leaks, a sample of the gas generated was submitted for mass spectrometric analysis and pressure, and temperature and release rate were determined. Visual examination of the reactor chamber was made; a small quantity of the reaction product solids was examined by x-ray diffraction techniques.

RESULTS AND DISCUSSIONS

The ability to fire the pyrotechnic system, TiH_x-$KClO_4$, was demonstrated in the unique reactor-receiver chamber. Fourteen firing experiments were performed involving the following pyrotechnic systems:

No. of Experiments	Pyrotechnic System	TiH_x-$KClO_4$ (Wt % ratio)
1	$TiH_{1.93}$-$KClO_4$	33/67
1	$TiH_{1.53}$-$KClO_4$	33/67
1	$TiH_{0.90}$-$KClO_4$	33/67
4	$TiH_{0.69}$-$KClO_4$	33/67
4	$TiH_{0.66}$-$KClO_4$	39/61
2	$TiH_{0.66}$-$KClO_4$	45/55
1	$TiH_{0.19}$-$KClO_4$	33/67

All of these experiments proceeded satisfactorily. A summary of the data obtained in these experiments is shown in Table 1. Results of the mass spectrometric analysis of the gas generated from the various TiH_x/$KClO_4$ systems are tabulated in Table 2.

Moisture content was measured by employing a Panametrics probe. As indicated in Table 1, a variation in (moisture) values was obtained. There appears to be, to some degree, some correlation

between the amount of oxidant present and·the resultant amount
of moisture generated. Moisture values increase with increased
amounts of oxidant used. As one can readily discern values of
~6, 3, and 0.03% moisture were obtained for 67, 61, and 55 wt %
oxidant present, respectively (Table 1).

To more completely characterize the system, it was also possible
to know the temperature in the immediate vicinity of the reactor
chamber cavity just after firing. Provisions were made, as indicated
in the experimental description section of this paper, to obtain
this measurement in several of the firing studies. Temperatures
exceeding 1300 K were evident in this particular reactor-receiver
system. Placing the thermocouple almost flush with the cavity
wall gave, as expected, substantially lower temperature values.

The time interval from ignition to onset of an initial pressure
increase is the value reported. Also included in Table 1, where
available, is the time span from moment of actual firing of the
system to the attainment of equilibrium conditions. The heat
generated from the rapid exothermic reaction upon ignition of
the bridgewire was quickly absorbed on the (thick) reactor walls
acting much like a heat sink. This fact, temperature variations
within the reactor chamber, plus the actual transducer location
tended to give substantially lower equilibrium pressure conditions
and values.

Initial firing experiments with the pyrotechnic mix, when housed
in bridgewire assemblies, led to copious quantities of gaseous
carbon derivatives (Table 2). Experiments 4, 5, 6, and 7 indicate
this trend. The major source of this "carbon impurity" is
primarily from the glued (epoxyed) ceramic inserts (sleeves)

employed in the assembly as described in the Equipment section of this paper. Quite possibly the variable quantity of carbon derivatives noted is directly proportional to the amount of epoxy used.

Eliminating the epoxy in the assembly resulted, as expected, in a marked reduction of carbon derivatives obtained when the gaseous combustion products were analyzed (Table 2, experiments 8, 9, 10, and 12). Note also the reduced values for the amount of moisture present when analyzed by mass spectrometry. As one is aware, presence of moisture and oxygen are extremely detrimental to a mass spectrometric instrument. Additionally, moisture condensing on the walls of the receiver chamber prior to actual mass spectrometric analysis would naturally tend to yield lower values. As a consequence, only when absolutely necessary were gaseous products subjected to mass spectrometric analysis.

Samples of the material in the receiver chamber following firing were analyzed by x-ray diffraction. The results of these analyses showed: X-ray diffraction data of the fired pyrotechnic were indicative of three major phases: 1) KCl (JCPDS #4587); 2) TiO_2 (JCPDS #21-1276), rutile, and 3) TiO_2 (JCPDS #21-1272), anatase. All of the diffraction lines on the powder pattern were identified. In addition, diffraction patterns which closely matched those of Fe_2TiO_5 (JCPDS #9-182) and α Al_2O_3 (JCPDS #10-173) were also noted in some instances. Some unreacted TiH_{2-y} was also observed (Experiment 4). In the 45/55 fuel to oxidizer ratio, traces of Ti_3O_5 (JCPDS #23-606) were observed in the x-ray diffraction pattern.

The lattice parameters were refined by a full matrix least squares analysis. Both TiO_2 phases possessed the tetragonal crystal system with the following lattice parameters and space group designation.

Rutile: a = 4.593 Å $P4_2/mnm$

              c = 2.959 Å $Z = 2$

Anatase: a = 3.875 Å $I4_1/amd$

              c = 9.514 Å $Z = 4$

These data were in good agreement with the ASTM tables.

It should be stated that firing of the various pyrotechnic mixes resulted in black solid products being generated. In every experiment performed, there was no white powder residue as one would expect from the generalized and unbalanced equation:

$$TiH_x + KClO_4 \rightarrow \underset{\text{white}}{TiO_{2\,(s)}} + H_2O + O_2 + \underset{\text{white}}{KCl_{(s)}} \tag{1}$$
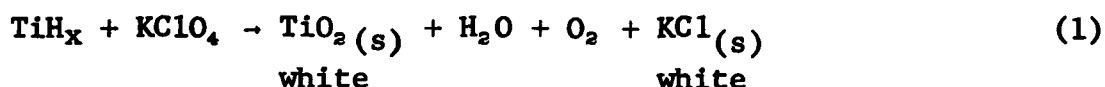
Additionally, the residue formed was an extremely fine powder adhering throughout the system in a thin layer.

Theoretical Considerations

The $TiH_{0.66} + KClO_4$ system using a fuel-to-oxidizer ratio of 39/61 and a total mix of 80 mg can be expressed in the following equation:

$$0.08\ TiH_{0.66} + 0.44\ KClO_4 \rightarrow 0.08\ TiO_2 + 0.077\ H_2O +$$

$$0.18_8\ H_2 + 0.44\ KCl \tag{2}$$
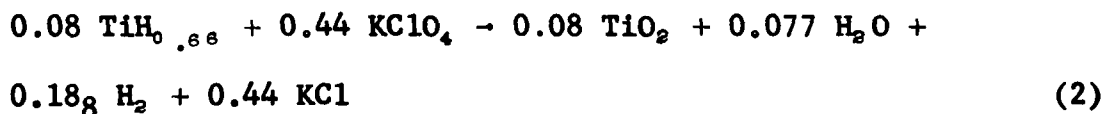
This expression indicates a value of 0.265 millimole of gaseous products is obtained. Using the ideal gas equation and solving for temperature:

$$T = \frac{PV}{nR} \tag{3}$$

where T = temperature (K)

        P = pressure (atmospheres)

        V = volume (cubic centimeters)

        n = moles of gas

and   R = gas constant

one can calculate a reaction temperature of 7800 K for Experiment #7 where $P = 16.9_8$ atm and $V = 10$ cm^3 in the experimental system.

This temperature is obviously excessive. The products of the reaction are substantially more complicated than Equation 2 indicates and it appears the number of moles of gaseous products is not correct. One means of correcting for the discrepancies in the reaction products and reaction temperature is to utilize equilibrium thermodynamics considerations suggested by Reed, Ivey, and Steinmeyer.[1] The results of their calculations were used to determine the correction factors to be applied to the number of moles of gaseous products obtained in order to yield corrected temperature values. Figures 4, 5, and 6 show the calculated changes in composition as a function of temperature for $TiH_{0.66}$-$KClO_4$ having weight ratios of 33/67, 39/61, and 45/55 respectively and for a pressure region ranging from ~0.05 to 200 atmospheres. Additional figures can be constructed for other substoichiometric titanium hydride compounds containing various fuel-to-oxidizer ratios. Suffice to say the figures denoted here can be considered representative. Only major species are depicted and KCl is omitted. At lower temperatures there is little if any change in composition with temperature. When the temperature exceeds 1500-2000 K, major changes tend to limit the reaction temperature.

Generally speaking, these theoretical considerations tend to re-
enforce our experimental data. The species reported are confirmed
in the figures particularly in the 1000-1500 K temperature region.

To obtain the corrections for the number of moles of gaseous pro-
ducts required for temperature calculations additional data from
theoretical chemical equilibrium thermodynamics are needed.[1]
Plots of average molecular weight of gaseous products as a function
of temperature are required (Figures 7, 8 and 9). These average
molecular weights in these figures include the weight of the solid
products.

Again we used the ideal gas equation,

$$nT = \frac{PV}{R} .$$ (3)

The average molecular weight is the total mass of material divided
by the number of moles of gas. The number of moles of gas, in
turn, is the weight of reactants (80 mg) divided by the average
molecular weight of gaseous products. Thus, Equation (3) can be
rewritten in the form:

$$nT = \frac{0.08\ T}{M} = \frac{PV}{R}$$

or

$$T/M = \frac{PV}{0.08R}$$

and the ratio, T/M, is a constant for each observed pressure. By
an iterative process, the temperature and molecular weight can
be adjusted to obtain a best fit for a particular pyrotechnic
system being investigated. Again, using Experiment #7 as an example,
inserting the observed pressure of 1.72 MPa, one obtains a T/M
value of 25.86. Selecting an arbitary temperature from Figure 8,

a value of the molecular weight, M, can be obtained. If the T/M
obtained is not 25.86, an adjustment is made on T and the process
is continued until a satisfactory value of T/M is obtained. In
the case of Experiment #7, the value of T is ~3400 K. This technique
was used to approximate the reaction temperatures for those cases
where data are available. The calculated temperatures listed in
Table 1 were determined by this method.

Overall, the data generated from the firings compared reasonably
well with those based on theoretical considerations in terms of
species and reaction temperatures observed. Our ignitions occurred
in the 1000 K region whereas theoretical calculations suggest
temperatures substantially higher. However, one must be aware
the equilibrium conditions in the actual firing scheme depart
radically from those in the theoretical models for reasons previously
cited. It is not misleading, therefore, to make the comparisons
indicated being aware, of course, of the particular parameters
and conditions noted.

SUMMARY AND CONCLUSIONS

Unquestionably, the ignition of a particular pyrotechnic can be
realized with the system hardware and techniques employed. In
the experiments performed, ignition occurred rapidly (milliseconds),
releasing gaseous compounds that were subsequently identified and
leaving, as a consequence of the ignition, a black solid residue
composed primarily of TiO_2 and KCl.

Although the various pieces of data generated did not compare
favorably with those obtained from other sources, the work performed
is meaningful. Certainly, one would logically expect, in the

62

system used, the kinds of data obtained to be substantially
different from say, thermal decomposition (of the pyrotechnic)
in a closed system or from a system in which firings are done
in a gas overpressure environment.

The experiments, to say the least, were unique; the objective
of determining certain aspects of the pyrotechnic was met.

ACKNOWLEDGEMENTS

REFERENCES CITED

[1] J. W. Reed, J. L. Ivey and R. H. Steinmeyer, "Thermodynamics
of Initiation of the TiH_x-$KClO_4$ Pyrotechnic Composition",
presented at Fifth International Pyrotechnics Seminar,
Vail, Colorado, July 1976.

TABLE 1

Summary Tabulation of Data on Pyrotechnic Firing Experiments

Experiment No.	Pyrotechnic Composition Fuel/Oxidant Ratio[a] (Wt. %)	Moisture Content[b] (%)	Maximum Temperature (K)		Maximum Pressure Observed (Mpa)	Time[c] (millisec)	Time[d] (millisec)	Comments
			Observed	Calculated				
2	33/67	>10.0	490**	--	1.4*	2.3	92	
4	33/67	6.8	>1350	3000	1.79	1.6	448	
5	33/67	--	--	--	--	--	--	Fired to obtain gaseous products for analysis.
6	39/61	3.4	>1200	1800	0.4*	3.0	630	
7	39/61	--	--	--	--	--	--	Fired to obtain gaseous products for analysis.
8	33/67	5.4	--	1150	0.3_6*	3.2	--	
9	33/67	--	--	--	--	--	--	Absence of epoxy glue; fired to obtain gaseous products for analysis.
10	39/61	2.8	--	3400	1.72	2.6	394	
11	39/61	--	--	--	--	--	--	Absence of epoxy glue; fired to obtain gaseous products for analysis.
12	45/55	0.03_5	625**	--	--	--	--	
13	45/55	0.03	580**	3300	1.67	1.2	588	
14	33/67	0.04_8	380**	--	1.62	0.8	150	

a_80 mg charge pressed in bridgewire at 10 Kpsi.
b As determined by in-line Panametrics probe ~10-30 sec after initiation of charge.
c Time elapsed from inception to first noticeable pressure increase.
d Time elapsed from inception of pressure increase to attainment of equilibrium.
*Pressure transducer located ~1.5 in. (3.81 cm) downstream from reactor region.
**Thermocouple inserted just inside cavity wall.

TABLE 2

Mass Spectrometric Analysis of Generated Gas

Experiment No.	Pyrotechnic Composition (Ratio)	Composition (mole %)[a]									
		H_2(2)	CH_4(16)	H_2O(18)	C_2H_2(26)	CO(28)	N_2(28)	C_2H_4(28)	O_2(32)	Ar(40)	CO_2(44)
2	33/67	--	--	0.62	--	3.61	--	92.65	--	--	3.12
4	33/67	13.22	1.07	0.73	0.25	26.41	2.79	0.24	16.35	0.06	38.88
5	33/67	6.62	0.19	0.47	0.05	9.58	1.86	0.07	35.39	0.01	45.75
6	39/61	64.39	0.84	3.53	0.30	19.88	0.59	0.21	2.77	0.04	7.45
7	39/61	61.59	0.57	0.64	--	26.64	1.00	0.41	1.96	0.03	7.16
8	33/67	0.05	0.01	5.29	--	0.43	0.49	--	89.35	--	0.08
9	33/67	3.01	0.09	1.52	--	0.68	3.82	0.02	89.52	0.01	1.32
10	39/61	13.91	0.07	0.01	--	0.43	0.93	0.01	73.91	--	10.73
12	45/55	95.44	0.09	0.03	--	1.14	0.50	0.01	0.03	0.01	2.71
14	33/67	--	--	0.51	--	5.26	--	--	80.28	--	13.96

[a]Probable error for components with abundance >1.0 mole % is 0.5%; less abundant components could have a larger error.

TRANSDUCER

PANAMETRICS PROBE

0.417" (1.06cm)

0.15" Diameter (0.38cm)

THERMOCOUPLE

REACTOR SECTION

RECEIVER SECTION

1.0" (2.54 cm)

2.0" (5.08 cm)

2.917" (7.41 cm)

(1.27 cm)

0.50"

1.41" (3.58 cm)

10 μm FRIT

NUPRO VALVE

MALE SAMPLE PORT
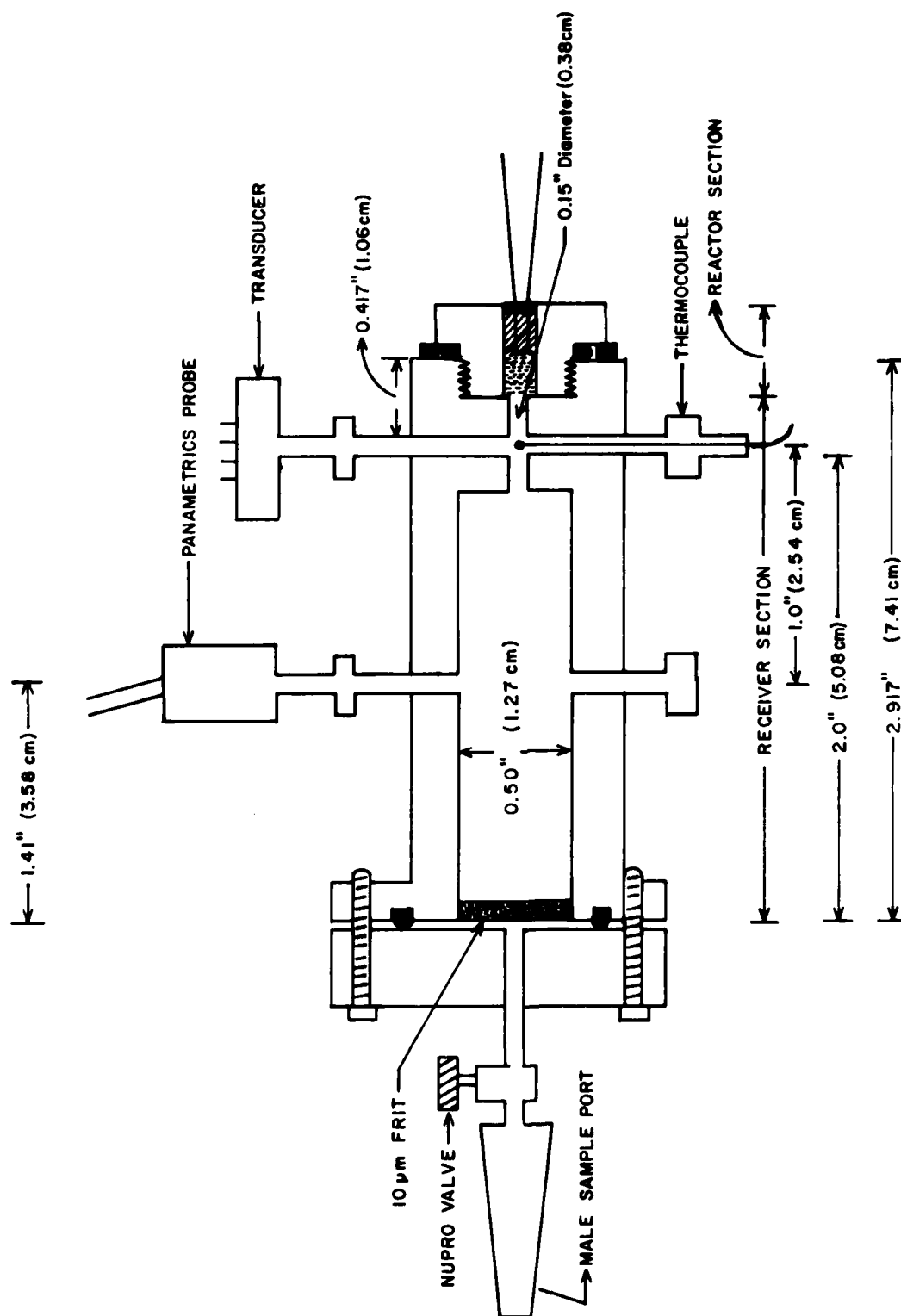
FIGURE 1

REACTOR–RECEIVER SYSTEM USED IN PYROTECHNIC FIRING EXPERIMENTS

(NOT TO SCALE)

66
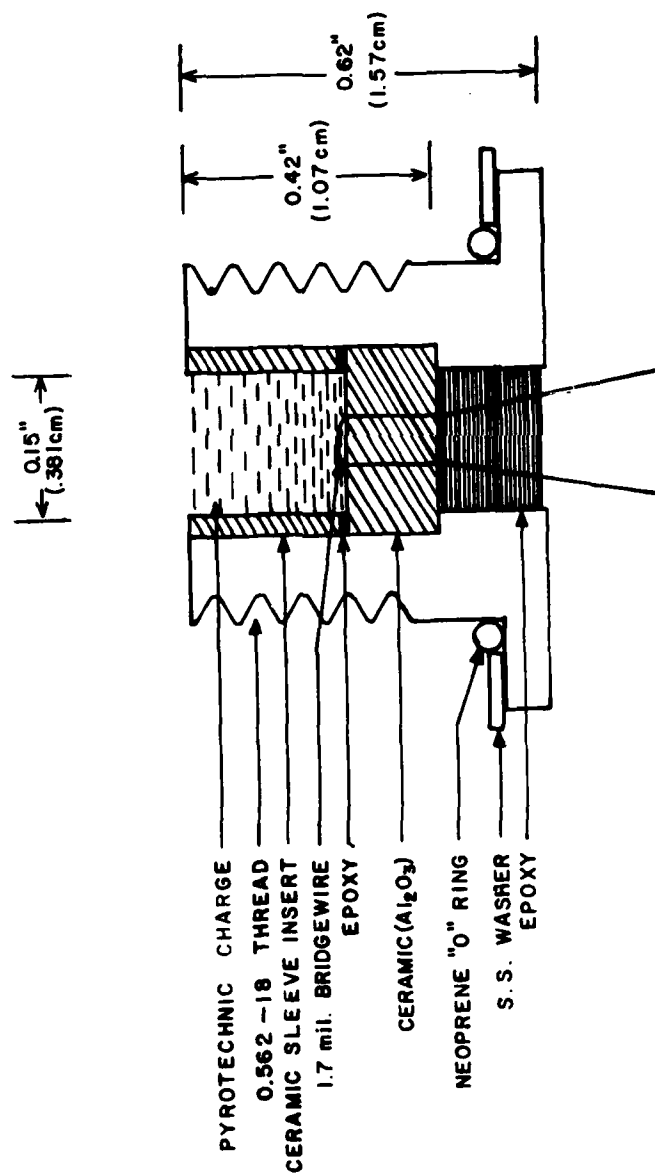
FIGURE 2

SKETCH OF BRIDGEWIRE (LOADED) ASSEMBLY HEADER

(NOT TO SCALE)
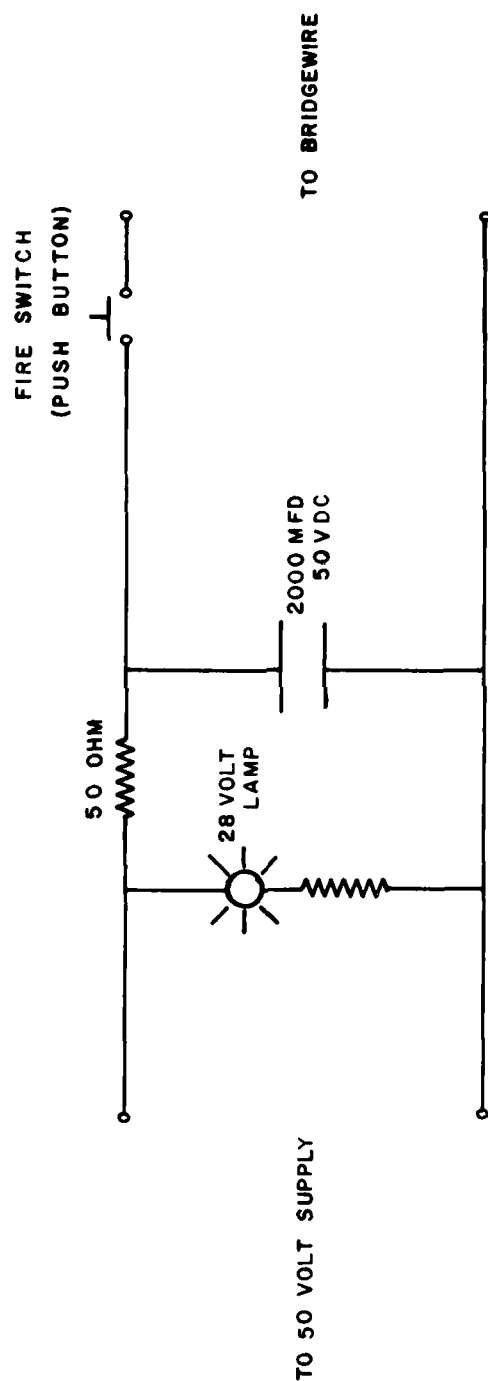
FIGURE 3

FIRING CIRCUIT

(SCHEMATIC)
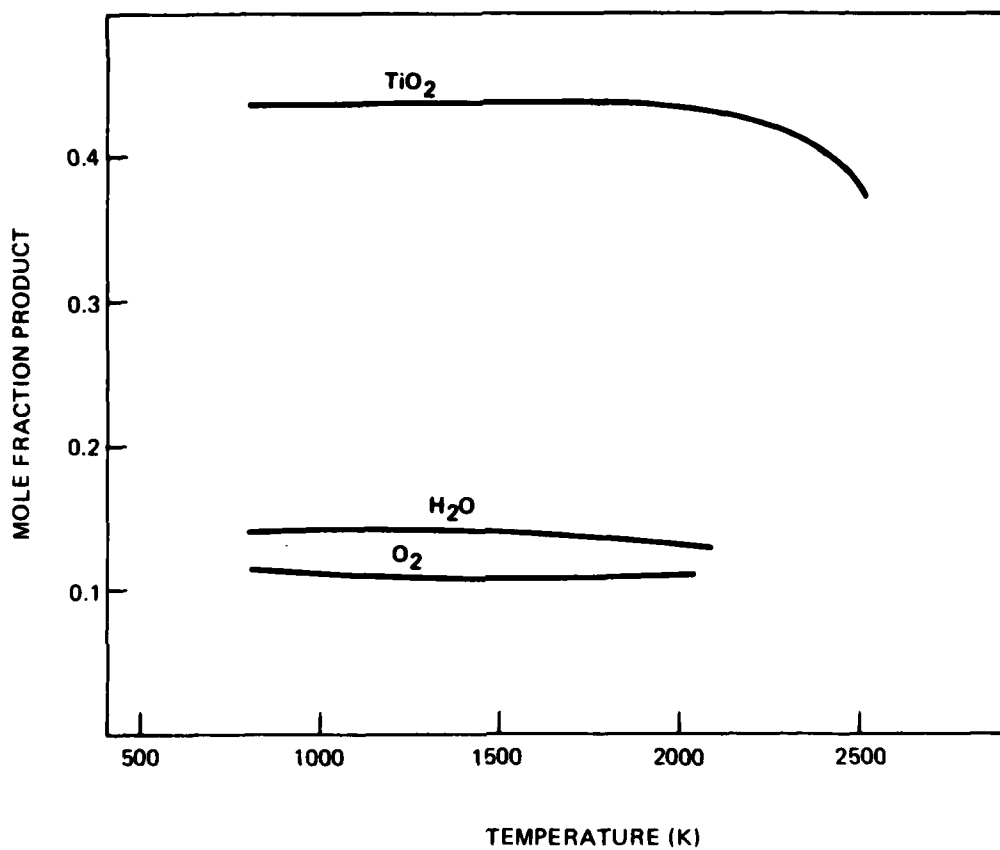
Figure 4 Reaction product composition as a function of temperature for
the system $TiH_{0.66}$ - - $KClO_4$, 33/67 weight ratio
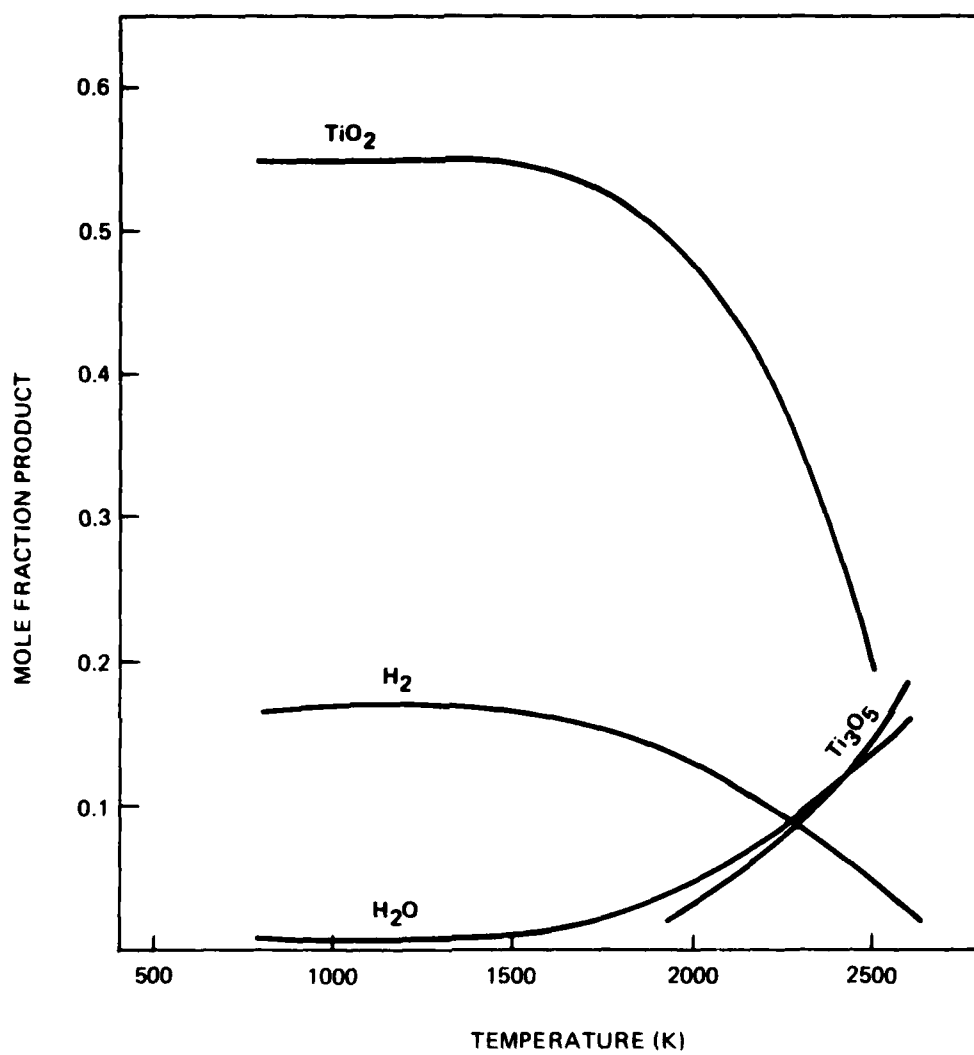
Figure 5 Reaction product composition as a function of temperature for the system $TiH_{0.66}$ - $KClO_4$, 39/61 weight ratio.
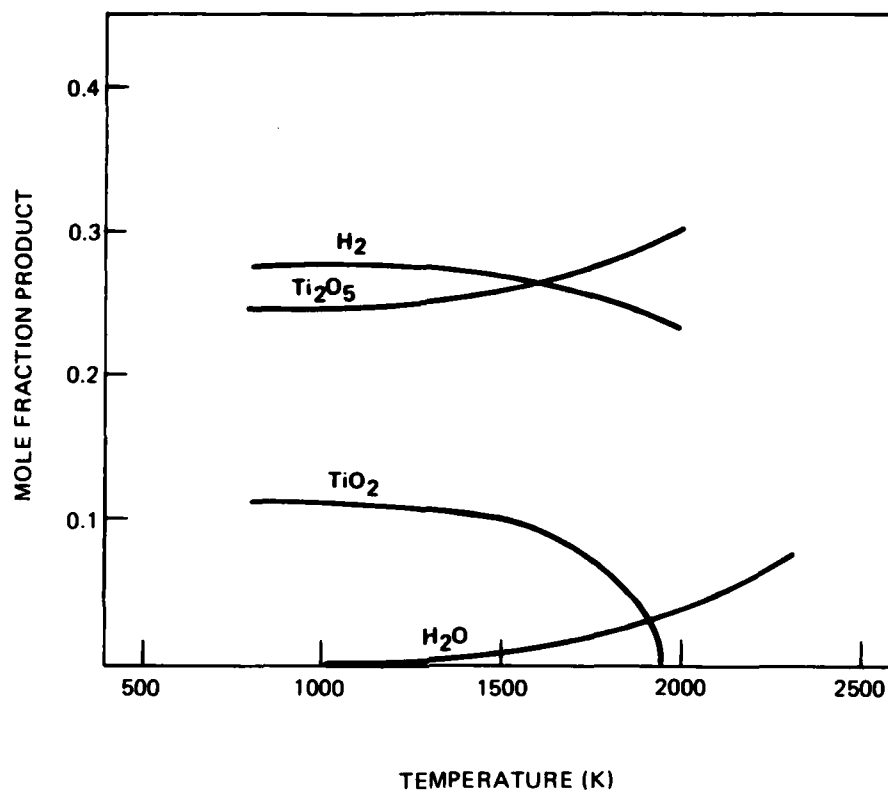
Figure 6   Reaction product composition as a function of temperature for the system $TiH_{0.66} \cdot KClO_4$, 45/55 weight ratio.
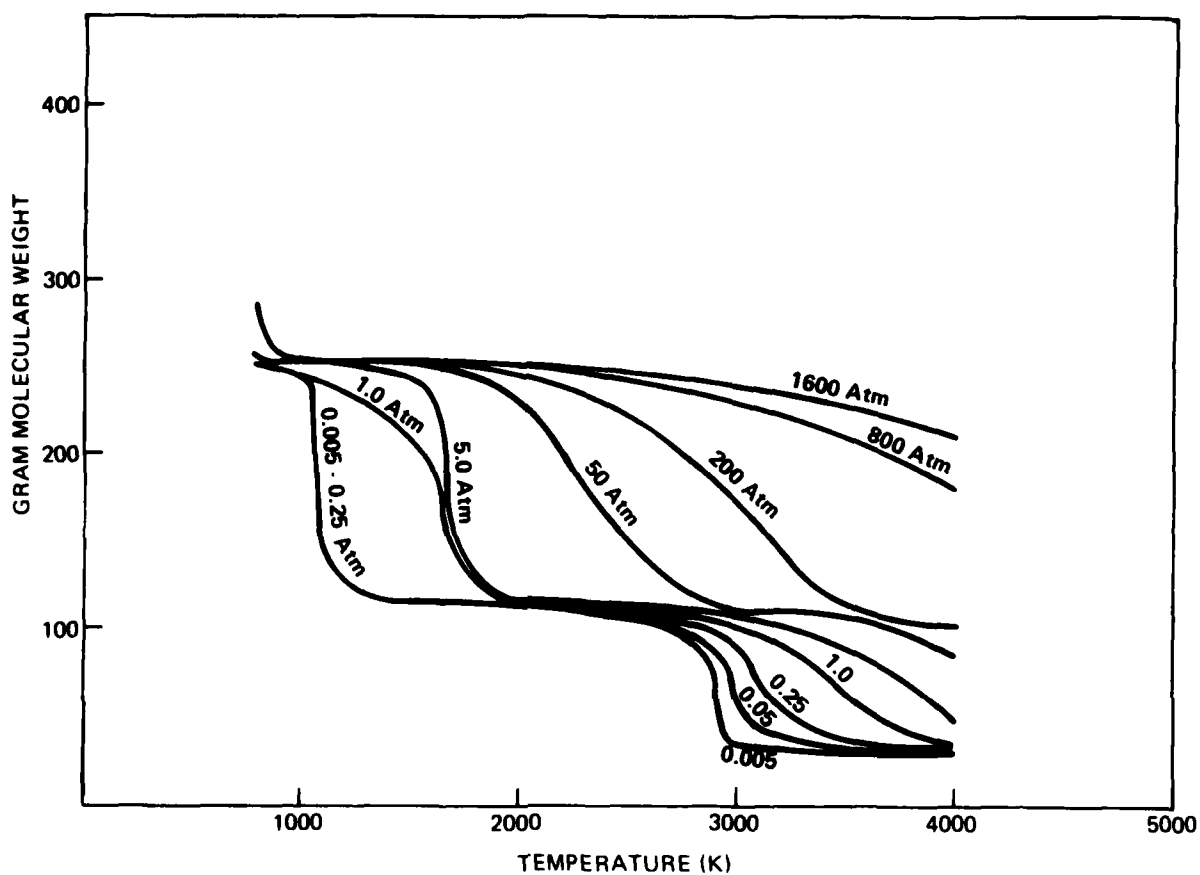
Figure 7 Molecular weight of reaction species mixture, including condensed phase components, as a function of equilibrium temperature for the system $TiH_{0.66}/KClO_4$ in a weight ratio 33/67
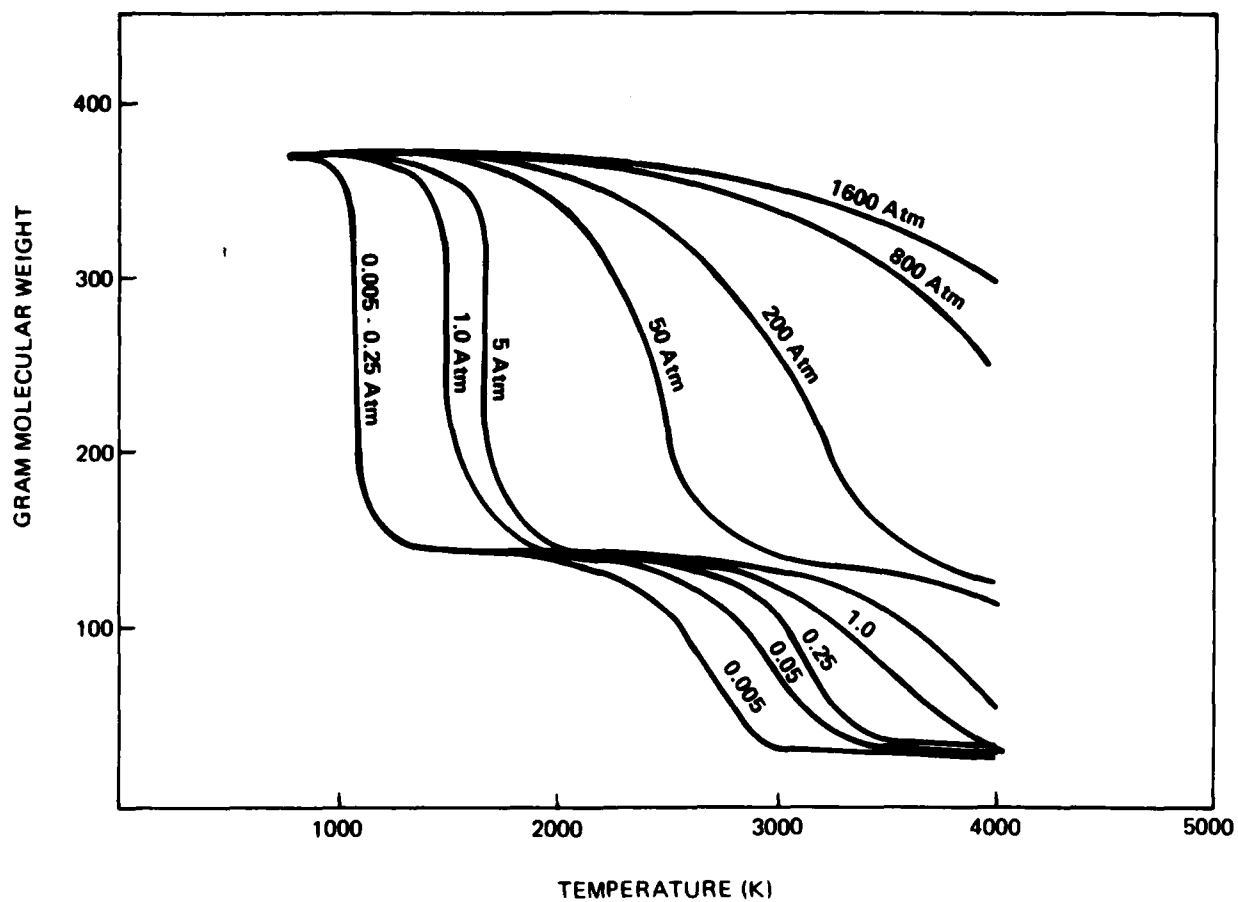
Figure 8 Molecular weight of reaction species mixture, including condensed phase components, as a function of equilibrium temperature for the system Ti $H_{0.66}$/$KClO_4$ in a weight ratio 39/61.
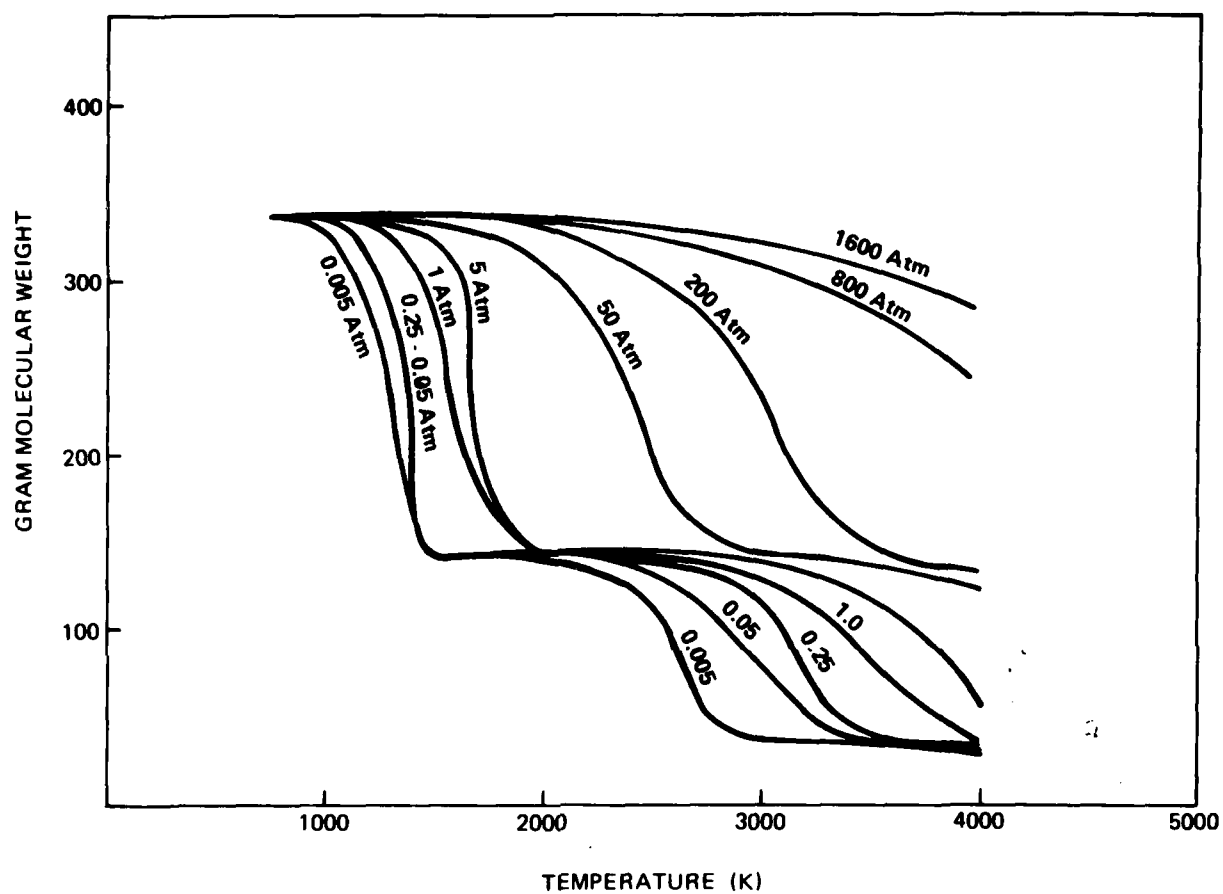
Figure 9 Molecular weight of reaction species mixture, including condensed phase components, as a function of equilibrium temperature for the system $TiH_{0.60}/KClO_4$ in a weight ratio 45/55

TWO ALL NON-PRIMARY EXPLOSIVE TIME
DELAY DETONATOR DEVICES

by

E. A. Day and P. B. Ritter

Systems, Science & Software
La Jolla, California

ABSTRACT

Two mechanically rugged, pyrotechnic time delay
detonator devices containing only materials that are insensi-
tive to spark and heat are described. Both delay devices
utilize the principles of the S^3 all-secondary-explosive,
low-voltage electric detonator ("Safe-detonator"). Time
delays from a few milliseconds to seconds can be attained.
The character and operation of the all-secondary explosive,
low-voltage detonator is reviewed, and the incorporation of
non-gassing delay mixes is described.

One type of delay device is designed for hot-wire
ignition by means of low-voltage electrical energy sources.
Design, construction and tests are presented. Material
selection is stressed to promote safety in manufacture,
storage, handling and use. Trade off of safety against
ignition by spurious electrical signals versus firing-set
energy requirements is discussed. All active materials in
this design are spark insensitive so that only normal
secondary-explosive handling procedures are required during
manufacture. Bonfire safety can be effected without de-
grading performance. The rugged construction of this elec-
trically-initiated delay device is equal to that of the S^3
"safe-detonator." The required confinement to make the
device function assures that the product is encased in a

strong body that mechanically can withstand severe accelerations even during the burning of the delay train.

The second pyrotechnic delay device described is similar to the first except the delay train is initiated by a mild detonating fuse instead of the heated bridgewire. This device has all the ruggedness and safety features of the electrically-initiated device, and because of the absence of the bridgewire circuit, does not have the potential vulnerability to spurious electrical impulse sources.

BACKGROUND

The present day delay electric blasting cap is designed to detonate at a predetermined time after electric current is applied to its bridgewire. The delay period is determined during the design and manufacture of the cap by the amount, configuration and the burning characteristics of a pyrotechnic delay powder. Delay periods range from several milliseconds to several seconds. The column of delay powder is ignited at one end by an ignition charge. Some delay materials evolve gas as they burn while others are essentially gasless during an exothermic reaction. For gas-evolving materials a void is generally provided to limit pressure buildup. Once the reaction front has traversed the delay column, the hot front heats more ignition charge which in turn heats a primary charge to detonation temperature. The primary charge in turn detonates a base charge which provides most of the power of the cap. In some configurations the primary charge is heated to detonation directly by the delay powder. Becker, et al described the general construction of some conventional detonators (Ref. 1).

Delay caps are available in which the delay column is initiated by various types of detonating cord in place of the heated bridgewires used in electric delay caps. All

of these delay detonating devices to our knowledge contain
a sensitive primary explosive which detonates when heated.

When heated, secondary explosives burn, they do not
detonate except under extreme conditions of confinement of
large masses. For this reason there have been many attempts
to develop practical detonators which use only secondary
explosives (Ref's 2,3,4,5,6,7,8,9). In 1971 Lemley, Seay
and Ritter (Ref. 10) reported their demonstration of the
feasibility of an all-secondary-explosive detonator which
incorporates the proper coupling of the following processes:

- Hot wire initiation of a self-sustaining deflagration
  in a "donor" secondary explosive.

- Release and acceleration of a metal impactor disc
  by confined product gases of the deflagration in
  the donor secondary explosive.

- Shock initiation-to-detonation of an acceptor
  secondary explosive upon impact by the accelerated
  impactor disc.

Later we showed that this concept could be made small in
size and operate with good reliability (Ref. 11). This
all-secondary-explosive detonator is shown in Figure 1.

In addition to the detonators referred to above, all
of which have low voltage ignition requirements, there is a
class of detonators which is initiated by the action of
exploding bridgewires. These EBW detonators use low density
pressings of secondary explosives such as PETN and RDX.
The electrical energy required for initiation is applied in
a very controlled manner, requiring capacitor discharge
from approximately 2000 volts. This ignition requirement
makes the EBW detonator very safe against static electri-
city, radio transmission, power line and other sources of
electricity.
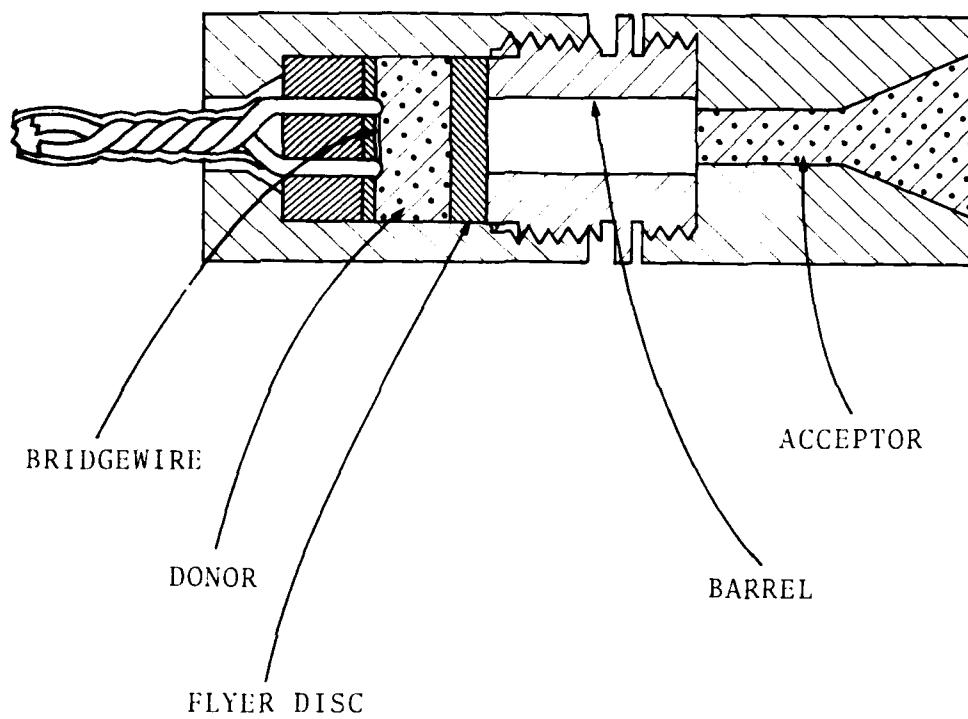
Figure 1.   All-Secondary-Explosive, Low-Voltage
            Electric Detonator for Instantaneous
            Operation (from Ref. 12).

HOTWIRE INITIATED DELAY DETONATOR

The "instantaneous" detonator shown in Figure 1 contains a donor which consists of highly compressed secondary explosive or a fast-burning gas-generating pyrotechnic material confined in a strong body. The flyer disc shears with internal pressure of from 50,000 to 60,000 psi. One can readily envision the addition of a time delay by including a suitable slow-burning material between the bridgewire and the donor charge. This material must be initiated with reliability by the bridgewire, must burn at a suitable rate for the desired delays, must burn with a near-constant volume without developing appreciable pressure, and must have a reaction front with sufficient temperature to ignite the donor charge. This combination of requirements could discourage the most optimistic researcher. However, a review of the properties of low-gassing mixes with powdered-metal bases produced hopeful results. Tungsten mixes per Formula 190 of ELLERN (Ref. 13) seemed to be good candidates if suitable burning rates could be achieved under conditions necessary for successful safe-detonator operation. These delay mixes are the subject of Specification MIL-T-23132 (1961) and are discussed also by Valenta (Ref. 14).

A tungsten delay powder with a burning time of 0.38 sec/in. in unobturated state fulfills all of the requirements if properly confined. Delay detonators with burning delays of from 8 to 30 msec have been successfully fired. It was found that under the confinement required to insure the detonator initiation, burning times were approximately one half those of these delay powders in the unobturated state. Other tungsten delay mixes of this general formulation with burning times up to 40 sec/in. in the unobturated state could be utilized for safe detonators with delay periods from several milliseconds to several seconds.

In the geometry shown in Figure 2, function times are repeatable to better than ±10% when fired at room temperature. (Function time is defined as the period starting when current is applied to the bridgewire and ending when the shock from detonation of the acceptor closes a contact switch.) Burning times are affected by combustion chamber design, confinement and operating temperature.

The employment of secondary explosives as donor and acceptor charges and spark and shock-insensitive delay materials has resulted in the development of a safe delay detonator sensitive only to the bridgewire current required for normal initiation.

MDF-INITIATED DELAY DETONATOR

Operations which require firing two or more charges after different delay intervals may be carried out with only one initiation source if time-delay connectors (Ref. 12) are used in a network of detonation trains. This procedure can offer important safety advantages if spurious electrical signals cannot be reliably controlled. If in the delay detonator described above, the bridgewire is replaced with the termination of a low-energy detonating cord (MDF), the inherently safe device becomes also insensitive to its only source of unplanned initiation, namely spurious electrical signals.

To ignite the delay column in a safe detonator it is necessary to provide a suitable energy source at the proper point within the pressure chamber. This must be accomplished without appreciably diminishing confinement of the delay column and donor charge. Furthermore, confinement must be retained throughout the delay burning period to allow reliable ignition of the donor charge and generation of pressure sufficient to rupture and accelerate the flyer disc. And

BRIDGEWIRE

DELAY MIX

DONOR

FLYER DISC

BARREL
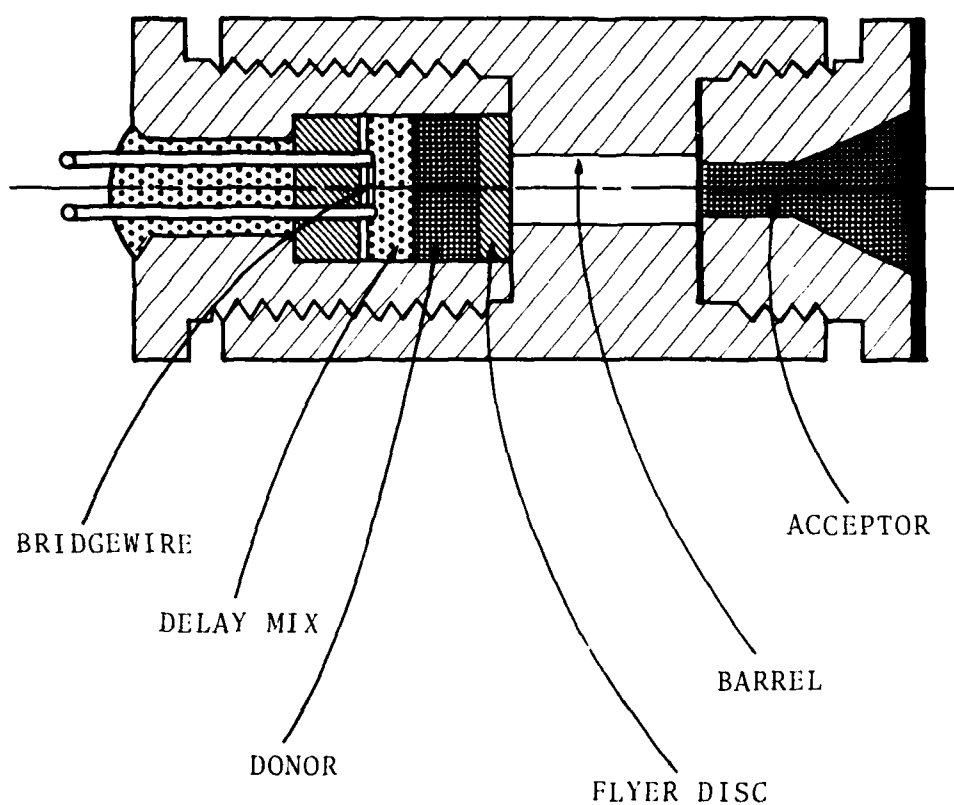
ACCEPTOR

Figure 2.   Non-Primary Explosive, Low-Voltage
            Electric Delay Detonator.

in addition, the flyer disc must be accelerated to a velocity high enough to insure impact detonation of the acceptor explosive. Components of the MDF-initiated delay detonator to be inserted in an MDF train are shown schematically in Figure 3. In this device the detonation front of the MDF terminates in a transition section or selective valve which permits ignition energy to enter the chamber. The selective valve closes, maintaining the required confinement and pressure for flyer plate acceleration. If required, the acceptor end of this device can also have the same design as for the electric delay detonator (see Figure 2) which then can be boosted for any initiation function.

Successful operation of this detonation-to-delay-to-detonation (DDD) device has been accomplished including time delay measurement.

CONCLUSIONS

Mechanically rugged electric delay detonators which contain only spark and shock-insensitive materials have been made and successfully fired with delays of from 8 to 30 msec. Slower-burning delay powders should permit extension of the possible delay range to several seconds.

Ignition of the delay detonator with MDF has been demonstrated, thus making possible multiple delays using a single initiation source. This can be one of the low-voltage safe detonators described above or an exploding bridgewire detonator, eliminating the need for any primary explosive or sensitive ignition materials.

With either method of initiation, the donor is highly compressed in a strong chamber which insures that the unit is very resistant to mechanical impact and acceleration. Accelerations of over one million g are
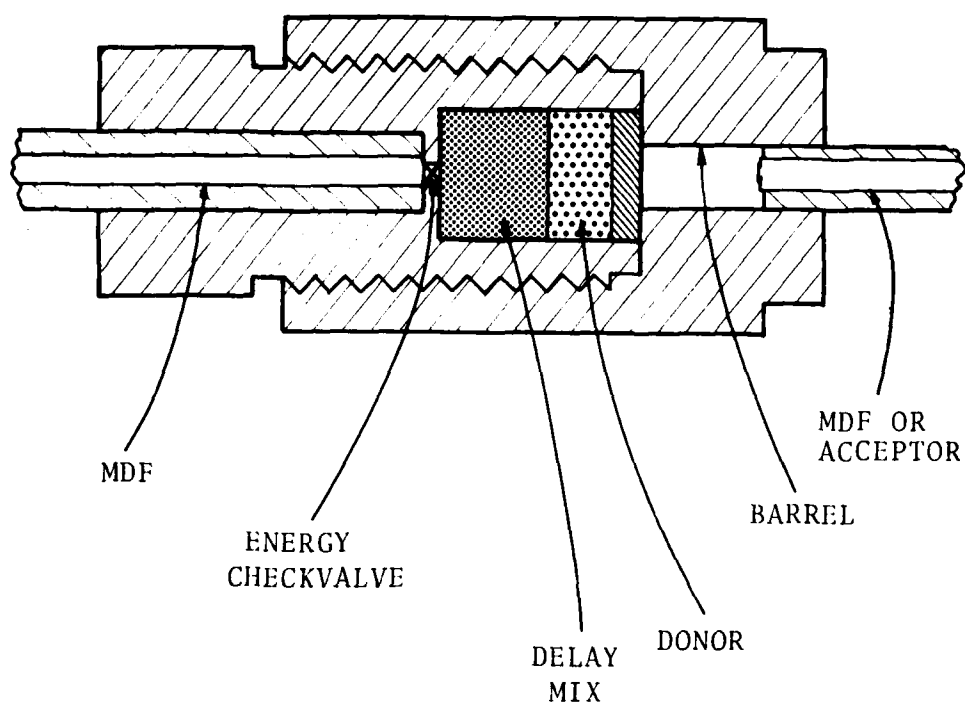
Figure 3. Non-Primary-Explosive Delay Assembly
for Detonation Initiation.

required to develop inertial forces equal to the pressing forces used in manufacture of the detonators. All of the materials used are as stable and insensitive as secondary explosives such as PETN, RDX and HMX.

The pyrotechnic material titanium hydride/potassium perchlorate burns with rapid evolution of gas and has proved to be a good donor material. The $T_i H_2/KC10_4$ mix has all the advantages of the above secondary explosives except that it is not quite as powerful. However, it can be ignited with less confinement, relaxing long-term storage confinement problems which might exist with the explosive materials, and permitting design variations directed toward cost limitations. Assembly by swaging without the need for threaded components has been successfully demonstrated.

Thermal stability of individually tested materials for delay mixes, donor and acceptors indicate the potential for development of higher temperature instantaneous and delay detonators. Efforts are currently underway to extend this concept to low-cost electric detonators with delays ranging from 25 msec to 3 sec; and to produce small millisecond detonators initiated by bridgewire and MDF.

REFERENCES

1. Becker, Karl C., John C. Cooper and Richard W. Watson: Impact and Thermal Sensitivity of Commercial Detonators, U. S. Bureau of Mines Report No. RI 8085, p. 3, 1975.

2. C. A. Houck, et al, U.S. Patent 2,883,931 (1959).

3. R. H. F. Stesau, U.S. Patent 2,981,186 (1961).

4. P. J. Franklin, U.S. Patent 2,996,007 (1961).

5. J. Savitt, et al, U.S. Patent 3,062,143 (1962).

6. A. McLellan Yuill, U.S. Patent 3,069,714 (1963).

84

7.   R. J. Reithel, U.S. Patent 3,158,098 (1964).

8.   M. Reyne, U.S. Patent 3,212,439 (1965).

9.   A. J. Dedman, et al, U.S. Patent 3,724,217 (1973).

10.   Lemley, V. F., P. B. Ritter, G. E. Seay and
      M. H. Purdy, Feasibility of an All-Secondary-Explosive,
      Low-Voltage, Electric Detonator, Air Force Armament
      Laboratory, Eglin AFB, Report AFATL TR-71-148, 1971.

11.   Day, E. A., P. B. Ritter and G. E. Seay, Development
      of a Miniature All-Secondary-Explosive, Low-Voltage,
      Electric Detonator, Air Force Armament Laboratory,
      Elgin AFB, Report AFATL TR-73-40, 1973.

12.   V. F. Lemley, et al, U.S. Patent Application
      SN 506,119.

13.   Military and Civilian Pyrotechnics, Ellern, Chemical
      Publishing Company Inc., 1968.

14.   Valenta, F. J., The State-of-the-Art of Navy Pyro-
      technic Delays, Proceedings Third International
      Pyrotechnics Seminar, Denver Research Institute,
      University of Denver, 1972.

15.   Blasters' Handbook, 15th Ed., E.I. duPont de NeMours,
      Wilmington, Delaware, 1969.

ACKNOWLEDGEMENTS

CONSIDERATIONS WHEN EMPLOYING
INTERACTIVE COMPUTER CONTROL FOR THE STUDY
OF COMPLEX FLAME SYSTEMS

M. Bonner Denton and M. W. Routh
Department of Chemistry
University of Arizona
Tucson, Arizona 85721

ABSTRACT

Investigations employing interactive computer control as a means
for effectively investigating fundamental processes occurring with-
in the complex heterogenous flame systems commonly employed for flame
spectrochemical analysis are described. The capabilities of the pre-
sent system for flame profiling and optimization as well as considerations
inherent in extending these techniques to the study of pyrotechnic flares
are presented.

INTRODUCTION

Due to the multiple interrelation and interaction of the numerous parameters governing heterogeneous flame systems, rigorous manual investigations involving multi-species flame mapping under varying conditions and multiparameter optimization for a given criterion can be exceedingly tedious and prohibitively time consuming. On-line interactive computer control of the parameters under study has proven to be a highly productive approach for conducting complex investigations in the class of flames commonly employed for flame spectrochemical analysis. While studies to date have been conducted with an experimental configuration developed explicitly to investigate the stable and relatively transparent flames employed for elemental analysis by flame atomic emission, atomic absorption, and atomic fluorescence spectrometry, many of the potential problems and possible solutions which can be expected in attempting to extend these techniques to pyrotechnic flares have become readily apparent.

EXPERIMENTAL

The present computer-controlled experimental system is diagrammed in Figure 1. Computer control is provided for varying the X and Y position of the flame observed, fuel and oxidant gas flow rates, photomultiplier high voltage, as well as the wavelength and slit width on the monochromator. Utilizing this configuration, flame profile maps such as those shown in Figures 2 through 8 can be generated and plotted in a matter

of several minutes. Studies involving interaction of various species within such flames can be conducted in a rigorous manner which would be logistically impossible in any reasonable time period utilizing conventional manual approaches. This series of profiles demonstrates an example of how barium species are affected by solvent variations. Figure 2 depicts the "gross signal" flame profile in the region of the barium oxide band (5493 Å) when 100 ppm barium (barium chloride) as a 90% methanol-10% aqueous solution is aspirated into a premixed oxygen-hydrogen flame. Two apparent maxima are observed; however, when the flame background emission map of Figure 3 is subtracted from the "gross signal" profile of Figure 2, the "net barium oxide" profile map of Figure 4 is generated. When Figure 4 is compared with the net barium oxide profile with 100% aqueous solvent of Figure 5, a displacement of the location of the maximum emission toward higher regions is observed in the non-aqueous case coupled with an increase in emission intensity. However when the nebulization rate for the methanol solvent case is adjusted to equal that obtained in the aqueous solution, the profile of Figure 6 is obtained, indicating that under equal rates of sample introduction the non-aqueous solvent system tends to impede the formation of the barium oxide species and, thus, enhances the atomic emission intensity observed at 5535.6Å. This effect is readily apparent when the atomic emission in the aqueous case (Figure 7) is compared to that observed with the nebulization rate-corrected organic solvent system (Figure 8).

While such mapping studies have provided and will continue to yield a great deal of valuable information about complex phenomena occuring

in flame systems, the application of the vast potential inherent in on-line interactive computer controlled optimization of the multiple inter-dependent parameters toward improving analysis is a tremendously appealing goal. In the course of implementing interactive optimization studies, a number of approaches to the required software were evaluated. Predictor-corrector-gradient techniques were found to be prohibitively slow. Add-itionally, after studying the conventional simplex (1) and even the more sophisticated Modified Simplex described by Nelder and Mead (2) it was felt that these approaches could be improved upon.

A simplex is merely a geometric figure defined by n + 1 points, where n is the number of variables. Thus, for two variables, the simplex is simply a triangle in two dimensional space (in three dimensional space it would be a pyramid, etc.). In practice, measurements are made of the function to be optimized at each of the points. The point producing the poorest response is then reflected through the line, plane, or hyper-plane defined by the other points. For the simplest case see Figure 9 where the initial simplex is defined by the triangle ABC. Since the response for A is the poorest of the three, it is reflected through the line connecting B and C and a new simplex B, C, D is generated.

In an attempt to overcome the simple simplex's inability to expand or contract, Nelder and Mead developed the Modified Simplex (MS) in which the replacement of the vertex with the worst reponse (Vw) can lead to one of four possible choices for the new vertex location (see Figure 10). The MS approach first determines the worst response vertex, Vw, then reflects this through the centroid and measures the response

at the reflected vertex, V_R; if the response at V_R is the best, then V_R is expanded an operator-specified constant percentage and the value at V_E is measured. If the value at V_E is not as favorable as that at V_R, V_R is incorporated in the new simplex. If the value at V_E is the most favorable, then the new simplex contains V_E. If the response at V_R is not the most favorable but second best, the new simplex incorporates V_R. If the response at V_R is worse than all but that at V_W, however, the simplex is contracted and the response at V_{CR} is evaluated and incorporated in the new simplex. If the response at V_R is worse than that at V_W, the simplex is contracted closer to V_W than V_R, and V_{CW} is contained in the new simplex.

A significantly improved approach, the Super Modified Simplex, which allows the computer to select one of a nearly infinite number of positions based on calculating the optimum new vertex by first fitting a second order curve through the responses obtained at V_W, the centroid of the hyperface V_P^- (line, etc.) and the reflected value V_R (see Figure 11), has been developed. Even in high dimensionality space only three response data points are required for this curve -- V_W which has already been measured; V_P^-, the midpoint of the vector connecting V_W and V_R; and V_R. (Acquisition of the response at V_P^- in general does not slow down the optimization since in most mechanically speed-limited systems the computer's response measurement and computational speeds are much faster than the system's ability to vary parameters. Since many or all parameters must pass through this point V_P^-, little or no time is lost in stopping their progression and making a high speed measurement on the way toward V_R.)

The shape of the calculated response is then evaluated and used to predict the V_{max} (the value employed for the next simplex). If the

curve is found to have a maximum somewhere between V_W and V_R, this point

is used as V_{max} (with the exception of a small zone surrounding the

centroid, since stopping on the centroid could result in loss of a

dimension in n space). If upward sloping curves are observed in either

direction (normally this occurs in the expanding direction of V_R, but

it is possible to encounter cases of multiple intersecting ridges where

expanding in the V_W direction is needed), the computer can either select

the endpoint of the curve giving the best response (V_{max}) or evaluate

the slope and calculate, using limits and previously provided restrictions,

the proper accelerated value for V_{max}, allowing the size of the simplex

to expand.

The Super Modified Simplex (SMS) technique has been found to be

superior to the Modified Simplex (MS) of Nelder and Mead. The SMS

requires fewer simplexes, fewer data points, and, hence, less time to

reach the optimum (see Figures 12 and 13). Additionally, while the

MS algorithm has been found to repeatedly fail in noisy signal environ-

ments, the SMS approach has demonstrated itself to be highly resistant

to noise limitations.

FUTURE

How can these flame mapping and parameter optimization techniques,

which have proven so useful in the study of analytical flame systems, be

extended toward the characterization of pyrotechnic flares?

Pyrotechnic flare systems offer several challenging, but formidable

restrictions when compared with analytical flames, including the transient
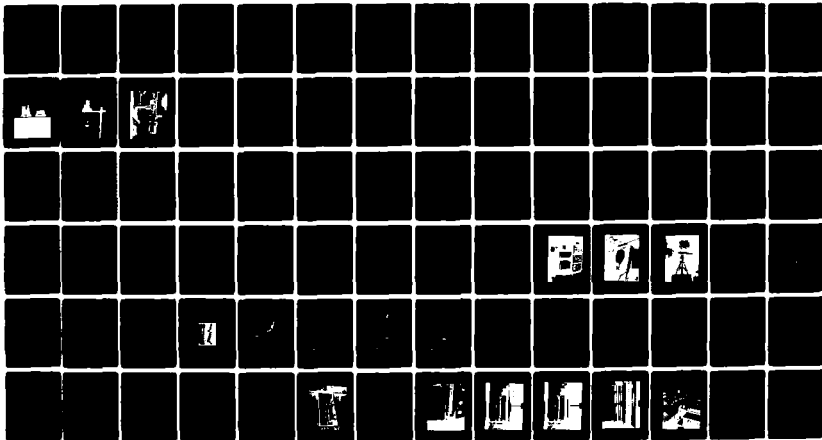
nature of the system under study, the high level of spectroscopic noise, and the existence of an optically dense plume, as well as difficulty in computer automation of certain critical parameters (i.e., candle composition, etc.).

Currently the high-speed mapping configuration shown in Figure 14 is under development. This system will provide sufficiently high scanning speed to accurately map emission from a flame or flare with total scan times of less than a second. Control algorithms will allow operator selection of important parameters, including size of region mapped, number of data points acquired, sampling speed, and delay between successive maps.

When the problems associated with mapping pyrotechnic flares are in hand, computer optimization techniques will be employed toward selecting conditions for extracting the desired data.

And in the future -- why not employ the computer to optimize overall system performance?

REFERENCES

1. W. Spendley, G. R. Hext, and F. R. Himsworth, <u>Technometrics</u>, <u>4</u>, 441 (1962).

2. J. A. Nelder and R. Mead, <u>Computer J.</u>, <u>7</u>, 308 (1965).
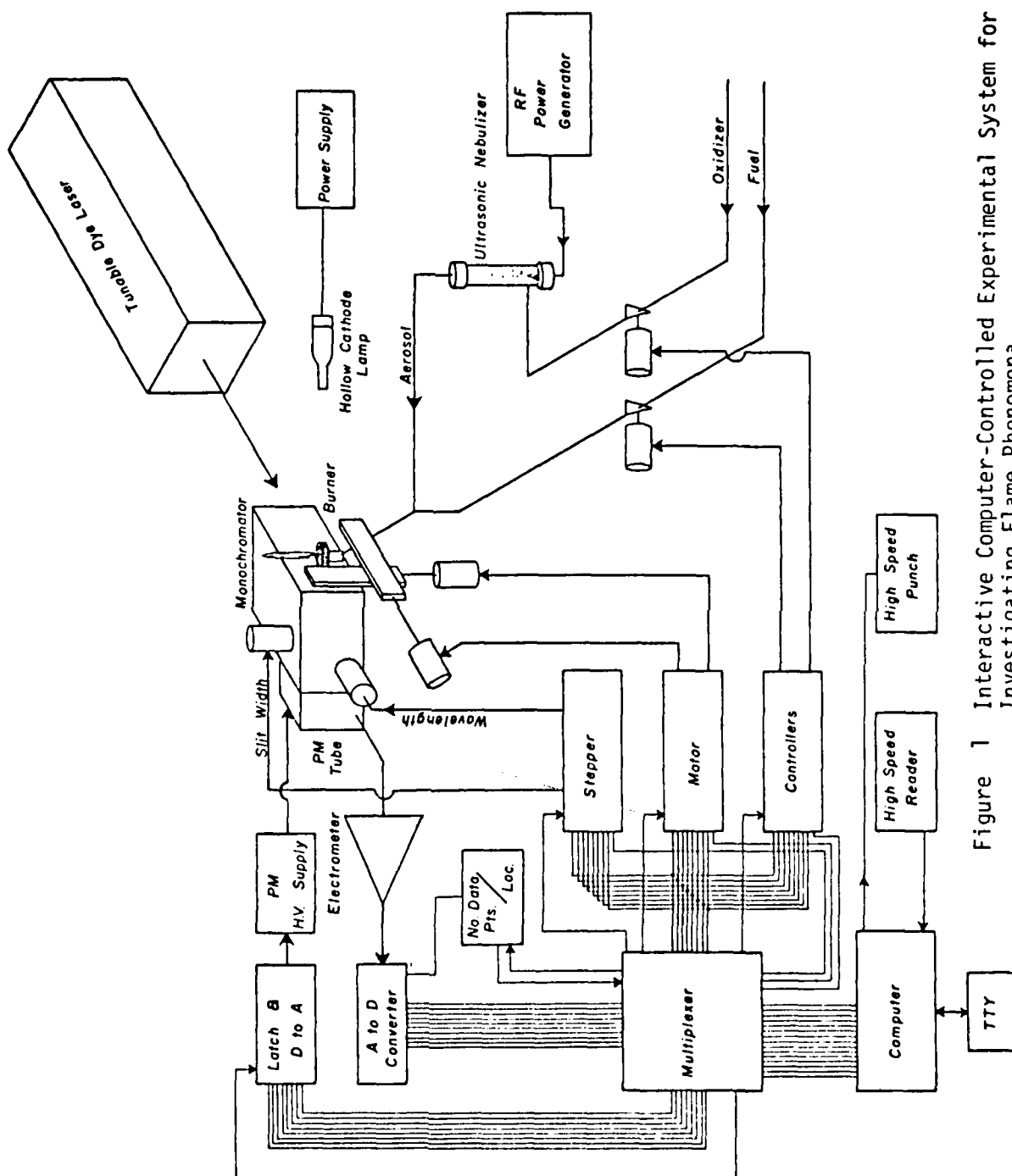
Figure 1   Interactive Computer-Controlled Experimental System for Investigating Flame Phenomena.
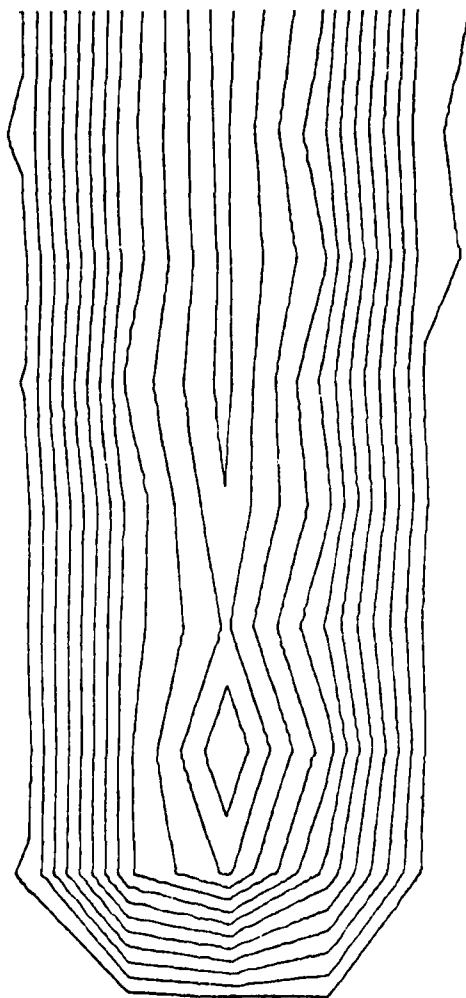
Figure 2   "Raw" flame profile observed at the oxide band of
             barium (5493 Å) in a 90% methanol-10% aqueous solution,
             exhibiting two apparent maxima.
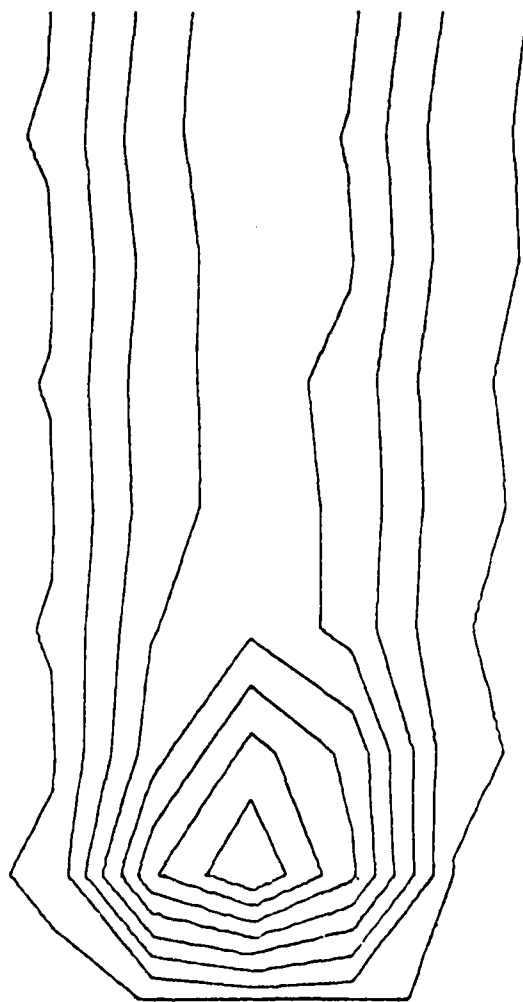
Figure 3   Background profile of a 90% methanol-10% aqueous
solution observed at the oxide band of barium (5493 Å).
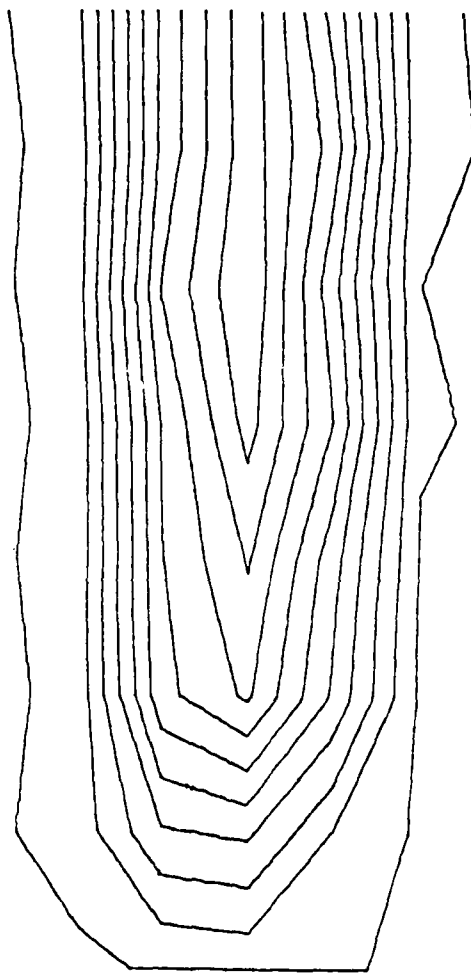
Figure 4   Net profile of barium observed at the oxide band
in a 90% methanol-10% aqueous solution.
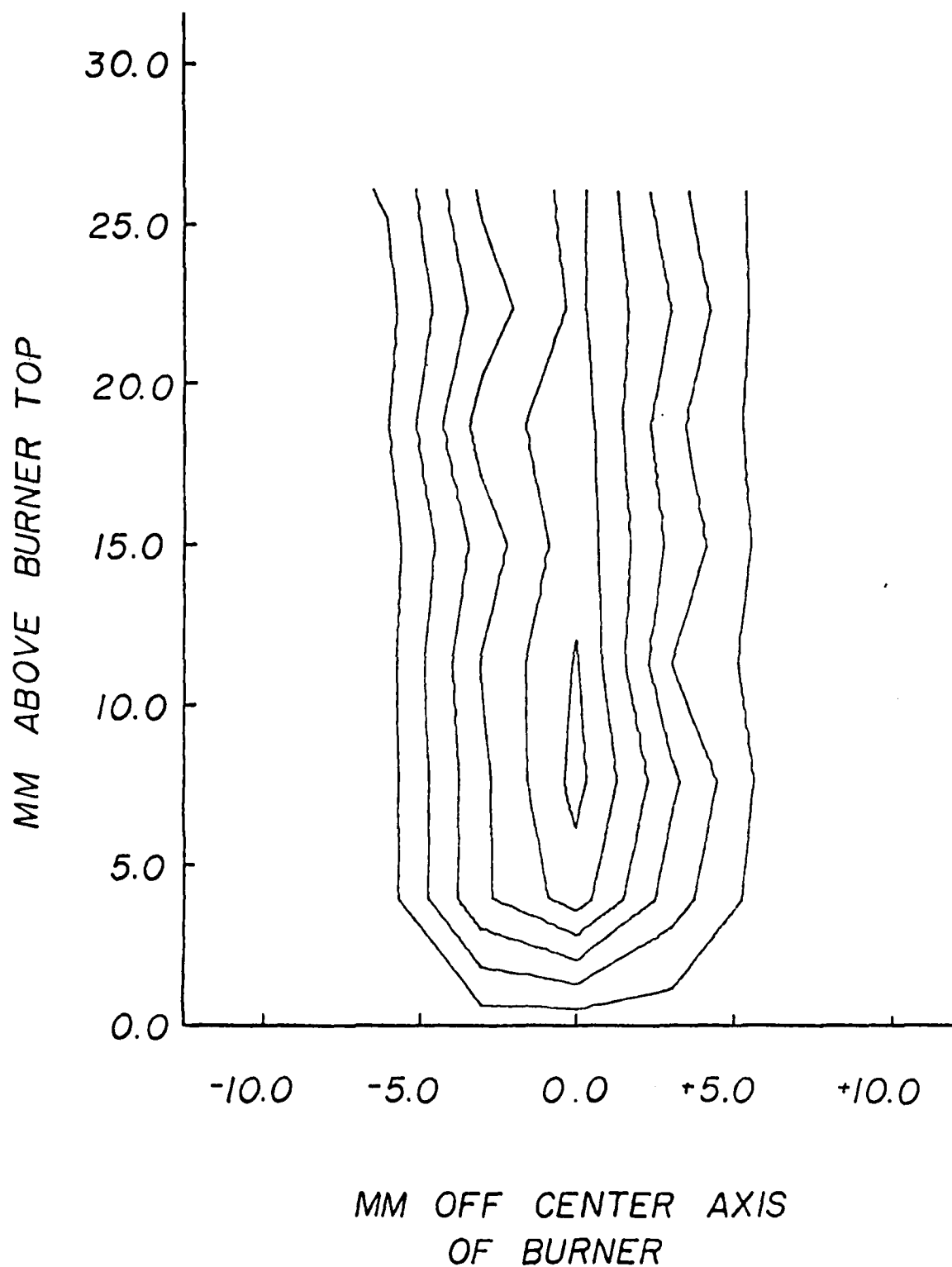
Figure 5 Background corrected (net) emission profile of 100 ppm. barium in water obtained at the oxide band head (5493 A) in a fuel-rich (oxygen/hydrogen = 0.30)premixed oxygen-hydrogen flame. Contours are drawn at 0.40 volt intervals.
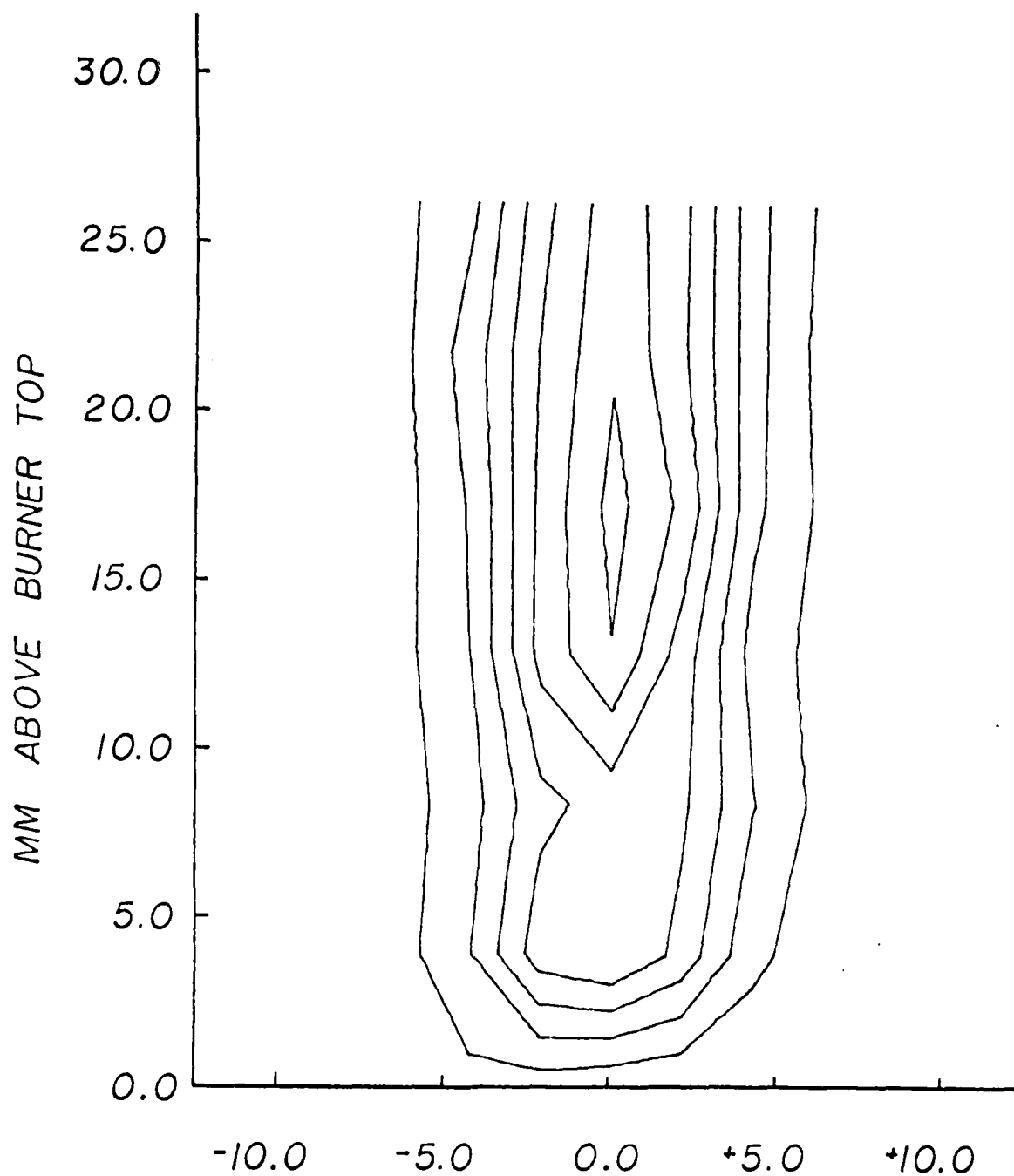
Figure 6   Background corrected (net) emission profile of 100 ppm
            barium in 90% methanol obtained at the oxide band head
            (5493 A) in a fuel-rich (oxygen/hydrogen = 0.30) premixed
            oxygen-hydrogen flame. The nebulization rate was adjusted
            to equal that obtained with water and the fuel was pre-
            saturated with 90% methanol to eliminate solvent evapora-
            tion from the sample cavity. Contours are drawn at 0.40
            volt intervals.
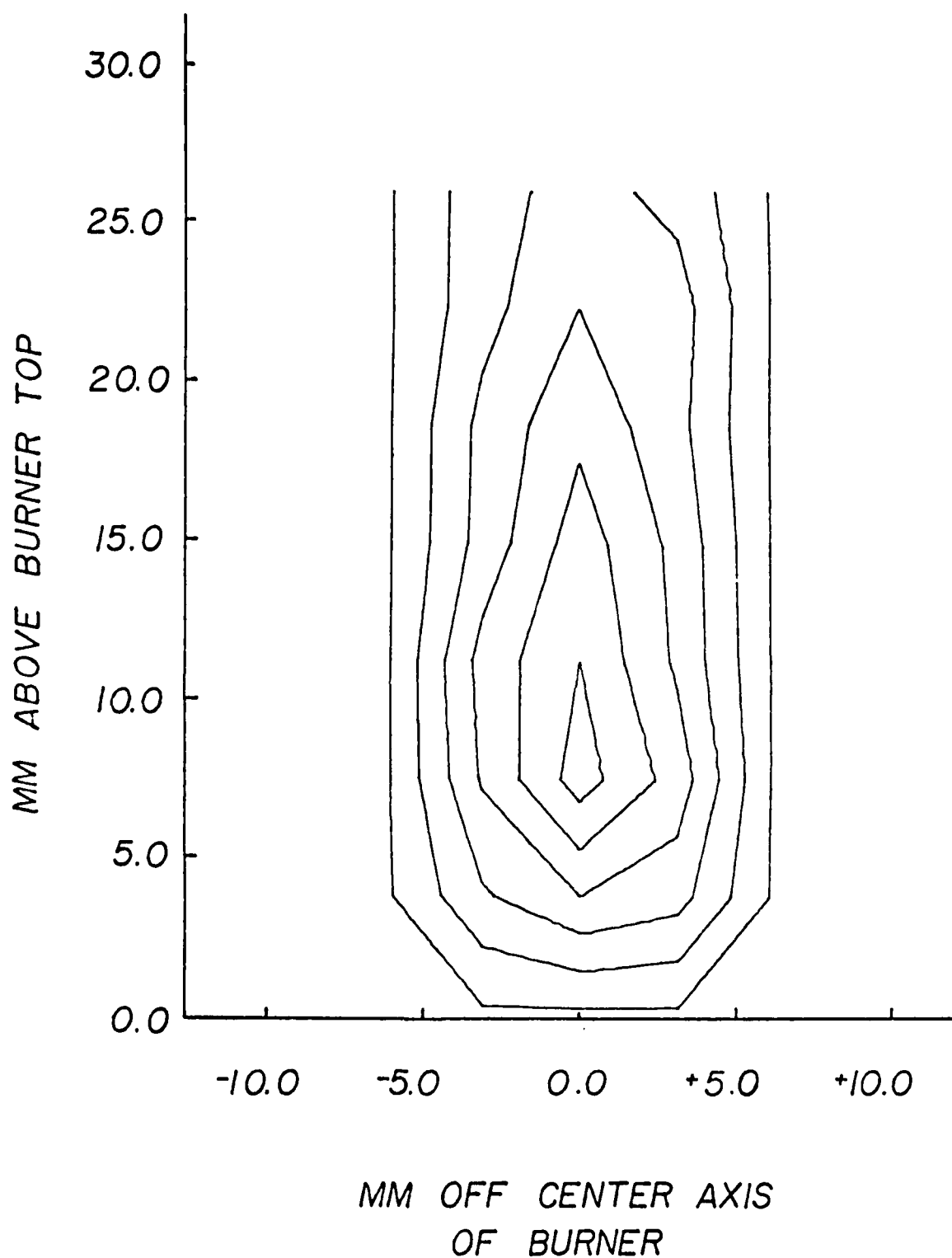
Figure 7 Background corrected (net) emission profile of 100 ppm barium in water obtained at the atomic resonance line (5535.6 Å) in a fuel-rich (oxygen/hydrogen = 0.30) premixed oxygen-hydrogen flame. Contours are drawn at 0.50 volt intervals.
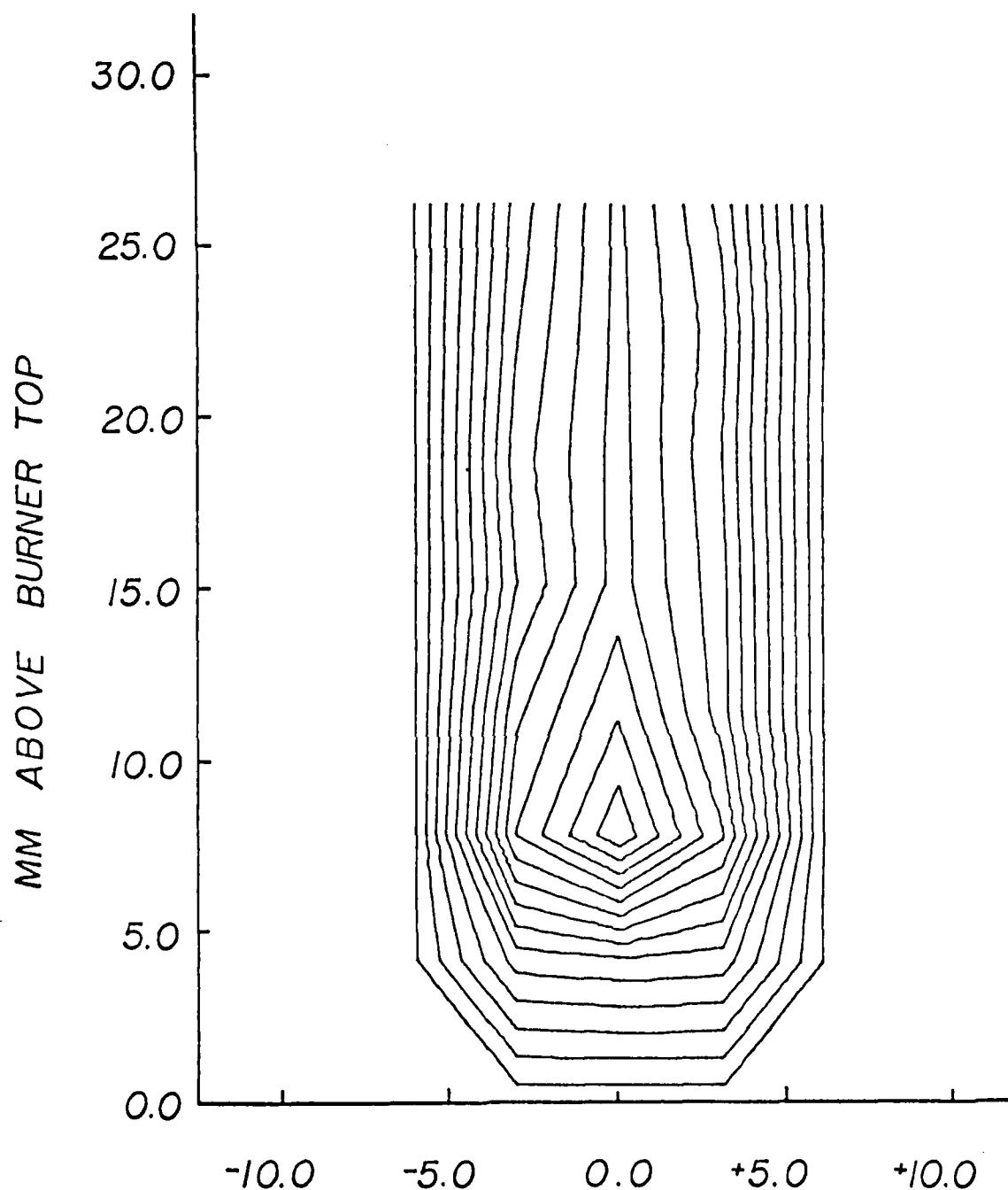
Figure 8. Background corrected (net) emission profile of 100 ppm barium in 90% methanol obtained at the atomic resonance line (5535.6 Å) in a fuel-rich (oxygen/hydrogen = 0.30) premixed oxygen-hydrogen flame. The nebulization rate was adjusted to equal that obtained with water and the fuel was presaturated with 90% methanol to eliminate solvent evaporation from the sample cavity. Contours are drawn at 0.50 volt intervals.
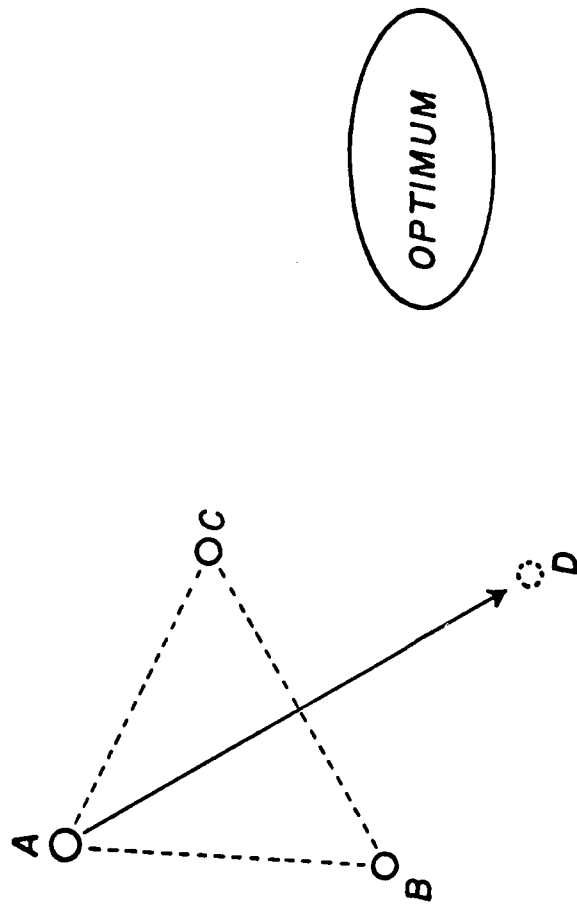
Figure 9   Simplified simplex in two dimensions. During optimization the vertex producing the poorest response is reflected through the opposite side resulting in a new simplex (BCD) closer to the optimum. This simplified approach suffers from several problems (see text).
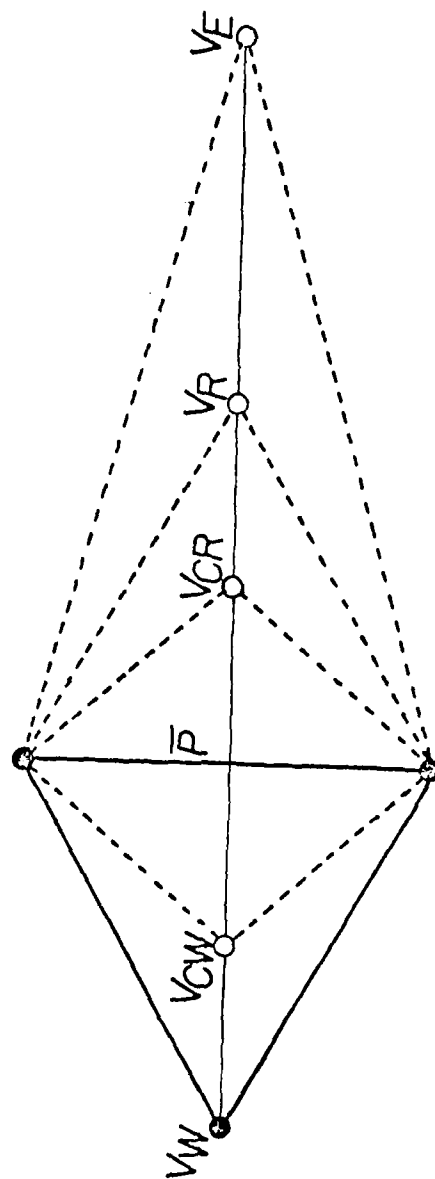
Figure 10 Two dimensional representation of the Nelder and Mead Modified Simplex which provides for sequential selection of one of four new locations.

V_R - location of the reflected vertex

V_E - location of the expanded vertex

V_{CR} - location of the contracted vertex

V_{CW} - location of the contracted vertex

$\bar{P}$ - centroid
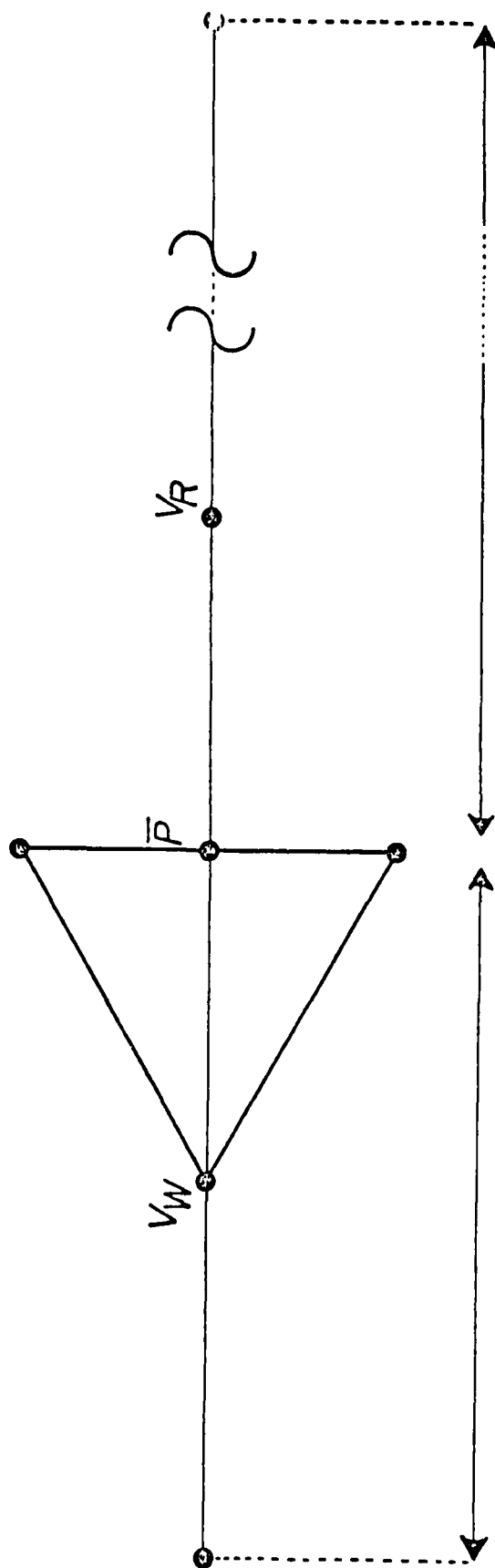
Figure 11   Two dimensional representation of the Super Modified Simplex. This approach provides an almost infinite range of possible values for the new vertex utilizing the computer-predicted optimum based on the evaluation of a second order curve fitted to the responses obtained at worst vertex V_W, the centroid $\bar{P}$, and the reflected vertex V_R.
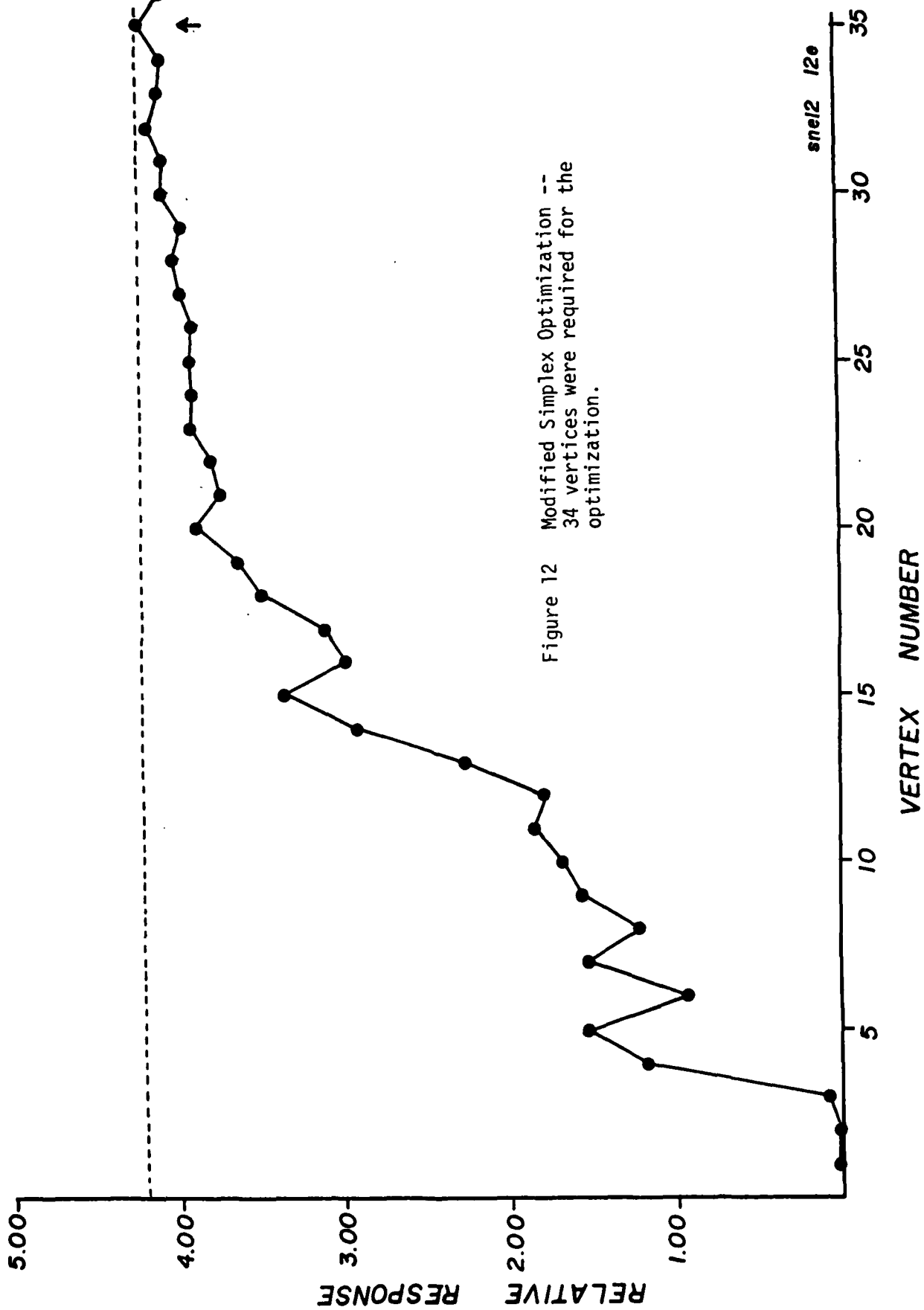
Figure 12   Modified Simplex Optimization -- 34 vertices were required for the optimization.

snel2 l2e

105

Figure 13   Super Modified Simplex-- Optimizing
same system as Figure 12 required
only 17 vertices.

smik2 4a
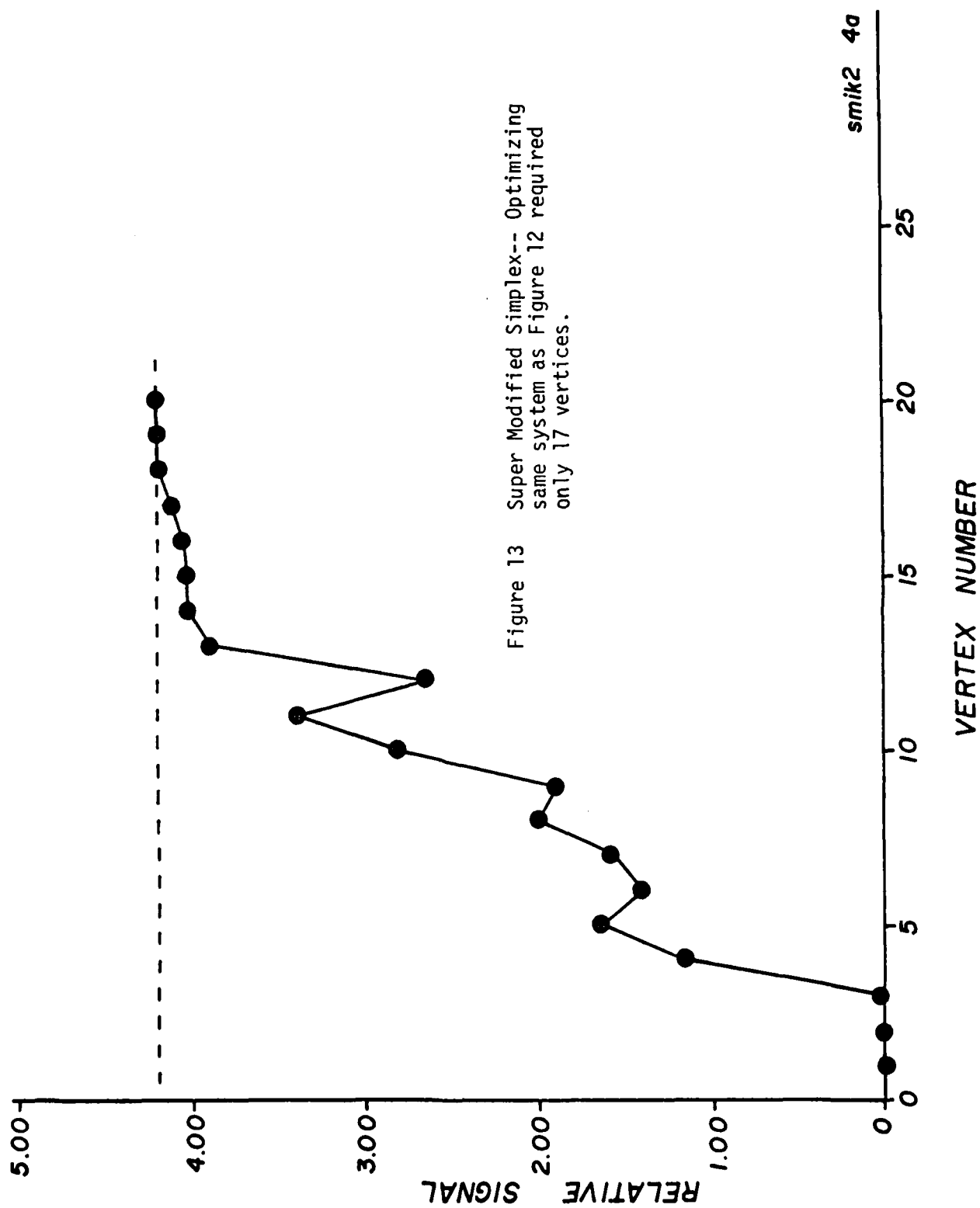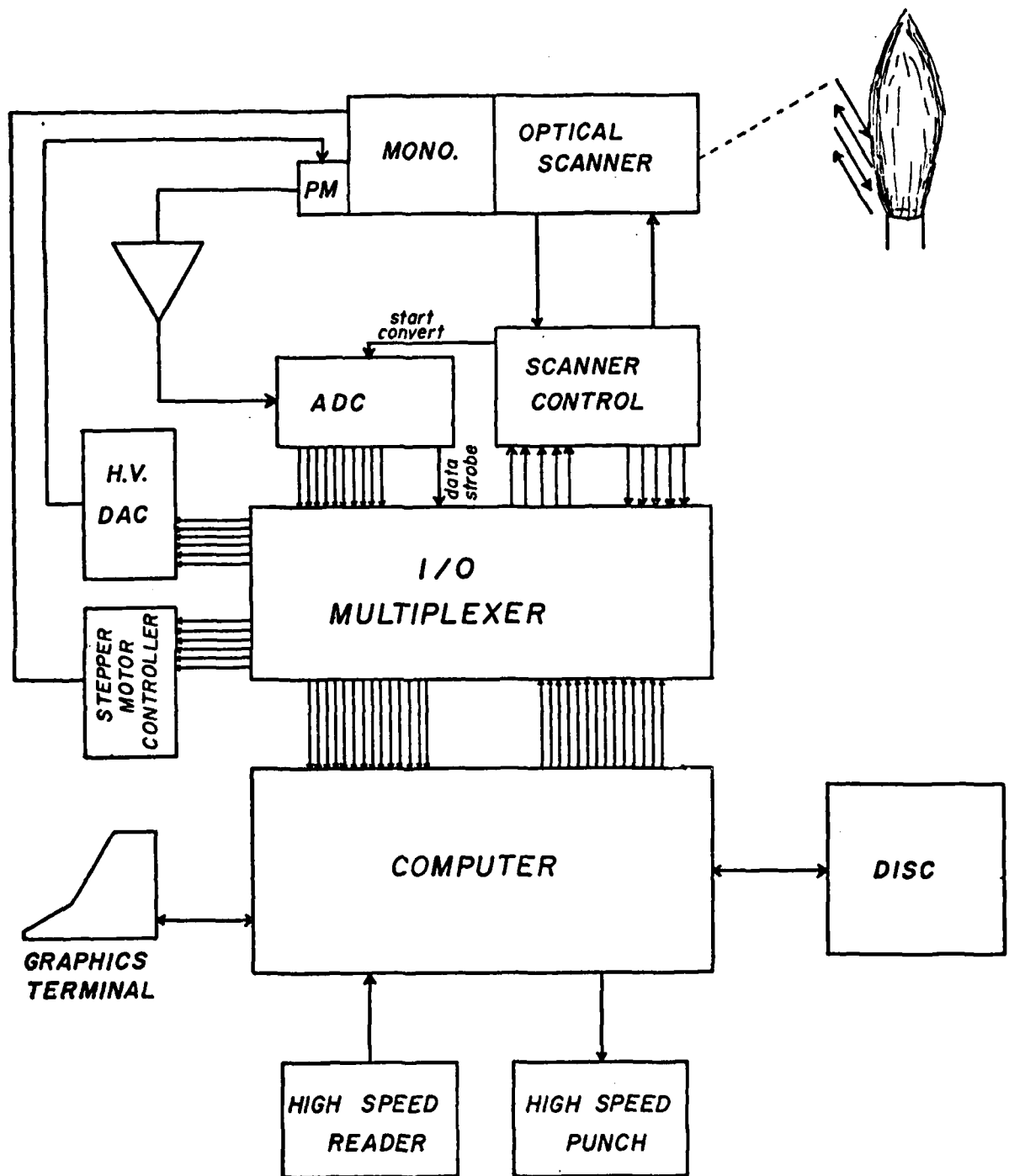
Figure 14   High speed computer controlled mapping system under development
for the study of flames and pyrotechnic flares.

CLOSED BOMB TESTING AT LONGHORN ARMY AMMUNITION PLANT

David R. Dillehay

Thiokol Corporation
Longhorn Division
Marshall, Texas 75670

A B S T R A C T

A novel and low cost closed bomb test system has been in use at Longhorn
Army Ammunition Plant for over 10 years. The system uses unique techniques
for data reduction that permit calculation of burning rate, burning rate
exponent, temperature sensitivity, specific impulse, impetus, and charac-
teristic velocity of propellants and pyrotechnic mixtures.

The system has been used for quality control of production propellant
mixes and for evaluation of pyrotechnic material hazards and problems.

A high degree of correlation was established with test motors for a variety
of propellant types.

108

INTRODUCTION

Laboratory methods for evaluation of propellant ballistic properties have long
been sought to provide rapid and inexpensive verification of production mix
quality and for testing the effects of raw material variations or formulation
adjustments. A novel and low cost closed bomb test system has been in use at
the Longhorn Army Ammunition Plant since 1962. The system has proved to be
useful for production quality control and for development programs where rapid
and inexpensive testing could be used to evaluate ballistic performance without
requiring test motor castings.

Some of the data reduction techniques are unique but the experimental results
obtained over the years have been highly successful in predicting ballistic
parameters in production systems.

EQUIPMENT

The closed bomb itself was developed and fabricated from off-the-shelf items
for convenience and to minimize cost. The pressure vessel is a Parr Oxygen
Type Calorimeter Bomb with a double valve head, modified to accept a strain
gauge pressure transducer and a pressurization line. The bomb has a working
pressure of 3000 psi. The body and head are primed with General Electric
SS-4004 Silicone Primer and lined with General Electric RTV-60 Silicone
Rubber for insulation. Stainless steel lines are used to connect the bomb
with a tank of argon gas for preload pressurization. A firing circuit was
constructed locally to switch on the recording oscillograph, step through a
calibration of the pressure transducer, apply firing voltage to the igniter
terminals, and switch off the oscillograph. A Honeywell Model 1508 Visicorder
Recording Oscillograph is used for recording the pressure-time trace.

The sample cup is machined from aluminum bar stock. The outside was dimensioned
to fit in the Parr Calorimeter sample holder. The inside diameter of the
sample cup was machined to 0.656 ± 0.002 inches. The dimension was recently
reduced to 0.500 inches to reduce the sample size. The depth of the cup is
0.200 ± 0.001 inches. Propellant may be cast directly in the cup and leveled
with a spatula and tested in the uncured state. Samples can be cured in the
cup and cut-back level to provide a fresh ignition surface. Sample "buttons"
have been cut from cured propellant in large rocket motors and placed in the
sample cup for testing. Other pyrotechnic samples have been tested directly
in the bomb, either as loose powder or in their loading configuration.

Ignition of the samples is accomplished with a Holex 1196-B Initiator.
The diaphragm of the igniter is cleaned of lacquer, scored lightly with an
"X" and punctured with a needle. This technique provides a uniform rupture
of the diaphragm and produces minimum surface disruption with uncured samples.
The igniter is wired across the Parr Calorimeter electrodes and positioned
approximately one-half inch above the surface to be ignited.

A schematic diagram of the complete system is shown in Figure 1. Photographs of the components are shown in Figures 2 through 4.

DATA REDUCTION

A typical sample test would involve loading the sample cup and placing it in the bomb with an igniter in place. The bomb would be flushed with argon to remove air and then pressurized to some predetermined test pressure. On firing, a pressure-time trace would be recorded, such as shown in the figure below.
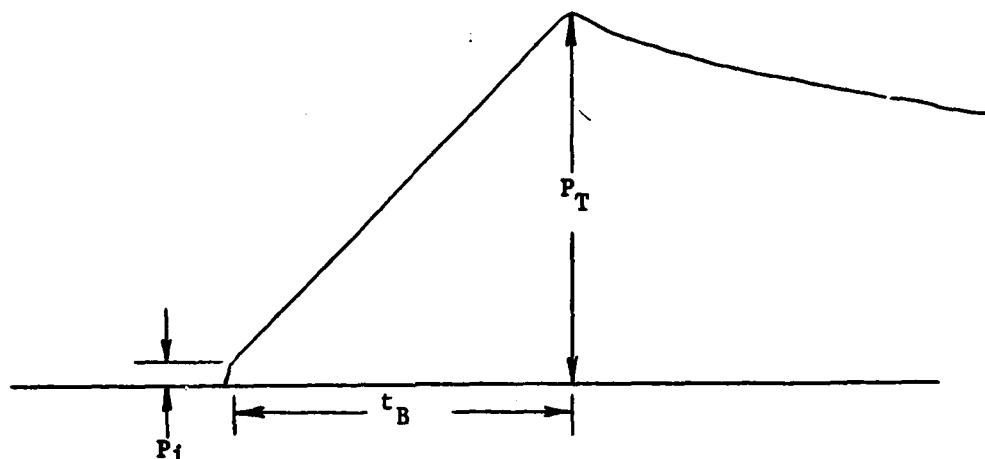
The linear pressure rise is typical when preload pressures, above a minimum required by the propellant type, are used. With no preload pressure the anticipated exponential pressure rise is obtained. Since the sample depth is closely controlled and the time from ignition to burn out can be determined from the trace, the closed bomb burning rate is defined to be

$$r_{cB} = \frac{0.200}{t_B}$$

The parameter P_{max} is defined as $(P_T - P_i)$ where P_T is the total pressure rise and P_i is the pressure rise from the igniter firing.

The total preload pressure is defined as the initial preload plus the igniter pressure rise.

It has been found that the closed bomb burning rate correlates with both strand burner and test motor burning rates with very good results. Further, it was found that the change in closed bomb burning rate with changes in preload pressure provides a measure of the burning rate exponent as determined from test motor or strand burner tests. See Figure 5.

The parameter P_{max} is used to calculate impetus (F) from closed bomb tests. Impetus can be used to calculate characteristic velocity and specific impulse of propellants. Impetus or force constant is a measure of the work potential of a propellant or pyrotechnic burned under constant volume conditions and is expressed in terms of energy per unit mass. In an ideal gas, impetus is

$$F = PV = nRT$$

110

In a closed bomb, impetus is determined by measuring the maximum pressure (P_{max}) obtained at a given propellant loading density. At low pressures the covolume effect is negligible and impetus may be calculated from the measured P_{max} if heat losses are assumed negligible. To obtain impetus in terms of ft-lb of work per pound of mass, the following equation may be used

$$F = 2.307 \, \frac{P_{max}}{W} \, V$$

where

F = impetus in ft-lb/lb.
2.307 = conversion constant
P_{max} = maximum pressure in psi
V = bomb volume in cm^3
W = sample weight in gms

To eliminate the effect of the preload gas, samples are tested at several preloads and P_{max} is plotted against preload pressure. By extrapolating the P_{max} to zero preload, a corrected P_{max} is obtained which is then used for the determination of impetus.

Characteristic velocity, c*, is a function of the combustion product gas properties in a rocket combustion chamber and can be expressed thermodynamically as

$$C^* = (g \, \gamma \, R \, T_c)^{\frac{1}{2}} (\frac{2}{\gamma + 1})^{\frac{1}{2}(\frac{1}{1 - \gamma})}$$

where

γ = specific heat ratio
R = gas constant divided by the molecular weight of the combustion products
T_c = chamber temperature
g = gravitational constant

It is seen, therefore, that both characteristic velocity and impetus are functions of nRT. However, impetus is a constant volume term and combustion in a rocket motor is generally under constant pressure conditions. In order to relate impetus and characteristic velocity, $(nRT)_V$ must be converted to $(nRT)_p$.

Gas composition and heat release can vary between constant volume conditions and constant pressure conditions. Thus, both n and T may vary. Since in the closed bomb only the product of n and T is obtained, an exact conversion of $(nRT)_V$ to $(nRT)_p$ cannot be made. However, an approximation can be made which appears to be sufficiently accurate for propellant characterization in the laboratory.

Let Q_p = heat change at constant pressure

Q_v = heat change at constant volume

T_p = combustion temperature at constant pressure

T_v = combustion temperature at constant volume

γ = C_p/C_v = specific heat ratio

The relationship between the heat change at constant pressure and heat change at constant volume may be expressed as

$$Q_p = Q_v + PdV$$

Where PdV represents the external work done by the system for a reaction carried out at constant pressure. If the assumption is made that the total heat release in a combustion reaction is much larger than PdV such that PdV can be assumed negligible, then

$$Q_p = Q_v$$

in which case

$$C_p T_p = C_v T_v$$

and

$$T_v = \gamma T_p$$

If the further assumption is made that n is constant in going from products at T_v to products at T_p, then

$$(nRT)_v = \gamma(nRT)_p$$

and

$$F = \gamma nRT_p$$

Substituting F in the expression for characteristic velocity gives

$$C^* = (gF)^{\frac{1}{2}} (\gamma)^{-1} \left(\frac{2}{\gamma+1}\right)^{\frac{1}{2}(\frac{1}{1-\gamma})}$$

Assuming a value of 1.25 for γ, the equation reduces to

$$C^* = 7.713 \ F^{\frac{1}{2}} \ ft/sec.$$

To show the dependence of c* on γ , the table below shows the effect of on the coefficient

γ	Coefficient
1.30	7.459
1.25	7.713
1.20	7.987
1.15	8.286

For the propellants tested, it has been found that n does not appear to vary significantly with temperature in the range from T_p to T_v. Good agreement has been obtained between the c* values from test motors and the c* values from the closed bomb. The theoretical c* equation is independent of chamber pressure when second order pressure effects on dissociation are neglected. If the effect of pressure on dissociation is significant, then the values of c* will be in error by the degree that n varies with pressure.

The specific impulse of a propellant is given by the equation

$$I_{sp} = \frac{C^* C_f}{g}$$

where

I_{sp} = specific impulse
C_f = nozzle coefficient

Therefore, in terms of impetus,

$$I_{sp} = C_f (F)^{\frac{1}{2}} (g)^{-\frac{1}{2}} (\gamma)^{-1} (\frac{2}{1+\gamma})^{\frac{\gamma+1}{2(1-\gamma)}}$$

and

$$C_f = \left\{ \frac{2\gamma}{\gamma-1} (\frac{2}{\gamma+1})^{\frac{\gamma+1}{\gamma-1}} \left[1 - (\frac{P_e}{P_c})^{\frac{\gamma-1}{\gamma}} \right] \right\}^{\frac{1}{2}}$$

where

P_e = pressure at nozzle exit
P_c = chamber pressure

Using a value of 1.25 for γ and a chamber pressure of 1000 psig, the sealevel $I_{sp} = 0.379 F^{\frac{1}{2}}$

Thus, it is seen that determination of impetus gives rather simple access to some propellant ballistic parameters which may be used for propellant comparisons.

Substituting preload pressure for chamber pressure and closed bomb burning rate for constant pressure burning rate, the equation

$$r = ap^n$$

can be solved for n. Good agreement between values from closed bomb tests and values for rocket motor or strand burner tests was obtained. The closed bomb rates were always higher than strand burner or test motor rates. It was observed that

$$r_{cB} = \gamma r_p$$

with fairly good agreement to give a reasonable estimate of a for experimental propellants. This would seem to support the equation

$$T_v = \gamma T_p$$

with the burning rate dependent on the combustion temperature.

EXPERIMENTAL RESULTS

This section will report on applications of closed bomb testing at Longhorn Army Ammunition Plant. A primary application has been in quality control. Samples of propellant were sent to the Chemical Laboratory prior to casting the production motors. Closed bomb burning rates were measured and compared with previous mix data to assure that no major weigh-up or processing errors had occurred. The mix was tested and released prior to casting. Correlations were developed and used with first and second stage Pershing propellant both in the star point and cylindrical core designs. Closed bomb testing was used in control of igniter propellants for Pershing and Nike-Hercules motors. Nike-Hercules and Sergeant polysulfide propellants were also tested routinely.

In a program to reduce crystallization of Sergeant propellant, a butyl formal polysulfide polymer was substituted for approximately 25% of the ethylformal polysulfide polymer. No changes were made in oxidizer content or BMA*. Test motors showed low pressures and burning rates. Laboratory mixes with the two polymers were tested in the closed bomb and the changes in ballistic performance were observed. Additional laboratory mixes were made with changes in the BMA and a modified formulation was found to match previous results. Production motors made with the new formulation performed satisfactorily (within 1% of predicted values).

Iron oxide is used as a burning rate catalyst in Pershing propellant. A change from one vender to another was eminent. Laboratory tests showed the particle size of the new iron oxide to be 0.22 microns compared with previous values of 0.24 microns. The production mix made with the new iron oxide was tested

---

*BMA is bimodalaggregate and refers to the ratio of ground and unground ammonium perchlorate.

in the closed bomb and a high burning rate was predicted. Test motors cast
and fired from the production mix verified that the new iron oxide produced
high burning rates. As a result of this experience, incoming lots of iron
oxide were tested with laboratory mixes fired in the closed bomb to determine
ballistic acceptability before committing production mixes.

The sensitivity of the closed bomb burning rate to BMA is shown in Figure 6.
The plateau region first detected by the closed bomb was later verified in
rocket motor tests.

A change in the burning rate exponent of Pershing propellant at high pressures
was first detected in the closed bomb and later verified by test motors.

The closed bomb system has also found application in pyrotechnic areas. The
impetus of black powder is readily determined in the closed bomb system.
Literature and standard impulse bomb measurements show black powder to have
an impetus of 100,000 ft-lbs/lb. Significant deviation from this value is
indicative of changes in composition or burning characteristics. For example,
signal propellant composition is made as black powder with approximately 9%
calcium carbonate added. The impetus of this composition as a function of
calcium carbonate content is shown in the table below.

% $CaCO_3$	Impetus, Ft-lb/lb.	c*, ft/sec
7.54	83,377	2231
8.42	81,314	2204
10.75	79,211	2177
10.83	80,341	2194
10.38	78,962	2169
11.62	74,821	2115
12.95	72,891	2084

These data show a correlation coefficient of 0.92 with an intercept (for 0%
calcium carbonate) of 97,600 ft-lb/lb.

Studies have been made on the effects of press pressure and moisture content
at the time of consolidation on signal propellant burn time. Figure 7 shows
the correlation between signal rocket motor burn times and closed bomb burn
times of propellant increments. The high slope results from the fact that
the propellant grain is progressive burning in the signal rocket motor whereas
the closed bomb data reflects constant pressure conditions obtained by
neutralizing the progressive burning by allowing end-burning to occur.
The correlation coefficient is 0.99.

Impetus measurements are useful in assessing the safety hazard of a composition.
Since impetus is a measure of the work potential of a composition it relates to
the amount of pressure that may be produced from accidental ignition. For

example, rocket motor propellants range from 300,000 to 400,000 ft-lbs/lb. compared to black powder which is only 100,000 ft-lbs/lb. A typical illuminant composition will test about 250,000 ft-lbs/lb. while Type I Yellow First Fire is only 66,000 ft-lbs/lb. The boron/barium chromate first fires have impetus values of around 5,000 ft-lbs./lb. The low values reflect that these compositions produce mostly solid reactants and heat, whereas propellants generate large quantities of gas. Delay compositions and heat transfer compositions will have very low impetus values and would be expected to burn without pressure build up. This would indicate that shielding for protection from hot particles would be satisfactory as opposed to pressure venting.

Burning rates of igniters and first fires can be tested at high pressures in the closed bomb and by preconditioning the samples over a temperature range, it is possible to get a measure of the temperature sensitivity of the composition.

Small delay carriers have been placed in the closed bomb to measure the burning rate of delay compositions at elevated pressures.

<div align="center">CONCLUSIONS</div>

An effective laboratory tool has been developed and proved useful for measuring ballistic properties of propellants and pyrotechnic compositions. They system is low in cost, simple to operate, and provides a high degree of correlation between laboratory results and production item performance.

Figure 1

LAAP Closed Bomb System

Firing Control Circuits

Oscillograph

Modified
Parr Bomb

Vent

Argon
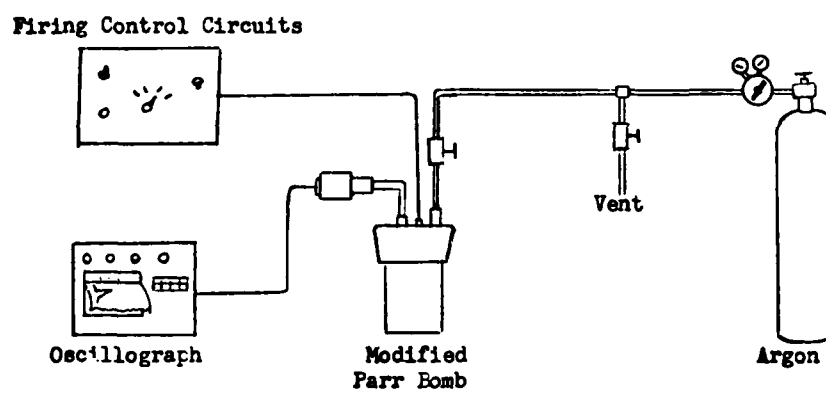
Figure 2

Modified and Unmodified Parr Bomb Heads

118
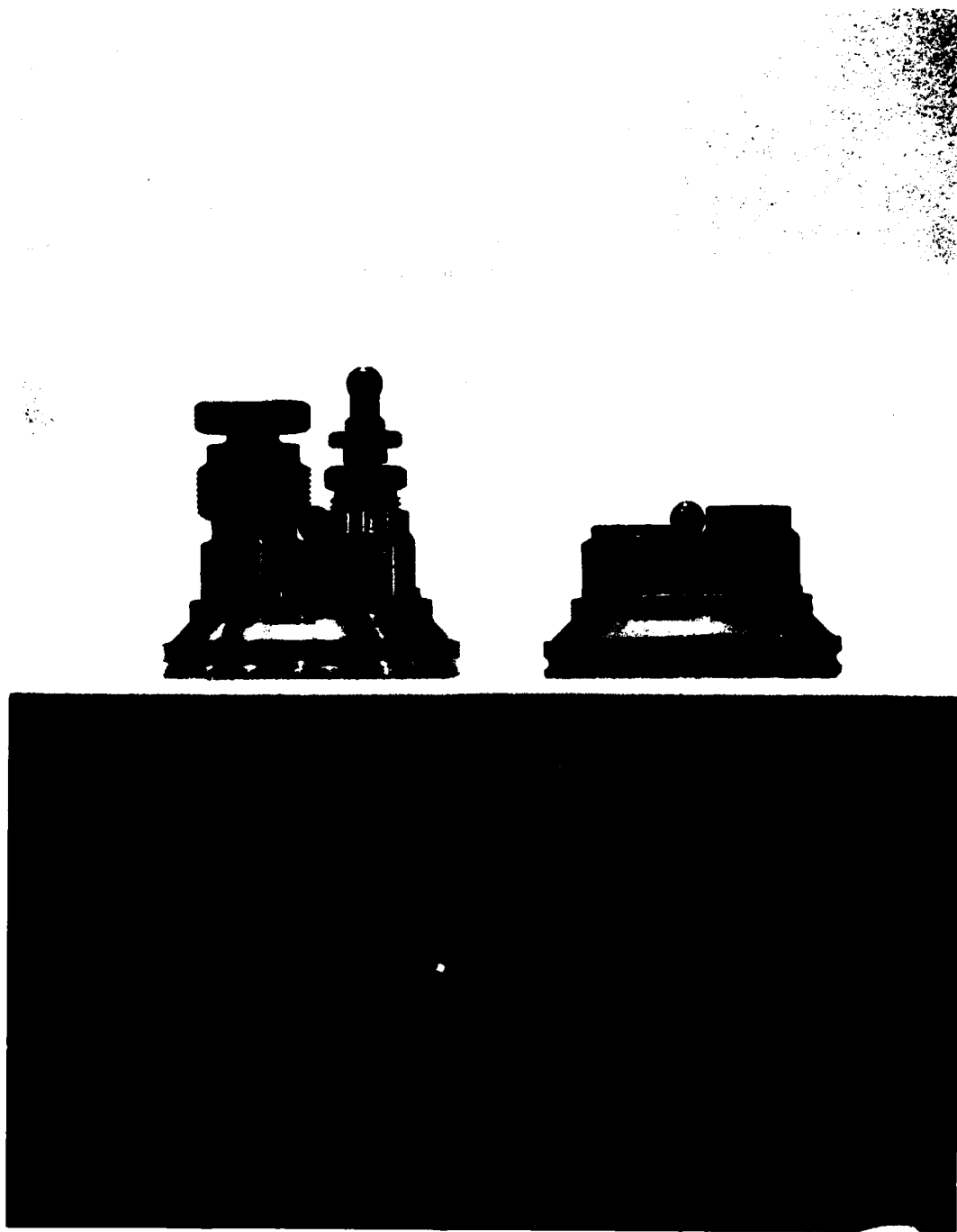
Figure 3

Sample Cup With Igniter in Position
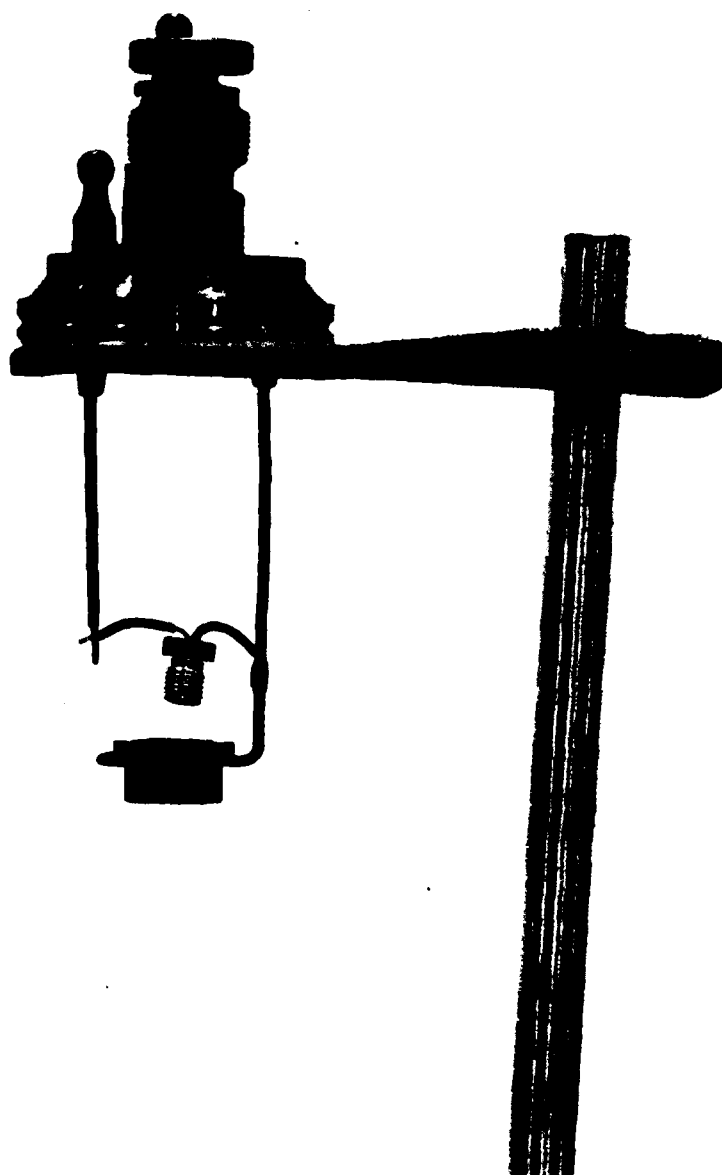
Figure 4

Complete System Ready to Fire
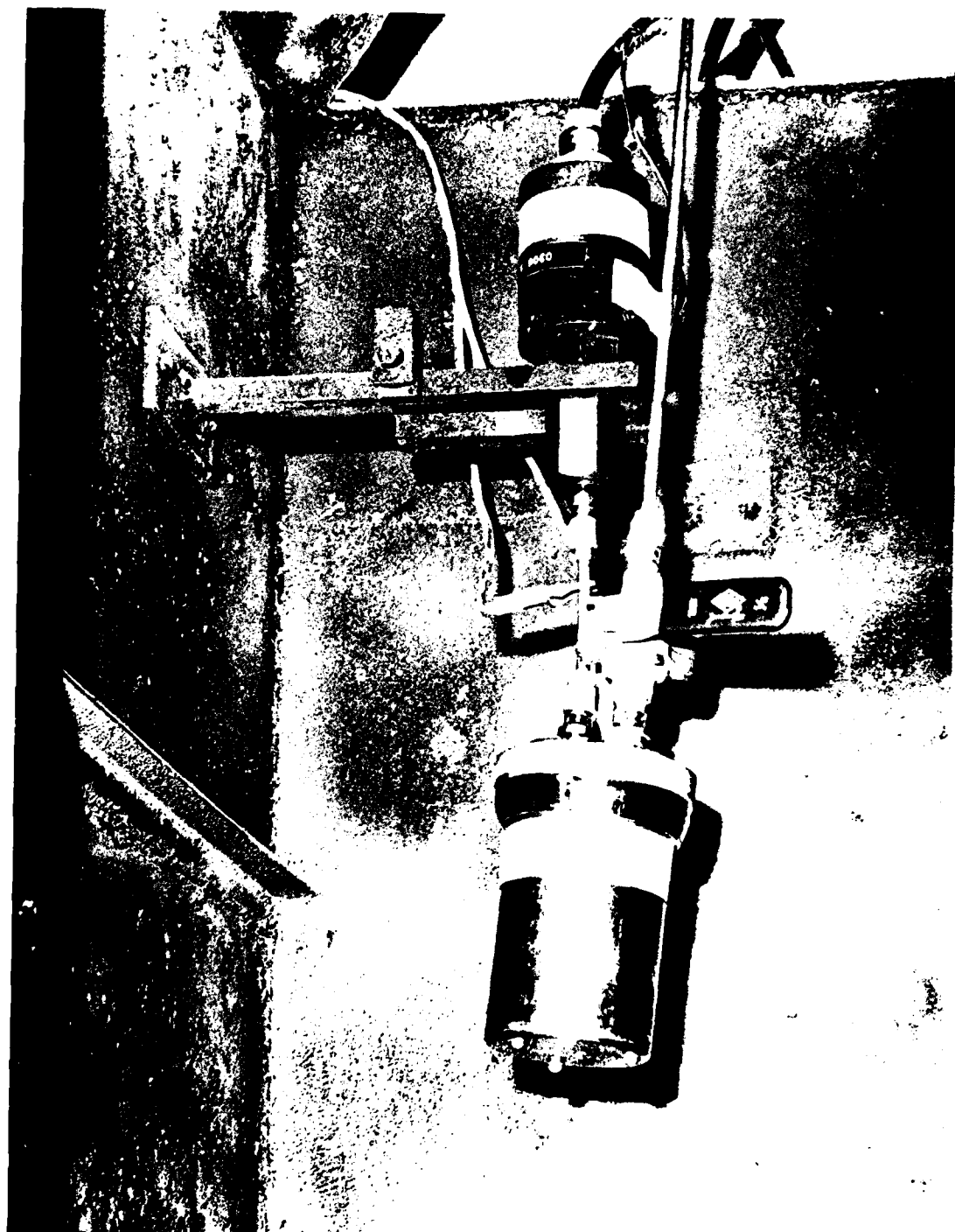
Figure 5

r_{CB} vs. r_{SB} and r_{TL-3}

Figure 6

r_{CB} vs. BMA

% Ground Oxidizer/% Unground Oxidizer

122
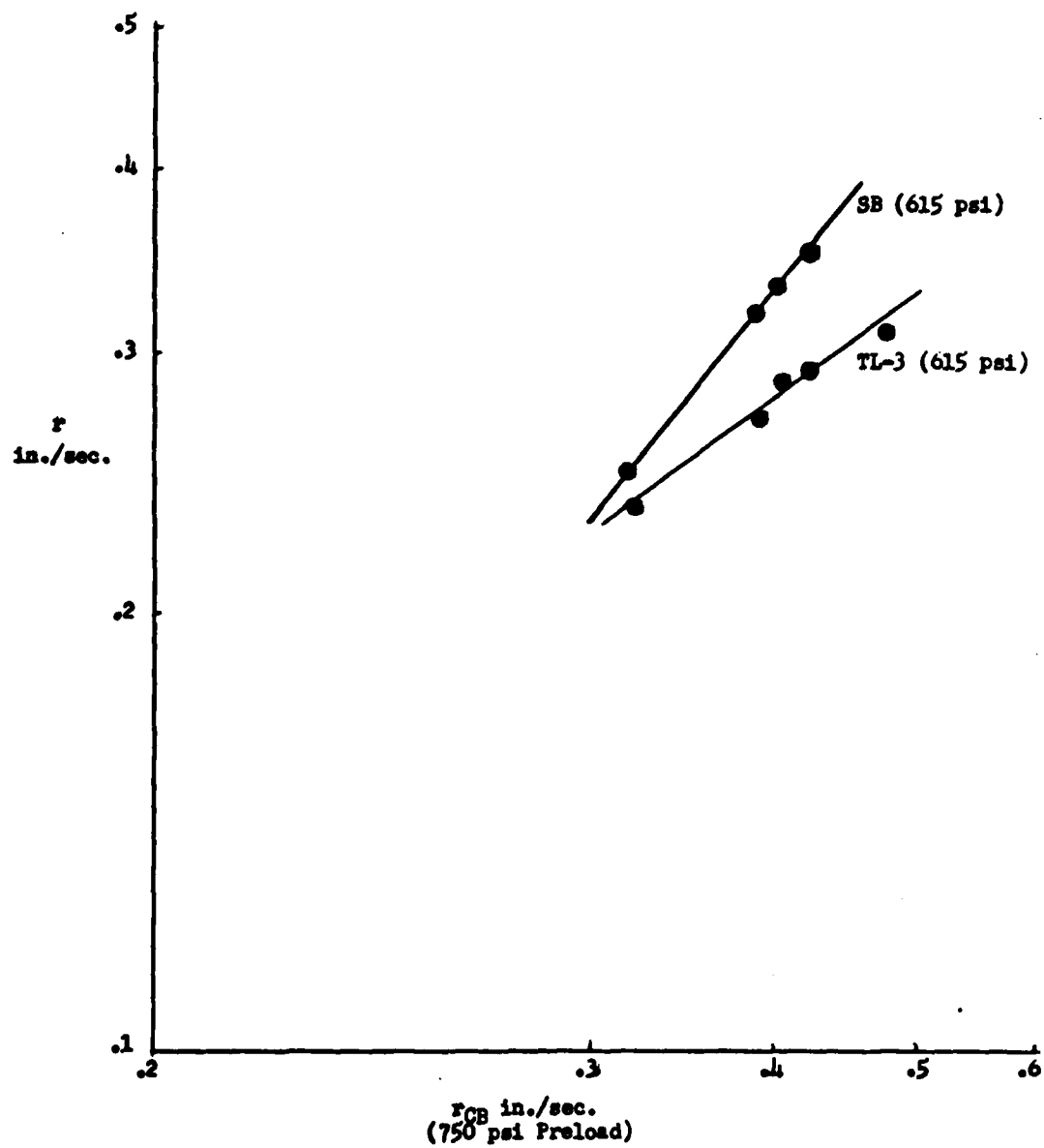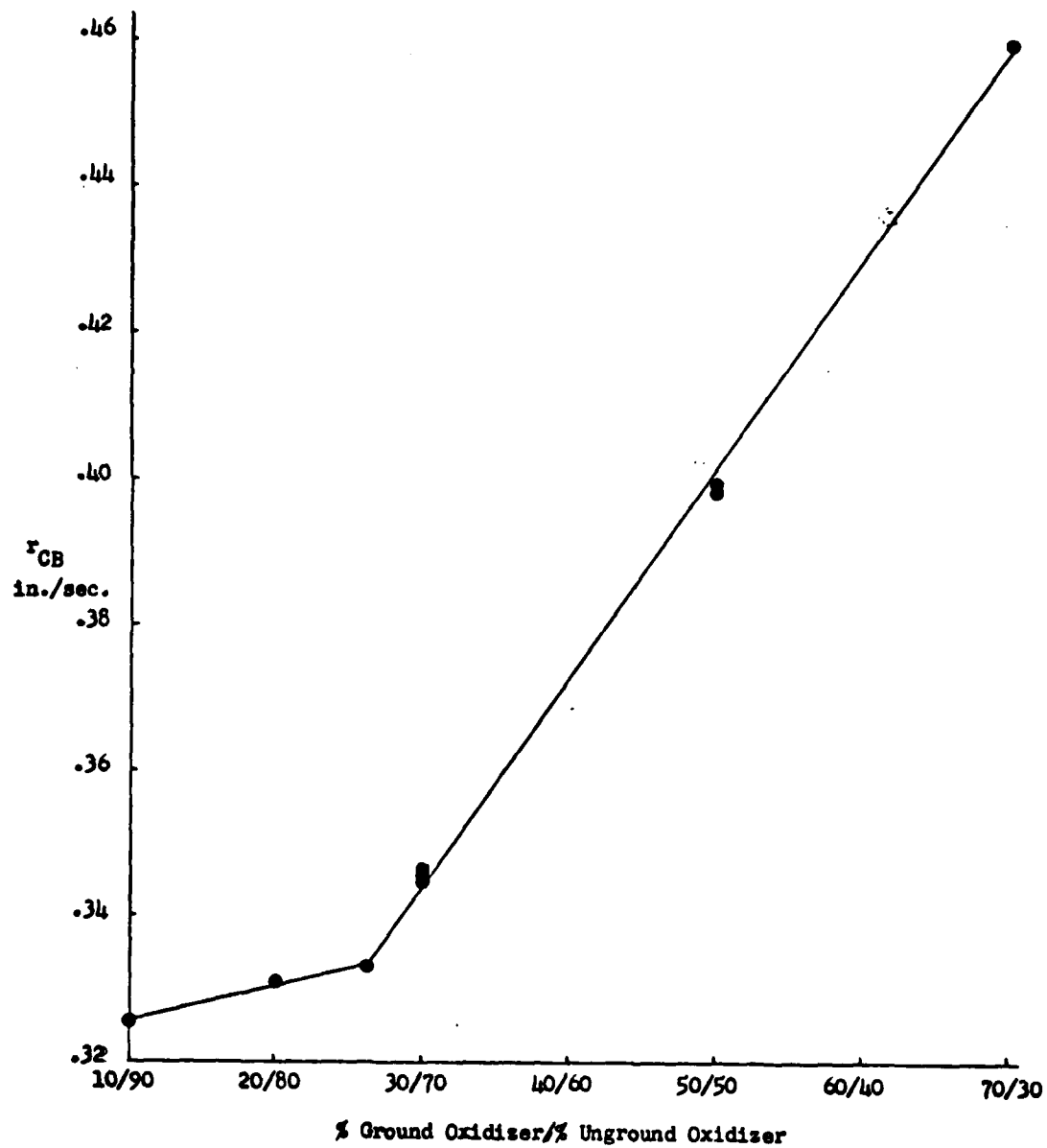
Figure 7

Propellant Burn Times in Signal Rocket Motors

Compared to Closed Bomb Burn Times
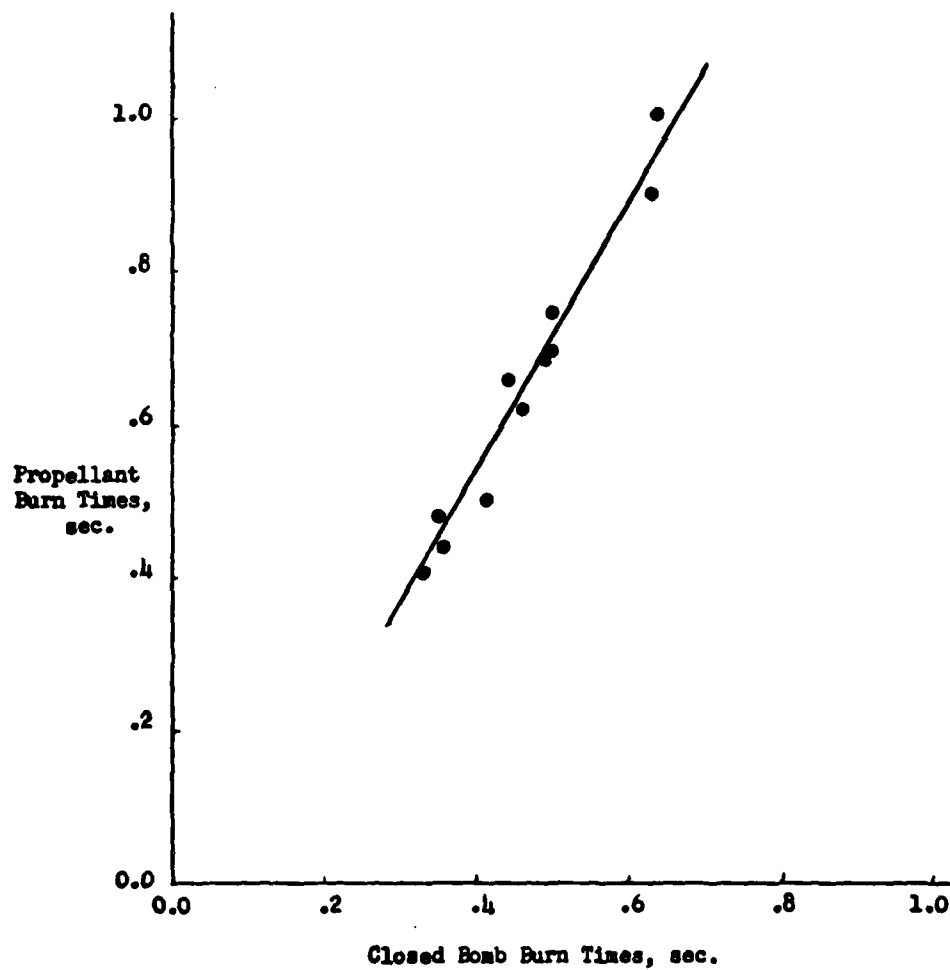
A B S T R A C T

Pyrotechnic Flame Modeling for Sodium D-Line Emissions

by
David R. Dillehay
Thiokol Corporation
Marshall, Texas 75670

Radiative transfer theory was first applied to sodium D-line radiation in an illuminant flame by Douda to study line broadening at reduced pressure. A two-line radiative transfer model of a pyrotechnic illuminating flare flame has been developed for the general case including the effect of ambient atmosphere. The model predicts the spectral radiant flux of illuminant compositions based on sodium atom radiation and considers formulation, diameter, pressure, ambient atmosphere, and rate of magnesium reaction. The parameters of the radiative transfer theory were obtained from the calculated thermodynamic properties of the flame.

Computed spectra at various locations in the flare plume show that broadening and D-line absorption are functions of position along the plume axis. The computer program allows computation of spectral profiles at positions off the plume axis.

PYROTECHNIC FLAME MODELING FOR SODIUM D-LINE EMISSION

The sodium D-line radiation in illuminant spectra is the major source of light. Radiative transfer has been proposed as the mechanism by which the sodium D-lines are broadened in the flare plume. Douda provided the initial work relative to radiative transfer, dealing with the special case of low pressure and no interaction with the ambient atmosphere. Expansion of the radiative transfer theory to the general case is the subject of this report. Since the theoretical background has been reported in detail previously (1, 5), the emphasis of this report will be to describe the plume modeling that has been applied to the general solution. A brief review of the theory is provided in the Appendix.

The model must take into consideration the mixing of the atmosphere into the flare plume and the radiant energy losses along the plume axis. Photographs of flare plumes were used to establish some of the physical constraints on the plume. Once fixed, however, the formulae are not adjusted for special cases, but provide, in fact, a general solution. Figure 1 shows the model of the illuminant plume that was derived. The outer boundaries are representative of the total interaction of the combustion gases with the ambient atmosphere. For the purposes of this paper the ambient atmosphere will be air. The overall length of the visible plume is defined as d/F, where d is the diameter of the candle in centimeters and F is a parameter relating the fraction of fuel in the air at which the computed temperature is 1800°K. Figure 2 shows the variation of F with % magnesium. The shift in F thus causes the plume to lengthen as the % magnesium increases. Since the length is also a function of d, the plume length increases as the candle diameter increases. The line marked d_{CL} is established by fitting a

parabola with vertex at A through point B. The line marked d'_{CL} is a mirror image of the parabola. These lines represent the inner boundaries of the air mixing with the plume. It is defined as the 0% air boundary for air entering the plume by turbulance or diffusion from one direction, i.e. air entering the plume from the left side of Figure 1 will have d_{CL} as the 0% air boundary. It was felt that the air would be rapidly introduced near the surface due to turbulance but that diffusion would be the primary means of transport within the inner regions of the plume. Accordingly, the air was introduced parabolically into the plume, as shown in Figure 3. Above the cross-over point of d_{CL} and d'_{CL}, the % air is determined as a sum of the mixing parameters. Using the NASA-Lewis SP-273 program for complex equilibra, the concentrations and temperatures were computed for the mixing of air with the combustion products at 10% intervals. By computing the % air at each position within the flare plume and interpolating between data points, it is possible to establish a temperature profile and a sodium atom concentration as a function of position within the plume. The Voigt parameter $\underline{a}$ was also calculated as a function of % air mixed. Using these computed data, it is possible to calculate a radiant energy profile for each wavelength of interest. The integrated area under the radiant power curve is then plotted against wavelength to develop the computed spectrum. Figure 4 shows a typical computed spectrum using only these data.

To provide a correction for the temperature loss along the plume axis, it was assumed that the temperature would drop parabolically along the centerline from the computed adiabatic temperature to 1800°K at d/F. Then the peak temperature at the optimum percent air was assumed to drop 200°K over the same distance.

The temperature profile was then fit to a parabola using the corrected peak temperature position as the vertex and either the outer air boundary or the centerline as the reference value. The correction of the temperature profile to account for radiant energy loss gives a computed spectrum as shown in Figure 5. This technique was used to approximate a radiant energy loss. The model may eventually be programmed to compute a radiant energy loss based on a step-wise progression along the plume axis. Figure 6 shows the spectra computed for three positions along the plume axis. All were for a 3 cm. diameter flare. These spectra show responses similar to experimental data reported by Blunt (7).

To test the model for response to various parameters, a number of spectra were computed. Figure 7 compares the spectra of four different diameter flares computed at a height of one diameter above the flare surface. The separation of the peaks has been reported to be proportional to the square root of the candle diameter (6). Figure 8 shows the relationship of computed peak separation to the square root of the diameter. The correlation coefficient was 0.9985.

Computations were made at 45% magnesium and at 50% magnesium. The spectra are shown in Figure 9. Each spectrum was calculated at a level of 10 cm. above the surface of a 3 cm. diameter flare. The area under the radiant power curve is greater for the 50% magnesium formulation than the 45% magnesium formulation. This is in the direction expected from experiments.

The spectra shown thus far were all calculated at a position along the centerline of the plume. At positions off the plume centerline, the optical path length, the temperature and specie concentrations are altered. Computation of spectra at positions off the centerline show changes in the spectral profile. See Figure 10.

The overall agreement of the computed spectra with experimental data is encouraging for the ultimate verification of the model. The model will then provide a useful tool for evaluating binders and additives and will provide a better understanding of the processes occurring in the flare plume. The complexity of the spatial distribution of energy points out the need for consistent definition of all parameters when taking or reporting spectra.

References

1) B. E. Douda, Radiative Transfer Model of a Pyrotechnic Flame, RDTR No. 258 Naval Ammunition Depot, Crane, Indiana, Sept. 1973. AD-769237

2) D. G. Moursund and C. S. Duris, Elementary Theory and Application of Numerical Analysis, McGraw-Hill Book Company, New York, 1967, p. 191.

3) S. Gordon and B. J. McBride, Computer Program for Calculation of Complex Chemical Equilibrium Compositions, Rocket Performance, Incident and Reflected Shocks, and Chapman-Jouguet Detonations, NASA-SP-273, Lewis Research Center, 1971

4) D. R. Dillehay, "Illuminant Combustion in Inert Atmospheres", Proceedings of the Fourth International Pyrotechnic Seminar, Sponsored by Denver Research Institute, Denver, Colorado, 1974

5) D. R. Dillehay, "Pyrotechnic Flame Modeling", Proceedings of Pyrochem International 1975, DDC No. AD-B006100L

6) Private communication with D. C. A. Izod, RARDE - Langhurst

7) R. M. Blunt, Spectral Distribution of Different Regions in Illuminating Flare Flames, RDTR No. 292, January, 1975

Figure 1

Plume Model
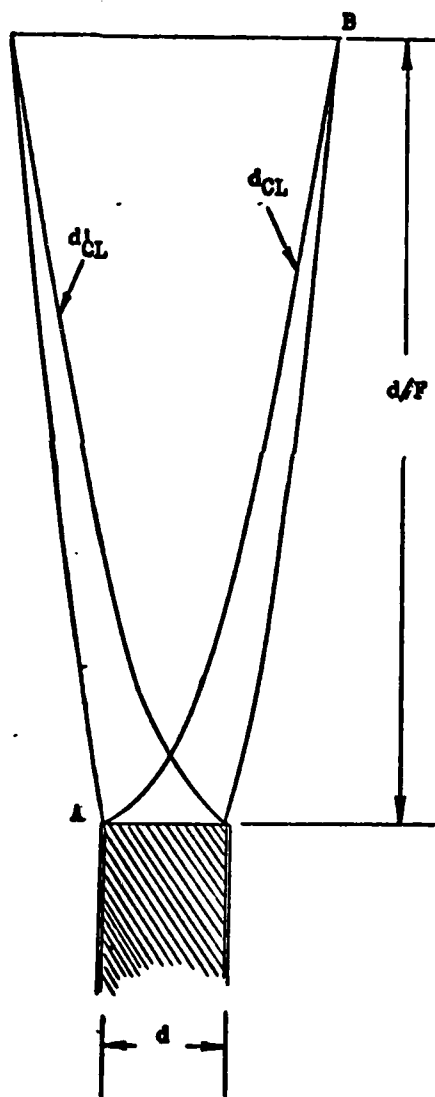
Figure 2

Fuel Fraction versus Temperature
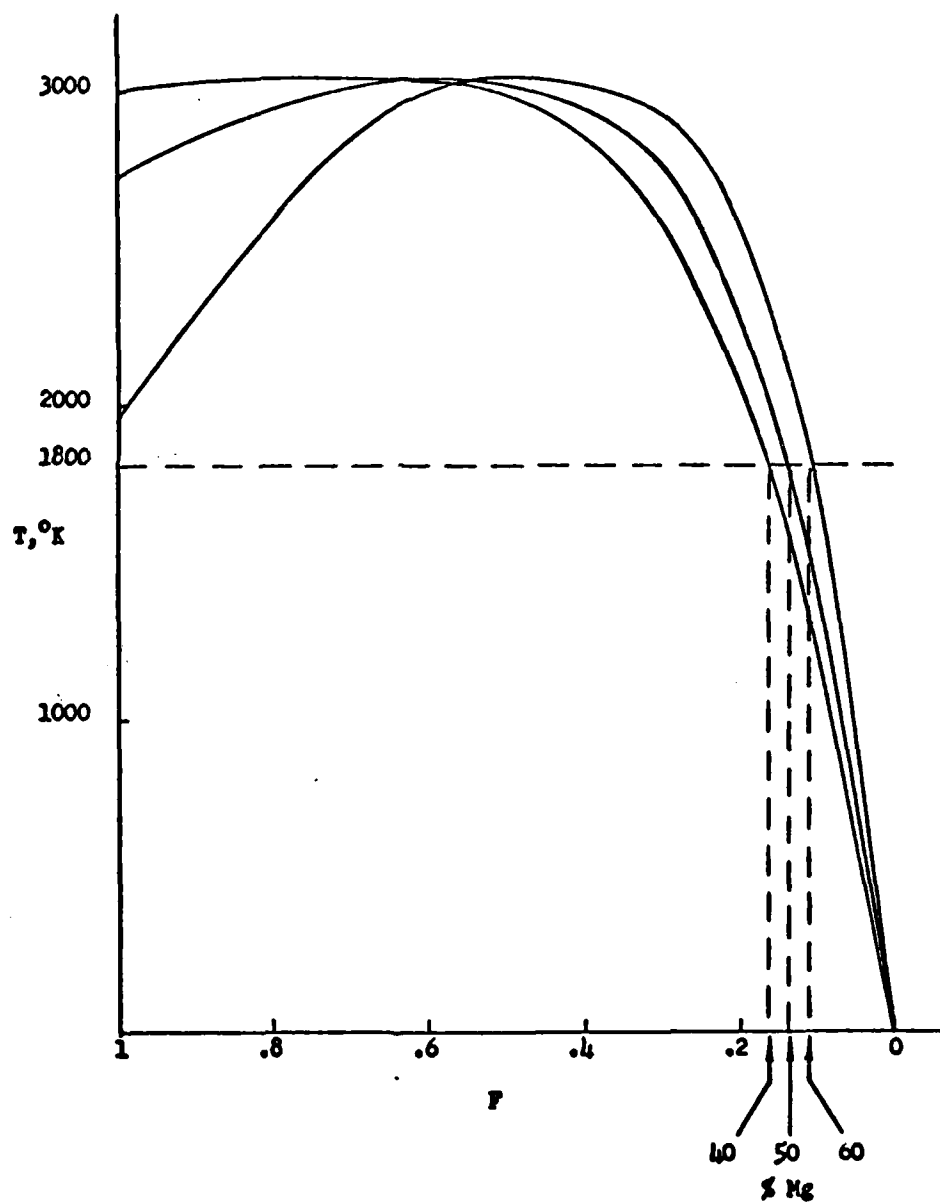
Figure 3

Mixing of Air at the Crossover of d_{CL} and d_{CL}^1

132
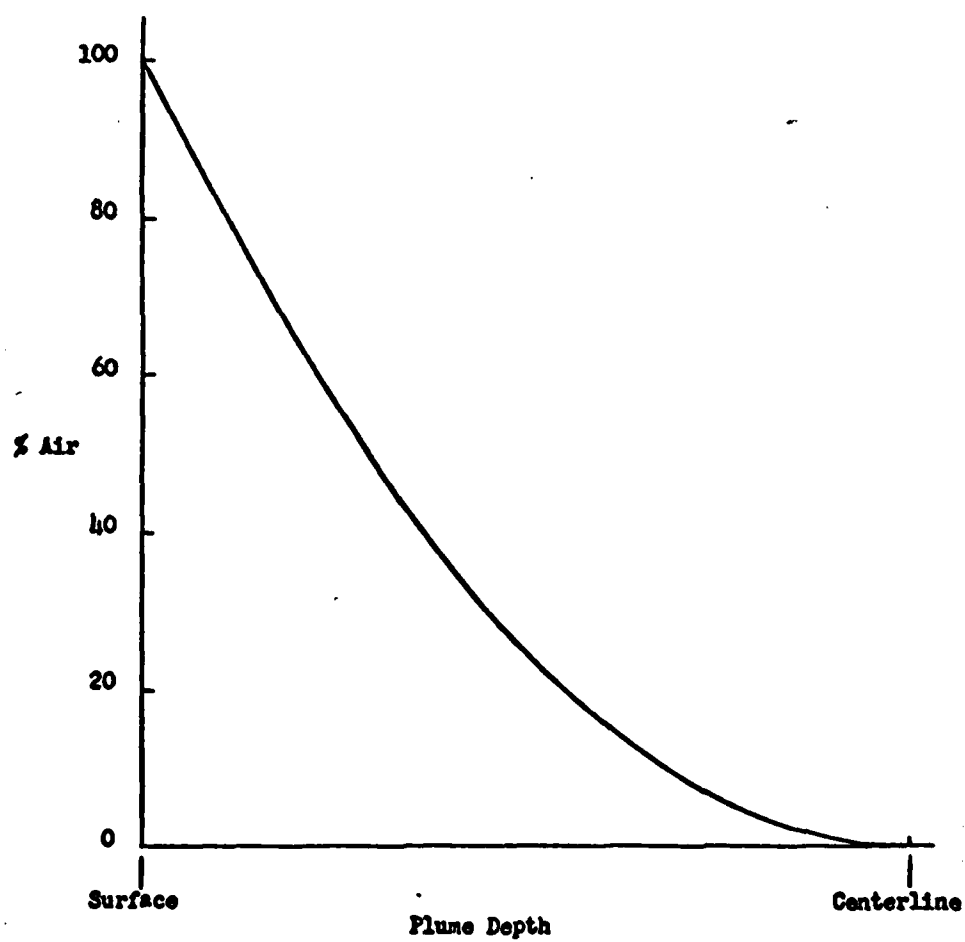
Figure 4

Normalized Computed Spectrum

3 cm. Diameter - 3 cm. Above Surface - 45% Mg
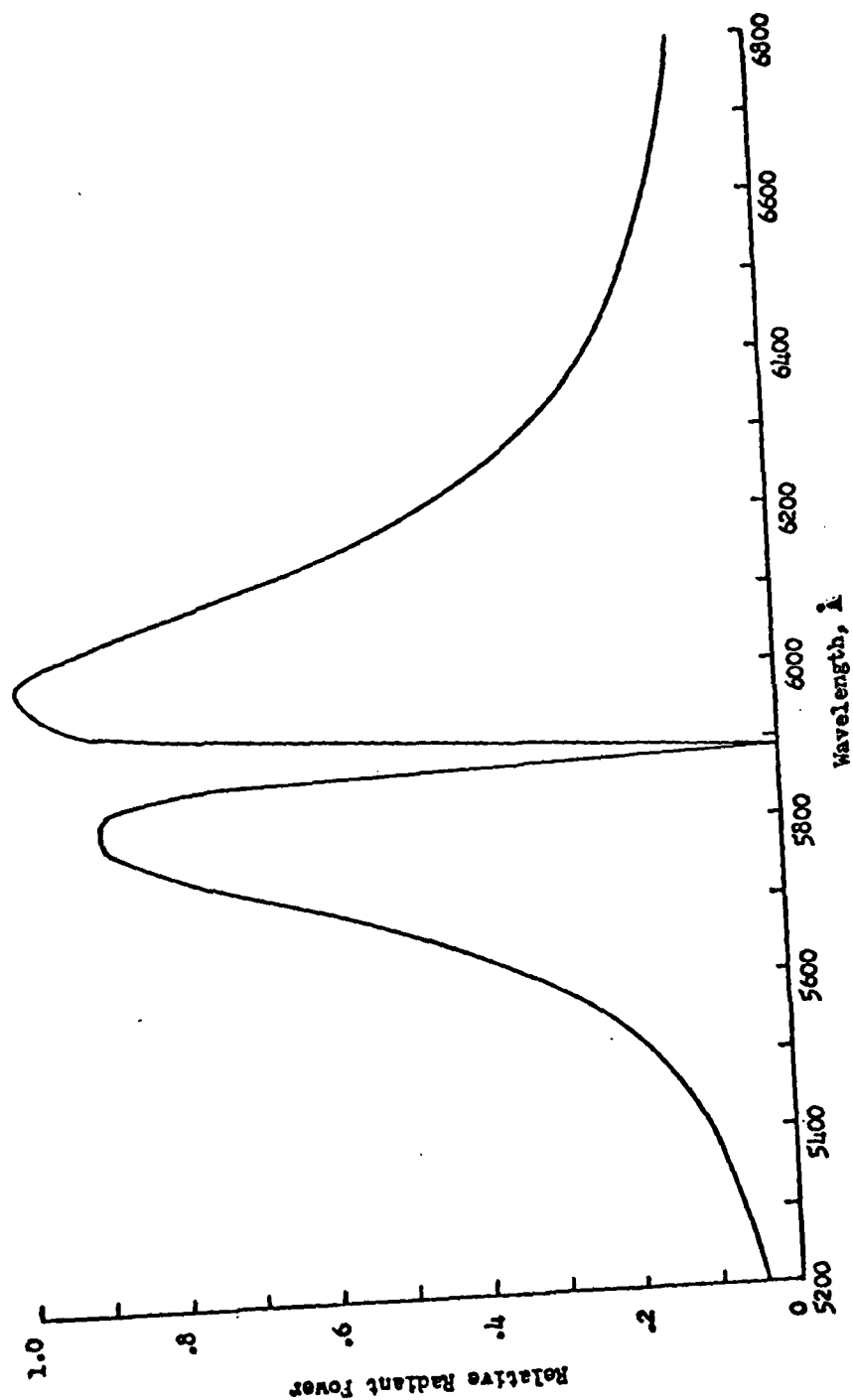
Figure 5

Computed Spectra With and Without Temperature Correction

3 cm. Diameter - 18 cm. Above Surface

——— Without Temperature Correction

– – With Temperature Correction

134
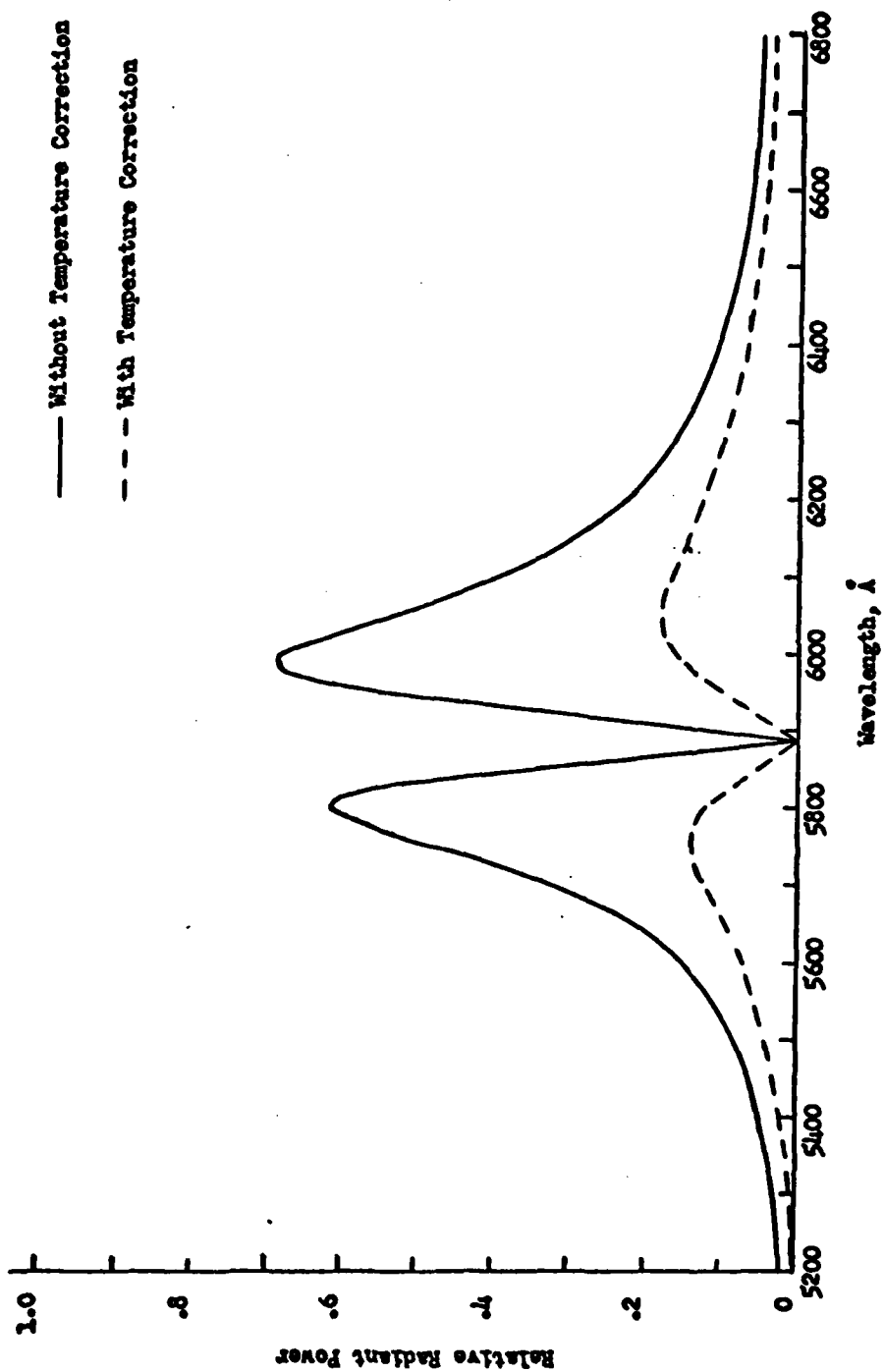
Figure 6

Computed Spectra at Three Heights Above Surface

3 cm. Diameter — With Temperature Correction
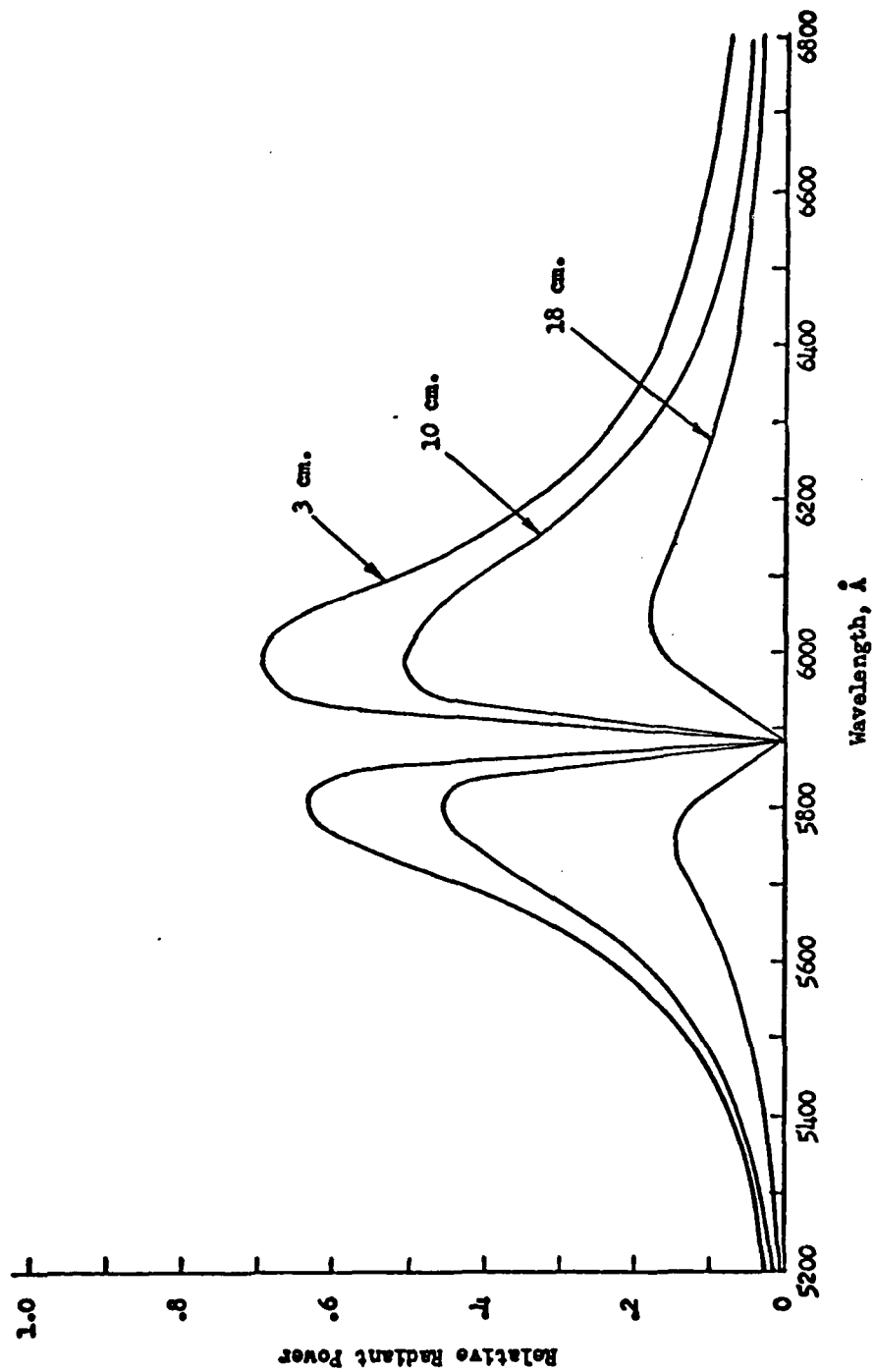
Figure 7

Computed Spectra for Four Different Diameter Flares

One Diameter Above Surface - 45% Mg
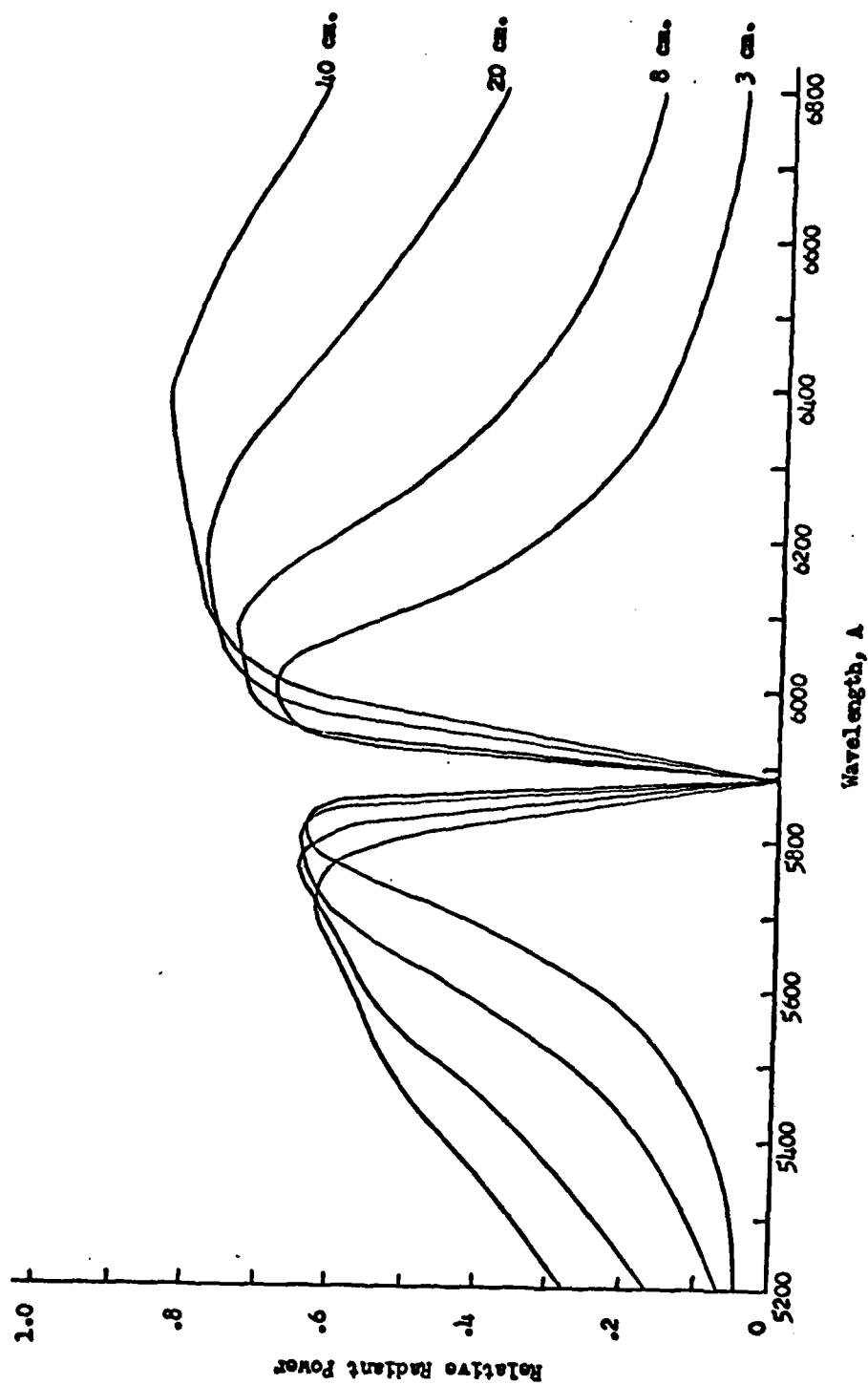
Figure 8

Correlation of Peak Separation with $\sqrt{D}$
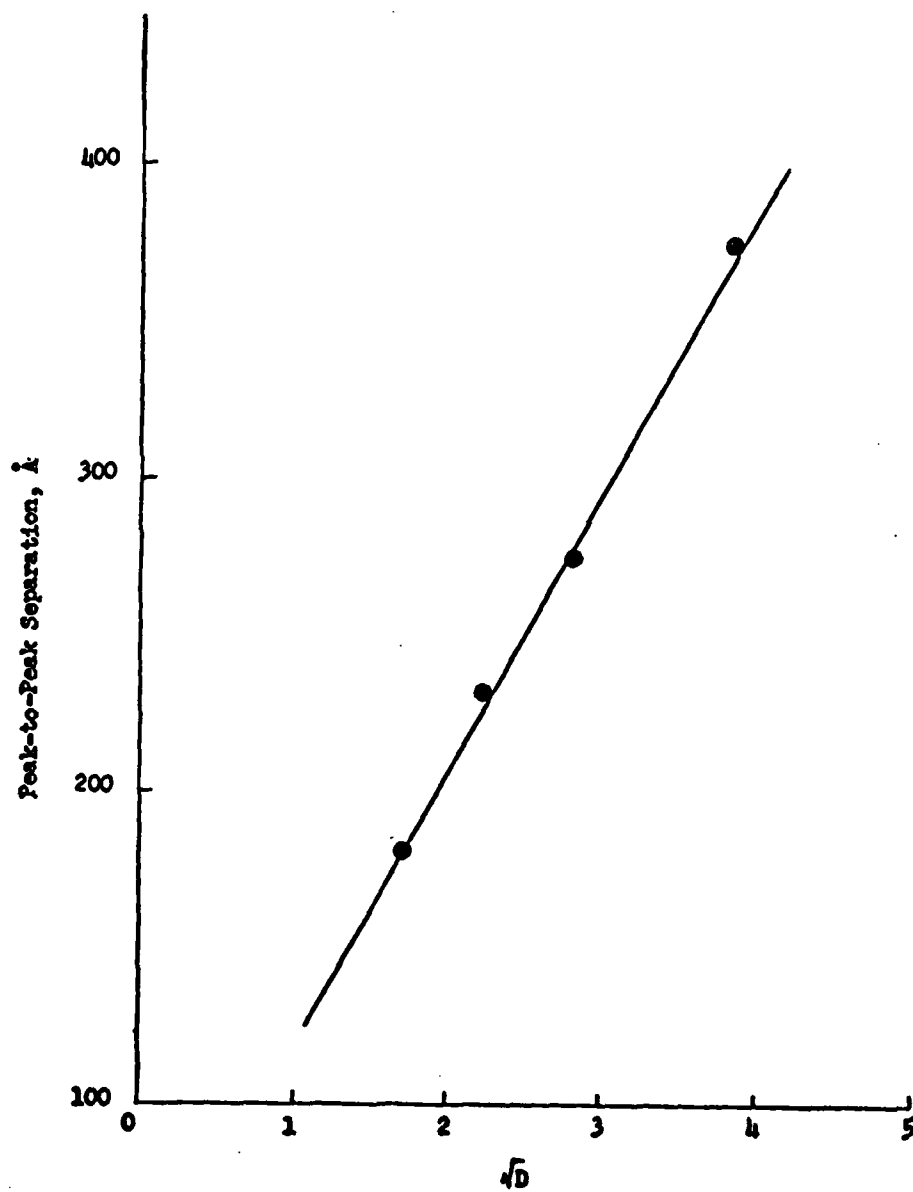
Figure 9

Computed Spectra for 45% and 50% Mg

3 cm. Diameter - 10 cm. Above Surface

138
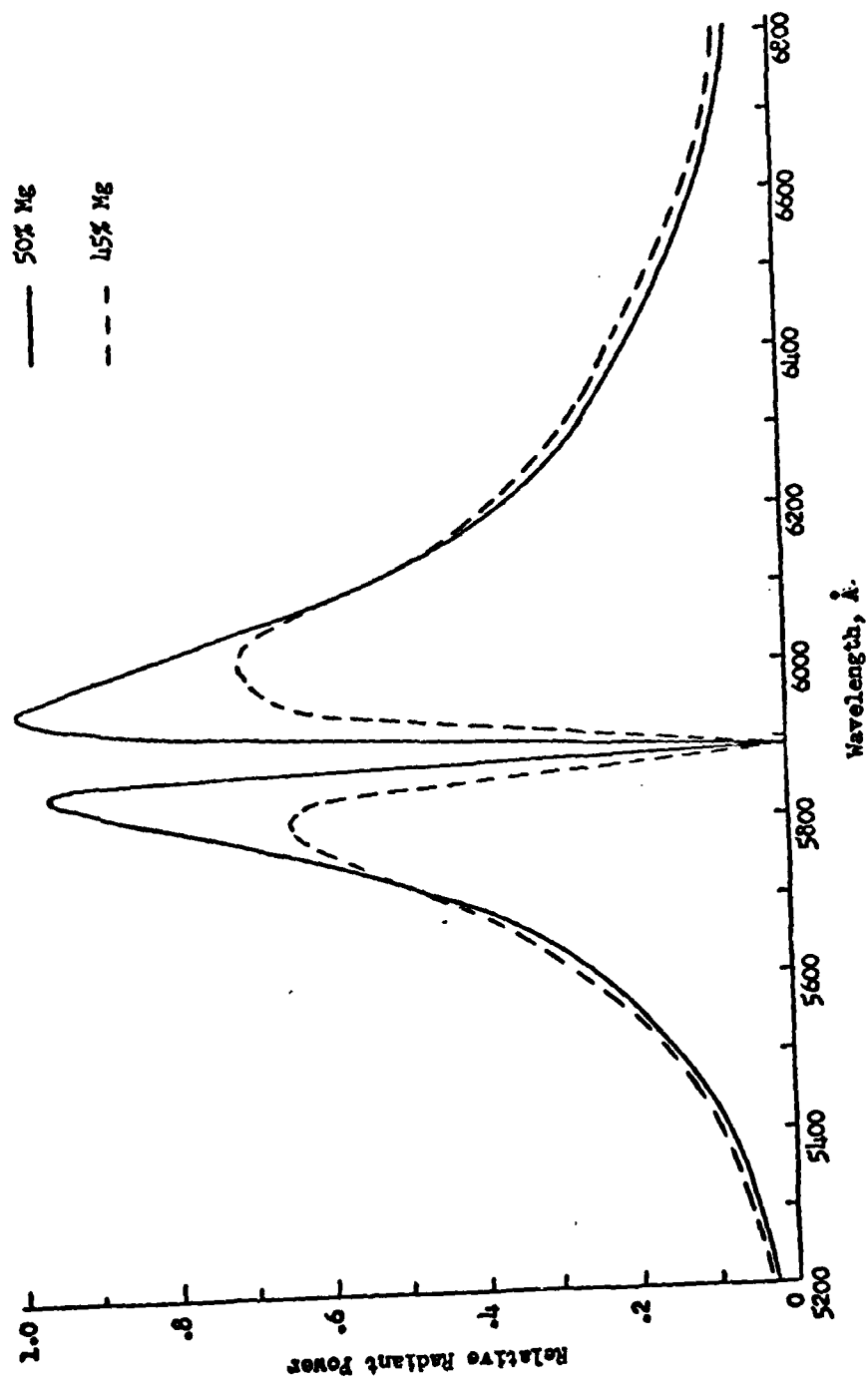
Figure 10

Normalized Computed Spectra

3 cm. Diameter — 10 cm. Above Surface
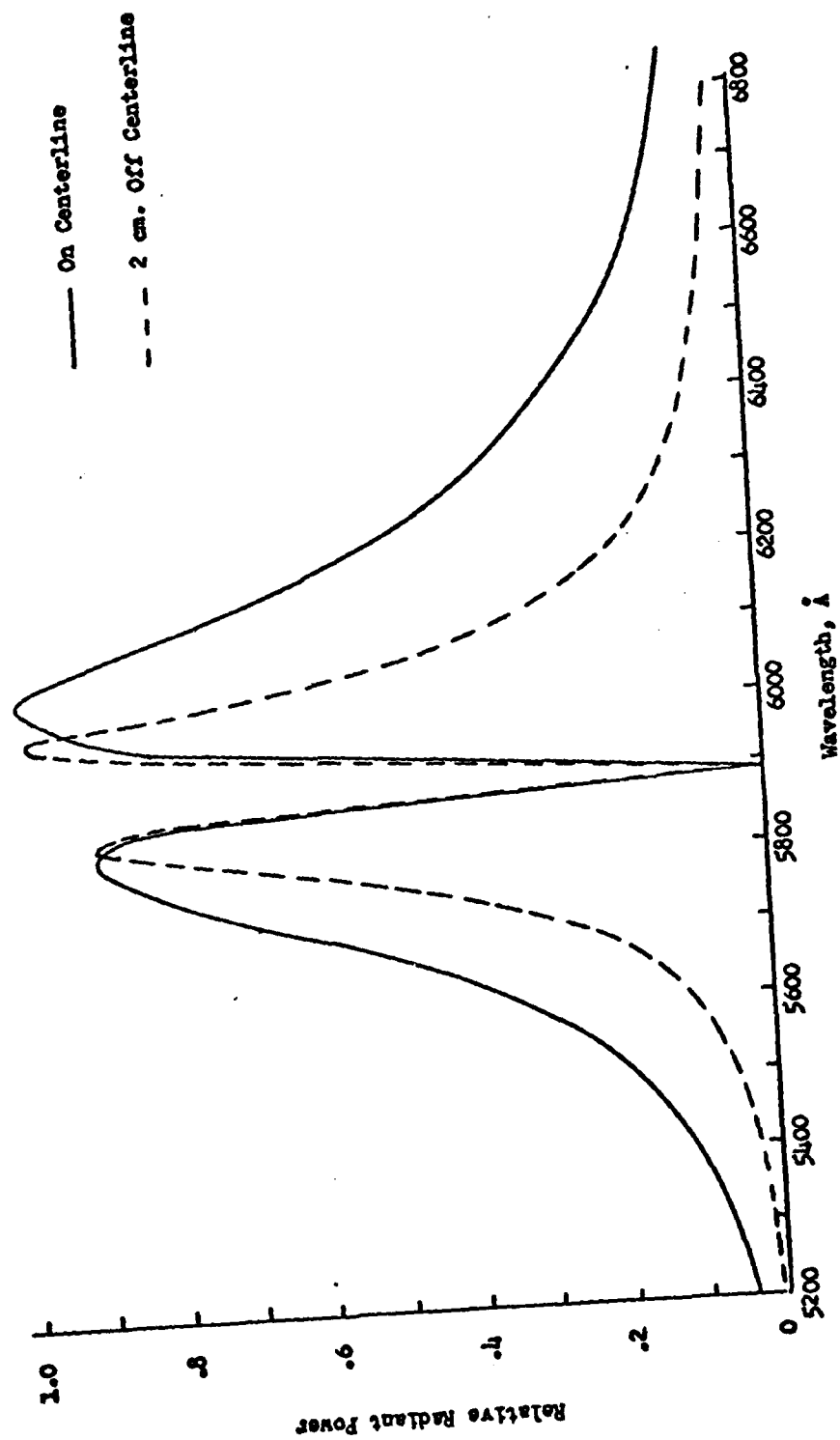
APPENDIX

TABLE OF SYMBOLS

a - Voigt parameter

A_{21} - Einstein coefficient for stimulated emission

B_{12} - Einstein absorption coefficient

B_{21} - Einstein induced emission coefficient

C_{21} - Rate of collisional deactivation

$B_\nu(T')$ - Planck function

c - Velocity of light

e - Elementary charge

f - Absorption f-value (oscillator strength = 1.0 for sodium doublet)

h - Planck's constant

I - Spectral intensity

k - Boltzman's constant

m_e - Electron rest mass

N_A - Avagadro's Number

$\Re$ - Universal gas constant

$S_\nu(r)$ - Line source function

$\Delta\lambda_N$ - Natural line broadening half-width

$\Delta\lambda_L$ - Lorentz line broadening half-width

$\Delta\lambda_R$ - Resonance line broadening half-width

$\Delta\lambda_Q$ - Quenching line broadening half-width

$\Delta\lambda_D$ - Doppler line broadening half-width

$\Delta\nu_0$ - Doppler half-width

σ_L - Optical cross-section

λ_0 - Line center wavelength

r - Optical depth

$\Phi_{\nu\alpha}$ - Normalized spectral profile of the absorption coefficient

PYROTECHNIC FLAME MODELING THEORY

To characterize the mechanisms of luminous energy generation in a flare plume, it is necessary to solve the general radiative transfer equation,

$$I_{\nu_1} = I_{\nu_2} \; EXP \; [(r_2 - r_1)\Phi_{\nu a}/\mu] + \int_{r=r_1}^{r=r_2} [S_\nu (r) \Phi_{\nu a}/\mu] EXP [-(r_2 - r_1)\Phi_{\nu a}/\mu] \, dr \quad (1)$$

where r_1 and r_2 are the optical depth integration limits from front to rear of the plume respectively, I_{ν_1} and I_{ν_2} are the spectral intensities at optical depths r_1 and r_2, $S_p (r)$ is the line source function, μ is the cosine of the angle of observation, and $\Phi_{\nu a}$ is the normalized spectral profile of the absorption coefficient. To solve this equation, the plume is represented by the following model:

1) The plume is a homogeneous gaseous atmosphere with plane-parallel stratification.

2) The gas consists of sodium atoms which can be excited to the $^2P_{\frac{1}{2}}$ or $^2P_{\frac{3}{2}}$ level and molecular species which can interact to perturb the D-line radiation.

3) There is local thermodynamic equilibrium (LTE) governed by the local temperature.

4) Energy exchange by radiation leads to radiative equilibrium.

5) The refractive index of the medium is unity.

6) The radiation is unpolarized when emitted and remains unpolarized on its interactions with flare species.

7) The temperature gradient can be constructed from the thermodynamic equilibrium temperature calculated for a limited surface penetration of the ambient atmosphere.

8) The absorption profile $\Phi_{\nu a}$ and the number density of sodium atoms are dependent on the calculated thermodynamic equilibrium compositions defined by the limited surface interactions with the ambient atmosphere.

Using these boundary conditions, the radiative transfer equation can be simplified by assuming that the observed flux is emerging normal to the surface ($\mu = 1$) and there is no flux incident on the rear surface of the plume ($I_{\nu_2} = 0$) and for the LTE case $S_\nu (r) = B_\nu (T')$ where $B_\nu (T')$ is the Planck function for the flare temperature at optical depth r. The monochromatic emergent intensity is now

$$I_\nu = \int_{r=0}^{r=TT} \Phi_{\nu a} B_\nu (T') \; EXP \; (-r\Phi_{\nu a}) \, dr \quad (2)$$

where TT is the total optical thickness.

A numerical integration of Eq. (2) using Simpson's rule of 2m intervals (2) yields a theoretical relative spectral radiant power for a given wavelength, proportional to spectral emergent intensity. By calculating values over a spectral frequency range, a theoretical flare spectrum can be generated.

In order to solve the transfer equation simultaneously for both of the sodium D-lines, Douda replaced the individual dispersion profiles, Φ_{va} in Eq. (2) with a 2-line Voigt function. This function included a superposition of broadening mechanisms and is described as

$$V_a(\nu) = \pi^{-\frac{1}{2}} \int_{-\infty}^{\infty} \frac{a \, EXP(-y^2)dy}{(\nu-y)^2 + a^2} \tag{3}$$

where ν is the frequency measured from the line center in units of Doppler half-width and $\underline{a}$ is a dispersion parameter.

The dispersion parameter, $\underline{a}$, is obtained from the equation

$$a = \left[(\Delta\lambda_N + \Delta\lambda_L + \Delta\lambda_R + \Delta\lambda_Q)/\Delta\lambda_D \right](\ln 2)^{\frac{1}{2}} \tag{4}$$

where $\Delta\lambda_N$, $\Delta\lambda_L$, $\Delta\lambda_R$, $\Delta\lambda_Q$, and $\Delta\lambda_N$ are the natural, Lorentz (unlike particle), resonance (like particle), quenching, and Doppler line broadening half-widths, respectively. It is worth repeating the equations for each of these broadening elements since these are variables in the general solution.

The equation for sodium D-line natural broadening half-width is

$$\Delta\lambda_N(\text{Å}) = 10^8 \lambda_o^2 A_{21}/2\pi c \tag{5}$$

where λ_o is the line center wavelength (cm) and A_{21} is the Einstein coefficient for stimulated emission. For the sodium D-lines $A_{21} = .65 \times 10^8 \, sec^{-1}$. The value of $\Delta\lambda_N$ for the sodium D_2 line is 1.2×10^{-4}Å. This magnitude is negligible and could be omitted without introducing significant error.

The Doppler broadening half-width for the sodium D_2 line is given by

$$\Delta\lambda_D(\text{Å}) = 2 \times 10^8 \left[(2\Re \ln 2)^{\frac{1}{2}}/c \right]\lambda_o(T_o/M)^{\frac{1}{2}} \tag{6}$$

where M is the sodium molecular weight (g). The value of $\Delta\lambda_D$ is proportional to the square root of the flame temperature and thus varies from 0.0385 Å at 1915^oK to 0.0487 A at 3067^oK.

The collisional or Lorentz broadening half-width due to unlike species is given by

$$\Delta\lambda_L(\text{Å}) = 10^8 (\lambda_o^2/c)\sigma_L n_2 (8 k T_o N_A/\pi \mu)^{\frac{1}{2}} \tag{7}$$

where σ_L is the optical cross section (cm^2), n_2 is the number density of perturbing species (cm^{-3}), N_A is Avagadro's number, and $\mu = (mM/(m+M))$, the reduced mass. If the mean relative velocity of colliding species $(cm \cdot sec^{-1})$ is

$$\bar{v}_j = (8k\,T_0 N_A / \pi \mu)^{\frac{1}{2}} \tag{8}$$

where j is the species index, Eq. 7 can be written.

$$\Delta \lambda_L (\AA) = 10^{-8} (\lambda_0^2/c)\,\sigma_L\,n_2\,\bar{v}_j \tag{9}$$

Using a value of $60 \times 10^{-16}\ cm^2$ for σ_L, the value of $\Delta \lambda_L$ ranges from $0.022\AA$ to $0.043\ \AA$ without accounting for interactions of the plume with the ambient atmosphere.

The reasonance broadening half-width can be derived from

$$\Delta \lambda_R (\AA) = [(6 \times 10^{8})\,e^2\,(N_0 \lambda_0^3)] / (4 \pi^2 c^2 m_e) \tag{10}$$

where e is the elementary charge $(cm^{\frac{3}{2}} \cdot gm^{\frac{1}{2}} \cdot sec^{-1})$, m_e is the electron rest mass (gm), and N_0 is the number density of sodium atoms. Resonance broadening of the sodium D-lines is the largest factor in the determination of the a parameter. Without considering the effects of interactions with the ambient atmosphere, $\Delta \lambda_R$ ranges from $0.87\ \AA$ down to $0.47\ \AA$.

The equation for quenching line half-width can be expressed as.

$$\Delta \lambda_Q (\AA) = 10^{8} \lambda_0^2 C_{21}(T) / 2 \pi c \tag{11}$$

where C_{21} is the rate of collisional deactivation or the number of quenching collisions per second. Typical values for $\Delta \lambda_Q$, without considering interactions with the ambient atmosphere, range from $0.0016\ \AA$ to $0.0005\ \AA$.

Using the above equations to calculate values of the Voigt a parameter, it is found that a ranges from 15.5 to 9.7 for typical illuminant formulations. These values do not, however, take into consideration the interactions of the ambient atmosphere with the plume which will be considered later.

To evaluate equation (2), an equation is needed to determine the total optical thickness for a given point within the plume. Douda's equation for optical thickness assumed that the number density of sodium atoms had an average value inside the flame. From this, the optical thickness is

$$\tau(z) = (h \nu_0 / 4 \pi \Delta \nu_0)(N_1 B_{12} - N_2 B_{21}) Z \tag{12}$$

where B_{12} and B_{21} are the Einstein absorption and induced emission coefficients, N_1 is the number density of sodium atoms in the lower (^2S) state and N_2 is the number density of sodium atoms in the upper (^2P) state, and Z is the flame depth (cm). The Doppler half-width, $\Delta \nu_0$, is in units of frequency. It may be shown that N_2 is negligible compared to N_1.

144

For a general solution, a model of the physical plume was constructed. The temperature and sodium atom density were calculated as a function of position in the plume. Now, the total optical thickness from the surface of the plume to a point within the plume can be written as

$$TT = \int_0^{\mathfrak{Z}} \tau \, d\mathfrak{Z} \tag{13}$$

where $\mathfrak{Z}$ is the depth in the plume (cm). For the computer solution, τ is calculated for each increment of $\mathfrak{Z}$ and a numerical integration is performed to give TT as a function of depth.

Now, using the established model, it is seen that the Voigt $\underline{a}$ parameter must be recalculated across the plume as the average center value will not be descriptive near the surface. Tables 1A and 2A and Figures 1A and 2A show the effects of composition and mixing with air on the components of the $\underline{a}$ parameter.

A solution of Eq. 2 is now possible using the established model and calculated parameters. Programs have been written for a Monroe Model 1860 Programmable Calculator and for a Wang 720C Programmable Calculator.

T A B L E   1A

Voigt a vs % Mg. (8% Binder)

% Mg.	$\Delta\lambda_L$ (Å)	$\Delta\lambda_R$ (Å)	$\Delta\lambda_D$ (Å)	$\Delta\lambda_Q$ (Å)	a
30	.024246	.799604	.048009	.001590	14.317
35	.025425	.735226	.048448	.001440	13.098
40	.027609	.651220	.048235	.001330	11.742
45	.030162	.565430	.047594	.001256	10.443
50	.033145	.499932	.046061	.001225	9.660
55	.038169	.486084	.042010	.001251	10.417
60	.042506	.484792	.038925	.001056	11.303
65	.042752	.477084	.038303	.000505	11.313

Figure 1A.

VOIGT a VS. % MAGNESIUM
AT
8% BINDER

Voigt a

% Magnesium
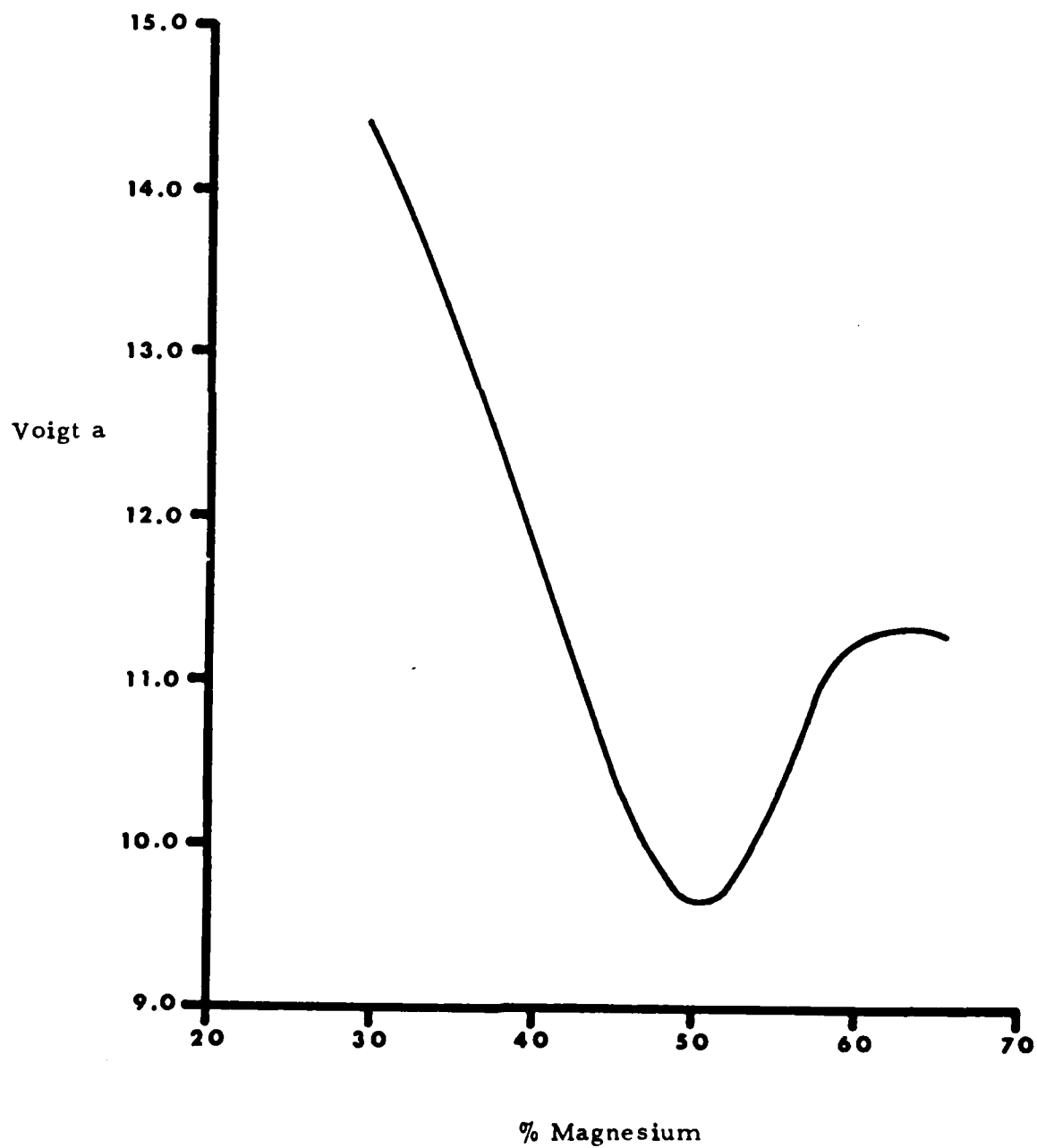
T A B L E   2A

Voigt $\underline{a}$ vs % Air (45% Mg, 8% Binder)

% Air	$\Delta\lambda_L (\mathring{A})$	$\Delta\lambda_R (\mathring{A})$	$\Delta\lambda_D (\mathring{A})$	$\Delta\lambda_Q (\mathring{A})$	a
0	.030162	.565430	.047594	.001256	10.443
20	.031027	.438486	.048264	.001517	8.127
30	.031754	.376574	.048358	.001667	7.061
40	.032732	.313504	.048243	.001822	6.009
50	.033966	.250442	.047887	.001975	4.981
60	.035558	.189738	.047118	.002131	4.021
70	.038222	.131984	.045127	.002335	3.186
75	.040719	.100349	.043065	.002506	2.778
80	.044400	.060270	.040213	.002752	2.227
85	.049483	.019424	.036607	.003085	1.640
90	.056736	.000493	.032103	.003539	1.579

148

Figure 2A.

VOIGT a
VS.
% AIR MIXED IN PLUME
(45% Mg AND 8% BINDER)
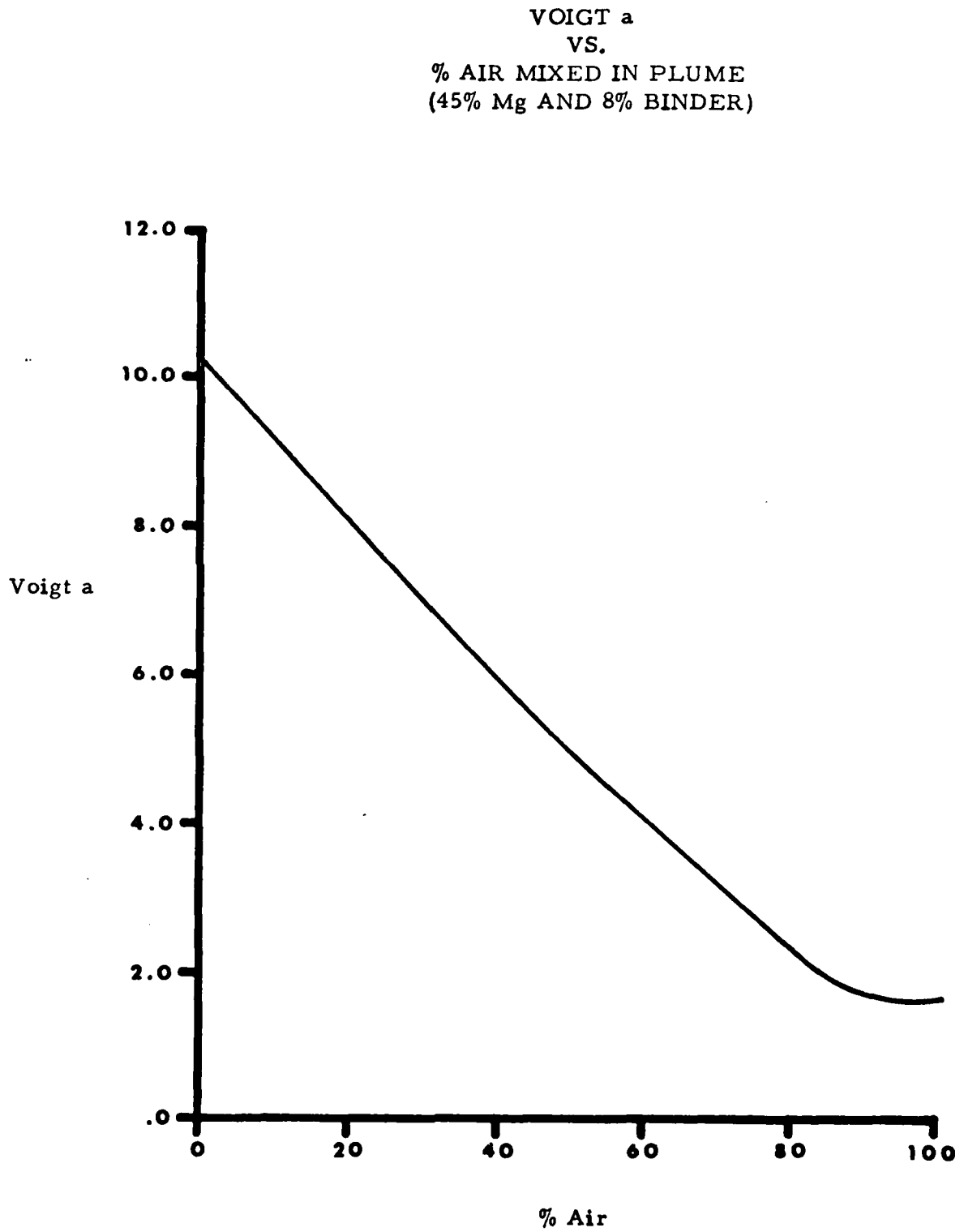
COMPUTERIZED RAPID-SCAN SPECTROSCOPY AT NAVWPNSUPPCEN, CRANE

Carl E. Dinerman
Applied Sciences Department
Naval Weapons Support Center, Crane, Indiana

ABSTRACT

This report contains a description of a computerized spectroscopic data acquisition and analysis system used to analyze flare emissions and smoke absorption. The system enables the computer generation of system corrected and signal averaged plots of spectral radiant intensity versus wavelength in the case of flare emissions, and the generation of plots of transmittance versus wavelength as a function of time in the case of smoke obscuration experiments.

The system consists of several commercially available components. A dual channel scanning spectrometer, presently set up for the 1.7 to 4.7 micrometer region, enables spectra to be obtained repetitively with scan times of 1, 50, 100, or 500 msec, and with a resolution (at the slowest scan times) of 0.004 micrometers. Two channels of spectroscopic data, a number of channels of radiometric data, and various synchronization pulses are recorded on a 14-channel analog tape recorder. The spectroscopic and radiometric data are then digitized, using as many as 2000 points per spectral scan per channel.

System corrected, absolute intensity spectra are generated in the computer by calculations involving the flare spectral data, spectra of a Globar source, and the radiometric data.

The system is flexible in that a variety of gratings, filters, and detectors make it possible to use this system in the near ultraviolet, visible, near, and middle infrared.

INTRODUCTION

Computerizing the handling of spectroscopic data generated from the Applied Sciences Department rapid scanning spectrometer is almost complete.

When finished, the capability to generate spectrometer system corrected, absolute intensity, signal averaged flare spectra, or the spectral transmittance of a smoke versus time, will exist.

The equipment and data acquisition procedures for flares and smokes will be discussed in the experimental section followed by the data digitization and computation processes for flares and smokes in the discussion section. Some examples of results to date will be presented in the results section. Finally, conclusions will be drawn.

EXPERIMENTAL[†]

Spectra are obtained with a Norcon 501 Rapid Scanning Spectrometer.[1,2] This is a dual channel grating instrument, which scans two spectral ranges at once (using two sets of exit slits, two detectors, and dual electronics). At present, it is being operated in the 1.7-3.2 μm (short wavelength scan) and the 3.0-4.7 μm region (long wavelength scan), for a total range of 1.7-4.7 μm. Spectra can be obtained repetitively with scan times of 1, 50, 100, or 500 msec. The time between scans is 25% of the scan time. For the results reported here, the 100 msec scan time was used. This means that spectra are 125 msec apart. Figure 1 shows a top view schematic of a typical arrangement used in the NAVWPNSUPPCEN Crane photometric tunnel for obtaining flare spectra. The flare is burned in the center of the tunnel and the emitted radiation is viewed by the spectrometer through a porthole. Also shown are the radiometers used for recording radiation in various spectral bands. The spectrometer field of view when focused at the center of the tunnel (a flare-to-entrance slit distance of 2.9 m) is approximately 10x2.5 cm. For smaller flares, a flare-to-entrance slit distance of 1.1 m is used, and the radiometer positions are adjusted accordingly. The spectrometer field of view then becomes approximately 3x0.5 cm. These radiometric data are used to convert the spectra from relative to absolute intensity. The radiometers consist of Hewlett-Packard Model 8334A Radiant Flux Detectors (with a field of view of 0.1 sr) and their mating electronic units, Model 8330A Radiant Flux Meters.[3]

Figure 2 shows the arrangement used for obtaining the spectral transmittance of smoke. Instead of a flare, the spectrometer views the radiation from a Glocoil[®] (a wirewound ceramic cylinder heated with 110V AC) as transmitted through the smoke.

[†]In order to specify procedures adequately, it has been necessary occasionally to identify commercial materials and equipment in this report. In no case does such identification imply recommendation or endorsement by the Navy, nor does it imply that the material or equipment identified is necessarily the best available for the purpose.
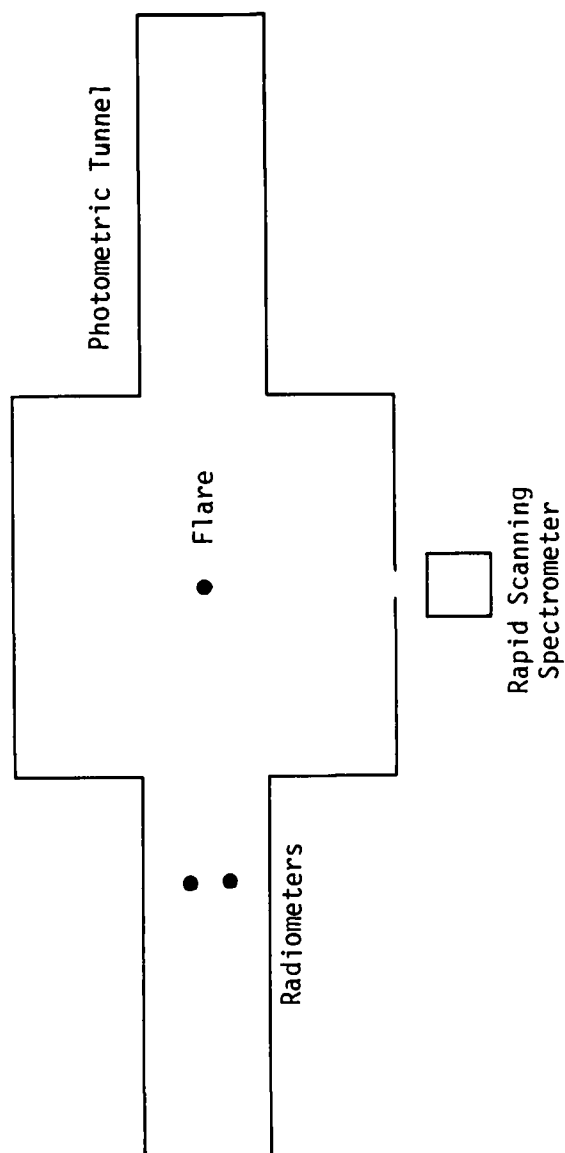
Figure 1. Typical Arrangement for Obtaining Flare Spectra. The flare is burned in the center of the NAVWPNSUPPCEN Crane photometric tunnel. The spectrometer views the radiation through a porthole, and radiometers view the radiation from one end of the tunnel.

152
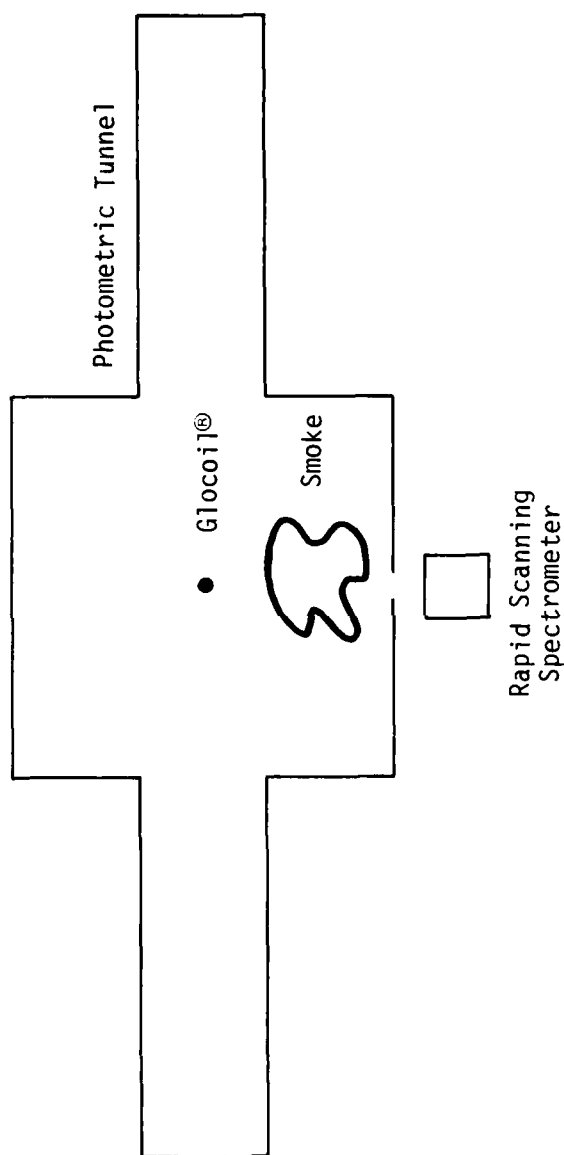
Figure 2. Arrangement for Obtaining Smoke Spectra. The spectrometer views a Glocoil®, which is a radiation source placed in the center of the tunnel. When the smoke is ignited between the Glocoil® and the spectrometer, the resulting reduction in transmitted radiation enables the spectral transmittance of the smoke to be calculated.

Figure 3 shows a view of the spectrometer (in background) and associated electronics (in left foreground). On the left electronics rack is one of the radiometers mentioned above. Figure 4 shows the interior of the spectrometer, detailing the rapid scanning mechanism (large wheel containing a series of corner mirrors), and the dual detectors (their liquid nitrogen dewars can be seen at extreme top of picture). The porthole is at the extreme right. Figure 5 shows two radiometers enclosed in shutter boxes and mounted on a tripod.

The outputs, in the form of analog voltages, of the spectrometer and the radiometers are fed into a Sabre III 14 channel analog magnetic tape recorder.[5] The spectrometer outputs consist of two channels of a series of spectra, as well as a series of synchronization pulses. Each series of spectra corresponds to one of the two spectral ranges mentioned above. Each radiometer output consists of a time-varying analog signal. Simultaneously, the spectra are displayed on a monitor oscilloscope for documenting by photography (see Figure 8), and the radiometric data are recorded on a strip-chart recorder. When flares are being studied, spectra from a Globar®[6] are also placed on the magnetic tape. It is a silicon carbide rod 5 cm in length and 0.5 cm in diameter, mounted in the spectrometer. It emits approximately graybody radiation. These spectra are needed in the calculations to be performed on the flare spectra as explained below, but are not used with smoke data.

DISCUSSION

The analog data are then digitized on a Data General Minicomputer.[7] As many as 2000 points per spectrum per spectral channel may be created, depending on the resolution of the spectrometer and the nature of the spectrum. The radiometric data also are digitized.

To summarize so far, the digital tape consists of data divided into general groups, one for each flare (or smoke). Within each group there are data corresponding to two series of spectra (up to a few hundred each), one series originating from the spectrometer short wavelength channel and the other series originating from the long wavelength channel. In each series of spectra each individual spectrum may have up to 2000 points. On a separate digital tape (for flares) are the radiometric data from a number of radiometers.

After the digitization process is completed, the digitized tapes are mounted on a Mohawk Data Sciences Corp. System 2400 computer[8] and sent over phone lines to a CDC 6600 computer[9] at a remote terminal, where new data tapes are created and stored. Calculations are done there using a program, also on tape.

A discussion of the calculations follows.

There are two subsections. The first subsection discusses calculations performed on flare spectra and radiometric data, and the second similarly for smoke spectra. Within each subsection an outline of the calculations is given, with a brief explanation of each calculation.

154
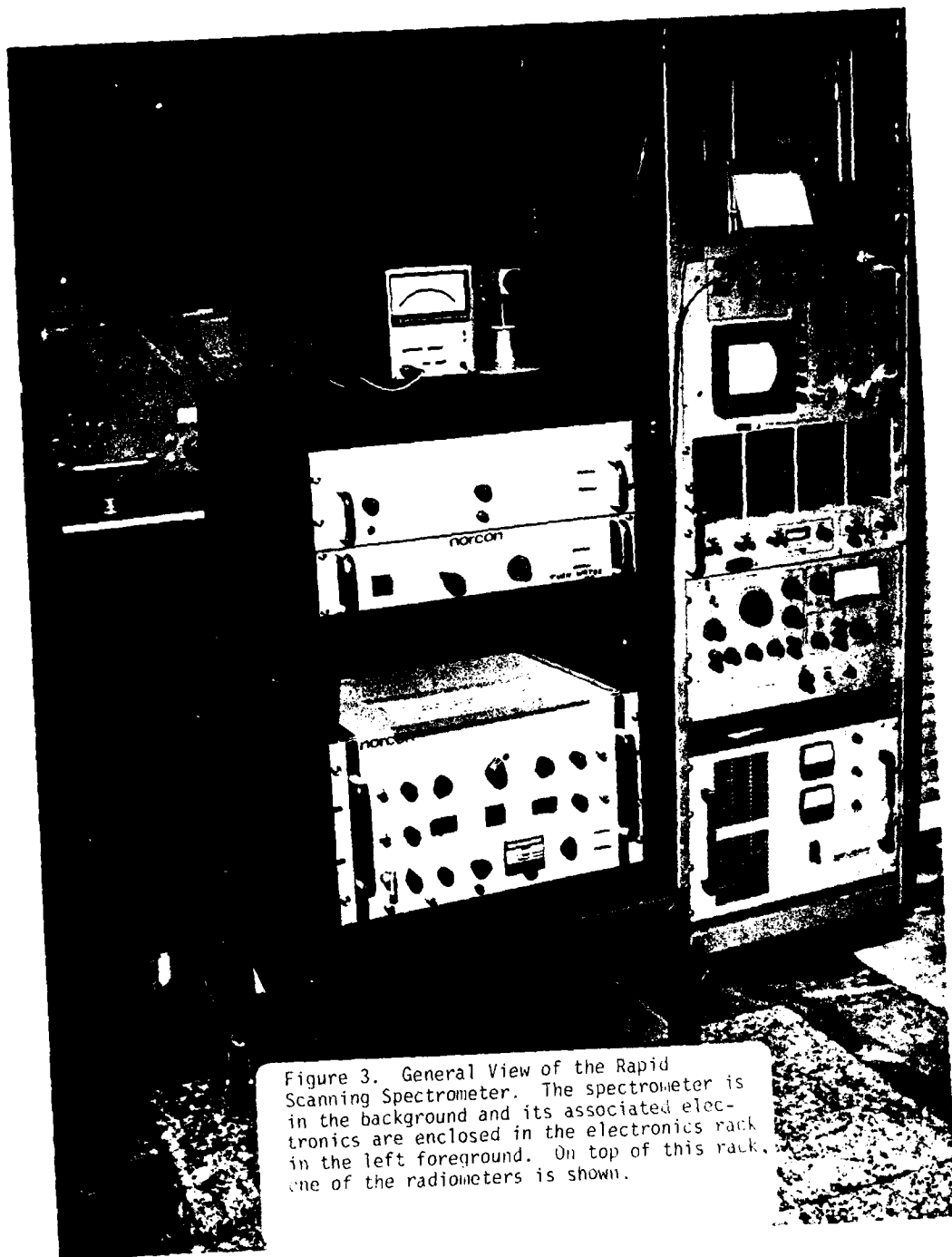
Figure 3. General View of the Rapid
Scanning Spectrometer. The spectrometer is
in the background and its associated elec-
tronics are enclosed in the electronics rack
in the left foreground. On top of this rack,
one of the radiometers is shown.
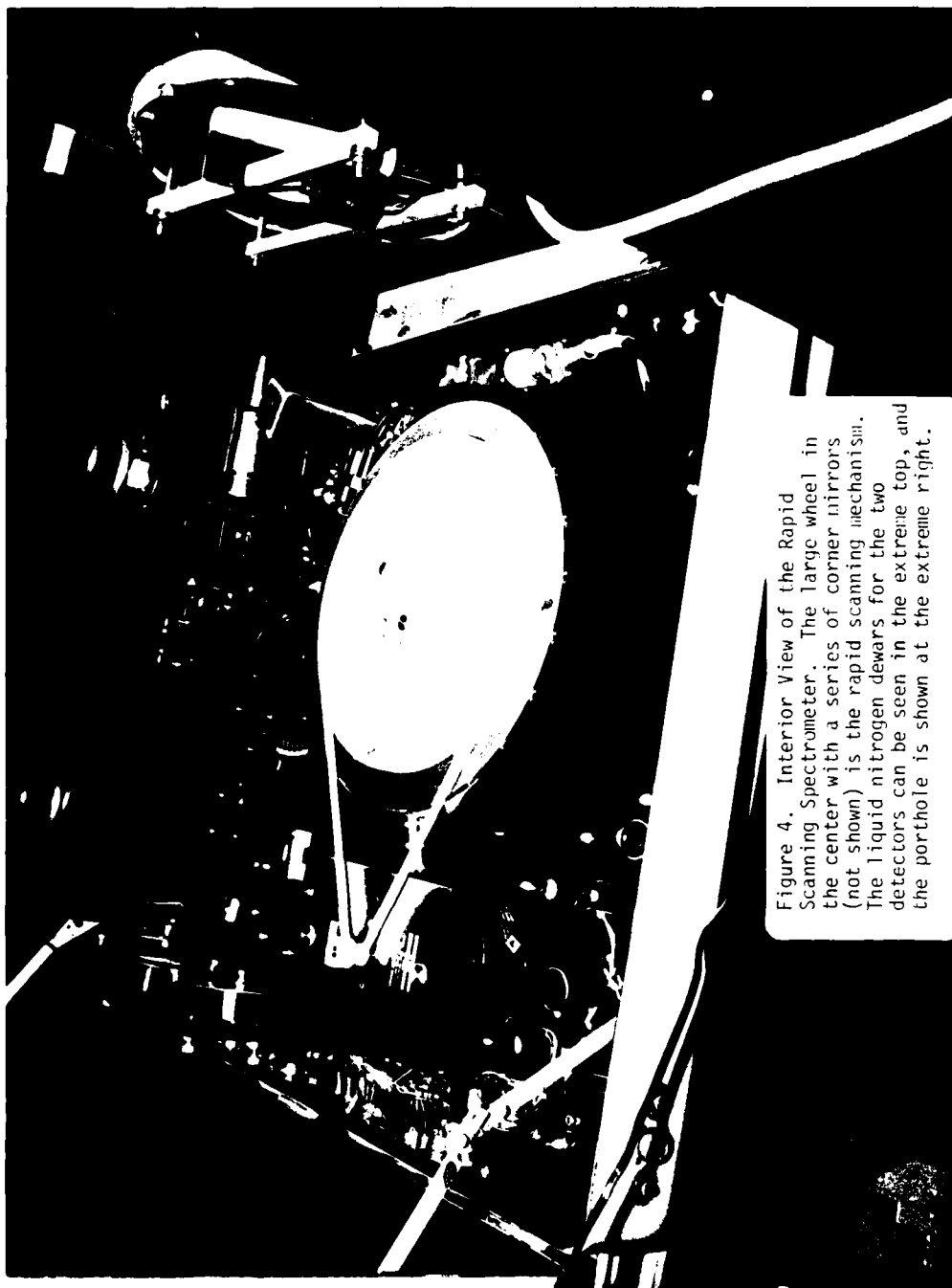
Figure 4. Interior View of the Rapid Scanning Spectrometer. The large wheel in the center with a series of corner mirrors (not shown) is the rapid scanning mechanism. The liquid nitrogen dewars for the two detectors can be seen in the extreme top, and the porthole is shown at the extreme right.

156
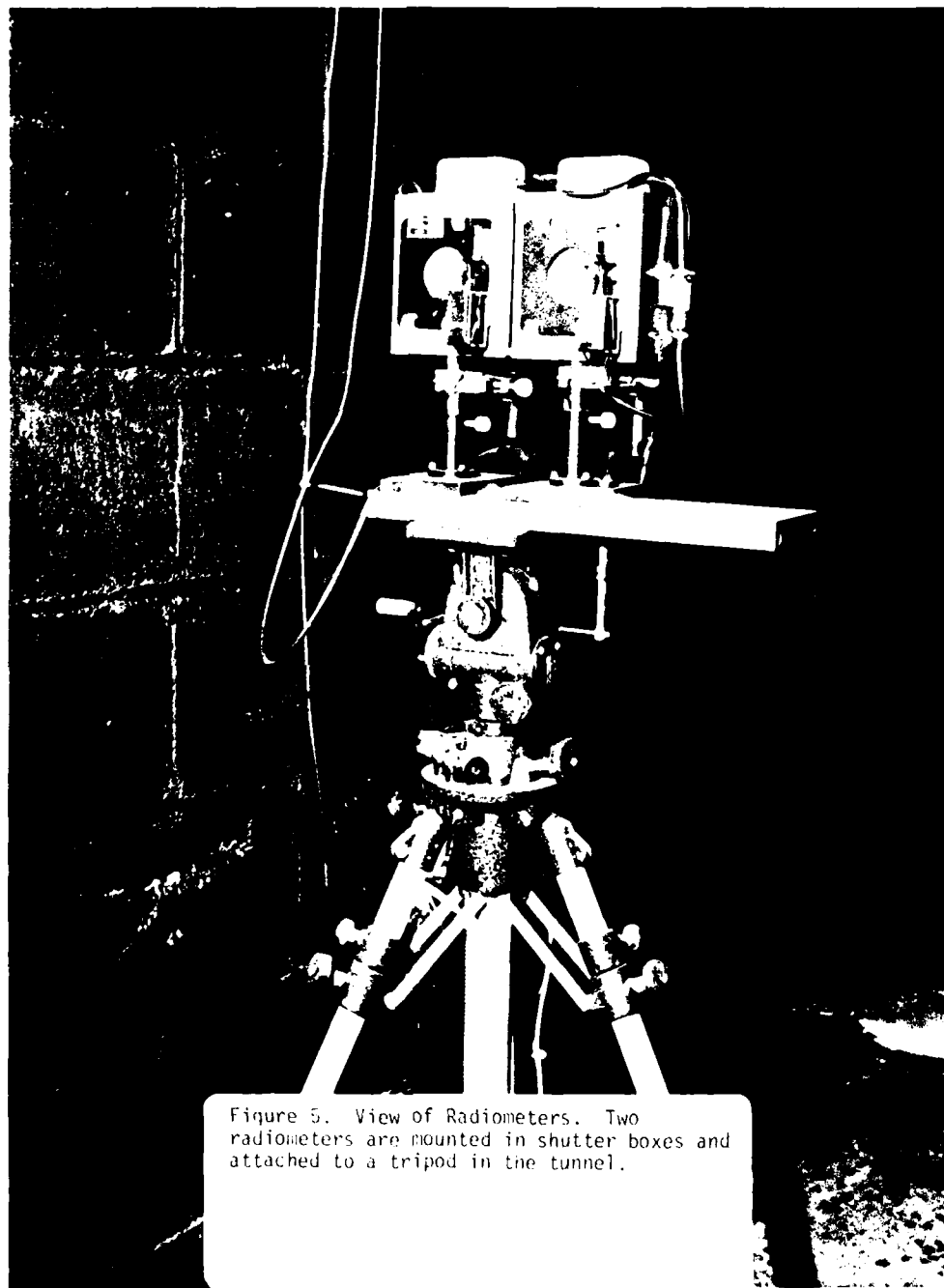
Figure 5. View of Radiometers. Two radiometers are mounted in shutter boxes and attached to a tripod in the tunnel.

Flare Data

1. Wavelength calibration
2. Correct Globar® spectrum for drift
3. Correct Globar® spectrum for atmospheric absorption
4. Correct flare spectra for drift
5. Correct flare spectra for spectrometer system response
6. Convert flare spectra to absolute intensity
7. Signal average all flare spectra

1. Wavelength Calibration

During digitization, known absorptions or emissions that are present in the flare spectra are related to their data points. For example, data point 376 (for each short wavelength spectrum) might correspond to a known peak at 1.870 µm. These peaks might be absorptions due to polystyrene film, or atmospheric water vapor and carbon dioxide, or other absorbing gases introduced into the spectrometer optical path. Emissions might be due to alkali metal species that may be present in pyrotechnic compositions.[2] Now a wavelength can be assigned to each data point. A linear interpolation-extrapolation is used, although in the future a higher order polynomial fit may be inserted if necessary. Figure 6 is an example of this wavelength calibration for a digitized Globar® spectrum. The short and long wavelength spectra have each been normalized to 1.00. No calculations, other than assigning wavelengths, have been performed on these data.

2. Correct Globar® Spectrum for Drift

In order to perform calculations involving division or multiplication of one spectrum by another, drift must be eliminated. The end points of any spectrum in the short and long wavelength scans should correspond to zero intensity (these points represent wavelengths beyond filter and/or detector cutoffs). Therefore, the actual signal at these points is equated to zero in each spectrum, with all other points in that same spectrum reduced by the same amount.

3. Correct Globar® Spectrum for Atmospheric Absorption

Eliminating the effects of atmospheric absorption from the Globar® spectra is necessary because the Globar® spectrum will be divided into the flare spectrum (step 5 below) as part of the correction for spectrometer system response; the result of this division must reflect the atmospheric absorption in the flare-detector path rather than a difference of absorption between the Globar®-detector path and flare-detector path. Rather than correct for this atmospheric absorption by introducing an atmospheric model, a series of linear interpolations was introduced, as seen in Figure 7. Justification for this is seen in reference 2, Figure 2.

4. Correct Flare Spectra for Drift

This is the same process as in step 2.

158
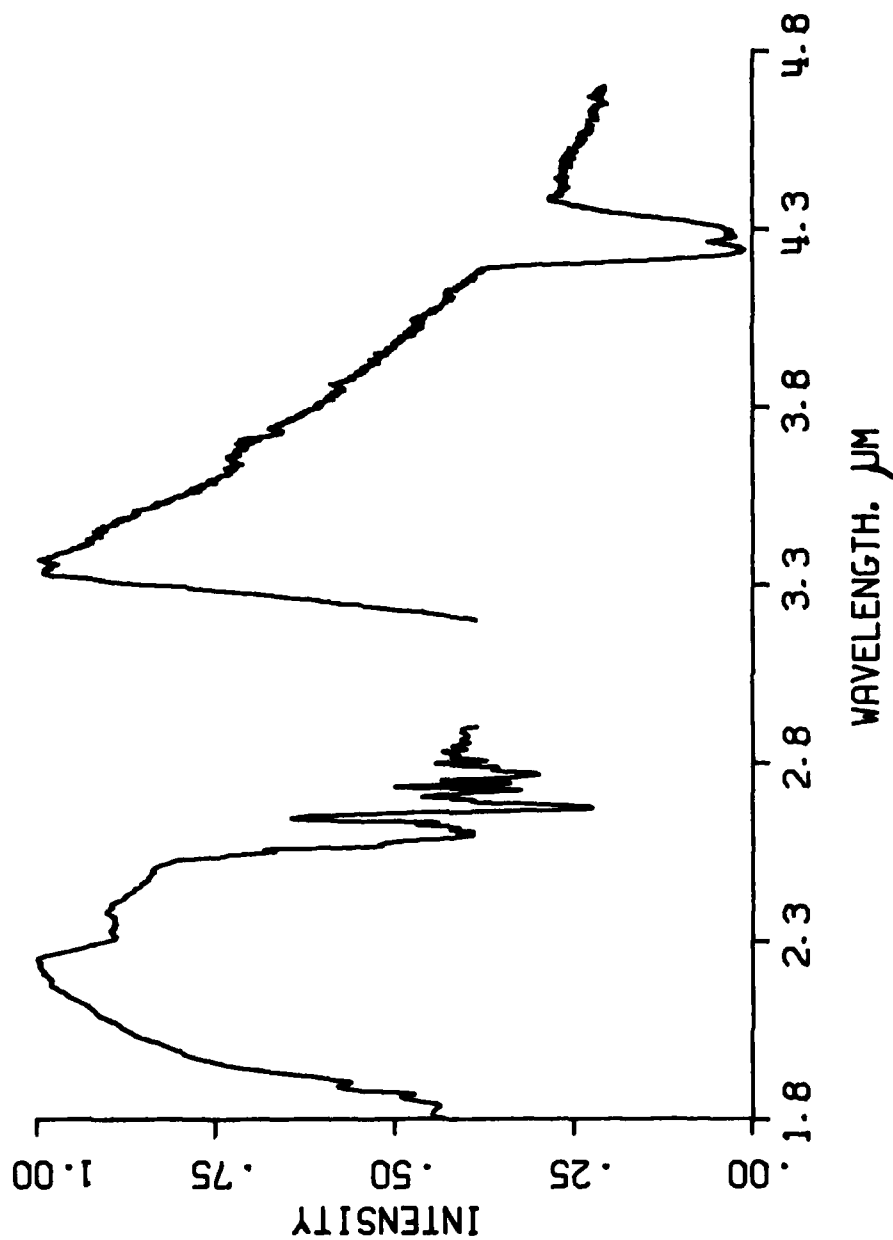
Figure 6. Globar© Spectrum. The short and long wavelength portions of this spectra have each been normalized to 1.00. No calculations, other than assigning wavelengths, have been made. The effects of detector, filter and grating responses can be seen, as well as the absorptions due to atmospheric water and carbon dioxide.
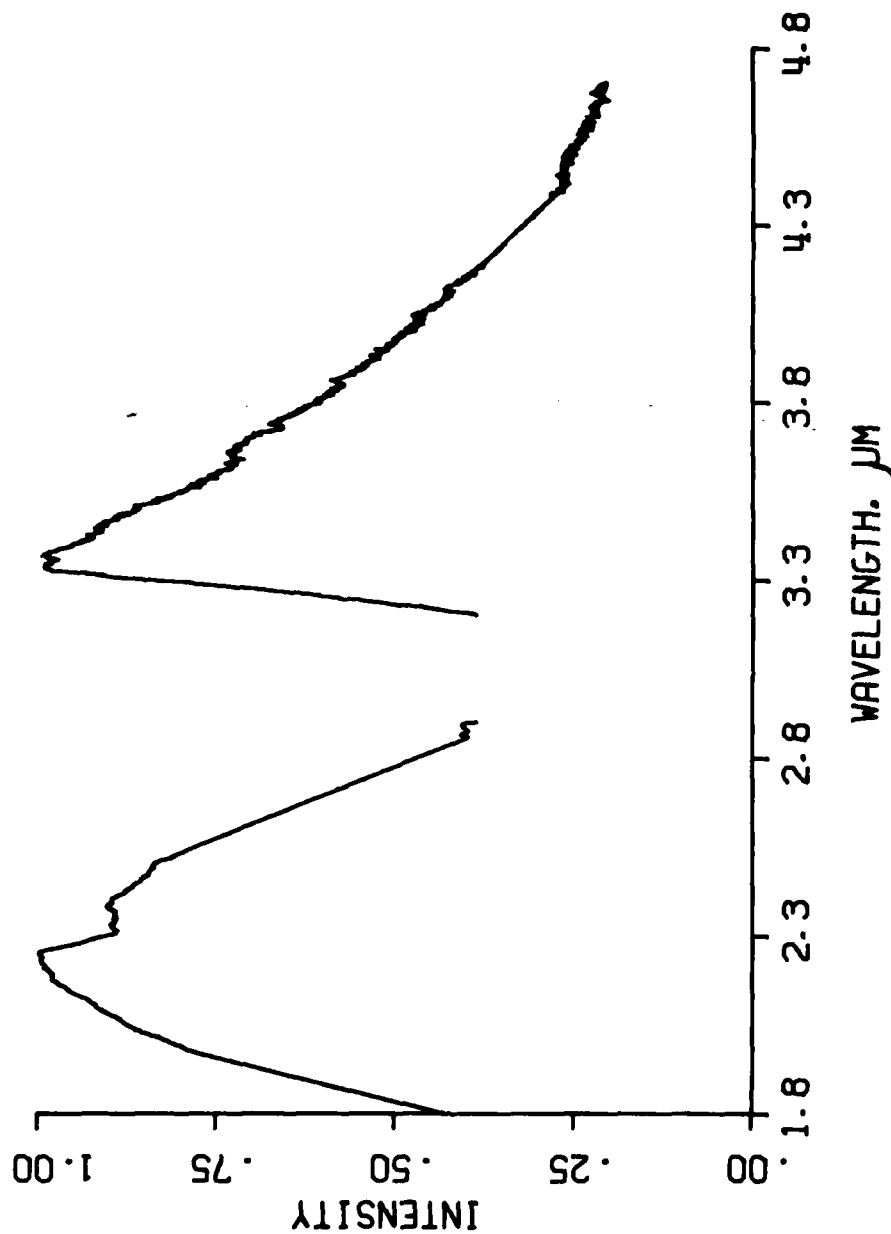
Figure 7. Globar® Spectrum Without Atmospheric Absorptions. A linear interpolation has been used to eliminate atmospheric absorptions from Figure 6, near 1.8, 2.7, and 4.3 μm. See text for details.

5.   Correct Flare Spectra for Spectrometer System Response

This is done by dividing each flare spectrum (both short and long wavelength) by the corresponding short or long wavelength Globar® spectrum from step 3. Next, this quotient is multiplied by the true Globar® curve, which is supplied by the manufacturer of the spectrometer.[1] This curve is that of a graybody with slightly varying emissivity.

6.   Convert Flare Spectra to Absolute Intensity

In order to do this, it is first necessary to calculate the output, in $W \cdot sr^{-1}$, from the radiometers, over the bandpass as a function of time, for example 2 ± 2.5 μm or 3-5 μm. This is done based on the radiometer calibration[+] and the radiometer output.

Each individual flare spectrum is integrated over the bandpass of a radiometer. This integral is then equated with the appropriate $W \cdot sr^{-1}$ value that corresponds approximately to the same time of the spectrum. This enables the intensity scale of each scan to be calibrated in $W \cdot sr^{-1} \cdot \mu m^{-1}$, thus calibrating the flare spectrum in absolute intensity terms.

7.   Signal Average All Flare Spectra

For each group of spectra (one group per flare burn), and within each of the two series of spectra per group, an average is taken of all the spectrometer system corrected, absolute intensity spectra, thus improving the signal-to-noise ratio.

After the above calculations are done, output tapes are created which may contain, for each flare, the two series of spectrometer system corrected, absolute intensity spectra, with the two signal averaged spectra. Also included are Globar® spectra and other information.

After the output tapes are created, the data can be sent back from the remote terminal to NAVWPNSUPPCEN Crane and printed on a line printer, converted to cards, or plotted on a Model DP-1-5 Complot® graphic plotter.[11]

Smoke Data

Smoke spectra are handled a little differently than the flare spectra. In the case of smokes, the spectra will consist of that of the

---

[+]This is done using a Barnes Engineering Co., Model 11-200T Blackbody[10] with a rated emissivity of 0.99±0.01. It was operated at 1273 K using a 0.33 cm^2 aperture, observing the usual precautions.

Glocoil®† that at first are at full intensity, then become weaker and may in fact approach zero as the smoke obscuration becomes heavier. After a period of time, the Glocoil® spectra return to full original intensity as the smoke dissipates.

1. Wavelength Calibration
2. Correct First Glocoil® Spectrum (Unobscured by Smoke) for Drift
3. Correct First Glocoil® Spectrum for Atmospheric Absorption
4. Correct the Glocoil® Spectra That are Obscured by Smoke for Drift

The above steps are basically the same as the corresponding steps in reduction of flare spectra.

5. Obtain Spectral Transmittance vs Time. The result of step 3 is divided into the result of step 4.

The output tapes for smoke would contain the spectral transmittance vs time for both short and long wavelength spectrometer scans for all smokes tested, as well as the Glocoil® spectrum, and other information.

RESULTS

Flare Data

Figure 8 shows an oscilloscope photograph (raw data) of emissions from a flare. The upper trace extends from 1.7-3.2 μm, and the lower trace extends from 3.0-4.7 μm. Figure 9 shows the corresponding spectrometer system corrected, signal averaged spectrum (averaged over 135 spectra). A 35 groove/mm grating, and 0.2 mm slits were used, producing a resolution of approximately 0.015 μm. With a 150 groove/mm grating and 0.2 μm slits, a resolution of 0.004 μm has been obtained. Figure 10 shows an expanded view of the emission in the 3.2-4.2 μm region. (This is primarily HCl emission.) Figure 11 and Figure 12 show, in a different flare from Figures 9 and 10, the effect of signal averaging in increasing the signal to noise ratio. Figure 12 is the result of averaging 30 scans such as Figure 11.

Smoke Data

Results for smokes have not yet been processed through the computer.

CONCLUSIONS

Eventually, this system will be generalized to handle spectroscopic data generated when the spectrometer is operated in the near ultra-violet, visible and near infrared, in addition to the present middle infrared arrangement.

---

†These spectra are very similar to that of the Globar® (the spectrometer internal secondary standard).
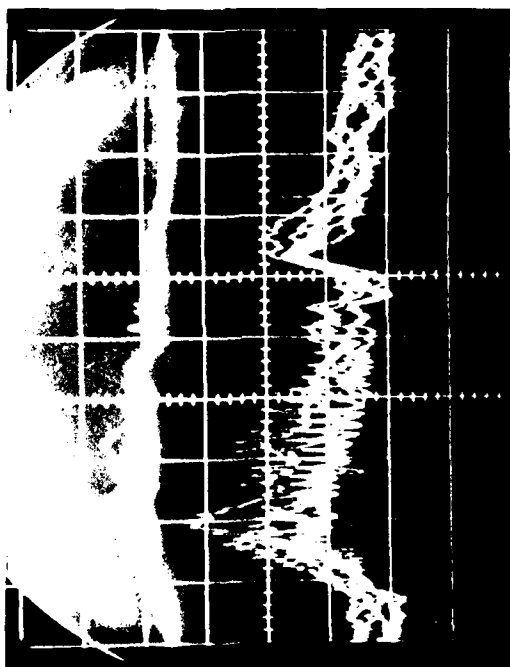
Figure 8. Oscilloscope Photograph of Flare Emission Spectra. The upper (short wavelength) trace extends from 1.7-3.2 μm and the lower (long wavelength) trace extends from 3.0-4.2 μm. Note the noise and fluxtuations.
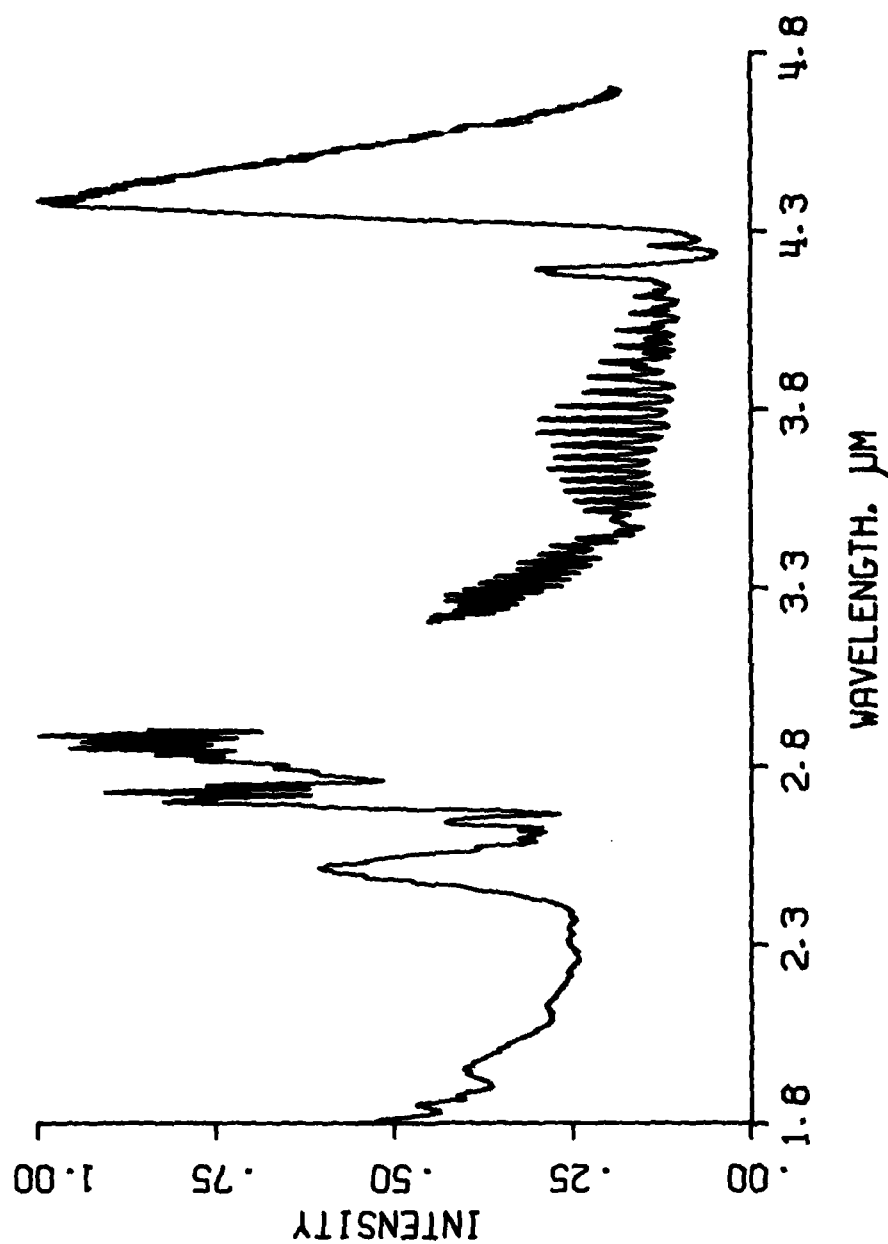
Figure 9. System Corrected, Signal Averaged Spectrum. This is the spectrometer system corrected, signal averaged spectrum corresponding to the raw data in Figure 8. The signal to noise ratio has been greatly improved by the averaging process.

164
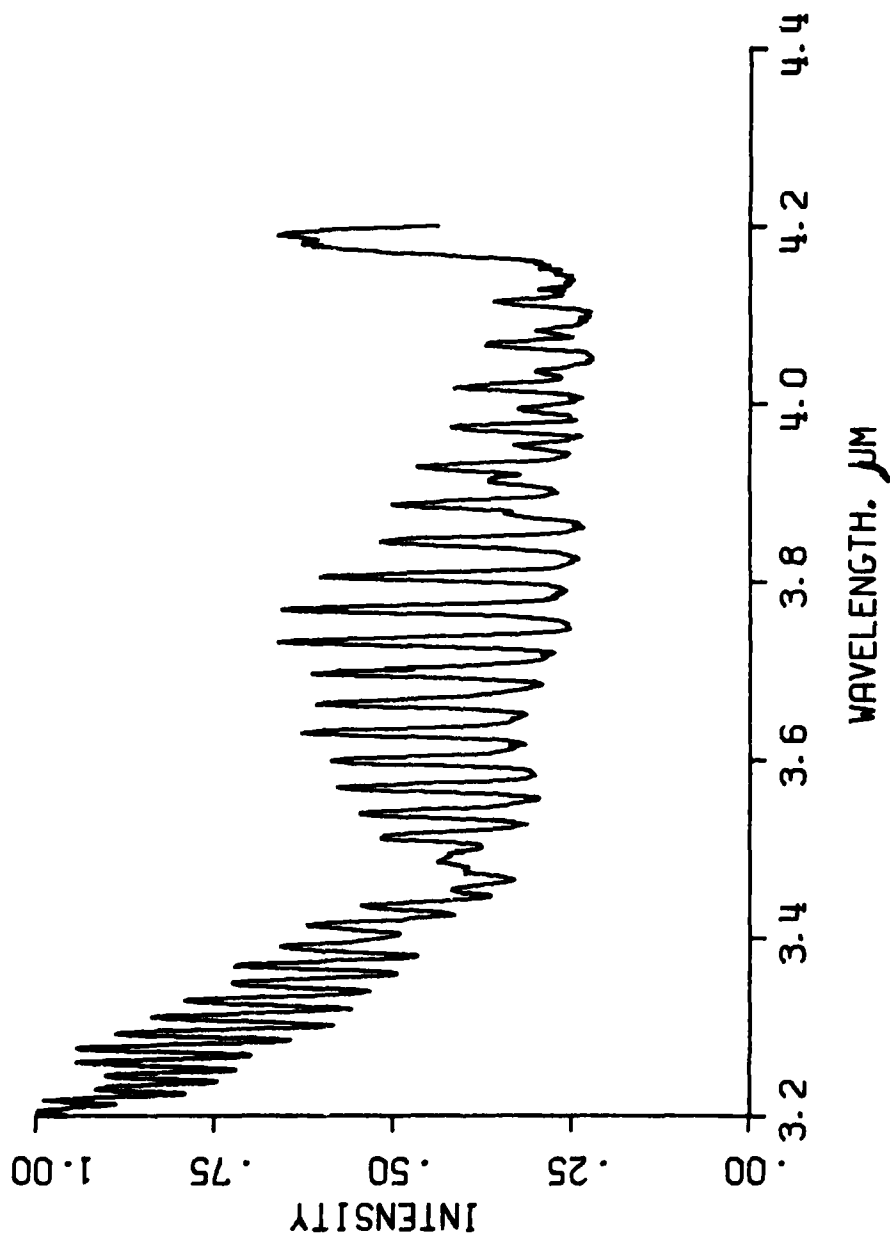
Figure 10. Expanded Portion of Fig. 9. The 3.2-4.2 μm region of Figure 9 has been expanded. The resolution is approximately 0.015 μm. This is primarily HCl emission.
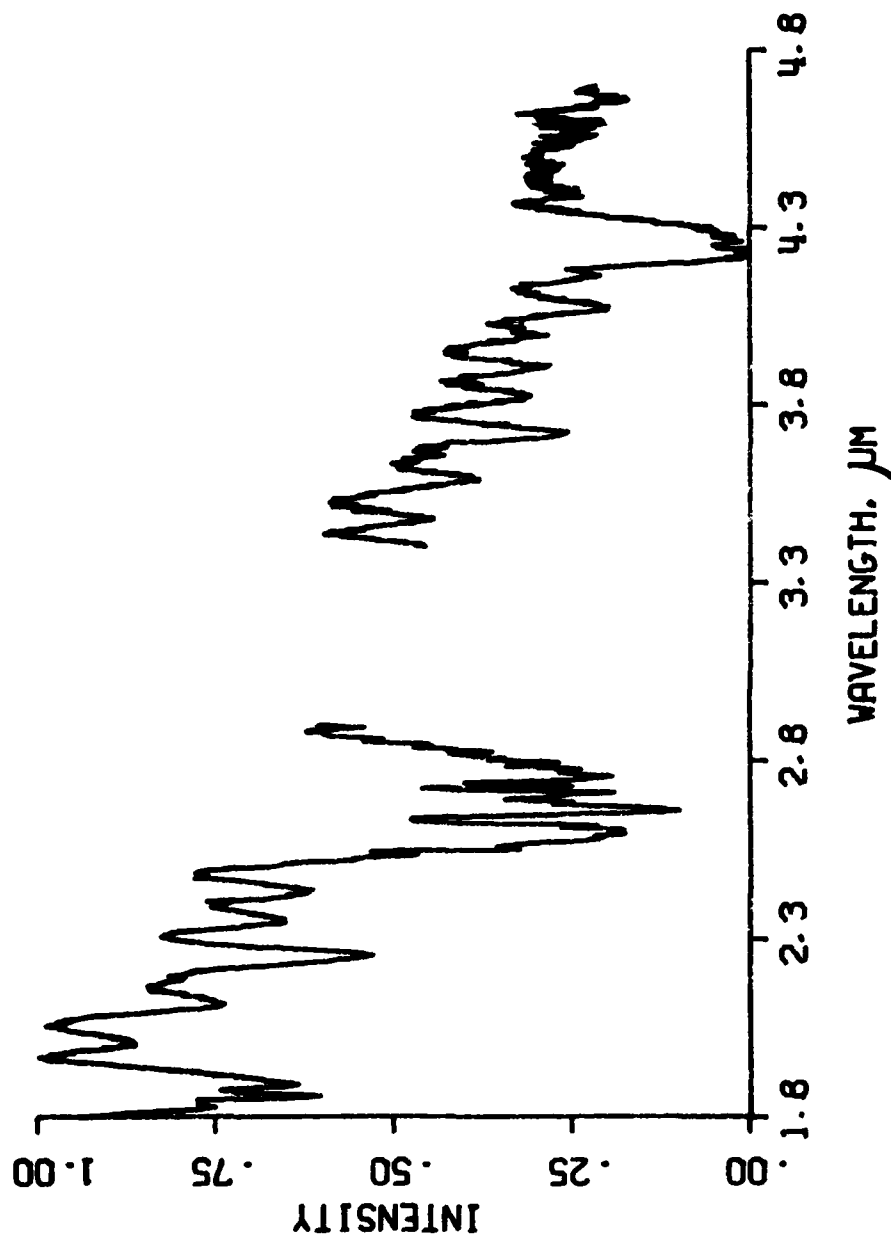
Figure 11. System corrected, but not signal averaged, spectrum. This is another example of the value of signal averaging. Compare with Figure 12.

166
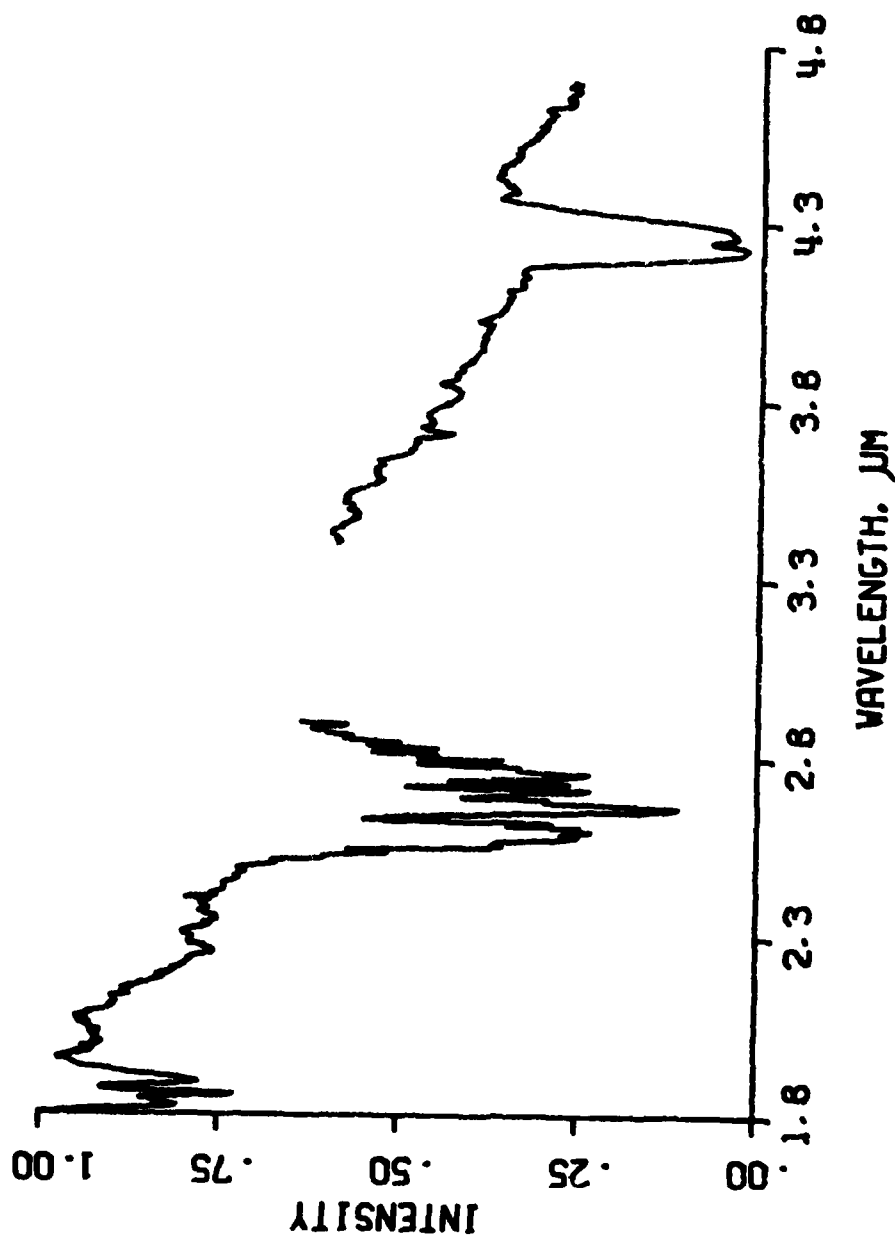
Figure 12. System Corrected, Signal Averaged Spectrum. This is the spectrometer system corrected, signal averaged spectrum corresponding to a series of spectra one of which is Figure 11.

REFERENCES

1. Norcon Instrument Co., Norwalk, Connecticut.

2. C. E. Dinerman, "Capabilities in Infrared Rapid Scan Spectroscopy", RDTR No. 268, Naval Ammunition Depot, Crane, Indiana (May 1974). Available from Defense Documentation Center, Cameron Station, Alexandria, Virginia 22314, AD 921141L.

3. Hewlett-Packard Co., Palo Alto, California.

4. Glocoil® is a trademark of Eagle Electric Manufacturing Co., Long Island, New York.

5. Sangamo Electric Co., Springfield, Illinois.

6. Globar® is a trademark of the Carborundum Co., Niagara Falls, New York.

7. Data General Corp., Southboro, Massachusetts.

8. Mohawk Data Sciences Corp., Utica, New York.

9. Control Data Corporation, Minneapolis, Minnesota.

10. Barnes Engineering Co., Stamford, Connecticut.

11. Complot® is a trademark of Houston Instrument Co., Bellaire, Texas.

168

ECOLOGICAL DISPOSAL/RECLAIM OF
NAVY COLORED SMOKE COMPOSITIONS

C. E. Dinerman and C. W. Gilliam
Applied Sciences Department
Naval Weapons Support Center, Crane, Indiana

ABSTRACT

This is a report on efforts sponsored by the Naval Sea Systems Command to dispose of or reclaim the approximately 9300 kg of colored smoke compositions within the Navy system in an ecologically permissible manner. These smoke compositions, which contain carcinogenic dyes, are contained in non-functional pyrotechnic devices.

After a consideration of many disposal/reclaim methods, two laboratory-scale approaches were selected: (1) controlled incineration, and (2) dye reclaim by solvent extraction.

For both methods, the smoke composition from the Mk 13 Mod 0 Signal (producing an orange smoke) was selected for the first tests, because this composition accounts for 6600 of the 9300 kg. This composition contains 1-methylaminoanthraquinone and xylene-azo-β-naphthol dyes.

1. <u>Incineration</u>. The first approach consists of incinerating the smoke composition as completely as possible to minimize toxic and/or carcinogenic effluents, as measured by gas chromatographic, infrared spectroscopic, and wet chemical analyses. A 75 cm long, 18 mm i.d. quartz-pyrex tube is used inside a multiple zone split tube combustion furnace. A one gram sample of the Mk 13 composition is placed, in a nickel combustion boat, inside one end of the tube, in a zone maintained at approximately 300-500K and an oxygen flow is introduced at approximately 7000-10000 cm^3/min.

The effluent passes into a second zone of the furnace, maintained at 1000 to 1100 K and packed with quartz wool to effect better heat transfer. Infrared analyses of the gaseous portion of the effluent using a 10 cm pathlength, shows CO_2, CO, CH_4, and NH_3 as major constituents. H_2O droplets were also observed forming on the cooler portions of the outlet end of the incinerator. This is evidence of partial oxidation and/or decomposition of the dye components of the smoke composition. Gas chromatographic analyses are preliminary but the presence of CO, CH_4 and H_2 has been shown, as well as other peaks which are as yet unidentified. The IR and GC results have not yet been quantitated. A second quartz-pyrex tube, which is designed to allow the effluent to traverse a 5.3 m path through the 1100 K zone, rather than 75 cm, has been constructed. This should increase the residence time of the effluent in the incinerator for better oxidation/decomposition than at present.

The results of this laboratory-scale incineration will be a statement of the conditions, such as temperature, residence time, and oxygen flow rates, needed for optimum oxidation/decomposition of smoke compositions. This information will be used in the construction of a pilot disposal plant.

2. <u>Solvent Extraction</u>. About five grams of Mk 13 smoke composition was placed in a test tube and treated with 25 cc of 50% sodium hydroxide solution. Two hours, with intermittent shaking at ambient conditions, were required to dissolve all the solubles. The residue, 1-methylaminoanthraquinone, was filtered. The filtrate contained the sodium salt of xylene-azo-β-naphthol dye, sucrose, sodium bicarbonate, and potassium chlorate. The filtrate was neutralized with 30% sulfuric acid solution with the expectancy of a quantitative yield of xylene-azo-β-naphthol dye. A red flocculant precipitate was formed in the neutralized solution. No attempt was made to quantify the amount of precipitate.

These efforts are part of a larger program to ecologically dispose of or reclaim chemical ingredients of non-functional colored smoke devices, dye marking devices, infrared decoy flare devices, and colored flare devices.

BACKGROUND

This is a report on efforts sponsored by the Naval Sea Systems Command to dispose of or reclaim the approximately 9300 kg of excess colored smoke compositions within the Navy system in an environmentally permissible manner. These smoke compositions, which contain carcinogenic or suspected carcinogenic dyes,[1-3] are contained in non-functional pyrotechnic devices.

The purpose of this work is to explore options and to develop alternative methods of reclaim or disposal of unserviceable Navy pyrotechnic smoke compositions so that a choice can be made as to which of these is most advantageous to the Navy.

These efforts are part of a larger program to dispose of or reclaim chemical ingredients of non-functional colored smoke devices, dye marking devices, infrared decoy flare devices, and colored flare devices.

APPROACH

A study was conducted of various techniques that exist for reclamation and/or disposal of devices containing organic dye smoke composition. Options that were uncovered during this study are:

1. Sale "as is"

2. Wet Air Oxidation Process

3. Molten Salt Process

4. Open Pit Incineration

5. Landfill

6. Reclaim of Organic Dyes

    a. Organic Solvent Extraction

    b. Sodium Hydroxide Extraction

    c. Water Extraction

7. Controlled Incineration of Pyrotechnic Smoke Compositions

As will be discussed below, options 6 and 7 were found more desirable than 1 to 5, and consequently are being pursued.

The smoke composition from the Mk 13 Mod 0 signal (producing an orange smoke) was selected for the first tests because this composition accounts for 6600 of the 9300 kg. This composition contains 1-methyl-aminoanthraquinone and xylene-azo-β-naphthol dyes. The exact formula is shown in Table 1.

DISCUSSION OF OPTIONS 1 TO 5

The following is a discussion of each of the first five options to indicate what the procedure is, any preliminary experiments that were performed, and the rationale for discarding each.

1.   Sale "as is"

One disposal alternative is the "as is" sale of the devices in accordance with the provisions of Defense Demilitarization Manuals DOD 4160.21M and DOD 4160.21M1. NAVSEASYSCOM has been requested to determine how appropriate this option is.

No further action is planned at this Center on this option.

2.   Wet Air Oxidation

The wet air oxidation of a sample of Mk 13 Mod 0 smoke composition in a laboratory autoclave at NSWC, Indian Head, Maryland was attempted. The results indicate that complete oxidation of the ingredients does not occur under the conditions present in this single experiment. These conditions are oxidation in the presence of water or dilute acid at temperatures between 478-588 K and operating pressures from 600 to 3000 psi.

The reaction liquors were tested for the presence of 2-naphthylamine, 2-naphthol and splitting of the diazo group. Ultraviolet spectroscopy showed the presence of 2-naphthol and possibly 2-naphthylamine. The presence of 2-naphthol was confirmed by the Erlich-Diazo test. This is an indication that the group was cleaved, thus forming 2-naphthol from the dye, xylene-azo-β-naphthol. A red precipitate formed when the effluents were treated with sodium 1,2-naphthoquinone-4-sulfonate indicating the presence of 2-naphthylamine. 2-naphthol is highly toxic and 2-naphthylamine is carcinogenic. This process was not pursued further because other options looked more promising.

3.   Molten Salt Process

The molten salt composition is a binary sodium carbonate-potassium carbonate eutectic with a melting point of 983 K. This binary mix can be operated up to 1273 K without appreciable decomposition. The organic material (smoke composition) is sized and contacted with the molten salt in a suitable combustor unit with an auxiliary air supply to oxidize the organics into their gaseous products.[4]

This process requires that the materials slated for combustion have a high organic material content such that residual ash is small. When ash and other non-combustible materials build up in the molten salt combustor, the salts must be changed to avoid reducing the efficiency of the process. If this process is to be considered for disposal of pyrotechnic smoke compositions, the compositions will have to be removed from their respective metal hardware. The amount of composition in the case of the Mk 13 smoke device, for example, is 50 gm

per unit. To process 45 kg of composition, 908 pieces of hardware would have to be handled. A reduction in size of the pressed smoke composition is necessary to process through the molten salt bath. The effect of 20% residual salts from the decomposition of smoke compositions upon the efficiency of the molten salt bath, and subsequent disposal of freeze (spent salt bath) are additional cost factors associated with this process. Taken collectively, these factors most probably would increase the operating cost of this process to the extent that the process becomes economically unfavorable when compared to other options. On this basis, this option will not be pursued further at this time.

4.   Open Pit Incineration

Open pit incineration is a cheap and dirty way of disposing of deteriorated and scrap pyrotechnic compositions. However, due to stringent state and federal regulations, this method of disposal is no longer an acceptable one for waste pyrotechnic compositions. This option will not be considered further.

5.   Landfill

The landfill method was used to bury materials generated from open pit incineration. Because of the potential hazards to the environment, i.e., soil and underground water sources, this method is no longer acceptable. This option will not be considered further.

DISCUSSION OF RECLAIM OF ORGANIC DYES

Organic Solvent Extraction

This method involves finding a solvent which selectively extracts the dye from the pyrotechnic composition with the least amount of coextraction of the other ingredients.

Water Extraction

Water extraction is a process to dissolve all water soluble materials from the composition. A typical water extract would contain potassium chlorate and sucrose. The residue would contain dye, binder and graphite. An additional separation would then be required to remove the dye(s).

Sodium Hydroxide Extraction

A dilute solution of sodium hydroxide, a strong base, should dissolve the acidic xylene-azo-β-naphthol dye, potassium chlorate and sucrose. The residue should be principally 1-methylaminoanthraquinone, graphite and binder which will require further separation. The dissolved materials (filtrate) can be acidified to reclaim the dye, xylene-azo-β-naphthol.

In the first experiment, a five gram sample of Mk 13 smoke composition was placed in a test tube and treated with 25cc of 50% sodium

hydroxide solution. (The tentative scheme for this experiment is shown in Fig. 1.) Two hours, with intermittent shaking at ambient conditions, were required to dissolve all the solubles. The residue, principally 1-methylaminoanthraquinone, was filtered. The filtrate contained the sodium salt of xylene-azo-β-naphthol dye, sucrose and potassium chlorate. The filtrate was neutralized with 30% sulfuric acid solution with the expectancy of a quantitative yield of xylene-azo-β-naphthol dye. A red flocculant precipitate was formed in the neutralized solution. No attempt was made to quantify the amount of precipitate.

In a second experiment, a ten gram sample of Mk 13 Mod 0 smoke composition was stirred for one hour in varying ratios of 50% sodium hydroxide and water solution to determine how efficiently xylene-azo-β-naphthol could be dissolved from the composition. Table 2 summarizes the results.

The last column in Table 2 was calculated from the assumption that all of the potassium chlorate and sucrose and none of the 1-methylamino-anthraquinone dissolves in the sodium hydroxide solution. Since the amount of potassium chlorate and sucrose that can be dissolved is known from Table 1, any excess of this amount is attributed to xylene-azo-β-naphthol. The excess weight is divided by the weight of the xylene-azo-β-naphthol in the composition to obtain the percentages. The average percentage of xylene-azo-β-naphthol that dissolved is about 21%.

The following is a summary of the work done on the reclaim of organic dyes option:

An experiment has shown that it may be feasible to separate xylene-azo-β-naphthol from 1-methylaminoanthraquinone by dissolving the former in sodium hydroxide solution and subsequently acidifying to precipitate it. A second experiment resulted in an average of 21% of the xylene-azo-β-naphthol being dissolved which shows that more work is needed to maximize the amount of dye that dissolves.

These experiments are:

1. To find the ratio which dissolves the maximum amount of xylene-azo-β-naphthol dye.

2. To determine how much of the dye is extractable from the filtrate of potassium chlorate and sucrose solution.

3. To ascertain how to best separate the 1-methyl-aminoanthraquinone from the solid residue.

FIG. 1.   RECLAIM SCHEME FOR SMOKE COMPOSITION
FROM MK 13 MOD 0 SIGNAL

SOLVENTS

Organic   Sodium Hydroxide   Water

Filtrate   Filtrate   Filtrate

| Dye |
| KClO$_3$ |
| C$_{12}$H$_{22}$O$_{11}$ |

| Na-Salt of |
| Xylene-azo-ß-naphthol Dye |
| KClO$_3$ |
| C$_{12}$H$_{22}$O$_{11}$ |

| KClO$_3$ |
| C$_{12}$H$_{22}$O$_{11}$ |

Residue

| Binder |
| Graphite (C) |

Residue

| 1-methylamino-anthraquinone Dye |
| Binder |
| Graphite (C) |

Residue

| 1-methylamino-anthraquinone Dye |
| Xylene-azo-ß-naphthol Dye |
| Binder |
| Graphite (C) |

Acidify

| Precipitate |
| Xylene-azo-ß-naphthol Dye |

| Filtrate |
| KClO$_3$ |
| C$_{12}$H$_{22}$O$_{11}$ |

TABLE 1. CHEMICAL COMPOSITION OF SMOKE
COMPOSITION OF MK 13 MOD 0 SIGNAL

Xylene-azo-β-naphthol	44.9%
1-methylaminoanthraquinone	15.3%
Sucrose	14.6%
Potassium Chlorate	18.9%
Graphite	1.5%
Sil-O-Cel®* (Binder)	4.8%

---

*This is a product of Johns-Manville Corp., New York, N.Y.

TABLE 2. SOLUBILITY OF MK 13 MOD 0 SMOKE COMPOSITION
IN VARYING RATIOS OF 50% NaOH/H_2O SOLUTION*

NaOH/H_2O Ratios	Mk 13 Mod 0 Smoke Comp Wt.	Percent Solubles	Percent Residue	Percent Xylene-azo-β-naphthol Dissolved
1:1	10 gms	54	46	19
1:3	10 gms	60	40	30
2:1	10 gms	57	43	27
5:1	10 gms	48	52	8

*Percent solubles refers to the total amount of composition, by weight, that dissolved in the sodium hydroxide solution. Percent residue is the difference between 100% and Percent Solubles.

The last column on the right was calculated from the assumption that all of the potassium chlorate and sucrose and none of the 1-methylamino-anthraquinone dissolves in the sodium hydroxide solution. Since the amount of potassium chlorate and sucrose that can be dissolved is known from Table 1, any excess of this amount is attributed to xylene-azo-β-naphthol. The excess weight is divided by the weight of the xylene-azo-β-naphthol in the composition to obtain the percentages.

DISCUSSION OF CONTROLLED INCINERATION OF
PYROTECHNIC SMOKE COMPOSITIONS

Controlled incineration consists of oxidizing the smoke as completely as possible to minimize the production of toxic and/or carcinogenic effluents, as measured by gas chromatographic, infrared spectroscopic, and wet chemical analyses. The bulk of the work has been accomplished on this option and it will be described in some detail.

This method was undertaken using information from previous work[4-12] and from standard technology.[13-16]

The utilization of this method has undergone several stages of evolution:

1. 75 cm Quartz-Pyrex Incinerator
2. 5.3 m 7-Pass Quartz-Pyrex Incinerator
3. 5.3 m 7-Pass Stainless-Steel-Pyrex Incinerator

Each stage will be discussed, along with the corresponding results. The nomenclature refers to the distance over which the effluent traverses the hottest zone of the incinerator.

1. In this stage, a 75 cm long, 18 mm i.d. quartz-pyrex tube was used inside a multiple zone split tube combustion furnace (Fig. 2). The quartz section was located in the hottest portions of the furnace, while the pyrex sections were used elsewhere for convenience in assembling the rest of the apparatus. The quartz and pyrex were connected through commercial quartz-pyrex graded seals. A one gram sample of the Mk 13 Mod 0 smoke composition was placed in a nickel combustion boat, inside one end of the tube, in a zone maintained at approximately 300-500 K and an air flow was introduced at approximately 1000 cm^3/min. (STP).

In this arrangement, the effluent passes into a second zone of the furnace, maintained at 1000 to 1100 K and packed with quartz wool to effect better heat transfer to the effluent. Fig. 3 shows the quartz wool packed in the quartz-pyrex tube. Infrared analyses of the gaseous portion of the effluent using a 10 cm pathlength cell, showed carbon dioxide, carbon monoxide, methane, and ammonia as major constituents. The gas chromatograph sampling bulb and infrared spectroscopic cell are not shown in Figs. 2 or 3. Water droplets were also observed forming on the cooler portions of the outlet end of the incinerator. This is evidence of partial oxidation and/or decomposition of the dye components of the smoke composition. Gas chromatographic analyses showed the presence of carbon monoxide, methane, and hydrogen as well as other peaks which are most likely aliphatic C_4-C_{20} and aromatics (see Appendix A for gas chromatograph conditions.)

The smoke effluent appeared grayish yellow (condensing as an oily film) as compared to the orange-red color of the undecomposed smoke which is also indicative of partial oxidation. At this point, no attempt was made to determine the amount of smoke versus gaseous effluent.

178

Figure 2
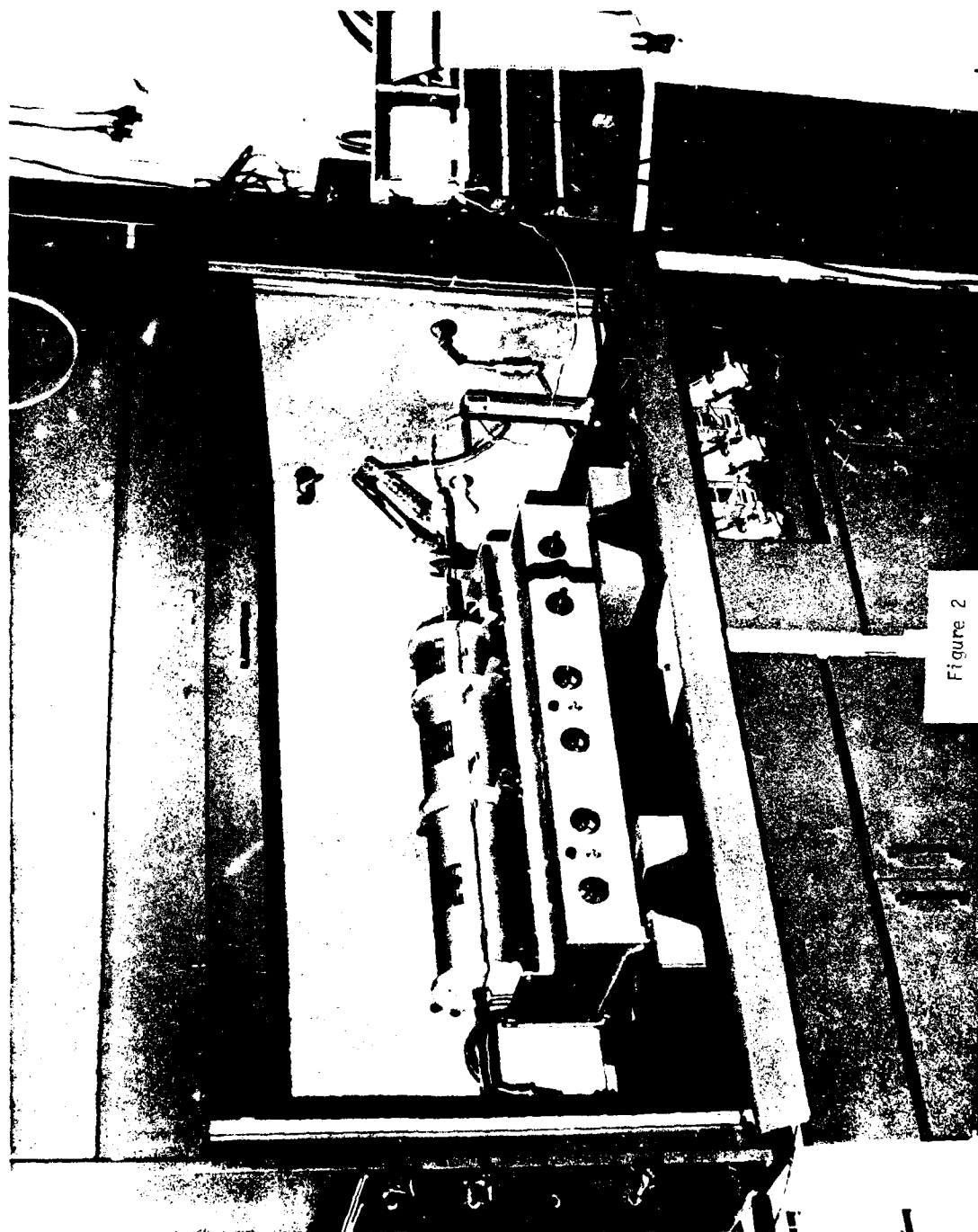
When pure oxygen at 1000 cm^3/min. (STP) was substituted for the air, this increase in oxidizing power produced a change in both the gas chromatograph (GC) and infrared spectrometer (IR) results. The total number of GC peaks decreased by 50 percent, and the IR peaks of carbon dioxide and carbon monoxide increased relative to the other gaseous constituents.

Also, the smoke portion of the effluent changed appearance from grayish yellow to mostly black, indicating that dye molecules were being broken down more completely than before.

To improve the oxidation/decomposition conditions, a second incinerator was constructed.

2. The second incinerator consisted of a series of seven parallel quartz tubes connected in series such that the effluent would traverse the hot zone of the furnace seven times before exiting to the sample collection devices. The quartz tubes were dimpled to increase turbulence. Provision was made to introduce additional oxygen about half way through the incinerator at the beginning of the fourth traversal. Figures 4 and 5 show a general view of the apparatus. Starting from the right in Fig. 5, oxygen enters the apparatus through the flowmeter at the horizontal stainless steel tube. Just above this tube, and parallel to it, is a thermocouple. Also at this point is a gauge to measure the system's back pressure. Further to the left is the sample boat, partially hidden under the heater tape. This is the low temperature zone. To the left are the quartz tubes connected in series. A close up of these tubes is shown in Fig. 6. In this figure, the short tube, capped with a black rubber bulb, extending out of the left side of the tube furnace, is a provision for introducing auxiliary oxygen. Also located at the left end is another thermocouple. Figure 7 shows a close up view of the sampling end of the apparatus. The cyclone collector is shown at A, the GC collection bulb at B, and the IR 10 cm cell at C. Thus, by attempting to follow the well-known principle of maximizing the three T's of time, temperature, and turbulence, it was expected that this second version of the incinerator would provide better conditions for combustion than the first version.

3. Unfortunately, the quartz tubes, when subjected to the 1000-1100 K temperatures, began devitrifying rapidly and quickly became brittle and weakened. It was not possible to perform experiments with this apparatus. It was found necessary to substitute Type 310 (high temperature) stainless steel (6.3 mm O.D., 1.2 mm wall) for the quartz. All the basic features mentioned in section 2 are preserved, except for the dimples. Commercial stainless-steel-pyrex seals replaced the quartz-pyrex seals mentioned above. Because of the decreased volume of this apparatus and to increase the residence time of the effluent, the oxygen flow rate was lowered to 150 cm^3/min. (STP).

With this apparatus, ammonia and another unidentified species, both of which had always been present, dropped to undetectable levels in the 10 cm IR cell.
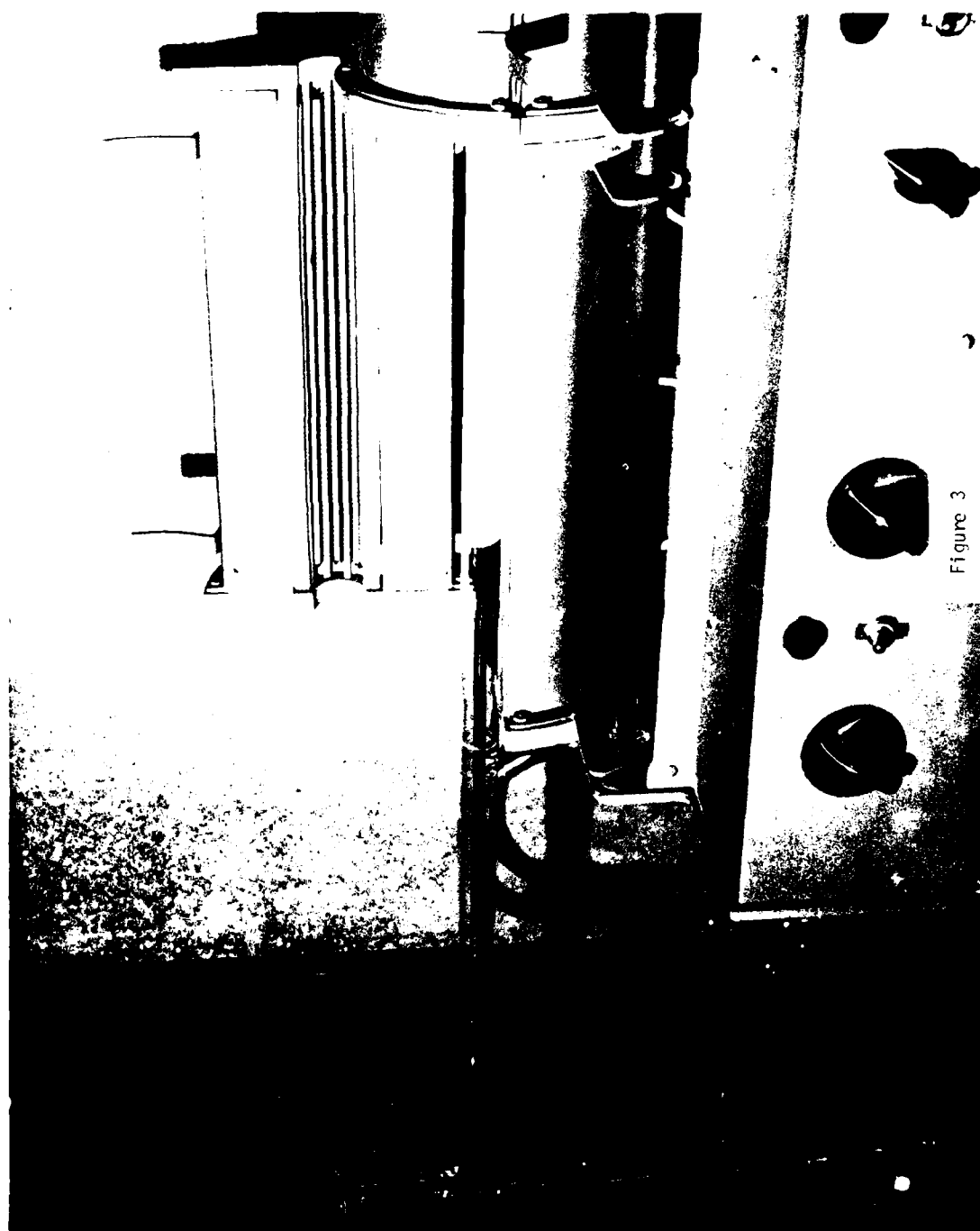
Figure 3
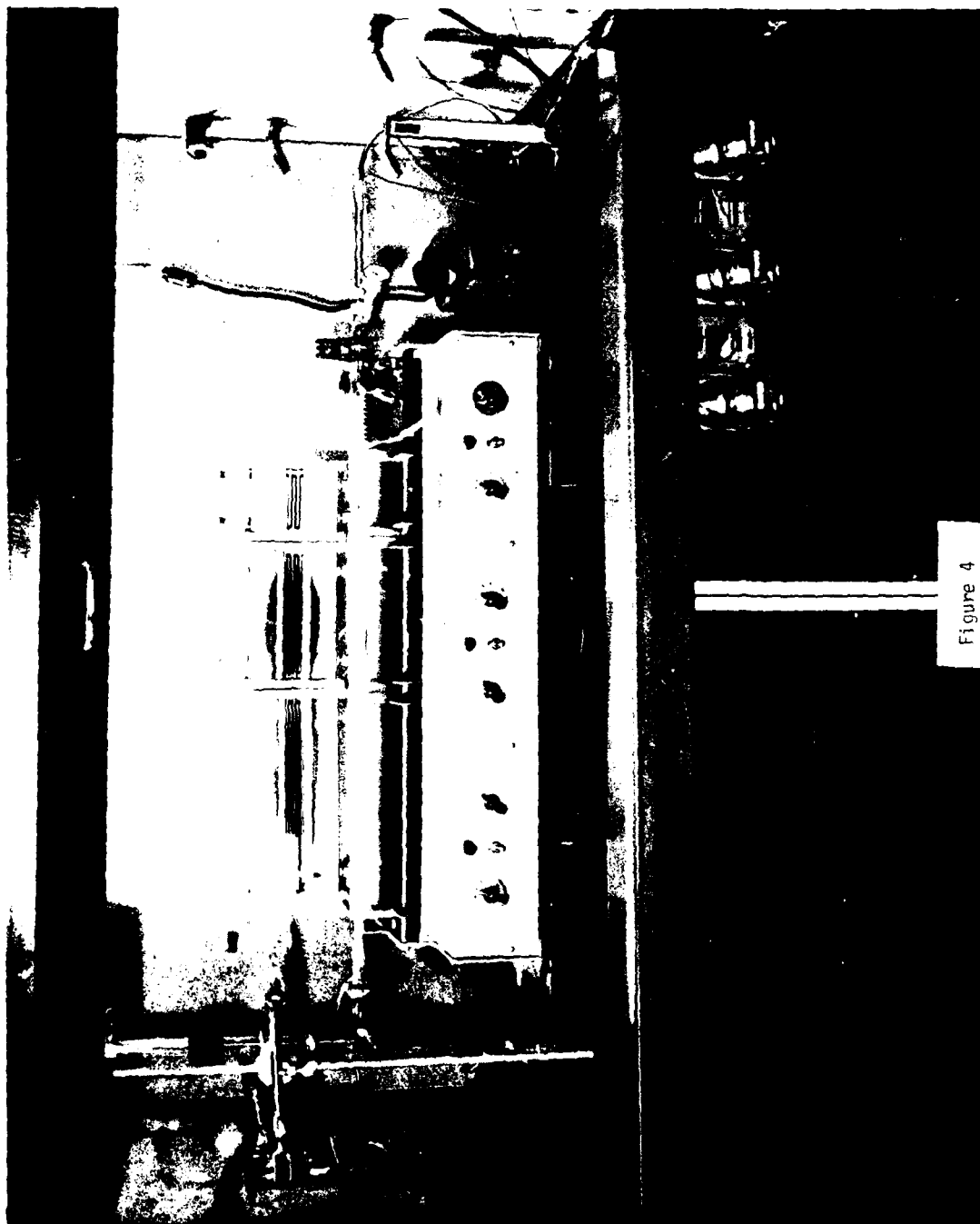
Figure 4
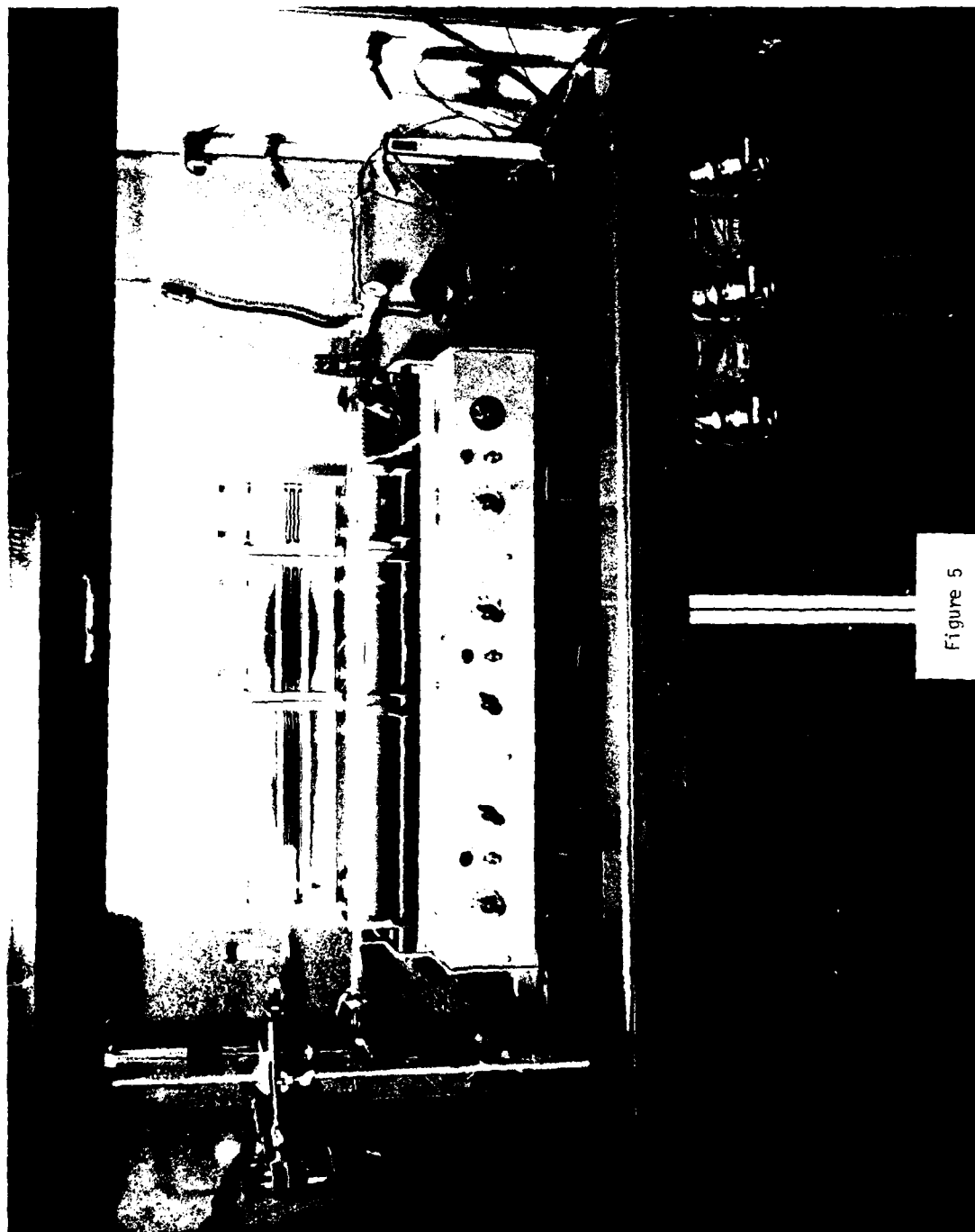
Figure 5

Figure 6
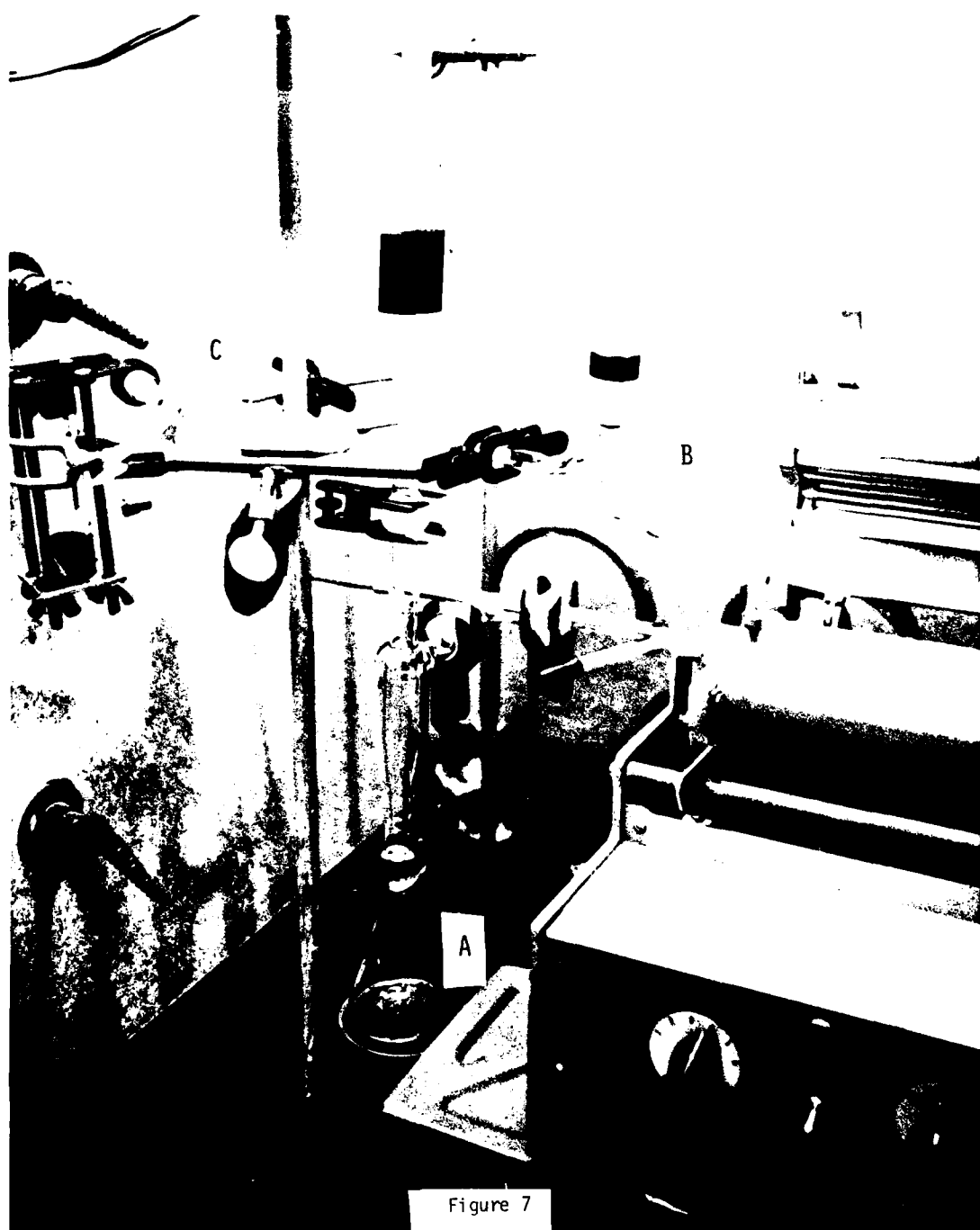
Figure 7

Also, the number of GC peaks decreased to 2 or 3, on a column designed to elute aliphatics C_4-C_{10} and then aromatics such as benzene, toluene, xylene, etc. (see Appendix A).

It was determined that a 1 gm sample of Mk 13 Mod 0 smoke composition severely overloaded the incinerator. When the sample size was reduced to 0.14 gm, the oxygen to fuel ratio increased to the extent that the ratio $(CO_2 + CO)/(CH_4 + NH_3)$ was increased many fold.

A NASA thermodynamic computer program was employed to predict the combustion species (assuming thermodynamic equilibrium) resulting from decomposition of Mk 13 compositions, for a series of ten temperatures ranging from 600-1500 K, and five oxidant/fuel ratios.[19]

The following summarizes the results of the controlled incineration method:

1. The ratio of carbon dioxide and carbon monoxide to other IR peaks is increasing as the experimental conditions are improved. Also, certain species are becoming much less abundant as evidenced in the disappearance of GC and IR peaks. These facts show that combustion is becoming more complete.

2. The appearance of the smoke portion of the effluent has changed from grayish yellow condensing as an oily film, to a black smoke condensing as soot. This change in appearance is evidence of a more extensive decomposition of the organic dye molecules. Increased oxidation of these primarily carbon-containing particles should be achieved with a greater oxygen to fuel ratio.

3. Optimum results should be obtained when oxidation takes place at temperatures above 1100 K, when the residence time of the effluent in this zone is greater than 2 or 3 seconds, and when the optimum oxygen to fuel ratio has been determined.

When experiments are completed on the Mk 13 Mod 0 smoke composition, similar experiments involving other colored smoke compositions will be initiated.

PLANS

Both the reclaim of organic dye and the controlled incineration methods will be the subject of further work. The relative merits of organic solvent, water, and sodium hydroxide extraction will be evaluated using the three schemes as shown in Fig. 1. Further experiments, as outlined in the Discussion of Reclaim of Organic Dyes section, will be pursued.

As for the controlled incineration method, experiments to improve incineration and collection techniques are continuing. The effect of adding auxiliary oxygen will be examined. When the incinerator conditions are optimized, a commercial 20 meter variable path IR cell[20] will be used instead of the 10 cm IR cell. This cell can be used to

complement the GC in the identification and quantification of trace compounds. Analyses of the solid portion of the effluent by IR, GC and various wet analytical methods and the determination of the amount of solid relative to gaseous effluents are continuing.

The resulting information will be used in the construction of a pilot reclaim or disposal plant, depending on which option is chosen by NAVSEASYSCOM.
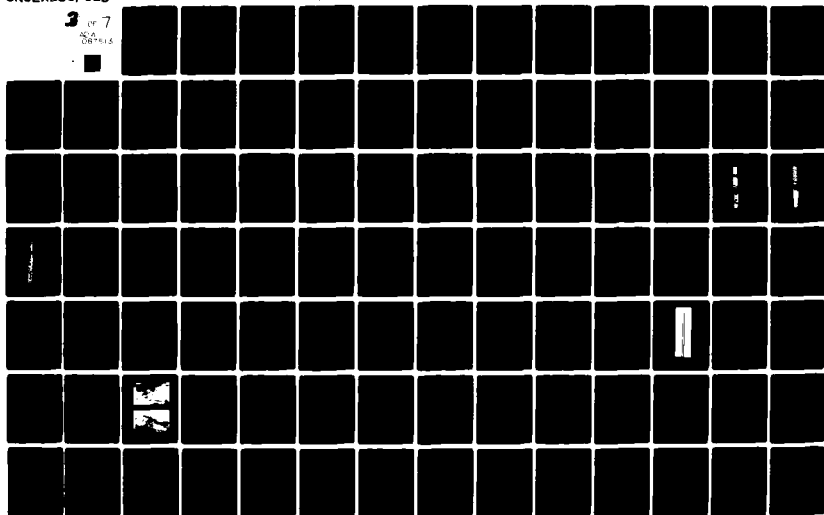
REFERENCES

1. E. J. Owens and D. M. Ward, *A Review of the Toxicology of Colored Chemical Smokes and Colored Smoke Dyes*, EB-TR-74064, Edgewood Arsenal, Aberdeen Proving Ground, Maryland (December 1974), available DDC-AD A003827.*

2. A. F. Tatyrek, *The Health Hazards of Certain Smoke Dyes in Current Use*, Technical Memorandum 1674, Feltman Research Labs, Picatinny Arsenal, Dover, New Jersey (September 1965).

3. M. H. Weeks and P. P. Yevich, *The Toxicity of Combustion Products of Pyrotechnics*, Technical Memorandum 26-12, U.S. Army Chemical Warfare Labs, Army Chemical Center, Maryland (May 1960), available DDC-AD 474403.

4. J. Mallis, *Disposal by Wet Air Oxidation* in *JANNAF Working Group on Safety and Environmental Protection, Minutes of August 1974 Semi-Annual Meeting, Supplement 5* (Chemical Propulsion Information Agency, The Johns Hopkins University, Applied Physics Laboratory, Silver Spring, Maryland, October 1974).

5. A. J. Darnell, L. Abraham, M. B. Frankel and S. J. Yosim, *Disposal of Explosives and Propellants by Use of Molten Salts*, AI-73-28, Atomics International Division, Rockwell International Corporation, Canoga Park, California (June 1973).

6. H. E. Malone and M. Santy, *Incineration Methods for the Disposal of Rocket Propellants and Propellant Ingredients* in *JANNAF Working Group on Safety and Environmental Protection, Minutes of August 1974 Semi-Annual Meeting, Supplement 4* (Chemical Propulsion Information Agency, The Johns Hopkins University, Applied Physics Laboratory, Silver Spring, Maryland, October 1974).

7. JANNAF Working Group on Safety and Environmental Protection, Environmental Protection Committee, *Environmental Impact Considerations for Disposal of Propellants and Ingredients*, CPIA Pub. 269, Chemical Propulsion Information Agency, The Johns Hopkins University, Applied Physics Laboratory, Laurel, Maryland (September 1975).

8. B. C. Kim and R. B. Landrigan, *A Study of Pyrotechnic Combustion Processes*, Battelle, Columbus Laboratories, 505 King Avenue, Columbus, Ohio (9 April 1975).

9. E. G. Kayser, *The Thermal Decomposition of Thirty Commercially Available Materials at 300°C*, NOL TR 74-44, Naval Ordnance Laboratory, White Oak, Silver Spring, Maryland (February 1974), available DDC-AD 783960.

---

*Available DDC indicates the document is available from Defense Documentation Center, Cameron Station, Alexandria, Virginia 22314.

10. H. H. Rosen, *Pesticide Pyrolysis Device*, Technical Report 74-89, Army Land Warfare Laboratory, Aberdeen Proving Ground, Maryland (June 1974), available DDC-AD 784553.

11. E. A. Boettner, G. L. Ball, and B. Weiss, *Combustion Products from the Incineration of Plastics*, EPA-670/2-73-049, Environmental Protection Agency, Cincinnati, Ohio (1973), available NTIS-PB 222-001.*

12. D. G. Nichols, *Incineration Studies of Colored Smoke Mix Wastes*, Edgewood Arsenal, Maryland (27 Mar 1970).

13. R. D. Ross, *Industrial Waste Disposal* (Reinhold Book Corporation, New York, 1968).

14. H. F. Lund, *Industrial Pollution Control Handbook* (McGraw-Hill Book Company, 1971).

15. V. E. Derr, et. al., *Remote Sensing of Pollutants: Computerized Reduction of Long-Path Absorption Data*, EPA-650/2-74-113, National Oceanic and Atmospheric Administration, Boulder, Colorado (July 1974).

16. W. Leithe, *The Analysis of Air Pollutants* (Ann Arbor-Humphrey Science Publishers, Ann Arbor-London, 1970).

17. Ace Glass, Inc., Vineland, New Jersey.

18. Kontes/Martin Co., Evanston, Illinois.

19. S. Gordon and B. J. McBride, *Computer Program for Calculation of Complex Chemical Equilibrium Compositions, Rocket Performance, Incident and Reflected Shocks, and Chapman-Jouguet Detonations*, NASA SP-273, Lewis Research Center (1971). Available NTIS-N71-37775.

20. Wilks Scientific Corporation, Norwalk, Connecticut.

*Available NTIS indicates the document is available from National Technical Information Service, 5285 Port Royal Road, Springfield, Virginia 22161.

APPENDIX A

DETAILS OF INFRARED SPECTROSCOPIC
AND GAS CHROMATOGRAPHIC ANALYSES

Infrared

IR data have been taken from 4000-450 cm^{-1} using a 10 cm pathlength infrared cell equipped with KBr windows of 0.5 cm thickness.

Before each experiment, the cell was evacuated to better than $1x10^{-2}$ torr and a spectrum taken of this empty cell to obtain a background.

The spectrometer was a Beckman Model IR-20A Infrared Spectrophotometer.[1]

Gas Chromatograph

The gas chromatograph is a Hewlett-Packard Model 7620A Research Chromatograph.[2] It is equipped with a Model 3307B Electronic Integrator and a dual pen strip chart recorder for recording and integrating the electrical signals. This instrument can be operated in an isothermal, linearly programmed or step programmed temperature mode with either a thermal conductivity (TC), flame ionization (FID) or electron capture (EC) nickel 63 detector. With the installation of the dual outlet effluent splitters, any combination of two detectors is possible. The FID-TC detector combination was used.

Three columns were used to examine the effluents: (1) A solid support of Chromosorb W-AW DMCS coated with 4% Silicone Gum SE 30 was packed in a 3 mm O.D., 3.7 m long stainless steel tube,[3,4] (2) a molecular sieve 5A, 60/80 mesh[5] in a 3 mm O.D., 1.8 m long stainless steel tube, and (3) a solid support of Chromosorb P-AW coated with 10% Diethylene Glycol Succinate in a 3 mm O.D., 2 m long stainless steel tube.[6]

Column (1) was used to examine the effluents from the first incinerator. This column is a slightly polar general purpose one which finds wide application for C_4-C_{10} aliphatics.[7] Ring cleavage was expected in the organic dyes of the Mk 13 Mod 0 smoke composition producing these aliphatic hydrocarbons. Column (1) separates hydrocarbons according to boiling point which to a great extent is linearly related to carbon number.[8] This column was run at 298 K for 10 minutes and then step programmed from 373 K to 493 K at 15 K per minute, with steps at 373K for 4 minutes, 404 K for 6 minutes, 443 K for 6 minutes and 493 K for 6 minutes. Since all of the peaks didn't elute at one temperature, the simple technique of relating relative retention time to carbon number[7] was not applicable.

Column (2) was used for its ability to separate permanent gases and light hydrocarbons. This column resolves hydrogen, oxygen, nitrogen, methane and carbon monoxide peaks at room temperature.

Column (3) is a highly polar one which was used to determine benzene and its homologs in the presence of aliphatics. It will elute C_4-C_{10}, then benzene, toluene, xylene, etc. This column was also step programmed from 373 K to 463 K at 15 K per minute with steps at 373 K for 4 minutes, 403 K for 4 minutes, 433 K for four minutes and 463 K for 6 minutes.

REFERENCES FOR APPENDIX A

1. Beckman Instruments, Inc., Fullerton, California.

2. Hewlett-Packard Corporation, Palo Alto, California.

3. Hewlett-Packard Part No. UCC-W982 (6120), Fullerton, California.

4. N. Iglauer, *Pyrolysis-Gas Chromatography - A Method for Rapid Identification of Polymers*, AFML-TR-72-274, Air Force Materials Lab, Wright-Patterson Air Force Base, Ohio (Dec 1972), available DDC-AD 755375.

5. SUPELCO, Inc., Part No. 02-0302, Bellefonte, Pennsylvania.

6. Hewlett-Packard Part No. 8501-1380, Fullerton, California.

7. O. E. Schupp and J. S. Lewis, *Gas Chromatographic Data Compilation*, ASTM AMD 25A S-1, Suppl. 1 (American Society for Testing and Materials, Philadelphia, Pennsylvania 19103).

8. J. D. Roberts and M. C. Caserio, *Modern Organic Chemistry* (W. A. Benjamin, Inc., New York, 1967), p. 58.

HOT WIRE IGNITION OF PYROTECHNIC MATERIALS*

by

A. B. Donaldson
Sandia Laboratories
Albuquerque, New Mexico 87115

ABSTRACT

The hot wire ignition of a pyrotechnic material is considered through
the use of a mathematical model. A system dependent "ignition temperature"
is obtained by observing the behavior of derivatives in the differential
equation as ignition develops. It is shown that this ignition criterion is
consistent with that which commonly appears in the Russian literature on
thermal explosion. Finally, the elapsed time required to achieve the igni-
tion temperature is obtained approximately by using the solution to the
"inert" heat conduction equation.

INTRODUCTION

Numerous theoretical (1,2,3,4,5) and experimental (6,7,8,9) investigations have been conducted on the topic of thermal ignition of pyrotechnic materials by electrically heated wires (bridgewires). Applications of these studies include components such as hot wire detonators, actuators, squibs, ignitors, etc.

The theoretical studies have been directed toward obtaining solutions to the nonlinear system which approximately describes thermal diffusion and chemical reaction in the pyrotechnic.

The end product of both the theoretical and experimental studies is the ignition or function time for a hot-wire stimulated pyrotechnic. As a means of affecting the ignition time at a particular current level, the diameter of the bridgewire is varied.

ANALYSIS

In consideration of ignition of a pyrotechnic material by electrically heated wires, a zeroth order Arrhenius model for the rate of heat liberation as a function of temperature is customarily used. Although some of the physics of the problem, such as reactant depletion, mechanism variation, and the often heterogeneous nature of the pyrotechnic, are neglected by this model, it does provide the conditions for ignition or thermal explosion. Analyses using this heat production model are often compared, with good success, to experimentally observed ignition characteristics, thus validating the procedure. Other assumptions used in the mathematical model are:

1) The system is assumed to be axially infinite and the pyrotechnic is radially infinite.

2) The bridgewire is in perfect thermal contact with the pyrotechnic.

3) Thermal properties of the pyrotechnic and bridgewire are homogeneous, isotropic and independent of temperature.

4) The bridgewire, because of its relatively high thermal conductivity and small diameter, can be treated as a lumped thermal mass so that radial temperature gradients can be neglected.

5) The current passing through the bridgewire remains constant for time > 0.

Based on these assumptions, the differential equation and boundary and initial conditions can be written as

194

$$\frac{1}{r}\frac{\partial}{\partial r}\left(r\frac{\partial T}{\partial r}\right) + \frac{\rho qz}{k} e^{-Ea/RT} = \frac{1}{\alpha}\frac{\partial T}{\partial t} \quad \begin{cases} t > 0 \\ a \leq r < 0 \end{cases}$$

B.C.   1. $-2\pi ak \frac{\partial T}{\partial r} = \frac{i^2 R}{\pi a^2} - \hat{\rho} \cdot \pi \hat{a}^2 \cdot \hat{c}\frac{d\hat{T}}{dt} \quad \begin{cases} t > 0 \\ r = a \end{cases}$

2. $T = \hat{T} \quad \begin{cases} t \geq 0 \\ r = a \end{cases}$

3. $T = Ti \quad \begin{cases} t \geq 0 \\ r \longrightarrow \infty \end{cases}$

I.C. $T = \hat{T} = Ti \quad \begin{cases} t = 0 \\ 0 \leq r < \infty \end{cases}$

In typical ignition applications, the bridgewire heating is sufficiently rapid that pyrotechnic ignition occurs at locations very near the bridgewire-pyrotechnic interface. Hence, as an approximation, ignition can be assumed to occur at the interface. The solution of the differential equation and boundary and initial conditions can be obtained by using a finite difference technique. From this solution, the behavior of the spatial and time derivatives at the boundary can be observed as functions of time. Both the first and second spatial derivatives are initially zero, but as heating commences they become negative. Temporarily corresponding to a minimum in the time derivative of temperature, the spatial derivatives also establish a minimum. This minimum corresponds to the appearance of the heat production term which reduces the amount of heat flux from the bridgewire to the pyrotechnic. Following this minimum, the two spatial derivatives change sign at a time only slightly preceding thermal explosion. Thus, it appears that the occurrence of the null in the first and second spatial derivatives can be used as ignition criteria. This occurrence follows the establishment of the minimum in the time derivative of temperature, which has been used as an ignition criterion by Gray, et al (10), and hence, gives a criteria which better corresponds to thermal explosion. The occurrence of a zero value of the first spatial derivative has been used previously by Enig (11) as an ignition criterion for thermal explosion problems.

Returning to the differential equation and first boundary condition and utilizing the occurrence of a null value in the first and second spatial derivatives results in

$$\frac{qz}{c} e^{-Ea/RT} = \frac{i^2 R}{\pi^2 a^4 \hat{\rho}\hat{c}}$$

or

$$T^* = \frac{Ea/R}{\ln \dfrac{\pi^2 a^4 \hat{\rho}\hat{c} \, qz}{i^2 R}} \quad .$$

These results correspond to the criterion often cited in Russian literature (1,6) that ignition occurs when the rate of energy added to the pyrotechnic equals the rate of heat production by the pyrotechnic. The "critical or ignition temperature," thus obtained, is not a unique value characteristic of a given pyrotechnic material since it depends on geometry, a, and the rate of heat addition, $\dfrac{i^2 R}{\hat{\rho}\hat{c}}$.

What is often of equal interest is the time to achieve this ignition temperature for a particular system. To determine this, one can use the method of Friedman (3) or Vilyunov (12) which decomposes the problem into two stages: the first stage consists of the inert problem, i.e., no reaction, and the second stage consists of adiabatic thermal explosion, i.e., no heat diffusion. Although this procedure should give good results, it becomes a bit cumbersome to apply. By examining the time corresponding to each of these two stages, it can be observed that often, the adiabatic thermal explosion time is short in comparison to the inert "heat-up" time. Hence, as an approximation, one can simply use the solution to the inert problem for the time which corresponds to the ignition temperature previously obtained. From Carslaw and Jaeger (13)

$$T^* = Ti + \frac{2}{\pi^3}\frac{Q}{k}\sigma^2 \int_0^\infty \frac{[1 - e^{-(\alpha t u^2/a^2)}]}{u^3 \Lambda(u)}\, du$$

where

$$\Lambda(u) = [uJ_0(u) - \sigma J_1(u)]^2 + [uY_0(u) - \sigma Y_1(u)]^2 .$$

Carslaw and Jaeger show further, that for limiting cases of short $(\alpha t/a^2 \le 0.1)$ and long $(\alpha t/a^2 \ge 10)$ times, respectively:

$$T^* - Ti \cong \frac{\sigma Q}{2\pi k}\left\{ \tau - \frac{4\sigma}{3\sqrt{\pi}}\tau^{3/2}\right\}$$

and

$$T^* - Ti \cong \frac{Q}{4\pi k}\left\{ \ln 4\tau - v\right\} .$$

Unfortunately, for many problems, ignition occurs at a time between the short time and long time approximations. On the other hand, the two solutions do

not differ greatly at the time of interest. Hence, so as to consider the
no-fire conditions with the same equation, the long-time solution can be
used to solve for the time corresponding to the occurrence of T*:

$$t = \frac{a^2}{4\alpha} \exp\left[\frac{4\pi k}{Q}(T* - Ti) + \gamma\right] .$$

Thus, if the required physical and thermochemical properties are known
for a material of interest, the ignition time can be determined as a
function of bridgewire diameter and applied current.

As an example, consider the ignition of a mixture of $TiH_2/KClO_4$ with
an Evanohm bridgewire. Properties which were used for this calculation are:

$$Ti = 300 \,°K$$
$$Ea/R = 12,000 \,°K^{-1}$$
$$q = 6900 \text{ joules/gm}$$
$$z = 1.0 \times 10^6 \text{ sec}$$
$$(\rho c) = 1.63 \times 10^6 \text{ joules/m}^3 \,°K$$
$$k = 0.88 \text{ watts/m} \,°K$$

With these values for the pyrotechnic and the appropriate values for Evan-
ohm bridgewire, Figure 1 was determined. Also shown are experimental data
points for ignition time versus applied current for a 0.0508 mm diameter
bridgewire (14). Because only estimates are available for the values of
Ea/R and z for this material, the values above were obtained by comparison
to the data of Reference 14. (These values are comparable to those which
have been successfully used in numerical analysis of hot wire ignition
problems.) However, it can be observed that the relationship between the
model and the experiment is rather good.

The procedure followed for the case of perfect thermal contact can be
extended to the case where contact resistance exists at the bridgewire-
pyrotechnic interface. In doing this, boundary condition 2 changes, but
this change does not modify the expression for critical temperature. Only
the value for time to achieve the ignition temperature is changed. Black-
well (15), gives an expression for the bridgewire temperature as a function
of time for the case of interface contact resistance. However, the
critical temperature corresponds to boundary pyrotechnic temperature which
is not now equal to the bridgewire temperature. Therefore, the solution
for boundary pyrotechnic temperature will be required for treating that
case by this procedure.
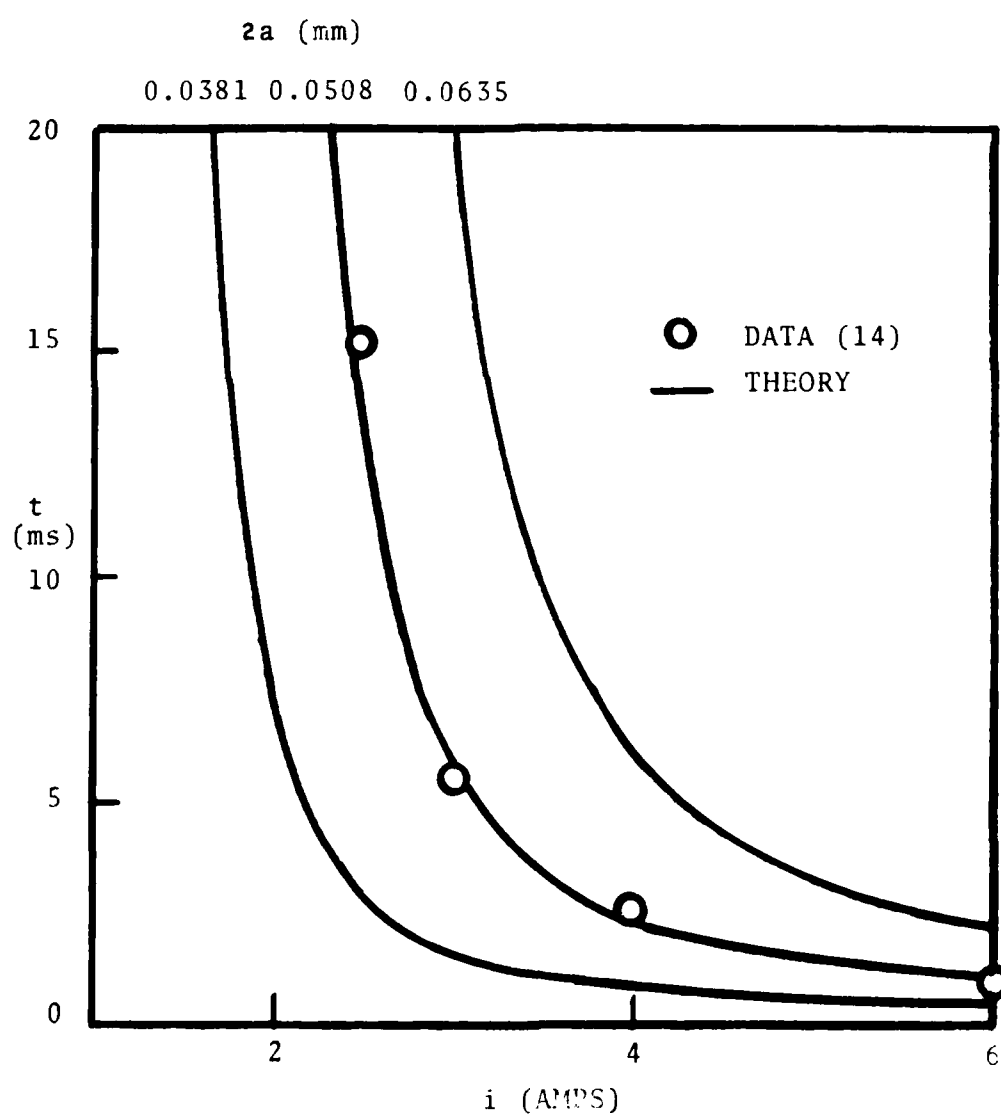
FIGURE 1   COMPARISON OF DATA AND MODEL

COMMENTS

Because of some of the assumptions made in the analysis, limitations in the model exist which will be discussed.

1. Although Figure 1 suggests a vertical asymptote for no-fire conditions, this limit cannot be obtained by the outlined procedure. This is because the model utilized the assumption of radial and axial infinity which does not lead to a theoretical steady-state temperature. In practice, however, a steady-state does occur as a result of finite dimensions.

2. Accurate experimental values are needed for the thermal and chemical properties of pyrotechnic before this model can be evaluated and before absolute values of ignition time can be calculated. In addition, it should be experimentally determined that the pyrotechnic of interest does indeed follow the Arrhenius model.

3. To give better accuracy at all times, the integral solution of the inert problem should be utilized. This would, however, require a procedure for solving the inverse problem, i.e., time as a function of temperature. Also, for those cases where it is appropriate, the adiabatic thermal explosion time should be included in calculations.

NOMENCLATURE

a	diameter of bridgewire
c	specific heat of pyrotechnic
$\hat{c}$	" " " bridgewire
E_a	activation energy of pyrotechnic
i	current passing through bridgewire
J_0, J_1, Y_0, Y_1	ordinary Bessel functions of zero and first order and modified Bessel functions of zero and first order, respectively
k	thermal conductivity of pyrotechnic
Q	energy supplied per unit length and per unit time by bridgewire ($\equiv i^2 \hat{R}/\pi a^2$)
q	heat of reaction of pyrotechnic
$\hat{R}$	resistivity of bridgewire
R	universal gas constant
r	radius variable
T	temperature of pyrotechnic
T^*	critical temperature of pyrotechnic (at bridgewire interface)
$\hat{T}$	temperature of bridgewire
T_i	initial temperature of the system (uniform)
t	time variable
u	integration variable
z	frequency factor
α	thermal diffusivity of pyrotechnic ($\equiv k/\rho c$)
ν	Eulers constant (= 0.5772....)
ρ	density of pyrotechnic

$\hat{\rho}$ density of bridgewire

σ volumetric heat capacity ratio ($\equiv 2\rho c/\hat{\rho}\hat{c}$)

REFERENCES

1. Averson, A. E., Barzykin, V. V. and Merzhanov, A. G., Doklady Akademii Nauk, SSSR, <u>178</u>, No. 1, p. 131 (1968).

2. Altman, D. and Grant, A. F., Fourth Symposium (International) on Combustion, p. 158, Williams and Wilkins, Baltimore (1953).

3. Friedman, M. H., Combustion and Flame, <u>13</u>, p. 567 (1969).

4. Baer, A. D. and Ryan, N. W., Combustion and Flame, <u>15</u>, p. 9 (1970).

5. Sernas, V., <u>Heat Transfer Model for Predicting Squib Ignition Times</u>, NASA, TM 33-655, (1974).

6. Zarko, V. E. and Khlevnoi, S. S., Combustion, Explosion and Shock Waves, <u>4</u>, No. 2, p. 89 (1968).

7. Jones, E., Proc. Roy. Soc. A, <u>198</u>, p. 522 (1949).

8. Klochkov, I. S. and Manachonskii, N. D., Fizika Goreniya i Vzryra, <u>9</u>, No. 4, p. 510 (1973).

9. Leopold, H. S., <u>Comparison of Constant Current and Capacitor Discharge Ignition of Normal Lead Styphnate</u>, Naval Ordnance Laboratory, NOLTR 70-236 (1971).

10. Gray, B. F. and Sherrington, M. E., Combustion and Flame, <u>19</u>, p. 435 (1972).

11. Enig, J. W., Proc. Roy. Soc. A, <u>305</u>, p. 205 (1968).

12. Vilyunov, V. N., Fizika Goreniya i Vzryva, <u>2</u>, No. 2, p. 77 (1968).

13. Carslaw, H. S. and Jaeger, J. C., <u>Conduction of Heat in Solids</u>, 2nd Ed., Clarendon Press, Oxford, p. 342 (1959).

14. Private Communication from Al Schwarz, Sandia Laboratories, Albuquerque, New Mexico, 4/26/76.

15. Blackwell, J. H., Journal of Applied Physics, <u>25</u>, No. 2, p. 137 (1954).

202

ESTIMATION OF THE THERMAL CHARACTERISTICS OF A
BRIDGEWIRE ENVIRONMENT BY AN ELECTROTHERMAL RESPONSE TEST*

A. B. Donaldson and A. C. Strasburg
Sandia Laboratories
Albuquerque, New Mexico 87115

ABSTRACT

The electrothermal response of an electroexplosive device is determined
by applying a subcritical square wave current pulse to the bridgewire and
monitoring the resultant temperature excursion. The temperature profile,
thus obtained, can be utilized with a mathematical model called the "Probe
Method" for approximating thermal properties. It is possible to estimate
the thermal conductivity and specific heat of the pyrotechnic and the thermal
contact conductance at the bridgewire/pyrotechnic interface by this technique.

INTRODUCTION

Parameters involved in modeling hot-wire ignition of a pyrotechnic composition include thermal constants of the bridgewire and pyrotechnic and the thermal coupling between them. Often the thermal conductivity of the pyrotechnic and coefficient of thermal conductance at the bridgewire/pyrotechnic interface are unknown. These parameters are a function of many variables including particle size and shape, pressing pressure, relaxation or centering processes following pressing, interstitial gas content, and others. Because pyrotechnic materials are hazardous to handle, they have not been studied extensively. In addition to the safety considerations, interface conductance is highly situation dependent and difficult to simulate in a laboratory model.

One approach to characterizing the unknown parameters is to use the explosive device itself as a test vehicle. A fully developed quality assurance test technique exists which utilizes a subcritical constant current to stimulate the actuator so that its response can be examined. The resultant temperature excursion from this test will be utilized in estimating the thermal characteristics of the bridgewire environment.

The concept of utilizing the electrothermal response of an explosive device as a quality assurance test was proposed by Rosenthal and Menicelli (1). In their model, the bridgewire is treated as a lumped thermal-mass system which dissipates heat through a contact conductance to constant temperature surroundings. Although this model has been successfully used in component development and testing, it provides no information on the thermal character istics of the pyrotechnic.

Sernas (2) studied pyrotechnic systems with a finite difference model and concluded that a contact conductance at the bridgewire/pyrotechnic interface should be included in bridgewire analyses. Using the Sernas model with variations in parameters to simulate observed responses one can predict values for the contact conductance and thermal conductivity of the pyrotechnic.

As an alternative to the finite difference model of the electrothermal response, the "Probe Method" of measuring thermal properties (3,4) can be utilized. Reference 4 gives an analytical solution to the problem which can be used in preference to a finite difference solution. The probe method utilizes, in essence, the thermal response of a cylindrical heat source which dissipates heat to variable temperature surroundings through a contact conductance. Data reduction consists of finding those thermal constants for which a match is obtained between the temperature-time response of the model and the experiment.

Because a bridgewire sometimes lies against an inert header, the thermal environment includes material which is not pyrotechnic. In this case, the values obtained will be a composite of values for both the pyrotechnic and the header. However, in system modeling, the composite values, rather than exclusively those of the pyrotechnic, will control rate of bridgewire heating.

If properties of the header and the pyrotechnic are individually known, the composite values can be used to indicate the header influence on the thermal response of the system.

ANALYSIS

Following the work of Blackwell (4), the problem is modeled as a cylindrical heat source surrounded by an infinite medium. The more significant assumptions utilized in the analysis are:

1) Axial effects are neglected.

2) The bridgewire temperature is a function of time only.

3) Thermal properties of both bridgewire and pyrotechnic are isotropic and independent of temperature.

4) The pyrotechnic is radially infinite and at a uniform initial temperature throughout.

Based on these assumptions, the differential equation can be stated as:

$$\frac{1}{r} \frac{\partial}{\partial r} \left[r \frac{\partial (\Delta T_2)}{\partial r} \right] = \frac{1}{\alpha} \frac{\partial (\Delta T_2)}{\partial t} \quad \begin{cases} a < r < \infty \\ t > 0 \end{cases}$$

with the boundary and initial conditions

$$- 2\pi a k_2 \frac{\partial (\Delta T_2)}{\partial r} = \frac{i^2 R}{\pi a^2} - \pi a^2 \rho_1 C_1 \frac{\partial (\Delta T_1)}{\partial t} \quad \begin{cases} r = a \\ t > 0 \end{cases}$$

$$- k_2 \frac{\partial (\Delta T_2)}{\partial r} = h(\Delta T_1 - \Delta T_2) \quad \begin{cases} r = a \\ t > 0 \end{cases}$$

$$\lim_{r \to \infty} \Delta T_2 = 0 \quad \begin{cases} r \to \infty \\ t > 0 \end{cases}$$

and

$$\Delta T_1 = \Delta T_2 = 0 \quad \begin{cases} r \geq 0 \\ t = 0 \end{cases}.$$

Blackwell gives the solution of this system for the temperature of the bridge-wire as a function of time. The result is

$$\frac{(\Delta T_1)k_2}{(i^2 R/\pi\alpha^2)} = \frac{2\sigma^2}{\pi^3} \int_0^\infty \frac{(1 - e^{-u^2\tau})du}{u^3 f(u)}$$

where

$$f(u) = [uJ_0(u) + (u^2/Bi - \sigma)J_1(u)]^2 + [uY_0(u) + (u^2/Bi - \sigma)Y_1(u)]^2$$

For $Bi \rightarrow \infty$, i.e., perfect thermal coupling between the bridgewire and pyrotechnic, the solution simplifies to the appropriate case treated in Carslaw & Jaeger (5). Hence, the nondimensional bridgewire temperature can be related to nondimensional time, the contact conductance, and the ratio of the volumetric-specific heats of the pyrotechnic to bridgewire.

EXPERIMENTAL

Test System

The input used in the electrothermal response test is a single square wave current pulse. Its amplitude is selected to produce a subcritical temperature excursion at the pyrotechnic/bridgewire interface. The duration of the pulse can be arbitrarily chosen. A typical pulse to achieve a nominal 100°C excursion may be an amplitude of 500 mA with a duration of 60 ms. Experimental data used in the present study were obtained with pulse amplitudes of 400 and 750 mA and durations in excess of the values needed for the parameter estimation. The data are shown in Table I.

The temperature excursion is monitored as the current-resistance drop across the bridgewire during application of the stimulus. Magnitude of change is on the order of one or two percent of the basic resistance. The excursion is isolated from response of the cold resistance by connecting the component as the unknown arm of a resistance bridge. Output of the bridge is zero at balance condition. Temperature (resistance) rise of the bridgewire unbalances the bridge and produces the characteristic output analog.

Peak amplitude of the output signal is on the order of 5 millivolts. Following suitable amplification, the analog is digitized at uniform intervals and stored in the memory of a waveform recorder. Data are then transferred to the memory of a programmable calculator for analysis and presentation of results.

Test Vehicle

The test vehicle contained a 26.5/73.5 mixture of $TiH_{1.9}/KClO_4$, pressed at 10,000 psi (2.18 gm/cm^3) into an actuator body. The header was glass and the bridgewire was 0.0457 mm diameter x 1.40 mm long Tophet C. The electro-thermal response test was performed shortly after the units were assembled. Data from the response test are shown in Table I for two current levels.

DISCUSSION

Determination of thermal parameters from experimental data requires the variation of parameter values until a fit is obtained between the theoretical solution and the data. Computation can involve any number of points, providing the number used is equal to or greater than the number of unknowns. However, as a general consideration, a larger number of points leads to greater accuracy in the parameters. For this study, we assume the unknown quantities to be the volumetric specific heat of the pyrotechnic, the thermal conductivity of the pyrotechnic and the thermal contact conductance at the bridgewire/pyrotechnic interface.

The procedure used was a variation of the parameters k_2, $(\rho C)_2$ and Bi until a fit was obtained between the analytic and experimental curves of ΔT_1 vs. t. A computer program was written which minimizes the difference of the squares at the locations used in the fit. Figure 1 shows a comparison between the theory and experiment for the data in Table I using a 10 point fit.

Values used in the theoretical curve calculation were:

$$k_2 = 0.379 \text{ J/ms} \cdot \text{K}$$

$$(\rho C)_2 = 6.27 \times 10^5 \text{ J/K} \cdot \text{m}^3$$

$$Bi = \begin{cases} 10 \text{ for the } 400 \text{ mA case} \\ \infty \quad " \quad " \quad 750 \quad " \quad " \end{cases}$$

TABLE I

Experimental Bridgewire Temperature
Excess as a Function of Time and Current

Time (msec)	$\Delta T_1 (K)$	
	i = 402.31 mA	i = 738.66 mA
1.00	10.87	33.42
2.00	18.19	58.02
3.00	22.85	74.66
4.00	26.84	87.68
5.00	30.16	97.45
6.00	32.16	105.05
7.00	34.82	111.56
8.00	36.15	115.90
9.00	36.82	120.24
10.00	38.15	124.22

208
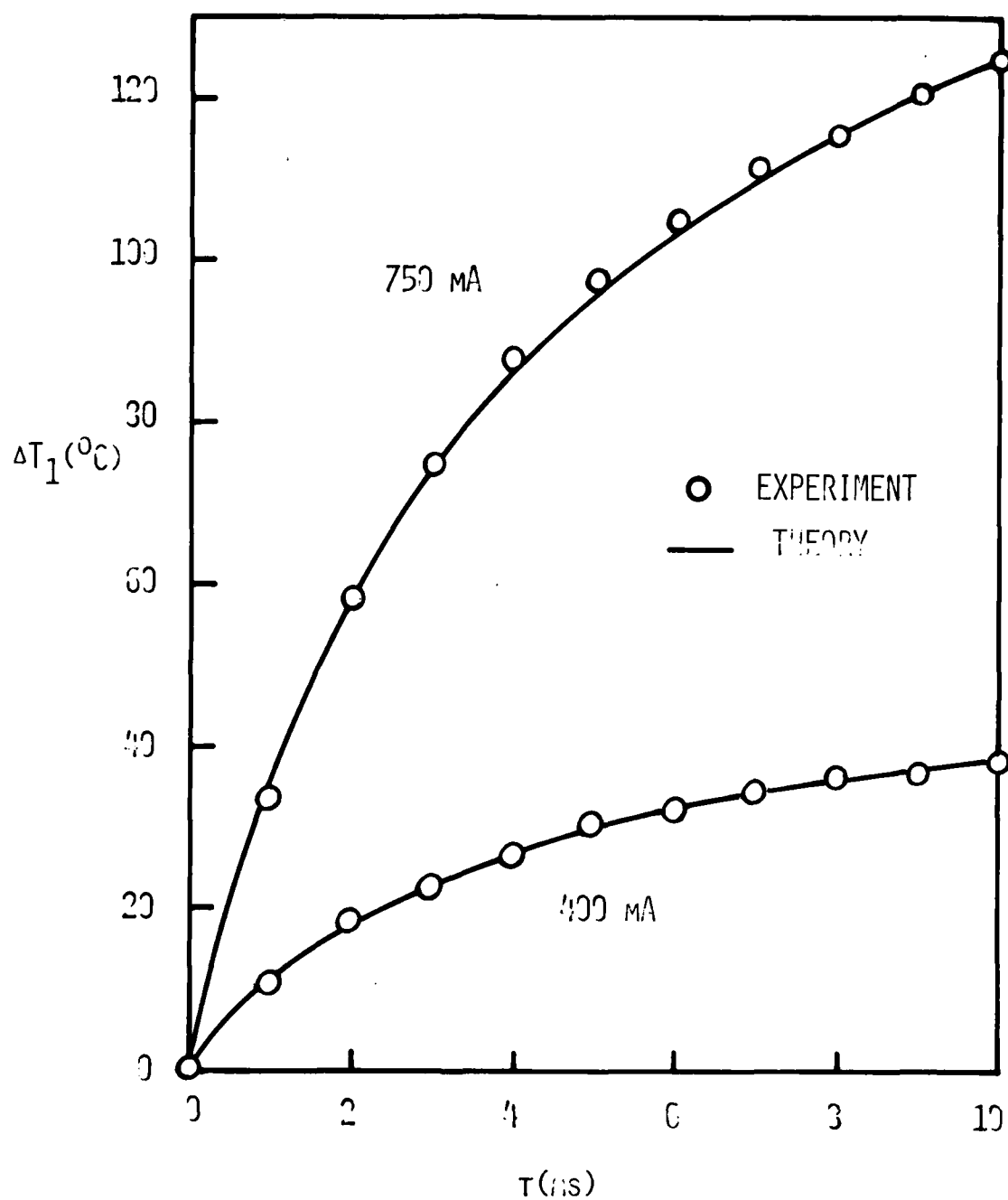
FIGURE 1   COMPARISON OF EXPERIMENT AND THEORY

These values can be compared to those estimated from other sources for similar material and to the values for the glass headers:

$$TiH_2/KClO_4 \quad (33/67) \qquad Glass$$

$$k_2 \quad 0.42 \qquad\qquad 1.42$$

$$(\rho C)_2 \quad 16.5 \times 10^5 \qquad 22.1 \times 10^5$$

Although the computed value for thermal conductivity falls between those of the pyrotechnic and the glass header, the value of the volumetric-specific heat does not. This may be because of incorrect assumptions incorporated in the analysis, or because of unsymmetric partitioning of energy between the bridgewire and its environment. Alternately, it has been observed that in the pressing of actuators, a strong density gradient can exist in the pyrotechnic. This effect generally leads to low densities in the vicinity of the bridgewire. Hence, the small indicated value of $(\rho C)_2$ could be real. Further studies are needed to better qualify this consideration. Another observation is that as the bridgewire temperature increases, so does the interface contact conductance. An explanation of this difference is that the interface contact conductance becomes larger for the 750 mA case due to thermal expansion of the bridgewire.

A final caution in utilizing the "Probe Method" is that data cannot be used at long times for parameter computation, i.e., in the region where thermal equilibrium is established, as the assumptions of axial and radial infiniteness no longer hold.

210

<div align="center">NOMENCLATURE</div>

a	radius of bridgewire
Bi	Biot Modulus for contact conductance $(\equiv \frac{ha}{k_2})$
h	thermal contact conductance
i	current passing through bridgewire
J_0, J_1, Y_0, Y_1	ordinary Bessel functions of zero and first order and modified Bessel functions of zero and first order, respectively
k_2	thermal conductivity of bridgewire environment
R	resistivity of bridgewire
r	radius variable
t	time variable
u	dummy variable of integrand
α	thermal diffusivity of pyrotechnic $\left[\equiv \frac{k_2}{(\rho C)_2}\right]$
ΔT_1, ΔT_2	temperature excess of bridgewire and pyrotechnic, respectively
θ	nondimensional bridgewire temperature $\left(\equiv \frac{\Delta T_1 k_2}{i^2 R/\pi a^2}\right)$
$(\rho C)_1$, $(\rho C)_2$	density-specific heat product of bridgewire and environment, respectively
σ	dimensionless volumetric heat capacity ratio $\left[\equiv 2(\rho C)_1/(\rho C)_0\right]$
τ	Fourier number $(\equiv \alpha t/a^2)$

REFERENCES

1. Rosenthal, L. A. and Menicelli, V. J., Nondestructive Testing of Insensitive Electroexplosive Devices by Transient Techniques, NASA Technical Report 32-1494, July 15, 1970.

2. Sernas, V., Heat Transfer Model for Predicting Squib Ignition Times, NASA Technical Memorandum 33-655, January 15, 1974.

3. Van der Held, E. M. F. and Van Drunen, F. G., Physica, Vol. 15 (1949), pp. 865-881.

4. Blackwell, J., Journal of Applied Physics, Vol. 25, No. 2 (1954), pp. 137-144.

5. Carslaw, H. S. and Jaeger, J. C., Conduction of Heat in Solids, 2nd Ed., Oxford Press, London, 1959, pp. 342-345.

PREDICTION OF LINE SHAPES IN PYROTECHNIC
FLARES CONTAINING LITHIUM

B. E. Douda
Applied Sciences Department
Naval Weapons Support Center, Crane, Indiana

ABSTRACT

A two line radiative transfer model of a pyrotechnic illuminating
flare flame was previously validated and reported for flames containing
sodium as the major emitter. The model is capable of predicting the
spectral radiant flux of different flares from known system variables
such as formula, size, and ambient pressure. The data presented
compares experimentally determined line shapes of flames containing
lithium with line shapes predicted by the model.

The origin of the parameters of the radiative transfer model is
discussed to show the differences between those needed for lithium and
those for sodium. Some thermodynamic properties of the flame are
included. The deficiency in the use of an average value inside the
flame for the number density of lithium atoms is described.

INTRODUCTION

A two line radiative transfer model of a pyrotechnic illuminating flare flame was previously validated,[1,2] and reported for flames containing sodium as the major emitter. The model is capable of predicting the spectral radiant flux of different flares from known system variables such as formula, size, and ambient pressure. For flares containing sodium, the agreement between theory and experiment was quite good even though the absorption profile and number density of sodium atoms were represented in the model as having average values inside the flame that are independent of the optical depth. Subsequently, Dillehay[3] presented an improved model which accounts for reduction in the sodium atom density at the plume boundary due to reaction with atmospheric oxygen and a reduced local plume temperature. Neither of the above models has been validated for alkali metals other than sodium. Primarily because the full half-width of the lithium resonance lines at 670.7 nm was observed to be smaller than expected, the present research was initiated to compare predicted spectra from the earlier model[1] to spectra of flares containing lithium. The purpose of the work was to determine why this difference exists. This paper is a report of that effort.

EXPERIMENTAL*

Initial Calculations

To completely accomplish the objectives of the work, a series of experimental flares was made which was designed to allow investigations of the emission spectra of high and low concentrations of atomic lithium as the emitter. An initial series of calculations was done using the NASA thermodynamics program[4] to optimize the magnesium, alkali metal nitrate, binder formulations to give the maximum adiabatic temperature. The organic binder level was fixed at five percent and the fuel to oxidizer ratio was varied until the maximum temperature was computed. The four final formulas used in this study are given in Table 1. The maximum computed adiabatic temperature and the alkali metal atom density at maximum temperature for each formula group are listed in Table 2.

An examination of Table 2 reveals that (a) the maximum temperature is nearly the same for all formulas; (b) groups 7307, 7312 and 7313, designed to contain a high lithium atom density, all have nearly the same atom density; and (c) group 7308 has nearly 1/100 lithium atom density as compared to the other formulas. Thus, these formulas made it possible to observe the spectral behavior of flares containing both high and low lithium atom density.

---

*In order to specify procedures adequately, it has been necessary occasionally to identify commercial materials and equipment in this paper. In no case does such identification imply recommendation or endorsement by the Navy, nor does it imply that the material or equipment identified is necessarily the best available for the purpose.

TABLE 1. FLARE FORMULATIONS

Group 7307

Magnesium	43.2%
Lithium Nitrate	51.1
Rubidium Nitrate	0.7
Binder	5.0

Group 7312

Magnesium	43.2%
Lithium Nitrate	51.05
Cesium Nitrate	0.75
Binder	5.0

Group 7308

Magnesium	39.6%
Sodium Nitrate	54.9
Lithium Nitrate	0.5
Binder	5.0

Group 7313

Magnesium	43.2%
Lithium Nitrate	50.65
Sodium Nitrate	0.55
Potassium Nitrate	0.60
Binder	5.0

TABLE 2. COMPUTED FLARE PARAMETERS

	Temperature	Li atoms/cm^3	Other atoms/cm^3
Group 7307	3081 K	5.00×10^{17}	2.96×10^{15} Rb
Group 7308	3073 K	4.55×10^{15}	
Group 7312	3083 K	5.06×10^{17}	4.33×10^{15} Cs
Group 7313	3083 K	4.99×10^{17}	7.01×10^{15} Na 6.01×10^{15} K

Construction of Flares

The chemicals used in making the formulations ranged from research grade lithium, rubidium and cesium nitrate to a practical grade sodium and potassium nitrate. These oxidizers were ground and dried prior to mixing. The particle size was approximately 30 μm. The magnesium was MIL-M-382, granulation 17, which has an approximate particle size of 75 μm. The binder[5] used was a combination of Dow Epoxy Resins©, DER 321 and DER 732 and a polyamine CX 3482.1 in the ratio DER 321 - 61.3%, DER 732 - 26.3% and CX 3482.1 - 12.4%. This is a typical epoxy binder formulation currently in use in illuminating flares. In an effort to prevent contamination, the mixing, screening and drying apparatus each were washed and dried between each formula change.

The flares were pressed into paper tubes at 10,000 pounds dead load. Fifty grams of composition were used for each candle. The finished size was 3.3 cm in diameter and 5.1 cm in length. Five grams of ignition composition were pressed on the surface of each candle.

Experimental Procedure

The flares were burned face up at a distance of 6.0 meters from the spectrographs. Visible spectra from 0.40 - 0.70 μm were recorded on a Bausch and Lomb 1.5 m grating spectrograph. This instrument has a 450 line/mm grating giving a dispersion of 15 Å/mm in the first order on the photographic film. Kodak Linagraph Shellburst© film[6] was used for recording these spectra. Spectra were also taken in the region of the resonance lines using a 1 m Spex spectrograph and Kodak© I-N plates. The Spex instrument has a 1200 line/mm grating and gives a first order dispersion of 8 Å/mm. Spectra of a 200 watt quartz-iodine lamp were recorded on the same plates to provide a film response correction. In these experiments the flares were masked in such a way that the spectrographs were observing a position in the flame seven centimeters above the surface of the candle.

The spectra were scanned and digitized on an Optronics S2000 densitometer. Points were taken at approximately 0.08 nm intervals. The resulting digital output was processed by standard procedures[7] and the film density converted to radiant power readings.

RESULTS

Experimental

As reported earlier by Webster,[8] these flares were prepared for multiple experiments. The Bausch and Lomb spectrograph was utilized to obtain spectra in the visible region, the cut-off being near the lithium resonance line. Accordingly, spectra acquired with this spectrograph were not useful for the present purposes. Only spectra of groups 7308 and 7312 taken with the Spex instrument are suitable for comparison to the theoretically predicted spectra. During testing of groups 7307 and 7313, the grating of the Spex instrument was set for a spectral region which did not include the lithium resonance line. Nevertheless, a

limited amount of information about groups 7307 and 7313 is included to facilitate comparison between experiment and theory.

Relative radiant power spectra obtained on the Spex instrument were plotted for each of the flares burned from groups 7308 and 7312. The burning rates on all the compositions were on the order of 0.084 cm/s. The full half-widths measured from each of the spectra are:

a.   For group 7308: 10.2 Å, 10.13 Å, 10 Å, 9 Å, and 10.13 Å for an average of 9.9 Å.

b.   For group 7312: 202.02 Å, 209.18 Å, 199.01 Å, 193.3 Å, 246.85 Å, and 151.33 Å for an average of 200.28 Å.

The experimental spectra in Figures 1 and 2, each being typical of the average of groups 7308 and 7312 respectively, are shown for later comparison to theoretically computed spectra.

Theoretical

Full half-widths were measured from spectra computed using the model described in reference (1) for all of the flare groups. The following parameters were used in the computation:

a.   flame diameter = 6 cm

b.   *lithium atom density* = value in Table 2

c.   Voigt profile a parameter was 1.2 for high lithium atom density (groups 7307, 7312, and 7313) and 0.3 for low lithium atom density (group 7308). These are the same values used for sodium containing flares as reported in reference (1).

d.   pressure = 101325 N/m^2

e.   temperature at flame center = value in Table 2

f.   boundary temperature = 1200 K, the same as used for sodium flares in reference (1).

Full half-widths resulting from the use of these parameters are about 2.5 times greater than observed experimentally. The reason for this difference will soon become clear. If one makes no other parametric changes except to use lithium atom densities which are one-seventh of those given in Table 2, the following full half-widths are computed.

a.   Group 7307   200.18 Å

b.   Group 7308   9.80 Å

c.   Group 7312   201.19 Å

d.   Group 7313   200.18 Å

These are in good agreement with the averages reported earlier for full half-widths measured from spectra obtained experimentally of groups 7308 and 7312. It remains to show why the use of a reduced (1/7) lithium atom density is needed whereas such is not the case for sodium flares and maybe for flares containing potassium, rubidium, or cesium. Figures 3 and 4 representing groups 7308 and 7312, respectively, are included for visual comparison with Figures 1 and 2. Although these full half-widths compare favorably with experiment, one notable difference is the more prominent absorption region at the resonance line center for the computed spectra. This too results from the approximation that the lithium atom density is an average value in the flame independent of optical depth, i.e. position in the flame. Why then is the computed metal atom number density acceptable for sodium containing flares but not for lithium? It is this question that will be examined next.

Thermodynamic Considerations

The mole fraction of each of the alkali metal atoms in the reaction products at the low density level was computed[4] as a function of temperature for each of formula groups 7307, 7308, 7312 and 7313. These are plotted in Figure 5. The main point of Figure 5 is to show that for flares containing sodium, potassium, rubidium, or cesium, the mole fraction is relatively constant between 1200 K (the flame boundary temperature) and the maximum temperature (flame center). On the other hand, the mole fraction of lithium atoms decreases rapidly by several orders of magnitude going from the region of maximum temperature to the flame boundary estimated to be 1200 K. This comparison tends to show why the use of the average number density computed at the maximum temperature is acceptable for predicting spectra of flares containing sodium but is not acceptable for flares containing lithium. For lithium, the effective atom number density is clearly less. The factor of one-seventh was established empirically.

The alkali metal mole fractions plotted in Figure 5 do not take into account any supplemental oxidation contributed by diffusion of ambient air into the flame. Such a process is known to cause further reduction of the metal atom concentration near the flame surface. Resonance line spectra of flares made with lithium seemingly are more sensitive to this process than those of the other alkali metals.

Below 1200 K, all of the alkali metal mole fractions of Figure 5 show a significant decrease except for rubidium. Although the data bank contained appropriate information about the oxides of rubidium, as well as for the other alkali metal oxides, the thermodynamic computation did not indicate the formation of enough oxides of rubidium above 800 K to cause a significant reduction in the rubidium metal atom mole fraction.

218

DISCUSSION

This paper shows that there is good correlation between spectral line shapes of the lithium resonance lines predicted by the radiative transfer model and experimental lithium line shapes when the lithium atom number density is taken to be one-seventh of the number density computed for the formula at its adiabatic temperature. No other parametric adjustments are needed. In addition, thermodynamic data (Figure 5) are presented to show why lithium is unique among the alkali metals in that its atom density within the flame is reduced greatly in regions near the flame surface, i.e. at lower temperatures. A similar adjustment was not needed to predict spectra of flares containing sodium.[1,2] It is anticipated that future research will demonstrate that potassium, rubidium, and cesium behave as does sodium.

The model reported by Dillehay[3] is an improved version of the model used for this research. Dillehay computes the value of the Voigt a parameter, the adiabatic temperature, and the alkali metal atom number density as a function of radial positions in the flame. While these computations require additional computer time, no adjustments should be required. In addition, Dillehay also accounts for reaction of the flame species with the surrounding atmosphere. It will be interesting to learn how well the Dillehay model predicts a lithium resonance line spectrum recognizing the unique properties of lithium discussed in this paper.

ACKNOWLEDGEMENTS

FIGURE CAPTIONS

Figure 1. Relative radiant power spectrum of a typical flare from formula group 7308 with low lithium atom number density. The spectrum shows the lithium resonance lines at 670.7 nm with a full half-width of 10 Å. The continuum underlying the resonance lines is due to the red wing of the broadened sodium resonance lines.

Figure 2. Relative radiant power spectrum of a typical flare from formula group 7312 with high lithium atom number density. The spectrum shows the lithium resonance lines at 670.7 nm with a full half-width of 199.01 Å.

Figure 3. Theoretical relative radiant power spectrum of the lithium resonance lines predicted for formula group 7303, the low lithium density case. The full half-width is 9.8 Å. The main model parameters are 6 cm flame diameter, 6.5×10^{14} lithium atom density, 0.3 Voigt a value, one atmosphere pressure, and 3073 K at flame center.

Figure 4. Theoretical relative radiant power spectrum of lithium resonance lines predicted for formula group 7312, the high lithium density case. The full half-width is 201.19 Å. The main model parameters are 6 cm flame diameter, 7.2×10^{16} lithium atom density, 1.2 Voigt a parameter, one atmosphere pressure, and 3083 K at flame center.

Figure 5. Computed mole fraction as a function of temperature of alkali metal atoms in the reaction products for formula groups 7307, 7308, 7312 and 7313. The lithium mole fraction decreases markedly with decreasing temperature. The other alkali metal mole fractions remain nearly constant between 1200 and 3000 K.

220
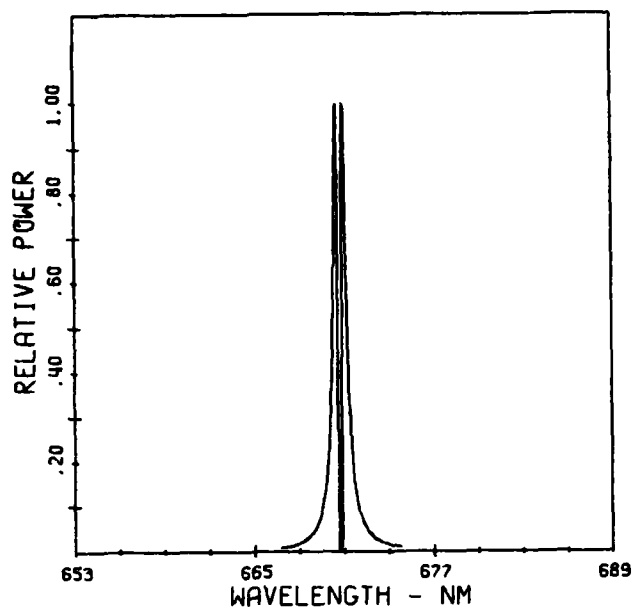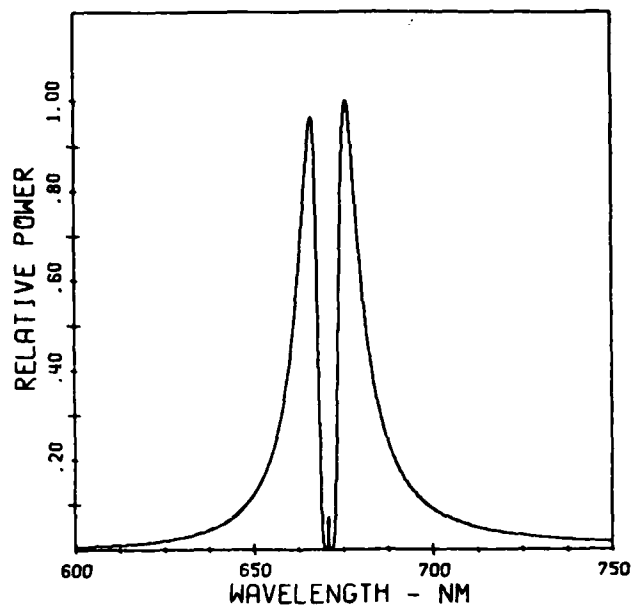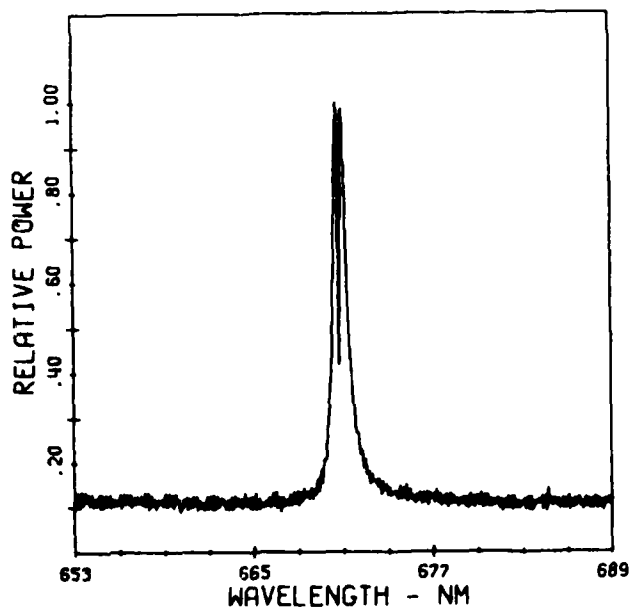
FIGURE 3

FIGURE 4

FIGURE 1
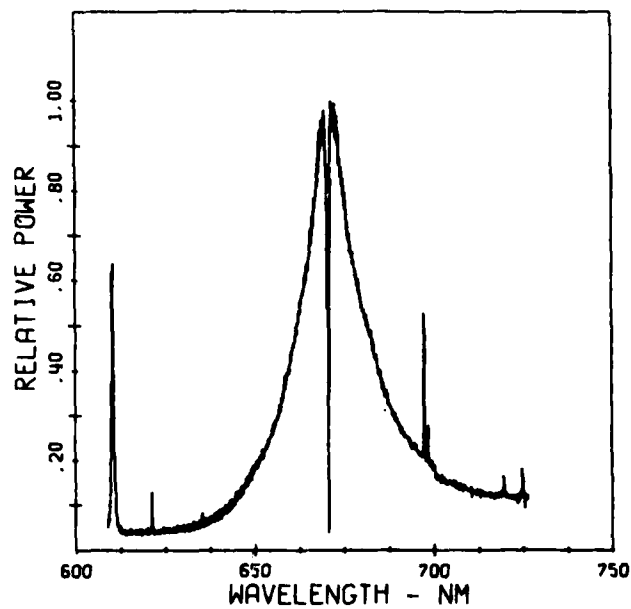
FIGURE 2
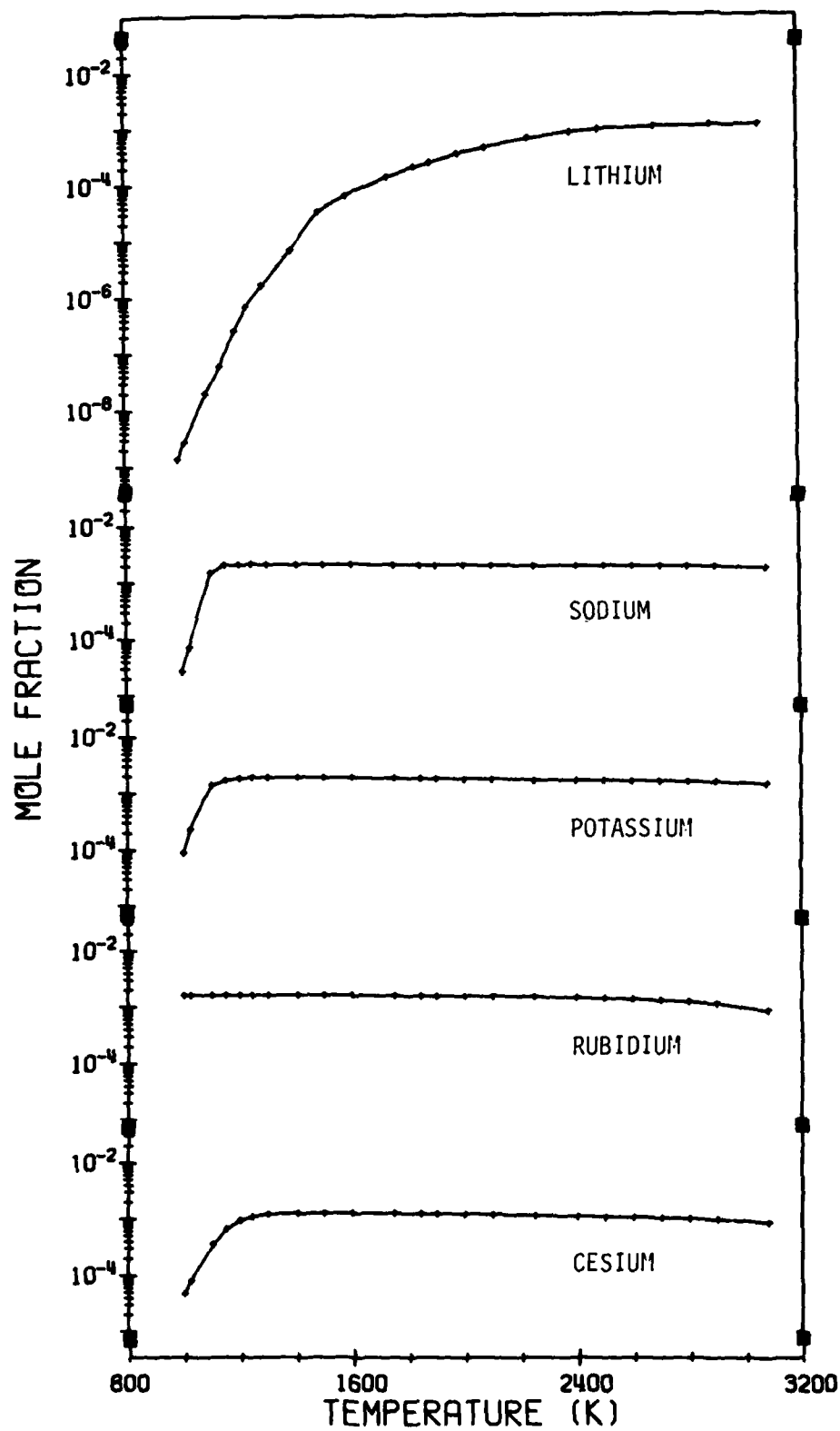
FIGURE 5

REFERENCES

1. B. E. Douda and E. J. Bair, *Radiative Transfer Model of a Pyrotechnic Flame*, J. Quant. Spectrosc. Radiat. Transfer $\underline{14}$, 1091-1105 (1974).

2. B. E. Douda, *Radiative Transfer Model of a Pyrotechnic Flame*, RDTR No. 258, Naval Ammunition Depot, Crane, Indiana (1973). Available NTIS--AD 769273.*

3. D. R. Dillehay, *Pyrotechnic Flame Modeling* in *PYROCHEM International 1975* held at University of Surrey, Guildford, U.K., 21-25 July 1975. (Sponsored by Royal Armament Research and Development Establishment), p. 5-1. Available DDC--AD-B006100L.**

4. S. Gordon and B. J. McBride, *Computer Program for Calculation of Complex Chemical Equilibrium Compositions, Rocket Performance, Incident and Reflected Shocks, and Chapman-Jouguet Detonations*, NASA SP-273, Lewis Research Center (1971). Available NTIS--N71 37775.

5. The binder resins are registered tradenames of the Dow Chemical Company, Midland, Michigan.

6. The referenced photographic films are registered tradenames of Eastman Kodak Company, Rochester, New York.

7. H. A. Webster and C. W. Gilliam, *Spectral Characteristics of Flares Containing Sodium Iodate as an Oxidizer*, RDTR No. 276, Naval Ammunition Depot, Crane, Indiana (1974). Available NTIS--AD 782510.

8. H. A. Webster III, *Alkali Metal Emitters. I. Analysis of Visible Spectra*, NWSC/CR/RDTR-16, Naval Weapons Support Center, Crane, Indiana (1975). Available NTIS--AD-A019367.

*Available NTIS indicates the document is available from National Technical Information Service, 5285 Port Royal Road, Springfield, Virginia 22161.

**Available DDC indicates the document is available from Defense Documentation Center, Cameron Station, Alexandria, Virginia 22314.

EFFECT OF HEAT LOSS ON DELAY COLUMN PERFORMANCE

Alexander P. Hardt and Peter V. Phung

Lockheed Palo Alto Research Laboratories
3251 Hanover Street, Palo Alto, California 94304

and

Frank J. Valenta

Naval Ordnance Station
Indian Head, Maryland 20640

ABSTRACT

Diffusion-limited reaction models were applied to propagation rate studies of gasless reactions. Simple geometries as represented by Pyrofuze wire and sheet were analyzed for adiabatic reactions, and the resulting propagation rates were compared with experimental data. The validity limits of such a one-dimensional analysis were established.

Causes of diverse reaction phenomena were examined and found to be related to oscillatory burning. Motion pictures and still photographs were obtained on representative intermetallic reactions. The equivalence of the diffusion-limited and the kinetically limited reaction model was demonstrated.

Combustion instability was ascribed to deviations from adiabaticity, and the reaction of heterogeneous mixtures was modeled in cylindrical coordinates and programmed for multidimensional analysis.

For identifiable parametric values, it was found that the propagation rate of the combustion front in the presence of radial heat loss diminishes until the reaction is quenched. Sample calculations were performed on unstable parametric configurations. Reaction front collapse was enhanced by high thermal conductivity of the mixture, large particles, high activation energy, low ambient temperature, and large delay column bodies.

For conventional systems of reasonable size and low conductance, the effect of radial heat loss on the temperature of the reaction zone was found to be negligible, and other contributing causes to performance variability were examined. The magnitudes and trends of the predicted parametric dependence of real delay columns correlate well with published data.

INTRODUCTION

In previous studies,[1,2] we have examined a simplified model of gasless reactions and showed that if one assumes a steady-state mass and heat transfer process, one can sufficiently describe the propagation rate and the reaction mechanism in terms of thermal and mass diffusion and so obtain a measure of the role of particle size, stoichiometry, and compaction on the propagation rate. In this paper we shall describe several complexities that are found in gasless reaction systems. One such complexity is the oscillatory mode of propagation.

To illustrate various types of reaction propagation, we are showing a motion picture of the burn of a stoichiometric mixture of nickel and aluminum powder and of titanium and carbon that were pressed into 1 × 1-cm rods. After pre-heating and igniting a Ni-Al specimen, it was observed that the luminous front migrates rapidly along the specimen. Soon the visible reaction ceases without traversing the specimen, and the remaining compact appears unreacted. Figure 1 shows such a specimen which was burned at room temperature and whose reaction ceased. After a brief period, a bright terminal flash occurs at the end of the specimen followed by a reflected heat pulse that races backward. Figure 2 shows the appearance of the specimen after the reaction. We shall have occasion later to discuss the various features that are observed in the specimen. Figure 3 shows the transition of steady-state reaction to oscillatory reaction in a reacting mixture of titanium and boron.

Other complexities arise from nonadiabatic reaction conditions leading to changes in reaction rate and ultimately to quenching. Such phenomena are of interest in the design of delay columns, and these have led to the extension of our previously reported work to nonadiabatic systems.

THE CONCEPT OF OSCILLATORY COMBUSTION

A. G. Merzhanov and coworkers[3] analyzed condensed phase reactions, programmed the differential equations, and observed that the computed reaction front characteristics (temperature and degree of completion) oscillated about a mean value. Whereas the model was specifically formulated for homogeneous systems, such oscillations have in fact been observed only in heterogeneous systems. This oscillatory behavior has been ascribed to variations in excess enthalpy in the combustion front.

The model may be explained as follows. As the temperature in a section reaches (by conduction from the preceding section), the ignition temperature, T_i, the heat in the section will rise to $\rho c \{ [(1 - F)Q/c] + T_i \}$, which includes an excess heat that resides in the combustion front and that, because of the higher reaction rates associated with the excess enthalpy, causes a steep temperature profile. To see how such excess enthalpy can give rise to oscillatory burning, consider a system which reacts slowly, because of high heat losses, or because of high melting points of the constituents, or because of low heat of reaction. Thermal diffusion

Scale 2:1

Fig. 1 Appearance of an Al–Ni Compact After Reaction. Ignition by a high-temperature first fire is followed by the ordinary mode of combustion characterized by a steep reaction front and a high propagation velocity. The change in mechanism is evident by the volume expansion which consists of Ni_2Al_3 and free nickel phases.[6] This zone is followed by extinction although partial reaction by dead sintering continues[4].

Scale 2:1

Fig. 2 Appearance of a Preheated Al–Ni Compact After Reaction. By increasing the reaction temperature through preheating to 250°C, the reaction resumes by a reflected front from the end of the specimen, after having stopped as shown in Fig. 1. Particle size of nickel: 44 μm: of aluminum: 74 μm.

Scale 2:1

Fig. 3 Titanium–Boron Compact After Reaction. Both oscillatory burning and normal burning are observed although, because of steeper reaction fronts, and higher reaction temperatures, transitions are not reversible as in the NiAl system. 10–44 μm titanium in amorphous boron.

may bring about dead sintering[4] so as to reduce the diffusion rate at T_i below the ignition level. Heat from the preceding hot zone continues to soak into the section, which may partially react, but because of heat losses, it will react with reduced conversion fraction. This heat soak will continue until a later section attains T_i, causing it to trigger another burst of energy, and by generating a steep temperature profile, causes a repetition of the above process. Systems can be made to react uniformly by preheating (Fig. 2), which is a way of increasing the reaction temperature throughout the sample.

Mixtures burning in the above oscillatory mode would have a lower reaction temperature, and hence a lower propagation velocity, than one would predict for adiabatic steady-state reaction. As early as 1941, Zel'dovich[5] showed that the minimum propagating velocity of a reaction accompanied by heat losses to the ambient medium is given by

$$v_{min} = \frac{v_a}{\sqrt{e}} = 0.61 \, v_a \tag{1}$$

where v_a is the rate for the adiabatic reaction, and v_{min} is the rate at the point of quenching. This theoretical treatment of combustion limits was experimentally verified and found to be applicable to gasless reactions.[6] The relationship between the pyrotechnic mixture characteristics and the oscillatory burning behavior has been found by analytical modeling of homogeneous systems to be[3]

$$\alpha = 9.1 \frac{c}{Q} \frac{\mathcal{R} T_r^2}{E} \left(1 - 0.27 \frac{Q}{c T_r}\right) \tag{2}$$

If $\alpha > 1$, the steady-state reaction is stable, but if $\alpha < 1$, the reaction becomes oscillatory. The domain of steady-state reaction is one of high reaction temperatures and high propagation rates. By diluting the mixture with an inert component, the heat output and hence the reaction temperature, are reduced, giving rise to a transition from stable combustion to the oscillatory combustion regime. This has been verified experimentally.[6] Interestingly, thermal conductivity does not enter into the analysis.

Exact quantitative experimental verification of Eq. (2) is difficult because of the requirements of knowing the kinetic activation energy, E. This activation energy in a diffusion-controlled system varies with concentration[6,7] because of the complex transition from interstitial to substitutional to molecular (liquid) diffusion, each being characterized by its own activation energy. Small particle size plays an important role in promoting narrow reaction zones and hence, high reaction temperatures, and steady-state reaction modes.[6]

We have never observed anything other than stable reactions in homogeneous systems (Pyrofuze), but find that oscillatory reactions are easily induced in heterogeneous intermetallic reaction mixtures, and oscillatory reactions have been reported in thermite compositions.[8] Moreover, precise modeling of the oscillatory reaction mechanism is difficult, because the appearance of

oscillations in computer printouts is as much a matter of fortuitous zoning as it is due to a firm grasp of all reaction variables. Merzhanov and others[3] have published schematic representations of the effect of oscillatory burning on propagation velocity, temperature, etc. We have reproduced such a representation in Fig. 4 to show how it helps to explain the appearance of reaction specimens as seen in Figs. 2 and 3. Some of the published data on representative gasless reactions are tabulated in Table 1.

ADIABATIC REACTION IN SIMPLE GEOMETRIES

We are extending now our previous work on adiabatic steady-state propagation in heterogeneous systems[1] to simple geometries. We are able to apply the results of this analysis to experimental data obtained on Pyrofuze[9] (*) sheet and single-strand wire. Consider a bimetallic sheet that reacts by mutual diffusion of two reagents through a layer of reaction product. This problem is reported to have been examined by Aldushin and Khaikin.[10] We did not have access to the reference at the time of this writing, but Merzhanov[3] states that the propagation could be analyzed one-dimensionally; i.e., the heat transfer normal to the direction of propagation is small compared with the propagation rate. We conclude that this assumption is applicable only to thin layers. We have derived a suitable rate expression for the slab geometry in the Appendix to this paper, and have estimated the limits of validity of the assumption of one-dimensional heat transfer.

Consider Fourier's equation in one dimension with a source term

$$\frac{\partial T}{\partial t} = \frac{k}{c\rho} \frac{\partial^2 T}{\partial x^2} - \frac{Q}{c} \frac{\partial F}{\partial t} \tag{3}$$

By relating the rate of reaction, $\partial F/\partial t$, to the rate of diffusion, one can compute a temperature profile. Fitting a quadratic polynomial to the temperature profile and differentiating, one finds the propagation rate in terms of geometric and kinetic parameters.

$$V = \frac{1}{a_o} \sqrt{\frac{2kD_o \exp(-E/\mathcal{R}T_a)}{c\rho W}} \tag{4}$$

We find from experimental studies[6] that E is approximately 125 kJ/mole for the Ni-Al system, a value which appears to reflect the rate-determining nature of the liquid-diffusion step. For solid-solid reactions, E values of more than

---

*Pyrofuze is the registered trademark of the Sigmund Cohn Corporation (Mt. Vernon, N.Y.). It consists of cold rolled sheets of palladium (or platinum) on aluminum and of swaged and drawn palladium wires that have an aluminum core. When initiated by heating to 550°C, Pyrofuze reacts with a bright flash, forming the intermetallic compound Pd(Pt)Al.
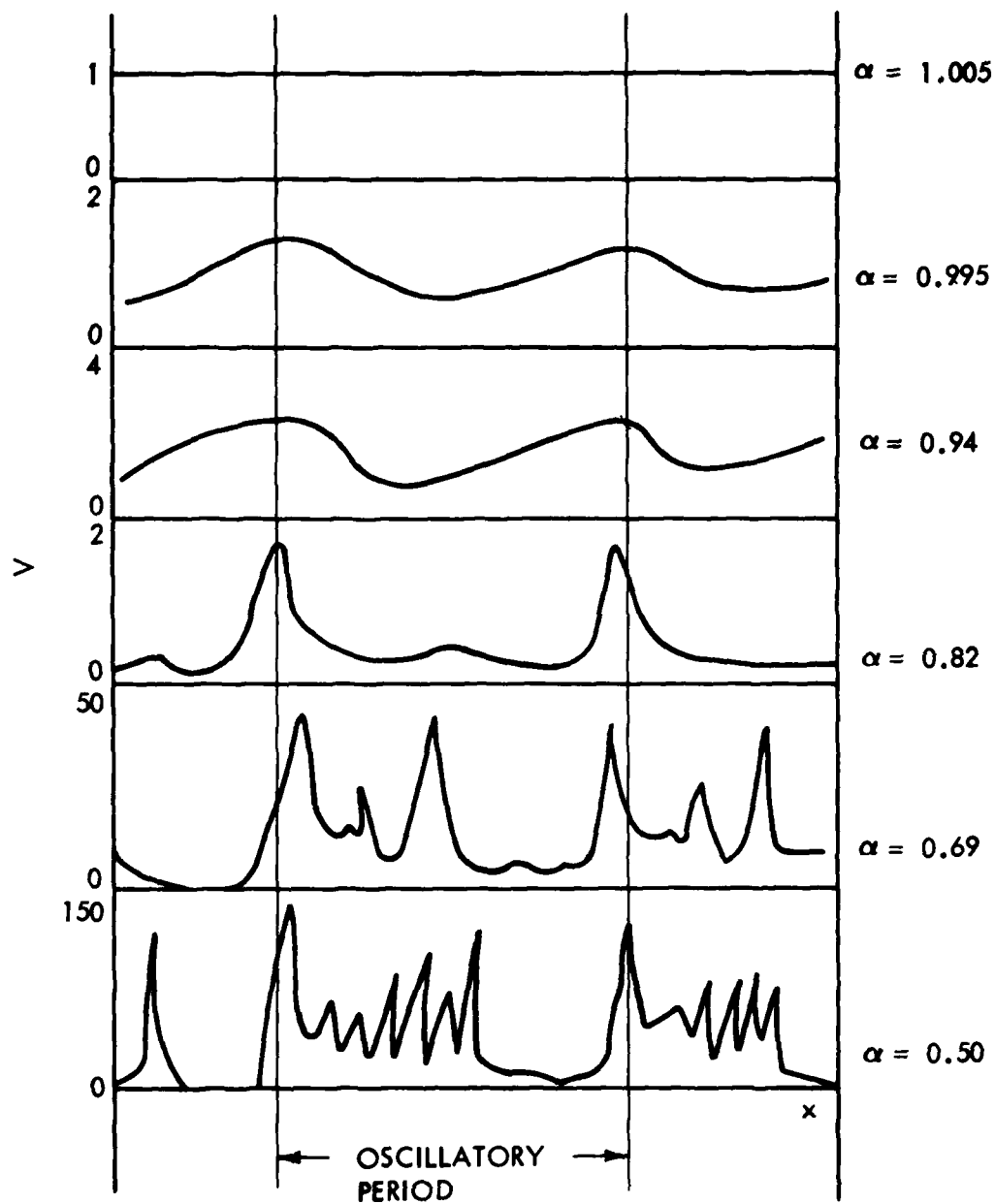
Fig. 4 Nature of Oscillatory Combustion After Merzhanov[3].

Table 1

PROPERTIES OF PUBLISHED GASLESS REACTION MIXTURES

(Numbers enclosed in parentheses apply to the literature cited in the References)

Reaction	E (kJ/mol)	T_a (K)	W	Q (J/g)	k (J/cm sec K)	c (J/g K)	α
Ti+2B	318(11)	3600(1)	3.05(2)	4835	5.5×10^{-3}(2)	1.281	0.8(11)
Zr+2B	310(11)	3800(1)	2.54(2)	2888	3.4×10^{-3}(2)	0.716	1.0(11)
Hf+2B	398(11)	4200(1)		1649[a]			0.55(11)
				1319[a]			0.50(11)
				825[a]			0.35(11)
Al+Ni	75[b]	1639(1)	2.53(2)	1377	0.65(1)	0.753	1.06(6)
	134[c]			1200[a]	0.22 (Estimated)	0.753	1.06(6)
	134(6)			1100[a]	0.033 (Estimated)	0.753	1.06(6)
	134(6)			900[a]	0.005 (Estimated)	0.753	0.50(6)
Al+Co	129(6)	1580(1)		1289			0.65(6)
Al+Pd	8.40[d]	2380(1)	1.885	1369	2 (Estimated)	0.418	
Al+Fe$_2$O$_3$		2450(11)	2.53(2)		4.9×10^{-3}(2)	0.753	
Ti+C		3600(1)	2.14(2)	3085	5.8×10^{-3}(2)	0.946	
Zr+C		3800(1)		1930	2.8×10^{-3}	0.753	

(a) Obtained by dilution with spent reaction product.
(b) For fine grained nickel, undiluted (6).
(c) For coarse grained nickel (6).
(d) 0.01 cm Pyrofuze Braid, bare, wrapped around a mandril (9).
    12 kJ/mole is reported for E of an ideal liquid systems (17).

300 kJ/mole have been reported.[11] We have used a value of 125 kJ/mole to calculate the propagation rates for various thicknesses of Pyrofuze sheet, as shown in Fig. 5. From the experimental data, we calculated a value of about 69 kJ/mole. This value may be still lower if the reaction were truly adiabatic and determined by liquid-liquid diffusion throughout the diffusion process. We have reason to believe that activation energies for liquid-liquid systems could be as low as 12 kJ/mole[17] so that the low experimental activation energy reported in Table 1 does not seem surprising.

The reaction rate [see Eq. (A.2) in the appendix to this paper] was derived in Ref. 1 for a planar geometry. To calculate the burning rate of wires, the rate should be rederived for a cylindrical geometry. For the present purpose, however, it was considered sufficient to use the propagation rate as it is expressed in Eq. (4), using an equivalent expression for a_o which is related to the wire radius R by

$$a_o = \frac{1}{W + \sqrt{W}} R \tag{5}$$

This formula specifies a sheet whose width equals the median circumference of the wire and whose two layers have the same volumes as those of the wire sheath and the wire core. By using this approximation, we have obtained the curve shown in Fig. 6. For wires, we find that the calculated activation energy is about 85 kJ/mole, reflecting greater heat loss than was the case in the sheet. Such heat loss may cause a larger participation of the solid phase in the diffusion process. Strictly speaking, therefore, the activation energy should reflect the degree of liquid presence in the diffusion process.

Figures 5 and 6 illustrate that the hyperbolic dependence of the burn rate on the thickness of the diffusion layer is correctly predicted, although the agreement is best when the thickness is small. To evaluate to what extent the one-dimensional diffusion model is valid, we have assumed as a first approximation that the heat loss due to the deviation from adiabaticity should be less than one half of the heat generated. We find for this assumption that the maximum permissible thickness of the sheet is

$$W a_o = \frac{2}{V} \sqrt{\frac{k}{\rho c} D_o \exp\left(-\frac{E}{R T_a}\right)} \tag{6}$$

Assuming an adiabatic propagation rate of 80 cm/sec at the center for the Pyrofuze system, the maximum permissible thickness will be no more than 4×10^{-3} cm. This thickness will be larger for slower reactions. This magnitude estimate is of interest when one wants to evaluate the applicability of Aldushin and Khaikin's analysis[10] to heterogeneous mixtures. Further, it indicates that the poor agreement in Fig. 6 may, among other reasons, be due to the large wire sizes used in the experimental study.
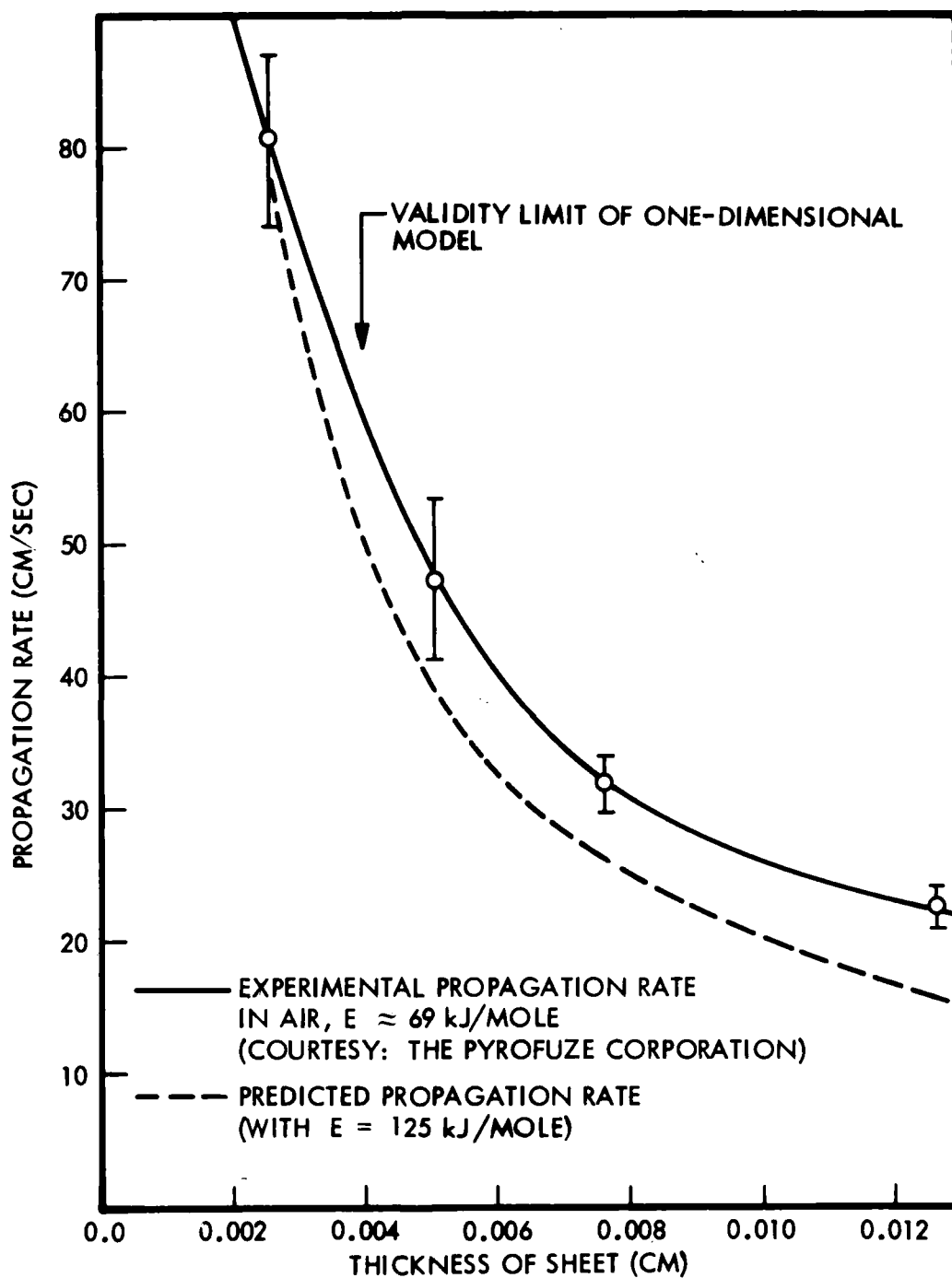
Fig. 5 Experimental and Computed Propagation Rates for Pyrofuze Sheet
E = 125 kJ/mole, k = 2 J/cm sec K.

234
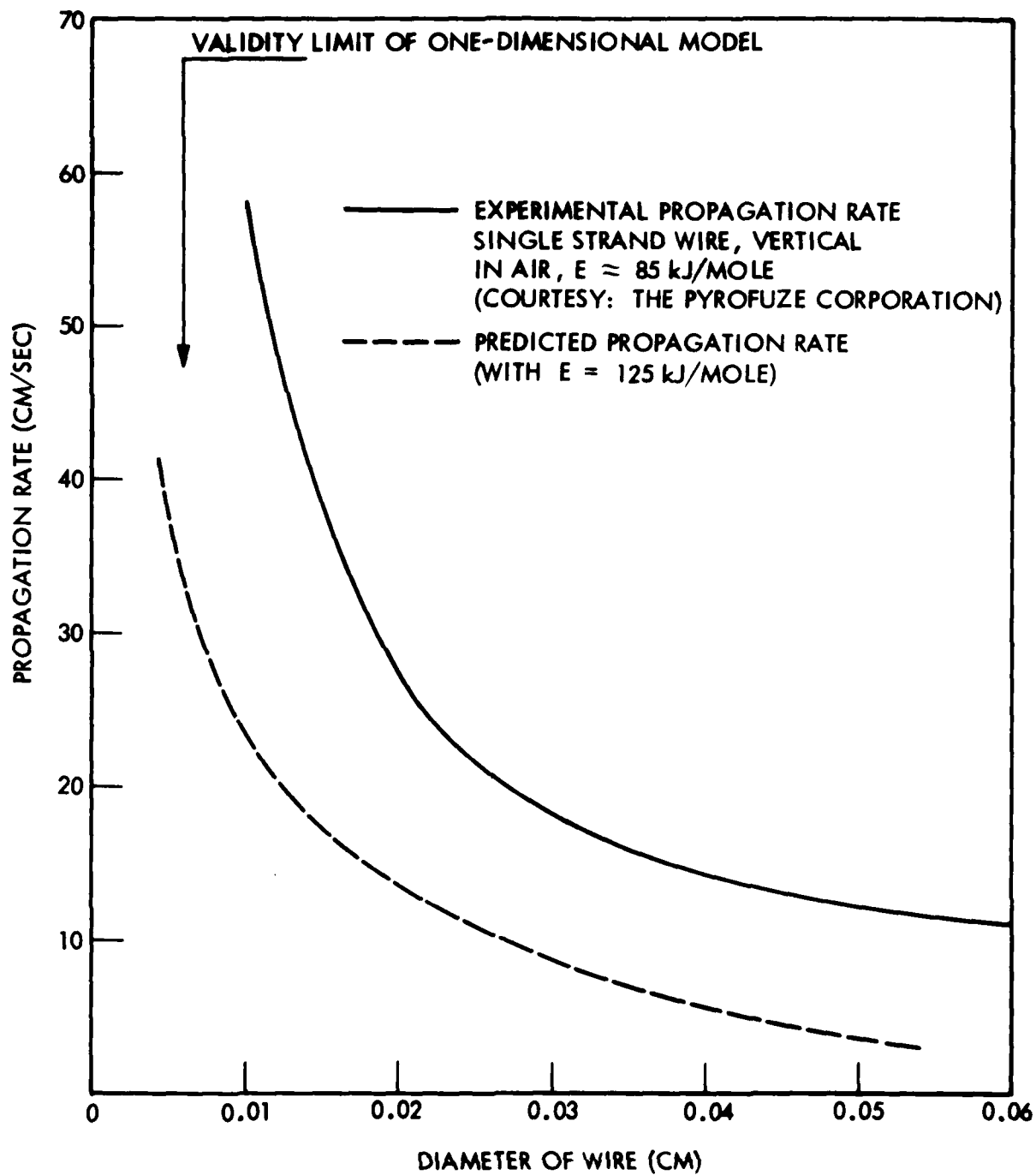
Fig. 6 Experimental and Computed Propagation Rates for Single Strand
Pyrofuze Wire E = 125 kJ/mole, k = 2 J/cm sec K.

To compare the diffusion-controlled rate expression, Eq. (4), with one that is derived from a conventional kinetic or Arrhenius model, we have examined Maximov and Shkadinskii's expression[12]

$$v = \sqrt{\frac{T_a^2 kZ \exp(-E/\mathcal{R}T_o)}{E(T_a - T_o)\rho}} \tag{7}$$

which does not consider the effect of the particle size. In practice, the frequency factor Z is obtained empirically, and it would therefore contain the particle size effect. Equation (4), on the other hand, requires a value for D_o. We have shown previously[1] that the propagation rate is quite insensitive to D_o; in this study, therefore, it as assumed to be equal to 1.0. We conclude that

$$\frac{D_o \exp(-E/\mathcal{R}T_a)}{Wa_o^2} \quad \text{corresponds to} \quad Z \exp\left(-\frac{E}{\mathcal{R}T_a}\right) \tag{8}$$

The factor

$$\frac{\mathcal{R}T_a^2}{E(T_a - T_o)\rho}$$

of Eq. (7) varies between 0.1 and 1.0 so that Eqs. (4) and (7) are seen to be equivalent if D_o is likewise allowed to assume values between 0.1 and 1.0 as was done in a previous study.[2]

THE EFFECT OF RADIAL HEAT LOSS

In real delay columns, we have seen that the propagation rates and the reaction mechanism are influenced by heat losses. This problem has been examined before,[5] but no parametric studies have been possible until the advent of high-speed computers. This is our first report on the results of computer modeling of gasless reactions in delay columns that experience radial heat losses. This method, however, is also useful in the study of ignition and other transient phenomena. Writing Eq. (3) in cylindrical coordinates, we obtain for the reactive core

$$c_1 \rho_1 \frac{\partial T}{\partial t} = k_1 \left(\frac{\partial^2 T}{\partial z^2} + \frac{\partial^2 T}{\partial r^2} + \frac{1}{r}\frac{\partial T}{\partial r}\right) - \rho Q \frac{\partial F}{\partial t}$$

$$\frac{\partial F}{\partial t} = \frac{D_o \exp(-E/\mathcal{R}T_a)}{Wa_o^2}(1 - F) \tag{9}$$

$$T = T_s, \quad z = 0, \quad t \leq t_i, \quad r \leq r_m$$

$$T = T_o \quad z > 0, \quad t = 0$$

and for the delay-column body,

$$c_2 \rho_2 \frac{\partial T}{\partial t} = k_2 \left(\frac{\partial^2 T}{\partial z^2} + \frac{\partial^2 T}{\partial r^2} + \frac{1}{r} \frac{\partial T}{\partial r} \right) , \quad r > r_m \qquad (10)$$

At this time we are presenting only the results for delay columns containing heterogeneous reaction mixtures, although the technique would be applicable to a homogeneous system as well. The variables of a real system produce a problem of extraordinary complexity. Fortunately, the effect of radial heat losses is small in the usual mixtures which have low thermal conductivities and small particles. Figures 7, 8, 9, and 10 show the quenching tendency of comparable, but hypothetical, gasless reaction systems that have particle size, thermal conductivity, activation energy and sheath size as variables. The computer runs show that Eq. (1) is approximately satisfied. These results show the limiting, no-go-conditions, but the performance of more typical systems can be inferred by extrapolation. Figure 11 shows the significant effect of ambient temperature on the quenching tendency of delay columns.

Figures 7 through 11 show that the quenching characteristics of delay columns are very sensitive to the value of the parameters. We have also examined the effect of body material on quenching tendency and find it not to be very significant. Quenching depends on the factor $\rho_2 c_2$ which is effectively a constant, even for ceramic bodies. Most real delay columns have reactive cores that are of the same magnitude as the thickness of the body, and changes in propagation rate in such columns due to radial heat losses will be small over the length of the column. The main reason for variations in rates will be because of end effects, inhomogeneities, surface impurities, ambient pressure,[13] or the anticipatory effect caused by gaseous ignitors or gaseous combustion fronts.[14] The effects of ambient temperatures, of column diameter, and of delay body composition and mass were investigated by Comyn and McIntyre,[15] who found that for tungsten delay mixtures the effect of the sheath on the reaction zone temperature is negligible. It was observed, however, that at subambient temperatures, the propagation in small diameter (< 0.50 cm) columns became erratic. We conclude, therefore, that our analytical results are consistent with experimental findings. We believe that a parametric analysis of the effects of heat transfer, and, at a later time, of mass transfer, will be an economical method of evaluating the effect of changes in mixture composition and of sheath design.

SUMMARY

We have examined complexities in gasless reactions of delay columns. Theoretical studies made by A. G. Merzhanov and coworkers have led them to formulate an oscillatory combustion model in systems that are subject to erratic burning behavior. These findings are interesting and will lead to further work.

We have derived rate expressions for the burning of Pyrofuze wire and sheet, and we have established validity limits for one-dimensional heat-transfer analysis in terms of maximum allowable dimensions. Comparison with experimental burning rate data suggests that the approach taken is a reasonable one.
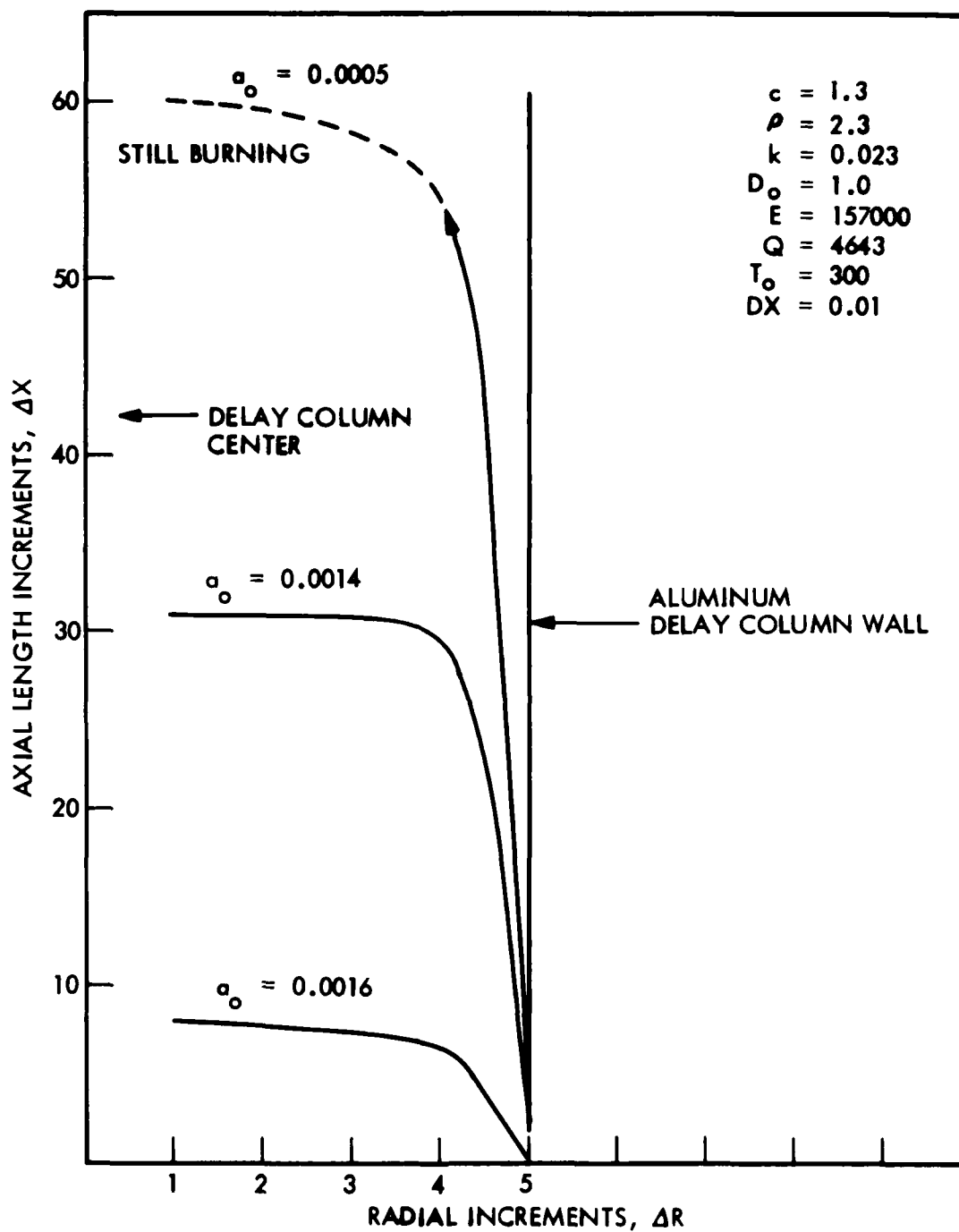
Fig. 7 Extinction Distance for Flame Propagation.   Effect of particle size.
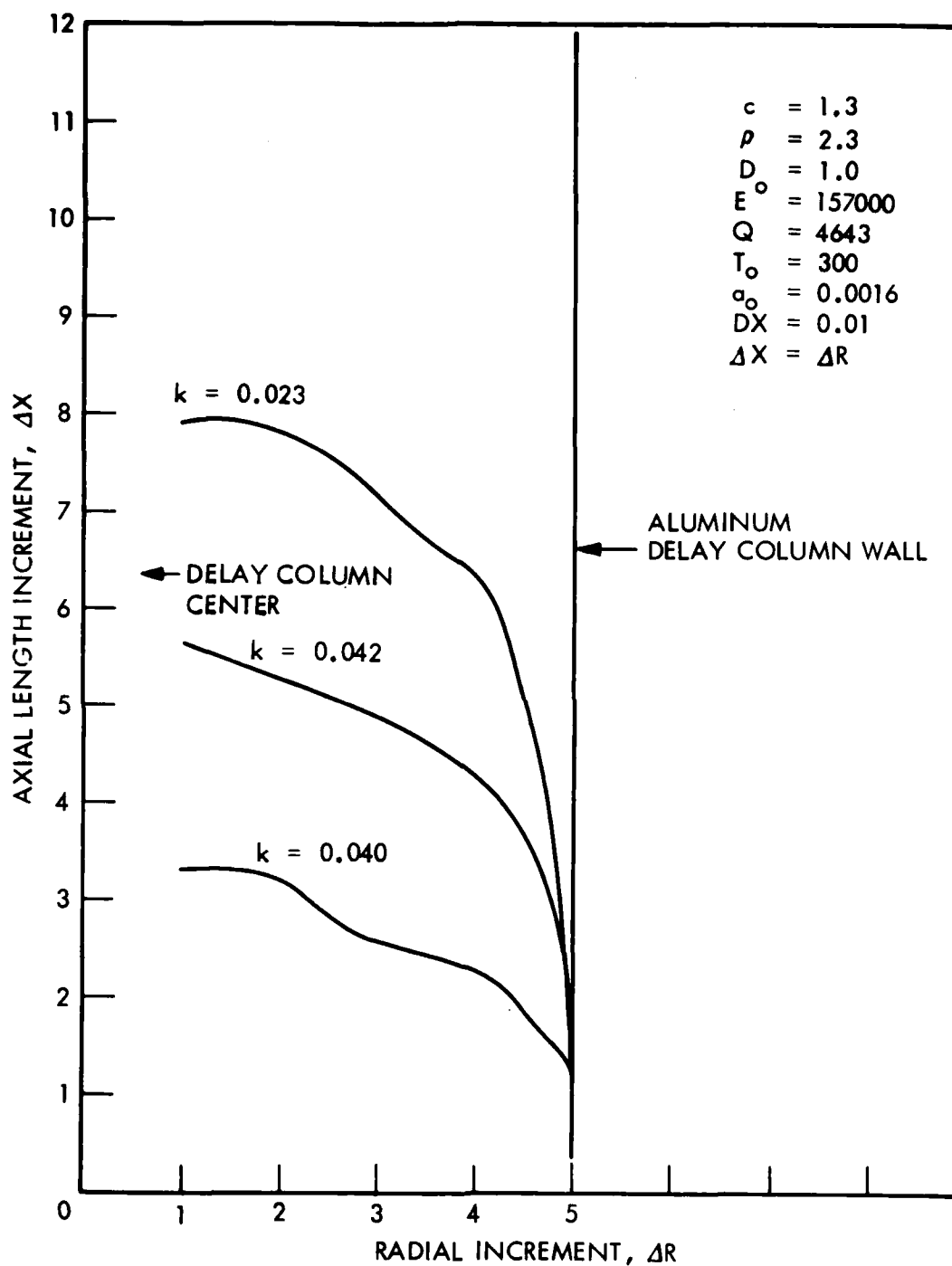
Fig. 8 Extinction Distance for Flame Propagation. Effect of thermal conductivity.
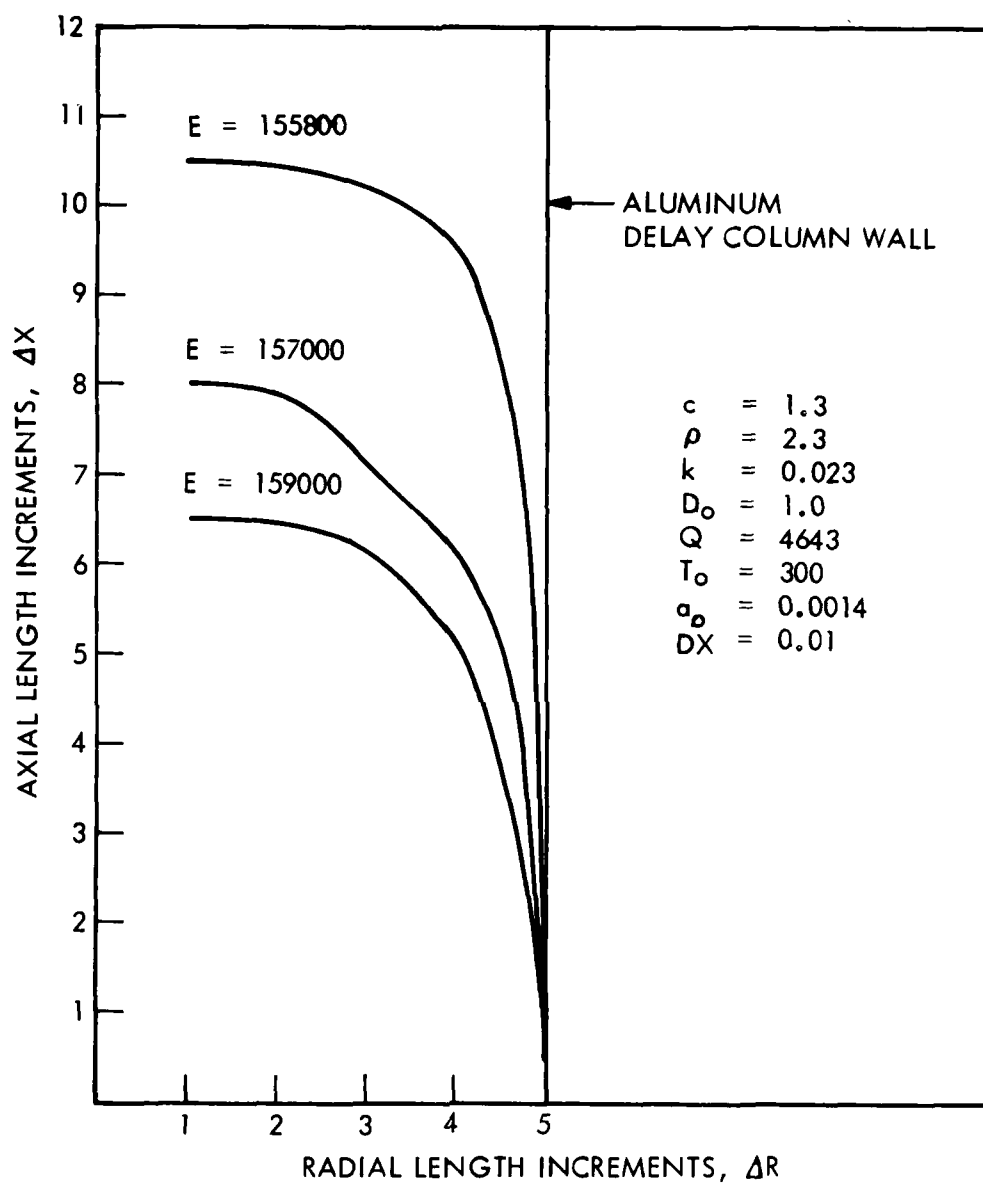
Fig. 9 Extinction Distance for Flame Propagation. Effect of activation energy.
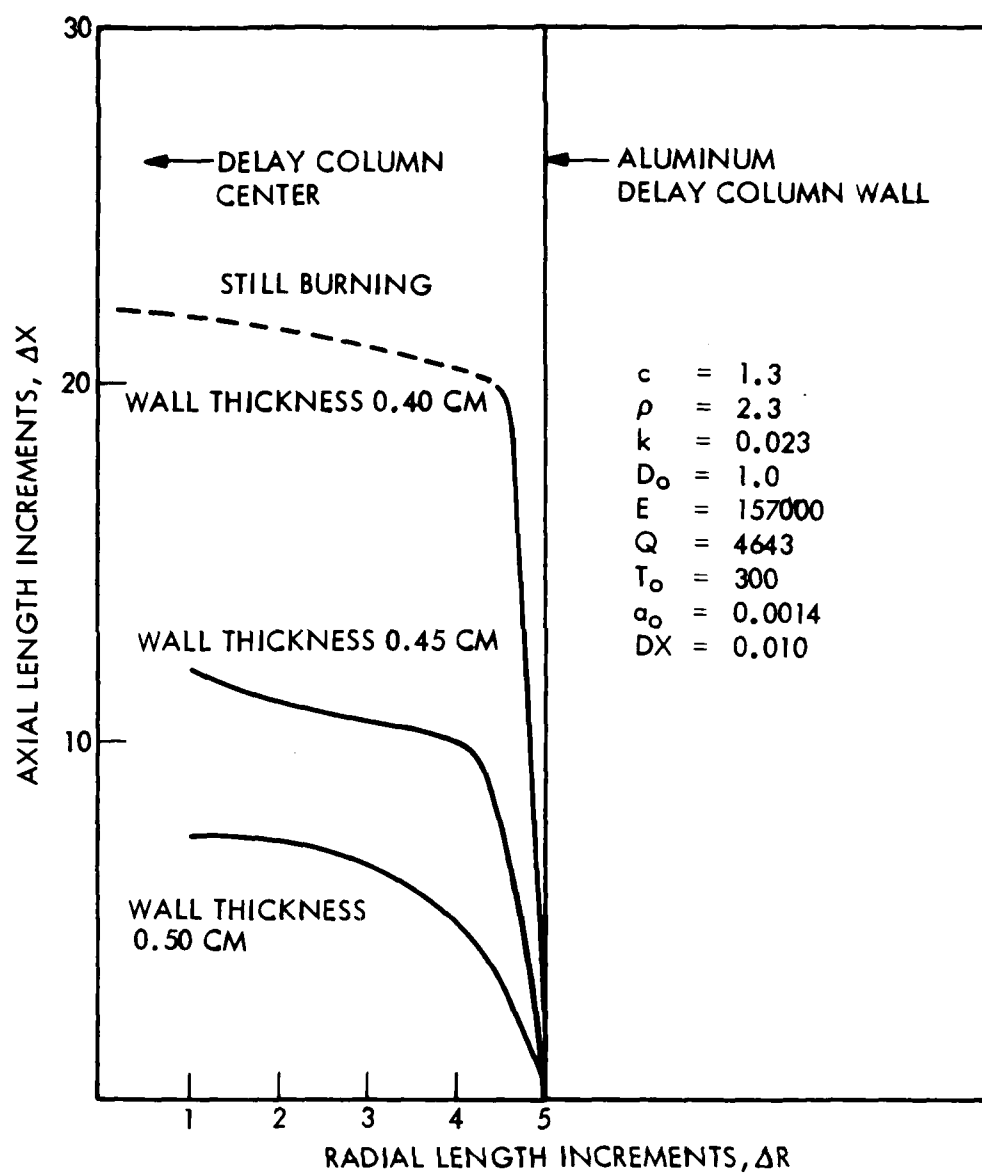
Fig. 10 Extinction Distance for Flame Propagation. Effect of wall thickness.
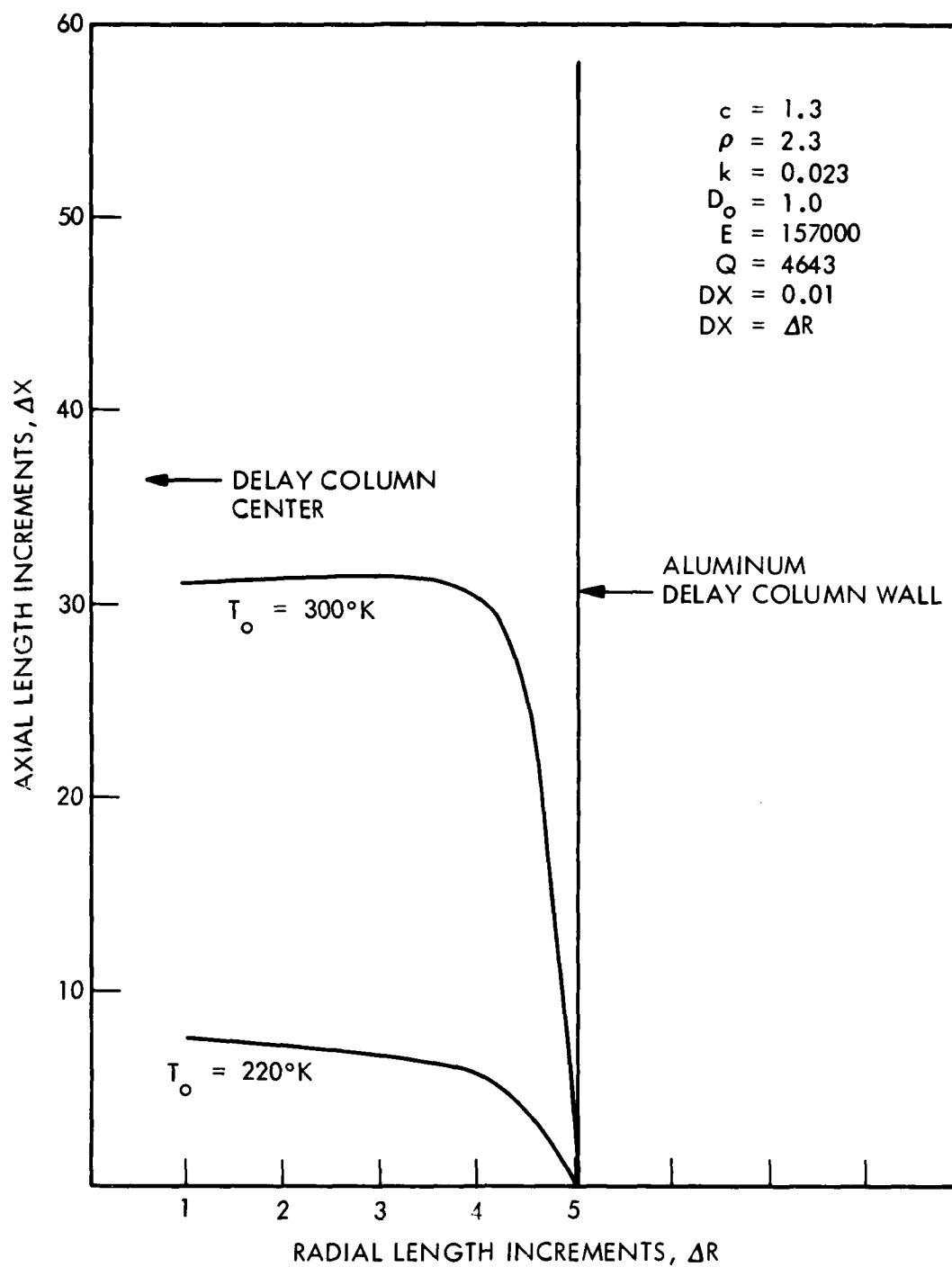
Fig. 11 Extinction Distance for Flame Propagation. Effect of ambient temperature.

Radial heat losses from delay columns were analyzed by a new computer program. The predicted parametric dependence agreed with findings in published studies on delay-column performance.

REFERENCES

(1) A. P. Hardt and P. V. Phung, Combustion and Flame 21, No. 1 (1973), pp. 77−89

(2) P. V. Phung and A. P. Hardt, Combustion and Flame 22, No. 3 (1974), pp. 323−335

(3) A. G. Merzhanov, "Theory of Gasless Combustion," Preprint. Submitted to the Polish Archives of Combustion Processes, 1973

Also see:
K. G. Shkadinskii, B. I. Khaikin, and A. G. Merzhanov, Fizika Goren. i Vzryva 7, No. 1 (1971), pp. 19−28

(4) A. P. Hardt and R. W. Holsinger, Combustion and Flame 21, No. 1 (1973), pp. 91−97

(5) Ya. B. Zel'dovich, ZhETF 11, No. 1 (1941), pp. 159−169

(6) Iu. S. Naiborodenko and V. I. Itin, Fizika Goren. i Vzryva 11, No. 3 (1975), pp. 343−353

(7) A. E. Berkowitz, F. E. Jaumot, Jr., and F. C. Nix, Physical Review 95, No. 5 (1954), pp. 1185−1189

(8) A. F. Belyaev and L. D. Komkova, Zh. Fiz. Khim. 11 (1950), p. 1301

(9) J. Cohn, U.S. Patent 2 911504 (1959)
Franklyn E. Stevens, Pyrofuze Corporation, private communication

(10) A. P. Aldushin and B. I. Khaikin: Metallotermicheskie Protessy v Khimii i Metallurgii, II, NAUKA, Novosibirsk (1973). Also see by the same authors Fizika Gorenia i Vzryva 10, No. 3 (1974), pp. 313−323

(11) I. P. Borovinskaya, A. G. Merzhanov, N. P. Novikov, and A. K. Philonenko, Fizika Goren. i Vzryva 10, No. 1 (1974), pp. 4−15

(12) E. I. Maximov and K. G. Shkadinskii, Fizika Goren. i Vzryva 7, No. 3 (1971), pp. 454−457

(13) F. J. Valenta, "Effects of Pressure on Burning Rates of Manganese and Tungsten Delay Compositions," IHTR 315, June 1970, AD 872897

(14) M. Gilford et al., "The Anticipatory Effect," PATR 3047, March 1964, AD 432537

(15) R. H. Comyn and R. E. McIntyre, "Investigation of the Effect of Delay Body Variables," TID-4500, August 1963, SC-4791-RR, N63-20944

(16) T. R. Goodman, "Advanced in Heat Transfer," Vol. I, N.Y., Academic Press, 1964

(17) C. S. Caldwell and A. L. Babb, J. Phys. Chem. 60 (1965), p. 51

LIST OF SYMBOLS

a_o	=	Particle size or layer thickness of reagent (cm)
α	=	Empirical reaction criterion (dimensionless)
A, B	=	Atomic weights of A and B
b_o	=	Layer thickness of reagent, $a_o (N_b B \rho_A / N_a A \rho_B)$ (cm)
c	=	Mean heat capacity (J/g K)
D_o	=	Diffusion prefix (cm^2/sec)
D	=	Diffusion coefficient (cm^2/sec)
E	=	Activation energy (J/mole)
F	=	Fraction unreacted (dimensionless)
f	=	Heat flow (J/cm^2)
k	=	Thermal conductivity (J/cm sec K)
N_A, N_B	=	Stoichiometric fractions
Q	=	Heat of reaction (J/g)
q	=	Heat generation (J/cm^2)
ΔR	=	Radial increment of bimetallic wire (cm)
r	=	Radial direction
$\mathcal{R}$	=	Gas constant (J/mole K)
ρ	=	Density (g/cm^3)
t	=	Time (sec)
T	=	Temperature (K)
V	=	Propagation velocity (cm/sec)
W	=	Stoichiometry ratio, $1 + (b_o/a_o)$ (dimensionless)
X	=	Longitudinal direction
Z	=	Frequency factor in Arrhenius equation (sec^{-1})
x, z	=	Longitudinal or axial direction
$\Delta X, \Delta Z$	=	Longitudinal or axial increment (cm), equal to ΔR

Subscripts

i	=	Ignition	s	=	Source or ignition temperature
a	=	Adiabatic	r	=	Reaction, not necessarily adiabatic
o	=	Initial or ambient	m	=	Metal body

1, 2 referring to system components.

ACKNOWLEDGMENT

Appendix

DERIVATIONS OF MATHEMATICAL EXPRESSIONS

PROPAGATION RATES IN SANDWICH MODEL (see Fig. A-1)

Assume one-dimensional heat transfer

$$\frac{\partial T}{\partial t} = \frac{k}{c\rho} \frac{\partial^2 T}{\partial x^2} - \frac{Q}{c} \frac{\partial F}{\partial t} \tag{A.1}$$

The reaction rate, $\partial F/\partial t$, has been derived in (1) and expressed in the form

$$\frac{\partial F}{\partial t} = -\frac{1}{Wa_o^2} \frac{D_o \exp(-E/\mathcal{R}T)}{(1-F)} \tag{A.2}$$

At steady state, the temperature profile is constant with time and moves with a constant velocity:

$$x = u + Vt \tag{A.3}$$

such that Eq. (A.1) takes the form

$$-V \frac{\partial T}{\partial u} = \frac{k}{c\rho} \frac{\partial^2 T}{\partial u^2} - \frac{Q}{c} \frac{\partial F}{\partial t} \tag{A.4}$$

This is a moving boundary problem similar to that of a solid that melts under the influence of a constant heat flux and in which the liquid layer is removed as it is formed.

The heat flux going into the unreacted material (see Fig. A-2)

$$\varphi = (T_a - T_o)c\rho V \tag{A.5}$$

Goodman[16] gives for the penetration depth, δ, into the unreacted material

$$\delta = \frac{2(T_a - T_o)k}{\varphi} = \frac{2k}{c\rho V} \tag{A.6}$$
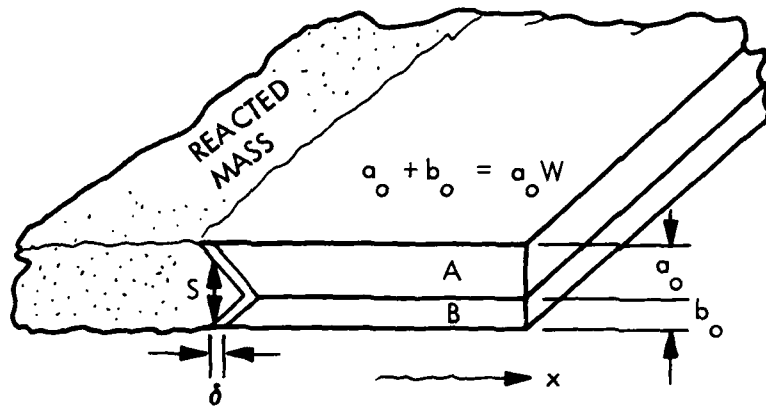
Fig. A-1 Sandwich Model.
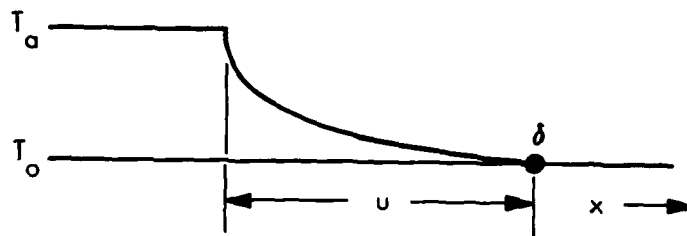
Fig. A-2 Temperature Profile.

We fit a quadratic polynomial to the temperature profile with an exact match at $u = 0$ and $u = \delta$ and with a zero slope at $u = \delta$. This result is

$$T = T_a - \frac{2(T_a - T_o)}{\delta} u + \frac{T_a - T_o}{\delta^2} u^2 \qquad \text{(A.7)}$$

Using Eqs. (A.6) and (A.7), one can write Eq. (A.4) at $u = 0$ as

$$V \frac{c\rho V(T_a - T_o)}{k} = \frac{k}{c\rho} \frac{(T_a - T_o)c^2\rho^2 V^2}{2k^2} - \frac{Q}{c} \left(\frac{\partial F}{\partial t}\right)_{u=0}$$

Remembering that $Q/c = T_a - T_o$, the propagation rate becomes

$$V = \frac{1}{a_o} \sqrt{\frac{2\rho D_o \exp(-E/\mathcal{R} T_a)}{c\rho W}} \qquad \text{(A.8)}$$

which is Eq. (4) in the text of the paper.

VALIDITY CRITERION FOR RATE EXPRESSIONS

The rate expression, Eq. (A.8), was derived on the assumption that the reaction front was reasonably flat and perpendicular to the bimetallic interface. This means that the reaction must proceed from the interface outward at a much faster rate than does the heat conduction in the plane of the sheet.

Consider a thin slice of thickness equal to the heated layer S. The interface layer reacts first, producing the heat Q which determines the instantaneous temperature before heat loss by conduction. The reaction proceeds outward at the rate

$$\frac{dS}{dt} = \frac{DW}{S} \qquad \text{(A.9)}$$

This rate decreases as S increases because of growth of the product layer acting as diffusion barrier. The time for completion is the time that S attains the total thickness of the sandwich, Wa_o:

$$\int_0^{a_o} S\,dS = DW \int_0^\tau dt$$

$$\tau = \frac{a_o^2}{2\,DW} \qquad \text{(A.10)}$$

During this time that the reacted material at the center loses heat by conduction, the flux of this heat is

$$\varphi = k \frac{T_a - T_o}{\delta}$$

The total heat loss is

$$f = \frac{k(T_a - T_o)\tau}{\delta}$$

From Eq. (A.6),

$$\delta = \frac{2k}{c\rho V}$$

Hence, the heat loss becomes

$$f = \frac{1}{2} \tau c\rho V(T_a - T_o) \tag{A.11}$$

The heat generated in slice δ is

$$q = \delta \rho Q = \frac{2kQ}{cV} \tag{A.12}$$

We now make the assumption that the one-dimensional analysis is acceptable if the heat loss f is less than half the heat generated, q. Substituting Eq. (A.10), one obtains

$$(T_a - T_o) \frac{c\rho V (a_o)^2}{4DW} \leq \frac{kQ}{cV}$$

Remembering that $T_a = (Q/c) + T_o$

$$Wa_o \leq \frac{2}{V} \sqrt{\frac{k}{c\rho} D_o \exp\left(-\frac{E}{\mathcal{R} T_a}\right)} \tag{A.13}$$

This is Eq. (6) in the text.

DIRECTIONAL VISUAL PENETRATION IN A CLOUD

Dr. Sidney Katz
Allen J. Tulis

IIT Research Institute
10 West 35th Street
Chicago, Illinois 60616

The development of a scientific concept often proceeds from theory to interpretive application and then, perhaps, to predictive application; we apply our new concept to explain existing phenomena and subsequently, as our confidence increases, we attempt to advance into new areas of application. Light scattering theory has been around for a long time and its use in the interpretation of a host of meteorological, optical and astronomical phenomena has been most impressive. It's value in the prediction of new phenomena and technologies has lagged for a number of reasons, including problems of material acquisition, control and manipulation.

One of the earliest attempts to predict a consequence based on light scattering, and then to move from theory to application is embodied in Figure 1. The problem was the attenuation of the high visibility of aircraft contrails. A solution based on an application of light scattering theory was proposed, with the results indicated. Before discussing this phenomena and those related to our present topic, I would like to review briefly some general principles of light scattering.

The basic theories of light scattering are derived from electromagnetic theory. Mie developed the first general theory (1908) and a detailed presentation appeared in Stratton's book on Electromagnetic Theory (1941).

In general, a small particle, illuminated by a distant point source will "scatter" the incident light and the emergent light will be omnidirectional and usually anisotropic. The theories of light scattering for spherical particles require three terms, refractive

index, particle size and the wavelength of the light. If we use the
complex refractive index, which contains the absorption term as well
as the refraction term, we may consider particles which are fully
transparent, partial absorbers or reflectors. The scatter of single
transparent spherical particles is illustrated, for two refractive
indices in Figure 2. The scattering efficiency, Q, is the ratio of
the actual total scatter to the calculated scatter based on classical
optics, i.e., the assumption that the particle scatters the light
intercepted by its geometric cross-section. Note that this is very
far from the actual situation. When the particle is very small,
compared with the wavelength, scattering efficiency is very low. This
effect, first described by Rayleigh, well in advance of Mie, explains
the low visibility of very small submicron particles even when the
total amount of material is substantial. As particle size increases,
a dimension of highest visibility is realized, followed by the
"damped oscillations" which form the rest of the curve. This curve
provides the basis of the operation illustrated in Figure 1. One may
assume that the contrails consist of water or ice particles condensing
on nuclei supplied by the aircraft exhaust debris, and that the
particle size is in a region corresponding to high visibility. If
one provided a large excess of additional nucleating centers, the
normal concentration of particles would shift to a very large concen-
tration of low scattering efficiency Rayleigh scatterers, and, if
nucleation were applied only to the left outboard engine the indi-
cated results should occur. As you can see, they did.

The radial distribution of the scattered intensity tends to be
a very complex function. Initially, let us consider transparent
particles, i.e., materials with "real" indices of refraction. A
Rayleigh scatterer, illustrated in Figure 3, is axially symmetrical,
but not radially. Because of its low total scattering efficiency,
it is of no present interest. Larger particles usually have a strong
forward and near forward scattering component, and a relatively small
scatter in other directions. A large amount of typical data indicate

forward-to-back ratios which may be of the order of several hundred to one as shown in Figure 4.

This leads into our present concept. The very complex subject of visual preception can be stated in an over-simplified form by the expression for visual contrast, C, thus,

$$C = \frac{B_o - B_b}{B_b}$$

where B_o and B_b are the brightness of the object and the background. A bright object is seen against a dark background, or a dark object is seen against a bright background as a function of the difference between the numerator terms. When the difference is zero, there is no contrast and the object is unresolved.

Actually a contrast "threshold" exists, and the object will not be perceived when B_o is small but not quite zero, or, alternatively when $B_b \gg B_o$. Thus, we cannot see a dark object against an intense background, for example, the sun.

Would it be possible to use an aerosol cloud of high differential scattering intensity as a wide-angle background? When illuminated from one direction, the cloud would be a strong forward and near-forward scatterer, while in the reverse direction, the scattered signal would be minimal. Thus, as Figure 5 shows, the forward field would be visible to a viewer between the cloud and the primary source of illumination against a low contrast background, while an observer with the cloud between him and the source of illumination would see the field against the high contrast background.

A number of laboratory investigations were attempted. The first, as a preliminary qualitative exploration, consisted of suspending particles in a liquid bath in a flat tank and examining the differential effects of directional illumination. The results were marginal, but they seemed real. From this we proceeded to large chamber operations using aerosol generators and visual charts. In

these experiments, the differences in visibility were substantial.
One field experiment with aerial support was attempted. The experiment was performed at noon on a sunny day with a moderate wind.
The observers in the aircraft reported a clear view of the field
during an interval during which their vehicle was not visible.

It was of considerable interest to learn subsequently of a
comparable experience, reported at a technical conference, by a flyer
studying phosphorus smoke obscuration. The report described a
terrain fully visible through the cloud by an observer in an
aircraft which was invisible to ground obervation (Figure 6).

Further investigations are needed to develop optimum materials
and deployment procedures. Insofar as materials are concerned,
high forward and low back scatter is associated with materials with
high "real" refractive indices. Some consideration has also l en
given to non-transmitting materials. Figure 7 shows the scatter
pattern of two interesting configurations, a specular reflector and
a diffusely reflecting surface. Note that the specular reflector
is an isotropic reflector. With equal scattered intensity in all
directions it would be completely useless in the present application.
On the other hand, the diffuse reflector with its predominant back
scatter and near zero forward scatter reverses the effect of
Figure 5. It could, for example, protect ground operations from
overhead observation without obscuring ground visibility. This
concept has an added attraction. Hollow light-weight glass and
plastic particles are commercially available and are cheap. They
can be metallized and their light weight has considerable logistic
appeal.

An interesting class of scatterers with high forward and back
scatter is shown in Figure 8. These materials would create low
visibility conditions in both the forward and back directions with
high lateral visibility. This suggests the possibility of, say, a
near ground level cloud with minimal visibility in both the forward
and back directions, but with a clear "window" for lateral observation.
Tactical applications are obvious.
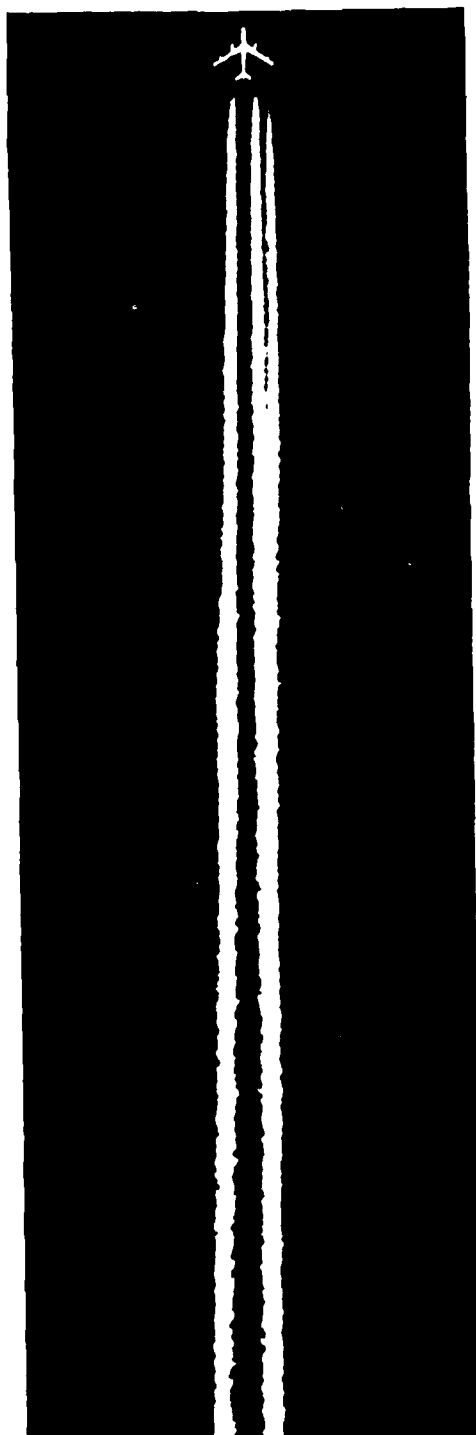
Figure 1. Aircraft Contrail Suppression

Contrail suppression has been applied to the left outboard engine. Note the faint residual contrail adjacent to the left inborad engine trail.
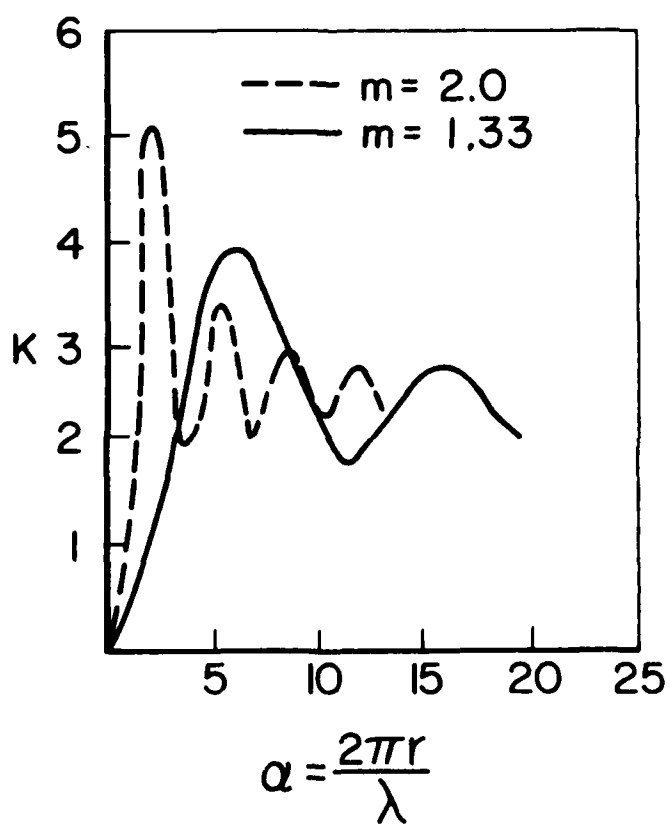
Figure 2.   Scattering Cross-Sections of Spherical Particles
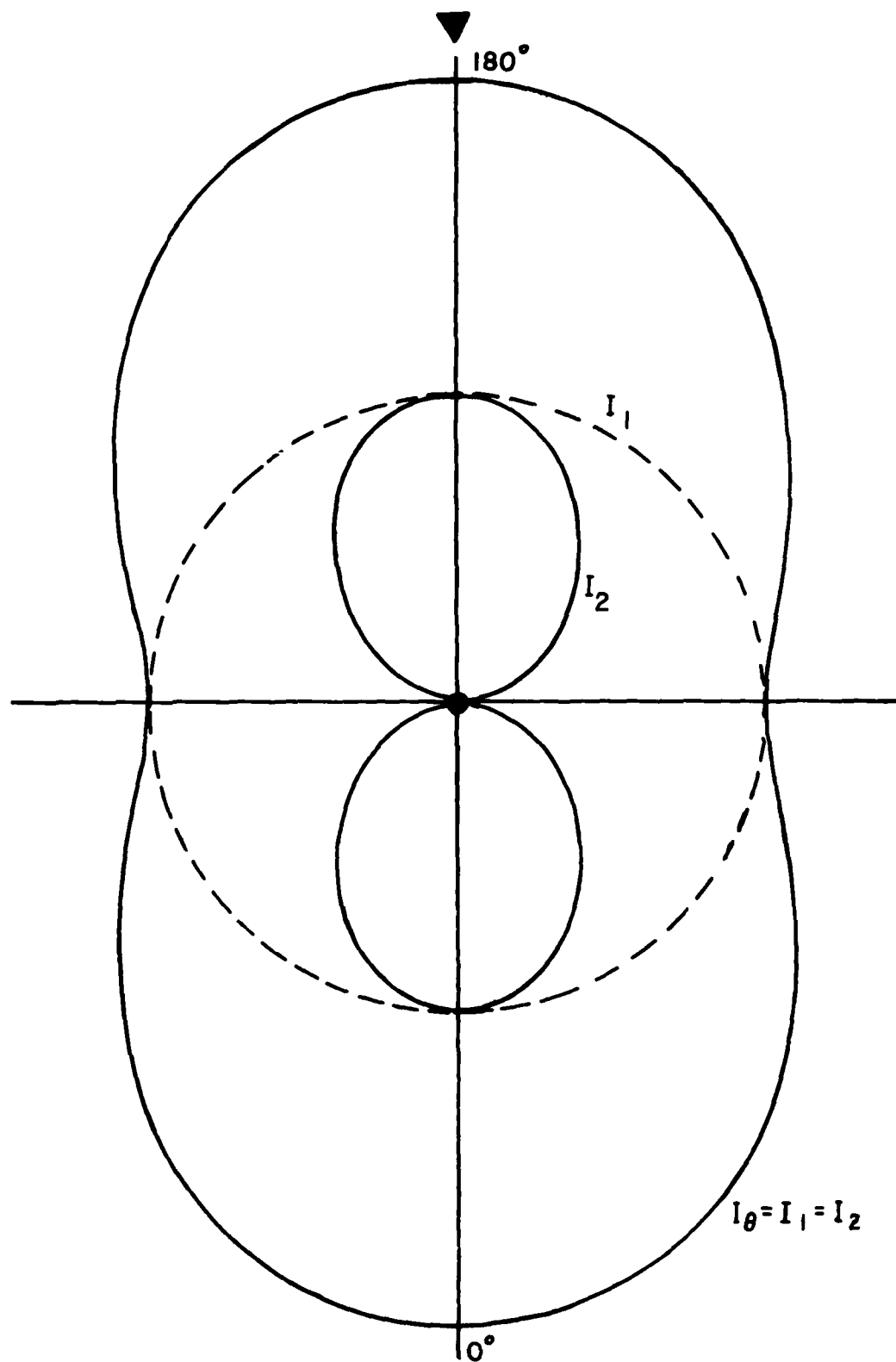
Figure 3: Polar diagram of the light scattered by a Rayleigh
scatterer when the incident radiation is unpolarized.
I_1 and I_2 are the two plane polarized components of
the scattered intensity. I_θ is the sum of $I_1 + I_2$

m = 1.33
α = 6.0

m = 1.33
α = 0.5
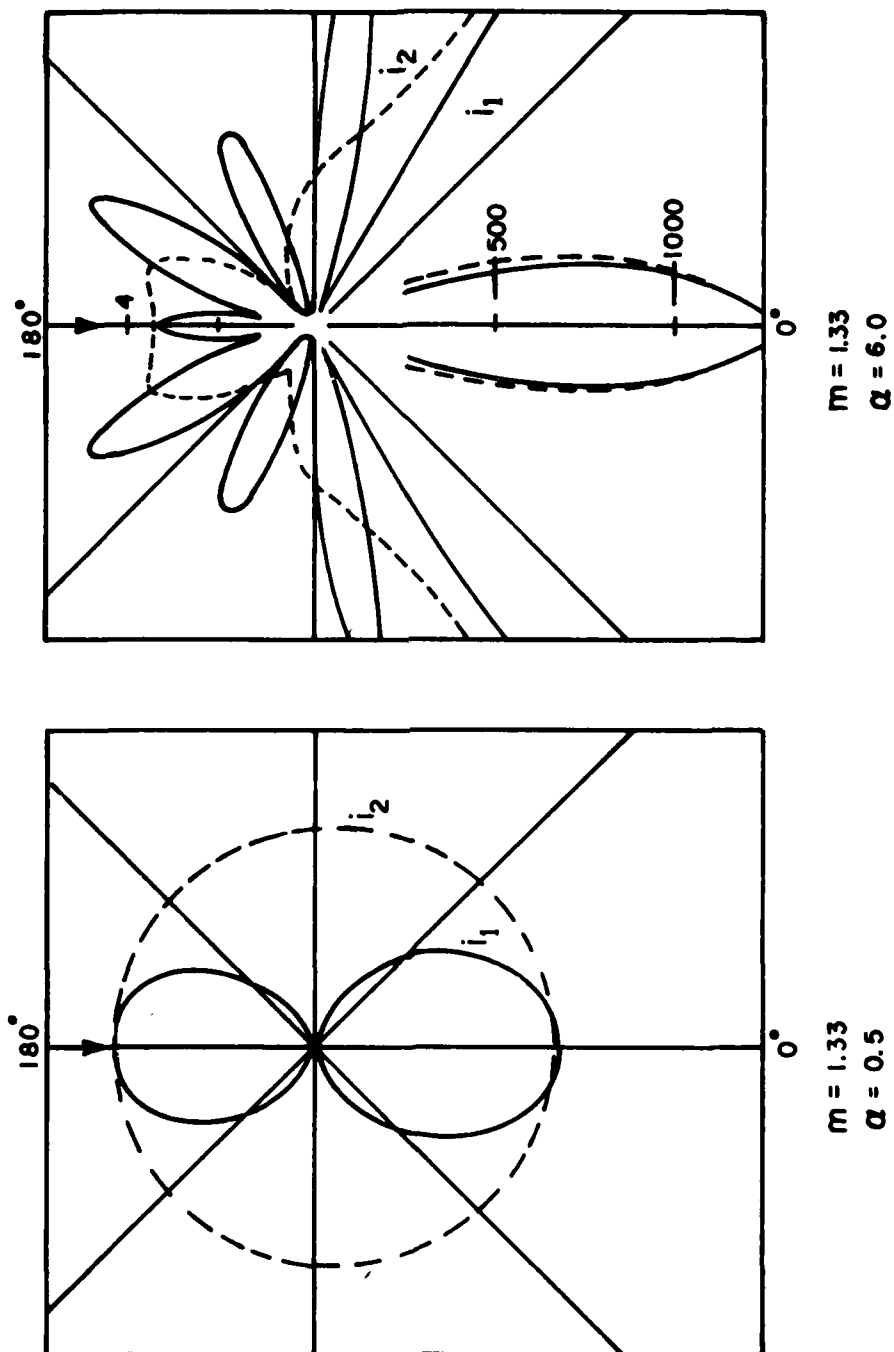
Figure 4:   Radial Distribution of Plane Polarized Components of Light
Scattered by Spherical Particles.
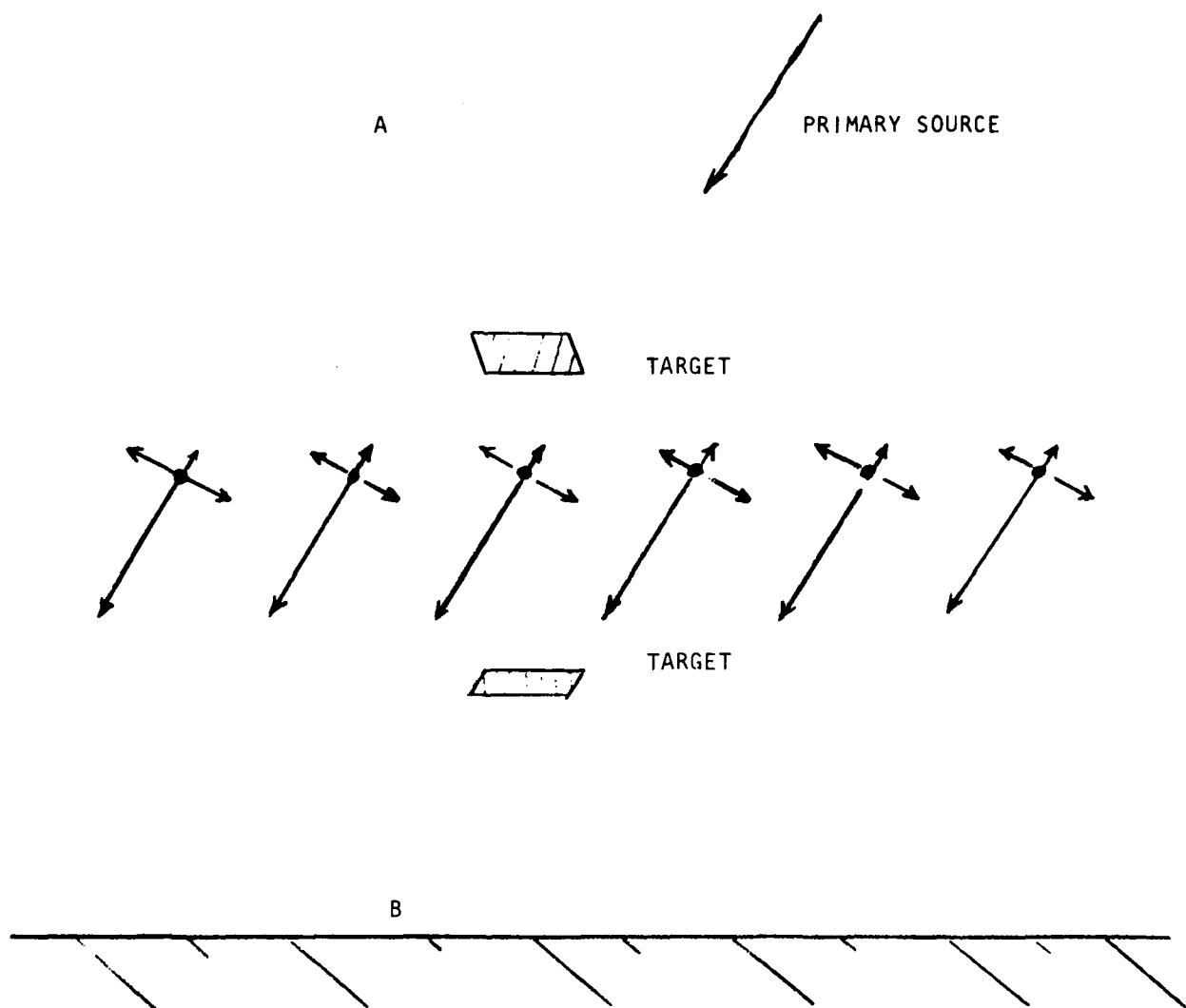
Figure 5.   Differential Visibility Against an Aerosol
Cloud Background.

Figure 6-A. WP Cloud Obscuring Helicopter as Viewed from Ground

Figure 6-B. Target Site at Intersection of Roads as Viewed by
Helicopter Pilot Through WP Cloud
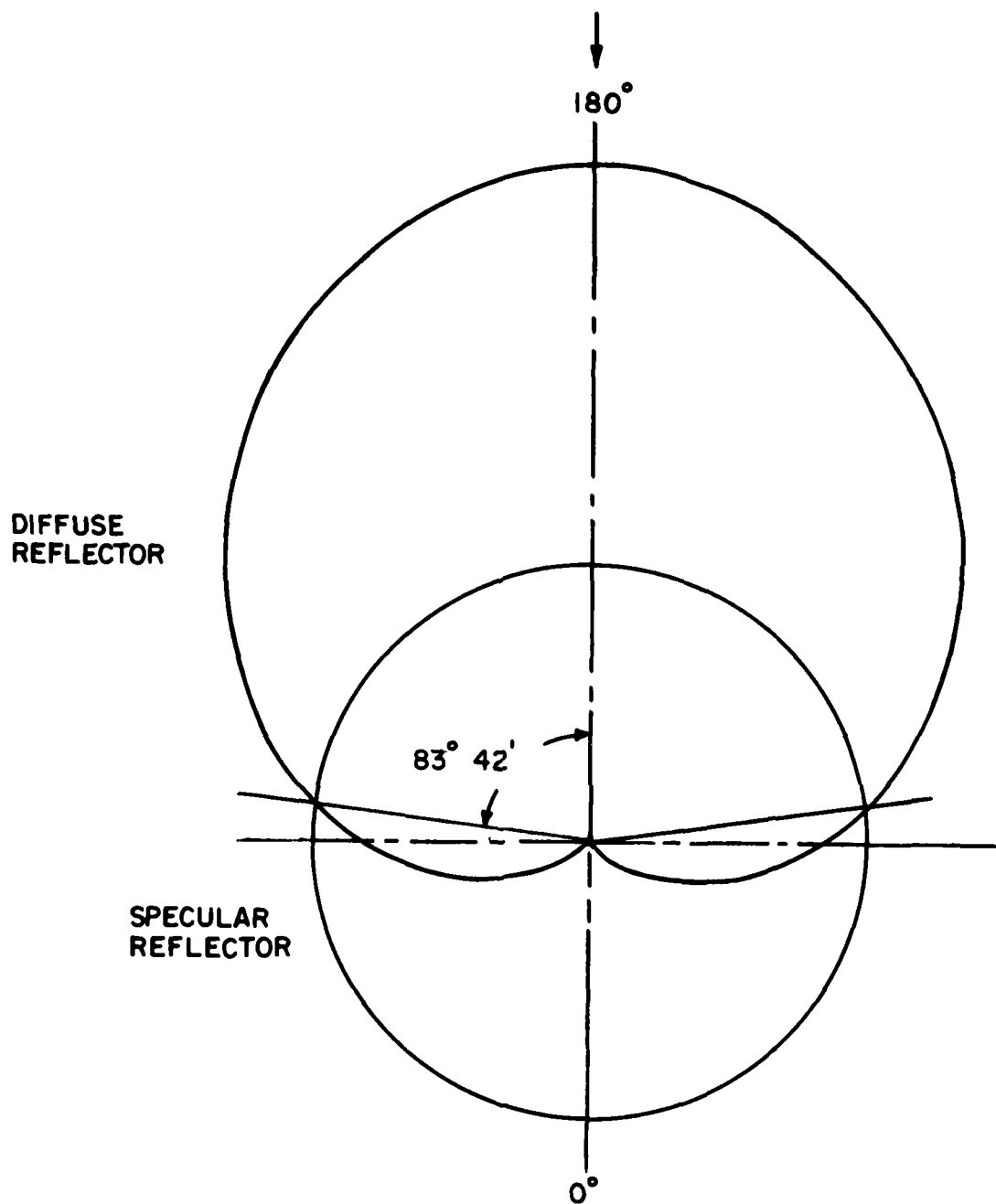
Figure 7:   Comparison of Radial Distribution of Reflected
            Intensity from Specular and Diffuse Reflectors
            Illuminated by a Distant Point Surface.

m=2
α = 4

m = 2
α = 3.6
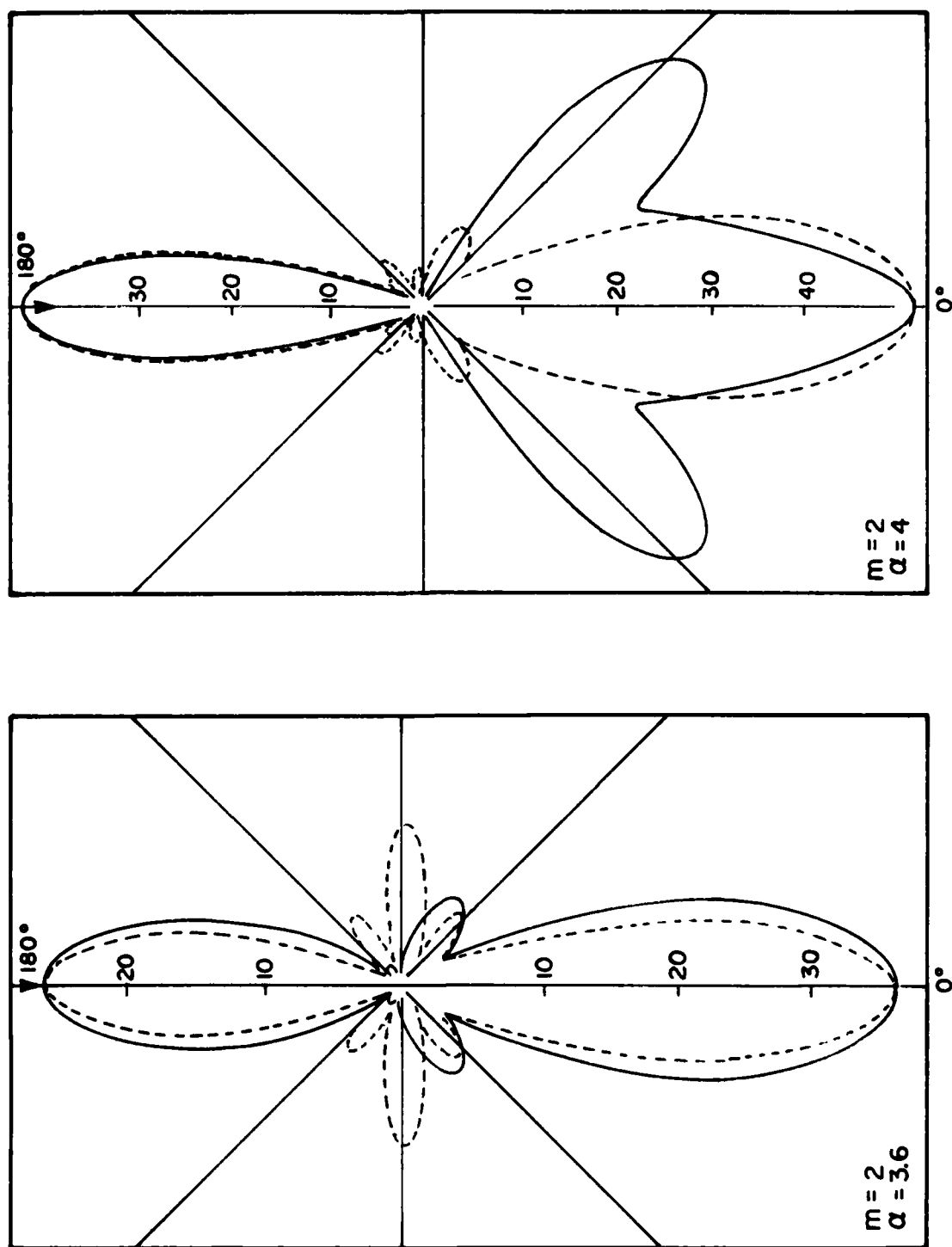
Figure 8:   Radial Distribution of Light Scattered by Particles of
Refractive Index 2 and α 3.6 and 4.0 Showing High
Relative Back to Forward Scatter.

5th International Pyrotechnic Seminar

DEVELOPMENT OF A SPARK INSENSITIVE
ACTUATOR/IGNITER*

by
E. A. Kjeldgaard
Initiating & Pyrotechnic Components Division
Sandia Laboratories
Albuquerque, New Mexico

ABSTRACT

The development of a new, spark insensitive pyrotechnic material, $TiH_x/KClO_4$, for actuators and igniters is discussed. The parametric investigation of the material is primarily aimed at answering the following question: "Can a pyrotechnic be sensitive to hot wire ignition, yet insensitive to ignition from a spark generated by a human body?"

A number of variables were studied, among which are the following: hydrogen and oxygen content, surface area and particle size, powder density at the bridgewire, component hardware configuration, ignition energy, and calorific output. Numerous examination and testing techniques were employed, such as: surface analysis (Auger, ESCA), particle analysis (Coulter counter, SEM), powder fractionation (particle classifier), NMR, BET surface area analysis, thermal analysis (DSC, bomb calorimeter), spark sensitivity (bulk and pressed powder), stability, impurity analysis, and hot wire ignition sensitivity.

The results of the investigation answered the question posed above in the affirmative. Spark sensitivity was found to be a function of hydrogen content and surface area, while bridgewire ignition sensitivity and reliability were primarily determined by the powder density at the bridgewire.

I. INTRODUCTION

For a number of years, efforts have been underway at Sandia Laboratories to develop hot wire initiated actuators and igniters that were safer than those typically containing sensitive, primary explosives such as lead styphnate. The basic safety problem associated with such devices is the electrostatic sensitivity of the explosive material, both as bulk powder and pressed into components. Thus the objective has been to develop an inherently spark insensitive actuator/igniter; that is, a component that does not rely on hardware techniques, such as spark gaps or shunt mixes, for resistance to ignition by an electrostatic discharge from a human body. The only obvious way of achieving that is to use an explosive or pyrotechnic material that is insensitive to electrostatic discharge, in both the bulk and compacted state.

Previous studies[1] at Sandia have examined the pyrotechnic mixtures titanium/potassium perchlorate ($Ti/KClO_4$) and titanium hydride/potassium perchlorate ($Ti_{1.9}/KClO_4$). The $Ti/KClO_4$ material was first investigated because of its high autoignition temperature. Other advantages are: 1) its ignition reliability and stability/compatibility have been proven on other Sandia components which have been in production for several years, and 2) it functions well as an igniter and actuator. The major disadvantage of $Ti/KClO_4$ is its spark sensitivity; it is extremely sensitive as a bulk powder, somewhat less sensitive in pressed form but still capable of ignition by a spark generated by a human body; a second disadvantage, for some applications, is the appearance of low values of resistance after fire (RAF) under certain conditions.

The $TiH_{1.9}/KClO_4$ mixture was the first material to be studied specifically with the inherent safety objective in mind. This pyrotechnic is extremely spark insensitive in both bulk and pressed form. It also has a high autoignition temperature and functions well in an actuator or igniter. In

addition, its RAF properties are better than for Ti/KClO$_4$. Within the past year, however, two major faults have come to light. First, a number of component ignition failures were observed at low temperatures (<219K). Second, stability and compatibility data were somewhat discouraging.

Table I summarizes the advantages and disadvantages of the two pyrotechnics.

Table 1

	Advantages	Disadvantages
Ti/KClO$_4$	Proven reliability Proven stability/ compatibility Functions well High autoignition temp.	Spark sensitive RAF properties
TiH$_{1.9}$/KClO$_4$	Spark insensitive High autoignition temp. Functions well Good RAF properties	Ignition failures Stability/compatibility

Thus the question arose: Is there a subhydride in the system TiH$_x$/KClO$_4$ that possesses the advantages of both and the disadvantages of neither? Specifically, are spark insensitivity and bridgewire sensitivity mutually exclusive properties? This paper describes the experimental program which was designed and executed to answer that question. The results are discussed in terms of the objective of developing an inherently spark insensitive actuator/igniter.

II. DEVELOPMENT PROGRAM DESCRIPTION

The following four major areas were covered in the investigation of TiH$_x$/KClO$_4$:

1. Stability/compatibility - Since current component lifetime requirements are typically in excess of twenty years,

the stability of the pyrotechnic mixture and its compability in a component is extremely important.

2.   Spark sensitivity - It is desirable to have a powder that is spark insensitive in the bulk form for increased handling safety, since a number of serious accidents have occurred at many locations during such operations as blending, packaging, and loading of spark sensitive pyrotechnics and primary explosives. An additional impetus to the development of an inherently spark insensitive actuator has been the recent requirement that the component have a demonstrated reliability of >0.999 against inadvertant ignition by electrostatic discharge from a human body. One suggested method of meeting such a requirement is 100% spark testing of the components. However, experience on a number of different components has shown that the probability of ignition on the second, fourth, or tenth pulse is about the same as for the first pulse. Thus the approach taken has been two pronged: first, design as much protection into the component hardware as possible, and second, use the least spark sensitive powder possible, consistent with other requirements. Only the latter approach will be discussed in this paper.

3.   Bridgewire ignition studies - Typically, hot wire explosive components must be ignited by a small current pulse (e.g., 3.5A for 10 ms through a 1 Ω bridgewire) over a wide temperature range and severe environmental conditions, with high reliability (e.g., 0.9999). Development of such a component using a pyrotechnic material considerably less sensitive than the commonly used primary explosives requires a degree of understanding much greater than in the past. Thus this topic received the major share of attention in the development program.

Ignition sensitivity and reliability of the $TiH_x/KClO_4$ system were studied as a function of the following three major variables:

1) Hydrogen content (x = 0.2-1.9)
2) Particle properties (surface area; particle size, shape, distribution)
3) Density of the powder at the bridgewire.

4. <u>Functional output</u> - The actuator/igniter under development will be used for two functions, to actuate a valve (i.e., stroke a piston) and to ignite a pyrotechnic train. The functional output was not influenced strongly by the value of x in the series $TiH_x/KClO_4$ studied and will not be discussed further.

III. EXPERIMENTAL DETERMINATIONS AND PROCEDURES

1. <u>Materials synthesis and characterization</u>

A. <u>Synthesis of TiH$_x$</u> - A number of synthesis techniques were explored, but the most successful procedure, and the one used to prepare all the subhydrides referred to in this paper, involved thermally dehydriding commercially available titanium hydride, $TiH_{1.9}$. The process involves a very carefully controlled vacuum heating cycle, followed by a controlled air oxidation step. The $TiH_{1.9}$ was purchased from Ventron Alfa Products, Beverly, Massachusetts as their commercial grade 2μ material. The properties of this material are tabulated in Table 2.

Table 2

BET surface area	2.3 m^2/g	Zr	400 ppm
Particle size	1.23μ	Al	300
Titanium	93.9%	Ni	300
Hydrogen	3.90%	Ca	100
Oxygen	1.2%	Fe	100
		Na	100
		Mg	10
		K	5

A number of subhydrides ranging in composition $TiH_{0.3}$ to

$TiH_{1.75}$ were prepared, analyzed, and studied. The material receiving the greatest attention was $TiH_{0.65}$. An important consideration if such a subhydride is to be used in any quantity is the batch to batch reproducibility, since only 150 g per batch were prepared. To this end a series of six 150 g batches of $TiH_{0.65}$ was prepared using identical synthesis procedures.[2] These batches were analyzed for hydrogen and oxygen content, and the surface area and particle size were determined. No significant differences were found. Several of the batches were blended with $KClO_4$ and the mixtures tested for spark sensitivity, calorific output, and bridgewire ignition. Again, no significant differences were apparent. Thus the synthesis procedure appears to be quite reproducible.

The potassium perchlorate used in the $TiH_x/KClO_4$ mixture was purchased from Barium and Chemicals, and had a particle size of nominally 9μ after passing through a 400 mesh seive.

    B. <u>Characterization</u> - The following analytical determinations were made on several of the subhydride samples:

    1) Hydrogen content - Pressure-volume and micro-combustion

    2) Oxygen content - Neutron activation analysis

    3) Surface area - BET gas adsorption

    4) Particle size - Coulter counter

    5) Particle shape - Scanning electron microscope

    6) Particle size distribution - Particle classifier

    7) Thermal properties - Bomb calorimeter, differential scanning calorimeter

    8) TiH_x phase relationships - Nuclear magnetic resonance (NMR)

    9) Crystal lattice properties - X-ray diffraction

    10) Trace impurities - Emission spectroscopy

    11) Surface analysis - ESCA, Auger spectroscopy

    2. <u>Spark sensitivity</u> - The definition of the test equivalent of a human body electrostatic discharge adopted by Sandia

is a 600 pf capacitor charged to 20 kV and discharged through
a 500 Ω series resistor. A sketch of the test fixture used
for testing bulk powder is shown in Figure 1.[1] The spark
ignition threshold of the bulk powder was measured by dis-
charging a 600 pf capacitor from a pointed electrode through
a sample of loose powder (~0.2g) to a ground plane. The volt-
age was varied until one ignition in ten trials was achieved
or until the voltage limit of the test equipment was reached.

High Voltage

Loose Powder

Ground Plane
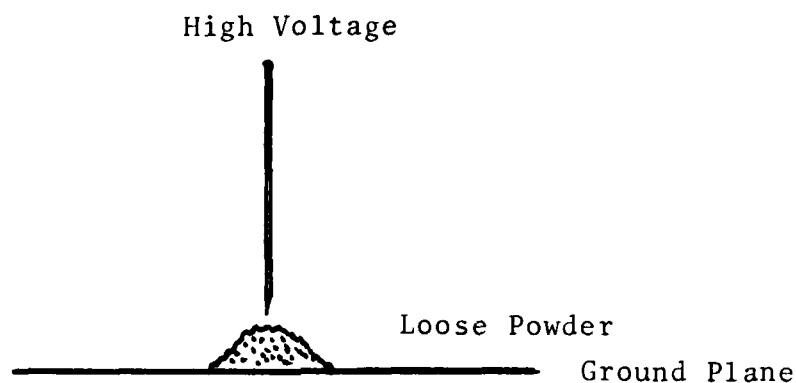
Figure 1. Test fixture for spark ignition of loose powder

A number of different methods were tried in attempting
to determine similar thresholds for pressed powders which
would correspond to the inherent sensitivity of the material
as present in the component. The standard component electro-
static sensitivity test (typically a go/no-go test at a pre-
set energy level) does not determine the sensitivity of the
powder, but merely the efficacy of spark gaps built into the
component hardware, either intentionally or inadvertently.
The test fixture which was found to give the most meaningful
data for conductive powders is shown in Figure 2. Here the
high voltage is applied to the bridgewire electrodes and the
steel ring is grounded. The spark then jumps between the
end of the pressed powder column and the ring.
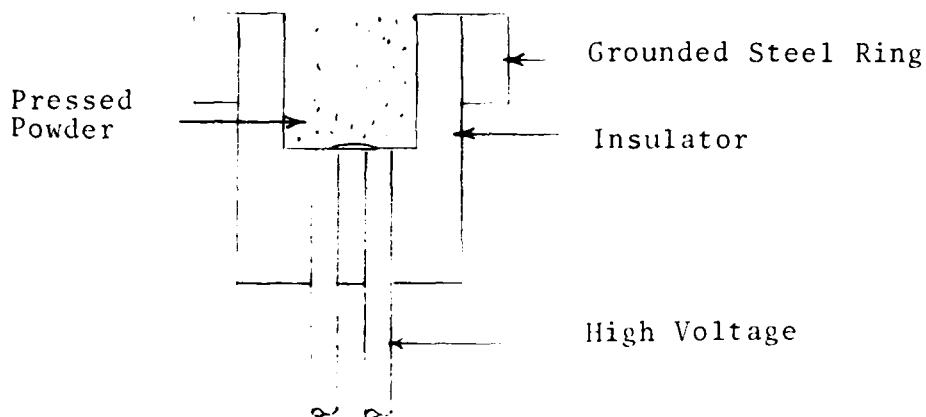
Figure 2. Test fixture for spark ignition of pressed powder

3. __Electrothermal response test__ - Electrothermal response testing (ETR) has been used extensively the past two years as an integral part of this actuator development program. It turned out to be of critical importance to the success of the program. The ETR test was first proposed by Rosenthal and Minichelli in 1970[3] and was then developed into a useful, usable tool by A. C. Strasburg of this Laboratory.[4,5] Considerable detail concerning theory and reduction to practice are available in references 3-5; suffice it to say that the ETR test is a means of non-destructively probing the bridgewire-powder interface. As the test is run at Sandia, a current pulse of a few hundred milliamperes is put through the bridgewire for 50-100 ms. The current level is picked to achieve a temperature rise in the bridgewire of ~75-100 K. By monitoring the change in resistance of the bridgewire, a number of parameters may be calculated. The most useful one is gamma (γ), which has the units of micro-

watts/degree K, which is related to the rate of heat loss
from the bridgewire (the larger the gamma, the greater the
thermal conductance at the interface). Gamma is strongly
affected by bridgewire size, the thermal conductivity of the
material surrounding the bridgewire (specifically the powder
and the header material, either glass or ceramic), and the
effective thermal contact of those materials with the bridge-
wire.

4. <u>Transmitted force measurements</u> - It had been sus-
pected for some time that the density of a pyrotechnic such
as $TiH_x/KClO_4$ next to the bridgewire is very important for
ignition and propagation. It was hoped that the electro-
thermal response (ETR) test would provide the necessary infor-
mation. By itself, however, the ETR test was insufficient
since the gamma values varied widely for different samples of
the $TiH_x/KClO_4$ series, even though the loading pressures and
procedures and the component configuration were held constant.
An important clue to the relationship of gamma and bridgewire
ignition reliability was provided by the results of an inves-
tigation into the pressing characteristics of several samples
of the $TiH_x/KClO_4$ series.

An MTS materials testing machine, fitted with two com-
pression load cells, was used to press several different sam-
ples into charge holders identical to those used in the
actuator. The experimental setup is shown in Figure 3.

Load cell on ram (Applied force)

Charge holder

Powder sample

Loading fixture

Load cell (Transmitted force)
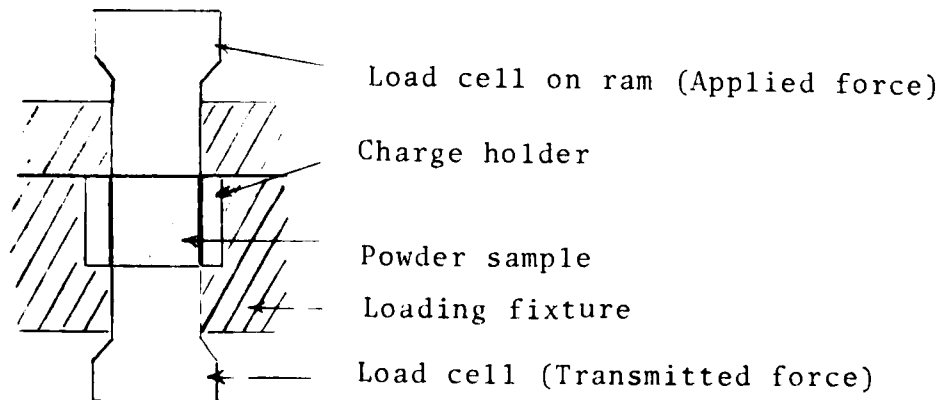
Figure 3. Test fixture for transmitted force measurements

The data generated are applied force and transmitted force plotted against powder column height as the powder is compacted. Representative data can be found in the Results and Discussion section. The variables investigated were the following: 1) composition of $TiH_x/KClO_4$ powder, 2) single and double pressing increments, 3) ram speed and dwell time, 4) charge holder material, dimensions, and surface finish.

IV. RESULTS AND DISCUSSIONS

1. <u>Stability and compatibility</u> - The stability and compatibility results[6] discussed in this paper were generated by T. M. Massis and P. K. Morenus of this Laboratory. The data presented in this section is abstracted from reference 6. As mentioned previously, $Ti/KClO_4$ has good stability/compatibility properties while $TiH_{1.9}/KClO_4$ does not. Experiments were designed to generate kinetic and thermodynamic information since both affect stability.

The reaction expected for TiH_x mixed in a stoichiometric ratio with $KClO_4$ can be described by the general equation:

$$2TiH_x + (1 + 0.25x) \; KClO_4 \longrightarrow 2TiO_2 + (1 + 0.25x) \; KCl + xH_2O \; ,$$
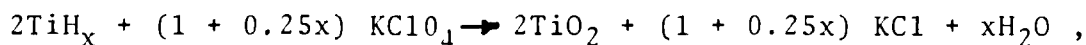
where x varies from 0.2 to 1.9. (The actual ratio used was a 33/67 weight percent $TiH_x/KClO_4$). It should be pointed out that the Mil. Spec. titanium used [7] is actually a subhydride, $TiH_{0.2}$, as determined by analysis and NMR results. In the remainder of this paper, the designation $TiH_{0.2}$ will be used.

The stability study was based upon the assumption that TiO_2, KCl, and H_2O would be the products of reaction during aging. Stability of the various pyrotechnics was determined by measuring the rate of formation of water with a gas chromatograph and that of chloride with a specific ion electrode.

Figure 4 shows the results of a stability study of several samples of $TiH_x/KClO_4$ (x = 0.2, 0.6, 1.5, 1.7, 1.9) carried out at 373 K. The results show that, as the amount of hydrogen

in TiH_x is reduced, the pyrotechnic mixture becomes more stable, approaching that found for Mil. Spec. titanium/potassium perchlorate ($TiH_{0.2}/KClO_4$).
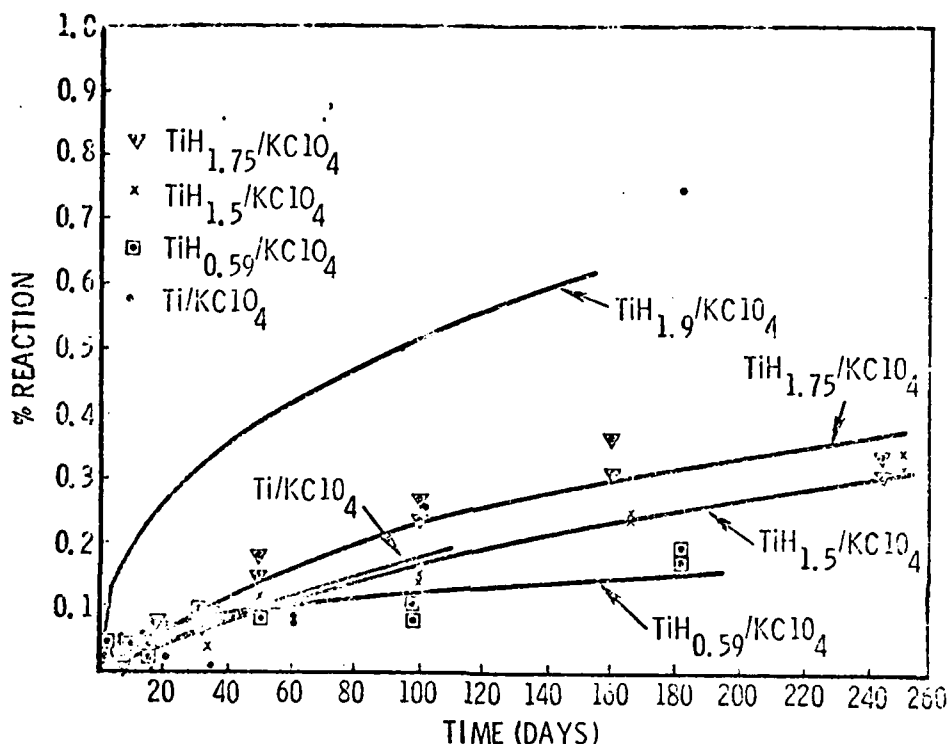
Figure 4. Stability of $TiH_x/KClO_4$
(Cl^- formation at 373 K)

Figure 5 presents the chloride stability data as a function of hydrogen content in TiH_x, measured at various time periods, which more clearly shows that once one deviates from $TiH_{1.9}$, stability increases dramatically. This would be expected since it has been shown that stability is a strong function of labile surface hydrogen, and the amount of surface hydrogen was observed to decrease rapidly as x drops below 1.9.
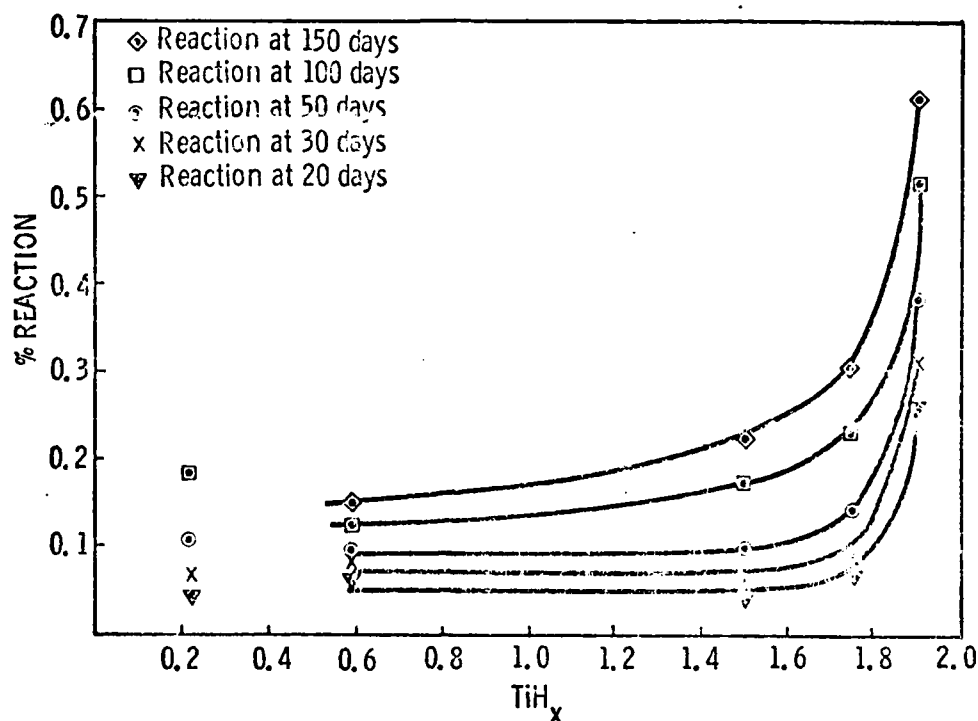
Figure 5. Stability versus TiH$_x$ composition
(Cl$^-$ formation at 373 K)

Activation energies for the formation of chloride and water in TiH$_{1.9}$/KClO$_4$ were determined to be 21 kcal/mole and 25 kcal/mole, respectively. Similar determinations for the subhydrides are in progress.

From a component compatibility standpoint, the production of water and chloride ion as decomposition products is cause for concern, especially in the area of bridgewire corrosion. Indeed, indications are that corrosion of the bridgewire may be occurring in sealed components containing TiH$_{1.9}$/KClO$_4$ that were aged for up to 225 days at 373 K and 423 K.

Examination of many other components containing TiH$_{0.2}$/KClO$_4$ that have been aged for long times at lower temperatures has revealed no evidence of corrosion. Since the stability

of the subhydrides is similar to the Mil. Spec. titanium, no
compatibility problems are anticipated. However, a compre-
hensive component compatibility program has been initiated.

   2. Spark sensitivity - A compilation of spark sensi-
tivity measurements of bulk $TiH_x/KClO_4$ as a function of x is
presented in Figure 6. The data points represent 10% thresh-
old levels. The tests were conducted using the apparatus
and test technique described earlier. The dashed line cor-
responds to Sandia's human body equivalent discharge level.
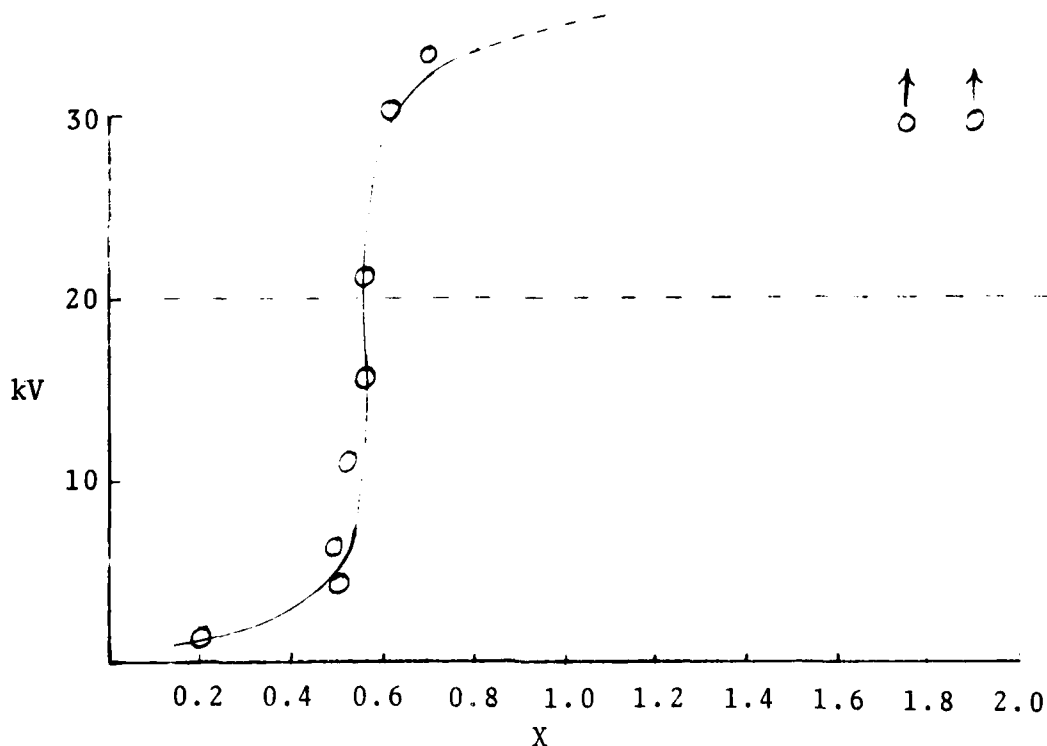
Figure 6. Spark sensitivity thresholds in kilovolts,
of bulk $TiH_x/KClO_4$ samples
as a function of hydrogen content

   Care must be exercised, however, in assuming that a
material that falls just above the 20 kV line is spark insen-
sitive. Consider the results of the following experiment.

A particular sample of $TiH_{0.5}/KClO_4$ exhibited one ignition out of ten trials at 20 kV. The same material was then subjected to 100 pulses at each of six voltage levels (10-30 kV in 5 kV intervals) with the result that 7-11 ignitions occurred at each level. The same material was then pulsed 100 times (20 times per day for 5 days) from a human body discharge. The charge was accumulated by walking on a nylon carpet; the voltage varied from 15-25 kV. A total of four ignitions occurred. [8]

From a fairly extensive parametric investigation of the effect of hydrogen content and surface area (and other particle parameters) of TiH_x on spark sensitivity and bridge-wire ignition, it was clearly evident that spark sensitivity decreases with increasing hydrogen content and increases with increasing surface area (or decreasing particle size). Table 3 lists several examples illustrating the trend.

Table 3

Sample	Surface Area (m^2/g)	Spark Threshold (kV)
$TiH_{1.75}/KClO_4$	~3	>50
$TiH_{1.70}/KClO_4$	9	10
$TiH_{1.53}/KClO_4$	1.5	>50
$TiH_{1.48}/KClO_4$	5.6	13
$TiH_{0.65}/KClO_4$	1	>50
$TiH_{0.63}/KClO_4$	6.4	8
$TiH_{0.01}/KClO_4$	0.4	20
$TiH_{0.2}/KClO_4$	8.8	< 1

Static sensitivity of $TiH_x/KClO_4$ mixtures is also affected by particle size distribution, which was demonstrated by the following experiments. The mixture $TiH_{0.7}/KClO_4$ is very spark insensitive (no fires in 100 trials at 30 kV). A sample of $TiH_{0.7}$ was separated into four fractions by a particle classifier. The properties of the four fractions and the starting material are listed in Table 4.

Table 4

Fraction	Particle Size(μ)	Surface Area(m^2/g)	H_2(%)	O_2(%)	Static sensitivity of $KClO_4$ mixture(kV)
I	1.0	2.36	0.96	3.8	8
II	1.25	1.59	1.2	2.7	28
III	1.4	1.03	1.4	2.0	>30
IV	1.7	.63	1.6	1.2	Not determined
$TiH_{0.7}$	1.6	1.08	1.46	1.7	>30

A summary of the results of spark testing $TiH_{0.65}/KClO_4$, a mixture that appears to have a number of favorable properties, is as follows:

Bulk powder -   No fires in 330 trials, voltage levels varied from 20-50 kV.

Pressed powder - No fires in 50 trials at 20 kV; no fires in 50 trials at 35 kV.

The bulk powder testing is fairly conclusive; several different blends were tested at two laboratories on several occasions. However, a more comprehensive test series is in progress. The data on pressed powder are insufficient for complete confidence; however, the results to date are encouraging.

3. <u>Bridgewire ignition</u> - During the course of the bridgewire ignition study, three different hypotheses were suggested to explain the failures previously observed and to understand the ignition properties of the $TiH_x/KClO_4$ series. The important variables investigated were hydrogen content, particle properties, and powder density at the bridgewire.

A. <u>Bridgewire ignition studies of $TiH_x/KClO_4$ as a function of hydrogen content (x)</u> - As mentioned previously, a number of ignition failures had been observed with $TiH_{1.9}/KClO_4$, while $TiH_{0.2}/KClO_4$ was very reliable. Examination of the spark sensitivity vs hydrogen content curve (Figure 6)

reveals that a sharp change in sensitivity occurs around $TiH_{0.6}$. The working hypothesis was that a composition that had a spark sensitivity threshold near 20 kV would also have acceptable bridgewire ignition properties. Thus, a number of subhydrides between $TiH_{0.55}$ and $TiH_{0.8}$ were synthesized, blended with $KClO_4$, and tested. A noticeable improvement was apparent, but failures of $TiH_{0.65}/KClO_4$ did occur at low temperatures.

    B. <u>Bridgewire ignition studies of $TiH_x/KClO_4$ as a function of particle properties and hydrogen content</u> - Typically, metal powders such as TiH_x are characterized by particle size. Based on Zeiss or Coulter counter particle size analysis, all the members of the TiH_x series and several Mil. Spec. titanium samples, were nearly identical. If however, BET surface areas are compared a rather dramatic difference is apparent. The subhydrides synthesized from $TiH_{1.9}$ had surface areas around 1 m^2/g while several Mil. Spec. titanium samples, which had proven reliability, had surface areas from 7-9 m^2/g.

Based on that information a parametric investigation was carried out where the hydrogen content was varied by dehydriding, and the surface area was varied by ball milling. Ball milling was carried out under water or octane; octane was used to achieve high surface area without the concomitant increase in oxygen content as occurs with water. Figure 7 depicts a representative experimental flow chart.

In some cases the ball milling and dehydriding steps were reversed; there were also multiple ball milling and/or dehydriding operations. In addition, some of the samples were fractionated by the particle classifier prior to blending. Approximately forty samples were blended and nearly 300 ignition tests made. The analysis included surface area, particle size, hydrogen and oxygen content, and sometimes SEM and x-ray diffraction.
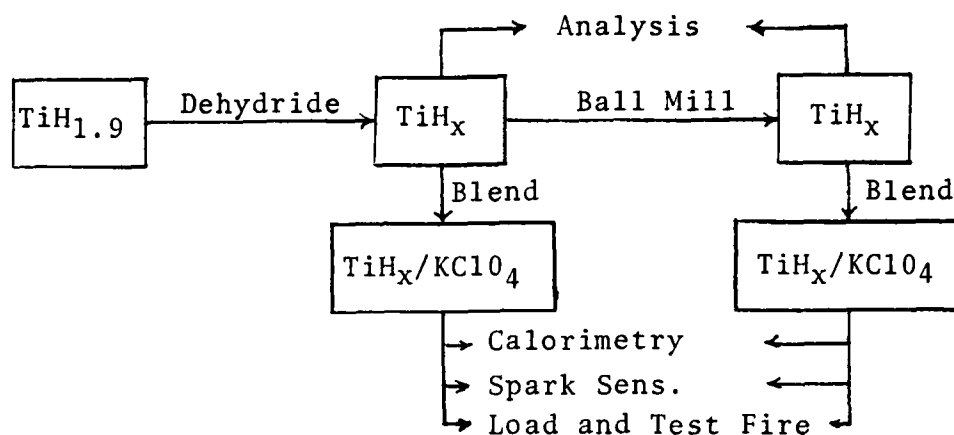
Figure 7. Experimental flow chart for
investigation of ignition properties of $TiH_x/KClO_4$
as a function of x and surface area

Table 5 is a list of the subhydrides made, surface area
and oxygen content, spark sensitivity threshold, and test fire
data for the $KClO_4$ blends. The test fire data includes bridge-
wire diameter (all one ohm), fire pulse current, test tem-
perature, number of units fired relative to number tested, and
bridgewire burnout time and sigma.

It is readily apparent that spark sensitivity correlates
with surface area and hydrogen content, while bridgewire igni-
tion sensitivity and reliability do not.

C. <u>Bridgewire ignition studies of $TiH_x/KClO_4$ as a
function of powder density near the bridgewire</u> - This section
discusses the relationship among powder pressing character-
istics, the electrothermal response (ETR) term gamma, and the
critical density of the powder at the bridgewire. The term
"critical density" here means that density at which ignition
failures begin to occur.

Early in the actuator program the loading precedure was
fixed at a single increment pressing at 69 MPa (10,000 psi)
for the following reasons: first, favorable results with Mil.
Spec. titanium/potassium perchlorate were obtained when the
length to diameter ratio of the pressed pellet was approxi-
mately one; second, when firing energy was determined as a

Table 5

Subhydride	O_2 (%)	Surface area (m^2/g)	Spark sensitivity of blend (kV)	Bridgewire Diameter (mm)	Firing Current (amp)	Test Temp. (K)	Units Fired/ Units Tested	Bridgewire Burnout Time and Sigma (ms)
$TiH_{1.93}$	1.2	2.3	>50	0.048	3.5	300	4/4	4.68(0.71)
				0.048	3.5	200	0/4	5.78(0.48)
$TiH_{1.70}$	6.6	8.9	10	0.043	3.5	200	3/5	2.62(0.17)
				0.048	3.5	200	0/5	4.33(0.64)
$TiH_{1.47}$	6.9	7.8	15	0.043	3.5	200	1/5	2.39(0.29)
				0.048	3.5	200	2/5	3.86(0.67)
$TiH_{0.63}$	8.9	6.4	8	0.043	5.0	200	4/5	0.95(0.08)
				0.048	5.0	200	5/5	1.32(0.24)
$TiH_{1.53}$	1.75	1.6	>50	0.043	3.5	200	3/5	2.80(0.36)
				0.048	3.5	200	1/5	4.18(0.86)
$TiH_{1.48}$	5.40	5.6	13	0.043	3.5	200	4/5	1.82(0.42)
				0.048	3.5	200	1/5	3.82(0.58)
$TiH_{1.83}$	3.21	7.3	8	0.043	3.5	200	1/5	2.70(0.18)
				0.048	3.5	200	3/5	5.02(0.29)
$TiH_{1.11}$	1.73	1.04	>50	0.043	3.5	200	4/5	2.60(0.45)
				0.048	3.5	200	4/5	5.42(0.32)
$TiH_{1.16}$	3.91	3.2	35	0.043	3.5	200	3/5	2.43(0.44)
				0.048	3.5	200	1/5	5.08(0.25)
$TiH_{1.13}$	2.29	2.9		0.043	3.5	200	4/5	2.65(0.37)
				0.048	3.5	200	3/5	4.62(0.18)
$TiH_{0.75}$	3.10	1.86	37 (13/100 @ 30, 3/50 @ 20, 0/50 @ 15)	0.038	3.5	200	5/5	1.36(0.14)
				0.043	3.5	200	5/5	3.44(0.29)
				0.043	3.5	200	4/4	2.54(0.50)
				0.043	5.0	200	4/4	1.20(0.10)
				0.043	10.0	200	4/4	0.35(0.02)
				0.048	3.5	200	5/5	2.96(0.29)
				0.048	3.5	200	4/4	4.52(0.56)
				0.048	5.0	200	3/4	2.06(0.09)
				0.048	10.0	200	2/4	0.54(0.02)
				0.043	3.5	422	5/5	1.47(0.02)
$TiH_{0.78}$	4.77	2.5	26	0.043	3.5	200	4/4	2.27(0.53)
				0.048	3.5	200	5/5	4.22(0.86)
				0.043	3.5	200	5/5	2.65(0.31)
				0.048	3.5	200	4/5	3.88(0.64)

function of loading pressure for $TiH_{1.9}/KClO_4$, the minimum occurred around 69 MPa where the standard deviation was also lowest; and third, with the lower subhydrides at pressures greater than 104 MPa (15,000 psi) the powder becomes quite conductive around the bridgewire and causes the effective resistance of the bridgewire to decrease.

During the course of the development program, however, various experimental observations were made which indicated that the density of the powder around the bridgewire might be implicated in some of the ignition failures; e.g., post-mortem examination of the powder-header interface of some failed units indicated lower density than expected, fewer failures occurred in component hardware with smaller ℓ/d ratios, and periodically, gamma values would appear that were abnormally high or low.

Transmitted force measurements made on a number of $TiH_x/KClO_4$ samples provided the clue which led to the critical powder density hypothesis. Figures 8 and 9 show curves of the applied force, F_A, and the transmitted force, F_T, for $TiH_{0.65}/KClO_4$ and $TiH_{0.2}/KClO_4$, respectively. The powder was pressed into ceramic charge holders, in a single increment, and F_T and F_A plotted against resultant powder column height. On the 3.73 mm (0.147") diameter ram, 756 N (170 pounds force) is equivalent to 69 MPa (10,000 psi) loading pressure.

Table 6 is a summary of the data generated to date on several samples of $TiH_x/KClO_4$. Note that all four Mil. Spec. titanium samples have considerably higher F_T/F_A ratios and three have lower density than the subhydrides or fully hydrided material. Note also that there is considerable deviation in the F_T/F_A ratio from run to run of the same sample.
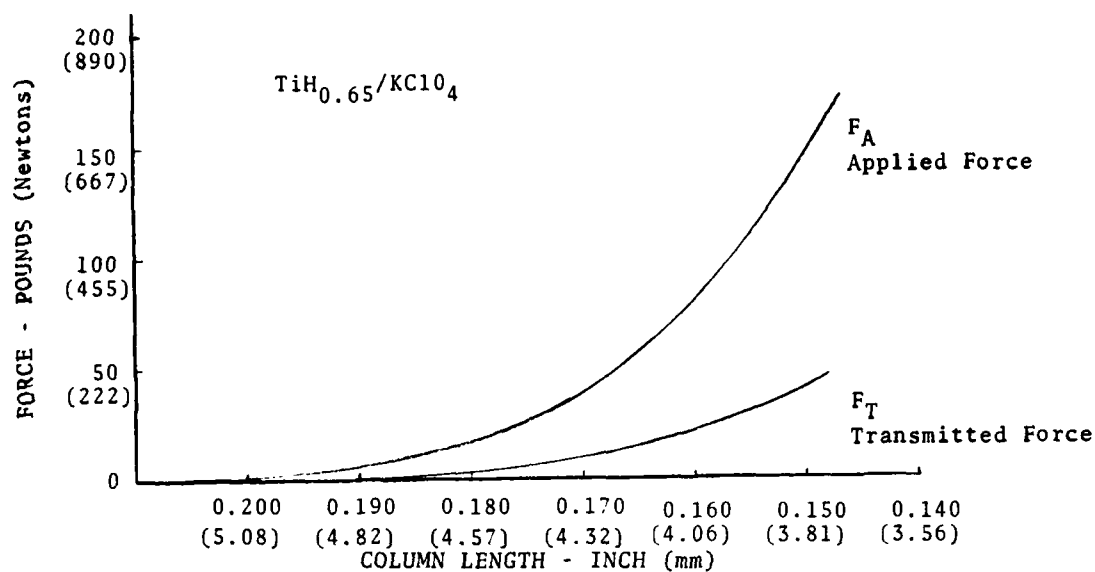
Figure 8. Transmitted force curve for
$TiH_{0.65}/KClO_4$ (P03043), 86.9 mg pressed
in single increment, plotted against powder column height
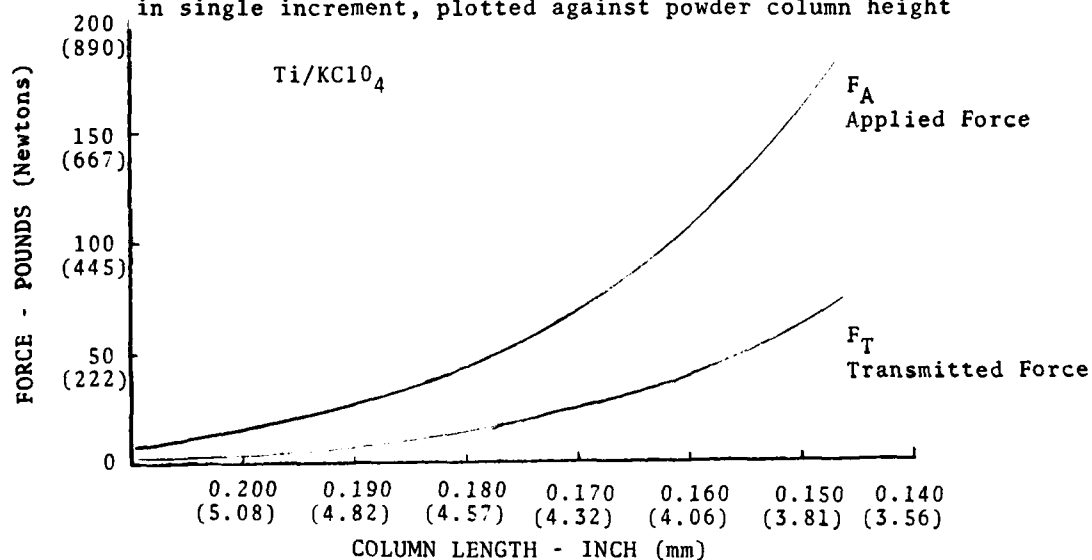
Figure 9. Transmitted force curve for
$TiH_{0.2}/KClO_4$ (P02019), 77.7 mg pressed
in single increment, plotted against powder column height

Table 6

Sample	Blend No.	No. of Runs	Density @ 69 MPa (g/cc)	F_T/F_A % and Sigma
$TiH_{1.9}/KClO_4$	PO3062	4	2.02	32.1 (2.4)
$TiH_{0.2}/KClO_4$	PO2019	6	1.84	34.6 (6.4)
$TiH_{0.2}/KClO_4$	PO2025	3	1.89	38.4 (0.4)
$TiH_{0.2}/KClO_4$	PO2032	5	1.87	37.6 (2.7)
$TiH_{0.01}/KClO_4$	PO2012	3	2.17	35.1 (3.5)
$TiH_{0.65}/KClO_4$	PO3043	4	2.08	28.4 (2.2)
$TiH_{0.65}/KClO_4$	PO3044	5	2.04	27.4 (2.5)

The data tabulated in Table 7 illustrates the results of pressing the same or similar materials into the same charge holder in two approximately equal increments, both at 69 MPa. Note the change in transmitted force and sigma.

Table 7

Sample	Blend No.	No. of Runs	F_T/F_A (1st increment) % and Sigma	F_T/F_A (2nd increment) % and Sigma
$TiH_{0.65}/KClO_4$	PO3040	4	54.9 (1.3)	44.3 (1.0)
$TiH_{0.2}/KClO_4$	PO2019	3	56.6 (2.0)	46.8 (1.2)
$TiH_{0.2}/KClO_4$	PO2032	3	53.9 (2.3)	44.8 (0.8)

Although the F_T/F_A ratios were all approximately equal, the density of the $TiH_{0.65}/KClO_4$ was still 10-15% greater than the $TiH_{0.2}/KClO_4$ samples, as determined by the quantities used to fill the charge holders.

The transmitted force data described above led to the hypothesis that the cause of the failures observed for $TiH_{0.65}/KClO_4$ was insufficient density of the powder at the bridgewire. If the hypothesis is correct, there should exist a density dependent ignition threshold. Consequently, a number of components were loaded with $TiH_{0.65}/KClO_4$ and $TiH_{0.2}/KClO_4$, in single increments, at various loading pressures. A sketch of

the test hardware used for all the bridgewire ignition tests reported in this paper is shown in Figure 10. The charge holder is the same as that used for the transmitted force measurements and is nominally 3.73 mm (0.147") in diameter by 3.73 mm (0.147") long. It will hold ~80 mg of $TiH_{0.2}$/ $KClO_4$ pressed at 69 MPa (10 kpsi). Before test firing an end cap is attached.
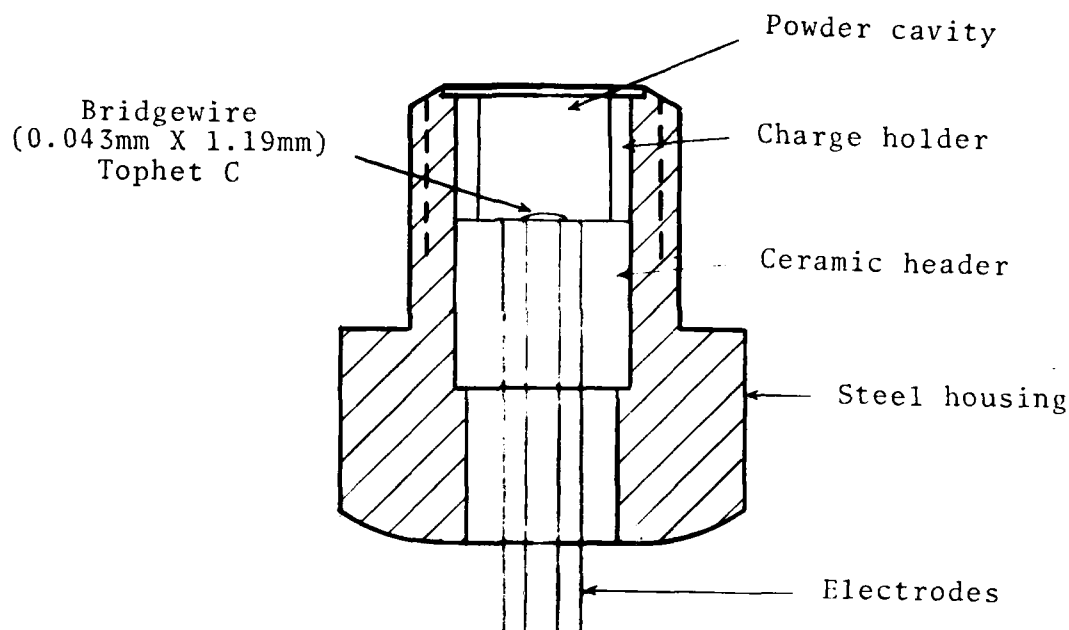
Figure 10. Test hardware sketch

Since the density of the powder at the bridgewire cannot be measured directly, it is inferred by a combination of gamma, which is measured on each unit, and transmitted force (actually transmitted pressure), which is calculated from the loading pressure used and the F_T/F_A ratios listed in Table 6.

The firing data is summarized in Table 8. All were fired at 200 K with 3.5 amps.

Table 8

| Loading Pressure | | Number of units fired/ Number of units tested | |
MPa	(kpsi)	$TiH_{0.65}/KClO_4$	$TiH_{0.2}/KClO_4$
69	(10)	3/3	3/3
55.2	(8)	2/3	3/3
41.4	(6)	5/8	3/3
27.6	(4)	0/3	0/3
20.7	(3)	0/5	
13.8	(2)	0/3	1/3

A plot of these data as a function of gamma and transmitted pressure is shown in Figure 11.
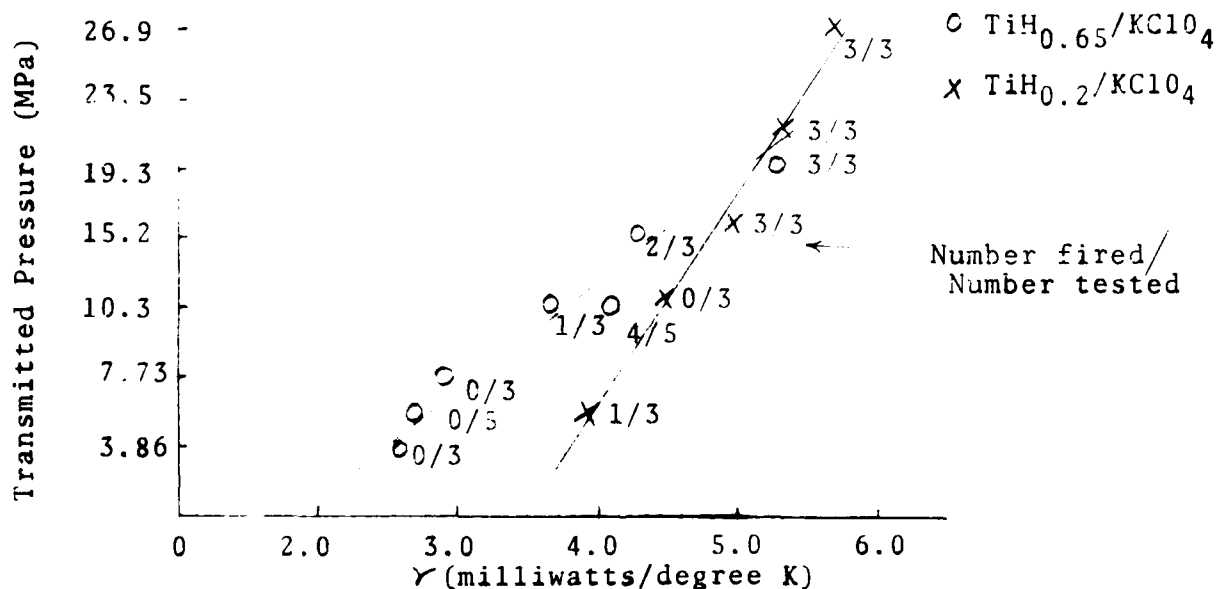
Figure 11. Test firing data as a function of transmitted pressure and gamma for $TiH_{0.65}/KClO_4$ and $TiH_{0.2}/KClO_4$

Clearly, a critical density exists for both $TiH_{0.65}/KClO_4$ and Mil. Spec. $TiH_{0.2}/KClO_4$. Previous ignition failures of $TiH_{0.65}/KClO4$ can now be rationalized. Three

failures out of 77 trials occurred, test fired under the same conditions as those in Figure 11. One group of four units loaded on a single day had an average gamma of 2.5; two out of four failed. A second group of five, loaded the same day as the previous group, exhibited an average gamma of 3.5 and had one failure. A number of other groups, totaling 68 units, had an average gamma of 5.8 and all fired. Thus, although all were supposed to have been loaded at 69 MPa (10 kpsi), the two groups of units that had failures exhibited bridgewire-powder interfaces similar to units loaded at 13-41 MPa (2-6 kpsi), where failures are expected, as shown in Figure 11.

The fact that components loaded with $TiH_{0.2}/KClO_4$ in a single increment at 69 MPa (10 kpsi) are more reliable than those with $TiH_{0.65}/KClO_4$ can be explained in the following manner. Although the critical density ignition threshold, as indicated by gamma, is similar for both materials, for a given loading pressure the transmitted pressure and hence the gamma is higher for $TiH_{0.2}/KClO_4$.

The results of a similar test series at a different laboratory, using $TiH_{0.65}/KClO_4$, are shown in Figure 12. Again failures are observed at low values of gamma corresponding to a low transmitted pressure.* The X's and 0's were single increment loads, fired with 3.5 amps at 200 K. The units designated Ⓧ were loaded in two increments at 69 MPa (kpsi), where the first increment was varied from 10-50 mg and the second increment filled the charge holder. They were tested at liquid nitrogen temperature (95 K) with 3.5 amps; all 24 fired. The transmitted pressure value was calculated from the F_T/F_A ratios listed in Table 7.

---

* There is a difference in gamma values at the two laboratories that is unexplained at the present time. The slopes of gamma vs transmitted pressure are the same, however.
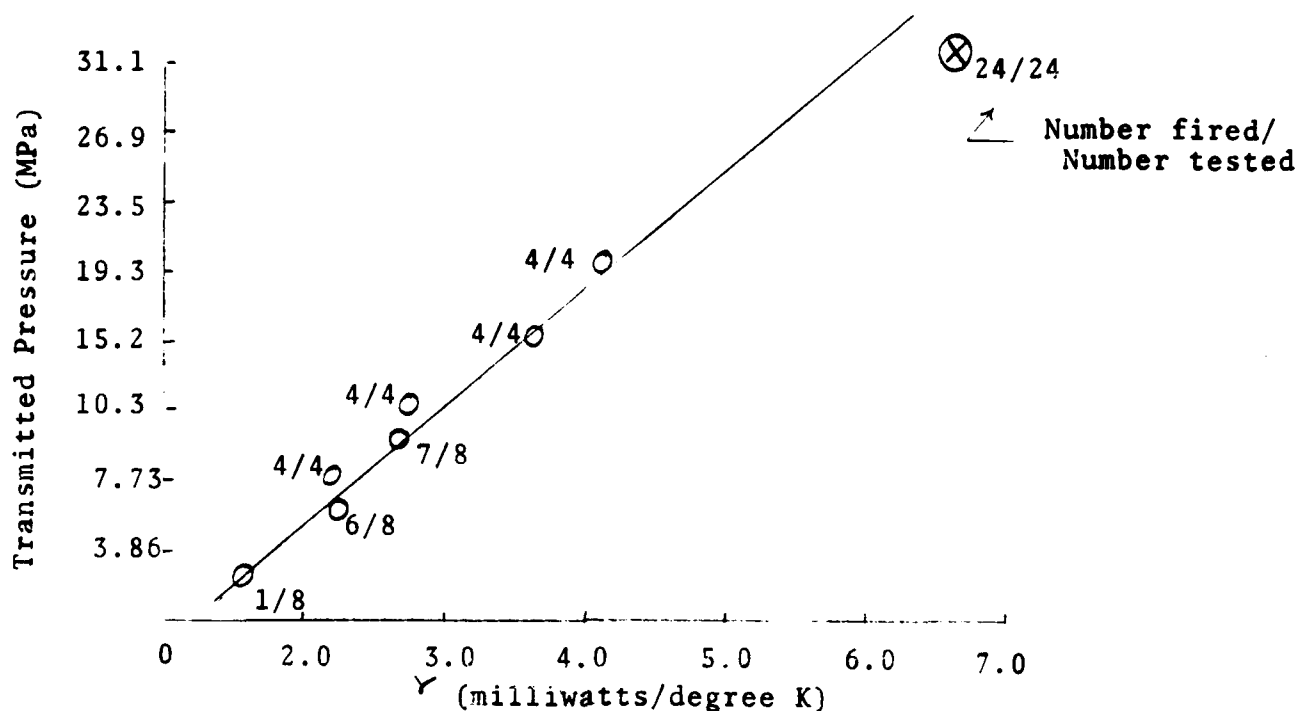
Figure 12.   Test firing data as a function of transmitted
pressure and gamma for $TiH_{0.65}/KClO_4$

From the foregoing analysis it is felt that, if the
pressing characteristics of a particular powder into a speci-
fic component are known, (the F_T/F_A ratio) and if the critical
density is determined as a function of gamma, then reliable
ignition can be obtained by specifying the loading procedure.
The reliability can be insured by measuring gamma on every
component, and rejecting those with gammas lower than a pre-
determined minimum.

Ignition failures can also occur at the other extreme
with conductive powders such as $TiH_x/KClO_4$, especially at
lower values of x. As the loading pressure is increased,
the electrical conductivity of the powder next to the bridge-
wire increases and lowers the effective resistance of the
bridgewire. The thermal conductivity is also increased as
evidenced by higher gamma values. Both effects increase the

all-fire energy; in the extreme, failures can occur with low energy firing pulses.

It has been found that thermal cycling and/or vibration can relieve this problem, presumably by causing a slight de-coupling of the powder from the bridgewire/electrode area. The ETR test is again valuable in insuring reliable ignition by allowing one to specify a certain minimum bridgewire resistance (one of the ETR test parameters measured) and maximum gamma, after thermal cycling and/or vibration.

V.   CONCLUSIONS

The investigation into the spark sensitivity and bridge-wire ignition properties of the pyrotechnic series $TiH_x/KClO_4$ (x = 0.2-1.9) has led to two major conclusions. First, spark sensitivity correlates well with hydrogen content (sensitivity increases with decreasing values of x) and surface area (sensitivity increases with increasing surface area), while bridge-wire ignition characteristics do not.

Second, the first order effect for ignition reliability from a hot wire is the density of the powder at the bridgewire. The powder density at the bridgewire can be inferred by a combination of the transmitted force data for a particular powder-charge holder pair and gamma values from electrothermal (ETR) testing of loaded components. The critical density, i.e. the density below which failures can occur, can be determined by loading components at various pressures, and plotting the firing results as a function of gamma and transmitted pressures. With the critical density established as a function of gamma and transmitted pressure, a loading procedure can be specified to give the proper density at the bridgewire, which can be monitored by ETR testing.

VI.   SUMMARY

An inherently spark insensitive actuator has been de-veloped which is highly reliable to hot wire ignition and should have a long shelf life (>24 years). The material used

is the pyrotechnic mixture, $TiH_x/KClO_4$, where x is >0.6 and
<1.9. The spark sensitivity of the pyrotechnic decreases as
the hydrogen content increases and increases as surface area
increases. Ignition reliability is primarily a function of
the density of the pyrotechnic near the bridgewire. Failures
to ignite and propagate occur when the density is below a
critical density; the critical density is influenced by the
pyrotechnic material properties and the component hardware.
Ignition failures can also be caused by excessive loading
pressures, where the ignition energy is limited, due to the
increased electrical and thermal conductivity of the powder
next to the bridgewire. The electrothermal response test is
an extremely valuable tool in nondestructively determining the
density next to the bridgewire.

VII. REFERENCES

1. Leslie, W. B. and Dietzel, R. W., Titanium Hydride-Potassium Perchlorate: A Spark Insensitive Pyrotechnic Material, Sandia Laboratories, Albuquerque, N. M., SAND74-0220, 1974.

2. Carlson, E. A., Monsanto Research Corp., Mound Labs, Miamisburg, Ohio, Private Communication, 1976.

3. Rosenthal, L. A. and Minichelli, V. J., Nondestructive Testing of Insensitive Electroexplosive Device by Transient Techniques, JPL Technical Report 32-1494, 1970.

4. Strasburg, A. C., Methodology for Computation of Interface Parameters of a Hot-Wire Explosive Device from the Electrothermal Response Analog, Sandia Laboratories, Albuquerque, N. M., SLA-73-1034, 1973.

5. Strasburg, A. C., A Data Requisition System for Transient Pulse Testing, Sandia Laboratories, Albuquerque, N. M., SAND75-0550, 1975.

6. Massis, T. M., Morenus, P. K., and Murill, R. M., Stability of the Pyrotechnic Mixture Titanium Hydrides (TiH_x)/ Potassium Perchlorate ($KClO_4$), Sandia Laboratories, Albuquerque, N. M., SAND-15-5889, 1976.

7. Military Specification Titanium Powder, MIL-T-13405C (MV).

8. Leslie, W. B., and Dietzel, R. W., Sandia Laboratories, Albuquerque, N. M., Private Communication, 1975.

288

VIII. ACKNOWLEDGEMENTS

SUPPRESSIVE SHIELDING APPLICATION TO PYROTECHNIC AND PROPELLANT OPERATIONS

R. G. THRESHER, MGR., and D. M. KOGER
Mechanical Process Technology Division
Edgewood Arsenal
Aberdeen Proving Ground, MD 21010

1.0 INTRODUCTION

The objective of this program was to proof test a vented enclosure that would suppress an accidential detonation of an explosive igniter slurry mix, and reduce flame and fireball from deflagration reactions to an operator tolerable level. The shield was designed so that, in the event of a process accident, maximum operation and facility protection would be provided while retaining facility flexibility at minimum cost.

The work was performed under the direction of the Edgewood Arsenal Resident Laboratory at the NASA National Space Technology Laboratories (NSTL) with support from the General Electric Company and Global Associates.

The suppressive shielding program (1) was initiated in 1969 to provide improved, cost-effective, safety-certified explosion suppressive protective structures in the form of homogeneously vented enclosures as an alternative to the use of US Army TM5-1300 walls. Previous tasks have demonstrated the concept feasibility and have shown that blast overpressure, fireball, and fragmentation hazards from an accidental detonation can be significantly reduced or suppressed. Full scale prototype structures have been developed for applications in Chemical Agent Munition Demilitarization Systems (2,3), white phosphorus munition processing (4), explosive ordnance disposal (5,6), and 81mm mortar round production lines (7,8).

In 1973 the program was given increased impetus by US Army authorization to provide, within three years, a sound technological base for the concept. At the direction of the Project Manager, USA Production Base Modernization and Expansion Office and with the cognizance of the Suppressive Shielding Technical Steering Committee, a simultaneous program was initiated to provide proven prototype hardware application to seven major categories of hazardous munition production operations. Work is currently in progress on all of the shield, and the testing of a prototype fixture for Category 5 applications is the subject of this report.

In addition to the basic definitions of Category 5, Army Ammunition Plant (AAP) surveys conducted during April 1974 resulted in selection of an igniter slurry mixing operation at the Longhorn AAP as a typical application for this shield. Specific consideration during the program was thus given to the candidate operation,

although the shield is applicable to the entire spectrum of Category 5 applications with only minor modifications required to address size restraints.

2.0   TECHNICAL INVESTIGATIONS

2.1   Test Fixture.   The design and fabrication details of the Category 5 suppressive shield will be published in a separate report.   The structure, in various stages of fabrication, is shown in figures 1-5.
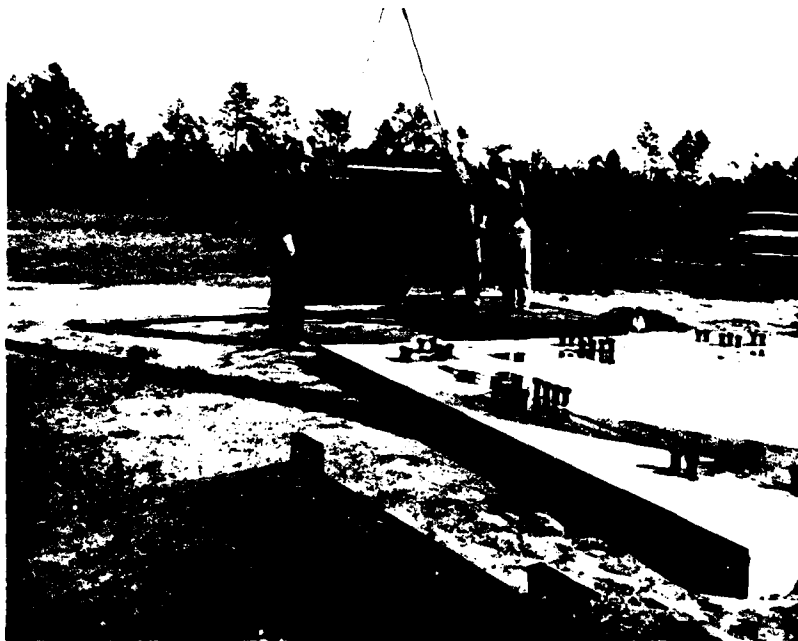
Figure 1.   Category 5 Suppressive Shield Wall Section
Being Positioned on Concrete Slab

2.2   Test Program Scope.   To evaluate the effectiveness of the suppressive shield design and to provide basic data for empirical input into the Applied Technology Program, a series of tests were performed within the structure as follows:

- Explosive tests were conducted inside the suppressive shield using spherical C-4 charges.   The final charge weight (2.44 lbs C-4) provided structural loading of 62.5 psi peak side-on overpressure at the wall and so represents a 25 percent blast pressure overload beyond the design point.

- Fragmentation confinement tests were conducted using simulated processing equipment from the candidate application, with an equivalent charge of high explosive.

Figure 2.   Category 5 Suppressive Shield Showing Six Wall Sections in Place
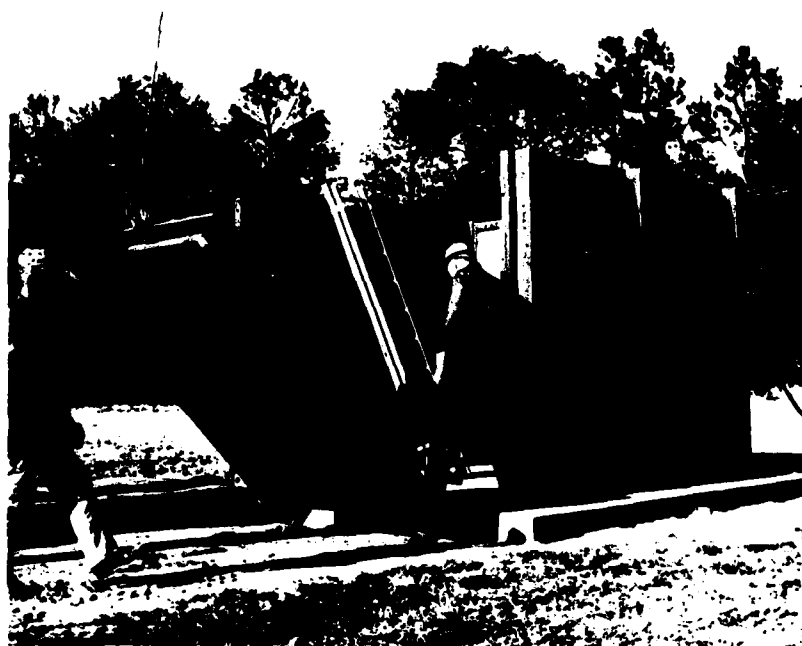
Figure 3.   Category 5 Suppressive Shield Wall Section Being Positioned
on Studs in Concrete Foundation
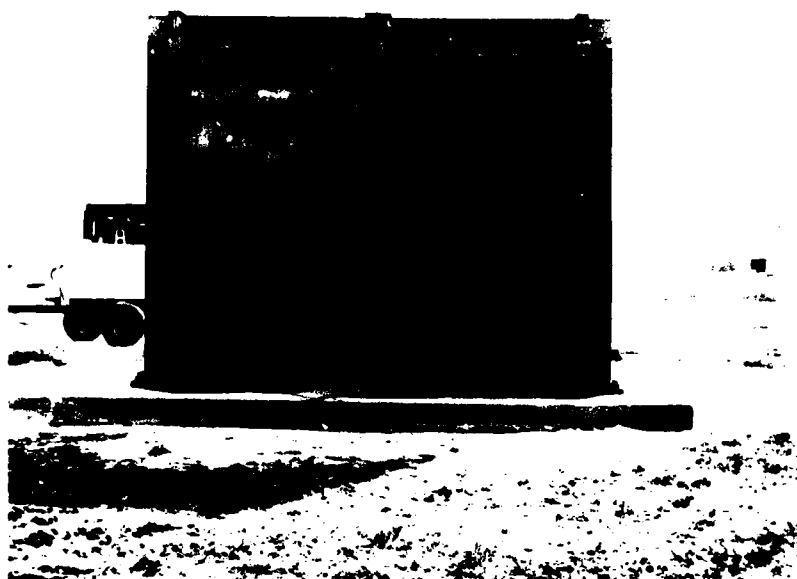
Figure 4. Completed Category 5 Suppressive Shield
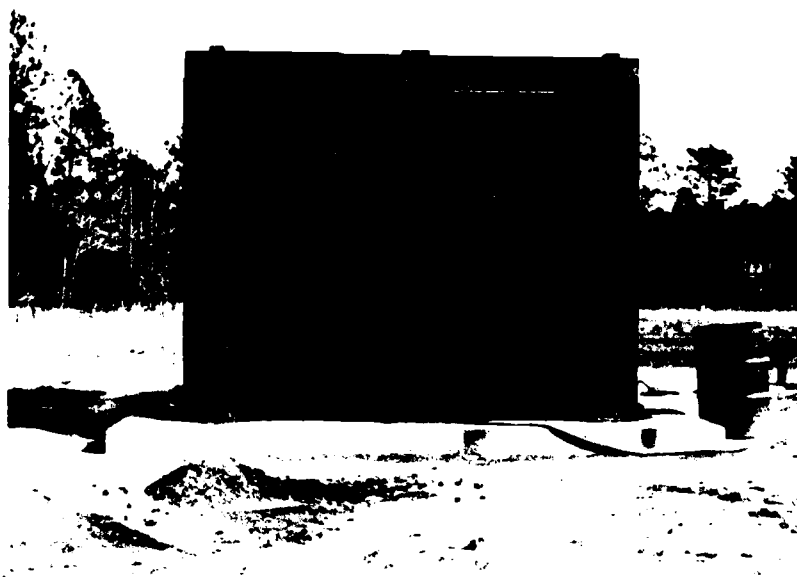
Figure 5. Category 5 Suppressive Shield Showing Personnel/Equipment
Access Door

- Flame and thermal confinement tests were conducted using an illuminant composition.

All tests were preceeded by appropriate free-air calibrations using equivalent weights of C-4 or illuminant mix.

A comprehensive report, detailing all tests, was previously published (9). This report will address only the flame and thermal confinement tests.

2.3   Fireball and Thermal Containment Tests. A series of tests were performed using 10, 20, 30, and 50 pound charges of a magnesium-sodium nitrate illuminant composition. The materials (55 percent $NaNO_3$/45 percent magnesium granules) were tumble-mixed immediately prior to testing, placed in a square cardboard box, and ignited with an electric match head boosted by approximately 100 grams of UTC No. 3001 solid rocket propellant. These tests were instrumented with internal temperature, external temperature, heat flux, and fireball duration sensors. Motion picture coverage included 200-1500 frame per second, 24 frame per second real time and 200-1500 frame per second infrared film. Figure 6 shows the test arrangement. Instrumentation for all thermal measurements is detailed in table 1. Similar tests were performed in free air, with the test layout shown in figure 7.

Table 1.   Instrumentation for Illuminant Tests, Category 5

Parameter	Transducer	Amplifier	Cable	Recording
Temperature	Chromel-Alumel 30 AWG Thermocouple w/150°F reference junction	NEFF Model 109-6	1100 ft. shielded 2 conductor 20 AWG	Sangamo 4700
	YSI # 44030 Thermistors	Transdata 2001G with NEFF 109-6	1100 ft. shielded 2 conductor 20 AWG	Honeywell 96
Heat Flux	Keithley 610 with probe	NA	1100 ft. RG58 C/U	Sangamo 4700
Burning Time	Monsanto MT-2 Photocell	Transdata 2001G with NEFF 109-6	1100 ft. shielded 2 conductor 20 AWG	Honeywell 96
Static Pressure	PCB 101A02	NEFF 109-6	1100 ft. RG58 C/U	Honeywell 96

3.0   RESULTS AND DISCUSSIONS

3.1   Thermal Measurements

3.2.1   Fireball Characteristics. Table 2 shows the fireball dimensions and duration for the high explosive charges fired in free field and inside the shield. No fireball was observed to extend beyond the walls of the shield for any of the
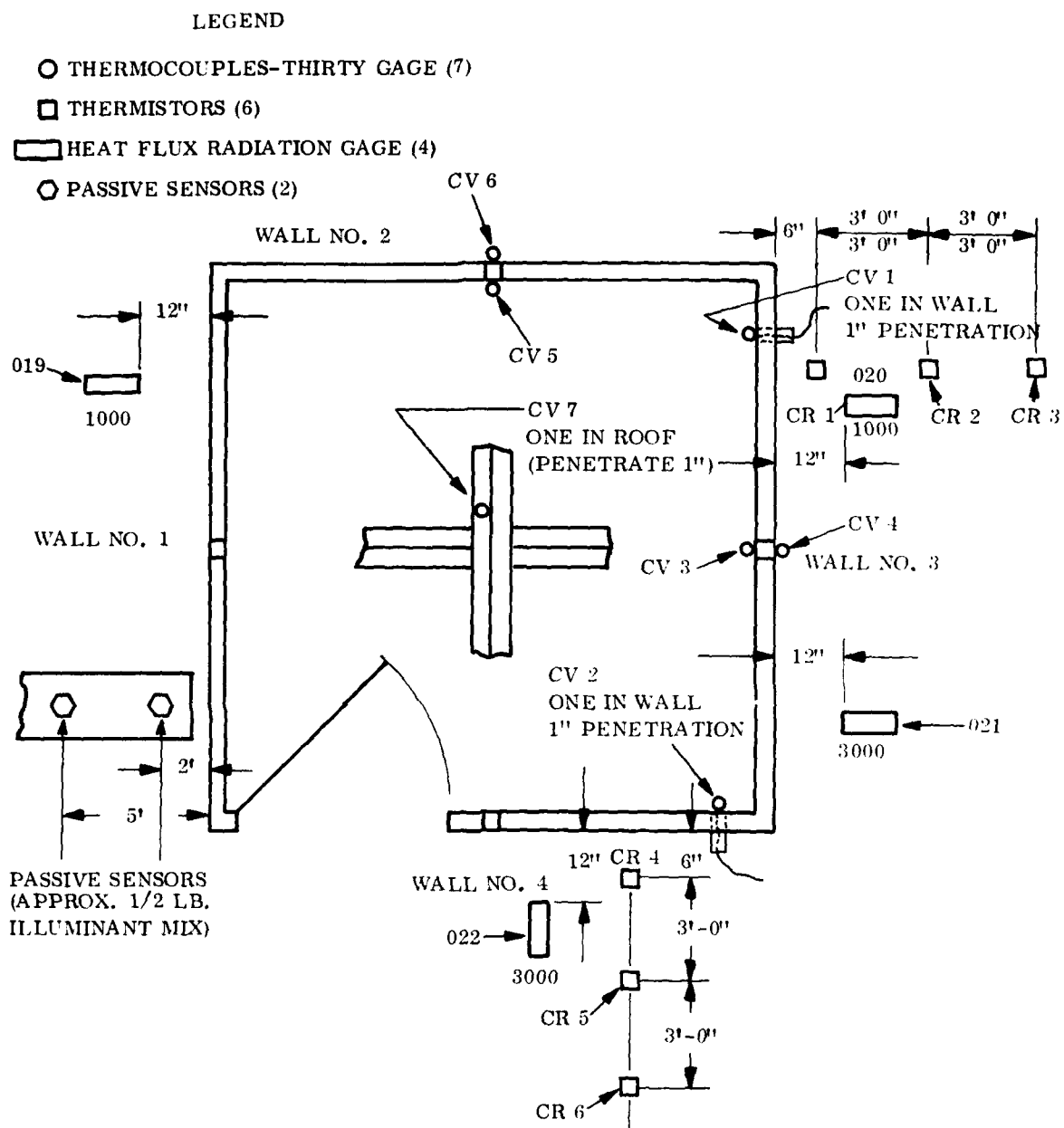
Figure 6. Category 5 Illuminant Test Setup and Instrumentation Locations

CV-004

THERMOCOUPLES — CV-003

CV-002

CV-001 — CV-005

11'-6"
TYP

EIGHT
RANGE POLES (TYP)

CHARGE IN
BOX AT
GROUND
LEVEL

5'-6"
TYP

CV-006

CV-007

CV-008

5'-0
TYP

8 - THERMOCOUPLES
4'-0" ABOVE GROUND

5'-0
TYP

5'-0
TYP

5'-0
TYP

5'-0
TYP

8'-6"
TYP

COLOR
FILM

BLACK
WHITE

IR CAMERAS

20 LB CHARGE - 30 FT. MINIMUM COVERAGE
30 LB CHARGE - 40 FT. MINIMUM COVERAGE
50 LB CHARGE - 60 FT. MINIMUM COVERAGE
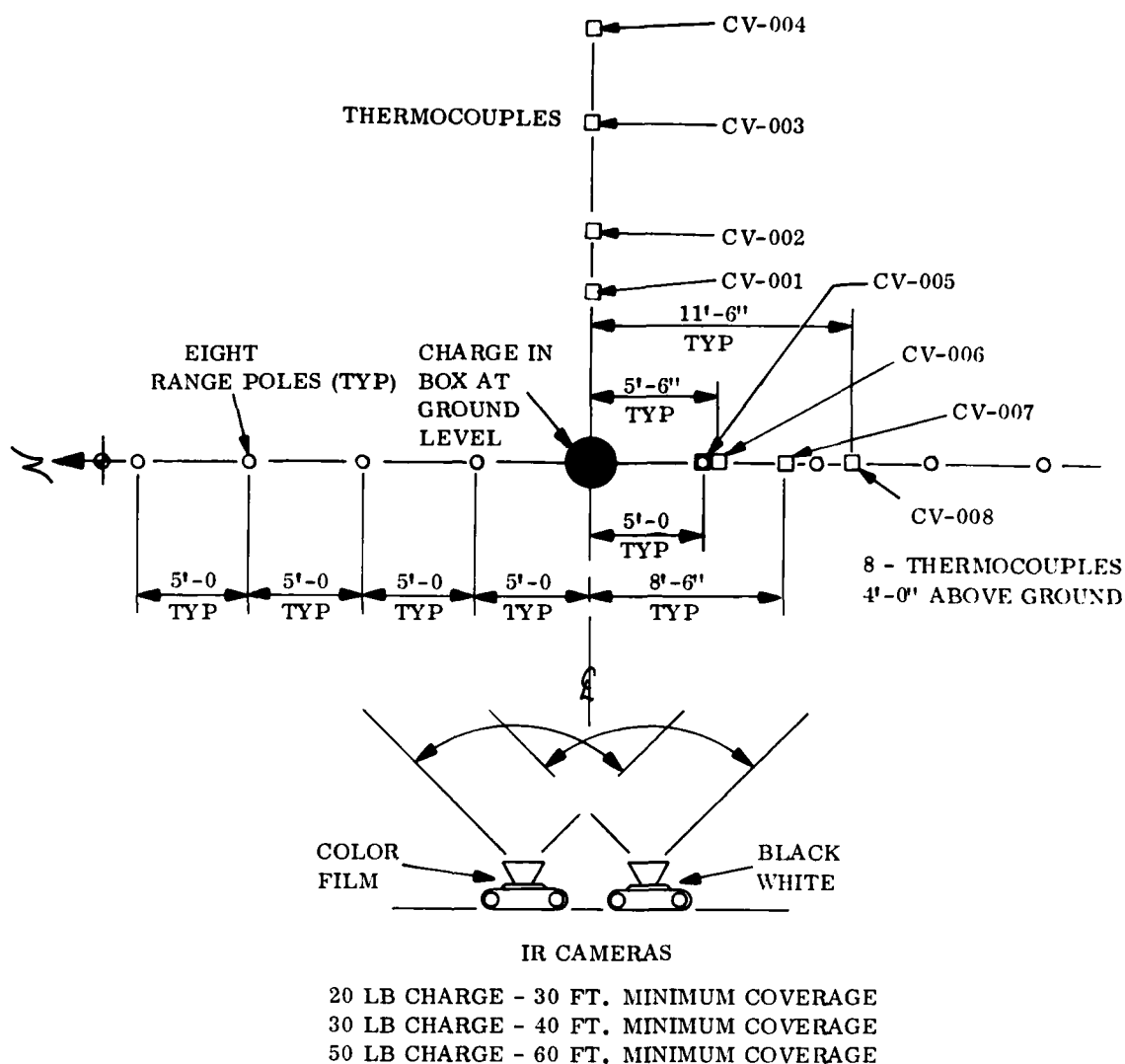
Figure 7. Free Field Illuminant Test Configuration

intershield high explosive tests, although the maximum free field fireball size, i.e., 11.8 ft. diameter x 12.7 ft. high (1.842 lb. charge) and 11.6 ft. diameter x 12.9 ft. high (2.442 lb. charge) would extend beyond dimensions of the shield (11.4 ft. long x 11.4 ft. wide x 9.2 ft. high).

Table 3 is a display of fireball dimensions and duration observed during the illuminant tests. For all charge weights, the fireball dimensions in the free field was greater than outside dimensions of the shield. This extension beyond the shield side walls ranged from approximately 1-1/2 feet in the worst case. The duration of this fireball beyond the walls ranged from 0.2 seconds for the 10 pound charge to 0.5 seconds for the 50 pound charge.

Table 2. Fireball Dimensions and Duration High-Explosive Charges

FREE FIELD DATA			SUPPRESSIVE STRUCTURE DATA		
Charge Weight (lb)	Maximum Fireball Dia. x Ht. (ft)	Fireball Duration (sec)	Charge Weight (lb)	Fireball Outside (ft)	Fireball Duration Outside (sec)
.572	7.4 x 6.9	.053	.572	None Observed	N/A
.970	6.9 x 6.4	.070	.970	None Observed	N/A
1.842	11.8 x 12.7	.106	.970	None Observed	N/A
2.442	11.6 x 12.9	.084	1.842	None Observed	N/A
			2.442	None Observed	N/A

Table 3. Fireball Dimensions and Duration - Illuminant Charges

FREE FIELD DATA				SUPPRESSIVE SHIELD DATA	
Charge Weight (lb)	Maximum Fireball Dia. x Ht. (ft)	Time to Maximum (sec)	Total Fireball Duration (sec)	Fireball Dimension (ft)	Observed Duration (sec)
10	18 x 18.5	1.031	3.325	1-2	.208
20	16.3 x 15.3	0.855	3.310	No Comparable Test	
30	27.8 x 23.3	0.817	2.650	1-2	.167
50	32 x 24	0.600	1.993	1-2	.504

Burning particles (fire brands) were observed to be projected 3 to 5 feet from the shield for all charge weights; the quantity and intensity varied directly as the charge weight. The total event time for this phenomena was less than 0.5 seconds.

3.1.2 Panel Configurations. The Category 5 shield panels were all of the same configuration as shown in figure 8 except the northern-most panel in wall number 1. This panel was fabricated with an aluminum basket weave material (Interweave by Harrington and King Perforating Company, Ramsey, New Jersey - 20 gauge aluminum (E&S), 53 percent vent area), which was designed as a fireball, fire brand flame impingement medium (see figure 9). All other panels were fabricated using four layers of standard aluminum, 16 x 16 mesh window screen as the fireball, fire brand, flame impingement medium. The vent area of each layer of screen was 62 percent. The effective venting ratio (α_{eff} for the four layers was then 15.5 percent. The interweave material yields an α_{eff} of 53 percent.

Observation of the high speed motion pictures of the illuminant tests inside the

3-1/2 x 3-1/2 x 1/4 ANGLE

16 GA. PERFORATED
PLATE (3)

15 ANGLES SPACED
AS SHOWN

2 x 2 x 1/8
16 ANGLES
EQUALLY
SPACED

SCREEN 16 x 16
MESH (4 PLACES)

3-1/2"
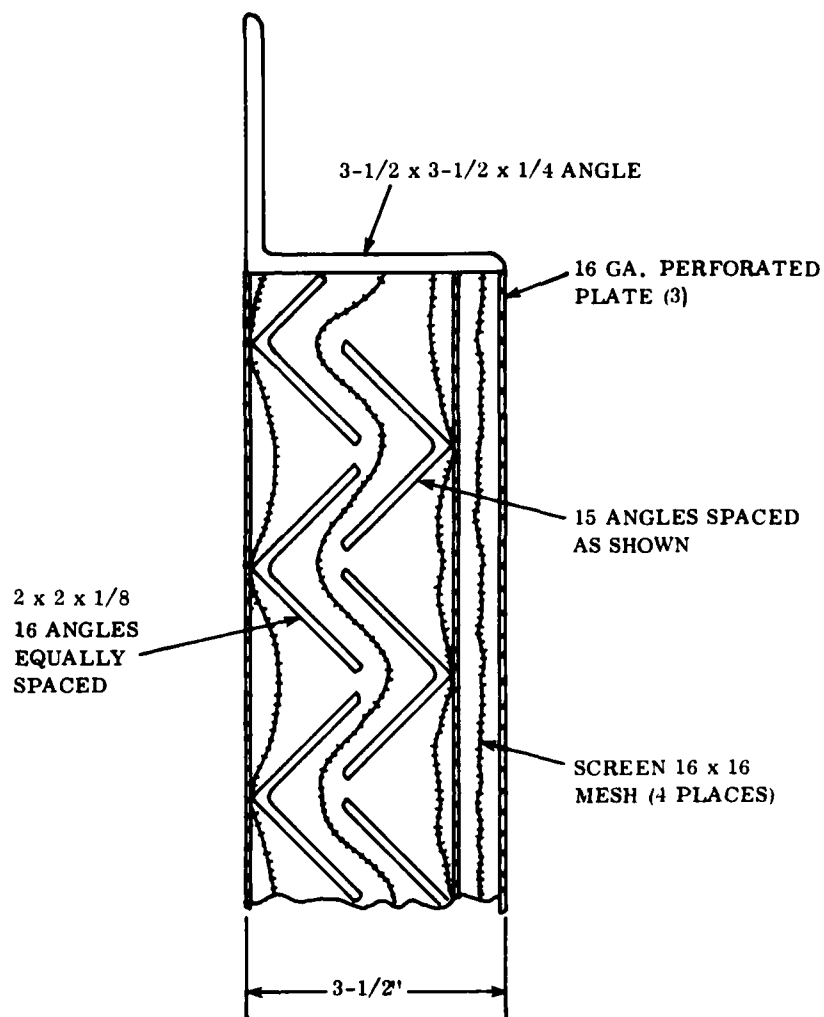
Figure 8.   Category 5 Panel Section

Side View
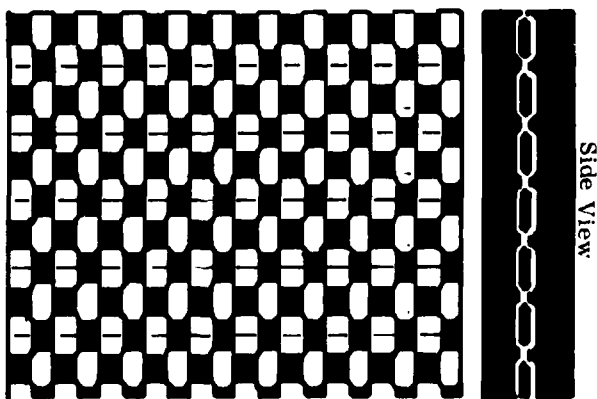
Figure 9.   Interweave - Approximately Fifty-Three Percent Open

shield showed that the interweave allowed passage of slightly more fireball/fire brand/flame than did the four layers of screening. The interweave withstood the heat much better than did the 16 x 16 mesh aluminum screening. The screening material almost entirely disintegrated during the 30 pound illuminant charge test. The effects of the disintegration was not readily apparent, however, when observing the motion pictures of the subsequent 50 pound illuminant test.

3.1.2   Ten Pound Illuminant Charge Test Data.   Table 4 shows the thermal data acquired during the 10 pound illuminant charge test. Of significance in this data comparison is the fact that the thermistors, arrayed at 0.5, 3.5 and 6.5 feet outside the shield wall, indicated virtually ambient temperature. Free air temperatures at similar distances ranged from 92°F at 6.5 ft., to 990°F at 0.5 feet. Of the seven chromel-alumel thermocouples that were inserted one inch deep into the structural steel of the shield, five were on the inside and two on the outside. The seven chromel-alumel thermocouples were located as shown in table 4 and as described for the 50-pound test, paragraph 3.1.4. Thus CV-3 and CV-5 indicate inside skin temperatures; CV-1, CV-2 and CV-7 indicate inside air temperatures; CV-4 and CV-6 indicate exterior skin temperatures. Two of the channels, CV-2 and CV-7 failed to function during the test. Of significance is that the two thermocouples located in the steel in the outer wall indicated only ambient temperature. The other thermocouples located inside registered temperatures of 123°F (CV-5), 161°F (CV-3) and 2500+°F (CV-1).

No comparable heat flux data was acquired due to an improper calibration range setting on the Keithly Model 860 heat flux meters.

No measurable pressures were observed from any of the four PCB transducers installed in the shield, indicating less than 0.2 psi of quasi-static pressure.

3.1.3   Thirty Pound Illuminant Charge Data.   Table 5 shows the thermal data acquired during the 30-pound illuminant charge test. Again, the temperatures at 0.5, 3.5 and 6.5 feet outside the shield were relatively low (75°F to 115°F) while temperatures at similar distances in free field ranged from 2500+°F at 5.0 ft. (approximate inside wall distance) to 850°F at 11.5 ft.

A comparison of peak heat flux in units of cal/cm^2 sec at a distance of one foot outside the shield wall is shown in table 5. Free field peak heat flux data acquired at a distance of 50 feet from the charge center was extrapolated back to 6.7 feet by application of inverse-square radiant heat flux laws. Thus, the heat flux at 6.7 feet, H_2, was given by:

$$H_2 = H \text{ (peak heat flux at 50 ft.)} \times \frac{(50 \text{ feet})^2}{(6.7 \text{ feet})^2}$$

3.1.4   Fifty Pound Illuminant Charge Test.   Table 6 displays the thermal data acquired during the 50 pound charge illuminant test. Temperatures at 0.5, 3.5,

Table 4. Illuminant Test Thermal Measurements for 10 Pound
Charge Weight - Test No. D-1-1 Burning Time .518 Second

Channel No.	Sensor	Distance From Chgr. (Feet)	Distance From Wall	Location Wall No.	Measured Values	Equiv. Free Air Values†	Δ *
CR-19	Heat Flux Meter	6.7	1.0 ft.	1	Over Range on all meters	N/A	N/A
CR-20		6.7	1.0 ft.	3	" " " " "		
CR-21		6.7	1.0 ft.	3	" " " " "		
CR-22		6.7	1.0 ft.	4	" " " " "		
Q-15	PCB Transducer	5.2	Flush w Inside	1	No Indication of Pressure		
Q-16			"	3	" " " "		
Q-17			"	3	" " " "		
Q-18			"	4	" " " "		
CV-1	Chromel-Alumel Thermocouple	5.2	1" inside	Inside 3	2500+°F		
CV-2		5.2	inside	Inside 4	No data		
CV-3		5.2	inside	Inside 3	161°F		
CV-4		5.7	outside	Outside 3	75°F		
CV-5		5.2	1" inside	Inside 2	123°F		
CV-6		5.7	outside	Outside 2	75°F		
CV-7		8.0	1" inside	Inside 5	No data		
CV-8			Ambient reference		75°F		
CR-1	Thermistor	6.2	0.5 ft.	3	79°F	990°F - 425°F -	911°F 346°F
CR-2		9.2	3.5 ft.	3	75°F	275°F -	200°F
CR-3		12.2	6.5 ft.	3	75°F	92°F -	17°F
CR-4		6.2	0.5 ft.	4	77°F	990°F - 425°F -	911°F 348°F
CR-5		9.2	3.5 ft.	4	75°F	275°F -	200°F
CR-6		12.2	6.5 ft.	4	75°F	92°F -	17°F

*Difference between free air and test values. †2400 BTU/HR/FT^2 extrapolated from 50 ft. radius to 6.7 ft. radius.

and 6.5 feet outside the wall ranged from 77°F at 6.5 feet to 181°F at 0.5 feet. At comparable distances in the free field, the temperatures ranged from 2500+°F at 5.0 feet (approximate inside shield wall distance) to 1172°F at 11.5 feet (compared to the 6.5 feet reading with the shield in place).

The three thermocouples located one inch inside the structure (CV-1, CV-2, CV-7) overranged the maximum chromel-alumel temperature (2500+°F). This indicates that the primary fireball essentially completely filled the enclosed volume. Thermocouples CV-3 and CV-5 were attached in contact with the interior panel members and indicated 321°F and 132°F, respectively. Such variation was observed in the other tests and is explained by off-center combustion of the illuminant mix and directional convection of the reaction products. Post test ash deposits on the floor of the structure at various locations were observed to corroborate the anisotropic thermal measurements. A measure of the shield thermal energy containment characteristics is afforded by exterior thermal sensors. Two thermocouples attached to the exterior frame steel (CV-4 and CV-6) indicated only ambient

Table 5. Illuminant Test Thermal Measurements for 30 Pound
Charge Weight - Test No. D-2-1 Burning Time .630 Sec.

Channel No.	Sensor	Distance From Chg.	Distance From Wall	Location Wall No.	Measured Values	Equil. Free Air Values †	△ •
CR-19	Heat Flux Meter	6.7	1.0 ft.	1	.054 cal/cm^2 sec	10.1 cal/cm^2 sec.	N/A
CR-20		6.7	1.0 ft.	3	.015 "	10.1 "	
CR-21		6.7	1.0 ft.	3	.015 "	10.1 "	
CR-22		6.7	1.0 ft.	4	.010 "	10.1 "	
Q-15	PCB Transducer	5.2	Flush w/ Inside	1	No indication of pressure	N/A	
Q-16		5.2		3	" " " "		
Q-17		5.2		3	" " " "		
Q-18		5.2		4	" " " "		
CV-1	Chromel-Alumel Thermocouple	5.2	1" inside	3	No Data Recorded	None	
CV-2		5.2	inside	4			
CV-3		5.2	inside	3			
CV-4		5.7	outside	3			
CV-5		5.2	inside	2			
CV-6		5.7	outside	2			
CV-7		8.0	1" inside	5			
CV-8		Ambient reference					
CR-1	Thermistor	6.2	0.5 ft.	3	90°F	2500+°F - 1992+°F -	2410°F 1902°F
CR-2		9.2	3.5 ft.	3	75°F	1285°F -	1210°F
CR-3		12.2	6.5 ft.	3	75°F	852°F -	777°F
CR-4		6.2	0.5 ft.	4	115°F	2500+°F - 1992+°F -	2385°F 1877°F
CR-5		9.2	3.5 ft.	4	108°F	1285°F -	1177°F
CR-6		12.2	6.5 ft.	4	81°F	852°F -	771°F

† 2400 BTU/HR/FT^2 extrapolated from 50 ft. radius to 6.7 ft. radius.

*Difference between free air and test values.

temperature (74°F). Thus the escaping energy was insufficient, during the mea-
surement time of greater than two seconds, to overcome the thermal inertia of
the steel structure. This information agrees well with computations of total
radiant heat loss from the heat flux measurements.

From table 6, it is obvious that the dramatic reduction in peak radiant heat flux
observed during the 30 lb. test was repeated in this case.

The radiant heat flux curves for the shield tests are shown in figure 10 compared
to the heat flux for the same charge in free field but at 50 ft. radius rather than
the 6.7 feet for the shield test. Integration of these curves to show total radiant
heat gain with time is shown in figure 11.

Table 6. Illuminant Test Thermal Measurements for 50 Pound Charge Weight - Test No. D-3-1 Burning Time .504 Sec.

Channel No.	Sensor	Distance From Chg.(Ft.)	From Wall	Location Wall No.	Measured Values	Dist. (Ft.) From Chgr.	Equiv. Peak Free Air Values *	Δ *
CR-19	Heat Flux Meter	6.7	1.0 ft.	1	.015 cal/cm² sec	6.7*	14.1 cal/cm² sec	N/A
CR-20		6.7	1.0 ft.	3	.027 "	6.7*	14.1 "	
CR-21		6.7	1.0 ft.	3	.11 "	6.7*	14.1 "	
CR-22		6.7	1.0 ft.	4	.019 "	6.7*	14.1 "	
Q-15	PCB Transducer	5.2	Flush	1	No Pressure Indicated		N/A	N/A
Q-16		5.2	"	3	" "	"		
Q-17		5.2	"	3	" "	"		
Q-18		5.2	"	4	" "	"		
CV-1	Chromel-Alumel Thermocouple	5.2	1" inside	3	2500+°F	N/A	None	
CV-2		5.2	inside	4	2500+°F			
CV-3		5.7	inside	3	321°F			
CV-4		5.7	outside	3	74°F			
CV-5		5.2	inside	2	132°F			
CV-6		5.7	outside	2	74°F			
CV-7		8.0	inside	5	2500+°F			
CV-8		Ambient Reference			74°F			
CR-1	Thermistor	6.2	0.5 ft.	3	181°F	5.0 / 5.5	2500+°F - / 2140°F -	2319°F / 1959°F
CR-2		9.2	3.5 ft.	3	99°F	8.5	1492°F -	1393°F
CR-3		12.2	6.5 ft.	3	79°F	11.5	1172°F -	1093°F
CR-4		6.2	0.5 ft.	4	145°F	5.0	2500+°F - / 2140°F -	2355°F / 1995°F
CR-5		9.2	3.5 ft.	4	81°F	8.5	1492°F -	1411°F
CR-6		12.2	6.5 ft.	4	77°F	11.5	1172°F -	1095°F

*Heat flux (3350 BTU/HR/FT²) extrapolated to 50 ft. radius

Selected photographs showing interior and exterior condition of the shield after completion of all tests are provided as figures 12 through 15. The only evidence of testing having been performed are the deposits of MgO/Na_2O combustion products and the deteriorated interpanel screening.

4.0 CONCLUSIONS

The primary conclusion that can be drawn as a result of reviewing and analyzing the test data is that all design and performance requirements described for the Category 5 suppressive shield were met. Both explosion and deflagration containment exceeded expectations, and the shield structurally withstood all tests.

It can be concluded that the interweave aluminum flame/fireball attenuation panel

302
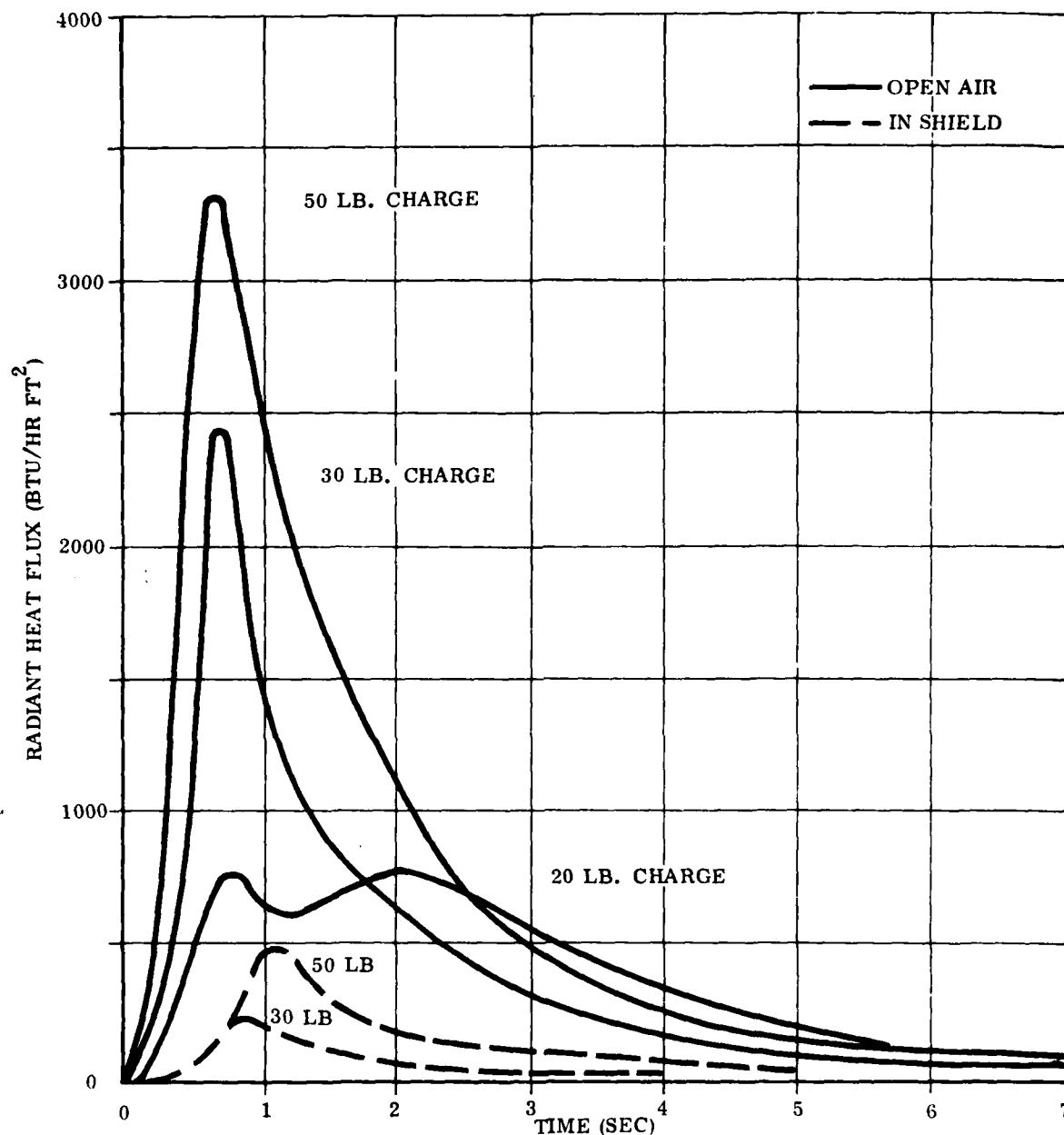
Figure 10. Heat Flux as a Function of Time

element (53 percent venting) is just as effective as the four layers of aluminum screen wire. The interweave is more cost effective since it requires only a single installation operation compared to four for the screening material. Furthermore, the interweave material withstands an adverse chemical environment whereas the fine mesh aluminum would have a tendency to deteriorate in a relatively short period of time.
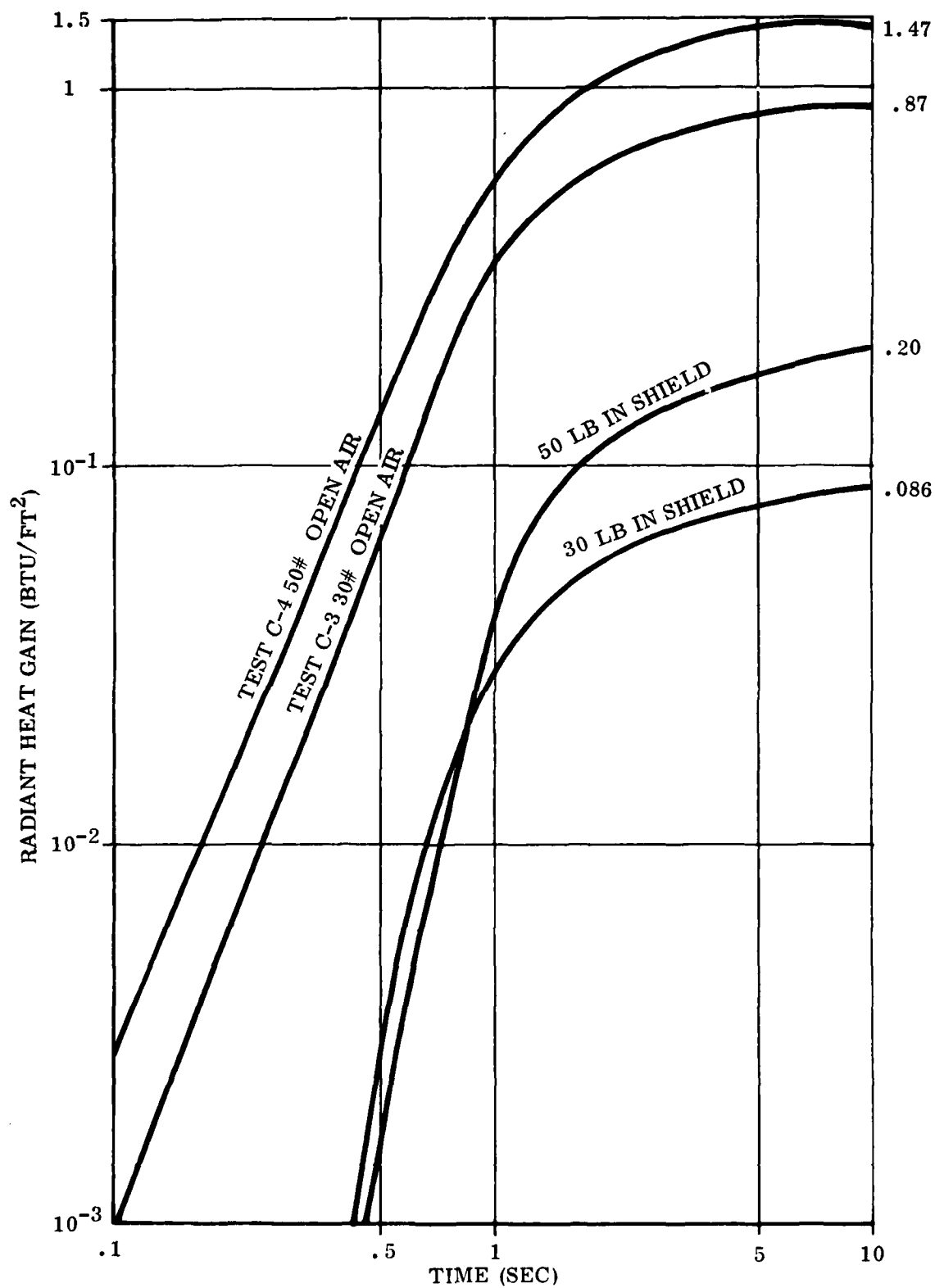
Figure 11.   Radiant Heat Gain Versus Time

304
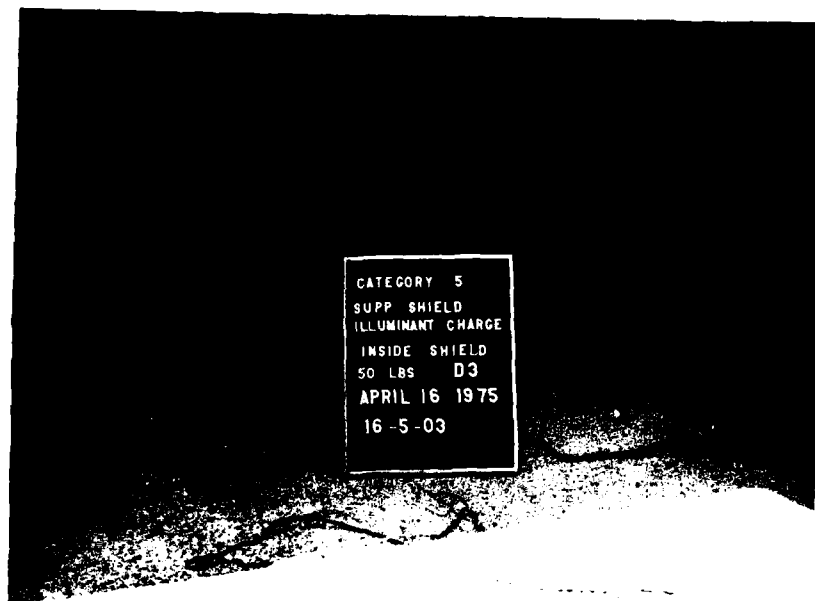
Figure 12. Post Test Interior View

Figure 13. Post Test Exterior Roof View

CATEGORY 5
SUPP SHIELD
ILLUMINANT CHARGE
SHIELD
50 LBS   D3
APRIL 16 1975
16-5-03
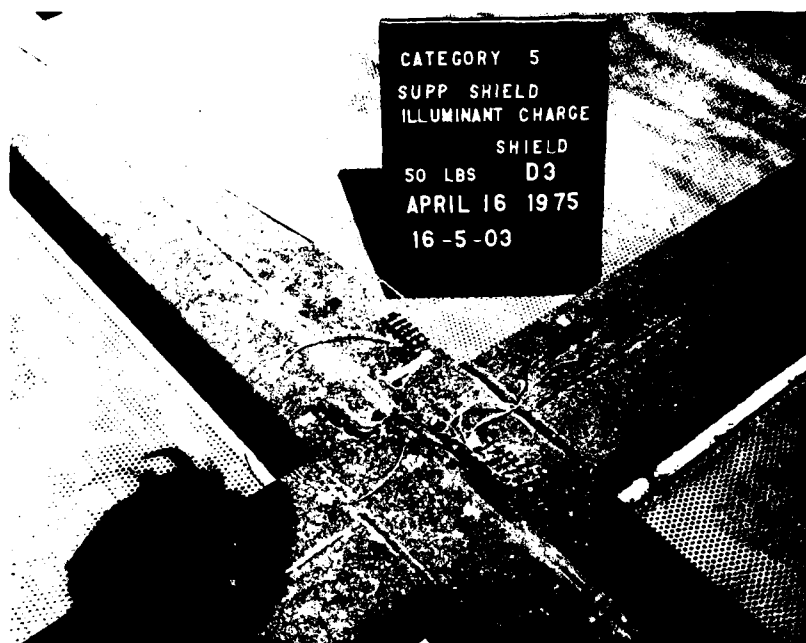
Figure 14.   Post Test Interior Roof View
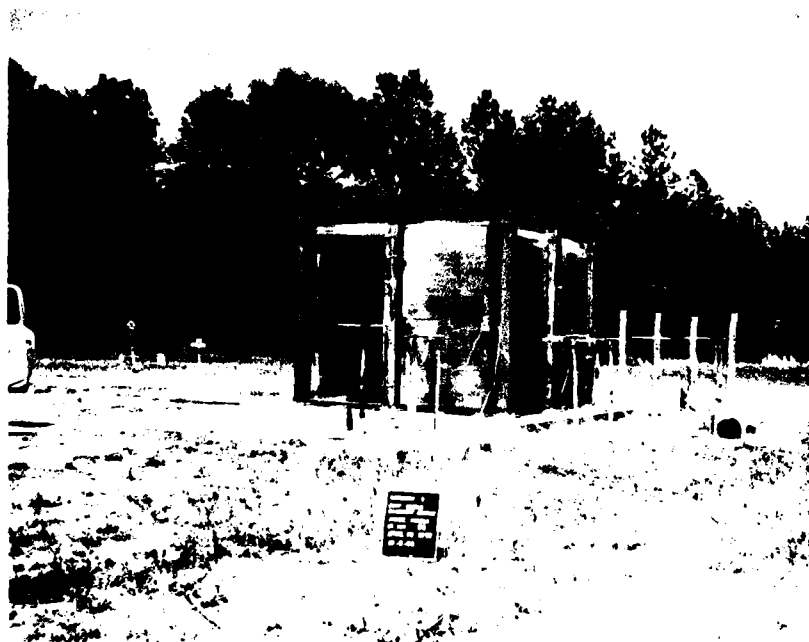
Figure 15.   Category 5 Suppressive After Completion of all Testing

REFERENCES CITED

1. PEMA 4932, Project 5751264, "Advanced Technology for Suppressive Shielding of Hazardous Production and Supply Operations".

2. Edgewood Arsenal Contractor Report, "Application of Suppressive Structure Concepts to Chemical Agent Munition Demilitarization System", in preparation.

3. Dugway Proving Ground Report, DPG - DR-74-303, Support Test for Evaluation of a Suppressive Shield - Containment Facility for Chemical Agent Munition Disposal Systems (CAMDS), April 1974.

4. General Electric Contractor Report, GE - MTSD-R-060, White Phosphorus Operational Shielding Studies Final Report, March 24, 1971.

5. General Electric Contractor Report No. EA-FR-2A07, Final Report on Design, Fabrication and Test of Prototype Transportable Suppressive Structure, December 1973.

6. Dugway Proving Ground Report No. DPG - DRI-74-313, Added Support Test of the Suppressive Shield for Naval Explosive Ordnance Disposal Facility, September 1974.

7. Edgewood Arsenal Contractor Report No. EM-CR-74050, EA-4E35F, 81MM Suppressive Shield, March 1975.

8. Edgewood Arsenal Technical Report No. EM-TM-76005, Supplemental Tests and Studies on the 81MM Suppressive Shield, September 1975.

9. Edgewood Arsenal Technical Report No. EM-TR-76001, Category 5 Suppressive Shield Test Report, October 1975.

BLACK NITE FLARE

by

Carl W. Lohkamp

The Army and the Navy have and are using image intensifiers and low light level televisions (LLLTV). These items are used at all levels, that is, from individual soldier in the Army to part of the fire control directorate for the TARTAR missile system in the Navy. These electro-optical (EO) devices, however, fail to perform adequately under 1/4 moon or less natural illumination conditions.

The EO image intensifiers and LLLTV devices which are now in or are soon to be in service utilize the S-1, improved S-20, or the S-25 photoemitter surfaces. Examination of these responses shows that the performance of the EO devices can be enhanced by visible and near infra-red flux. Spectra of several compositions having peak emissions in the near infrared portion of the spectrum will be shown as well as reflec-tance data on natural terrain.

Testing of these compositions in the laboratory as well as in the field has been completed. Flare output data for the visible and infrared portion of the spectrum will be included in the paper. Concluding the presentation will be a seven-minute videotape of the performance of a night observation device (NOD) under conditions of starlight, starlight with visible illuminating flare, and starlight with the Black Nite Flare.

Black Nite Flare

The services are using low light level televisions (LLLTV) tripod mounted image intensifiers, hand held and rifle mounted units, and goggle type devices. Image intensifiers are used at all authority levels and in all locations such as the B-52 bomber, the individual foot soldier and the TARTAR fire control system.

All image intensifiers rely on intensifying the image flux that is present to gain a usable image. Present day intensifiers do not perform adequately under one-quarter moonlight or less natural illumination conditions. Examination of the lunar cycle and cloud cover data reveals that in approximately 73% of the night hours you have one quarter moonlight or less natural illumination (1). To enhance the image produced by the intensifier and LLLTV, several techniques have been employed. These include: (a) use of visible illuminating flares; (b) use of spotlights filtered to remove the visible flux and transmit the near infrared flux; (c) use of laser illuminators; (d) use of a pyrotechnic flare having primarily near infrared emission (2).

Examine the disadvantages of the first three techniques of enhancement. Visible flares do enhance the performance of the system (3); however, they also allow all friendly and enemy forces to see. Drift of the visible flare can lead to exposure of friendly positions. Use of spotlights filtered to remove the visible flux is a technique used in the past, particularly on armored vehicles. This technique has one large drawback which is: if the enemy has night vision equipment, he can see exactly where the searchlight is and can direct his fire to destroy it and the carrying vehicle. The third technique of laser augmentation of the imaging system is presently being explored by at least the Navy and the Air Force. The major drawback is similar to the spotlight in that you give away your position when you activate your laser if the opposing forces have image intensifiers. An additional problem that is encountered is the need of pulse gating the systems such that the flux scattered in the laser beam in the intervening atmosphere between the source and the target being illuminated does not obscure the target.

The semi-convert near-infrared flare overcomes many of these problems; however, there are some drawbacks to using this type of flare also. Drawbacks to the infrared flare include having some visible candlepower and it is nearly impossible to deploy a flare without generating some acoustic signature.

To determine what types of near-infrared flares are desirable, examination of the spectral responsivity of the photoemitters is in order. Figure 1 is a plot of three of the more widely found surfaces in image intensifiers today. The S-1 photoemitter is found in the Metascope and many of the older devices and is usually used for visual tasks that are of short range. The S-20 surface was found in some of the older Starlight scopes. Newer Starlight scopes have an improved S-20 response which is closer to the S-25 response. The PVS-5 night goggles have a response closely approximated by that shown as the S-25 response.
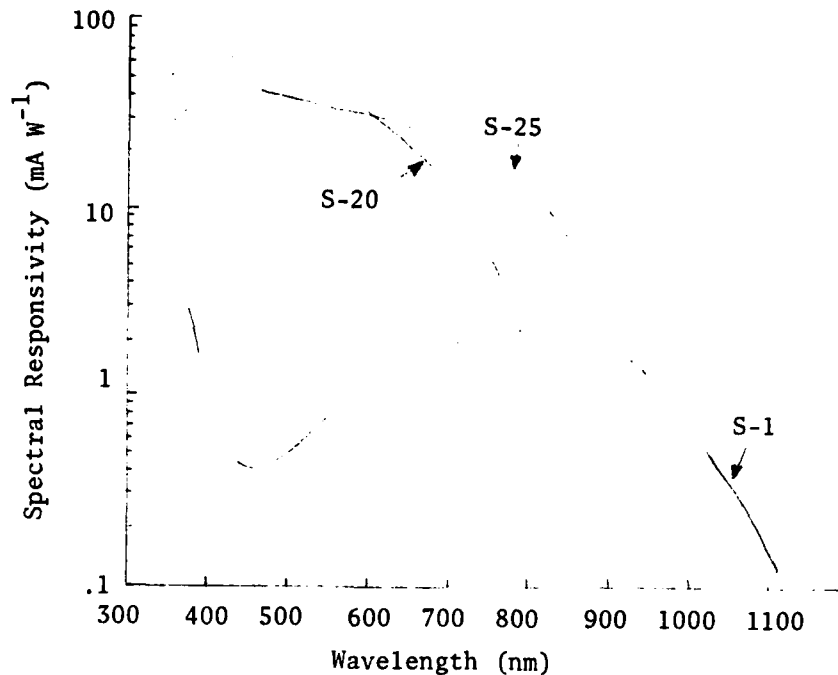
Figure 1. Visible and Near IR Photoemitter Characteristics.

With these responses in mind, we have obtained three types of compositions which have potential as sources. These compositions utilize alkali metal nitrates. They are potassium nitrate, rubidium nitrate and cesium nitrate. Figure 2 is the atomic line emission spectra (4) of the mentioned alkali metals.

Potassium having resonance line emission at .7698 and .7644 microns mates very well with the S-20 and S-25 responses shown in Figure 1, yet is just outside the visible spectrum which can be defined as .4 - .74 micron (y = .0001 at .760 micron). Broadening of these line emissions coupled with very limited eye response at .76 micron does give some visible flux. There is, of course, some flux in the visible due to other line emission and the temperature of the reaction.

In an attempt to reduce the visible emission and have the emission a bit farther in the infrared, rubidium nitrate was utilized as an oxidizer. The emissions near .79 micron mate reasonably well with the S-1 and S-25 curves. The general problem, however, is that there is a greater number of in-service image intensifiers having response properties between the S-20 and the S-25 curves than the S-25 to S-1 portion of the spectrum.

To obtain flux that is optimally compatible with the S-1 surface, cesium nitrate was utilized as an oxidizer in several flare formulations. Due to the temperature of the reaction, burn rates experienced in flare formulations, and atomic spectra, these flares had large IR power output; however, they also had greater visible flux emitted.

Typical formulations tested of all three types are shown in Table 1.
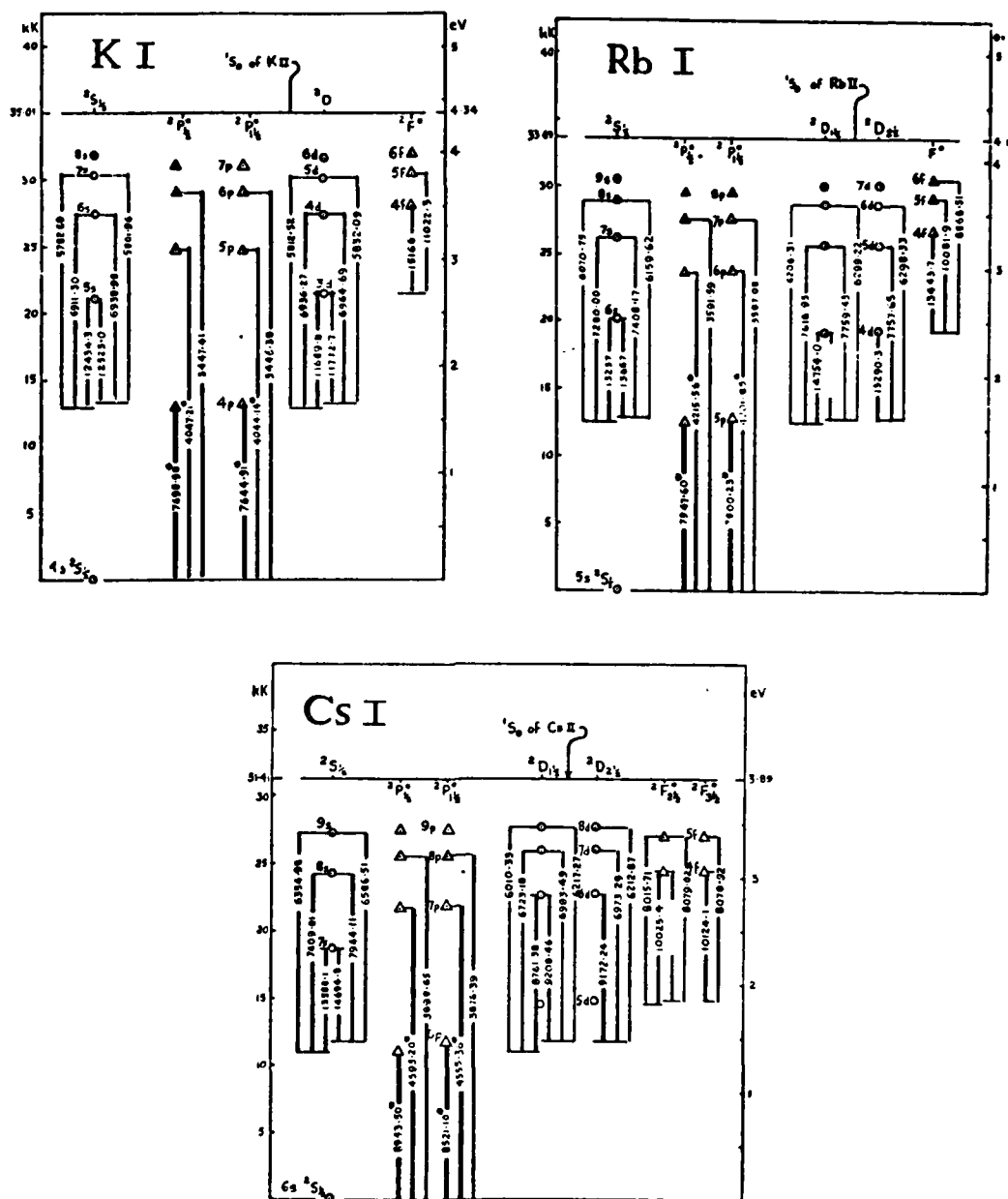
Figure 2. Atomic Spectra (taken from Candler)

Table I. Flare Formulas

	.76 Micron flare	.79 Micron flare	.8-.9 Micron flare
Silicon	10	10	16.3
Potassium nitrate	70		
Cesium nitrate			78.7
Rubidium nitrate		60.8	
Hexamethylenetetromine	16	23.2	
Epoxy resin (DER 321)	2.8	4.2	3.3
Epoxy hardener (DEH 14)	1.2	1.8	1.7

Flare candles composed of these compositions have been pressed into paper tubes having diameters from 1.6" to 4". Radiometric and spectra data on the potassium, which is the most interesting to NAVSEA and NAVAIR applications, have been taken. Table II contains a summary of data of primary interest to the design agents.

Table II. Flare Performance

	Watts/Steradian (.7-1 Micron)	Candlepower (.4-.74 Micron)	Burn rate (sec/in)
40 MM	14	65	45
MK 45 size (4.25")	160	900	45
*EX-18 size (3.375")	85	600	45
**155 MM size	80-100	600	40

* Candle composition pressed into the 5" EX-18 projectile paper.
** Pressed in steel containers that are used for the 155 MM illuminating load.

An interesting point noted during experimentation with the 40 MM size is that 20-30% of the visible flux originates from the burning of the paper tube on the flare candle. A large part of this flux is from the sodium impurity found in the paper. The spectral data taken on the near infrared flares shows that a predominant portion of the flux in the near infrared originates from the resonance lines. The visible emission is primarily composed of the gray body emission due to temperature and to the sodium impurity in the ingredients. A lesser amount of flux originates from the atomic lines in the visible spectrum.

One portion of the problems left unaddressed is that of the reflective properties of the elements in the natural scenario. Figures 3 and 4, although representing only a few materials formed in the battlefield, do indicate a general pattern. Most items are more reflective in the near infrared than in the visible.
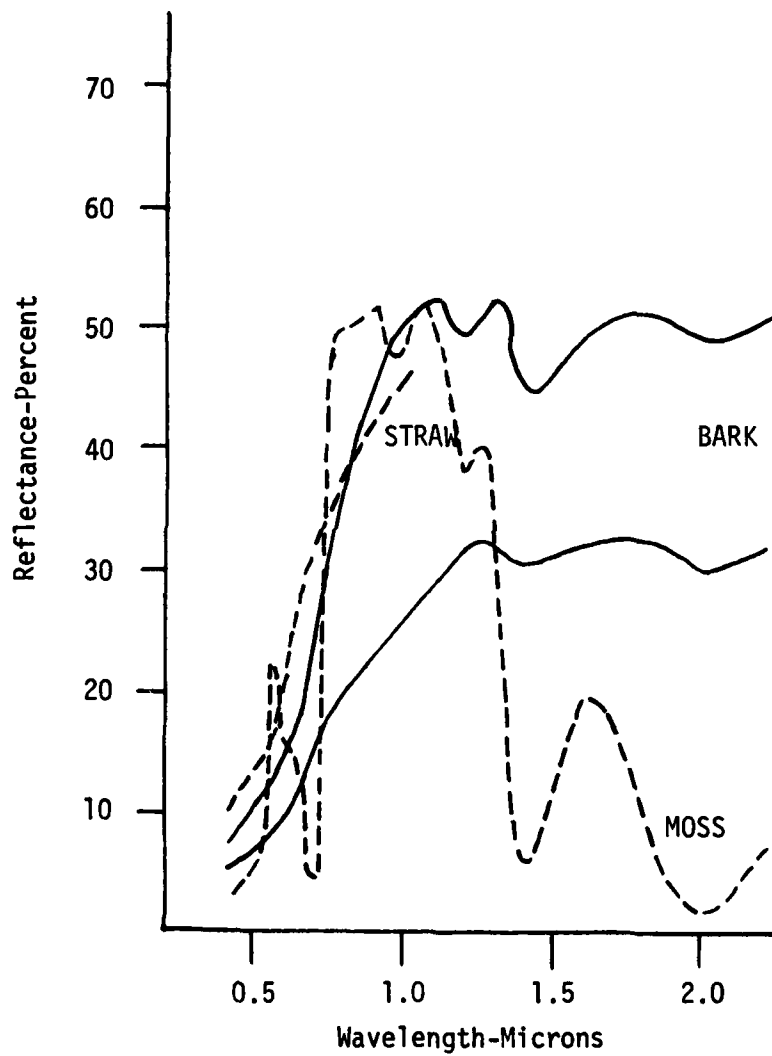
FIGURE 3

SPECTRAL REFLECTANCE OF TYPICAL EXAMPLES OF
MOSS, TREE BARK, AND DRY STRAW
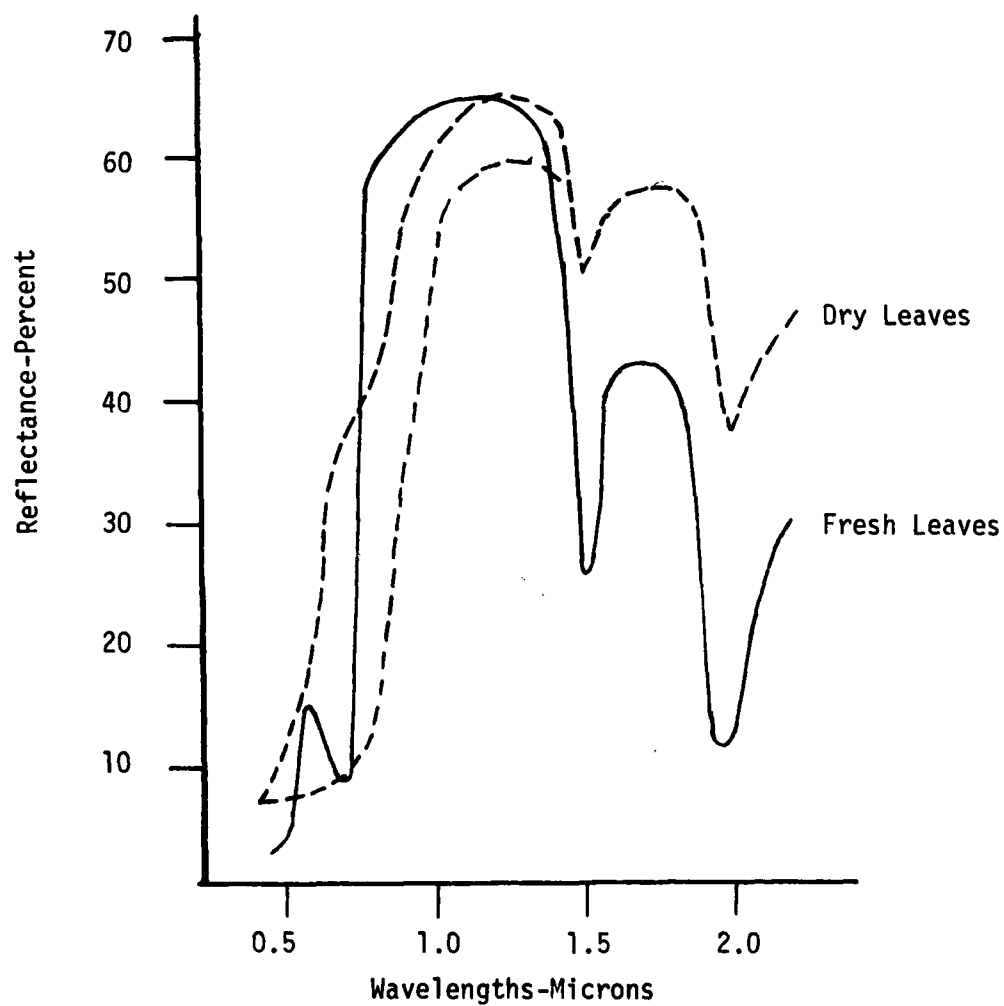
FIGURE 4

SPECTRAL REFLECTANCE OF TYPICAL LEAVES OF DECIDUOUS TREES

Video tape of the performance of image intensifiers under conditions of starlight, with visible flares and with near-infrared (EX-18 size) potassium flares, has been obtained. This tape, shown at the conference, demonstrates the vast improvement in target detection capability that can be obtained with the flares. The performance through the scope is comparable when utilizing visible and infrared flares. The visible flares fully illuminate, to the naked eye, everyone in the total test area while only those having night vision devices were capable of utilizing the flux from the IR flares. Further test and demonstrations are planned in the time between submission of this paper and when it is presented. These tests and results will be given during the conference presentation.

REFERENCES

1. *Electro-Optics Handbook*, RCA/Commercial Engineering, Harrison, New Jersey, 1968.

2. C. Lohkamp, *Near Infrared Illuminating Composition*, Patent Number 3,733,223, assigned to U.S.A., 15 May 1973.

3. LCDR D. Krieger, USN, *FLIR and LLLTV in the Navy*, Naval Research Laboratory, June 1975 (Confidential).

4. C. Candler, *Atomic Spectra and the Vector Model*, D. Van Nostrand Company, New Jersey, 1964.

DEVELOPMENT OF A .38-CALIBER MINATURIZED
FLUERIC CARTRIDGE INITIATOR

Joseph W. Morris
Mechanical Engineer
Naval Ordnance Station
Indian Head, Maryland

Vincent P. Marchese
Chief Engineer
EMX Engineering
Cedar Grove, New Jersey

ABSTRACT

A Flueric (pneumatic, no moving parts) Cartridge Initiator (FCI) is under development. Initially, a stores separation cartridge was utilized because of its larger envelope. Efforts were directed toward eliminating gas backflow through the FCI, and in providing adequate propellant ignition. FCI input gas supplies which have been evaluated include bottled nitrogen, helium, hydrogen, and cartridge generated gas. Function times of less than 10 ms were achieved, depending on the gas source and pressure.

The present year's effort involved miniaturizing the FCI to mate with .38-caliber cartridges, more typical of the size cartridge used in aircrew escape systems. A miniaturized resonance tube was developed that provides shorter function times at lower pressures. Vent and nozzle area and chamber length and diameter were reduced to interface with .38-caliber geometry.

A standard Navy .38-caliber cartridge configuration was used. Modifications to the cartridge case were kept at a minimum. Methods of vent sealing against hostile environments were investigated.

Test firings were made and the data were compared with existing mechanical initiation/ cartridge performance parameters. Comparisons were also made with standard electric igniter performance.

PROGRAM BACKGROUND

Increased aircraft performance envelopes and variable mission profiles have resulted in more complex aircrew automated escape systems (AAES). Because more stringent AAES performance requirements are needed to ensure safe crewmember recovery, additional maintenance and safety problems with potential consequent degradation of AAES performance and reliability have become apparent.

In order to obtain AAES performance improvement, more accurate event sequencing and timing has been required. However, current AAES technology can provide pyrotechnic delay cartridges with an accuracy of only $\pm 15\%$ over the temperature range of $-65°$ F to $200°$ F. These pyrotechnic time delay cartridges provide nominal fixed time delays for the entire aircraft operational envelope, which are not optimum for all ejection conditions.

Current Navy pyrotechnic delay cartridges have an installed life of 18 months, while aircraft scheduled depot level maintenance cycles are normally 36 months. This is forcing AAES maintenance to be performed at the squadron level, and with the increased AAES complexities, it is straining squadron maintenance capabilities from a skill level standpoint.

As a result of the aforementioned, the Naval Ordnance Station, Indian Head, Cartridge Actuated Device (CAD) Engineering Branch (Code 5123) is investigating fluidics as a possible candidate for AAES incorporation. A category 6.2 Exploratory Development Program was instituted in FY-75 to determine feasibility of utilizing fluidics for AAES sequencing and cartridge initiation.

PROGRAM OVERVIEW

Because of current AAES problem areas and the potential solution offered by fluidics, efforts were begun in FY-75 to investigate the feasibility of incorporating fluidic technology in AAES. The effort addressed two areas: initiation and sequencing/timing.

Initiation: The Flueric Cartridge Initiator (FCI), also known as the Flueric Match and Flueric Explosive Initiator (FEI), was investigated to determine feasibility of pyrotechnic cartridge initiation. The Mk 125 stores separation cartridge was selected as the test vehicle primarily because of envelope considerations and because it is a worst case condition in regard to gas blowback. Efforts in FY-76 addressed miniturizing the FCI to meet the .38-caliber cartridge requirements. Because of FCI and fluidic sequencer operational pressure compatibility, the FCI is being considered for existing firing pin/shear replacement. Problems such as ballistic gas blowback, ignition capabilities, and function times were approached in a three-phase program.

Sequencing/Timing: A sequencer was designed and fabricated to determine feasibility for AAES usage. Time delays representing a candidate ejection seat sequence were chosen, and mechanical inputs were used to simulate altitude and velocity sensor inputs. Methods of temperature and supply pressure compensation were examined. A sequencer breadboard was fabricated and tested over the temperature range of - 65° F to 200° F.

This paper will deal only with the cartridge initiation portion of the program.

FLUERIC CARTRIDGE INITIATOR DEVELOPMENT

Background

A Flueric Explosive Initiator (FEI) had been developed by Singer Kearfott, Little Falls, N. J., and later EMX Engineering Inc., Cedar Grove, N. J., for various military and NASA applications where initiation of explosive and/or propellant was required. This device consists of two essential component parts, a resonance tube and an excitation nozzle as shown schematically in Figure 1. The device functions when the open end of the resonance tube cylinder is placed in the compression region of a free jet emanating from the nozzle. When the flow emerges, it accelerates to supersonic speed and then readjusts to subsonic speed by compression through a shock wave. The process creates a series of diamond-shaped cells of alternate supersonic and subsonic flow. These cells or conical shock waves (Mach diamonds) intersect the jet axis throughout the length of the jet (Figure 2).
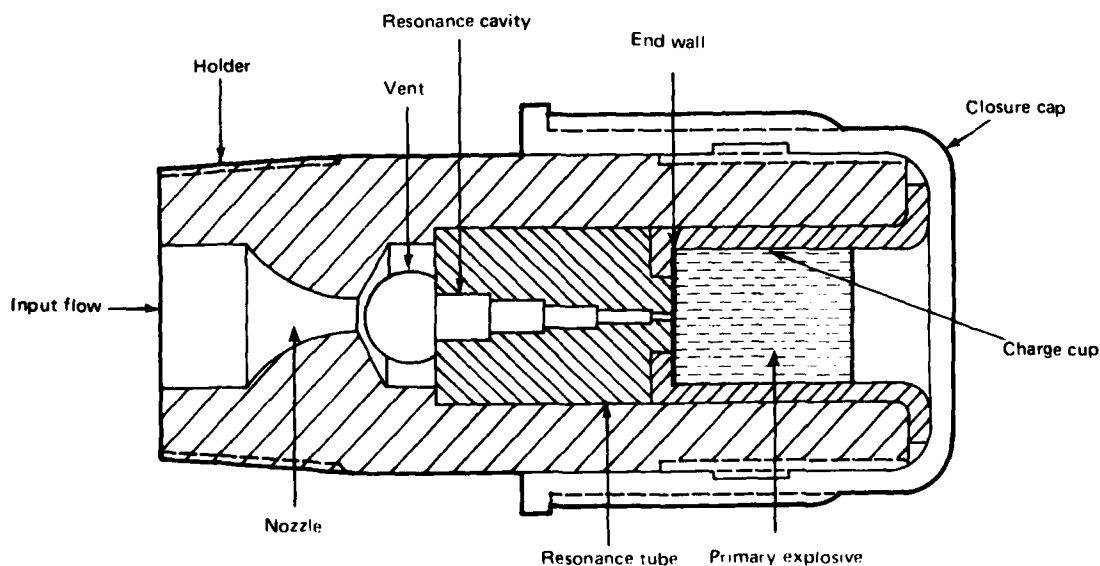
FIGURE 1. FLUERIC EXPLOSIVE INITIATOR ASSEMBLY

320
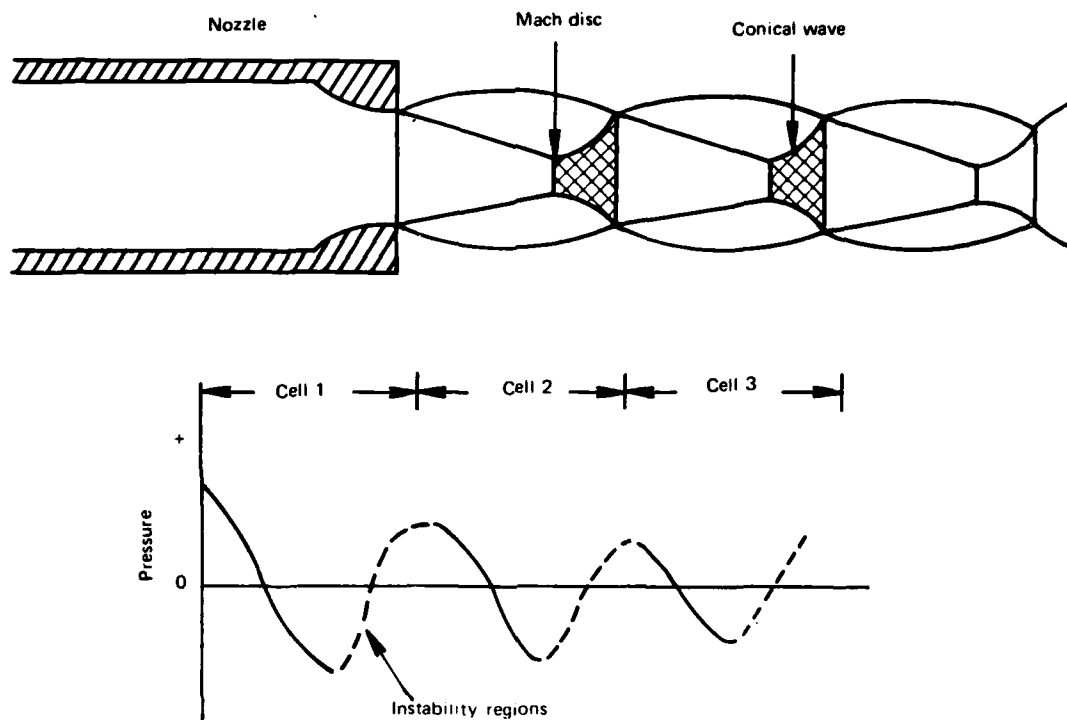
FIGURE 2. PRESSURE VARIATION–SHOCK WAVES

Intervals of instability (indicated by the crosshatching in Figure 2) are located between these points. Hartmann[1] who did the first reported work in this field found that placing a cavity in one of the intervals of instability would cause a self-sustaining system of oscillations to be created by driving the gas in the cavity into resonance. The location of the instability region is directly downstream of the Mach disk. The jet impinges on the open end of the resonance tube with resulting change in the flow field.

Although there is continuous flow into and out of the resonance cavity, a portion of the gas remains trapped at the closed end and undergoes many cycles of periodic compression and rarefaction. This periodic compression and expansion of the gas, within the rigid cavity of the resonance tube, produces irreversible temperature increases, which may be several times the initial adiabatic temperature head. The thermal energy generated by this process is concentrated at the closed end of the resonance tube and can be utilized to initiate exothermal processes requiring elevated temperature and/or heat flux as the initiation mechanism.

Initial Development:

Initial development[2] of the FEI for explosive initiation was begun in 1968. The feasibility of using this concept to initiate explosives was proven during the course of a subsequent development contract. Additionally, the parameters effecting the performance were identified. Based on satisfactory resonance tube performance obtained during the initial program, a second more comprehensive program was initiated in 1970.[3] The primary objective of this second program was to optimize resonance heating phenomena in order to develop a fast rise time, inexpensive, safe and reliable FEI. This program, again primarily experimental, was directed toward obtaining a maximum rise in end wall temperature in a minimum of time. The effects of external environments including ambient pressure, ambient temperature, and acoustic noise were also evaluated. The program resulted in the design of an FEI capable of generating temperatures of 1,000° C in 30 ms and igniting primary explosives in less than 10 ms. A program to extend this research and development to a reliable explosive initiator design which would interface with an existing explosive valve was later established, and methods of mass producing inexpensive resonance tubes were also addressed.[4] Helium was extensively evaluated as the excitation gas during these programs.

Squib for Explosive Cutter Valve:

An effort[4] was initiated to develop a cold gas power supply for a fluidic missile control system. Initiation of these supplies had previously depended upon electrically initiating a pyrotechnic powered cutter valve. A program to combine the FEI and the power supply to produce an all fluidic cold gas power supply was also undertaken.[5]

Two types of FEI's were developed and fabricated for use with an existing cutter valve assembly. This explosively activated valve uses a blunt ram to remove a closure on a gas bottle charged to 8,000 psi. A self-sealing FEI was designed to seal off both the gas supply and the vents. Although the self-sealing hardware worked perfectly and sealed as required, it was subsequently discovered that a much simpler nonsealing pneumatic initiator would perform satisfactorily, and all subsequent testing with the cutter valve was performed with the nonsealing initiator. Forty-six explosive tests of the complete system were conducted under various environments. None of the squibs failed to fire when supplied with gas at pressures from 150 to 1,500 psi. The lowest air supply pressure at which firing occurred was about 40 psi at 74° C ambient gas supply temperature. Nitrogen and helium were also evaluated during the program.

Time Delay Explosive Initiator:

The feasibility of using the FEI as a time delay igniter for an explosive weapon system was analytically and experimentally investigated.[6] The time delay igniter developed is a simple and rugged device which is ejected from the weapon on impact and detonates after a predetermined settable time delay in the range of 100 to 1,000 ms. The FEI designed to accomplish this time delay consisted of a small gas container, a nozzle, a resonance tube, and the explosive charge. The gas container is initially charged to a pressure considerably higher than the functioning pressure of the FEI's nozzle/resonance tube combination. When the assembly is ejected, the gas in the container flows through the nozzle and vents to the atmosphere, thereby reducing the pressure until it reaches the level at which resonance tube heating occurs.

Ram Air Safe and Arm (S&A):

The FEI was adapted for use on projectile weapons as a means of safing, arming, and/or fuzing the projectile.[7] During flight, ambient air enters a nozzle and exits into an internal chamber where a resonance tube is located. The ram air excites the tube into resonance, generating sufficient thermal energy to cause either an explosive to be initiated or a thermal responding element to be activated. The explosive energy may be used for arming of the round or fuzing. The thermally activated element can lock or unlock S&A mechanisms. Wind tunnel tests showed the feasibility of utilizing the initiator with ram air for all projectiles whose velocities are Mach 0.8. Flight tests conducted at the Yuma Proving Grounds, Yuma, Ariz., demonstrated that the igniter would survive and operate after exposure to 10,000 g's axial acceleration and 300,000 rad/s^2 radial acceleration.

Solid Propellant Rocket Igniter:

A fluidic ignition system for sounding rockets was developed for NASA, Langley, Va. The objective of this program[8,9] was to develop and demonstrate an inexpensive and safe ignition system concept for solid propellant rocket motors. Although first proposed for use in a sounding rocket, this system has broad potential applications in all solid propellant motor vehicles in first stage ground launch, or in upper stages utilizing fluidic programmers. Temperatures in excess of 800° C were generated in the resonance tube driven by a simple hand pump as the only energy source. Using a consumable nitrocellulose resonance tube, boron potassium nitrate ($BKNO_3$), a commonly used rocket motor material, was successfully initiated with air supply pressures as low as 45 psi. The program evaluation included a determination of power supply requirements, igniter geometry and alignment, igniter/ propellant interfacing, and the effects of ambient temperatures and pressure. It was demonstrated that an operator using a simple hand pump could ignite $BKNO_3$ at a standoff distance of 300 feet with the only connection to the igniter being a piece of plastic pneumatic tubing. Extensive testing with low pressure air, 30 to 150 psi, was required for this program.

Flueric Cartridge Initiator

In demonstration tests at Dayton, T. Brown Inc., Bohemia, N. Y., it was shown that the FEI could successfully ignite cartridges but that there was a significant backflow problem because the FEI components could not withstand the cartridge ballistic gas environment. The goal for the initial effort was to develop an FCI which would withstand ballistic gas pressures and function within current cartridge specification requirements. A stores separation cartridge was used because of its larger physical size.

The following were required in order to accomplish these objectives:

(1) A heat resistant or composite material resonance tube possessing adequate shock strength and thermal generating ability, since destruction or serious damage to the resonance tube would cause significant ballistic gas backflow through the FCI.

(2) New sealing techniques to eliminate possible backflow paths around the resonance tube.

(3) Modifications to the ignition train to ensure proper cartridge functioning.

After meeting the above objectives, follow-on effort has involved miniaturizing the FCI for the .38-caliber cartridge application. The Mk 125 stores separation cartridge, FCI design/development program[10] will first be discussed followed by the CCU-36/A .38-caliber cartridge, FCI effort. Test data and analyses are presented in Appendices A and B.

Mk 125 Cartridge Hardware Development/Design:

Resonance Tube Material Selection:

In order to be an effective resonance tube material for cartridge initiator usage, the selected material must possess the following properties:

(1) Low thermal conductivity to ensure the heat generated by the entrapped gas is transferred through the steel disk (end wall) to the ignition mix, not radially through the resonance tube walls. This will ensure reliable cartridge initiation.

(2) High service temperature to withstand the temperatures generated in the resonance tube after cartridge ignition.

(3) Resistance to thermal shock because of the rapid temperature increases of the gas entrapped in the resonance tube and cartridge ballistic gases.

(4) High compressive strength because of the high ballistic pressures required in some cartridge actuated device applications.

(5) Low porosity to prevent gas leakage through the resonance tube wall, and resultant heat loss.

(6) Easily moldable, castable, or machinable for production purposes.

The two methods employed to evaluate the resonance tube material candidates were:

(1) Thermocouples made from 0.003-inch-diameter chromel and alumal wire were placed in the resonance tube. The FCI was functionally tested and temperature versus time histories were recorded (Figure 3). Based on the ignition materials under consideration, an ignition temperature of 350° C was used.

(2) Small quantities of KDNBF (potassium dinitrobenzfuroxane) were loaded in aluminum cups with ultrasonically welded steel disks. The cups were functionally tested in closed bombs, and ignition times were recorded.

Based on the above testing as well as material properties testing, the Corning machinable glass ceramic (MGC) appeared to hold the most promise for successful test firing. However, the test results indicated that polyester has the best thermal generating performance, could be cast, and has the significant advantage of being clear (thus allowing for visual inspection); but it has a low service temperature and compressive strength. Ultra Cast 553 had the highest service temperature, thereby having the capability of easily withstanding the anticipated high temperatures; but of the three materials, it has the lowest strength. Both the Ultra Cast 553 and the polyester tubes were destroyed each time during initial cartridge testing. This produced low cartridge output pressures caused by backflow through the broken tube. The Corning MGC did withstand the temperature and forces produced by the cartridge. Table I summarizes these data.

Resonance Tube Design:

The Corning MGC resonance tube consisted of five cylindrical cavities of different diameters ranging from 0.062 to 0.015 inch. MGC design changes during the developmental program included (1) a diameter change in the final step from 0.015 to 0.010 inch and (2) a stepped inlet to permit the use of a copper washer/gasket for sealing purposes. These changes will be addressed in more detail.
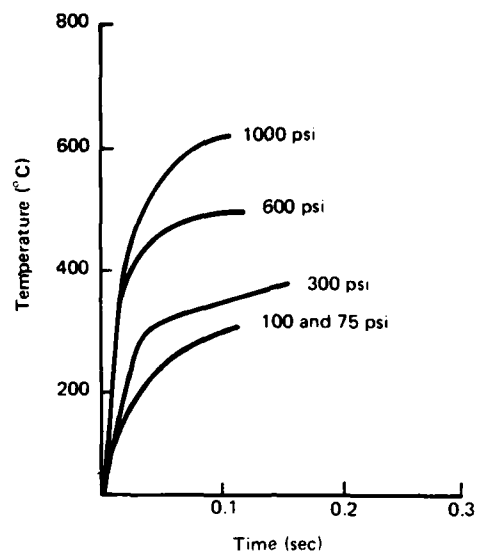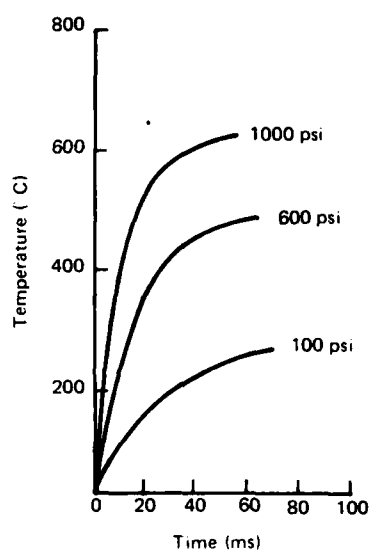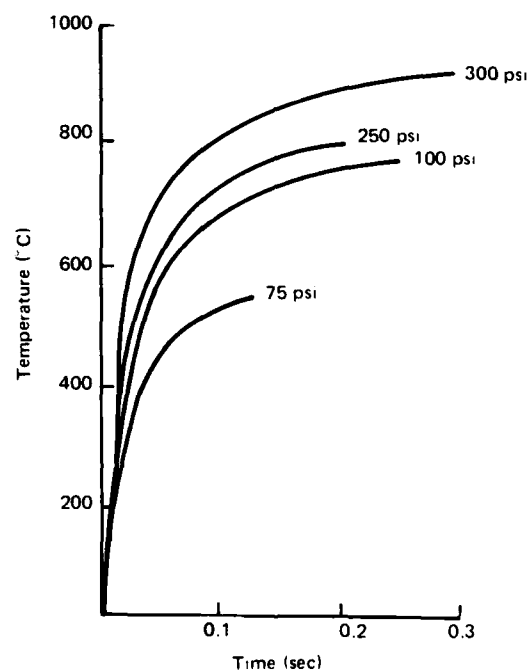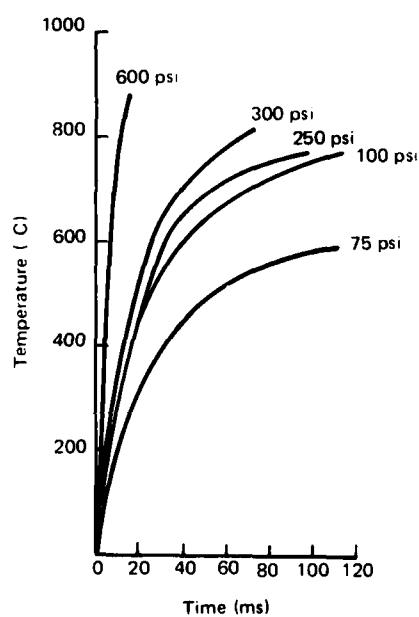
FIGURE 3. TEMPERATURE VERSUS TIME FOR VARIOUS INPUT PRESSURES OF
AIR AND HELIUM WITH MGC CERAMIC RESONANCE TUBES

Table I

SUMMARY OF PROPERTIES FOR THREE CANDIDATE RESONANCE TUBE MATERIALS

Material	Compressive strength (kpsi)	Thermal conductivity (Btu)	Service temperature (°C)	Performance temperature[1] (°C)	Survived cartridge functioning
Acme 555/655 (polyester)	15.0	2	275	700	No
Ultra Cast 553	3.5	9	4,000	600	No
Corning MGC	50.0	12	1,800	600	Yes

[1] Resonance tube gas temperature after 25 ms with a 300 psi helium supply.

Ignition Holder Design:

The KDNBF, responding to the thermal output of the resonance tube, ignites other materials to eventually burn the propellant in the cartridge. Some other ignition materials successfully used during the previously discussed developmental programs included lead styphnate, lead azide, and cellulose nitrate. KDNBF was chosen because it is safer to handle and exhibits a slightly better response time. However, it was necessary to provide a means of protecting the KDNBF from being disrupted by the hot resonating gases. The use of a thin metal protective disc (Figure 1, endwall) between the resonance tube and ignition mix had been successful during past programs. During the course of the developmental program, several igniter designs were evaluated.

The major design changes from previous FEI's involved incorporating a two-piece versus one-piece holder to allow for a good leak-tight seal at the copper washer interfaces. The copper would deform during loading, effectively sealing off the ignition chamber except for the hole through the resonance tube. The two holder pieces were fabricated from stainless steel for strength and thermal resistance. A notch for crimping was also provided to ensure complete igniter pellet ignition. The vent area was reduced to allow FCI operation at high gas pressures and provide for an increased resonance tube bearing areas. The fifth design, FCI/5 (Figure 4) evolved which made use of all previous improvements from the FCI/1 through FCI/4 deisgns. The new output charge holder reduced the resonance tube area upon which the 13,000 psi acted to only 0.003 in.² which limits the force on the tube to 40 pounds.

Flueric Cartridge Initiator Miniaturization for the .38-Caliber Cartridge Configuration

Resonance Tube Design:

The key to overall miniaturization involved the reduction of the resonance tube envelope. Problems of tube cracking during torquing operations (assembly) in the Mk 125 application because of resonance tube/holder bearing surface were also addressed.
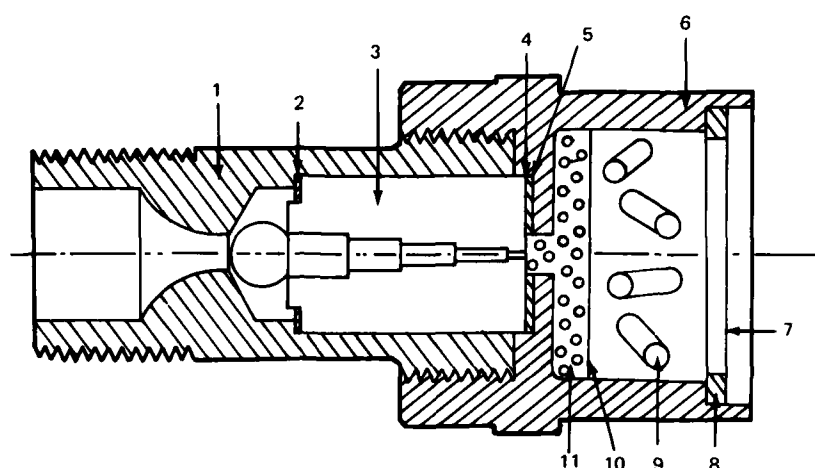
Item	Description	Material	Quantity
1	Tube holder	Stainless steel 303	1
2	Input copper washer	Copper	1
3	Resonance tube	Ceramic	1
4	Thermal disk	Stainless steel 15-7PH	1
5	Output copper washer	Copper	1
6	Output charge holder	Stainless steel 303	1
7	Sealing disk, 1-mil	Aluminum mylar	1
8	Crimp washer	Copper	1
9	Transfer charge	Unique	250 mg
10	Closure disk, 1-mil	Mylar	1
11	Ignition material	KDNBF	50 mg

FIGURE 4. FCI/5 THIN LAYER DESIGN FOR MK 125
STORES SEPARATION CARTRIDGE APPLICATION

The .38-caliber resonance tube design employed steel, copper (sealing), and MGC for the first, second, and third through fifth steps, respectively, to form the resonance tube cavity. The basic design still uses the Mk 125 S-9 resonance tube concepts except the overall length has been reduced by half, now designated the S-11 resonance tube.

Thermocouple tests indicated inadequate performance caused by improper sealing. To eliminate leakage, the copper disk was reduced to 0.01 inch thickness and used to form part of the first step. The design, shown in Figure 5, incorporated a copper/steel first step, four MGC steps, and a copper washer (sealing)/steel disk. This improved sealing and provided an adequate bearing surface for the resonance tube, eliminating tube cracking during torquing operations.
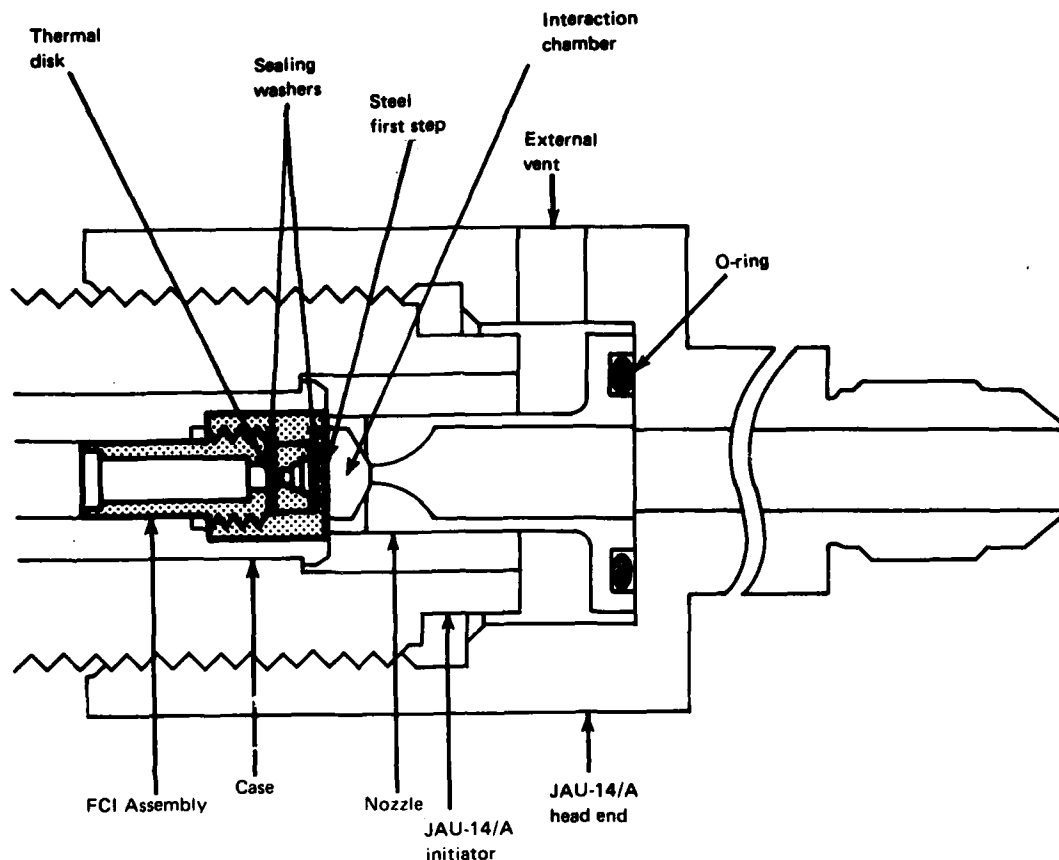
FIGURE 5. MINIATURIZED FCI FOR .38-CALIBER CARTRIDGE

Thermal Disk Design:

In the Mk 125 FCI/5 design, a 1-mil 15-7 P-H stainless steel disk survived ballistic gas pressures in excess of 15,000 psi while standard 302 stainless steel disks (FEI design) did not. However, when the miniaturized FCI was test fired, the initiator suffered blowback (i.e., the 1-mil 15-7 P-H stainless steel disks did not remain intact) although pressures were only in the 8,000 psi range.

Originally, it was felt the disks were failing under the high temperatures generated by the S-11 resonance tube. During one special test without ignition charge installation, a 0.010 inch hole was burned in a steel disk. Rhenium, because of its high strength and melting point, was chosen as an alternative disk material. However, rhenium was less successful than steel during functional testing.

Failure analysis indicated the disks seemed to be failing under shock, instead of tension loading. The cause was isolated to shock phenomenon from the smaller diameter KDNBF column which served to concentrate the KDNBF ignition transient on the disk.

New disk materials are being considered, with the prime candidate being Inconel 718 because of its high strength, its high temperature resistance, and primarily, its toughness. At the time of this paper preparation, the Inconel 718 disks were in the process of being annealed to obtain elongation in the 15% to 20% range. Material properties are summarized in Table II.

Table II

THERMAL DISK MATERIAL CANDIDATES

Material	Yield stress (kpsi)	Ultimate stress (kpsi)	Melting point (°F)	Elongation in 2 in. (%)
302 Stainless	75	90	2550	35
15-7 P-H[1]	260	265	>2500	4
Rhenium	270	280	5760	
Inconel 718[2]	196	171	2400	20

[1]Heattreated in the CH900 condition.
[2]Annealed and aged.

Supply Pressure and Function Time Optimization:

Earlier FEI programs determined the criticality of the separation distance between the nozzle exit and resonance tube. Also the vent area is critical to FCI/FEI performance.

The FCI/5 design functioned in the 10 to 20 ms range with a 500-psi input pressure. Function times of less than 10 ms with 200-psi helium pressure were desired with the miniaturized FCI.

Therefore, the separation distance was reduced by 25% and the vent area was also reduced slightly. Preliminary indications are that, while performance increased at 200 psi, more optimum performance is possible with further geometry changes.

The nozzle geometry design was dictated by the JAU-14/A initiator standard firing pin housing envelope which served as the test vehicle for the miniaturized FCI. An exterior vent drilled in the initiator head was necessary to permit the flow conditions necessary for resonance tube operation to exist. It was found that the size of this vent also affected performance. A single 1/4-inch diameter vent provided the best performance. The vents are designed to be choked to eliminate altitude effects.

Because of the length of the S-11 tube (each step is 0.025 inch), it was difficult to obtain adequate thermocouple data. However, FCI function times for the .38-caliber application versus the Mk 125 were reduced by a factor of two. Test data summaries appear in Appendices A and B.

Vent Seal Design:

Because of the severe environments a cartridge must function in; e.g., temperature and humidity, sand and dust, and salt spray; a method of sealing the exterior vents is required. The simplest method involves using a rupture disk/sealant combination. To ascertain the effect of vent sealing on FCl function time performance, cellophane-type tape of different thickness was placed over the vent during thermocouple testing. Figure 6 summarizes the data.
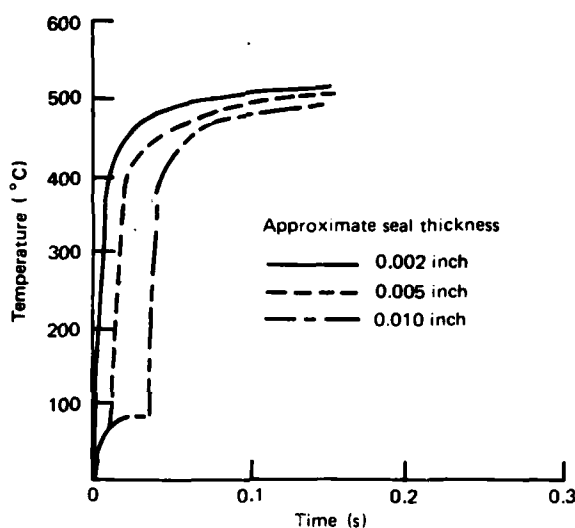
FIGURE 6. TEMPERATURE VERSUS TIME FOR VARIOUS
VENT SEAL THICKNESS

It can be seen that the thicker the seal, the longer the function time (desired temperature is 500° C). Initial heating occurs until the interaction chamber pressure (P) exceeds $P_{critical}$ in which case the heating stops until the seal ruptures. Thus, the seal material must rupture at low pressures to ensure short function times and yet be strong enough to survive all environments. At the time of this writing a vent sealing candidate design was being readied for testing.

CONCLUSIONS

The feasibility of initiating a cartridge with the FCI has been demonstrated through a continuing exploratory research and development program. The specific accomplishments of this program are:

- Cartridge ignition has been demonstrated for both the Mk 125 and the CCU-36/A .38-caliber cartridges.

- Consistent function times of less than 10 ms have been demonstrated in the CCU-36/A.

- An FCI that will survive the ballistic environment has been designed. developed and tested at -65° F, 70° F, and 200° F.

- A design for a vent seal has been generated and will soon be tested.

- Ultrasonic cleaning was demonstrated as an acceptable method of cleaning the resonance tubes after assembly to prevent ceramic dust clogging that occurred during the Mk 125 FCI program. The ceramic dust resulted from the resonance tube machining operation.

REFERENCES

(1) J. Hartmann and B. Troll, "On a New Method for the Generation of Sound Waves," *Phys. Rev.*, **20**:719-727 (1922).

(2) Singer-General Precision, Inc., *Development of a Flueric Explosive Ignition Device* by E. L. Rakowsky, C. Miller, and J. Donaghue, ARC Final Report 1590-6811, December 1968.

(3) Singer Co., Kearfott Division, Little Falls, N. J. *Flueric Explosive Initiator* by V. P. Marchese, Final Report KD71-8, April 1971.

(4) Singer Co., Kearfott Division, Little Falls, N. J. *Flueric Explosive Initiator* by V. P. Marchese, Final Report KD71-69, December 1971.

(5) Singer Co., Kearfott Division, Little Falls, N. J. *A Pneumatic Explosive Initiator for an Explosive Cutter* by V. P. Marchese and F. G. Vander Vliet, Final Report KD72-131, December 1972.

(6) Singer Co., Kearfott Division, Little Falls, N. J. *A Flueric Second Event Initiator for Fuel Air Explosives* by V. P. Marchese, Final Report KD72-67, August 1972.

(7) Singer Co., Kearfott Division, Little Falls, N. J. *Flueric Safing and Arming of Selected Ammunition* by V. P. Marchese, Final Report KD72-68, August 1972.

(8) Singer Co., Kearfott Division, Little Falls, N. J. *Flueric Sounding Rocket Motor Ignition* by V. P. Marchese, Final Report KD71-69, December 1971.

(9) Singer Co., Kearfott Division, Little Falls, N. J. *Development and Demonstration of Flueric Sounding Rocket Motor Ignition* by V. P. Marchese, Final Report KD73-40, September 1973.

(10) J. W. Morris and V. P. Marchese, "Flueric Cartridge Initiator Development," 1975 Annual Meeting of Pyrotechnics and Explosives Applications Sections, American Defense Preparedness Association, October 1975.

Appendix A

MK 125 CARTRIDGE TEST RESULTS

Table A-I

FLUERIC CARTRIDGE INITIATOR RESONANCE TUBE MATERIAL/DESIGN DETERMINATION TESTING IN THE MK 125

Tube materials	Helium supply pressure (psi)	Solenoid time (ms)	Function time (ms)	Maximum cartridge pressure (psi)	Time to maximum pressure (ms)	Backflow (psi)	Resonance tube intact after firing	Remarks
				FCI/2				
Polyester	300	$-^1$	$-^1$	8,271	$-^1$	532	No	
Polyester	300	$-^1$	$-^1$	7,754	$-^1$	1,000	No	
Polyester	300	$-^1$	$-^1$	9,473	$-^1$	920	No	
Ultracast	300	$-^1$	$-^1$	9,305	$-^1$	1,100	No	
Ultracast	300	$-^1$	$-^1$	8,777	$-^1$	1,200	No	
MGC	300	$-^1$	$-^1$	5,690	$-^1$	$-^1$	Yes	Holder eroded
MGC	300	$-^1$	$-^1$	8,097	$-^1$	$-^1$	Yes	Holder eroded
MGC	300	$-^1$	$-^1$	9,535	$-^1$	$-^1$	Yes	Holder eroded
Stainless steel/polyester	300	$-^1$	$-^1$	9,507	$-^1$	$-^1$	Yes	Holder ruptured
Stainless steel/polyester	300	$-^1$	$-^1$	1,334	$-^1$	$-^1$	Yes	No orifice
				FCI/5				
MGC	477	$-^1$	327	10,575	18	$-^1$	Yes	No O-ring
MGC	318	$-^1$	31	11,632	16	$-^1$	Yes	No O-ring
MGC	474	$-^1$	74	12,160	14	$-^1$	Yes	No O-ring
MGC	367	23	25	10,033	12	$-^1$	Yes	No O-ring
MGC	468	39	39	12,775	13	$-^1$	Yes	O-ring
MGC	434	35	35	13,110	13	$-^1$	Yes	O-ring
MGC	434	28	28	13,500	12	$-^1$	Yes	O-ring
MGC	481	30	100	13,511	12	$-^1$	Yes	Blocked tube

[1] Not recorded.

334

Table A-II

MK 125 CARTRIDGE TEMPERATURE TESTING WITH STANDARD ELECTRICAL INITIATION AND FCI/5

Electrical initiation	FCI/5 initiation	He input pressure (psi)	Solenoid time (ms)	Function time (ms)	Cartridge maximum pressure (psi)	Time to maximum pressure (ms)	Electrical delay time (ms)
70° F Temperature Conditioned							
1					11,688	15	6
2					12,089	14	6
3					12,089	10	10
4					12,356	13	6
5					—	—	—
	1	477	13	20	12,386	14	
	2	504	14	15	12,557	12	
	3	517	12	22	15,028	10	
	4	504	13	16	13,358	12	
	5[1]	—	—		—	—	—
	Average			18.25			
	σ			3.3			
−65° F Temperature Conditioned							
6					11,612	16	8
7					13,892	17	7
8					12,022	17	8
	6	523	17	29	12,757	12	
	7	527	13	16	12,823	13	
	8	530	13	13	11,688	12	
	9	517	12	12	13,024	11	
	10	520	13	13	12,624	12	
	11[2]	—	—	—	—	—	
	12	498	14	30	11,956	14	
	13	517	14	12	12,757	11	
	14	517	13	11	14,652	13	
	15	530	14	25	12,623	12	
	Average			17.89			
	σ			7.82			
200° F Temperature Conditioned							
9					14,960	15	10
10					16,093	12	7
11					15,028	10	7
	16	517	11	11	16,364	10	
	17	520	15	16	15,292	10	
	18	517	15	15	17,365	10	
	19	504	14	11	15,361	11	
	20	523	15	16	15,361	11	
	21	517	14	14	16,364	10	
	22	516	15	14	17,365	9	
	23	471	15	11	15,048	9	
	24	490	15	12	15,495	10	
	25	506	13	13	15,361	11	
	Average			13.30			
	σ			2.0			

[1] No-fire, tube blocked.
[2] No-fire, concave end.

Table A-III

FCI/5 FUNCTIONAL TESTNG FLUERIC CARTRIDGE INITIATOR ONLY

Gas input supply	Pressure (psi)	Function time (ms)
Helium	470	14
	480	14.5
	500	19
	480	No-fire[1]
Hydrogen	475	7.5
	475	8.0
	475	10.0
	480	10.5
	480	218[1]

[1] Resonance tube not cleaned.

Cartridge functional times of 11 ms have been obtained with helium input gas. The data indicated that the FCI function times are related to solenoid operations the faster the valve functions, the faster the FCI functions. Results of the limited hydrogen FCI testing (Table A-III) seemed to confirm analytical predictions that the hydrogen would provide faster function times than helium.

During the two series of tests (Tables A-II and A-III), three no-fires and a long function time (Table A-III, 218 ms) occurred. One of the no-fires was directly attributable to poor machining of the resonance tube. The back end was concave, preventing contact with the thermal transfer disk. The other two were clogged as was the one with the long function time. The material clogging was caused by a fine ceramic dust resulting from the resonance tube machining operation. However, cleaning the resonance tube via industrial ultrasonic cleaning in a suitable solution has been shown to provide a technique for ensuring dust removal.

336

Appendix B

.38-CALIBER CARTRIDGE TESTING

CCU-36/A cartridges with the FCI/6 .38-caliber configuration were functionally tested in modified JAU-14/A initiators. Test data are summarized in Table B-I.

Table B-I

FCI/6 FUNCTIONAL TESTING AT AMBIENT TEMPERATURE

Test No.	Function time (ms)	Helium input pressure (psi)
1	7.0	398
2	7.0	398
3	7.0	410
4	10.0	298
5	21.0	314

Test data analysis revealed the following:

(1) The cause of the long function time (test No. 5) was caused by grease from the upstream pressure transducer partially blocking the FCI nozzle.

(2) All five thermal disks experienced a pinhole type burnthrough. Post test analysis performed with unloaded FCI/6 units indicated this condition was caused by the heat generated within the FCI itself. The S-11 resonance tube, one half the length of the FCI/5 design, generates sufficiently high temperatures to cause steel disk burnthrough. Solutions which were being investigated are

    (a) Heat treating the 1-mil 15-7 P-H disks to improve their high temperature properties.

    (b) Investigation of alternate disk materials. The two most promising materials under consideration were rhenium and tantalum. The tantalum was not available in 1-mil stock and will not be investigated under the current program because of time and cost limitations. Rhenium sheets (1-mil thick) have been obtained and were evaluated. It should be

noted that this disk failure does not prevent proper FCI functioning. The 0.010-inch-diameter hole which results from burnthrough only reduces cartridge output slightly, but not critically.

(3) The FCI function times improved relative to the previous efforts which were in the 15-ms range. Also, pressure requirements have been reduced, thereby improving FCI/fluidic sequencer compatability.

Table B-II

FCI/6 INPUT PRESSURE AND THERMAL DISK MATERIAL DETERMINATION[1]

Round No.	Disk material[2]	Function time (ms)	Actuation pressure (psi)	Output pressure (psi)
FCI-1	SS	6.0	184	NA
FCI-2	SS	8.0	187	NA
FCI-3	SS	11.5	184	NA
FCI-4	SS	17.0	174	NA
FCI-5	SS	11.0	184	NA
FCI-6	SS	23.0	179	NA
FCI-7	SS	11.0	274	NA
FCI-8	SS	24.5	270	NA
FCI-9	SS	7.0	367	NA
FCI-10	SS	7.0	367	NA
FCI-11	SS	9.0	294	NA
FCI-12	SS	15.0	271	NA
FCI-13	R	6.5	367	NA
FCI-14	R	8.0	365	NA
CTGT-1	SS	6.0	368	10,000
CTGT-2	SS	4.5	368	12,000
CTGT-3	SS	5.0	368	9,000
CTGT-4	R	4.5	368	12,675
CTGT-5	R	4.0	368	9,000
CTGT-6	R	6.0	184	9,300

[1] 0.075-inch resonance tube/nozzle separation distance.
[2] SS   15-7 PH stainless steel
    R   rhenium.

Posttest analysis of the second series revealed that:

(1) All thermal disks ruptured (cartridge rounds designated CTGT).
(2) All rhenium and 40% of the stainless steel thermal disks ruptured (FCI rounds).

Because of the failure of the rhenium and steel disks at relatively low ballistic gas pressures (30% to 50% less than the Mk 125 application), it is believed that the resultant pinhole type ruptures are due to a shock phenomenon caused by the ignition material vice a thermal disk material tensile failure.

A change of the ignition material was attempted to reduce the shock effect. Table B-III summarizes the data. The reduction in KDNBF did not eliminate disk rupturing. At the time of this writing, Inconel 718 is being considered as a possible replacement because of its toughness. Also, effort will continue to improve function times at 200 psi.

Table B-III

.38-CALIBER TESTS WITH 10 MG OF KDNBF AND 150 MG OF A-1A

Round No.	Disk material[1]	Function time (ms)	Actuation pressure (psi)	Output pressure (psi)
1	R	17.5	200	4,982
2	SS	11.0	189	7,314
3	R	8.0	207	5,347
4	SS	9.0	207	8,967
5	SS	11.0	408	8,401

[1]SS = 15-7 P-H stainless steel
R = rhenium.

Appendix C

FUNCTIONAL TEST SETUP AND PROCEDURE

A schematic of the test setup is shown in Figure C-1. It consists of a firing source of compressed gas connected to a refill system, a firing system, and a pressure monitoring system.
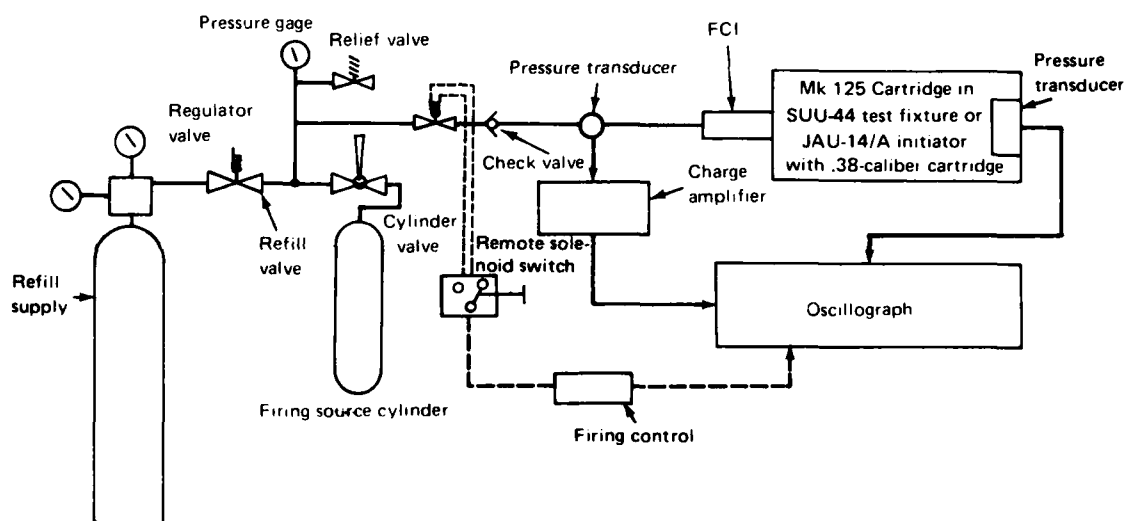
FIGURE C-1. FLUERIC CARTRIDGE INITIATOR FUNCTIONAL TEST SCHEMATIC

The important parameters associated with FCI functional testing are as follows:

(1) Fire/no-fire

(2) Input gas pressure

(3) Peak pressure output

(4) Time to ignition (function time) defined as the time from start of gas supply (solenoid opens) to the first indication of pressure output from the cartridge.

In another definition, the function time is taken as the time from supply of electrical energy to the solenoid to initial cartridge pressure. Thus, it includes the time that it takes for the solenoid to open (15 to 30 ms). For the purposes of this report, function time starts when pressure is recorded at the input pressure transducers. Functional testing was accomplished with the various FCI assemblies previously described.

METALS, ALLOYS AND INTERMETALLIC COMPOUNDS

Metals and metallic substances are characterized by a distinctive set of physical properties, including high electrical and thermal conductivity, metallic luster, ductility and malleability and the chemical property of electropositivity. It is this chemical property, of course, which is of primary interest to chemists and pyrotechnicians, but some of the physical properties are also important.

For example, large surface area or small particle size is important to the pyrotechnics and explosive industry, but the grinding properties of metals are dependent on their malleability and ductility. Powdered aluminum of small particle size is created by atomization or by ball milling. Magnesium powders, however, are much more difficult to reduce in size. The magnesium – aluminum compound Al_3Mg_4 is quite frangible, and this will grind easily into the small particles so desirable and the chemical properties are also quite unique. Obviously, therefore we have modified the forces holding these atoms together.

What has this done to the chemical properties? Will the heat of combustion of one mole of Al_3Mg_4 be equal to, less or greater than that of three gram atoms of aluminium and four of magnesium? The literature[1] is none too clear on the heat of formation of this compound. Various methods and investigators give a range of -780, -4110 and -7000 calories per gram atom. It is however obvious from phase diagrams that a compound is formed of a distinct atomic ratio, and that this compound will have less heat of reaction than a comparable amount of the metal mixture.

When metals are used as reducing agents in pyrotechnic reactions, an important property is the heat of reaction. The calculation is made utilizing

---

(1) D. Kubaschewski and J. A. Catterall, "Thermochemical Data of Alloys", Pergamon Press, London and New York, 1956, pages 31, 32 and cited literature.

that rule of thermo-chemistry that assumes the heat of formation of an element in its standard state is zero.

The following illustration is used to point out some other considerations that must be kept in mind.

$$3CuO_{(s)} + 2Al_{(s)} = Al_2O_{3(s)} + 3Cu_{(s)} + heat$$
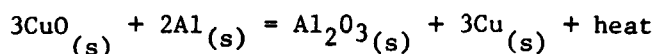
The calculated heat of reaction obtained using the heats of formation of CuO and Al_2O_3 is 287,7 K cal. This is only true however if the amount of energy required to break Al-Al bonds is exactly recovered by formation of the produced Cu-Cu bonds. If the Cu-Cu bonds are not formed then the delivered heat of reaction is not as large as calculated. This is true for this reaction because the copper comes off as monatomic gas particles, thus the realized heat of reaction is less by the amount of energy needed to sublime two gram atoms of aluminum.

One way to get all the heat out of the reaction would be to start with atomic aluminum. Unfortunately we have not invented such a grinder but as we all know we approach this by pulverizing etc. What we are doing is breaking as many aluminum-aluminum bonds before use. When we break an aluminum crystalloid into pieces we create surfaces, edges and corners. The Al atoms on surfaces etc. are not bonded in the same way because their coordination number is no longer 12 but 3, 4, 5, 6 and obviously require less energy to pull apart.

Obviously grinding is not the only way to break or weaken metallic bonds. Anything that loosens the lattice will also accomplish this - doping. If we can create imperfections by size or valence differential, we can do the same thing.

Doping doesn't always weaken the lattice. Carbon steel is an example which strengthens it. Carbon is the right size to fit into the interstices and also forms stronger bonds (Fe-C is stronger than Fe-Fe), consequently we have tool steels - harder and denser.

Silicon however in aluminum does loosen the lattice and specific impulse increase in solid propellants is claimed (U.S. Patent 3,053,708).

Some other metals and alloys of interest to our field are the following:

Ni-Zr alloys - with $KClO_4$ as delays

Al-Pd - Pyrofuze

$CaSi_2$ - Starter mix and self heating food can

NiAl - Pyronol torch

Ce-Pb - Sparking alloy

Be-Cu - Non-spark tools

Hg-Al - Stress cracking

Metals of course are used widely -

Zr - Heat mixes, white sparks, starter mixes, primers.

Al - Flares, salutes

Ni - Delays

Mg - Flares

B - Starters, delays

Si - Starters, delays

Ti - Starters, delays

W - Starters, delays

Zn - Fireworks and smoke

Sb - Delays and white stars

Cu - Heat conductor, blue and green stars

Cr - Delays

Mn - Delays and starters

Fe - Delays

Mo - Delays

Ag - Delays

Bi - Delays

Ce, La, Nd - Mischmetall

Pb - Zr - Lighter "flints"

INTERMETALLIC COMPOUNDS

Intermetallic compounds have been known for years and yet strangely they have never occasioned any great interest to chemists. Perhaps it is because there has been no great unifying theory of valence, such as ionic or covalent.[2] The following discussion is not intended to be an exhaustive or definitive treatment of the metallic bond. Hopeful. it will serve as an introduction to a fascinating but so far neglected area of chemistry and stimulate further study of the classic publications of the area. (1, 2, 3).

Equilibrium diagrams as below are indispensable to the determination of compound formation.

FIGURE I
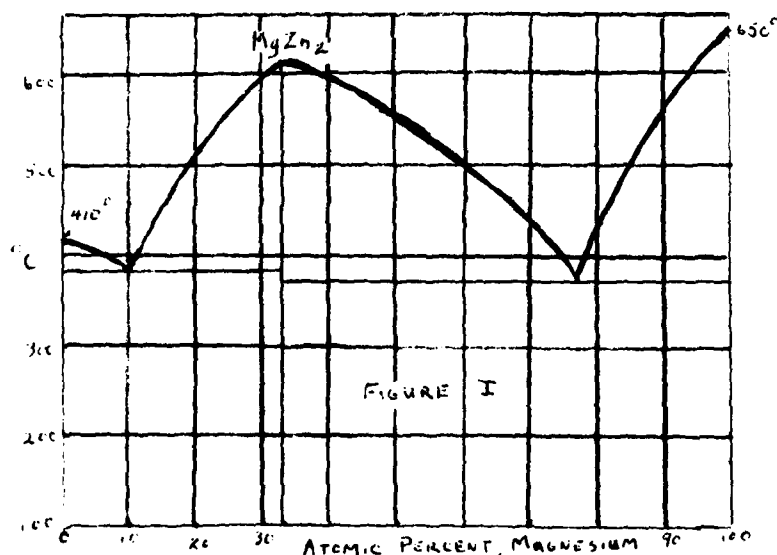
(2) Pauling, Linus, "The Nature of the Chemical Bond", Cornell Univ. Press.

Compound formation usually leads to a maximum in the equilibrium diagram such as $MgZn_2$ in the above example.

Once it is known that a compound is formed and its stoichiometry has been determined an attempt can be made to classify its bonding. Bonding is generally classified by one of three types as follows:

(a) "Semi-Ionic" Bonding

Perhaps the easiest place to start is the metal-metalloid compounds because of its close relationship to ionic bonding that we know so well.

Some examples of this type of compound are:

Ca_2Si	Mg_2Pb
Mg_3Bi_2	Mg_2Si
Mg_3Sb_2	Zn_3Sb_2
Ca_3As_2	Mg_2Sn
Ba_2Pb	Cu_3Al

(b) Laves Compounds - "Size factor compounds"

A large number of binary compounds of the general composition AB_2 have a particular stable arrangement in space. If the atomic diameters are approximately in the ratio of 1,2 to 1,0 the unit cell is cubic with 24 atoms per unit cell. The smaller atoms lie at the corners of tetrahedra which are joined point to point and leave a dodocahedral hole into which the larger atom is fitted. There are three main types of these compounds as shown in the following:

MgCu$_2$ type	MgZn$_2$ type	MgBi$_2$ type
CaAl$_2$	BaMg$_2$	HfCr$_2$
KBi$_2$	CaCd$_2$	HfMn$_2$
TiBe$_2$	FeBe$_2$	ReBe$_2$
ZrFe$_2$	ZrCr$_2$	
ZrW$_2$	TiFe$_2$	

The chemical properties of these compounds are sensitive to the change in size of adulterant metals as well as electrons per atom.

(c) <u>Hume-Rothery Compounds</u> [3]

Certain intermetallic compounds of similar structure but apparently unrelated stoichiometry can be considered to have the same ratio of valence electrons to number of atoms. For example, consider the β phases of the systems Cu-Zn, Cu-Al and CuSn which are all cubic close packed and their compositions are CuZn, Cu$_3$Al and Cu$_5$Sn. If copper is univalent, zinc bivalent, aluminum trivalent and tin quadrivalent the ratio of valence electrons to atoms has the value $3/2$ for these compounds.

$$CuZn \quad (1 + 2)/2 \quad = 3/2$$

$$Cu_3Al \quad (3 + 3)/4 \quad = 3/2$$

$$Cu_5Sn \quad (5 + 4)/6 \quad = 3/2$$

---

(3) Hume-Rothery, William, "Electrons, Atoms, Metals and Alloys", Dover Publications, N.Y., N.Y. 1963.

Some other in this class are CuBi, AgZn, AgMg and Ag_3Al.

The Υ alloys which include Cu_5Zn_8, Cu_9Al_4, $Cu_{31}Sn_8$ and Fe_5Zn_{21} the ratio of valence electrons to atoms has the value $21/13$.

Cu_5Zn_8 $(5 + 16)/13$ $=$ $21/13$

Cu_9Al_4 $(9 + 12)/13$ $=$ $21/13$

$Cu_{31}Sn_8$ $(31 + 32)/39$ $=$ $21/13$

Fe_5Zn_{21} $(0 + 42)/26$ $=$ $21/13$

It is to be noted that Fe, Co, Ni, Rh, Pd and Pt are assigned zero

valence electrons in order that the ratio ratin its value. (Also

presumably Os, Ir and Ru).

What then should be the structure of Ni-Al and Pd-Al? From the above

the most stable should be

NiAl $(0 + 3)/2$ $=$ $3/2$

Pd-Al $(0 + 3)/2$ $=$ $3/2$

and they should be β phases with an A2 structure.

Are there any other possibilities? Ni_6Al_7 but probably not because it is

too close to the 1-1 atomic ratio. Laves compounds possibility do exist

however because the atomic diameters are as follows:

Pd 1.283

Ni 1.154

Al 1.248

There can then be the possibility of $PdAl_2$ and $AlNi_2$.

SPECIAL APPLICATIONS

The Pd-Al system has found fairly wide application in the pyrotechnic and explosives areas. It is marketed under the name "Pyrofuze" and its advantages as a delay and ignition element are

1. reproducibility

2. no waterproofing

3. long term storage stability

4. low volume

5. no pressing or mixing necessary

Pyrofuze is prepared in a wire, sheet or granular form. The wire is made by swaging aluminum core in a palladium cladding. Its composition is 79,81 per cent Pd and 20,19 per cent Al. Its heat of alloying is 327 calories per gram and 3263 calories per cubic centimeter. Its ignition temperature is 670°C (Tm of Al + 660°C). Its per cent composition corresponds to a PdAl formula.

Other exothermic alloying reactions are also of interest such as the NiAl compound which is used in a modified thermite mix in powder form to give additional heat and velocity. Suitably cased and directed this reaction does cut through four inches of stainless steel in 0,25 second. Its composition is 31,5% Al and 685% Ni or NiAl. The heat of alloying is 329 calories per gram and 2290 calories per cubic centimeter. The Ni-Al combination does not react in wire or sheet form but only in a powder mixture.

Pt-Al (87,5 - 12,5%) will react in the same manner as Pd-Al yet its heat of alloying is only 216 calories per cc which is the important requirement.

Kubaschewski and Catterall give the heat of formation of the NiAl compound as 17 000 at 293 K and state that it is "obviously due to the new covalent bonds formed between dissimilar atoms."

Both of these systems have been investigated by Ferro and Capelli[4] and their heats of alloying and their equilibrium diagrams are shown in figure (2).

It can be seen that there are the following compounds:

Al_3Ni

$AlNi$

AlN_3

$AlPd_3$

A recent application of Al-Pd compound has just been patented in Germany. When the usual copper, brass or aluminum metallic cones for shaped charges are replaced by the pyrofuze alloy, significantly increased penetrations are claimed.

SUMMARY

Because I have seemingly devoted this entire paper to the discussion of crystalline order in intermetallic compounds as evidenced by stoichiometry and crystal formation, I think that I should restate the creed of the solid state chemist which are - unlike gases in which the properties are predicted with confidence by relying on the average, solids are immensely affected by very small departures from perfection. For example, the conductivity of a semiconductor can be increased a thousand fold with the addition of 0.1% of an impurity.

---

(4) Ferro, R. and Capelli, R., "Rendiconti dell' Accademia dei Lincei", 34, 659-664 (1963)

A homely simile (not Homeric) is, it is not the tail wagging the dog, it is the flea on the end of the tail. Yes, doping is important and can be made more so and with more precision by knowledge of the metal or metallic compound to be doped.
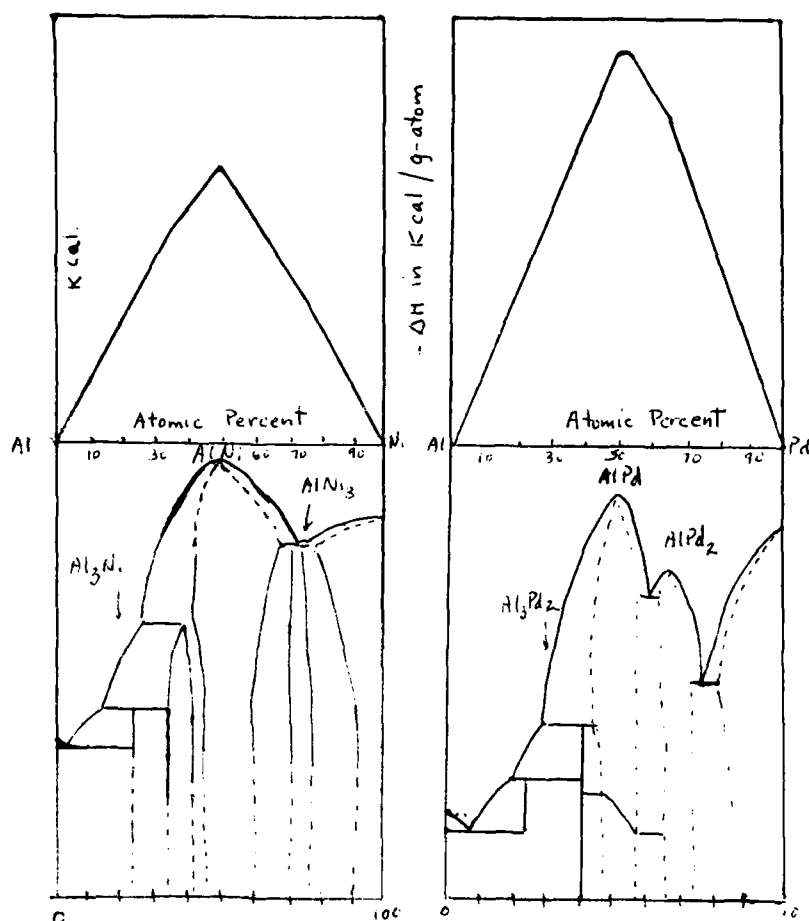
FIGURE II

EXAMINATION OF THE VARIATION OF INFRARED FLARE

ENERGY WITH GRAIN CONFIGURATION AND BINDER

by

Melvin P. Nadler
Applied Science Branch
Propulsion Development Department

April 1976

NAVAL WEAPONS CENTER
China Lake, California 93555

ABSTRACT

The infrared emission of flares is discussed, with emphasis on the variation of radiant intensity in the 2-3μm and 3-5μm regions as a function of grain configuration, oxidizer/fuel (O/F) ratio, and binder. Four O/F ratios, two different binders, and six different grain configurations were tested at 5.5 psi (38 kPa). Radiant intensity (w/sr), burn time, mass flow rate (g/s), radiant efficiency (J/g·sr), and motion picture coverage were obtained. The radiant intensity was found to be proportional to mass flow rate, with the binder having a significant effect on the proportionality constant. The ratio of the radiant intensity in the 3-5μm to that in the 2-3μm region was greatly influenced by mass flow rate, configuration, O/F ratio, binder, and flare plume conditions. The above ratio of radiant intensity was inversely related to the radiant efficiency.

The observed results are explained in detail. "Chamber" pressures are calculated for the internal burners and related to critical flow conditions. Thermodynamic computer calculations of chamber species and temperatures, and exit species and temperatures, are discussed. Thermodynamic calculations of afterburning species and temperatures are also given. Plume velocity, mass flow rate, exit species, and mixing ratios are shown to be important parameters in determining emitting species and plume temperatures as afterburning efficiency decreases from ideal thermodynamic conditions. Optically-thin and optically-thick plume emission models are discussed and compared to the experimentally measured radiant intensities and radiant efficiencies.

INTRODUCTION

The process of radiant emission from flare plumes is a complex phenomenon and is not generally predictable by present analytical procedures. Many factors influence the emissions from particle-laden flare plumes, including combustion species concentrations and distributions, temperature distributions, species emissivities, heat transfer between particles and gases, plume afterburning, mixing ratios, scattering, optical densities, etc. Species concentrations and combustion temperatures can be calculated using thermodynamic computer programs: however, these predictions for flare combustion are inaccurate compared to predictions for rocket motor combustion. The non-equilibrium combustion of flares is due to their relatively low combustion pressures and short residence times (compared to rocket motor combustion). Introduction of reaction kinetics improves species concentration prediction, but uncertainties in rate constants and the importance of diffusion-controlled processes during flare combustion leave many unanswered questions. The temperature distribution of the flare plume is one of the most important parameters for the prediction of radiant intensity, since the intensity is proportional to the fourth power of the absolute temperature (for graybody emission). The variation of plume temperature and its effect on the infrared (IR) radiant intensity of flares is discussed in this report.

Species emissivities can be predicted for gas phase species, but for liquid and solid species the variation of emissivity with wavelength, particle size, and temperature is uncertain unless the plume is optically-thick and unless graybody emission can be assumed. Some solid particles, such as carbon, can be considered to emit as graybodies over a large particle size range.[1] Others, such as MgO, have high emissivities in the far IR and low emissivities in the 2-5μm window[2] and their emissivities vary with particle size. More details on particle emissivity is given later in this report.

Flare formulations are generally very fuel rich in order to take advantage of atmospheric oxygen for afterburning. Afterburning allows more radiant intensity (W/sr) to be generated per weight of flare material and, therefore, higher radiant efficiencies (J/g·sr).[1] Exothermic afterburning reactions maintain higher plume temperatures, which result in higher radiant intensities. However, the increased radiant efficiency due to afterburning is reduced as atmospheric pressure decreases and wind shear velocities increase. Flare plume afterburning is a complex process, depending on fundamental parameters such as plume velocity, exit pressure, mass flow rate, reaction kinetics, turbulent mixing, mixing ratio of air to plume products, and temperature distribution. These fundamental parameters are related to flare parameters such as grain configuration,

---

[1] Radiant efficiency $= \dfrac{\text{radiant intensity}}{\text{mass flow rate}} = \dfrac{W/sr}{g/s} = J/g \cdot sr$

binder, oxidizer/fuel (O/F) ratio, and linear burning rate. Finally, both sets of parameters are connected to the variation of IR flare radiant intensity and radiant efficiency in the 2-5µm window.

Much work has been done on the theoretical prediction of IR emissions from rocket motor plumes with only limited success.[3-5] Reasonable predictions a·e accomplished for optically-thin plumes expanding into a vacuum. Even in this simplified case, lack of optical data to calculate particle emissions can cause uncertainties. When afterburning plumes are considered, the best alternative is to measure IR emissions experimentally. Some work has been done on the prediction of visible emissions of flares,[6] but many of the parameters are fitted from experimental data.

In this report the approach is to experimentally measure radiant intensity in the 2-3µm and 3-5µm regions of fuel-rich flares burning at 5.5 psi (38 kPa), and then attempt to explain these results theoretically. Emphasis is on afterburning, turbulent mixing, and particle emissivity.

EXPERIMENTAL SETUP AND RESULTS

Radiometric measurements were made on four fuel-rich flare formulations using two different binders and six different grain configurations. The four formulations used are shown in Table I. These formulations are all similar in that Mg is the fuel, AP is the oxidizer, and all use a castable binder; however, particle size of Mg is varied, binder is changed from a dimethyl siloxane (Sylgard-182) to a hydrocarbon (HTPB), and O/F ratios are varied. The main variable in this study is grain configuration. The six configurations used are designated A through F:

Configuration	Description
A	End burner, 1.25 inch (3.175 cm) diameter x 2.5 inches (6.35 cm) long. Initial burning surface area $S_o = 1.23$ in^2 (7.94 cm^2)
B	End burner, 2.25 inches (5.72 cm) diameter x 2.5 inches (6.35 cm) long. $S_o = 3.97$ in^2 (25.6 cm^2)
C	Internal burner (uninhibited), 1.25 inch (3.175 cm) diameter x 5 inches (12.7 cm) long x 0.375 inch (0.9525 cm) diameter central bore. $S_o = 27.7$ in^2 (179 cm^2)
D	Internal burner, 1.25 inch (3.175 cm) diameter x 5 inches (12.7 cm) long x 0.375 inch (0.9525 cm) diameter central bore. $S_o = 8.1$ in^2 (52.3 cm^2)

Configuration	Description
E	Internal burner with oblong port, 1.25 inch (3.175 cm) diameter x 5 inches (12.7 cm) long. Port dimensions: 0.4 inch (1.02 cm) x 0.2 inch (0.51 cm) with 0.2 inch (0.51 cm) radius semicircles at the 0.2 inch (0.51 cm) ends. S_o = 12.2 in^2 (78.7 cm^2)
F	Internal burner with six-point star, 1.25 inch (3.175 cm) diameter x 5 inches (12.7 cm) long. Star dimensions: inner radius 0.3 inch (0.76 cm), outer radius 1.0 inch (2.54 cm), star points 30 degrees wide and 30 degrees apart, star points 0.08 inch (0.20 cm) apart on inner radius and 0.25 inch (0.635 cm) wide at outer radius. S_o = 32.5 in^2 (210 cm^2)

These six configurations allowed variation of mass flow rate, burning surface area, internal vs external burning, internal pressure, exit velocity, and plume volume.

Sylgard 182 is a Dow Corning silicone polymer having the structure of a dimethyl siloxane, and with a small percentage of a silica filler in the resin. The formulation is:

Resin 182 ....65.8%
Dow Corning 200 Fluid (10 centistokes)..27.8%
Curative 182 .... 6.4%

The hydrocarbon binder is composed of R45 polymer (91.6%) and isophorane-diisocyanate curative (8.4%).

The formulations were mixed under vacuum and pressure cast into Micarta cases with Teflon mandrels for the ported configurations (Figure 1). The Sylgard mixes were cured in an oven at 60°C for 24 hours, and the HTPB at 60°C for 3 days.

The flares were burned at 5.5 psi (38 kPa) in a 6,870 ft^3 (194 m^3) chamber to accentuate the effects of low-pressure flare combustion. The radiant intensity of the flares in the 2-5μm region was measured through two sapphire chamber windows. A PbS detector with a 2-3μm filter was used to measure radiant intensity in the 2-3μm region [J(2-3)]. A PbSe detector with a 3-5μm filter was used to measure radiant intensity in the 3-5μm region [J(3-5)]. Both detectors were liquid nitrogen cooled. The radiometric signals were amplified and recorded on an O-graph and magnetic tape, then integrated by computer to obtain average radiant intensity of the whole flare plume. All flares were fired horizontally and

perpendicularly to the radiometers. Burn time (t_b), average mass flow rate ($\dot{m}$), radiant efficiency,[2] and the ratio of radiant intensities [J(3-5)/J(2-3)], were also computed. Motion picture coverage was obtained through the quartz window.

Four flares of each of the six configurations and four formulations were teste., for a total of 96 tests. The experimental data are reported as the average, plus or minus the average mean deviation, in Tables 2-5. The following observations can be made from the data in Tables 2-5.

1. Radiant intensity increases with mass flow rate for all four formulations and in both wavelength regions. Figures 2 and 3 show J(2-3) and J(3-5) vs $\dot{m}$ for configurations A, D, E, and F of the Sylgard and HTPB formulations. (Note: Previous work is from five lower density castings of configuration D.) Figure 2 shows J(3-5) increased more rapidly than J(2-3) for both Sylgards. The equations for the straight lines [ignoring the curvature into (0,0)] are as follows:

$$322 \text{ Sylgard} \quad \begin{cases} J(3-5) = 64\ \dot{m} + 510 & (1) \\ J(2-3) = 31\ \dot{m} + 700 & (2) \end{cases}$$

$$368 \text{ Sylgard} \quad \begin{cases} J(3-5) = 59\ \dot{m} + 390 & (3) \\ J(2-3) = 34\ \dot{m} + 300 & (4) \end{cases}$$

Figure 3 shows that the slopes for the HTPB formulations are much greater than for the Sylgards, and their straight line equations are as follows:

$$284 \text{ HTPB} \quad \begin{cases} J(2-3) \quad J(3-5) = 365\ \dot{m} & (5) \end{cases}$$

$$277 \text{ HTPB} \quad \begin{cases} J(3-5) = 225\ \dot{m} + 170 & (6) \\ J(2-3) = 167\ \dot{m} + 200 & (7) \end{cases}$$

The 284 HTPB does not show the increased slope for the J(3-5) over J(2-3) that occurs in the other three formulations.

2. In general, the radiant efficiencies for the HTPB flares were higher than for the Sylgard flares. However, radiant efficiency varied with mass flow rate (except for 284 HTPB), as can be seen in Figure 4. The two Sylgard formulations show relatively high efficiency at low $\dot{m}$ and approach a limit at high $\dot{m}$. Equation (1) gives E(3-5) $\rightarrow$ 64 J/g·sr for 322 and equation (3) gives E(3-5) $\rightarrow$ 59 J/g·sr for 368 in the limit of high $\dot{m}$. The 277 HTPB appears similar to the Sylgards, while 284 HTPB maintains a constant radiant efficiency. The HTPB formulations had much lower linear burning rates than the Sylgard formulations, so high $\dot{m}$'s could not be obtained for the configurations used in this study, and extrapolation to high $\dot{m}$ cannot be made as with the Sylgards.

---

[2] Radiant efficiency in the 2-3 and 3-5μm regions are hereafter abbreviated E(2-3) and E(3-5), respectively.

358

3. There also appears to be an inverse relationship between radiant efficiency and the ratio J(3-5)/J(2-3), which is called reversal (R). Figure 5 is a plot of R versus E(3-5) for all configurations with a constant plume diameter (configurations A, D, E and F). This inverse relation, Rα1/E, holds except for E(3-5) < 100 J/g·sr, where there appears to be a leveling-off in R. The energy radiated per unit mass flow per unit area increases with temperature for a blackbody. Also, R = K(3-5)/K(2-3),[3] which is plotted versus temperature in Figure 6. Figure 6 shows that as temperature increases, R decreases. Therefore, for a blackbody, as radiant efficiency/unit area increases due to a temperature increase, R must decrease, and qualitatively the inverse relationship between E and R can be understood. The inverse relation should hold for graybodies also, and R = K(3-5)/K(2-3) will also be true. This provides a method of calculating temperature from R, assuming graybody emission. The temperature calculated from Figure 6, using the experimentally-measured reversals, would be the average plume temperature, assuming the plume emits graybody with no atmospheric absorption between the plume and the radiometers. Figures 7 and 8 are plots of E(2-3) and E(3-5) versus calculated graybody temperature for all the flares tested. The points appear to fall on two straight lines (except 284 B and C), one for the Sylgard and one for the HTPB. The range of temperatures is not large enough to determine the real temperature dependence, and the magnitude of the temperatures may not be correct because of the graybody assumption. However, if the log-log dependence is assumed, the following absolute temperature exponents are calculated:

$$\text{Sylgard} \quad \begin{cases} E(2-3) \propto T^{3.8} \\ E(3-5) \propto T^{3.1} \end{cases}$$

$$\text{HTPB} \quad \begin{cases} E(2-3) \propto T^{4.7} \\ E(3-5) \propto T^{3.6} \end{cases}$$

For a real graybody the temperature dependence would be T^4. An important point to be noted is that there appears to be a temperature variation within a particular formulation as the configuration changes. This and other related points will be examined in more detail in the Discussion section.

4. The type of binder has a significant effect on the linear burning rates. The linear burning rate was 0.206 cm/s (0.081 in/sec) for 322 Sylgard compared to only 0.083 cm/s (0.033 in/sec) for 284 HTPB (determined from tests of configuration A). The large increase in burning rate for Sylgard formulation over HTPB formulation is surprising since (1) the O/F ratios are similar, (2) the HTPB formulation had a greater percentage of fine magnesium, and (3) HTPB has a positive heat of formation while Sylgard is negative [-1860 cal/mol (-7.8 kJ/mol)].

---

[3] K(3-5) is the fraction of energy radiated in the 3-5μm region and K(2-3) the fraction radiated in the 2-3um region, assuming blackbody radiation.

Three possible reasons for the difference in regression rate are:

     a.   The Dow Corning 200 Fluid used as a diluent (1.3%) is a low-molecular-weight dimethyl siloxane and has a flash point of 163°C and an ignition temperature of 452°C.[7,8]

     b.   The Sylgard binder did not "wet" the AP particles as well as HTPB; so more surface area was available for reaction. (Poor physical properties and large numbers of voids would also cause increased burning rates, but the densities of both binder formulations were about 98% of theoretical.)

     c.   HTPB propellants are known to have poor combustion properties at low pressures[9]. During this study it was noted that the Sylgard formulations ignited readily while the HTPB formulations were difficult to ignite at 5.5 psi (38 kPa). Strand burning tests performed from 15-250 psi (103-1722 kPa) showed the HTPB formulations have a higher pressure exponent than the Sylgard formulations, but extrapolation to 5.5 psi (38 kPa) may be in error.

     5. The radiant intensity [J(3-5)] versus time data are plotted in Figure 9 for 322 Sylgard configurations A, C, D, E and F. Nothing unusual is observed; configuration F, which has the highest initial surface area, has the fastest rise time followed by E and C, then D. Configuration C has the highest peak intensity since it is uninhibited and burns on the outside surface as well as internally.

     It was noted from the motion picture coverage that not all flares had the rapid flame propagation of 322 Sylgard. The HTPB flares showed poor flame propagation properties, and it took a significant fraction of the burn time for the complete burning surface area to ignite properly.

DISCUSSION

     This section gives theoretical explanations for the observed flare data in an attempt to put the generation of IR flare energy on a more scientific basis. In any study of IR emissions, it is important to know the species and temperatures: therefore, a thermodynamic computer program was used to determine the equilibrium products of combustion and the flame temperature. The NWC Propellant Evaluation Program (PEP) was used for these calculations. Four inputs are needed to run the PEP: weight percent of each flare component, heats of formation, combustion chamber pressure, and exit pressure. The exit pressure used was 5.5 psi (38 kPa), but the chamber pressure for a flare is not easily defined. External-burning-flare combustion takes place under the ambient pressure (38 kPa), but internal burning flares will combust at higher than ambient pressure. This internal flare pressure must be calculated for

use in the PEP. It should be noted that this program gives products
and temperatures of complete equilibrium combustion and isentropic
expansion.

INTERNAL FLARE PARAMETERS

For rocket motor flow the pressure expansion from the chamber to
the exit takes place isentropically, and the nozzle is designed to
give sonic flow at the throat. In the case of an internal burning
flare, the expansion does not take place isentropically, but can be
considered as steady adiabatic flow with mass addition at constant
enthalpy. This case has been analyzed by E.W. Price[10] for flow in
a constant area port. The analysis can be applied to internal burning
flares, even though the port area is not constant, by calculating
pressures at specific port area intervals during the burn. Another
complication arises in dealing with the flares tested in this study
because the internal burners were opened at both ends. Therefore,
stagnation conditions must be considered to exist at the center of the
port. Under these conditions the internal flare pressure at the center
of the port (stagnation pressure) can be calculated from[10]

$$P_o = \frac{\dot{m}}{A_p \theta_* \delta} \tag{8}$$

and

$$\frac{p}{P_o} = \frac{1 + \gamma (1 - \delta^2)^{1/2}}{\gamma + 1} \tag{9}$$

where

$$\theta_* = \gamma/[2(\gamma - 1)(\gamma + 1)C_p T_s]^{1/2} \tag{10}$$

P_o = stagnation pressure (chamber pressure at the
center of the port), dynes/cm^2

$\dot{m}$ = mass flow rate, g/s

A_p = cross sectional area of port, cm^2

δ = dimensionless variable ($0 \leq \delta \leq 1$)

p = pressure at a specified point along port, dynes/cm^2

γ = ratio of specific heats (C_p/C_v)

C_p = specific heat at constant pressure (erg/g·K)

T_s = stagnation temperature, K

The critical pressure ratio for sonic flow can be calculated from equation (9) when $\delta = 1$:

$$\frac{p^*}{p_o} = \frac{1}{\gamma + 1} \tag{11}$$

where

p^* = pressure when velocity is sonic.

If p^* at the exit plane is greater than or equal to the ambient pressure, then choked flow occurs and the exit velocity is sonic. Under choked flow conditions, $\delta = 1$ and equation (8) is easily solved for p_o. However, if $p^* \le p_a$ (ambient pressure) then $\delta < 1$ and equations (8) and (9) must be solved simultaneously while iterating a value for δ until $p = p_a$. When the correct value of δ is obtained, the p_o from equation (8) is the internal flare pressure. Before equation (8) can be solved, θ_* must be calculated from equation (10); this requires γ, C_p, and T_s to be known. In order to determine γ, C_p, and T_s, the thermodynamic computer program must be run for each of the four flare formulations, but this requires p_o. This circular problem was solved by running the PEP program at several p_o's [6 psi (41 kPa) to 50 psi (344 kPa)] to find γ, C_p, and T_s, and then calculating p_o from equations (8)-(10) until the calculated p_o and the p_o input to the PEP program agreed. It was noted that in the pressure range of 6-15 psi (41-103 kPa), the γ, C_p, and T_s calculated were insensitive to the chamber pressure (p_o) input to the PEP program. This insensitivity allowed a simplification of the complex iterative process by using only $p_o = 10$ psi (69 kPa) as an input to the PEP calculations; this was approximately the average internal flare pressure calculated. (See Appendix for PEP calculations.) Another important point to be made before the internal flare pressure results are presented is that the $\dot{m}$ in equation (8) must be calculated for a particular flare configuration at a particular port cross-section. The $\dot{m}$ also must be one-half of the total mass flow rate, since the stagnation pressure is at the center of the port and expansion takes place in two directions. Therefore, in order to use equations (8 through 10), only one-half of the flare is considered, as shown in the diagram of configuration D below.

p_a

p_e $\qquad$ p_o $\qquad$ p_e
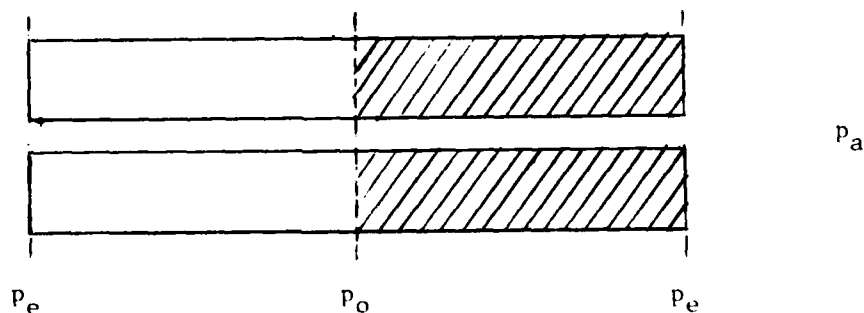
Another way of looking at this is: if the total burning surface area of the flare is considered by using the total $\dot{m}$, the stagnation pressure calculated would be for a flare closed at one end and p_o would be at the closed end. The mass flow rate for a solid propellant is:

$$\dot{m} = A_b \rho_p \dot{r} \tag{12}$$

where

A_b = burning surface area, cm^2

ρ_p = propellant density, g/cm^3

$\dot{r}$ = linear burning rate, cm/s

For configuration D

$$A_b = \pi d l \tag{13}$$

where

d = port diameter, cm

l = port length, cm

Calculations were performed at four port diameters: 0.9525 cm (the initial diameter), 1.51 cm, 2.06 cm, and 3.175 cm (the final diameter). Table 6 shows the results of the internal flare pressures for all configuration D flares. Column 1 gives the thermodynamic computer results for γ, C_p, and T_s at p_o = 10 psi (69 kPa)(Appendix). Columns 2 and 3 compare adiabatic and isentropic critical pressure ratios needed for sonic flow. It should be noted that a greater expansion ratio is needed to achieve sonic flow under adiabatic conditions. Columns 4 and 5 give the critical chamber pressures needed for choked flow at the flare exit plane when the ambient pressure is 5.5 psi (38 kPa). Column 6 gives the calculated internal flare pressures at the port diameters shown in column 7. The first set of pressures in column 6 is calculated using equation (12) for $\dot{m}$ and $\dot{r}$ = constant (the constant $\dot{r}$ is shown in column 12 for each formulation); the second set of pressures is for $\dot{r}$ = function (p), which will be explained later. Note that for the $\dot{r}$ = constant case, only the initial internal flare pressure for the two Sylgard formulations is high enough to give choked flow at the exit. The HTPB formulations show lower pressures and no choked flow. Column 8 gives the calculated times to reach the given diameters assuming constant $\dot{r}$ and assuming $\dot{r}$ = f(p). The total $\dot{m}$'s are shown in column 9. The first set of $\dot{m}$'s are calculated from equation (12) assuming constant $\dot{r}$; the second set is for $\dot{r}$ = f(p). Column 10 gives the value of the dimensionless variable (δ) for $\dot{r}$ = constant and $\dot{r}$ = f(p). The exit velocity of the flare plume can be calculated from equation (14)[10] and is shown in column 11.

$$v = v_* \frac{1 - (1 - \delta^2)^{1/2}}{\delta} \tag{14}$$

where

$$v_* = \text{sonic velocity} = \gamma/[\Theta_*(\gamma + 1)]$$

The first set of velocities in column 11 is again for the $\dot{r}$ = constant case, and the second set is for $\dot{r}$ = f(p). The variation of plume velocity vs calculated burn time is shown in Figure 10 for all configuration D flares ($\dot{r}$ = constant).

In rocket motor calculations, $\dot{r}$ is a function of pressure, so strand burning tests were conducted at 15-250 psi (103-1722 kPa) to find the pressure dependence. The lowest pressure was only 15 psi (103 kPa) during strand burning, so the results were extrapolated to 5.5 psi (38 kPa), which possibly gave an incorrect pressure dependence at the lower pressures [5.5-15 psi (38-103 kPa)]. The Sylgard 322 formulation gave

$$\dot{r} = 0.0813 \, p^{0.57} \quad \text{cm/s} \tag{15}$$

with   p in psi (1 psi = 6.9 kPa)

The pressure used in equation (15) varies with distance in the port, since expansion takes place from $p_o \rightarrow p_e$. If a linear average is assumed and equation (9) is used, then

$$p \, (\text{average}) = \frac{p_o}{2} \left[1 + \left(\frac{1 + \gamma(1-\delta^2)^{1/2}}{\gamma + 1} \right) \right]. \tag{16}$$

Introduction equation (16) into equation (12) and using $\ell/2$ for the length, equation (8) is solved for p_o.

$$p_o = 1.18 \times 10^{-14} \left(\frac{\rho_p \ell}{\delta d \Theta_*} \right)^{2.326} \left\{ (\gamma + 2) + \gamma(1 - \delta^2)^{1/2} \right\}^{1.326} \tag{17}$$

Equation 17 is for Sylgard 322 configuration D, and p_o is in psi, not dynes/cm². The internal flare pressure can be found by using the same iterative procedure described earlier, that is, using equations (17) and (9). The values of p_o, t, $\dot{m}$ (total), δ, and v are shown in Table 6. It should be noted that p_o, $\dot{m}$, and v are higher than the corresponding values calculated for $\dot{r}$ = constant. Figure 11 shows a plot of p_o versus burn time for Sylgard 322D: p_o* (critical chamber pressure) and the experimental burn time are also shown. The p_o calculated for the $\dot{r}$ = f(p) case has a high initial pressure, pressures above t_o* for about 1 second, and the flare only burns for 3.1 seconds. For the p_o calculated from the $\dot{r}$ = constant case, there is a slower drop in pressure, a burn time of 5.4 seconds, and pressure above p_o* for about 0.7 second. The burn time

calculated for the $\dot{r}$ = constant case agrees well with the experimental burn time of 6.1 ± 0.1 sec (Table 2). The reason for the $\dot{r}$ = f(p) case having more error could be the extrapolation to lower pressures, or most likely the fact that the initial flare burning surface area was not as high as the calculated surface area. As mentioned earlier, the film coverage showed that flame propagation was not instantaneous, so the initial pressure spike shown in Figure 11 for the $\dot{r}$ = f(p) case is erroneous. This also applies to the $\dot{r}$ = constant case, so the calculated initial pressures are high by some undetermined amount. The mass flow rate calculations are shown in Figure 12 for 322D; these data again show the agreement for the $\dot{r}$ = constant case with the experimental average mass flow rate. The $\dot{r}$ = constant case is more nearly in agreement with experimental data than the $\dot{r}$ = f(p) case because of the ignition delay of the flares to complete-burning-surface-area coverage. It should be noted that HTPB 284 shows very poor agreement between experimental (Table 4) and calculated (Table 6) burn times and average mass flow rates. This indicates a severe ignition delay problem, which was observed for HTPB 284 from the motion picture coverage.

Similar calculations must be performed for the other configurations so that comparisons of p_0, v, $\dot{m}$, and t_b can be made as a function of configuration. Configuration F internal parameters were calculated using the $\dot{r}$ = constant method described above. Equations (8) and (9) were used to determine p_0 and δ, equation (14) was used to find v, and equation (12) was used for $\dot{m}$. A problem arises in the calculation of cross sectional area (A_p) and burning surface area (A_b) since they are not simple functions of the diameter. This problem was solved by calculating A_b and A_p at four intervals during the burning of the star configuration: initial, final, and two intervals between. The web burned was changed by a known interval so that time to each interval could be calculated from $\dot{r}$. It should be noted again that the $\dot{m}$ used in equation (8) was one-half of the total average mass flow rate calculated from equation (12). The results of these internal parameter calculations are shown in Table 7 for all four formulations of configuration F. The calculated burn times (Table 7) are about half the experimental burn time (Tables 2 through 5) and the calculated $\dot{m}$'s are twice the experimental $\dot{m}$'s. This indicates that, for large internal surface area flares burned at 5.5 psi (38 kPa), the ignition delay or flame propagation problem becomes more severe as the initial surface area becomes larger. Another reason for the discrepancy in burn times and mass flow rates is poor combustion efficiency because of the high flow velocities. The exit velocities for configuration F are higher initially than those of configuration D, but rapidly decrease until the velocities for D and F are equal at the end of burn. The $\dot{m}$'s for configuration F decrease with time, while those for configuration D increase with time.

Configurations A and B are not internal burners, but initial plume velocities can be calculated from the continuity equation ($\dot{m} = \rho v A$). Equation (12) can be used to calculate $\dot{m}$; the cross sectional area (A) and the burning surface area (A_b) are equal to $\Pi d^2/4$; and the gas density (ρ) is $p_a M/RT$ (M = average gas molecular weight, R = 82.1 $cm^3 \cdot atm/mol \cdot K$, p_a = 0.37 atm). The $\dot{m}$ from equation (12) must be multiplied by the weight fraction of gas, so that the gas mass flow rate is used to calculate velocity. Inputs to calculate ρ come from the PEP calculations at ambient pressure. Table 8 gives the calculated data for configurations A and B. The agreement between burn time and mass flow rate in Tables 2-5 and Table 8 is excellent because of the constant A_b and low flow velocities. The exit velocities for configurations A and B are generally a factor of 10 lower than for configurations D and F.

Before these internal flare parameters are related to afterburning efficiency in the next section, two important points should be noted:

1. The expansion from $p_0 \rightarrow p_e$ for the internal burners causes a decrease in temperature as shown in equation (18)[10].

$$\frac{T}{T_s} = 1 - \frac{\gamma - 1}{\gamma + 1} \left[\frac{1 - (1 - \delta)^{1/2}}{\delta} \right]^2 \tag{18}$$

This drop in temperature is small, and reaches a maximum under choked flow conditions ($\delta = 1$)

$$\frac{T^*}{T_s} = \frac{2}{\gamma + 1} \tag{19}$$

It should be noted that for an isentropic expansion the same temperature drop occurs as in equation (19). This decrease in temperature at the exit for the internal burners will cause a drop in radiant efficiency (Figures 7 and 8) and a shift in IR intensity to longer wavelengths (see Figure 6). Both of these results are observed experimentally (except for HTPB 284). Figure 4 shows a decrease in radiant efficiency for the high mass flow rate internal burners; Figures 7 and 8 show a drop in E(2-3) and E(3-5) with temperature, and Figure 5 shows an increase in reversal for the internal burners.

2. The increase in exit velocity from configurations A and B, to D, and then to F, correlates with the increase in reversal from configuration A → F (compare Tables 6-8 with Tables 2-5). Also, the decrease in average velocity for all configuration D flares (Figure 10) in the order 368-322-277-284 correlates with the decrease in reversal for the configuration D flares (Tables 2-5).

AFTERBURNING AND TURBULENT MIXING

To establish a basis for discussion, the PEP was run to determine afterburning species and temperature as a function of weight air/weight propellant (m_a/m_p). The results are given in the Appendix for (1) m_a/m_p = 0, 0.25, 0.50, 0.75, 1.0, 2.0, 5.0, 10, 25, and 50, (2) each formulation, and (3) p_o = 10 psi (69 kPa) expanded to $p_e = p_a$ = 5.5 psi (38 kPa). The weight of flare mix or fuel-rich combustion products is kept at 100 grams, and air is added to make the weight ratios given above. The concentrations of products are given in moles/100 grams of propellant plus weight of air.

Figure 13 shows a plot of the thermodynamic afterburning temperatures versus m_a/m_p. All the temperature distributions are similar; they show a sharp rise to a maximum at the stoichiometric afterburning ratio of m_a/m_p, then decrease as more air is added. Table 9 shows the flare O/F ratios, the propellant exit temperatures, and the approximate stoichiometric m_a/m_p needed to completely burn the fuel-rich exhaust products. It should be noted that the most fuel-rich formulation (284) has the lowest exit temperature and requires the most air to completely afterburn, but its maximum afterburning temperature is about the same as the other three formulations (within resolution of PEP runs shown).

At this point it is appropriate to introduce afterburning efficiency, that is, how close does actual flare afterburning approach the thermodynamic prediction. The effects of exit temperature, exit velocity, flare configuration, exit species, reaction kinetics, and turbulent mixing on afterburning efficiency are discussed in the following paragraphs. For the inhibited flares, the mixing takes place outside the flare nozzle (or port), as shown in Figure 14. The Reynolds numbers (Re) for the internal burning configurations are much greater than 2000, and fully-developed turbulent flow will be obtained (Re $\sim$ 12000 for 322D and Re $\sim$ 7400 for 284D). The end burners have lower velocities but a larger characteristic length (ℓ^*) than the internal burners, and the Reynolds numbers vary from about 500-2000 at flame temperatures. As air mixes into the flame, the temperature will drop, thereby decreasing the viscosity (ν) and increasing the Reynolds numbers [Re = $v\ell^*/\nu$]. The best estimate is that the end burners are in the laminar-turbulent transition region since the Reynolds numbers calculated are only approximate.

Figure 14 shows four regions: (1) the potential core, where velocity and concentration of the nozzle gases remain unchanged; (2) the mixing region, where momentum and mass are transferred perpendicularly to the flow direction; (3) the transition region, whose length is about 10 nozzle diameters; and (4) the fully-developed region.[11] The axial and radial distribution of velocity and concentration in the fully-developed region can be calculated from empirical equations as a function of x/d (axial distance along the jet axis/nozzle diameter) or r/d (where r is radial distance). It should be noted that velocity, concentration, and temperature fall off more rapidly in the radial direction than along the jet axis for non-reactive flows.[11]

Another important property of turbulent flows is the entrainment
of air into the nozzle gases, or the mixing ratio of m_{air}/m_{prop}. For
turbulent jets the following entrainment equation holds:[11]

$$\frac{\dot{m}_{air}}{\dot{m}_{prop}} = 0.32 \left(\frac{\rho_a}{\rho_o}\right)^{1/2} \frac{x}{d} - 1 \qquad (20)$$

where

$\dot{m}_{air}$ = mass flow of entrained air, g/s

$\dot{m}_{prop}$ = mass flow of nozzle fluid, g/s

ρ_a = density of entrained air, g/cm^3

ρ_o = density of nozzle fluid at exit, g/cm^3

x = distance along jet axis, cm

d = nozzle diameter, cm

Equation (20) will allow calculation of the weight ratio of air to
nozzle gases as a function of x/d, or the calculation of x/d for a
particular $\dot{m}_{air}/\dot{m}_{prop}$. If the velocity along the x-axis is known, then
the time to reach a particular x/d can be calculated. This time is
very important since reactions do not take place instantaneously and
turbulent mixing of fuel and air does not occur at the molecular level
instantaneously. If the concept of the Damkohler number (D_o), which is
the chemical reaction rate/turbulent mixing rate,[12] is introduced, then
the above discussion, and the afterburning efficiency of flares, becomes
clear. Turbulent mixing takes place in different stages. First, the
mixing occurs on a scale that is large compared to the mean free path,
and chemical reactions can take place only on the surfaces of these
large eddies. Second, the energy distribution shifts, and the mixing
scale approaches the mean free path, where chemical reactions are kinet-
ically controlled. Finally, the turbulent mixing energy is dissipated.
If an eddy diffusivity (ϵ) is defined analogous to molecular diffusivity,
the mixing time (t^*) is inversely proportional to ϵ. Turbulent mixing
times are much shorter than laminar mixing times since the eddy diffusiv-
ity is larger than the molecular diffusivity. Since turbulent mixing
times are not instantaneous, if reaction times are less than or of the
same order of magnitude as t^*, then chemical reactions may not take place
or will be diffusion limited. In terms of the Damkohler number, if $D_o >$
1, chemical reactions will not go to completion until mixing on the

molecular level occurs. It should also be noted that as the nozzle gases move along the jet axis, their temperature and concentration decreases. Also, as the mixing ratio (m_a/m_p) moves away from stoichiometric and the temperature drops below the ignition temperature, afterburning efficiency will decrease or afterburning will not occur.

To put this discussion on a more quantitative basis, the time to $m_a/m_p = 1$ and stoichiometric m_a/m_p can be calculated for configurations A, B, and D, using equation (20) and the plume exit velocities. The nozzle or port diameter for configuration D varies, so times must be calculated for the four diameters in Table 6. The exit velocities of Tables 6 and 8 can be used as long as $m_a = m_p$ or as long as the stoichiometric m_a/m_p occurs at an x/d within the potential core, since the velocity remains unchanged within the potential core. The axial distances and times to $m_a/m_p = 1$ and stoichiometric m_a/m_p are shown in Tables 10 through 12. Several observations can be made from the data in Table 10 through 12.

1. Stoichiometric fuel-air ratios are reached at relatively short distances from the flare nozzle compared to the total plume length.

2. The planes in which stoichiometric fuel-air ratios are reached occur within the potential core and mixing region.

3) Table 10 shows that the times to reach $m_a = m_p$ increase in the order 368D – 322D – 277D – 284D. This is the same order for increasing apparent temperature (Figures 7 and 8), and decreasing reversal (Tables 2 through 5).

4. Configurations A and B require an order of magnitude longer time to reach $m_a = m_p$.

5. The times to reach stoichiometric m_a/m_p increase in the order 368D – 322D –277D –284D – 368A – 322A –277A – 284A for configurations A and D. The stoichiometric time for 284 increased more, relative to the other formulations, over the time to reach $m_a = m_p$. All A and B configurations show relatively long times compared to configuration D.

6. It should be noted that the times to reach stoichiometric m_a/m_p for configuration F would be slightly faster than those for configuration D.

To give the times to stoichiometric m_a/m_p more than just a relative meaning, the chemical reactions times and turbulent mixing times must be calculated for comparison. Turbulent mixing times cannot be calculated from the data available, but an estimate can be made if it is assumed that turbulent and laminar mixing times are analogous if an eddy diffusivity (ϵ) is substituted for the molecular diffusivity (D)[13]

$$t^* = \frac{d^2 X_o}{16\epsilon X_{st}} \tag{21}$$

where X_o = initial mole fraction of fuel in jet

X_{st} = mole fraction of fuel in stoichiometric mixture

ϵ = eddy diffusivity, cm^2/s

Now the eddy diffusivity must be approximated by an empirical equation used for pipe flow.[13]

$$\epsilon = 0.00255 f v_o d \tag{22}$$

where f = constant ~1

v_o = initial velocity

Combining equations 22 and 21 and using f=1

$$t^* = 24.5 \frac{d \, X_o}{v_o \, X_{st}} \tag{23}$$

The initial mole fraction of fuel can be calculated from the PEP calculations considering only species that will oxidize; X_{st} can be calculated from $(m_a/m_p)_{st}$; and d and v_o have already been calculated. The last column of Table 12 gives the calculated t^*. Turbulent mixing times (t^*) are about a factor of 20 greater than the times for the plume to reach the stoichiometric m_a/m_p. This indicates that mixing to the molecular level requires a longer time than is available when stoichiometric conditions exist. It should be noted, however, that the t^* calculated is only an approximation.

The important questions are: how do times to $(m_a/m_p)_{st}$ and t^* compare with chemical reaction times, and how fast is the plume temperature decreasing before afterburning ignition occurs? A single number for reaction time cannot be calculated due to the complexity of the

afterburning reactions, but an order of magnitude reaction time can be
calculated for a specific reaction. The reaction time of a bimolecular
reaction can be expressed as

$$t_r = \frac{1}{k_2 c} \tag{24}$$

where k_2 = rate constant, cm^3/molecule·s

c = concentration, molecules/cm^3

For example, the reaction of $CO \rightarrow CO_2$ occurs as follows

$$CO + OH \xrightarrow{k_2} CO_2 + H \tag{25}$$

and $k_2 = 9 \times 10^{-13} \exp(-540/T)$.[14] Doing the calculation for 322 Sylgard
and using the exit plane conditions $T = 1744K$ and $[CO] = 0.024$ mol/
100 g [1.4×10^{16} molecules/cm^3], $t_r = 0.1$ ms. Similar calculations can
be performed for other reactions: $t_r \sim 0.01$-1.0 ms is a good ballpark
estimate. Table 12 shows that the times to reach a stoichiometric mix-
ture are of the same order of magnitude as t_r. Since the times to
stoichiometric mixture are faster for Sylgard flares than for the HTPB
flares, it can be concluded that the Sylgard flares would give less
reaction efficiency (afterburning efficiency). The mixing times (Table
12) are longer than the reaction time, so complete reaction is unlikely
unless temperature can be maintained until mixing at the molecular level
occurs. It should also be noted that the combustion of particles such
as carbon or silicon carbide may take several milliseconds to go to
completion (depending on particle size). The most important conclusions
to be drawn from this discussion of afterburning efficiency are:

1. Thermodynamic predictions of temperatures and species may not
be correct due to incomplete combustion.

2. Even turbulent mixing is not fast enough to mix air and fuel on
the molecular level when plume velocities are at or near sonic.

3. If afterburning is delayed past the point where stoichiometric
conditions exist, the plume temperature may drop below the ignition
temperature (this has been observed by Schadow[15]). Even if reactions
are taking place at a decreased rate, the average temperature of the
plume will decrease from that predicted thermodynamically.

4. Afterburning efficiency can be ranked in three classes: (1) low
afterburning efficiency—little chemical reaction occurs during after-
burning and temperature decreases due to radiation and convention:

(2) complete reaction takes place and afterburning efficiency is about 100%; and (3) reactions occur at reduced rates and may be diffusion-limited; afterburning efficiency is intermediate.

5. 368F, E, then D and 322F, E, then D are in the low afterburning efficiency class, which gives a lower average plume temperature than Figure 13 indicates. This agrees with Figures 7 and 8 and with the high reversals observed (Tables 2 and 3).

6. 277D would have a lower afterburning efficiency than 284D, but both are more efficient than the corresponding Sylgards. The times to $(m_a/m_p)_{st}$ in Table 12 for 284D are comparable to t_r, and 284D could have a high afterburning efficiency, which agrees with the low reversals (Table 4), and high radiant efficiencies (Table 4 and Figure 4).

7. The times to $(m_a/m_p)_{st}$ for configuration A and B flares are long, and they should have the highest afterburning efficiencies and the highest average plume temperatures. This agrees with the low reversals (Tables 2-5) and high radiant efficiencies (Tables 2-5). This comparison is the best since it compares configurations within the same formulation. The reasons for decreasing radiant efficiency and increased reversal as mass flow rate increases can now be understood. The leveling off of radiant efficiency, and reversal (Figure 4 and Tables 2-5) at high $\dot{m}$, are also explained in terms of afterburning efficiency.

So far, nothing has been said about afterburning species, which will significantly affect the radiant emissions of flares. The afterburning species shown in the Appendix will be increasingly affected as the afterburning efficiency decreases. This will make prediction of plume species concentrations impossible unless the afterburning effi-ciency is about 0 or 100%. Figures 15-21 show the variation of im-portant plume species as a function of m_a/m_p, assuming equilibrium (taken from the Appendix).

RADIANT EMISSION OF FLARE PLUMES

The emission properties of the major afterburning species are discussed before plume emission models are given. The experimental emission data would seem to indicate that the plume emits primarily as a graybody. This indicates mainly particle emission or an optically-thick plume; however, particles do not always emit graybody. It has been shown that "small"[4] particles emit only at their dipole resonance frequency, which depends upon the optical properties of the solid and

---

[4] "Small" is of the order, or smaller than, the wavelength of the emission band.

upon lattice force constants.[16] As the particles become larger compared to the wavelength, the sharp resonance emission decreases and the emission finally appears graybody (i.e., the particles become optically-thick). For large numbers of particles in an emitting cloud, the effects of scattering and self-absorption must be considered. As the optical density of the particle cloud increases, the emission properties change, and at optically-thick densities the emission appears graybody. Most particles have dipole resonances in the long wavelength IR from about 8μm to several hundred micrometers, which are not important in the 2-5μm IR window.[17, 18]

Figure 15 shows $Mg(g)$ versus m_a/m_p for all four formulations. The concentrations are high, but $Mg(g)$ emits mainly in the visible and ultraviolet.[19] When the plume temperature drops below 1373 K, graybody emission from $Mg(l)$ droplets will become important if any Mg remains unoxidized past $m_a/m_p > 5$.

Figure 16 shows that MgO (s) concentration is high, but small MgO (s) particles will emit at their dipole resonance wavelength of about 17μm.[2] Therefore, no emissions in the 2-5μm region from $MgO(s)$ will be observed unless the plume is optically-thick or the particle sizes are > 20μm.

The variation of C(s) is shown in Figure 17. Note that the C(s) concentration increases in the order 368 - 322 - 277 - 284; this is the same order observed for increasing radiant efficiency (Figure 4). The carbon concentrations are probably maintained at higher levels than the thermodynamics indicate since combustion times for C(s) are slow compared to mixing times. Carbon emits graybody (no allowed IR dipole resonance) and is the most important emitting species due to its high emissivity in the 2-5μm region.[2, 20]

Figure 18 shows the $CO(g)$ concentration variation. $CO(g)$ has an emission band at 4.6μm,[21] and the HTPB formulations show about a factor of two higher concentrations than the Sylgards. The peak $CO(g)$ concentrations occur at low m_a/m_p, which is very close to the flare grain. As more air is added, the plume becomes optically-thin in CO. Since m_a/m_p of about 50 is obtained for the plume lengths observed, the $CO(g)$ emissions will not be of major importance.

The $CO_2(g)$ concentration is shown in Figure 19 for equilibrium combustion and perfect mixing. In the 2-5μm region, $CO_2(g)$ has a strong band at 4.3μm and a weaker band at 2.7μm.[21] The low emissivity of gases compared to C(s) and the low optical density of CO_2 would indicate only a small emission contribution from $CO_2(g)$. The high $CO_2(g)$ concentration of 284 HTPB and the high afterburning efficiency of 284 HTPB would also indicate that C(s) emission dominates $CO_2(g)$ emission since the experimentally-observed reversals for 284 HTPB are low.

Figure 20 shows SiC(s) and SiO(g) for the Sylgard formulations. Small SiC(s) particles will emit at their dipole resonance wavelength of about 13μm[16]. The SiO(g) emits at 8.1μm and 11.9 μm[22].

The variation of $H_2O(g)$ versus m_a/m_p is shown in Figure 21. Water has strong bands at 6.3, 2.7, and 1.9μm, and weak bands at 3.2, 1.4, 1.1, and 0.94μm.[21] The high concentration of $H_2O(g)$ can influence emission in the 2-3μm region if high afterburning efficiencies exist.

Minor species such as $MgSiO_3(g)$, HC1, HF, and others found in the Appendix will probably have little influence on the plume emissions in the 2-5μm region.

In summary, the C(s) is probably the most important emitting species in the 2-5μm region, with contributions from Mg(1), Mg(s), large MgO(s) and SiC(s) particles, CO, CO_2, and H_2O. However, without spectral data it is difficult to make any definite conclusions about plume emitting species.

The prediction of IR signatures of a hot plume of particles and gases is a complex problem. However, two extreme models can be discussed: (1) optically-thin; and (2) optically-thick. The emissions calculated from these models can be compared to the experimental radiant intensities and radiant efficiencies.

Optically-thin Plume

Assuming that the plume expands to low pressures and that plume diameters are small, then gaseous radiation is a second order effect compared to particle emission and the plume is then optically-thin. Also, if the plume is at low pressures, convective heat loss between particles and gases can be ignored, and particles will lose energy only by radiation. It must also be assumed that afterburning makes no contribution to plume energy. thus the only energy loss mechanism for the hot particles is radiation and[23]

$$J(\lambda_1-\lambda_2)_i = \frac{4.185}{4\pi} \dot{m}_i \int_{T_f}^{T_o} K(\lambda_1-\lambda_2) \, C_{p_i} \, dT \qquad (26)$$

374

where $J(\lambda_1-\lambda_2)_i$ = radiant intensity in $\lambda_1-\lambda_2$ region due to particle i, W/sr

$\dot{m}_i$ = solid particle mass flow rate for particle i, g/s

Cp_i = specific heat for particle i, cal/g·K

and

$$K(\lambda_1-\lambda_2) = \int_{\lambda_1}^{\lambda_2} \varepsilon_p\, N_\lambda(\lambda,T)d\lambda \bigg/\!\!\int_0^\infty \varepsilon_p\, N_\lambda(\lambda,T)d\lambda \qquad (27)$$

(the fraction of energy emitted between λ_1&λ_2)

ε_p = particle emissivity

$N_\lambda(\lambda,T)$ = blackbody spectral radiance, W/cm^2·sr·μm

T_o – initial particle temperature, K

T_f – final particle temperature, K

The total radiant intensity is

$$J(\lambda_1-\lambda_2) = \sum_i J(\lambda_1-\lambda_2)_i, \qquad (28)$$

and the radiant efficiency is

$$E(\lambda_1-\lambda_2) = \frac{1}{\dot{m}} \sum_i J(\lambda_1-\lambda_2)_i \qquad (29)$$

where $\dot{m}$ = total mass flow rate, g/s

Note that $\dot{m}_i/\dot{m}$ is just the weight fraction of the ith species, and can be calculated from the PEP data. E(2-3) and E(3-5) for the four formulations can be calculated if (1) the average C_p and average $K(\lambda_1 - \lambda_2)$ are used, (2) the exit temperature is used for T_o, and (3) $T_f = 273K$. The top numbers in Table 13 show the calculations for the E(2-3) and E(3-5) using the exit temperature and considering only carbon emissions. These radiant efficiencies are much lower than the experimental data in Tables 2 through 5 and Figures 7 and 8. The bottom set of numbers in Table 13 uses the highest afterburning temperature and considers all the solid species present. These radiant efficiencies are in better agreement with the experimental data for high mass flow rate Sylgard flares. (Tables 2 through 5 show measured E(2-3) $\sim$ 40-60 J/g·sr and E(3-5) $\sim$ 65-90 J/g·sr for the high mass flow rate Sylgard flares.)

The poor agreement of radiant efficiencies of the optically-thin model is not surprising, since the heat term due to afterburning has not been completely considered, aerodynamic heating is ignored, heat transfer may be important, gaseous emission cannot be completely ignored, and the scattering contribution cannot be neglected. However, the radiant efficiencies in Table 13 should be a lower limit.

Optically-thick Plume

The radiant intensity for the optically-thick plume is

$$J(\lambda_1 - \lambda_2) = \frac{A \, \varepsilon(\lambda_1 - \lambda_2) K(\lambda_1 - \lambda_2)}{\pi} \sigma T^4 \qquad (30)$$

Where A = projected area of radiating surface, cm^2

σ = Stefan-Boltzmann constant = 5.7×10^{-12} $W/cm^2 \cdot K^4$

$\varepsilon(\lambda_1 - \lambda_2)$ = average emissivity in $\lambda_1 - \lambda_2$ region

Equation (30) is the radiant intensity of a surface emitting as a gray-body ($\varepsilon < 1$) and shows no dependence on mass flow rate. To calculate the radiant intensity of optically-thick flare plumes, a reasonable temperature and projected area must be determined. The average afterburning temperature (from $m_a/m_p = 0$ to $m_a/m_p = 50$) seems appropriate; however, a linear average would be incorrect. A T^4 average must be used to give the higher temperatures the proper weighting. For example, using Figure 13 the linear average afterburning temperature for 322 Sylgard is 1150K, but the T^4 average is 1610K. By using 1610K in equation (30) $J(\lambda_1 - \lambda_2)$ is, in effect, integrated over the axial temperature distribution of the plume. The projected area of the plume can be estimated from the motion picture coverage, but this will only give the visible projected area, which is smaller than the emitting area in the 2-5μm region. Using the visible projected area averaged over the burn time is a reasonable

approximation, since $J(\lambda_1 - \lambda_2)$ depends on the first power of the area only. For this optically-thick approximation, $\varepsilon(2-5) = 1$ can be used, but differences between $\varepsilon(2-3)$ and $\varepsilon(3-5)$ will be important in determining $J(2-3)$ and $J(3-5)$. The value of $K(\lambda_1 - \lambda_2)$ must be averaged over the temperature range; in this case a linear average is appropriate, which will tend to weight the lower temperatures. The optically-thick calculations are shown in Table 14 for 322 Sylgard and 284 HTPB configurations A, B, C, D, and F. The radiant efficiencies in Table 14 were calculated by dividing the experimental mass flow rates into the calculated radiant intensities. It should be noted that the radiant efficiencies in Table 14 are about a factor of two to three higher than the experimental radiant efficiencies in Tables 2 and 4.

Several final observations can be made from the calculations in Tables 13 and 14 as compared to the experimental emission data.

1. The optically-thick model agrees more favorably with the experimental data than the optically-thin model.

2. Even when the maximum afterburning temperature was used, the optically-thin model gave low radiant efficiencies.

3. The T^4 average afterburning temperatures used in the optically-thick model are high because of the diminished afterburning efficiency discussed in the Afterburning and Turbulent Mixing section. The high mass flow rate Sylgard flares had low afterburning efficiency. A drop to 1200-1300K for the T^4 average plume temperature would give good agreement between optically-thick radiant efficiencies and experimental radiant efficiencies.

4. If the temperatures in Figures 7 and 8 (calculated from the experimental reversals) are used in equation (30), the resultant calculated radiant intensities are too low.

SUMMARY

The experimentally-observed radiant efficiencies are between the predictions from optically-thick and optically-thin plume models.

The very low values of radiant efficiency for the optically-thin model with no afterburning show the importance of the afterburning of flare plumes on generating high radiant efficiencies.

Afterburning efficiency explained in terms of the relative times for reaction and turbulent mixing shows the reasons for decreased radiant efficiency and increased reversal when a higher mass flow rate configuration is used.

In general, the lower the plume velocity, the higher the afterburning efficiency and the lower the reversal.

Solid carbon appears to be the most important emitting species, with contributions from $Mg(1)$, $MgO(s)$, $SiC(s)$, CO, CO_2, and H_2O.

The Sylgard binder gave higher linear burning rates, which in turn led to lower radiant efficiencies and higher reversals than the corresponding HTPB configurations.

O/F ratios were all fuel-rich in order to achieve increased energy from afterburning; the most fuel-rich formulation (284) gave the highest $C(s)$ concentration. $C(s)$ is the most efficient radiating species in the $2-5\mu m$ region.

378

REFERENCES

1. V.R. Stull and G.N. Plass. "Emissivity of Dispersal Carbon Particles", J. Opt. Soc. Am., 50. 1960, pp. 121-129.

2. Space and Missile Systems Organization. "Handbook of the Infrared Optical Properties of Al_2O_3, Carbon, MgO, and ZrO_2", by M.E. Whitson, Jr., Aerospace Corporation, El Segundo, Calif., SAMSO-TR-75-131, 1975.

3. Aerodyne Research, Inc. "Rocket Exhaust Aluminum Oxide Particle Properties", by B.W. Worster and R.H. Kadomiya. ARI, ARI-RR-30, August 1973.

4. Aerodyne Research, Inc. "Particulate Infrared Radiation in Aluminized Solid-Fuel Rocket Plumes", B.W. Worster. ARI, ARI-RR-19, March 1973.

5. S.J. Morizumi and H.J. Carpenter. "Thermal Radiation from the Exhaust Plume of Aluminized Composite Propellant Rocket", J. Spacecraft, 1(5), pp. 501-507, 1964.

6. Naval Weapons Support Center. "A Mathematical Model of Flare Plume Combustion and Radiation", by J.F. Tanner, Jr. NWSC, Crane, Indiana, NWSC/CR/RDTR-9, June 1975.

7. Dow Corning. "Dow Corning 200 Fluid", Dow Corning Bulletin 05-061, November 1963.

8. Academic Press. Inorganic Polymers, ed. F.G.A. Stone and W.A.G. Graham. 1962, p. 247.

9. Private Communication with Russell Reed, Jr., Naval Weapons Center, China Lake, Calif.

10. E.W. Price. "One-Dimentional, Steady Flow with Mass Addition and the Effect of Combustion Chamber Flow on Rocket Thrust", Jet Propulsion, 15(2). 1955, pp. 61-66.

11. John Wiley and Sons, Inc. Comubustion Aerodynamics, J.M. Beer and N.A. Chigier, 1972.

12. F.M. Page, W.G. Roberts, and H. Williams. 15th International Combustion Symposium, 1974, p. 617.

13. Princeton University Press. Combustion Processes, ed. B. Lewis, R.N. Peace, and H.S. Taylor, 1956, pp. 312-404.

14. Rocket Propulsion Establishment. "Gas-Phase Reaction Rate Coefficients for Rocketry Applications, by D.E. Jensen and G.A. Jones, RPE, Westcott, RPE-TR-71/9, 1971.

15. K. Schadow. "Fuel-Rich, Particle-Laden Plume Combustion". AIAA 13th Aerospace Sciences Meeting, Pasadena, Calif., Jan. 1975, AIAA Paper 75-245.

16. Private communication with D.L. Decker, Code 6018, Naval Weapons Center, China Lake, Calif.

17. G.R. Hunt and L.M. Logan. "Variation of Single Particle Mid-Infrared Emission Spectrum with Particle Size", App. Opt. 11, p. 142, 1972.

18. G.R. Hunt. "LWIR Emissive Behavior of Materials for Use in Pyrotechnic Decoys", AFCRL, (to be published).

19. John Wiley and Sons, Inc. Flame Spectroscopy, by R. Mavrodineanu and H. Boiteux, 1965.

20. O.Halpern and H. Hall. "The Ionization Loss of Energy of Fast Charged Particles in Gases and Condensed Bodies", Phys. Rev., 73, 1945, pp. 477-486.

21. Office of Naval Research. Handbook of Military Infrared Technology, ed. W. L. Wolfe, 1965.

22. Van Nostrand Reinhold Company. Spectra of Diatomic Molecules, by G. Herzberg, 1950, p. 570.

23. W.S. Rothwell and H.L. Schick. "Emission Spectra from a Stream of Cooling Particles", J. Spacecraft, 11, 1974, p. 597.

TABLE 1. Flare Formulations.

Ingredient	322	368	284	277
Mg (gran 16) (coated with 3% Viton-A)	19.9% (0.6% Viton)			
Mg (gran 17) (coated with 5% Viton-A)	39.0% (1.9% Viton)			
Mg (gran 16)			64%	54%
Mg (gran 17)		57.9%		
AP (5μm)	19.5%	23.7%	20%	30%
Sylgard 182 binder	21.6%	18.4%		
Hydroxy terminated polybutadiene (HTPB) binder			16%	16%

TABLE 2.   322 Test Results.

Grain configuration	Number of flares in average	Burn time, seconds	Radiant intensity, W/sr		Efficiency, J/g·sr		Mass flow rate, g/s	Reversal
			2-3μm	3-5μm	2-3μm	3-5μm		
A	4	30.7 ±2.5	736 ±23	632 ±32	290 ±18	251 ±33	2.6 ±0.2	0.86 ±0.04
B	1[a] 3 inhibitor failures	21.3	2,510	2,570	218	224	11.5	1.03
C	4	4.6 ±0.4	4,070 ±480	4,550 ±310	136 ±7.5	153 ±13.5	29.8 ±1.9	1.12 ±0.09
D	3[b]	6.1 ±0.1	1.455 ±28	2,075 ±100	65 ±1.7	93 ±4.7	22.3 ±0.4	1.43 ±0.05
E	4	5.6 ±0.1	1,355 ±175	1,955 ±37.3	66 ±7.8	94 ±2.8	20.8 ±0.4	1.48 ±0.23
F	2[c]	3.2 ±0.4	1,720 ±284	2,360 ±145	57 ±3.0	80 ±4.0	30.0 ±4.0	1.40 ±0.10

[a]Inhibitor or grain rupture at end of burn.

[b]One inferior casting not fired.

[c]One inferior casting and other poor burn eliminated statistically.

TABLE 3.   368 Test Results.

Grain configuration	Number of flares in average	Burn time, seconds	Radiant intensity, W/sr		Efficiency, J/g·sr		Mass flow rate, g/s	Reversal
			2-3μm	3-5μm	2-3μm	3-5μm		
A	1[a]	25.4	432	468	140	151	3.1	1.08
B	2[b]	28.0 ±1.0	1,595 ±24	1,780 ±12	170 ±4	190 ±3	9.3 ±0.2	1.12 ±0.01
C	4	6.9 ±0.6	1,255 ±118	1,690 ±106	68 ±3	93 ±4	18.4 ±1.5	1.36 ±0.08
D	4	6.3 ±0.3	941 ±81	1,560 ±129	46 ±3	77 ±5	20.3 ±0.7	1.66 ±0.02
E	4	6.0 ±0.3	999 ±36	1,640 ±44	53 ±3	87 ±3	18.9 ±1.0	1.64 ±0.06
F	4	2.7 ±0.4	1,520 ±173	2,385 ±274	43 ±4	67 ±2	36.0 ±4.5	1.57 ±0.10

[a]Three inhibitor failures and one failed near end of burn.

[b]Two inhibitor failures.

TABLE 4. 284 Test Results.

Grain configuration	Number of flares in average	Burn time, seconds	Radiant intensity, W/sr		Efficiency, J/g·sr		Mass flow rate, g/s	Reversal
			2-3μm	3-5μm	2-3μm	3-5μm		
A	4	74.0 ±1.0	297 ±18	325 ±26	302 ±15	331 ±33	0.98 ±0.03	1.10 ±0.07
B	3[a]	79.0 ±2.5	948 ±59	1,170 ±76	310 ±14	382 ±18	3.06 ±0.04	1.23 ±0.01
C	4	18.4 ±4.6	2,040 ±409	2,590 ±665	279 ±21	351 ±4.5	7.39 ±1.91	1.27 ±0.10
D	4	21.0 ±5.0	1,950 ±608	1,980 ±488	334 ±32	342 ±30	5.87 ±1.34	1.10 ±0.09
E	2[b]	21.0 ±3.0	1,935 ±251	1,990 ±184	372 ±6	385 ±20	5.25 ±0.75	1.03 ±0.03
F	3[c]	9.1 ±0.8	3,290 ±345	3,340 ±373	356 ±8	361 ±10	9.23 ±0.80	1.02 ±0.02

[a]One flare statistically eliminated.
[b]One poor casting and other no radiometric data.
[c]One erratic burn.

TABLE 5. 277 Test Results.

Grain configuration	Number of flares in average	Burn time, seconds	Radiant intensity, W/sr		Efficiency, J/g·sr		Mass flow rate, g/s	Reversal
			2-3μm	3-5μm	2-3μm	3-5μm		
A	4	74.0 ±2.0	377 ±20	405 ±14	360 ±12	387 ±11	1.04 ±0.03	1.07 ±0.06
B	3[a]	76.0 ±2.0	1,080 ±80	1,130 ±42	336 ±29	352 ±18	3.21 ±0.05	1.05 ±0.06
C			Would not release from case					
D	3[b]	14.0 ±3.0	1,395 ±20	1,890 ±100	154 ±30	207 ±30	9.40 ±1.70	1.35 ±0.06
F	3[c]	14.0 ±0.6	1,280 ±81	1,665 ±58	164 ±7.0	214 ±4.0	7.80 ±0.40	1.31 ±0.05
I	3[c]	8.3 ±0.2	1,965 ±274	2,460 ±232	188 ±20	235 ±18	10.4 ±0.3	1.27 ±0.15

[a]One no burn.
[b]No radiometric data.
[c]Poor casting.

TABLE 6. Internal Flare Parameters for Configuration D

	γ,Cp,Ts (p_o=10 psi)	Po/p* ADIAB	Po/p* ISEN	ADIABATIC Choked Po (p_a=5.5 psi)	ISENTROPIC Choked Po (p_a=5.5 psi)	Po,(psi) at Center for Config. D t=const r=f(po)	Diameters used in Calc., cm	Times to Diameters r=c / r=f(po) (Average)	ṁ, g/s		δ		v,ft/s †		r=c cm/s
322 ρp=1.60	1.18 0.36 cal/gK 1818K	2.18	1.76	≥12.0	≥9.7	15.6 10.1 8.1 / 6.6	47.3 16.2 9.4 / 7.0	d_0=.9525 d_1=1.51 d_2=2.06 d_f=3.175	0 1.35 2.69 / 5.39	0 .591 1.38 / 3.10	12.4 19.9 27.1 / 41.2 25.2	37.5 32.2 33.8 / 47.2 37.7	1 .987 .91 .71	1 1 .971 .77	2190 1865 1410 915	2190 2190 1720 1030	.206
368 ρp=1.58	1.19 0.35 1876K	2.19	1.77	≥12.0	≥9.7	18.3 11.6 8.9 / 6.9	49.7 17.0 9.5 / 7.0		0 1.19 2.37 / 4.75	0 0.58 1.35 / 3.12	14.1 22.3 30.4 / 46.8 28.4	38.3 32.9 33.4 / 46.8 37.8	1 .995 .952 .79	1 1 .977 .78	2265 2050 1650 1110	2265 2265 1825 1090	.234
284 ρp=1.55	1.20 0.35 1520K	2.20	1.77	≥12.1	≥9.7	7.2 6.1 5.85 / 5.62			0 3.36 6.67 / 13.4		4.9 7.8 10.6 / 16.3 9.9		.81 0.6 .46 .31		2081** 1065 695 510 330		.083
277 ρp=1.57	1.21 0.37 1902K	2.21	1.78	>12.2	≥9.8	7.75 6.41 6.02 / 5.75			0 3.36 6.67 / 13.4		5.0 7.9 10.7 / 16.5 10.0		.89 .68 .53 .36		2454** 1500 965 700 460		.083

* 1 psi = 6.89 kPa

† 1 ft/sec = 30.5 cm/sec

** sonic velocity

TABLE 7.   Internal Flare Parameters for Configuration F

	A_p, cm²	A_b, cm²	t_b, seconds	$\dot{m}$ (total), g/s	P_o, psi*	δ	v, ft/sec‡
322	2.83 5.17 7.16 7.92	201 190 133 127	0 0.62 1.23 1.54	66.2 62.6 43.8 41.8	21.0 10.9 7.0 6.6	1 0.996 0.79 0.71	2190 2000 1075 915
368	"	"	0 0.54 1.09 1.36	74.0 70.0 49.0 47.0	24.2 12.5 7.5 6.9	1 1 0.85 0.79	2265 2265 1260 1110
284	"	"	0 1.53 3.06 3.83	25.9 24.4 17.1 16.3	8.4 6.2 5.8 5.6	0.92 0.64 0.35 0.31	1375 750 375 330
277	"	"	0 1.53 3.06 3.83	26.2 24.7 17.3 16.5	9.5 6.6 5.8 5.7	0.97 0.72 0.41 0.36	1915 1040 525 460

‡ 1 ft/sec = 30.5 cm/sec

* 1 psi = 6.89 kPa

TABLE 8. Flare Parameters for Configurations A and B

	Experimental ṙ, cm/s	ṁ (total), g/s	t_b, seconds	v, ft/sec‡	Weight Fraction of Gas (from Appendix) at $p_a = 0.37$ atm
322A	0.206	2.6	30.8	113	0.47
332B		8.5		113	
368A	0.234	2.9	27.1	136	0.51
368B		9.4		136	
284A	0.083	1.02	76.5	40	0.52
284B		3.3		40	
277A	0.083	1.03	76.5	56	0.60
277B		3.3		56	

‡ 1 ft/sec = 30.5 cm/s

TABLE 9. Fuel/Oxidizer Ratios

Formulation	Mg/AP	Total Fuel/AP	Exit Temperature, K	Stoichiometric m_a/m_p
284	3.2	4.0	1460	~3.5
322	2.9	4.0	1741	~2.5
368	2.4	3.2	1812	~2
277	1.8	2.3	1840	~2

TABLE 10. Times and Axial Distances to $m_a = m_p$
For Configuration D

	d, cm	v, cm/s	ρ_o, g/cm³	ρ_a, g/cm³	x, cm (to $m_a = m_p$)	t, μs (to $m_a = m_p$)	x/d (when $m_a = m_p$)
322D	0.9525	6.7×10^4	5.7×10^{-5}	4.4×10^{-4}	2.1	31	2.2
	1.51	5.7×10^4			3.4	60	
	2.06	4.3×10^4			4.6	107	
	3.175	2.8×10^4			7.1	250	
368D	0.9525	6.9×10^4	5.8×10^{-5}	4.4×10^{-4}	2.1	30	2.2
	1.51	6.2×10^4			3.4	55	
	2.06	5.0×10^4			4.6	92	
	3.175	3.4×10^4			7.1	209	
284D	0.9525	3.2×10^4	6.1×10^{-5}	4.4×10^{-4}	2.2	69	2.3
	1.51	2.1×10^4			3.5	167	
	2.06	1.5×10^4			4.8	320	
	3.175	1.0×10^4			7.3	730	
277D	0.9525	4.6×10^4	4.9×10^{-5}	4.4×10^{-4}	1.9	41	2.0
	1.51	2.9×10^4			3.1	107	
	2.06	2.1×10^4			4.2	200	
	3.175	1.4×10^4			6.5	460	

388

TABLE 11. Times and Axial Distances to $m_a = m_p$
For Configuration A and B

	d, cm	v, cm/s	x, cm (to $m_a = m_p$)	t, ms (to $m_a = m_p$)	x/d (when $m_a = m_p$)
322A	3.175	3450	7.1	2.1	2.2
B	5.715	3450	12.9	3.7	2.2
368A	3.175	4130	7.1	1.7	2.2
B	5.715	4130	12.9	3.1	2.2
284A	3.175	1230	7.3	5.9	2.3
B	5.715	1230	13.2	10.7	2.3
277A	3.175	1715	6.5	3.8	2.0
B	5.715	1715	11.8	6.9	2.0

TABLE 12. Times and Axial Distances to Stoichiometric m_a/m_p

	Stoichiometric m_a/m_p	Nozzle Diameter d, cm	Stoichiometric Mixture Occurs at x, cm	x/d	t, ms	X_{st} and (X_o)	t*, ms
322D	~2.5	0.9525	3.7	3.9	0.06	0.24	1.2
		1.51	5.9		0.10	(0.77)	2.1 } t*=20.2t
		2.06	8.1		0.19		3.8
		3.175	12.5		0.45		8.9
322A	~2.5	3.175	12.5	3.9	3.6		72
322B	~2.5	5.715	22.5	3.9	6.5		131
368D	~2	0.9525	3.2	3.4	0.05	0.29	0.93
		1.51	5.1		0.08	(0.75)	1.5 } t*=18.6t
		2.06	6.6		0.13		2.4
		3.175	10.7		0.31		5.8
368A	~2	3.175	10.7	3.4	2.6		48
368B	~2	5.715	19.3	3.4	4.7		87
284D	~3.5	0.9525	5.0	5.2	0.16	0.17	3.7
		1.51	7.9		0.38	(0.84)	8.8 } t*=23.3t
		2.06	10.7		0.71		17
		3.175	16.5		1.7		40
284A	~3.5	3.175	16.5	5.2	13.4		312
284B	~3.5	5.715	29.7	5.2	24.1		560
277D	~2	0.9525	2.9	3.1	0.06	0.26	1.5
		1.51	4.7		0.16	(0.82)	4.0 } t*=24.9t
		2.06	6.4		0.30		7.5
		3.175	9.8		0.70		17
277A	~2	3.175	9.8	3.1	5.7		142
277B	~2	5.715	17.7	3.1	10.0		250

TABLE 13. Optically-Thin Radiant Efficiencies

	$T_o(K)$ (Afterburning Maximum Temperature)	Weight Fraction C(s) and (Total Solids)	Average C_p for Carbon (Total Solids)	Average K(2-3)	Average K(3-5)	E(2-3), J/g·sr	E(3-5), J/g·sr
322	1744 (2760)	0.04 (0.53)	~0.5 (~0.4)	.18 (.19)	.25 (.21)	1.8 (34)	2.4 (37)
368	1812 (2780)	0.02 (0.49)	~0.5 (~0.4)	.19 (.19)	.25 (.21)	0.97 (31)	1.3 (34)
284	1460 (2790)	0.14 (0.48)	~0.5 (~0.4)	.16 (.19)	.26 (.21)	4.4 (31)	7.2 (34)
277	1840 (2760)	0.11 (0.40)	~0.5 (~0.4)	.19 (.19)	.25 (.21)	5.5 (25)	7.2 (28)

TABLE 14. Optically - Thick Radiant Intensities and Radiant Efficiencies

	Visible Projected Area, cm²	Plume Temperature T⁴ Average (Linear Average)	K(2-3) at Linear Average	K(3-5) at Linear Average	J(2-3), kW/sr	J(3-5), kW/sr	E(2-3), J/g·sr	E(3-5), J/g·sr
A	800				2.5	3.3	960	1300
B	1600	1610 K			5.1	6.6	440	570
322 C	3000		0.26	0.34	9.4	12.3	320	410
D	1400	(1150 K)			4.4	5.7	200	260
F	2000				6.3	8.2	210	270
A	400				1.3	1.6	1300	1600
B	800	1660 K			2.6	3.2	850	1050
284 C	2500		0.27	0.33	8.2	10.0	1100	1350
D	1400	(1210 K)			4.6	5.6	780	950
F	2000				6.6	8.1	710	880

FIGURE 1. End View of Ported Cases and Mandrels.
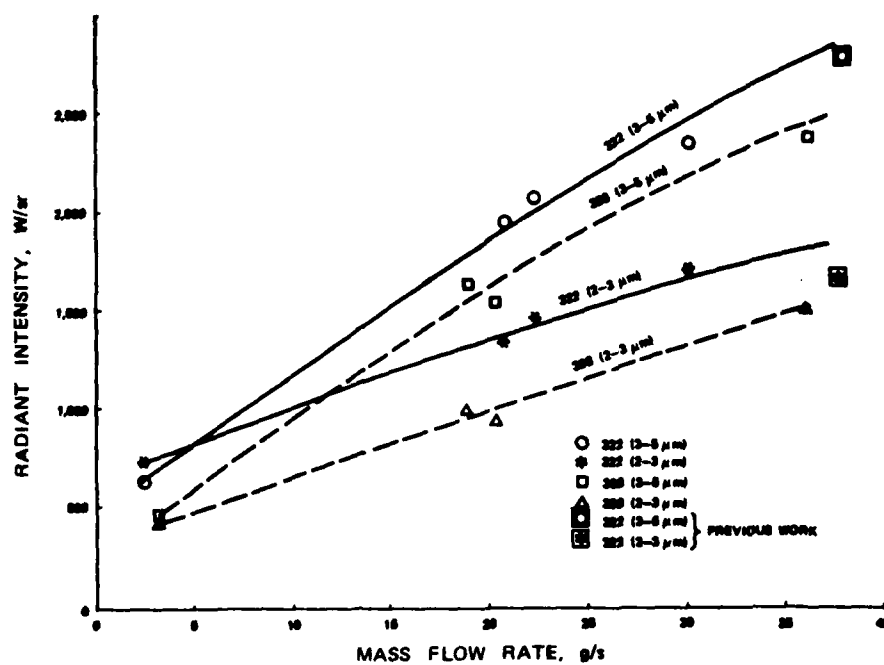
FIGURE 2. Radiant Intensity Versus Mass Flow Rate for
Sylgard Formulations
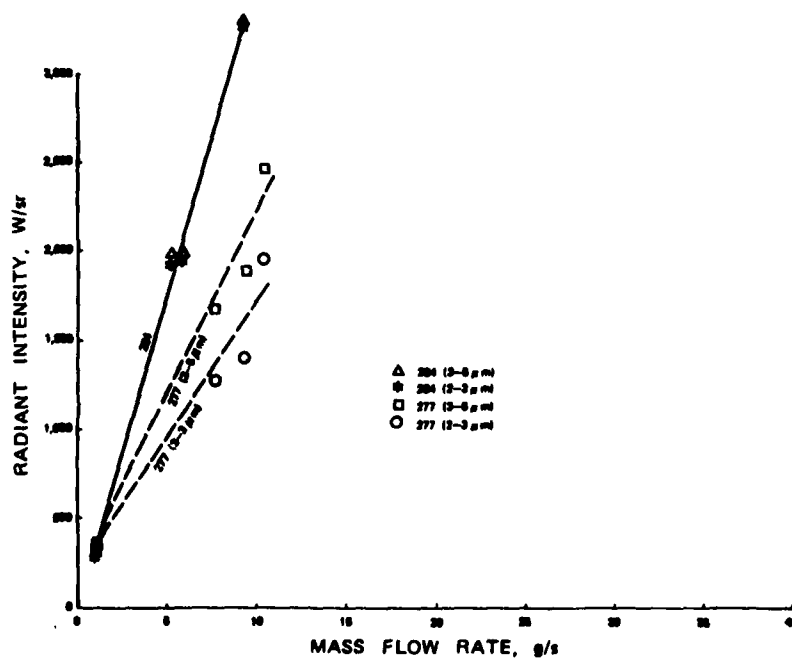
FIGURE 3. Radiant Intensity Versus Mass Flow Rate for HTPB Formulations.
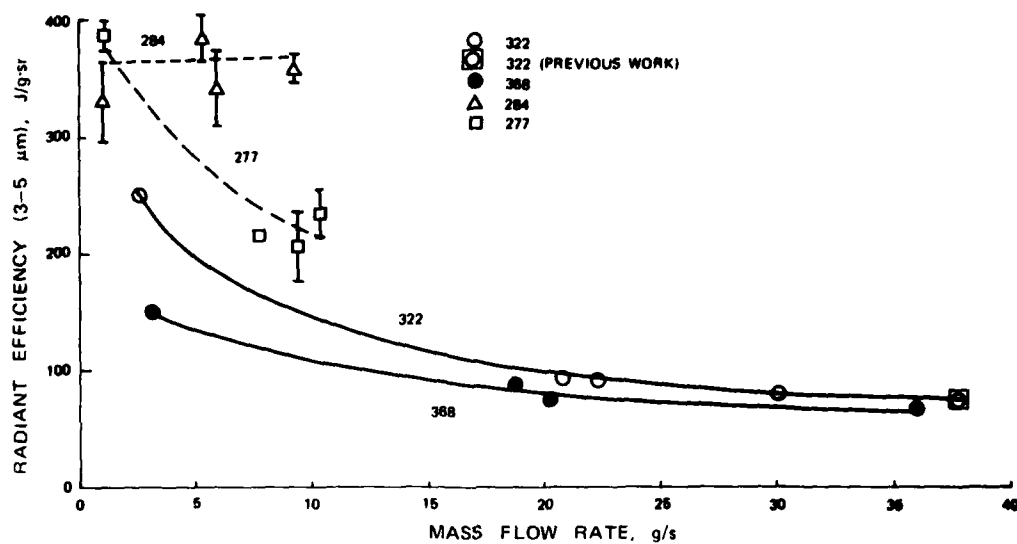
FIGURE 4. Efficiency (3-5μm) Versus Mass Flow Rate
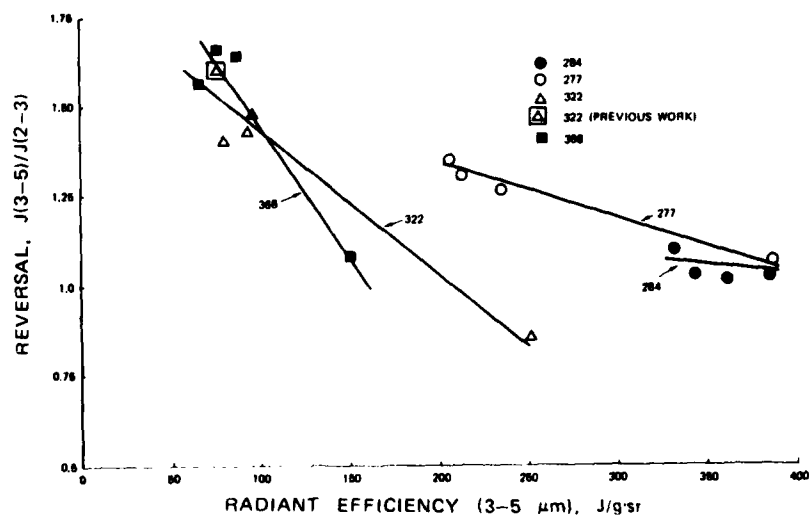
FIGURE 5. Reversal Versus Efficiency (3-5μm)
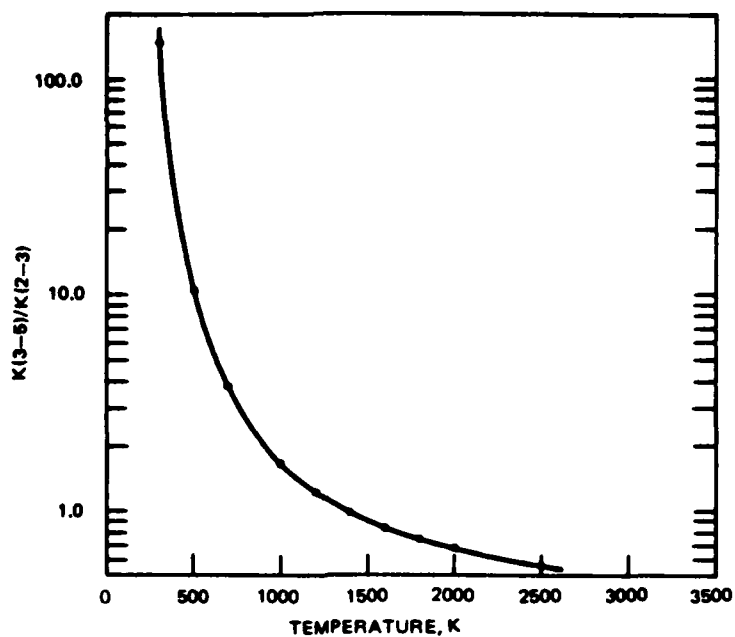
FIGURE 6. Blackbody IR Energy Distribution versus Temperature.
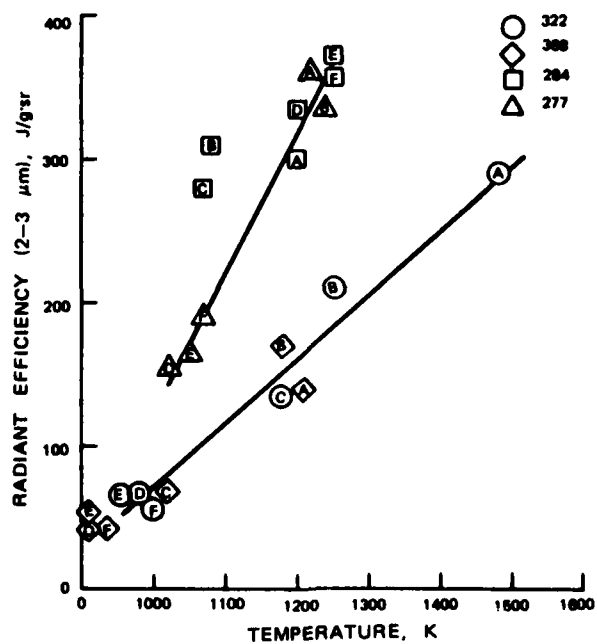
FIGURE 7. Radiant Efficiency (2-3μm) versus Temperature.

396
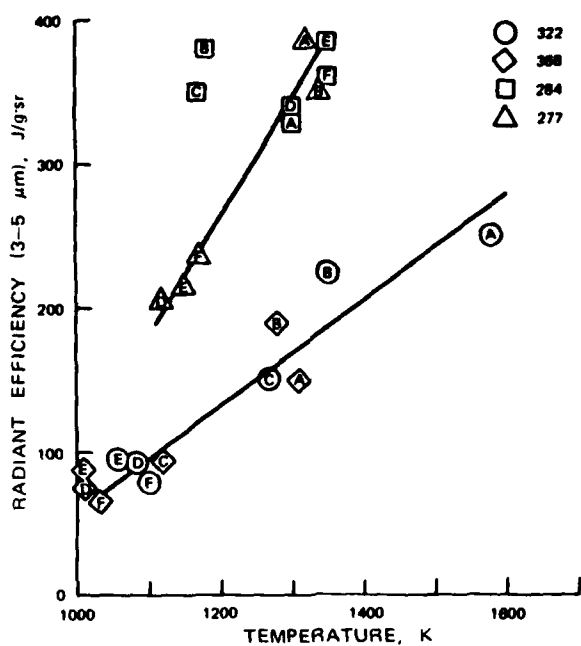
FIGURE 8. Radiant Efficiency (3–5μm)
versus Temperature.
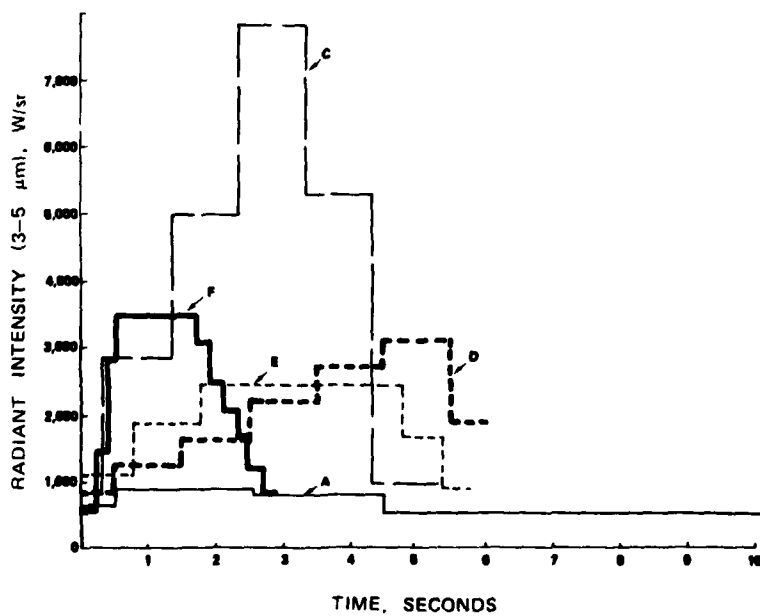
FIGURE 9. Radiant Intensity (3-5μm) Versus Time for
Five Different Configurations of Sylgard-322.
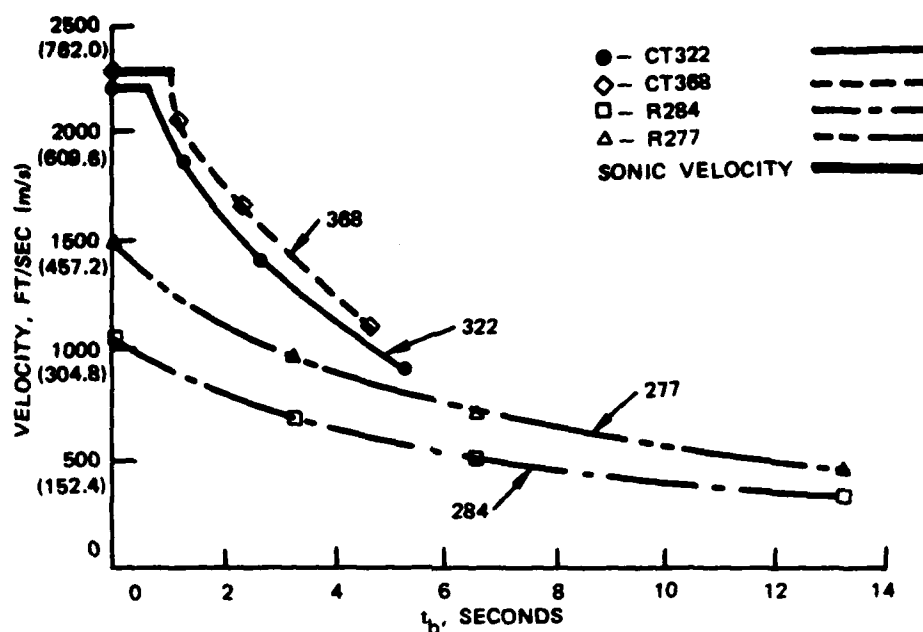
FIGURE 10.   Configuration D Plume Velocity.
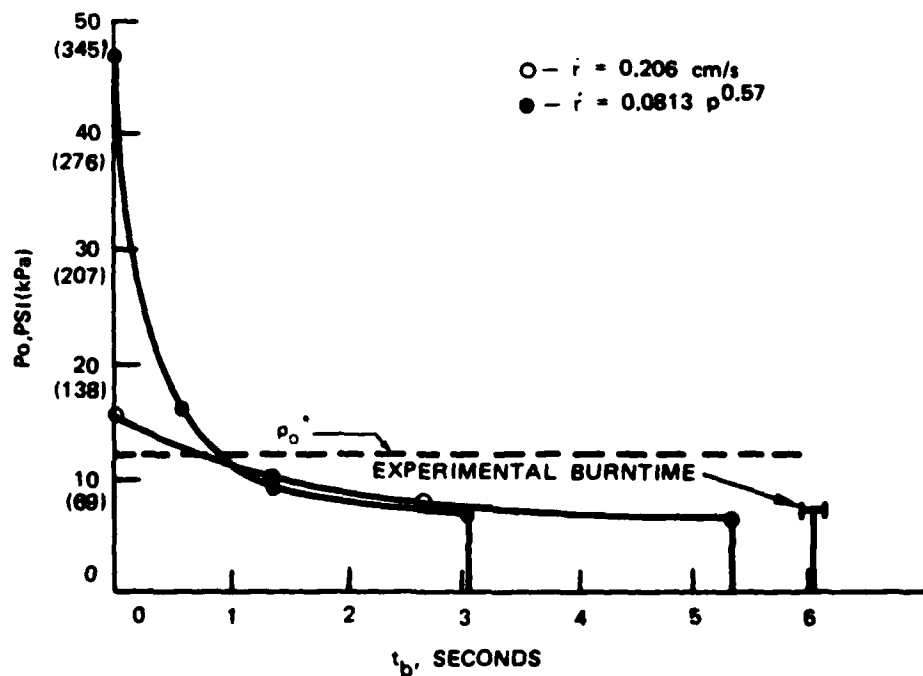
FIGURE 11.   Sylgard 322 Configuration D Internal Pressures.
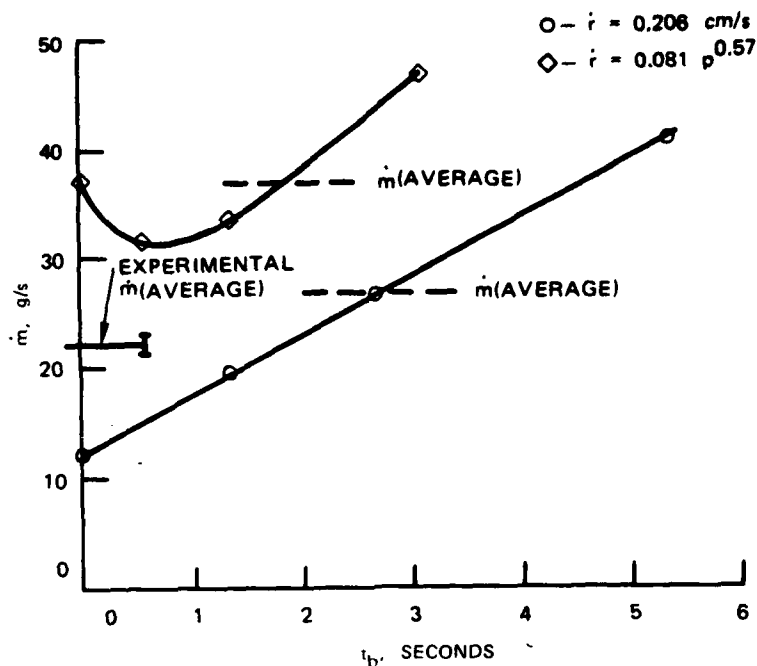
FIGURE 12. Sylgard 322 Configuration D Mass
Flow Rates.
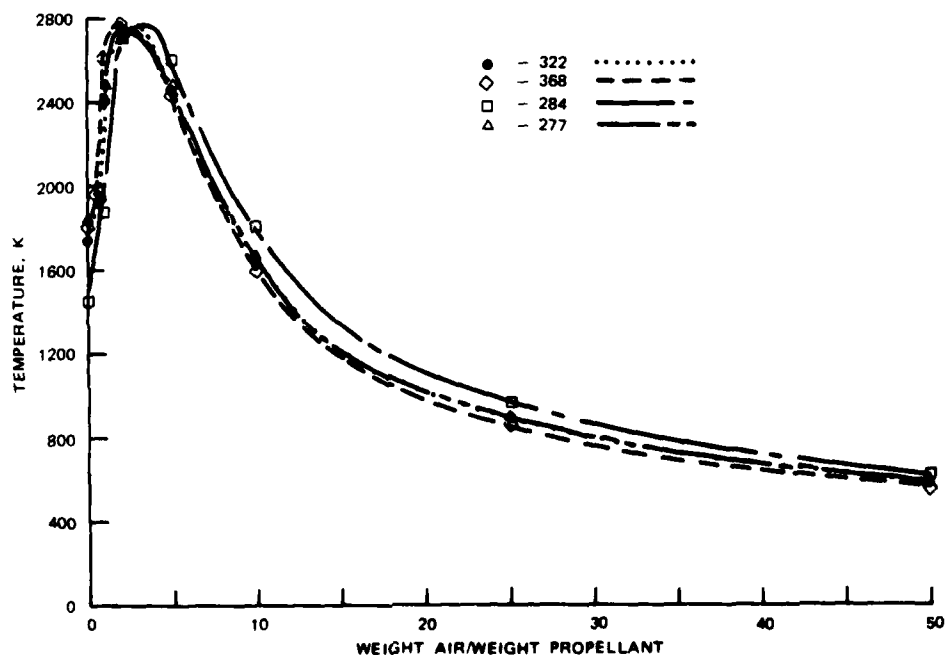
FIGURE 13. Thermodynamic Afterburning Temperature versus
Weight Air/Weight Propellant.
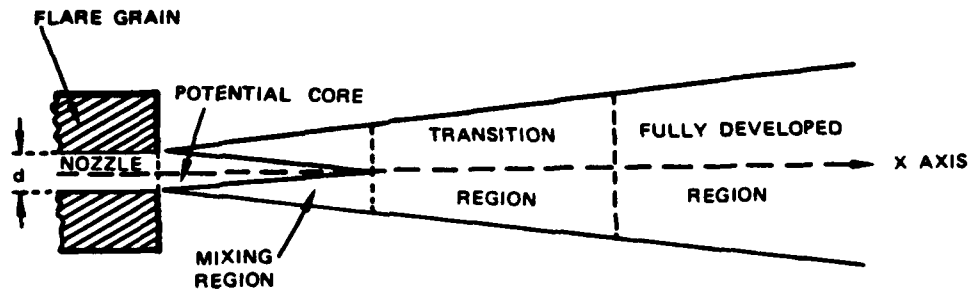
FIGURE 14.   Turbulent Free Jet Outside Flare Nozzle.
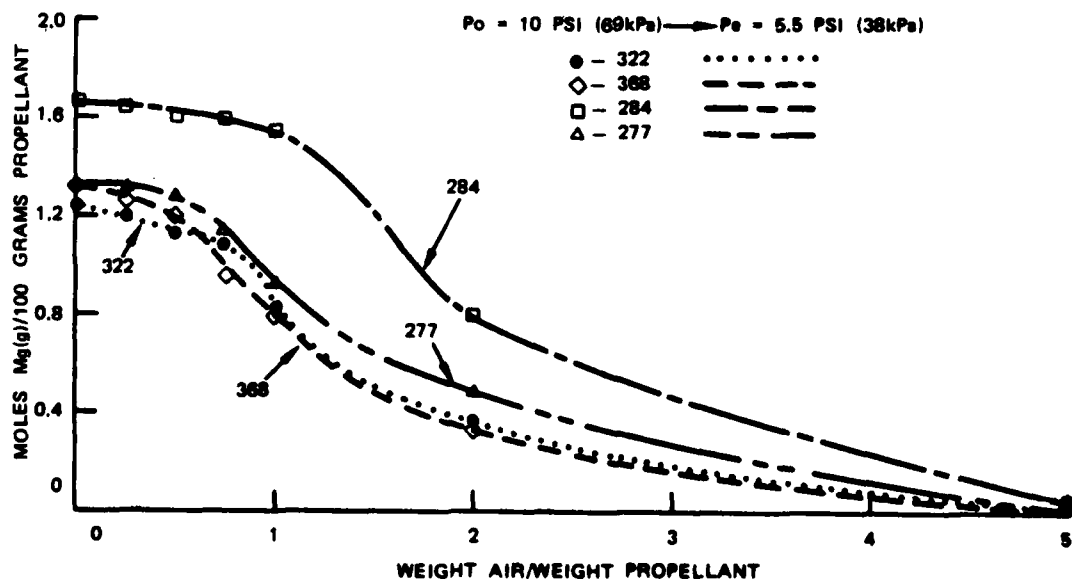
FIGURE 15.   Thermodynamic Mg(g) versus Weight Air/Weight Propellant.
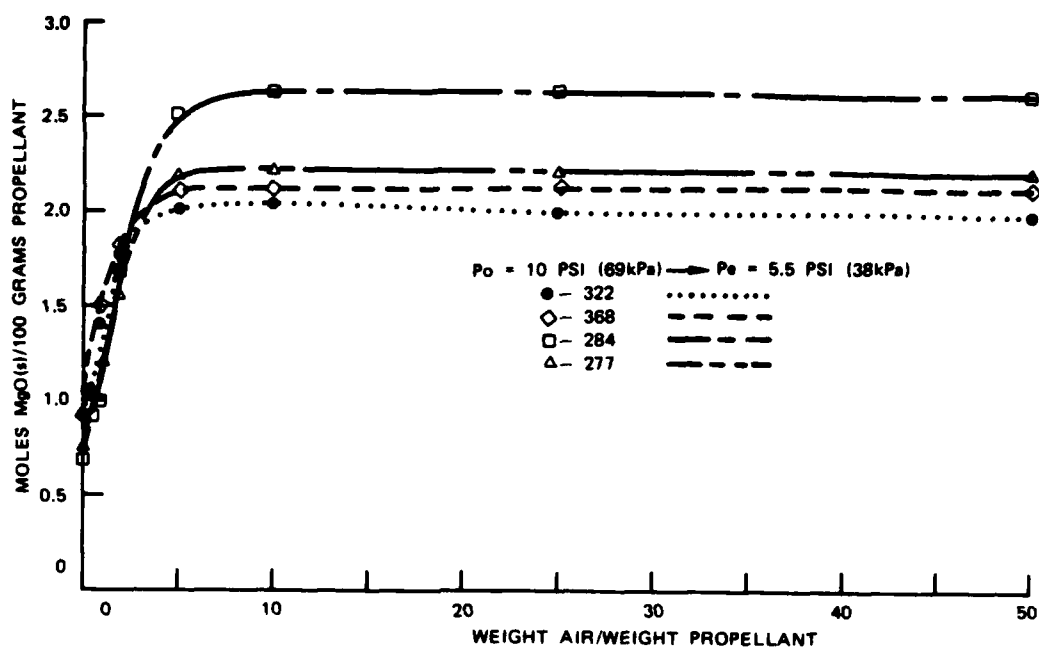
FIGURE 16.   Thermodynamic MgO(s) versus Weight Air/Weight Propellant.
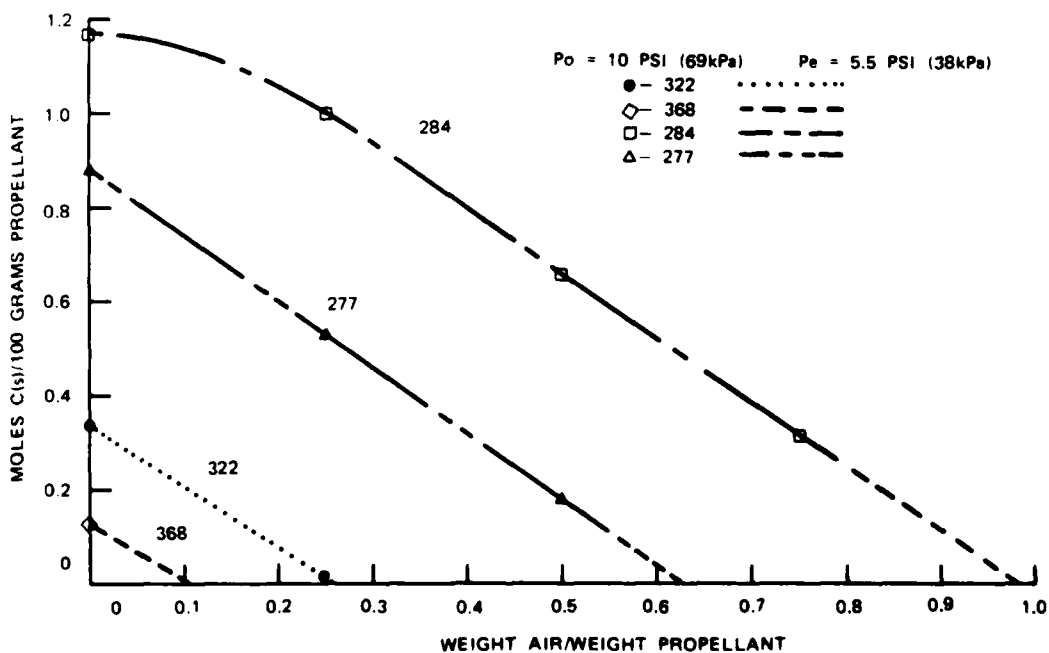
FIGURE 17.   Thermodynamic C(s) versus Weight Air/Weight Propellant.
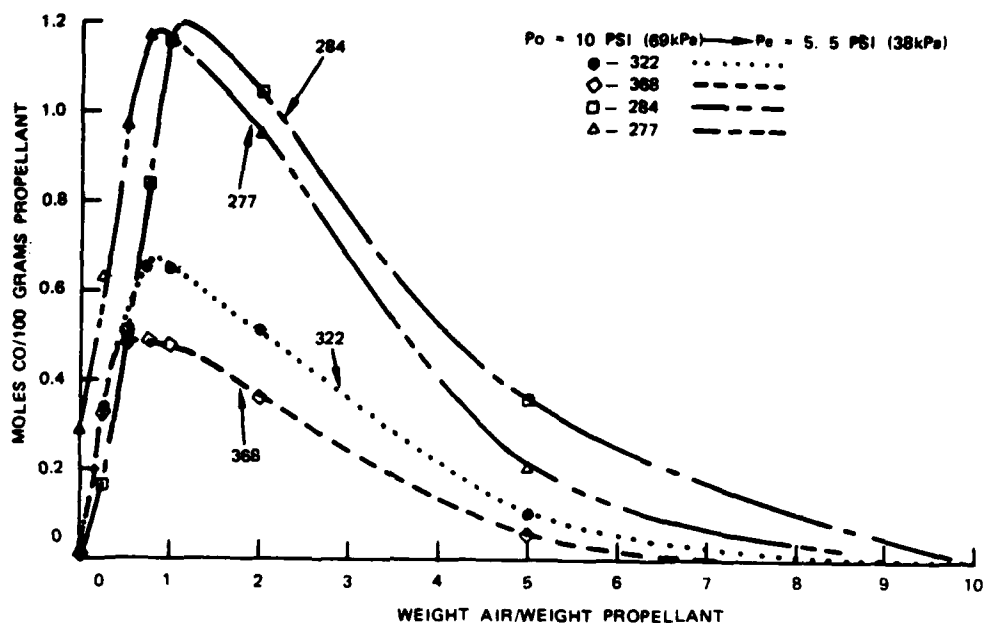
FIGURE 18.   Thermodynamic CO(g) versus Weight Air/Weight Propellant.
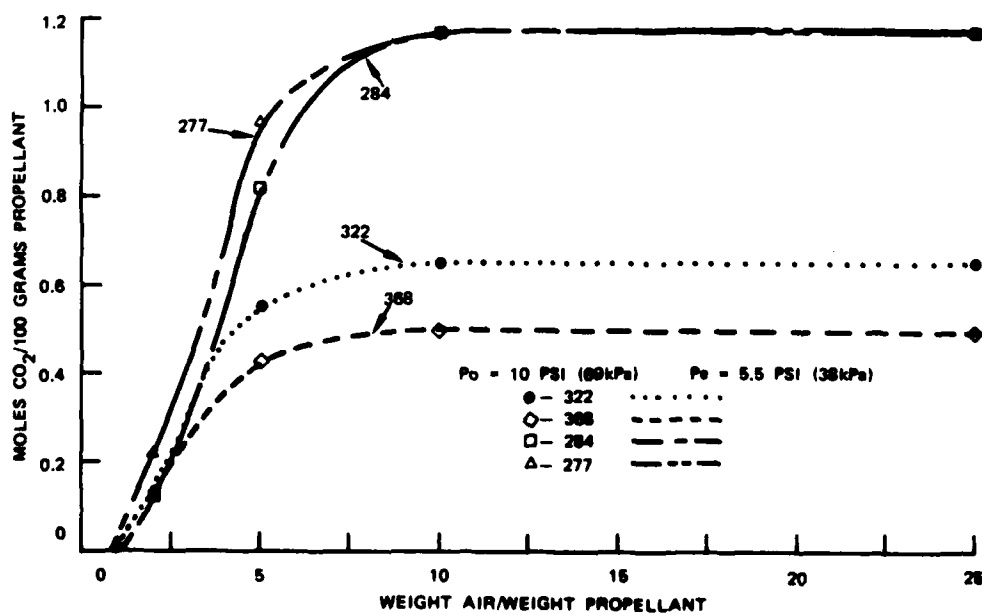
FIGURE 19.   Thermodynamic CO_2(g) versus Weight Air/Weight Propellant.
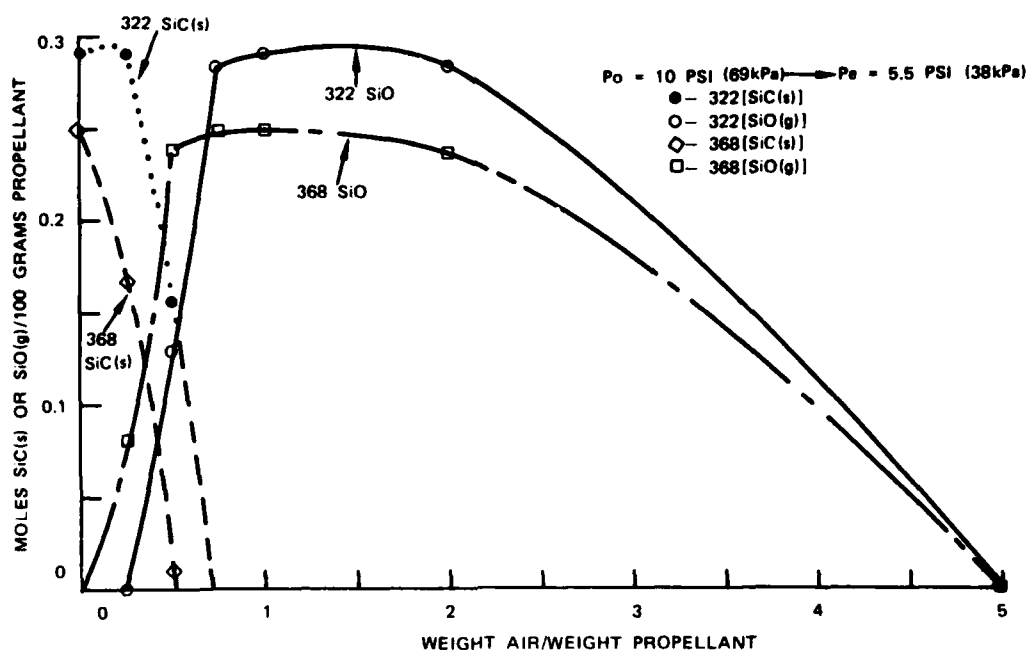
FIGURE 20. Thermodynamic SiC(s) and SiO(g) versus Weight Air/ Weight Propellant.
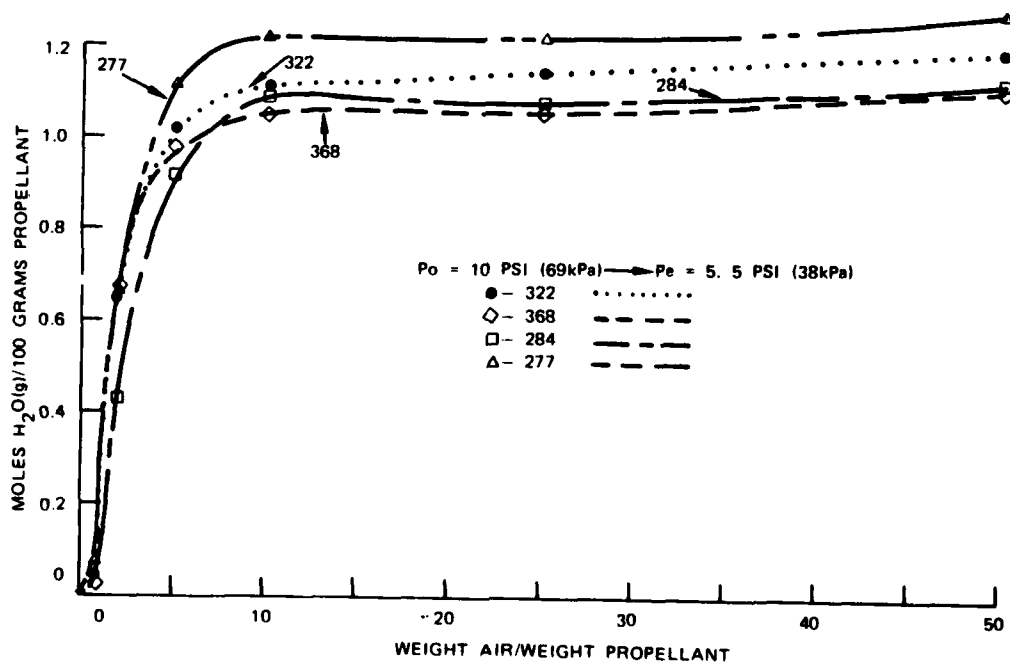
FIGURE 21. Thermodynamic $H_2O(g)$ versus Weight Air/Weight Propellant.

Appendix

THERMODYNAMIC COMPUTER CALCULATIOND

INGREDIENTS

	H	C	N	O	F	MG	SI	CL	AR			WEIGHT	CAL./G.	DENSITY
MAGNESIUM (PURE CRYSTALINE)	.000	.000	.000	.000	.000	.001	.000	.000	.000	.000	.000	56.400	0.	.0628
VITON A	.206	.274	.000	.000	.342	.000	.000	.000	.000	.000	.000	2.500	-1890.	.0658
AMMONIUM PERCHLORATE (AP)	.004	.000	.001	.004	.000	.000	.000	.001	.000	.000	.000	19.500	-602.	.0704
SYLGARD	.006	.002	.000	.001	.000	.000	.030	.000	.000	.000	.000	21.600	-1850.	.0000
AIR (DRY AT SEA LEVEL)	.000	.000	.835	.224	.000	.000	.000	.000	.005	.000	.000	.000	0.	.0000

SYSTEM WT. IS 100.000GRAMS

(H)	(C)	(N)	(O)	(F)	(MG)	(SI)	(CL)	(AR)
2.462237	.651047	.165962	.975109	.085529	2.319079	.291262	.165962	.000000

CHAMBER RESULTS TEMP.(K) 1816. TEMP.(F) 2810. PRESS.(ATM) .68 PRESS.(PSI) 10.0000 ENTHALPY -56.64 ENTROPY 172.67 CP/CV 1.1759 MOLS GAS 2.755 RT/V .2469

MG	1.2572/ 1.26+00	H2	1.2211/ 1.22-00	CS	3167/ 3.17-01
SICS	.2911/ 2.91-01	N2	.0815/ 8.15-02	CO	.0395/ 3.95-02
MGCLF	.0556/ 3.56-02	MGF2	.0177/ 1.77-02	MGF	.0120/ 1.20-02
MGH	.0022/ 9.00-03	CNH	.0030/ 2.93-03	HF	.0024/ 2.39-03
H	.0009/ 9.07-04	C2H2	.0003/ 2.82-04	SIO	.0001/ 9.73-05
SIF2	.0001/ 5.03-05	SIF3	.0000/ 2.17-05	H2O	.0000/ 3.16-06
NH3	.0000/ 2.73-06	CL	.0000/ 1.60-07	SIH2F2	.0000/ 6.84-07
SIF4	.0000/ 2.67-07	SI	.0000/ 1.70-06	SICL2	.0000/ 9.65-08
SIH3CL	.0000/ 8.89-08	SIF	.0000/ 6.78-08	CO2	.0000/ 2.64-08
SICL	.0000/ 1.36-08	CH2O	.0000/ 8.27-09	SIH	.0000/ 4.67-09
AR	.0000/ 3.23-09	MGHO	.0000/ 2.81-09	CH2	.0000/ 1.11-09
SICLF3	.0000/ 9.33-10	NH	.0000/ 6.25-10	SIH2CL	.0000/ 1.90-10
HO	.0000/ 1.56-10	SIH	.0000/ 1.35-10	N	.0000/ 2.78-11
CH	.0000/ 1.20-11	CL2	.0000/ 6.00-12	SIHCL3	.0000/ 2.34-12
C	.0000/ 1.73-12	SIO2	.0000/ 1.60-12	NO	.0000/ 1.07-12

EXHAUST RESULTS TEMP.(K) 1741. TEMP.(F) 2675. PRESS.(ATM) .37 PRESS.(PSI) 5.5000 ENTHALPY -62.42 ENTROPY 172.67 CP/CV 1.1734 MOLS GAS 2.718 RT/V .1377

MG	1.2452/ 1.25+00	H2	1.2239/ 1.22+00	CS	.3350/ 3.35-01
SICS	.2912/ 2.91-01	N2	.0819/ 8.19-02	MGCLF	.0346/ 3.46-02
CO	.0223/ 2.23-02	MGF2	.0155/ 1.55-02	MGF	.0093/ 9.32-03
MGH	.0063/ 6.93-03	MGF2*	.0043/ 4.34-03	CNH	.0021/ 2.08-03
HF	.0019/ 1.90-03	H	.0006/ 6.39-04	C2H2	.0002/ 1.51-04
SIO	.0000/ 4.28-05	SIF2	.0000/ 3.16-05	SIH3F	.0000/ 2.04-06
NH3	.0000/ 1.79-06	H2O	.0000/ 1.46-06	MGN	.0000/ 6.94-07
SIH2F2	.0000/ 4.07-07	SIF4	.0000/ 2.01-07	SI	.0000/ 6.37-08
SIF2	.0000/ 4.77-08	SIH3CL	.0000/ 4.42-08	MGO	.0000/ 1.97-08
CO2	.0000/ 7.46-09	SICL	.0000/ 5.20-09	CH2O	.0000/ 2.70-09
SIH	.0000/ 1.92-09	CHO	.0000/ 1.32-09	MGHO	.0000/ 8.48-10
SICLF3	.0000/ 5.16-10	CH2	.0000/ 3.77-10	F	.0000/ 1.39-10
SIH2CL	.0000/ 8.05-11	HO	.0000/ 4.25-11	SI2	.0000/ 3.23-11

HYPOTHESIS	IMPULSE	IS EXP	THR. T	THR. P	CF	ISP.	OPT EX	EXH V	RHO-ISP	ELLIS PARA.	A*/M.	EX T
FROZEN	70.3	1.1770	1668.	.39	.689	126.4	1.00	2263.	.0	.0	10.2152	1660.
SHIFTING	70.9	1.1025	1749.	.40	.678		1.00	2282.	.0	.0	10.4592	1741.

NADLER

NADLER

INGREDIENTS	H	C	N	O	F	MG	SI	CL	AR	WEIGHT	CAL./G.	DENSITY
MAGNESIUM (PURE CRYSTALINE)	.000	.000	.000	.000	.000	.001	.000	.000	.000	56.400	0.	.0628
VITON A	.206	.274	.000	.000	.342	.000	.000	.000	.000	2.500	-1890.	.0658
AMMONIUM PERCHLORATE (AP)	.004	.000	.001	.004	.000	.000	.001	.003	.000	19.500	-602.	.0704
SYLGARD	.006	.002	.000	.001	.000	.001	.001	.000	.005	21.600	-1860.	.0704
AIR (DRY AT SEA LEVEL)	.000	.000	.835	.224	.000	.000	.000	.000	.005	50.000	0.	.0000

SYSTEM WT. IS 150.000GRAMS

(H)	(C)	(N)	(O)	(F)	(MG)
2.462937	.651047	2.862230	1.678504	.085529	2.319079

(SI)	(CL)	(AR)		
.291262	.165962	.016149		

CHAMBER RESULTS

TEMP.(K)	TEMP.(F)	PRESS.(ATM)	PRESS.(PSI)	ENTHALPY	ENTROPY	CP/CV	MOLS GAS	RT/V
1932	3127.	.68	10.0000	-56.64	299.43	1.2225	4.668	.1457

N2	1.4279/	H2	1.2145/	MG	1.1724/	MG$	1.0092/	1.01+00		
CO	.5154/	SIO	.1539/	SICS	.1325/	MGCL2	.0523/	5.23-02		
MGCLF	.0281/	MGCL	.0221/	AR	.0161/	MGF	.0143/	1.43-02		
MGF2	.0127/	HCL	.0110/	MGH	.0079/	HF	.0070/	7.02-03		
H	.0044/	SIF2	.0037/	CN	.0031/	SIF3	.0010/	1.04-03		
H2O	.0001/	SI	.0001/	SIH3F	.0000/	CL	.0000/	3.02-05		
SICL2	.0000/	SIF	.0000/	C2H2	.0000/	CH4	.0000/	1.02-05		
SIHF2	.0000/	MGN	.0000/	CO2	.0000/	SIF4	.0000/	8.26-06		
SICL	.0000/	NH3	.0000/	SIOF2	.0000/	SIHF3	.0000/	3.46-06		
MGO	.0000/	SIH3CL	.0000/	SI2	.0000/	CHO	.0000/	1.18-07		
SIO2	.0000/	MGHO	.0000/	SICLF3	.0000/	CH2O	.0000/	5.97-08		
SIH4	.0000/	SIH	.0000/	HO	.0000/	NH	.0000/	1.90-08		
F	.0000/	SIH2CL	.0000/	N	.0000/	SIN	.0000/	1.93-09		
NO	.0000/	CH2	.0000/	SIHCL3	.0000/	CL2	.0000/	2.55-10		
SICL3F	.0000/	O	.0000/	CHOF	.0000/	CH	.0000/	5.78-11		

EXHAUST RESULTS

TEMP.(K)	TEMP.(F)	PRESS.(ATM)	PRESS.(PSI)	ENTHALPY	ENTROPY	CP/CV	MOLS GAS	RT/V
1929.	3012.	.37	5.5000	-67.41	299.43	1.2173	4.584	.0816

N2	1.4303/	H2	1.2167/	MG	1.1304/	MG$	1.0562/	1.06+00
CO	.4924/	SICS	.1563/	SIO	.1299/	MGCL2	.0538/	5.38-02
MGCLF	.0290/	MGCL	.0188/	AR	.0161/	MGF2	.0129/	1.29-02
MGF2	.0125/	HCL	.0105/	HF	.0070/	MGH	.0055/	5.52-03
H	.0038/	SIF2	.0033/	CNH	.0024/	SIF3	.0012/	1.20-03
H2O	.0001/	SI	.0000/	CL	.0000/	SIH3F	.0000/	2.15-05
SICL2	.0000/	SIF	.0000/	SIF4	.0000/	C2H2	.0000/	8.75-06
SIHF2	.0000/	CH4	.0000/	CO2	.0000/	MGN	.0000/	5.22-06
SIHF3	.0000/	SICL	.0000/	SIOF2	.0000/	NH3	.0000/	3.03-06
MGO	.0000/	SIH3CL	.0000/	SI2	.0000/	SICLF3	.0000/	7.36-08
CHO	.0000/	SIO2	.0000/	MGHO	.0000/	CH2O	.0000/	3.27-08
SIH4	.0000/	HO	.0000/	SIH	.0000/	NH	.0000/	9.71-09
F	.0000/	SIHCL	.0000/	N	.0000/	SIN	.0000/	8.36-10
NO	.0000/	CH2	.0000/	SIHCL3	.0000/	SICL3F	.0000/	1.86-10
CL2	.0000/	O	.0000/	CHOF	.0000/	CH	.0000/	2.34-11

HYPOTHESIS	IMPULSE	IS EXP	THR. T	THR. P	THR. P	CF	ISP*	OPT EX	EXH V	EXH T	AMB-ISP	ELLIS PARA.	A*/M.	EX T
FROZEN	77.9	1.2234	1791.	.38	.695		143.3	1.00	2508.		1.00	.0	11.2129	1785.
SHIFTING	79.0	1.1903	1936.	.40	.677			1.00	2543.			.0	11.6053	1929.

NADLER

INGREDIENTS	H	C	N	O	F	MG	SI	CL	AR				WEIGHT	CAL./G.	DENSITY
MAGNESIUM (PURE CRYSTALINE)	.000	.000	.000	.000	.000	.001	.000	.000	.000	.000	.000	.000	56.400	0.	.0628
VITON A	.206	.274	.000	.000	.342	.000	.000	.000	.000	.000	.000	.000	2.500	-1890.	.0658
AMMONIUM PERCHLORATE (AP)	.004	.000	.001	.004	.000	.000	.001	.000	.000	.000	.000	.000	19.500	-602.	.0704
SYLGARD	.006	.002	.000	.001	.000	.000	.001	.000	.000	.000	.000	.000	21.600	-1860.	.0000
AIR (DRY AT SEA LEVEL)	.000	.000	.835	.224	.000	.000	.000	.005	.005	.000	.000	.000	75.000	0.	.0000

SYSTEM WT. IS 175.000GRAMS

(H)	(C)	(N)	(O)	(F)	(MG)	(SI)	(CL)	(AR)
2.442937	.651047	4.211400	2.040552	.085629	2.319079	.291262	.165062	.024224

CHAMBER RESULTS

TEMP.(K)	TEMP.(F)	PRESS.(ATM)	PRESS.(PSI)	ENTHALPY	ENTROPY	CP/CV	MOLS GAS	RT/V
2129.	3372.	.68	10.0000	-56.64	360.43	1.2319	5.544	.1227

N2 2.1054/ 2.11+00	H2 1.2023/ 1.20+00	MGOG 1.0094/ 1.10+00	MG 1.0852/ 1.09+00
CO .6505/ 6.50-01	SIO .2895/ 2.90-01	MGCL2 .0453/ 4.53-02	MGCL .0271/ 2.71-02
MGCLF .0242/ 2.52-02	AR .0242/ 2.42-02	HCL .0230/ 2.30-02	MGF .0172/ 1.73-02
HF .0146/ 1.46-02	MGF2 .0124/ 1.24-02	H .0116/ 1.16-02	MGH .0072/ 7.25-03
SIF2 .0013/ 1.35-03	H2O .0007/ 7.45-04	CNH .0005/ 4.89-04	SIF3 .0003/ 3.22-04
CL .0002/ 1.04-04	CO2 .0001/ 8.09-05	SI .0000/ 3.83-05	MGO .0000/ 3.36-05
MGN .0000/ 1.70-05	SICL2 .0000/ 1.20-05	SIF .0000/ 1.19-05	SIOF2 .0000/ 7.44-06
NH3 .0000/ 3.93-06	SICL .0000/ 3.93-06	SIH3F .0000/ 3.30-06	SIF4 .0000/ 2.13-06
SIO2 .0003/ 1.72-06	SIH2F2 .0000/ 1.52-06	HO .0000/ 8.78-07	SIHF3 .0000/ 7.64-07
MGHO .0000/ 6.25-07	CHO .0000/ 4.65-07	CHO .0000/ 2.44-07	C2H2 .0000/ 2.07-07
SIHSCL .0000/ 1.86-07	F .0000/ 1.12-07	F .0000/ 1.04-07	NH .0000/ 8.50-08
CH2O .0000/ 6.06-08	SI2 .0000/ 5.12-08	SICLF3 .0000/ 3.04-08	SIH .0000/ 2.81-08
N .0000/ 2.13-08	NO .0000/ 6.09-09	SIH4 .0000/ 4.60-09	SIH2CL .0000/ 2.76-09
CL2 .0000/ 2.37-09	O .0000/ 2.00-09	CH2 .0000/ 4.05-10	SICL3F .0000/ 1.69-10
CHOF .0000/ 1.59-10	SIN .0000/ 1.57-10	CH .0000/ 4.80-11	C .0000/ 3.42-11
SICL4 .0000/ 2.16-11	SIHCL3 .0000/ 8.17-12	CLF .0000/ 2.70-12	O2 .0000/ 1.61-12
	NHO .0000/		

EXHAUST RESULTS

TEMP.(K)	TEMP.(F)	PRESS.(ATM)	PRESS.(PSI)	ENTHALPY	ENTROPY	CP/CV	MOLS GAS	RT/V
1937.	3027.	.37	5.5000	-63.93	360.43	1.2337	5.523	.0677

N2 2.1046/ 2.10+00	H2 1.2155/ 1.22+00	MGOG 1.1074/ 1.11+00	MG 1.0840/ 1.08+00
CO .6468/ 6.49-01	SIO .2310/ 2.84-01	MGCL2 .0537/ 5.37-02	MGCLF .0272/ 2.72-02
AR .0242/ 2.42-02	MGCL .0187/ 1.87-02	HCL .0124/ 1.24-02	MGF .0117/ 1.17-02
MGF2 .0114/ 1.14-02	HF .0077/ 7.63-03	SIF2 .0055/ 5.48-03	MGH .0048/ 4.84-03
H .0044/ 4.39-03	CH .0022/ 2.20-03	SIF3 .0017/ 1.66-03	H2O .0001/ 9.54-05
SI .0001/ 5.41-05	CL .0000/ 3.41-05	SICL2 .0000/ 2.81-05	SIH3F .0000/ 2.31-05
SIF .0000/ 1.81-05	SIF4 .0000/ 1.42-05	CO2 .0000/ 1.18-05	SIH2F2 .0000/ 9.53-06
SIOF2 .0000/ 6.17-06	MGN .0000/ 5.73-06	SICL .0000/ 5.29-06	C2H2 .0000/ 5.12-06
SIH3 .0000/ 4.19-06	CH4 .0000/ 4.03-06	NH3 .0000/ 3.00-06	MGO .0000/ 2.35-06
SIHSCL .0000/ 9.56-07	SI2 .0000/ 9.22-07	SIH2 .0000/ 1.68-07	SICLF3 .0000/ 1.06-07
CHO .0000/ 7.75-08	MGHO .0000/ 4.62-08	CH2O .0000/ 3.56-08	HO .0000/ 2.98-08
SIH .0000/ 2.60-03	N .0000/ 2.08-08	NH .0000/ 1.28-08	F .0000/ 9.79-09
SIHCL .0000/ 8.17-09	SIN .0000/ 1.35-09	SIN .0000/ 1.56-09	NO .0000/ 1.23-09
CH2 .0000/ 4.50-10	SIHCL3 .0000/ 3.33-10	SICLF .0000/ 3.15-10	CL2 .0000/ 2.34-10
O .0000/ 8.15-11	CHOF .0000/ 4.56-11	SICL4 .0000/ 4.07-11	CH .0000/ 2.21-11

HYPOTHESIS	IMPULSE	IS EXP	CF	ISP*	THR. T	THR. P	TIR. T	OPT EX	EXIT V	RHO-ISP	ELLIS PARA.	A*/M.	EX T
FROZEN	81.2	1.2333	.637		1906.	.38		1.00	2612.	0.	.0	11.6594	1901.
SHIFTING	81.5	1.1693	.691	146.3	1945.	.38		1.00	2822.	0.	.0	11.7887	1937.

407

INGREDIENTS	WEIGHT	CAL./G.	DENSITY
MAGNESIUM (PURE CRYSTALINE)	56.400	0.	.0628
VITON A	2.500	-1890.	.0658
AMMONIUM PERCHLORATE (AP)	19.500	-602.	.0704
SYLGARD	21.600	-1860.	.0000
AIR (DRY AT SEA LEVEL)	100.000	0.	.0000

	H	C	N	O	F	MG	SI	CL	AR
	.000	.000	.000	.000	.000	.001	.000	.000	.000
	.206	.274	.000	.000	.342	.000	.000	.000	.000
	.004	.000	.001	.004	.000	.000	.000	.001	.000
	.006	.002	.000	.001	.000	.000	.001	.000	.005
	.000	.000	.835	.224	.000	.000	.000	.000	.005

(H)	(C)	(N)	(O)	(F)	(MG)	(SI)	(CL)	(AR)
2.462937	.651047	5.555879	2.402100	.085529	2.319079	.291262	.165962	.032299

SYSTEM WT. IS 200.000GRAMS

CHAMBER RESULTS

TEMP.(K)	TEMP.(F)	PRESS.(ATM)	PRESS.(PSI)	ENTHALPY	ENTROPY	CP/CV	MOLS GAS	RT/V
2561.	4151.	.68	10.0000	-56.64	417.08	1.2135	6.062	.1122

N2	2.7798/ 2.78+00	MGO$	1.3624/ 1.36+00	MG	.8599/ 8.60-01
CO	.6432/ 6.43-01	SIO	.2909/ 2.91-01	HCL	.0651/ 8.51-02
H2O	.0783/ 7.83-02	HF	.0475/ 4.75-02	MGCL	.0318/ 3.18-02
MGF	.0182/ 1.82-02	MGCL2	.0170/ 1.70-02	MGO	.0099/ 8.92-03
CO2	.0078/ 7.81-03	MGH	.0062/ 6.16-03	MGF2	.0052/ 5.18-03
HO	.0016/ 1.65-03	SIO2	.0003/ 3.26-04	O	.0001/ 1.04-04
MGHO	.0001/ 8.16-05	MGN	.0001/ 5.65-05	F	.0000/ 1.21-05
SI	.0000/ 5.93-06	SICLF2	.0000/ 4.69-06	O2	.0000/ 3.26-06
N	.0000/ 2.51-06	NH3	.0000/ 2.30-06	SIF3	.0000/ 1.69-06
SIF	.0000/ 1.05-06	SICL	.0000/ 9.23-07	SICL2	.0000/ 1.05-07
CL2	.0000/ 2.35-07	N+O	.0000/ 4.37-08	SIF4	.0000/ 2.99-08
SIH	.0000/ 4.66-09	SIN	.0000/ 3.54-09	SIHF3	.0000/ 2.46-09
HO2	.0000/ 1.19-09	CLF	.0000/ 8.13-10	CHOF	.0000/ 5.49-10
SIH3CL	.0000/ 3.98-10	CH4	.0000/ 2.76-10	SI2	.0000/ 2.51-10
C	.0000/ 7.19-11	CH2	.0000/ 2.72-11	SIH2CL	.0000/ 2.64-11
NF	.0000/ 1.28-11	SIH4	.0000/ 8.25-12	SICL3F	.0000/ 6.48-12

EXHAUST RESULTS

TEMP.(K)	TEMP.(F)	PRESS.(ATM)	PRESS.(PSI)	ENTHALPY	ENTROPY	CP/CV	MOLS GAS	RT/V
2414.	3886.	.37	5.5000	-74.46	417.08	1.2116	5.995	.0624

N2	2.7799/ 2.78+00	MGO$	1.4108/ 1.41+00	MG	.8183/ 8.18-01
CO	.6469/ 6.47-01	SIO	.2911/ 2.91-01	H	.0707/ 7.07-02
HF	.0458/ 4.58-02	H2O	.0410/ 4.10-02	HCL	.0276/ 2.76-02
MGF	.0213/ 2.13-02	MGF	.0160/ 1.60-02	MGF2	.0060/ 6.05-03
CO2	.0042/ 4.24-03	CO2	.0042/ 4.16-03	MGCLF	.0031/ 3.11-03
HO	.0005/ 4.91-04	SIO2	.0001/ 1.42-04	O	.0000/ 2.84-05
MGN	.0002/ 2.68-05	MGHO	.0000/ 2.60-05	SIF2	.0000/ 2.16-05
F	.0000/ 5.33-06	SI	.0000/ 4.97-06	SIO2	.0000/ 4.94-05
NH3	.0000/ 1.38-06	CHO	.0000/ 1.04-06	SIF3	.0000/ 4.35-06
SICL2	.0000/ 6.40-07	SIF	.0000/ 4.59-07	N	.0000/ 8.96-07
CL2	.0000/ 1.15-07	CH2O	.0000/ 2.63-08	O2	.0000/ 4.58-07
SIH3F	.0000/ 5.30-09	SIH2F	.0000/ 4.44-09	N+O	.0000/ 1.49-08
SICLF3	.0000/ 5.25-10	CH4	.0000/ 4.94-10	SIH	.0000/ 4.22-09
CLF	.0000/ 2.80-10	CHF	.0000/ 2.72-10	SIN	.0000/ 3.63-10
C	.0000/ 2.75-11	SIH2CL	.0000/ 2.58-11	SI2	.0000/ 9.03-11
C2H2	.0000/ 9.77-12	SICL3F	.0000/ 7.99-12	CH	.0000/ 1.59-11
				SIHCL3	.0000/ 7.78-12

HYPOTHESIS	IMPULSE	IS EXP	THR.T	THR.P	CF	ISP*	OPT EX	EXH V	R+D-ISP	ELLIS PARA.	A*/M.	EX T
FROZEN	87.3	1.2150	2313.	.39	.694		1.00	2808.	.0	0	12.5787	2304.
SHIFTING	88.1	1.1557	2436.	.39	.683	159.0	1.00	2833.	.0	.0	12.8982	2414.

NADLER

INGREDIENTS

	H	C	N	O	F	MG	SI	CL	AR	WEIGHT	CAL./G.	DENSITY
MAGNESIUM (PURE CRYSTALLINE)	.000	.000	.000	.000	.000	.001	.000	.000	.000	56.400	0.	.0628
VITON A	.206	.274	.000	.000	.342	.000	.000	.000	.000	2.500	-1890.	.0658
AMMONIUM PERCHLORATE (AP)	.004	.001	.001	.004	.000	.000	.000	.001	.000	19.500	-602.	.0704
SYLGARD	.006	.002	.000	.001	.000	.000	.001	.000	.000	21.600	-1860.	.0000
AIR (DRY AT SEA LEVEL)	.000	.000	.335	.224	.000	.000	.000	.000	.005	200.000	0.	.0000

SYSTEM WT. IS 300.000GRAMS

(H)	(C)	(N)	(F)	(O)	(F)	(MG)	(SI)	(CL)	(AR)
2.462957	.651047	10.653797	4651.	3.649091	.053523	2.319079	.291262	.165962	.064598

CHAMBER RESULTS

	TEMP.(K) 2839.	TEMP.(F)	PRESS.(ATM) .68	PRESS.(PSI) 10.0000	ENTHALPY -56.64	ENTROPY 629.64	CP/CV 1.2056	MOLS GAS 8.708	RT/V .0781
N2	5.4569/ 5.46+00	MGOB	1.6961/ 1.69+00	H2O	.6508/ 6.51-01	CO	.5112/ 5.11-01
MG	.4182/ 4.18-01	H2	.3456/ 3.46-01	SIO	.2815/ 2.82-01	H	.1961/ 1.96-01
MGO	.1750/ 1.75-01	CO2	.1399/ 1.40-01	HO	.1071/ 1.07-01	HO	.0937/ 9.87-02
HF	.0662/ 6.62-02	AR	.0646/ 6.46-02	NO	.0400/ 4.00-02	CL	.0389/ 3.89-02
O	.0355/ 3.86-02	O2	.0236/ 2.36-02	MGCL	.0164/ 1.64-02	MGF	.0114/ 1.14-02
SIO2	.0097/ 9.75-03	MGCL2	.0044/ 4.45-03	MGCLF	.0031/ 3.13-03	MGF2	.0023/ 2.33-03
MGH	.0016/ 1.59-03	MGHO	.0006/ 5.81-04	F	.0002/ 1.84-04	MGN	.0001/ 6.12-05
N	.0000/ 3.86-05	NH	.0000/ 8.85-06	HO2	.0000/ 5.57-06	SIOF2	.0000/ 4.62-06
NHO	.0000/ 3.00-06	CL2	.0000/ 2.29-06	SI	.0000/ 9.50-07	SIF2	.0000/ 8.84-07
CHO	.0000/ 7.16-07	NH3	.0000/ 2.91-07	SIF	.0000/ 1.44-07	SIF3	.0000/ 7.60-08
CNH	.0000/ 6.71-08	SICL	.0000/ 6.49-08	SICL2	.0000/ 3.15-08	CLF	.0000/ 1.73-08
CH2O	.0000/ 7.85-09	O3	.0000/ 9.85-10	NF	.0000/ 4.90-10	CHOF	.0000/ 4.33-10
SIH	.0000/ 3.95-10	SIF4	.0000/ 1.72-10	SIN	.0000/ 1.29-10	C	.0000/ 3.36-11
SIHF3	.0000/ 3.25-11	SIH2F2	.0000/ 1.48-11	O2F	.0000/ 1.47-11	SICLF3	.0000/ 1.24-11
SIH3F	.0000/ 7.91-12	COCLF	.0000/ 4.05-12	CO2F2	.0000/ 3.65-12	CH	.0000/ 3.30-12

EXHAUST RESULTS

	TEMP.(K) 2734.	TEMP.(F) 4463.	PRESS.(ATM) .37	PRESS.(PSI) 5.5000	ENTHALPY -85.23	ENTROPY 629.64	CP/CV 1.2014	MOLS GAS 8.566	RT/V .0437
N2	5.4621/ 5.46+00	MGOB	1.7935/ 1.79+00	H2O	.6497/ 6.50-01	CO	.5116/ 5.12-01
MG	.3679/ 3.68-01	H2	.3582/ 3.58-01	SIO	.2825/ 2.83-01	H	.1843/ 1.84-01
MGO	.1534/ 1.39-01	MGO	.1250/ 1.25-01	HCL	.1041/ 1.04-01	HO	.0880/ 8.80-02
HF	.0694/ 6.94-02	AR	.0646/ 6.46-02	CL	.0375/ 3.75-02	MGF	.0296/ 2.96-02
O	.0291/ 2.91-02	O2	.0216/ 2.16-02	MGCL	.0131/ 1.31-02	MGF2	.0090/ 9.02-03
SIO2	.0087/ 8.72-03	MGCL2	.0042/ 4.20-03	MGCLF	.0029/ 2.88-03	MGN	.0020/ 2.05-03
MGH	.0010/ 1.03-03	MGHO	.0003/ 3.49-04	F	.0001/ 1.41-04	HO2	.0000/ 3.21-05
N	.0000/ 2.37-05	NHO	.0000/ 5.21-06	SIOF2	.0000/ 4.46-06	SI	.0000/ 3.03-06
CL2	.0000/ 1.80-06	NH3	.0000/ 1.67-06	SIF2	.0000/ 7.78-07	HO2	.0000/ 6.02-07
CHO	.0000/ 4.26-07	CH	.0000/ 3.97-08	SIF	.0000/ 9.50-08	SIF3	.0000/ 7.18-08
SICL	.0000/ 4.12-08	O3	.0000/ 3.64-10	SICL2	.0000/ 2.37-08	CLF	.0000/ 1.09-08
CH2O	.0000/ 4.60-09	SIF4	.0000/ 1.75-10	CHOF	.0000/ 2.48-10	NF	.0000/ 2.15-10
SIH	.0000/ 1.84-10	SICLF3	.0000/ 1.05-11	SIN	.0000/ 5.65-11	SIHF3	.0000/ 2.57-11
C	.0000/ 1.36-12	COCLF	.0000/ 2.16-12	SIH2F2	.0000/ 9.98-12	O2F	.0000/ 5.18-12
SIH3F	.0000/ 4.52-12			CO2F2	.0000/ 2.03-12	CH	.0000/ 1.25-12

HYPOTHESIS	IMPULSE	IS EXP	THR. T	THR. P	THR. P	CF	ISP	ISP*	OPT EX	EX V	RHO-ISP	ELLIS PARA.	A*/M.	EX T
FROZEN	90.0	1.2069	2573.	.38		.693		165.0	1.00	2895.	.0	.0	12.9910	2562.
SHIFTING	91.1	1.0990	2745.	.40		.678			1.00	2930.	.0	.0	13.4401	2734.

INGREDIENTS		WEIGHT	CAL./G.	DENSITY
MAGNESIUM (PURE CRYSTALINE)		56.400	0.	.0628
VITON A		2.500	-1890.	.0658
AMMONIUM PERCHLORATE (AP)		19.500	-602.	.0704
SYLGARD		21.600	-1860.	.0000
AIR (DRY AT SEA LEVEL)		500.000	0.	.0000

SYSTEM WT. IS 600.000GRAMS

	H	C	N	O	F	MG	SI	CL	AR
MAGNESIUM	.000	.000	.000	.000	.000	.001	.000	.000	.000
VITON A	.206	.274	.000	.000	.342	.000	.000	.000	.000
AMMONIUM PERCHLORATE	.004	.000	.001	.004	.000	.000	.001	.000	.000
SYLGARD	.006	.002	.000	.001	.000	.000	.001	.000	.000
AIR (DRY AT SEA LEVEL)	.000	.000	.835	.224	.000	.000	.000	.000	.005

(H)	(C)	(N)	(O)	(F)	(MG)	(SI)	(CL)	(AR)
2.462937	.651047	27.135549	8.190064	.085529	2.319079	.291262	.165962	.161495

CHAMBER RESULTS	TEMP.(K) 2622.	TEMP.(F) 4261.	PRESS.(ATM) .68	PRESS.(PSI) 10.0000	ENTHALPY -56.64	ENTROPY 1241.54	CP/CV 1.2140	MOLS GAS 17.552	RT/V .0388
N2	13.4179/ 1.34+01		MGO$	1.9732/ 1.97+00	O2	1.2690/ 1.27+00	H2O	.9639/ 9.64-01
CO2	.4995/ 4.99-01		NO	.2996/ 3.00-01	MGSIO3	.2749/ 2.75-01	HO	.2249/ 2.25-01
AR	.1615/ 1.61-01		CO	.1516/ 1.52-01	O	.1462/ 1.46-01	HCL	.0935/ 9.35-02
HF	.0795/ 7.96-02		CL	.0656/ 6.56-02	MGO	.0483/ 4.83-02	H2	.0458/ 4.58-02
H	.0454/ 4.54-02		MG	.0149/ 1.49-02	SIO	.0123/ 1.23-02	SIO2	.0040/ 4.04-03
MGCL2	.0019/ 1.87-03		MGCLF	.0016/ 1.60-03	MGCL	.0015/ 1.52-03	MGF2	.0014/ 1.39-03
MGF	.0013/ 1.33-03		F	.0002/ 2.43-04	HO2	.0001/ 5.81-05	MGHO	.0001/ 5.10-05
N	.0000/ 1.59-05		MGH	.0002/ 1.35-05	CL2	.0000/ 7.92-06	NHO	.0000/ 5.63-06
SIOF2	.0000/ 3.13-06		NH	.0000/ 1.54-06	MGN	.0000/ 1.48-06	O3	.0000/ 1.17-07
CLF	.0000/ 4.81-08		SIF2	.0000/ 4.03-08	CHO	.0000/ 3.18-08	SIF3	.0000/ 1.66-08
NH3	.0000/ 1.31-08		SI	.0000/ 1.27-09	SIF	.0000/ 8.57-10	SICL2	.0000/ 6.17-10
O2F	.0000/ 5.30-10		CNH	.0000/ 5.05-10	NF	.0000/ 3.99-10	SICL	.0000/ 2.78-10
SIF4	.0000/ 1.81-10		CH2O	.0000/ 1.56-10	CHOF	.0000/ 7.27-11	SICLF3	.0000/ 6.83-12

EXHAUST RESULTS	TEMP.(K) 2464.	TEMP.(F) 3976.	PRESS.(ATM) .37	PRESS.(PSI) 5.5000	ENTHALPY -109.45	ENTROPY 1241.54	CP/CV 1.2129	MOLS GAS 17.395	RT/V .0215
N2	13.4516/ 1.35+01		MGO$	2.0077/ 2.01+00	O2	1.2950/ 1.30+00	H2O	1.0139/ 1.01+00
CO2	.5521/ 5.52-01		MGSIO3	.2867/ 2.86-01	NO	.2334/ 2.32-01	HO	.1662/ 1.66-01
AR	.1615/ 1.61-01		HCL	.1009/ 1.01-01	CO	.0990/ 9.90-02	O	.0932/ 9.32-02
HF	.0819/ 8.19-02		CL	.0602/ 6.02-02	H2	.0304/ 3.04-02	H	.0253/ 2.53-02
MGO	.0161/ 1.61-02		MG	.0043/ 4.29-03	SIO	.0034/ 3.43-03	SIO2	.0016/ 1.55-03
MGCL2	.0015/ 1.51-03		MGCLF	.0012/ 1.19-03	MGF2	.0009/ 9.09-04	MGCL	.0006/ 5.77-04
MGF	.0005/ 4.79-04		F	.0001/ 1.42-04	HO2	.0000/ 3.44-05	MGHO	.0000/ 2.22-06
CL2	.0000/ 7.89-06		N	.0000/ 5.18-06	NHO	.0000/ 2.60-06	MGH	.0000/ 1.24-05
SIOF2	.0000/ 1.87-06		NH	.0000/ 4.63-07	MGN	.0000/ 2.09-07	O3	.0000/ 5.84-08
CLF	.0000/ 3.12-08		SIF2	.0000/ 1.20-08	SIF3	.0000/ 8.51-09	CHO	.0000/ 8.03-09
NH3	.0000/ 4.60-09		O2F	.0000/ 2.16-10	SIF4	.0000/ 1.63-10	SICL2	.0000/ 1.47-10
NF	.0000/ 1.06-10		SIF	.0000/ 9.86-11	CNH	.0000/ 9.46-11	SI	.0000/ 8.99-11
CH2O	.0000/ 3.83-11		SICL	.0000/ 3.11-11	CHOF	.0000/ 2.61-11	SICLF3	.0000/ 4.53-12

HYPOTHESIS	IMPULSE	IS EXP	THR. T	THR. P	THR. P	CF	ISP	ISP*	OPT EX	EXH V	RHO-ISP	ELLIS PARA.	A*/M.	EX T
FROZEN	86.8	1.2154	2657.	.38		.694		158.0	1.00	2791.	.0	.0	12.5024	2359.
SHIFTING	87.5	1.1392	2477.	.39		.683			1.00	2816.	.0	.0	12.8126	2464.

NADLER

NADLER

INGREDIENTS

INGREDIENTS	H	C	N	O	F	MG	SI	CL	AR	WEIGHT	CAL./G.	DENSITY
MAGNESIUM (TYPE CRYSTALINE)	.000	.000	.000	.000	.000	.001	.000	.000	.000	56.400	0.	.0628
VITON A	.205	.274	.000	.000	.342	.000	.000	.000	.000	2.500	-1890.	.0658
AMMONIUM PERCHLORATE (AP)	.004	.000	.001	.004	.000	.000	.000	.000	.000	19.500	-602.	.0704
SILANED	.006	.002	.000	.001	.000	.000	.001	.005	.000	21.600	-1850.	.0000
AIR (DRY AT SEA LEVEL)	.000	.000	.835	.224	.000	.000	.000	.005	.005	1000.000	0.	.0000

SYSTEM WT. 151100.000GRAMS

(H)	(C)	(N)	(O)	(F)	(MG)	(SI)	(CL)	(AR)
2.465937	.651047	54.105136	15.425019	.0855-3	2.519079	.291262	.165962	.322989

CHAMBER RESULTS
TEMP.(K) 1821. TEMP.(F) 2818. PRESS.(ATM) .68 PRESS.(PSI) 10.0000 ENTHALPY -56.64 ENTROPY 2219.82 CP/CV 1.2544 MOLS GAS 34.452 RT/V .0197

N2	26.0846/	2.70+01	O2	4.9738/	4.98+00	MGO$	2.0272/ 2.03+00
CO2	.6505/	6.51-01	AR	.3230/	3.23-01	MGSIO3	.2913/ 2.91-01
NO	.1353/	1.35-01	HF	.0852/	8.52-02	CL	.0220/ 2.20-02
O	.0023/	2.33-03	CO	.0005/	5.23-04	MGCL2	.0004/ 3.83-04
MGCLF	.0002/	1.73-04	CL2	.0001/	7.70-05	MGF2	.0001/ 6.57-05
HO2	.0000/	8.39-06	F	.0000/	3.54-06	MGO	.0000/ 8.07-07
NHO	.0000/	1.13-07	MGCL	.0000/	1.05-07	SIOF2	.0000/ 7.10-08
O3	.0000/	3.42-08	CLF	.0000/	2.41-08	MG	.0000/ 9.16-09
N	.0000/	1.91-09	SIF4	.0000/	1.94-09	SIF3	.0000/ 2.22-10
MGHO	.0000/	1.50-10	O2F	.0000/	6.34-11	NH3	.0000/ 1.01-11

(H2O 1.1097/ 1.11+00, HCL .1429/ 1.43-01, HO .0149/ 1.49-02, H2 .0002/ 2.30-04, H .0000/ 4.58-05, SIO2 .0000/ 1.57-07, MGF .0000/ 6.32-08, SIO .0000/ 5.09-09, NH .0000/ 1.66-10, SICLF3 .0000/ 9.38-12)

EXHAUST RESULTS
TEMP.(K) 1629. TEMP.(F) 2473. PRESS.(ATM) .37 PRESS.(PSI) 5.5000 ENTHALPY -127.36 ENTROPY 2219.82 CP/CV 1.2604 MOLS GAS 34.446 RT/V .0109

N2	27.0188/	2.70+01	O2	5.0194/	5.02+00	MGO$	2.0276/ 2.03+00
CO2	.6510/	6.51-01	AR	.3230/	3.23-01	MGSIO3	.2913/ 2.91-01
HF	.0854/	8.54-02	NO	.0674/	6.74-02	CL	.0129/ 1.29-02
O	.0004/	4.33-04	O	.0002/	1.69-04	CO	.0001/ 1.04-04
MGCLF	.0001/	6.77-05	H2	.0000/	4.37-05	MGF2	.0000/ 1.94-05
HO2	.0000/	2.41-06	F	.0000/	6.71-07	N+O	.0000/ 1.73-08
CLF	.0000/	1.13-08	CLF	.0000/	9.81-09	O3	.0000/ 8.27-09
SIO2	.0000/	2.56-09	SIF4	.0000/	2.13-09	MGF	.0000/ 1.88-09
N	.0000/	6.27-11	SIF3	.0000/	2.54-11	SIO	.0000/ 2.16-11

(H2O 1.1101/ 1.11+00, HCL .1524/ 1.52-01, HO .0049/ 4.86-03, CO .0001/ 7.99-05, H .0000/ 4.63-06, MGO .0000/ 1.53-08, MGCL .0000/ 3.37-09, MG .0000/ 7.48-11, O2F .0000/ 1.14-11)

HYPOTHESIS	IMPULSE	IS EXP	THR. T	THR. P	OPT EX	ISP*	CF	THR.(T)	ISP*	EXH V	RHO-ISP	ELLIS PARA.	A*/M.	EX T
FROZEN	74.5	1.2570	1614.	.38	1.00	133.8	.700			2397.	0	0	10.6511	1611.
SHIFTING	74.8	1.2281	1634.	.38	1.00		.608			2407.	0	0	10.7208	1629.

INGREDIENTS

	WEIGHT	CAL./G.	DENSITY
MAGNESIUM (FLAKE CRYSTALINE)	56.400	0.	.0628
VITON A	2.500	-1890.	.0658
AMMONIUM PERCHLORATE (AP)	19.500	-602.	.0704
SYLGARD	21.600	-1860.	.0000
AIR (DRY AT SEA LEVEL)	2500.000	0.	.0000

	H	C	N	O	F	MG	SI	CL	AR
	.000	.000	.000	.000	.000	.001	.000	.000	.000
	.206	.274	.000	.000	.342	.000	.000	.000	.000
	.004	.000	.001	.004	.000	.000	.000	.001	.000
	.006	.002	.000	.001	.000	.000	.001	.000	.000
	.000	.000	.835	.224	.000	.000	.000	.000	.005

SYSTEM WT. IS 2600.000 GRAMS

(H)	(C)	(N)	(O)	(F)	(MG)	(SI)	(CL)	(AR)
2.462937	.65104	7135.013897	37.129884	.085529	2.319079	.291262	.165962	.807473

CHAMBER RESULTS

	TEMP.(K)	TEMP.(F)	PRESS.(ATM)	PRESS.(PSI)	ENTHALPY	ENTROPY	CP/CV	MOLS GAS	RT/V
	1009.	1356.	.68	10.0000	-6.64	4974.00	1.3146	86.210	.0079
N2	67.5054/ 6.75+01	O2	15.9073/ 1.59+01		MGO$	2.0060/ 2.01+00		H2O	1.1302/ 1.13+00
AR	.8075/ 8.07-01	CO2	.6510/ 6.51-01		MGSIO3	.2913/ 2.91-01		HCL	.1605/ 1.61-01
HF	.0419/ 4.19-02	MGF2$	.0218/ 2.18-02		NO	.0031/ 3.12-03		CL2	.0026/ 2.58-03
CL	.0003/ 2.60-04	HO	.0000/ 4.30-06		MGCL2	.0000/ 5.29-07		MGCLF	.0000/ 5.98-08
O	.0000/ 9.06-09	HO2	.0000/ 8.59-09		SIF4	.0000/ 2.73-09		MGF2	.0000/ 2.74-09
CLF	.0000/ 3.86-10	H2	.0000/ 3.57-10		CO	.0000/ 1.48-10		O3	.0000/ 5.72-11

EXHAUST RESULTS

	TEMP.(K)	TEMP.(F)	PRESS.(ATM)	PRESS.(PSI)	ENTHALPY	ENTROPY	CP/CV	MOLS GAS	RT/V
	874.	1114.	.37	5.5000	-152.92	4974.00	1.3229	86.191	.0043
N2	67.5066/ 6.75+01	O2	15.9073/ 1.59+01		MGO$	1.9889/ 1.99+00		H2O	1.1499/ 1.15+00
AR	.8075/ 8.07-01	CO2	.6510/ 6.51-01		MGSIO3	.2913/ 2.91-01		HCL	.1555/ 1.55-01
MGF2$	.0390/ 3.90-02	HF	.0076/ 7.61-03		CL2	.0052/ 5.22-03		NO	.0006/ 5.92-04
CL	.0001/ 5.13-05	NO2	.0001/ 4.93-05		HO	.0000/ 2.53-07		MGCL2	.0000/ 4.14-08
MGCLF	.0000/ 7.22-10	HO2	.0000/ 5.55-10		O	.0000/ 1.18-10		CLF	.0000/ 1.40-11
SIF4	.0000/ 6.29-12	H2	.0000/ 5.20-12		MGF2	.0000/ 4.06-12		O3	.0000/ 3.05-12

HYPOTHESIS	IMPULSE	IS EXP	THR. T	THR. P	CF	ISP*	OPT EX	EXH V	RHO-ISP	ELLIS PARA.	A*/M.	EX T
FROZEN	56.8	1.3188	870.	.37	.708		1.00	1826.	.0	.0	8.0192	873.
SHIFTING	56.8	1.3181	871.	.37	.707	100.9	1.00	1827.	.0	.0	8.0266	874.

NADLER

412

NADLER

INGREDIENTS

	H	C	N	O	F	MG	SI	CL	AR		WEIGHT	CAL./G.	DENSITY
MAGNESIUM (PURE CRYSTALINE)	.000	.000	.000	.000	.000	.001	.000	.000	.000		56.400	0.	.0628
VITON A	.206	.274	.000	.000	.342	.000	.000	.000	.000		2.500	-1890.	.0658
AMMONIUM PERCHLORATE (AP)	.004	.000	.001	.004	.000	.000	.001	.001	.000		19.500	-602.	.0704
SYLGARD	.006	.002	.000	.001	.000	.000	.000	.000	.005		21.600	-1960.	.0000
AIR (DRY AT SEA LEVEL)	.000	.000	.835	.224	.000	.000	.000	.000	.005		5000.000	0.	.0000

SYSTEM WT. 155100.000GRAMS

(H)	(C)	(N)	(O)	(F)	(MG)	(SI)	(CL)	(AR)
2.462937	6510.7269.861832	73.304750	.085529	2.319079	.291262	.195762	1.614345

CHAMBER RESULTS	TEMP.(K)	TEMP.(F) 676.	PRESS.(ATM) .68	PRESS.(PSI) 10.0000	ENTHALPY -96.64	ENTROPY 9342.14	CP/CV 1.3436	MOLS GAS 172.493	RT/V .0039
	757.								

N2	134.9308/ 1.35+02	O2	33.9815/ 3.40+01	M50$	1.9351/ 1.93+00	AR	1.6149/ 1.61+00
H2O	1.1307/ 1.18+00	CO2	.6510/ 6.51-01	MGSIO3	.2913/ 2.91-01	HCL	.1015/ 1.01-01
MGF2B	.0427/ 4.27-02	CL2	.0373/ 3.23-02	HF	.0001/ 9.40-05	N2O2	.0000/ 3.94-05
NO	.0000/ 3.17-05	CL	.0000/ 9.26-07	HO	.0000/ 4.50-10	MGCL2	.0000/ 6.85-11

EXHAUST RESULTS	TEMP.(K) 578.	TEMP.(F) 581.	PRESS.(ATM) .57	PRESS.(PSI) 5.5000	ENTHALPY -134.86	ENTROPY 9342.14	CP/CV 1.3383	MOLS GAS 172.483	RT/V .0022

N2	134.9308/ 1.35+02	O2	33.9718/ 3.40+01	MGO$	1.9351/ 1.99+00	AR	1.6149/ 1.61+00
H2O	1.2001/ 1.20+00	CO2	.6510/ 6.51-01	MGSIO3	.2913/ 2.91-01	HCL	.0626/ 6.26-02
CL2	.0517/ 5.17-02	MGF2B	.0428/ 4.28-02	NO2	.0000/ 1.13-05	HF	.0000/ 4.60-06

HYPOTHESIS	IMPULSE	IS EXP	THR. T	THR. P	CF	ISP*	OPT EX	ISP*	EXH V	RHO-ISP	ELLIS PARA.	A*/M.	EX T
FROZEN	46.8	1.3540	574.	.35	.712			82.9	1505.	.0	.0	6.5680	578.
SHIFTING	46.8	1.3552	574.	.35	.712		1.00		1505.	.0	.0	6.5694	578.

NADLER

INGREDIENTS

	H	C	N	O	MG	SI	CL	AR	WEIGHT	CAL./G.	DENSITY
MAGNESIUM (PURE CRYSTALINE)	.000	.000	.000	.000	.001	.000	.000	.000	57.900	0.	.0628
AMMONIUM PERCHLORATE (AP)	.004	.000	.001	.004	.000	.000	.001	.000	23.700	-602.	.0704
SYLGARD	.006	.002	.000	.001	.000	.001	.000	.000	18.400	-1860.	.0000
AIR (DRY AT SEA LEVEL)	.000	.000	.835	.224	.000	.000	.005	.000	.000	0.	.0000

SYSTEM WT. IS 100.000GRAMS

(H)	(C)	(N)	(O)	(MG)	(SI)	(CL)	(AR)
2.295502	.496224	.201708	1.054941	2.380757	.248112	.201707	.000000

CHAMBER RESULTS TEMP.(K) 1876. TEMP.(F) 2917. PRESS.(ATM) .68 PRESS.(PSI) 10.0000 ENTHALPY -48.49 ENTROPY 176.94 CP/CV 1.1917 MOLS GAS 2.860 RT/V .2378

MG	1.3494/ 1.35+00	H2	1.1364/ 1.14+00	MGO$	.9113/ 9.11-01	SIC$	.2477/ 2.48-01
CO	.1432/ 1.43-01	C$	.1002/ 1.00-01	N2	.0988/ 9.88-02	MGCL2	.0870/ 8.70-02
MGCL	.0226/ 2.26-02	MGH	.0105/ 1.05-02	HCL	.0051/ 5.08-03	CN	.0041/ 4.15-03
H	.0014/ 1.43-03	SIO	.0004/ 4.28-04	C2H2	.0004/ 4.17-04	CH	.0002/ 1.74-04
H2O	.0000/ 7.77-06	CL	.0000/ 4.91-06	NH3	.0000/ 2.31-06	MGN	.0000/ 2.18-06
SI	.0000/ 5.05-07	SICL2	.0000/ 3.85-07	CO2	.0000/ 2.39-07	MGO	.0000/ 2.06-07
SIH3CL	.0000/ 1.30-07	SICL	.0000/ 5.39-08	CH2O	.0000/ 2.63-08	CHO	.0000/ 2.28-08
MGHO	.0000/ 8.28-09	SIH+	.0000/ 4.89-09	AR	.0000/ 3.23-09	CH2	.0000/ 2.28-09
NH	.0000/ 1.35-09	HO	.0000/ 7.45-10	SI2	.0000/ 5.86-10	SIH2CL	.0000/ 4.97-10
SIH	.0000/ 4.21-10	N	.0000/ 8.52-11	CH	.0000/ 4.05-11	CL2	.0000/ 2.84-11
SIO2	.0000/ 2.03-11	SIHCL3	.0000/ 1.01-11	C	.0000/ 8.07-12	NO	.0000/ 6.47-12

EXHAUST RESULTS TEMP.(K) 1812. TEMP.(F) 2802. PRESS.(ATM) .37 PRESS.(PSI) 5.5000 ENTHALPY -54.70 ENTROPY 176.94 CP/CV 1.1876 MOLS GAS 2.809 RT/V .1332

MG	1.3281/ 1.33+00	H2	1.1391/ 1.14+00	MGO$	.9373/ 9.37-01	SIC$	.2478/ 2.48-01
CO	.1273/ 1.27-01	CO	.1174/ 1.17-01	N2	.0993/ 9.93-02	MGCL2	.0891/ 8.91-02
MGCL	.0189/ 1.89-02	MGH	.0074/ 7.40-03	HCL	.0046/ 4.63-03	CN	.0031/ 3.12-03
H	.0012/ 1.15-03	SIO	.0003/ 2.87-04	C2H2	.0003/ 2.55-04	CH	.0001/ 1.21-04
H2O	.0000/ 4.82-06	CL	.0000/ 3.63-06	NH3	.0000/ 1.48-06	MGN	.0000/ 1.17-06
SI	.0000/ 2.75-07	SICL2	.0000/ 2.50-07	CO2	.0000/ 1.29-07	MGO	.0000/ 9.91-08
SIH3CL	.0000/ 7.05-08	SICL	.0000/ 2.85-08	CH2O	.0000/ 1.24-08	CHO	.0000/ 9.93-09
MGHO	.0000/ 3.43-09	AR	.0000/ 3.23-09	SIH+	.0000/ 2.16-09	CH2	.0000/ 9.77-10
NH	.0000/ 6.34-10	HO	.0000/ 3.23-10	SI2	.0000/ 2.53-10	SI2	.0000/ 2.19-10
SIH	.0000/ 1.64-10	N	.0000/ 3.89-11	SIH2CL	.0000/ 1.54-11	CH	.0000/ 1.45-11
SIO2	.0000/ 7.67-12	SIHCL3	.0000/ 5.28-12	CL2	.0000/ 2.89-12	NO	.0000/ 2.49-12

HYPOTHESIS	IMPULSE	IS EXP	THR. T	THR. T	THR. P	CF	ISP*	OPT EX	EXH V	RHO-ISP	ELLIS PARA.	A*/M.	EX T
FROZEN	72.7	1.1937	1710.	1710.	.38	.691		1.00	2339.	.0	.0	10.5245	1703.
SHIFTING	73.5	1.0335	1819.	1819.	.40	.677	133.2	1.00	2365.	.0	.0	10.8550	1812.

NADLER

INGREDIENTS	WEIGHT	CAL./G.	DENSITY
MAGNESIUM (PURE CRYSTALINE)	57.900	0.	.0628
AMMONIUM PERCHLORATE (AP)	23.700	-602.	.0704
SYLGARD	18.400	-1850.	.0000
AIR (DRY AT SEA LEVEL)	25.000	0.	.0000

	H	C	N	O	MG	SI	CL	AR
	.000	.000	.000	.000	.001	.000	.000	.000
	.064	.000	.001	.004	.000	.001	.001	.000
	.065	.002	.000	.001	.000	.001	.001	.000
	.000	.000	.855	.224	.000	.000	.005	.005

SYSTEM WT. IS 125.000GRAMS

(H)	(C)	(N)	(O)	(MG)	(SI)	(CL)	(AR)
2.259502	.493224	1.550187	1.416689	2.380757	.249112	.201707	.008075

CHAMBER RESULTS TEMP.(K) 1998. TEMP.(F) 3137. PRESS.(ATM) .68 PRESS.(PSI) 10.0000 ENTHALPY -48.49 ENTROPY 240.63 CP/CV 1.2146 MOLS GAS 3.789 RT/V .1795

MG	1.2034/ 1.29+00	H2	1.1340/ 1.13+00	MGO$	.9433/ 9.68-01	N2	.7739/ 7.74-01
CO	.3471/ 3.47-01	SIC$	.1468/ 1.47-01	SIO	.1012/ 1.01-01	MGCL2	.0804/ 8.04-02
MGCL	.0292/ 2.92-02	HCL	.0116/ 1.15-02	MGH	.0034/ 3.42-03	AR	.0081/ 8.07-03
H	.0040/ 4.01-03	CN	.0023/ 2.31-03	H2O	.0001/ 6.97-05	SI	.0000/ 4.41-05
CL	.0000/ 3.63-05	SICL2	.0000/ 2.55-05	C2H2	.0000/ 1.43-05	CH4	.0000/ 1.09-05
MGN	.0000/ 8.81-06	SICL	.0000/ 5.03-06	CO2	.0000/ 4.70-06	NH3	.0000/ 3.91-06
MGO	.0000/ 2.69-06	SIH3CL	.0000/ 1.67-06	SI2	.0000/ 8.12-07	CHO	.0000/ 8.70-08
MGHO	.0000/ 7.36-08	SIO2	.0000/ 5.09-08	SIH4	.0000/ 4.66-08	CH2O	.0000/ 4.61-08
SIH	.0000/ 3.47-08	HO	.0000/ 2.40-08	NH	.0000/ 1.43-08	SIH2CL	.0000/ 1.39-08
N	.0000/ 1.56-08	SIN	.0000/ 1.38-09	CH2	.0000/ 1.21-09	NO	.0000/ 7.17-10
SIHCL3	.0000/ 5.18-10	CL2	.0000/ 3.15-10	O	.0000/ 6.32-11	CH	.0000/ 5.64-11

EXHAUST RESULTS TEMP.(K) 1933. TEMP.(F) 3020. PRESS.(ATM) .37 PRESS.(PSI) 5.5000 ENTHALPY -57.26 ENTROPY 240.63 CP/CV 1.2100 MOLS GAS 3.725 RT/V .1004

MG	1.2607/ 1.26+00	H2	1.1362/ 1.14+00	MGO$	1.0057/ 1.01+00	N2	.7742/ 7.74-01
CO	.3286/ 3.29-01	SIC$	.1658/ 1.66-01	MGCL2	.0828/ 8.28-02	SIO	.0823/ 8.23-02
MGCL	.0249/ 2.49-02	HCL	.0111/ 1.11-02	AR	.0081/ 8.07-03	MGH	.0066/ 6.62-03
H	.0034/ 3.40-03	CN	.0018/ 1.76-03	H2O	.0000/ 4.90-05	SI	.0000/ 2.76-05
CL	.0000/ 2.53-05	SICL2	.0000/ 1.91-05	C2H2	.0000/ 9.00-06	CH4	.0000/ 7.32-06
MGN	.0000/ 4.85-06	CO2	.0000/ 3.30-06	SICL	.0000/ 3.10-06	NH3	.0000/ 2.46-06
MGO	.0000/ 1.49-06	SIH3CL	.0000/ 9.58-07	SI2	.0000/ 3.70-07	CHO	.0000/ 4.55-08
MGHO	.0000/ 3.45-08	SIO2	.0000/ 2.67-08	CH2O	.0000/ 2.51-08	SIH4	.0000/ 2.14-08
SIH	.0000/ 1.56-08	HO	.0000/ 1.26-08	SIH2CL	.0000/ 7.84-09	NH	.0000/ 7.24-09
N	.0000/ 9.19-10	SIN	.0000/ 5.83-10	CH2	.0000/ 5.60-10	NO	.0000/ 3.39-10
SIHCL3	.0000/ 3.13-10	CL2	.0000/ 1.97-10	SICL4	.0000/ 3.64-11	O	.0000/ 2.86-11

HYPOTHESIS	IMPULSE	IS EXP	THR. T	THR. P	CF	ISP*	OPT EX	EXH V	RHO-ISP	ELLIS PARA.	A*/M.	EX T
FROZEN	77.1	1.2134	1803.	.38	.694	141.7	1.00	2482.	.0	.0	11.1122	1796.
SHIFTING	78.2	1.0917	1940.	.40	.677		1.00	2515.	.0	.0	11.5512	1933.

INGREDIENTS	WEIGHT	CAL./G.	DENSITY
MAGNESIUM (PURE CRYSTALINE)	57.900	0.	.0628
AMMONIUM PERCHLORATE (AP)	23.700	-602.	.0704
SYLGARD	18.400	-1860.	.0000
AIR (DRY AT SEA LEVEL)	50.000	0.	.0000

	H	C	N	O	MG	SI	CL	AR
	.000	.000	.000	.000	.001	.000	.000	.000
	.004	.001	.001	.004	.000	.001	.000	.000
	.006	.002	.000	.001	.000	.001	.000	.005
	.000	.000	.835	.224	.000	.000	.000	.000

SYSTEM WT. IS 150.000GRAMS

(H)	(C)	(N)	(O)	(MG)	(SI)	(CL)	(AR)
2.295502	.496224	2.808666	1.778437	2.380757	.248112	.201707	.016149

CHAMBER RESULTS

TEMP.(K)	TEMP.(F)	PRESS.(ATM)	PRESS.(PSI)	ENTHALPY	ENTROPY	CP/CV	MOLS GAS	RT/V
2090.	3302.	.68	10.0000	-48.49	302.21	1.2315	4.713	.1443

N2	1.4469/ 1.45+00	MG	1.2302/ 1.23+00	H2	1.1286/ 1.13+00	MGO$	1.0345/ 1.03+00
CO	.4954/ 4.95-01	SIO	.2480/ 2.48-01	MGCL2	.0737/ 7.37-02	MGCL	.0337/ 3.37-02
HCL	.0204/ 2.04-02	AR	.0161/ 1.61-02	MGH	.0085/ 8.45-03	H	.0081/ 8.13-03
CNH	.0008/ 7.78-04	H2O	.0003/ 3.18-04	CL	.0001/ 1.09-04	SI	.0001/ 5.29-05
CO2	.0000/ 2.87-05	SICL2	.0000/ 2.51-05	MGO	.0000/ 1.55-05	MGN	.0000/ 1.49-05
SICL	.0000/ 6.27-06	NH3	.0000/ 3.69-06	CH4	.0000/ 1.20-06	C2H2	.0000/ 7.94-07
SIO2	.0000/ 6.41-07	SIH3CL	.0000/ 5.24-07	SI2	.0000/ 3.61-07	MGHO	.0000/ 3.23-07
HO	.0000/ 2.63-07	CHO	.0000/ 1.66-07	CH2O	.0000/ 5.15-08	NH	.0000/ 4.78-08
SIH	.0000/ 3.94-08	NO	.0000/ 1.24-08	SIH4	.0000/ 1.19-08	N	.0000/ 9.79-09
SIH2CL	.0000/ 7.43-09	SIN	.0000/ 2.33-09	CL2	.0000/ 1.62-09	O	.0000/ 1.38-09
CH2	.0000/ 5.78-10	SIHCL3	.0000/ 4.22-10	SICL4	.0000/ 6.03-11	CH	.0000/ 5.23-11

EXHAUST RESULTS

TEMP.(K)	TEMP.(F)	PRESS.(ATM)	PRESS.(PSI)	ENTHALPY	ENTROPY	CP/CV	MOLS GAS	RT/V
1945.	3041.	.37	5.5000	-59.66	302.21	1.2297	4.661	.0803

N2	1.4484/ 1.45+00	MG	1.2127/ 1.21+00	H2	1.1351/ 1.14+00	MGO$	1.0558/ 1.06+00
CO	.4844/ 4.84-01	SIO	.2381/ 2.39-01	MGCL2	.0816/ 8.16-02	MGCL	.0249/ 2.49-02
AR	.0161/ 1.61-02	HCL	.0134/ 1.34-02	SICS	.0099/ 9.93-03	MGH	.0057/ 5.72-03
H	.0041/ 4.13-03	CNH	.0018/ 1.83-03	H2O	.0001/ 7.57-05	SI	.0001/ 5.76-05
MGN	.0000/ 3.99-05	CL	.0000/ 3.71-05	CO2	.0000/ 7.44-06	SICL	.0000/ 6.60-06
MGO	.0000/ 5.99-06	C2H2	.0000/ 5.11-06	CH4	.0000/ 4.09-06	NH3	.0000/ 2.62-06
CHO	.0000/ 2.30-06	SIH3CL	.0000/ 1.26-06	SI2	.0000/ 1.13-06	SIO2	.0000/ 1.21-07
SIH	.0000/ 6.32-08	MGHO	.0000/ 4.66-08	CH2O	.0000/ 2.93-08	SIH	.0000/ 2.93-08
N	.0000/ 2.44-08	HO	.0000/ 2.42-08	SIH2CL	.0000/ 1.24-08	NH	.0000/ 1.12-08
CH2	.0000/ 1.67-09	SIN	.0000/ 1.51-09	NO	.0000/ 9.06-10	SIHCL3	.0000/ 5.86-10
CL2	.0000/ 4.84-10	CL2	.0000/ 3.07-10	SICL4	.0000/ 7.99-11	O	.0000/ 6.84-11

HYPOTHESIS	IMPULSE	IS EXP	THR. T	THR. P	CF	ISP*	OPT EX	EXH V	RHO-ISP	ELLIS PARA.	A*/M.	EX T
FROZEN	80.1	1.2333	1871.	.38	.696	145.2	1.00	2578.	.0	.0	11.5061	1866.
SHIFTING	80.5	1.1016	1951.	.40	.684		1.00	2590.			11.7637	1945.

NADLER

INGREDIENTS

							WEIGHT	CAL./G.	DENSITY
POLYBUTADIENE (KRYSTALINE)							57.900	0.	.0628
AMMONIUM PERCHLORATE (AP)							23.700	-602.	.0704
SILGARD							18.400	-1860.	.0000
AIR (USE AT SEA LEVEL)							75.000	0.	.0000

SYSTEM WT. IS 175.000 GRAMS

	H	C	N	O	MG	SI	CL	AR	
	.000	.000	.000	.000	.001	.000	.000	.000	
	.004	.000	.001	.004	.000	.001	.001	.000	
	.005	.002	.000	.001	.000	.001	.000	.005	
	.000	.000	.835	.224	.000	.000	.005	.005	

(H)	(C)	(N)	(O)	(MG)	(SI)	(CL)	(AR)
2.05602	4.34224	4.247145	2.140185	2.520757	.248112	.201707	.024224

CHAMBER RESULTS — TEMP.(K) 2597. / TEMP.(F) 4215. / PRESS.(ATM) .68 / PRESS.(PSI) 10.0000 / ENTHALPY -48.49 / ENTROPY 359.22 / CP/CV 1.2093 / MOLS GAS 5.224 / RT/V .1302

	PRESS.(ATM)		PRESS.(PSI)	
N2	2.1234/ 2.12+00	MGOS	1.3021/ 1.30+00	H2	.9882/ 9.68-01
CO	.4903/ 4.90-01	SIO	.2478/ 2.43-01	HCL	.0985/ 9.85-02
H2O	.0741/ 7.41-02	MGCL	.0442/ 4.42-02	AR	.0242/ 2.42-02
MGH	.0111/ 1.11-02	MGH	.0075/ 7.49-03	CO2	.0059/ 5.93-03
HO	.0018/ 1.80-03	SIO2	.0003/ 2.83-04	O	.0001/ 1.26-04
H2HO	.0001/ 1.02-04	MGN	.0001/ 6.70-05	O2	.0003/ 3.98-06
N	.0000/ 2.73-06	CNH	.0000/ 2.76-06	NH3	.0000/ 1.74-06
CHO	.0000/ 8.10-07	SICL2	.0000/ 6.53-07	CL2	.0000/ 3.81-07
CH2O	.0000/ 3.61-08	N2O	.0000/ 3.20-08	HO2	.0000/ 1.52-09
SIN	.0000/ 5.49-10	SIH3CL	.0000/ 4.20-10	C	.0000/ 7.90-11
SI2	.0000/ 7.18-11	SIH2CL	.0000/ 2.88-11	CH2	.0000/ 2.62-11
SIH4	.0000/ 7.68-12	SIHCL3	.0000/ 4.98-12	SICL4	.0000/ 1.50-12

EXHAUST RESULTS — TEMP.(K) 2455. / TEMP.(F) 3959. / PRESS.(ATM) .37 / PRESS.(PSI) 5.5000 / ENTHALPY -64.08 / ENTROPY 359.22 / CP/CV 1.2078 / MOLS GAS 5.163 / RT/V .0725

	PRESS.(ATM)		PRESS.(PSI)	
N2	2.1235/ 2.12+00	MGOS	1.3458/ 1.35+00	MG	.9549/ 9.55-01
CO	.4938/ 4.93-01	SIO	.2480/ 2.48-01	H	.0766/ 7.66-02
H2O	.0415/ 4.15-02	MGCL	.0388/ 3.83-02	AR	.0242/ 2.42-02
MGH	.0052/ 5.24-03	CL	.0051/ 5.09-03	CO2	.0034/ 3.37-03
HO	.0006/ 6.07-04	SIO2	.0001/ 1.36-04	N2HO	.0000/ 3.56-05
MGN	.0000/ 3.31-05	O	.0000/ 3.07-05	CNH	.0000/ 2.99-06
NH3	.0000/ 1.21-06	N	.0000/ 1.02-06	SICL2	.0000/ 7.84-07
SICL	.0000/ 5.31-07	CHO	.0000/ 5.23-07	CL2	.0000/ 1.99-07
CH2O	.0000/ 2.16-08	SIH	.0000/ 6.84-09	SIH3CL	.0000/ 4.70-10
SIN	.0000/ 2.95-10	HO2	.0000/ 2.50-10	SI2	.0000/ 7.23-11
C	.0000/ 3.12-11	CH2	.0000/ 3.05-11	CH	.0000/ 1.19-11
SIH4	.0000/ 6.57-12	C2H2	.0000/ 5.86-12	SICL4	.0000/ 1.93-12

	HYPOTHESIS IMPULSE	IS EXP	THR. T	THR. P	CF	ISP*	OPT EX	EXH V	R+O-ISP	ELLIS PARA.	A*/M.	EX T
FROZEN	87.2	1.2114	2349.	.38	.694	159.0	1.00	2807.	.0	.0	12.5829	2340.
SHIFTING	88.0	1.1304	2466.	.39	.632		1.00	2833.	.0	.0	12.9095	2455.

INGREDIENTS
MAGNESIUM (PURE CRYSTALINE)
AMMONIUM PERCHLORATE (AP)
SYLGARD
AIR (DRY AT SEA LEVEL)

	H	C	N	O	MG	SI	CL	AR		WEIGHT	CAL./G.	DENSITY
	.000	.000	.000	.000	.001	.000	.000	.000		57.900	0.	.0628
	.004	.000	.001	.004	.000	.001	.001	.000		23.700	-602.	.0704
	.005	.002	.000	.001	.000	.001	.000	.000		18.400	-1860.	.0000
	.000	.000	.835	.224	.000	.000	.005	.005		100.000	0.	.0000

SYSTEM WT. IS 200.000GRAMS

(H)	(C)	(N)	(O)	(MG)	(SI)	(CL)	(AR)
2.256502	.490234	5.595655	2.501932	2.380757	.248112	.201707	.032299

CHAMBER RESULTS	TEMP.(K) 2748.	TEMP.(F) 4488.	PRESS.(ATM) .68	PRESS.(PSI) 10.0000	ENTHALPY -48.49	ENTROPY 413.57	CP/CV 1.2052	MOLS GAS 5.859		RT/V .1161
N2	2.7955/ 2.80+00	MGO$	1.4150/ 1.42+00	MG	.8543/ 8.54-01	H2	.7488/ 7.49-01
CO	.4732/ 4.73-01	SIO	.2467/ 2.47-01	H2O	.2411/ 2.44-01	H	.1720/ 1.72-01
HCL	.1165/ 1.17-01	MGO	.0534/ 5.34-02	MGCL	.0376/ 3.76-02	AR	.0323/ 3.23-02
CO2	.0231/ 2.31-02	CL	.0187/ 1.87-02	HO	.0150/ 1.50-02	MGCL2	.0144/ 1.44-02
MGH	.0057/ 5.65-03	NO	.0025/ 2.52-03	O	.0022/ 2.21-03	SIO2	.0014/ 1.38-03
MGHO	.0040/ 3.47-04	O2	.0003/ 2.95-04	MGN	.0001/ 8.97-05	N	.0000/ 1.16-05
NH	.0000/ 5.82-06	SI	.0000/ 3.13-06	CL2	.0000/ 1.13-06	NH3	.0000/ 1.06-06
CHO	.0000/ 9.61-07	CNH	.0000/ 5.62-07	N+O	.0000/ 3.36-07	SICL	.0000/ 2.62-07
SICL2	.0000/ 1.73-07	HO2	.0000/ 9.75-08	CH2O	.0000/ 2.36-08	SIH	.0000/ 2.27-09
SIN	.0000/ 3.47-10	C	.0000/ 7.96-11	SIH3CL	.0000/ 3.87-11	CH	.0000/ 1.68-11
CH4	.0000/ 1.31-11	CH2	.0000/ 7.73-12	SI2	.0000/ 6.60-12	SIH2CL	.0000/ 3.94-12

EXHAUST RESULTS	TEMP.(K) 2633.	TEMP.(F) 4280.	PRESS.(ATM) .37	PRESS.(PSI) 5.5000	ENTHALPY -67.08	ENTROPY 413.57	CP/CV 1.2015	MOLS GAS 5.771		RT/V .0648
N2	2.7971/ 2.80+00	MGO$	1.4906/ 1.49+00	MG	.8061/ 8.06-01	H2	.8005/ 8.01-01
CO	.4774/ 4.77-01	SIO	.2471/ 2.47-01	H2O	.2030/ 2.03-01	H	.1532/ 1.53-01
HCL	.1219/ 1.22-01	MGCL	.0325/ 3.25-02	AR	.0323/ 3.23-02	MGO	.0320/ 3.20-02
CO2	.0193/ 1.89-02	CL	.0165/ 1.65-02	MGCL2	.0154/ 1.54-02	HO	.0092/ 9.23-03
MGH	.0040/ 3.96-03	NO	.0014/ 1.36-03	O	.0012/ 1.16-03	SIO2	.0010/ 9.84-04
MGHO	.0002/ 1.81-04	O2	.0001/ 1.21-04	MGN	.0000/ 4.83-05	N	.0000/ 6.14-06
NH	.0000/ 3.13-06	SI	.0000/ 2.23-06	CL2	.0000/ 7.97-07	N+3	.0000/ 7.24-07
CHO	.0000/ 5.57-07	CNH	.0000/ 4.21-07	SICL	.0000/ 1.32-07	SICL2	.0000/ 1.64-07
N+O	.0000/ 1.33-07	HO2	.0000/ 3.00-06	CH2O	.0000/ 1.44-08	SIH	.0000/ 1.20-09
SIN	.0000/ 1.68-10	C	.0000/ 3.36-11	SIH3CL	.0000/ 2.75-11	CH4	.0000/ 9.25-12
CH	.0000/ 7.01-12	S12	.0000/ 3.79-12	CH2	.0000/ 3.71-12	SIH2CL	.0000/ 2.81-12

HYPOTHESIS	IMPULSE	IS EXP	THR. T	THR. P	CF	ISP	OPT EX	ISP*	EXH V	EXH V	RHO-ISP	ELLIS PARA.	A*/M.	EX T
FROZEN	89.0	1.2067	2431.	.38	.693		1.00		.2862.		.0	.0	12.8424	2481.
SHIFTING	89.9	1.1079	2544.	.40	.679	162.8	1.00		.2893.		.0	.0	13.2469	2633.

INGREDIENTS

	H	C	N	O	MG	SI	CL	AR		WEIGHT	CAL./G.	DENSITY
MAGNESIUM (PURE CRYSTALINE)	.000	.000	.000	.000	.001	.000	.000	.000		57.900	0.	.0628
AMMONIUM PERCHLORATE (AP)	.004	.000	.001	.004	.000	.000	.001	.000		23.700	-602.	.0704
SYLGARD	.005	.002	.000	.001	.000	.001	.000	.005		18.400	-1860.	.0000
AIR (DRY AT SEA LEVEL)	.000	.000	.835	.234	.000	.000	.000	.000		200.000	0.	.0000

SYSTEM WT. IS 300.000GRAMS

(H)	(C)	(N)	(O)	(MG)	(SI)	(CL)	(AR)
2.17952	.45224	10.5835+2	3.04923	2.300757	.248112	.201707	.064598

CHAMBER RESULTS

TEMP.(K)	TEMP.(F)	PRESS.(ATM)	PRESS.(PSI)	ENTHALPY	ENTROPY	CP/CV	MOLS GAS	RT/V
2877.	4720.	.68	10.0000	-48.49	623.93	1.2028	8.562	.0795

N2	5.4617/	MGO$	1.7283/	1.73+00	H2O	.0641/	MG	.3055/	3.89-01
CO	.5513/	H2	.2570/	2.57-01	MGO	.2367/	SIO	.2367/	2.37-01
H	.1909/	HO	.1480/	1.48-01	CO2	.1343/	HCL	.1126/	1.13-01
CL	.0478/	O	.0633/	6.93-02	NO	.0650/	AR	.0646/	6.46-02
MGH	.0579/	MGCL	.0192/	1.92-02	SIO2	.0115/	MGCL2	.0060/	6.01-03
HO2	.0013/	MGHO	.0007/	6.60-04	MGN	.0001/	N	.0001/	5.03-05
SI	.0000/	NH	.0000/	9.25-06	CL2	.0000/	NHO	.0000/	4.33-06
SICL2	.0000/	CHO	.0000/	4.81-07	NH3	.0000/	SICL	.0000/	5.76-08
SIH	.0000/	CNH	.0000/	3.04-08	CH2O	.0000/	O3	.0000/	4.17-09
		SIN	.0000/	9.76-11	C	.0000/	CH	.0000/	1.91-12

EXHAUST RESULTS

TEMP.(K)	TEMP.(F)	PRESS.(ATM)	PRESS.(PSI)	ENTHALPY	ENTROPY	CP/CV	MOLS GAS	RT/V
2777.	4540.	.37	5.5000	-77.00	623.93	1.1984	8.417	.0445

N2	5.4681/	MGO$	1.8340/	1.83+00	H2O	.6744/	CO	.3578/	3.58-01
MG	.3438/	H2	.2583/	2.58-01	SIO	.2372/	H	.1813/	1.81-01
MGO	.1807/	CO2	.1394/	1.33-01	HO	.1298/	HCL	.1177/	1.18-01
AR	.0646/	O2	.0622/	6.22-02	O	.0503/	CL	.0576/	5.76-02
NO	.0533/	MGCL	.0194/	1.54-04	SIO2	.0109/	MGCL2	.0055/	5.54-03
MGH	.0008/	MGHO	.0004/	4.15-04	MGN	.0000/	N	.0000/	3.26-05
HO2	.0000/	NH	.0000/	5.58-06	CL2	.0000/	NHO	.0000/	2.59-06
SI	.0000/	CHO	.0000/	2.83-07	NH3	.0000/	SICL	.0000/	3.57-08
SICL2	.0000/	CNH	.0000/	1.67-08	CH2O	.0000/	O3	.0000/	1.98-09

HYPOTHESIS	IMPULSE	IS EXP	THR. T	THR. P	CF	ISP*	OPT EX	EXH V	RHO-ISP	ELLIS PARA.	A*/M.	EX T
FROZEN	89.9	1.2040	2611.	.38	.693		1.00	2891.	.0	.0	12.9790	2600.
SHIFTING	90.9	1.0556	2788.	.40	.677	164.8	1.00	2426.	.0	.0	13.4304	2777.

INGREDIENTS
MAGNESIUM (PURE CRYSTALINE)
AMMONIUM PERCHLORATE (AP)
SYLGARD
AIR (DRY AT SEA LEVEL)

	WEIGHT	CAL./G.	DENSITY
	57.900	0.	.0628
	23.700	-602.	.0704
	18.400	-1860.	.0000
	500.000	0.	.0000

SYSTEM WT. IS 600.000GRAMS

(H)	(C)	(N)	(O)	(MG)	(SI)	(CL)	(AR)
2.225502	.493224	27.171295	8.283345	2.380757	.248112	.201707	.161495

	H	C	N	O	MG	SI	CL	AR
	.000	.000	.000	.000	.001	.000	.000	.000
	.004	.000	.001	.004	.000	.000	.000	.000
	.006	.002	.002	.001	.001	.000	.001	.000
	.030	.000	.835	.224	.000	.000	.005	.000

CHAMBER RESULTS

TEMP.(K) 2598.   TEMP.(F) 4218.   PRESS.(ATM) .68   PRESS.(PSI) 10.0000   ENTHALPY -48.49   ENTROPY 1234.19   CP/CV 1.2146   MOLS GAS 17.489   RT/V .0389

N2	13.4501/ 1.34+01	MGO$	2.0920/ 2.09+00	O2	1.4733/ 1.47+00	H2O	.9283/ 9.29-01
CO2	.3959/ 3.97-01	NO	.3110/ 3.11-01	MGSIO3	.2355/ 2.37-01	HO	.2138/ 2.14-01
AR	.1615/ 1.61-01	O	.1412/ 1.41-01	HCL	.1138/ 1.14-01	CO	.0933/ 9.93-02
CL	.0509/ 8.09-02	MGO	.0378/ 3.78-02	H	.0369/ 3.69-02	H2	.0367/ 3.67-02
MG	.0102/ 1.02-02	SIO	.0084/ 8.36-03	SIO2	.0032/ 3.23-03	MGCL2	.0028/ 2.76-03
MGCL	.0015/ 1.47-03	HO2	.0001/ 6.01-05	MGHO	.0000/ 3.68-05	CL2	.0000/ 1.35-05
N	.0000/ 1.30-05	MGH	.0000/ 8.19-06	NHO	.0000/ 5.22-06	NH	.0000/ 1.20-06
MGN	.0000/ 9.50-07	O3	.0000/ 1.38-07	CHO	.0000/ 1.75-08	NH3	.0000/ 9.66-09
SICL2	.0000/ 6.78-10	SI	.0000/ 6.29-10	CNH	.0000/ 2.48-10	SICL	.0000/ 2.01-10

EXHAUST RESULTS

TEMP.(K) 2431.   TEMP.(F) 3916.   PRESS.(ATM) .37   PRESS.(PSI) 5.5000   ENTHALPY -100.54   ENTROPY 1234.19   CP/CV 1.2140   MOLS GAS 17.352   RT/V .0216

N2	13.4672/ 1.35+01	MGO$	2.1196/ 2.12+00	O2	1.5180/ 1.52+00	H2O	.9777/ 9.78-01
CO2	.4362/ 4.36-01	MGSIO3	.2451/ 2.45-01	NO	.2359/ 2.37-01	AR	.1615/ 1.61-01
HO	.1521/ 1.52-01	HCL	.1236/ 1.24-01	O	.0848/ 8.48-02	CL	.0732/ 7.32-02
CO	.0600/ 6.00-02	H2	.0228/ 2.28-02	H	.0188/ 1.88-02	MGO	.0109/ 1.09-02
MG	.0024/ 2.43-03	MGCL2	.0022/ 2.19-03	SIO	.0019/ 1.93-03	SIO2	.0011/ 1.09-03
MGCL	.0005/ 4.55-04	HO2	.0000/ 3.46-05	CL2	.0000/ 1.39-05	MGHO	.0000/ 7.62-06
N	.0000/ 3.74-06	N O	.0000/ 2.29-06	MGH	.0000/ 1.08-06	NH	.0000/ 3.20-07
MGN	.0000/ 1.08-07	O3	.0000/ 6.72-08	CHO	.0000/ 3.81-09	NH3	.0000/ 3.11-09
SICL2	.0000/ 1.39-10	CNH	.0000/ 3.89-11	SI	.0000/ 3.20-11	CH2O	.0000/ 1.76-11

HYPOTHESIS

	IMPULSE	IS EXP	THR. T	THR. P	THR. T	CF	OF	ISP*	OPT EX	EXH V	RHO-ISP	ELLIS PARA.	A*/M.	EX T
FROZEN	86.2	1.2160	2345.	.38	2345.	.694	1.00	156.7	1.00	2773.	.0	.0	12.4207	2337.
SHIFTING	85.9	1.1471	2443.	.39	2443.	.604	1.00		1.00	2706.	.0	.0	12.7010	2431.

NADLER

INGREDIENTS
MAGNESIUM (PURE CRYSTALLINE)
AMMONIUM PERCHLORATE (AP)
SYLGARD
AIR (DRY AT SEA LEVEL)

	H	C	N	O	MG	SI	CL	AR		WEIGHT	CAL./G.	DENSITY
	.000	.000	.000	.000	.001	.000	.000	.000	.000	57.900	0.	.0628
	.004	.000	.001	.004	.000	.000	.001	.000	.000	23.700	-602.	.0704
	.006	.002	.000	.001	.000	.001	.000	.000	.000	18.400	-1850.	.0000
	.000	.000	.000	.214	.000	.000	.005	.005	.000	1000.000	0.	.0000

SYSTEM WT. 151100.000GRAMS

(H)	(C)	(N)	(O)	(MG)	(SI)	(CL)	(AR)

CHAMBER RESULTS   TEMP.(K) 1742.   TEMP.(F) 2405.   PRESS.(ATM) .69   PRESS.(PSI) 10.0000   ENTHALPY -48.49   ENTROPY 2209.59   CP/CV 1.2569   MOLS GAS 34.453   RT/V .0197

N2	27.0073/	5.2310/	5.23+00	MGO	2.1321/	2.13+00	H2O
CO2	.4449/	.3230/	3.23-01	MGSIO3	.2431/	2.48-01	HCL
NO	.1763/	.0252/	2.52-02	HO	.0123/	1.23-02	O
MGCL2	.0105/	.0003/	2.88-04	H2	.0002/	1.62-04	CL2
H	.0000/	.0000/	7.28-06	H2O	.0000/	4.30-07	MGO
SIO2	.0000/	.0000/	7.61-08	O3	.0000/	3.14-08	MG
SIO	.0000/	.0000/	1.16-09	N	.0000/	9.67-11	MGHO

EXHAUST RESULTS   TEMP.(K) 1590.   TEMP.(F) 2403.   PRESS.(ATM) .37   PRESS.(PSI) 5.5000   ENTHALPY -117.64   ENTROPY 2209.59   CP/CV 1.2625   MOLS GAS 34.447   RT/V .0109

N2	27.0411/	5.2703/	5.27+00	MGO	2.1324/	2.13+00	H2O
CO2	.4462/	.3230/	3.23-01	MGSIO3	.2431/	2.48-01	HCL
NO	.0587/	.0139/	1.39-02	HO	.0036/	3.57-03	O
MGCL2	.0002/	.0002/	1.89-04	CO	.0000/	3.60-05	H2
H	.0000/	.0000/	1.88-06	MGO	.0000/	1.14-08	O3
MGCL	.0000/	.0000/	1.68-09	SIO2	.0000/	8.48-10	N

HYPOTHESIS   IMPULSE   IS EXP   THR. T   THR. P   CF   ISP*   OPT EX   EXH V   RHO-ISP   ELLIS PARA.   A*/M.   EX T

	IMPULSE	IS EXP	THR. T	THR. P	CF	ISP*	OPT EX	EXH V	RHO-ISP	ELLIS PARA.	A*/M.	EX T
FROZEN	73.9	1.2508	505.	.38	.700			.577.	1.00	.0	10.5572	1584.
SHIFTING	74.0	1.2525	1593.	.38	.699	132.2		2380.	1.00	.0	10.5862	1590.

NADLER

INGREDIENTS	H	C	N	O	MG	SI	CL	AR					WEIGHT	CAL./G.	DENSITY
MAGNESIUM (PURE CRYSTALINE)	.000	.000	.000	.000	.001	.000	.000	.000	.000	.000	.000	57.900	0.	.0628
AMMONIUM PERCHLORATE (AP)	.004	.000	.001	.004	.000	.000	.000	.000	.000	.000	.000	23.700	-602.	.0704
SYLGARD	.006	.002	.000	.001	.000	.001	.000	.000	.000	.000	.000	18.400	-1860.	.0000
AIR (DRY AT SEA LEVEL)	.000	.000	.855	.224	.000	.000	.005	.005	.000	.000	.000	2500.000	0.	.0000

SYSTEM WT. 15600.000GRAMS

(H)	(C)	(N)	(O)	(MG)	(SI)	(CL)	(AR)
2.294502	.498234	155.045043	37.224717	2.380757	.248112	.201707	.807473

CHAMBER RESULTS	TEMP.(K)	TEMP.(F)	PRESS.(ATM)	PRESS.(PSI)	ENTHALPY	ENTROPY	CP/CV	MOLS GAS		RT/V
	986.	1315.	.68	10.0000	-48.49	4956.46	1.3165	86.231		.0079
N2	67.5235/ 6.75+01		O2	16.1530/ 1.62+01	MGO6	2.1326/ 2.13+00		H2O	1.0517/ 1.05+00	
AR	.8075/ 8.07-01		CO2	.4962/ 4.96-01	MGSIO3	.2481/ 2.48-01		HCL	.1921/ 1.92-01	
CL2	.0047/ 4.70-03		NO	.0025/ 2.45-03	CL	.0002/ 2.50-04		NO2	.0001/ 1.11-04	
HO	.0000/ 2.66-06		MGCL2	.0000/ 5.64-07	HO2	.0000/ 5.69-09		O	.0000/ 4.57-09	

EXHAUST RESULTS	TEMP.(K)	TEMP.(F)	PRESS.(ATM)	PRESS.(PSI)	ENTHALPY	ENTROPY	CP/CV	MOLS GAS		RT/V
	853.	1076.	.37	5.5000	-142.54	4956.46	1.3249	86.229		.0043
N2	67.5245/ 6.75+01		O2	16.1516/ 1.62+01	MGO6	2.1326/ 2.13+00		H2O	1.0565/ 1.06+00	
AR	.8075/ 8.07-01		CO2	.4962/ 4.96-01	MGSIO3	.2481/ 2.48-01		HCL	.1825/ 1.82-01	
CL2	.0096/ 9.60-03		NO	.0004/ 4.40-04	CL	.0000/ 4.59-05		NO2	.0000/ 4.50-05	
HO	.0000/ 1.41-07		MGCL2	.0000/ 3.94-08	HO2	.0000/ 3.34-10		O	.0000/ 5.10-11	

HYPOTHESIS	IMPULSE	IS EXP	THR. T	THR. P	CF	ISP*	OPT EX	EXH V	RHO-ISP	ELLIS PARA.	A*/M.	EX T
FROZEN	56.1	1.3207	850.	.37	.708		1.00	1805.	.0	.0	7.9255	853.
SHIFTING	56.1	1.3223	850.	.37	.708	99.7	1.00	1805.	.0	.0	7.9264	853.

NADLER

INGREDIENTS		WEIGHT	CAL./G.	DENSITY
MAGNESIUM (PURE CRYSTALINE)		57.900	0.	.0628
AMMONIUM PERCHLORATE (AP)		23.700	-602.	.0704
SYLGARD		18.400	-1860.	.0000
AIR (DRY AT SEA LEVEL)		5000.000	0.	.0000

SYSTEM WT. 155100.000GRAMS

	H	C	N	O	MG	SI	CL	AR	
	.000	.000	.000	.000	.001	.000	.000	.000	.000
	.004	.000	.001	.004	.000	.000	.001	.000	.000
	.006	.002	.000	.001	.001	.000	.000	.000	.000
	.000	.000	.835	.224	.000	.000	.005	.005	.000
									5000.000

(H)	(C)	(N)	(O)	(MG)	(SI)	(CL)	(AR)
2.225502	.49622	269.837579	73.404492	2.380757	.248112	.201707	1.614945

CHAMBER RESULTS

	TEMP.(K)	TEMP.(F)	PRESS.(ATM)	PRESS.(PSI)	ENTHALPY	ENTROPY	CP/CV	MOLS GAS		RT/V
	663.	733.	.68	10.0000	-48.49	9315.79	1.3510	172.529		.0039
N2	134.9487/ 1.35+02		O2	34.2203/ 3.42+01	MOS	2.1326/ 2.13+00		AR	1.6149/ 1.61+00
H2O	1.0944/ 1.09+00		CO2	.4962/ 4.96-01	MGS103	.2481/ 2.48-01		HCL	.1067/ 1.07-01
CL2	.0475/ 4.75-02		NO2	.0000/ 3.55-05	NO	.0000/ 2.31-05		CL	.0000/ 7.28-07

EXHAUST RESULTS

	TEMP.(K)	TEMP.(F)	PRESS.(ATM)	PRESS.(PSI)	ENTHALPY	ENTROPY	CP/CV	MOLS GAS		RT/V
	561.	561.	.37	5.5000	-174.22	9315.79	1.3597	172.518		.0022
N2	134.9487/ 1.35+02		O2	34.2092/ 3.42+01	MOS	2.1326/ 2.13+00		AR	1.6149/ 1.61+00
H2O	1.1167/ 1.12+00		CO2	.4962/ 4.96-01	MGS103	.2481/ 2.48-01		CL2	.0698/ 6.98-02
HCL	.0620/ 6.20-02		NO2	.0000/ 9.90-06	NO	.0000/ 1.44-06		CL	.0000/ 2.77-08

HYPOTHESIS	IMPULSE	IS EXP	THR. T	THR. P	THR. P	CF	ISP*	OPT EX	ISP*	EXH V	RHO-ISP	ELLIS PARA.	A*/M.	EX T
FROZEN	46.3	1.3554	563.	.36		.713			1.00	1490.	.0	.0	6.5022	566.
SHIFTING	46.3	1.3565	563.	.36		.712	82.1		1.00	1490.	.0	.0	6.5037	567.

INGREDIENTS

	WEIGHT	CAL./G.	DENSITY
MAGNESIUM (PURE CRYSTALINE)	64.000	0.	.0628
AMMONIUM PERCHLORATE (AP)	20.000	-602.	.0704
HTPB (SINCLAIR)	16.000	13.	.0352
AIR (DRY AT SEA LEVEL)	.000	0.	.0000

	H	C	N	O	MG	CL	AR
	.000	.000	.000	.000	.001	.000	.000
	.004	.000	.001	.004	.000	.001	.000
	.103	.073	.000	.001	.000	.000	.000
	.000	.000	.835	.224	.000	.005	.000

SYSTEM WT. IS 100.000GRAMS

(H)	(C)	(N)	(O)	(MG)	(CL)	(AR)
2.334446	1.171953	.170218	.693323	2.631579	.170217	.000000

CHAMBER RESULTS: TEMP.(K) 1520. TEMP.(F) 2277. PRESS.(ATM) .68 PRESS.(PSI) 10.0000 ENTHALPY -11.83 ENTROPY 171.81 CP/CV 1.1987 MOLS GAS 3.001 RT/V .2257

MG	1.7010/ 1.70+00	CS	1.1708/ 1.17+00	H2	1.1606/ 1.16+00	MGO$	.6969/ 6.97-01
MGCL2	.0813/ 8.13-02	MG3N2$	.0451/ 4.51-02	N2	.0398/ 3.98-02	MGH	.0097/ 9.72-03
MGCL	.0073/ 7.27-03	CH4	.0007/ 6.95-04	CNH	.0004/ 3.90-04	HCL	.0003/ 3.07-04
H	.0001/ 5.05-05	C2H2	.0000/ 1.56-05	CO	.0000/ 1.23-05	NH3	.0000/ 3.34-06
MGN	.0000/ 2.06-07	CL	.0000/ 1.09-08	H2O	.0000/ 4.85-09	AR	.0000/ 3.23-09
MGO	.0000/ 3.29-11	CH2	.0000/ 7.95-12	NH	.0000/ 5.40-12	MGHO	.0000/ 3.25-12
CH2O	.0000/ 2.60-12						

EXHAUST RESULTS: TEMP.(K) 1460. TEMP.(F) 2169. PRESS.(ATM) .37 PRESS.(PSI) 5.5000 ENTHALPY -17.09 ENTROPY 171.81 CP/CV 1.1945 MOLS GAS 2.944 RT/V .1271

MG	1.6611/ 1.66+00	CS	1.1712/ 1.17+00	H2	1.1626/ 1.16+00	MGO$	.6969/ 6.97-01
MGCL2	.0822/ 8.22-02	MG3N2$	.0597/ 5.97-02	N2	.0253/ 2.53-02	MGH	.0067/ 6.68-03
MGCL	.0055/ 5.55-03	CH4	.0005/ 5.28-04	HCL	.0002/ 2.33-04	HCL	.0002/ 2.05-04
H	.0000/ 3.25-05	C2H2	.0000/ 7.60-06	CO	.0000/ 5.33-06	CNH	.0000/ 1.80-06
C2H4	.0000/ 5.06-07	MGN	.0000/ 7.61-08	CL	.0000/ 5.37-09	NH3	.0000/ 3.23-09
H2O	.0000/ 1.84-09	C2H6	.0000/ 8.48-10	MGO	.0000/ 8.63-12	AR	.0000/ 3.23-09
CH2	.0000/ 2.32-12	NH	.0000/ 1.43-12			C2H6	.0000/ 8.09-12

HYPOTHESIS

	IMPULSE	IS EXP	THR. T	THR. P	CF	ISP*	CPT EX	EXH V	RHO-ISP	ELLIS PARA.	A*/M.	EX T
FROZEN	67.0	1.1993	1382.	.38	.692		1.00	2156.	.0		9.6869	1376.
SHIFTING	67.7	1.1100	1466.	.40	.679	122.5	1.00	2177.	.0		9.9042	1460.

NADLER

INGREDIENTS	H	C	N	O	MG	CL	AR	WEIGHT	CAL./G.	DENSITY
MAGNESIUM (PURE CRYSTALINE)	.000	.000	.000	.000	.001	.000	.000	64.000	0.	.0628
AMMONIUM PERCHLORATE (AP)	.004	.000	.001	.004	.000	.001	.000	20.000	-602.	.0704
HTPB (SINCLAIR)	.103	.073	.000	.001	.000	.000	.000	16.000	13.	.0332
AIR (DRY AT SEA LEVEL)	.000	.000	.835	.224	.000	.005	.005	25.000	0.	.0000

SYSTEM WT. IS 125.000GRAMS

(H)	(C)	(N)	(O)	(MG)	(CL)	(AR)
2.334446	1.171953	1.518396	1.058570	2.631579	.170217	.008075

CHAMBER RESULTS

TEMP.(K) 1872. TEMP.(F) 2910. PRESS.(ATM) .68 PRESS.(PSI) 10.0000 ENTHALPY -11.83 ENTROPY 239.06 CP/CV 1.2139 MOLS GAS 3.906 RT/V .1741

MG	1.6685/ 1.67+00	H2	1.1521/ 1.15+00	C$	.9590/ 9.59-01	MGO$	.8580/ 8.58-01
N2	.7537/ 7.54-01	CO	.2007/ 2.01-01	MGCL2	.0715/ 7.15-02	MGCL	.0225/ 2.25-02
CNH	.0114/ 1.14-02	MGH	.0111/ 1.11-02	AR	.0081/ 8.07-03	HCL	.0048/ 4.77-03
H	.0016/ 1.64-03	C2H2	.0004/ 4.12-04	CH4	.0001/ 1.32-04	H2O	.0000/ 8.20-06
MGN	.0000/ 6.26-06	CL	.0000/ 5.20-06	NH3	.0000/ 4.80-06	CO2	.0000/ 3.51-07
MGO	.0000/ 2.62-07	CH2O	.0000/ 2.74-08	CHO	.0000/ 2.70-08	MGHO	.0000/ 9.15-09
NH	.0000/ 3.61-09	CH2	.0000/ 2.21-09	HO	.0000/ 8.82-10	N	.0000/ 2.59-10
CH	.0000/ 4.44-11	CL2	.0000/ 2.41-11	NO	.0000/ 2.09-11	C	.0000/ 1.01-11

EXHAUST RESULTS

TEMP.(K) 1808. TEMP.(F) 2796. PRESS.(ATM) .37 PRESS.(PSI) 5.5000 ENTHALPY -20.29 ENTROPY 239.06 CP/CV 1.2089 MOLS GAS 3.834 RT/V .0976

MG	1.6352/ 1.64+00	H2	1.1558/ 1.16+00	C$	.9993/ 9.99-01	MG0$	.8952/ 8.95-01
N2	.7551/ 7.55-01	CO	.1635/ 1.64-01	MGCL2	.0735/ 7.35-02	MGCL	.0189/ 1.89-02
CNH	.0085/ 8.53-03	AR	.0081/ 8.07-03	MGH	.0078/ 7.84-03	HCL	.0044/ 4.36-03
H	.0013/ 1.32-03	C2H2	.0003/ 2.51-04	CH4	.0001/ 9.21-05	H2O	.0000/ 5.08-06
MGN	.0000/ 3.84-06	MGN	.0000/ 3.35-06	NH3	.0000/ 3.07-06	CO2	.0000/ 1.88-07
MGO	.0000/ 1.25-07	CH2O	.0000/ 1.29-08	CHO	.0000/ 1.17-08	MGHO	.0000/ 3.76-09
NH	.0000/ 1.68-09	CH2	.0000/ 9.42-10	HO	.0000/ 3.80-10	N	.0000/ 1.18-10
CH	.0000/ 1.57-11	CL2	.0000/ 1.30-11	NO	.0000/ 7.97-12	C	.0000/ 3.59-12

HYPOTHESIS	IMPULSE	IS EXP	THR. T	THR. P	CF	ISP*	OPT EX	EXH V	RHO-ISP	ELLIS PARA.	A*/M.	EX T
FROZEN	75.8	1.2154	1690.	.38	.694		1.00	2438.	.0	.0	10.9185	1664.
SHIFTING	76.7	1.0370	1815.	.40	.678	139.0	1.00	2469.	.0	.0	11.3299	1808.

NADLER (stamped, left margin)

INGREDIENTS	WEIGHT	CAL./G.	DENSITY
MAGNESIUM (PURE CRYSTALINE)	64.000	0.	.0638
AMMONIUM PERCHLORATE (AP)	20.000	-602.	.0704
HTPB (SINCLAIR)	16.000	13.	.0332
AIR (DRY AT SEA LEVEL)	50.000	0.	.0000

	H	C	N	O	MG	CL	AR
	.000	.000	.000	.000	.001	.000	.000
	.004	.000	.001	.004	.000	.001	.000
	.103	.073	.000	.001	.000	.000	.000
	.000	.000	.835	.224	.000	.005	.005

SYSTEM WT. IS 150.000GRAMS

(H)	(C)	(N)	(O)	(MG)	(CL)	(AR)
2.354446	1.171953	2.867176	1.420418	2.631579	.170217	.016149

CHAMBER RESULTS

TEMP.(K)	TEMP.(F)	PRESS.(ATM)	PRESS.(PSI)	ENTHALPY	ENTROPY	CP/CV	MOLS GAS	RT/V
1898.	2957.	.68	10.0000	-11.83	302.52	1.2364	4.909	.1336

MG	1.6552/ 1.66+00	H2	1.4249/ 1.42+00	H2	1.1486/ 1.15+00	MG0$	.8725/ 8.72-01
C$	.6055/ 6.06-01	CO	.5479/ 5.48-01	MGCL2	.0701/ 7.01-02	MGCL	.0239/ 2.39-02
CNH	.0174/ 1.74-02	AR	.0161/ 1.61-02	MGH	.0100/ 1.00-02	HCL	.0062/ 6.22-03
H	.0022/ 2.24-03	C2H2	.0005/ 4.98-04	CH4	.0001/ 9.63-05	H2O	.0000/ 1.58-05
CL	.0000/ 9.26-06	MGN	.0000/ 8.59-06	NH3	.0000/ 4.97-06	CO2	.0000/ 1.80-06
MGO	.0000/ 5.50-07	CHO	.0000/ 7.49-08	CH2O	.0000/ 5.87-08	MGHO	.0000/ 1.62-08
CHO	.0000/ 6.66-09	CH2	.0000/ 3.07-09	HO	.0000/ 2.46-09	N	.0000/ 6.09-10
CH2	.0000/ 8.38-11	CH	.0000/ 8.32-11	CL2	.0000/ 4.86-11	C	.0000/ 2.38-11
CH	.0000/ 3.67-12						

EXHAUST RESULTS

TEMP.(K)	TEMP.(F)	PRESS.(ATM)	PRESS.(PSI)	ENTHALPY	ENTROPY	CP/CV	MOLS GAS	RT/V
1837.	2847.	.37	5.5000	-22.64	302.52	1.2305	4.816	.0777

MG	1.6088/ 1.61+00	H2	1.4269/ 1.43+00	H2	1.1527/ 1.15+00	MG0$	.9235/ 9.23-01
C$	.6610/ 6.61-01	CO	.4969/ 4.97-01	MGCL2	.0721/ 7.21-02	MGCL	.0201/ 2.01-02
CNH	.0161/ 1.61-02	AR	.0134/ 1.34-02	MGH	.0070/ 7.01-03	HCL	.0059/ 5.87-03
H	.0019/ 1.87-03	C2H2	.0003/ 3.15-04	CH4	.0001/ 6.61-05	H2O	.0000/ 1.07-05
CL	.0000/ 7.32-06	MGN	.0000/ 4.67-06	NH3	.0000/ 3.15-06	CO2	.0000/ 1.17-06
MGO	.0000/ 2.89-07	CHO	.0000/ 3.71-08	CH2O	.0000/ 3.07-08	MGHO	.0000/ 7.25-09
CHO	.0000/ 3.28-09	CH2	.0000/ 1.39-09	HO	.0000/ 1.21-09	N	.0000/ 2.98-10
CH2	.0000/ 3.68-11	CH	.0000/ 3.25-11	CL2	.0000/ 2.90-11	C	.0000/ 9.48-12
CH	.0000/ 1.53-12						

HYPOTHESIS	IMPULSE	IS EXP	THR. T	THR. P	CF	ISP*	OPT EX	EXH V	RHO-ISP	ELLIS PARA.	A*/M.	EX T
FROZEN	78.0	1.2319	1606.	.39	.697	143.4	1.00	2509.	.0	.0	11.1869	1691.
SHIFTING	79.2	1.1023	1843.	.40	.678		1.00	2548.	.0	.0	11.6781	1837.

426

INGREDIENTS	WEIGHT	CAL./G.	DENSITY
MAGNESIUM (PURE CRYSTALINE)	64.000	0.	.0628
AMMONIUM PERCHLORATE (AP)	20.000	-602.	.0704
HTPB (SINCLAIR)	16.000	13.	.0332
AIR (DRY AT SEA LEVEL)	75.000	0.	.0000

	H	C	N	O	MG	CL	AR									
MAGNESIUM (PURE CRYSTALINE)	.000	.000	.000	.000	.001	.000	.000	.000	.000	.000	.000	.000	.000	.000	.000	.000
AMMONIUM PERCHLORATE (AP)	.004	.000	.001	.004	.000	.001	.000	.000	.000	.000	.000	.000	.000	.000	.000	.000
HTPB (SINCLAIR)	.103	.073	.000	.001	.000	.000	.000	.000	.000	.000	.000	.000	.000	.000	.000	.000
AIR (DRY AT SEA LEVEL)	.000	.000	.835	.224	.000	.005	.000	.000	.000	.000	.000	.000	.000	.000	.000	.000

SYSTEM WT. IS 175.000 GRAMS

(H)	(C)	(N)	(O)	(MG)	(CL)	(AR)
2.35+446	1.171953	4.215655	1.782166	2.631579	.170217	.024224

CHAMBER RESULTS   TEMP.(K) 1903.   TEMP.(F) 2967.   PRESS.(ATM) .68   PRESS.(PSI) 10.0000   ENTHALPY -11.83   ENTROPY 365.26   CP/CV 1.2258   MOLS GAS 5.933   RT/V .1147

N2	2.0970/ 2.10+00	MG	1.6483/ 1.65+00	CO	.9015/ 9.02-01	
MGO$	.8306/ 8.81-01	C$	.2477/ 2.48-01	AR	.0242/ 2.42-02	
MGCL	.0241/ 2.41-02	CNH	.0216/ 2.16-02	HCL	.0070/ 7.05-03	
H	.0026/ 2.57-03	C2H2	.0005/ 5.17-04	H2O	.0000/ 2.09-05	
CL	.0000/ 1.20-05	MGN	.0000/ 9.70-06	CO2	.0000/ 3.92-06	
MGO	.0000/ 7.41-07	CHO	.0000/ 1.15-07	MGHO	.0000/ 1.96-08	
NH	.0000/ 8.60-09	HO	.0000/ 3.78-09	N	.0000/ 8.88-10	
NO	.0000/ 1.58-10	CH	.0000/ 1.02-10	C	.0000/ 3.29-11	
O	.0000/ 6.48-12					
		H2	1.1464/ 1.15+00			
		MGCL2	.0695/ 6.95-02			
		MGH	.0091/ 9.09-03			
		CH4	.0001/ 7.80-05			
		NH3	.0000/ 4.92-06			
		CH2O	.0000/ 7.96-08			
		CH2	.0000/ 3.28-09			
		CL2	.0000/ 6.49-11			

EXHAUST RESULTS   TEMP.(K) 1844.   TEMP.(F) 2859.   PRESS.(ATM) .37   PRESS.(PSI) 5.5000   ENTHALPY -24.93   ENTROPY 365.26   CP/CV 1.2491   MOLS GAS 5.818   RT/V .0643

N2	2.0995/ 2.10+00	MG	1.5893/ 1.59+00	MGO$	.9444/ 9.44-01	
CO	.8377/ 8.38-01	C$	.3169/ 3.17-01	AR	.0242/ 2.42-02	
MGCL	.0203/ 2.03-02	CNH	.0167/ 1.67-02	MGH	.0063/ 6.32-03	
H	.0022/ 2.15-03	C2H2	.0003/ 3.30-04	H2O	.0000/ 1.44-05	
CL	.0000/ 9.67-06	MGN	.0000/ 5.24-06	CO2	.0000/ 2.65-06	
MGO	.0000/ 3.95-07	CHO	.0000/ 5.87-08	MGHO	.0000/ 8.91-09	
NH	.0000/ 4.28-09	HO	.0000/ 1.91-09	N	.0000/ 4.40-10	
NO	.0000/ 7.17-11	CH	.0000/ 4.05-11	C	.0000/ 1.34-11	
O	.0000/ 2.79-12					
		H2	1.1508/ 1.15+00			
		MGCL2	.0716/ 7.16-02			
		HCL	.0067/ 6.72-03			
		CH4	.0001/ 5.35-05			
		NH3	.0000/ 3.12-06			
		CH2O	.0000/ 4.26-08			
		CH2	.0000/ 1.51-09			
		CL2	.0000/ 3.96-11			

HYPOTHESIS	IMPULSE	IS EXP	THR. T	THR. P	CF	ISP*	OPT EX	EXH V	RHO-ISP	ELLIS PARA.	A*/M.	EX T
FROZEN	73.4	1.2511	1666.	.38	.700	146.2	1.00	2554.	.0	.0	11.3401	1683.
SHIFTING	80.7	1.1022	1849.	.40	.678		1.00	2597.	.0	.0	11.9043	1844.

INGREDIENTS

	H	C	N	O	MG	CL	AR	WEIGHT	CAL./G.	DENSITY
MAGNESIUM (PURE CRYSTALINE)	.000	.000	.000	.000	.001	.000	.000	64.000	0.	.0628
AMMONIUM PERCHLORATE (AP)	.004	.000	.001	.004	.000	.001	.000	20.000	-602.	.0704
HTPB (SINCLAIR)	.103	.073	.000	.001	.000	.000	.000	16.000	13.	.0332
AIR (DRY AT SEA LEVEL)	.000	.000	.335	.224	.000	.000	.005	100.000	0.	.0000

SYSTEM WT. IS 200.000GRAMS

(H)	(C)	(N)	(O)	(MG)	(CL)	(AR)
2.334446	1.171953	5.584135	2.143914	2.631579	.170217	.032299

CHAMBER RESULTS	TEMP.(K)	TEMP.(F)	PRESS.(ATM)	PRESS.(PSI)	ENTHALPY	ENTROPY	CP/CV	MOLS GAS	RT/V
	2091.	3305.	.68	10.0000	-11.83	427.25	1.2593	6.821	.0997

N2	2.7813/ 2.78+00	MG	1.5574/ 1.56+00	CO	1.1703/ 1.17+00	H2	1.1468/ 1.15+00
MGOS	.9730/ 9.73-01	MGCL2	.0583/ 5.83-02	MGCL	.0339/ 3.39-02	AR	.0323/ 3.23-02
HCL	.0197/ 1.97-02	H	.0100/ 9.96-03	MGH	.0090/ 8.98-03	CNH	.0015/ 1.52-03
H2O	.0004/ 3.77-04	CL	.0001/ 1.27-04	CO2	.0001/ 7.92-05	MGO	.0000/ 2.30-05
MGN	.0000/ 2.19-05	NH3	.0000/ 3.61-06	C2H2	.0000/ 1.57-06	CH	.0000/ 1.19-06
MGHO	.0000/ 4.01-07	H2O	.0000/ 3.77-07	CHO	.0000/ 3.32-07	CH2O	.0000/ 8.53-08
NH	.0000/ 6.77-08	NO	.0000/ 2.45-08	N	.0000/ 1.67-08	O	.0000/ 2.38-09
CL2	.0000/ 1.50-09	CH2	.0000/ 8.31-10	CH	.0000/ 9.05-11	C	.0000/ 6.43-11
NHO	.0000/ 3.42-12						

EXHAUST RESULTS	TEMP.(K)	TEMP.(F)	PRESS.(ATM)	PRESS.(PSI)	ENTHALPY	ENTROPY	CP/CV	MOLS GAS	RT/V
	1879.	2924.	.37	5.5000	-27.87	427.25	1.2618	6.795	.0551

N2	2.7769/ 2.78+00	MG	1.5517/ 1.55+00	CO	1.1614/ 1.16+00	H2	1.1529/ 1.15+00
MGOS	.9825/ 9.82-01	MGCL2	.0596/ 6.96-02	AR	.0323/ 3.23-02	MGCL	.0219/ 2.19-02
CNH	.0104/ 1.04-02	HCL	.0091/ 9.09-03	MGH	.0059/ 5.86-03	H	.0031/ 3.09-03
C2H2	.0001/ 9.23-05	H2O	.0000/ 3.16-05	CH4	.0000/ 1.88-05	CL	.0000/ 1.87-05
CO2	.0000/ 7.75-06	MGN	.0000/ 6.51-06	NH3	.0000/ 2.89-06	MGO	.0000/ 9.84-07
CHO	.0000/ 9.14-08	CH2O	.0000/ 5.01-08	MGHO	.0000/ 1.86-08	NH	.0000/ 7.56-09
HO	.0000/ 6.51-09	CL2	.0000/ 1.12-09	N	.0000/ 1.00-09	NO	.0000/ 2.99-10
CL2	.0000/ 9.21-11	CH	.0000/ 4.23-11	C	.0000/ 1.77-11	O	.0000/ 1.35-11

HYPOTHESIS	IMPULSE	IS EXP	THR.T	THR.P	CF	ISP*	OPT EX	EXH V	RHO-ISP	ELLIS PARA.	A*/M	EX T
FROZEN	83.3	1.2616	1849	.38	.700		1.00	2680.	.0	.0	11.8954	1847.
SHIFTING	83.5	1.2238	1885	.38	.695	149.6	1.00	2688.	.0	.0	12.0177	1879.

NADLER

INGREDIENTS

INGREDIENTS	H	C	N	O	MG	CL	AR								WEIGHT	CAL./G.	DENSITY
MAGNESIUM (PURE CRYSTALINE)	.000	.000	.000	.000	.001	.000	.000	.000	.000	.000	.000	.000	.000	64.000	0.	.0628
AMMONIUM PERCHLORATE (AP)	.004	.000	.001	.004	.000	.001	.000	.000	.000	.000	.000	.000	.000	20.000	-602.	.0704
HTPB (SINCLAIR)	.103	.073	.000	.001	.000	.000	.000	.000	.000	.000	.000	.000	.000	16.000	13.	.0332
AIR (DRY AT SEA LEVEL)	.000	.000	.835	.224	.000	.000	.005	.000	.000	.000	.000	.000	.000	200.000	0.	.0000

SYSTEM WT. IS 300.000GRAMS

(H)	(C)	(N)	(O)	(MG)	(CL)	(AR)
2.334446	1.171953	10.558052	3.590305	2.631579	.170217	.064598

CHAMBER RESULTS

TEMP.(K) 2827.　TEMP.(F) 4629.　PRESS.(ATM) .68　PRESS.(PSI) 10.0000　ENTHALPY -11.83　ENTROPY 645.20　CP/CV 1.2205　MOLS GAS 9.217　RT/V .0738

N2	5.4699/ 5.47+00	MGOS	1.5562/ 1.56+00	MG	.8696/ 8.70-01
H2	.5142/ 5.14-01	H2O	.4535/ 4.53-01	MGO	.1672/ 1.67-01
CO2	.1336/ 1.34-01	HCL	.0986/ 9.86-02	HO	.0598/ 5.98-02
CL	.0315/ 3.15-02	MGCL	.0276/ 2.76-02	O	.0174/ 1.74-02
O2	.0063/ 6.26-03	MGCL2	.0063/ 6.26-03	MGHO	.0007/ 6.66-04
MGN	.0001/ 1.21-04	N	.0000/ 3.64-05	CHO	.0000/ 1.68-06
NHO	.0000/ 1.61-06	CL2	.0000/ 1.48-06	NH3	.0000/ 5.04-07
CNH	.0000/ 3.36-07	CH2O	.0000/ 2.25-08	O3	.0000/ 9.10-11
CH	.0000/ 1.56-11	CH2	.0000/ 3.70-12		

EXHAUST RESULTS

TEMP.(K) 2717.　TEMP.(F) 4431.　PRESS.(ATM) .37　PRESS.(PSI) 5.5000　ENTHALPY -41.93　ENTROPY 645.20　CP/CV 1.2157　MOLS GAS 9.065　RT/V .0413

N2	5.4731/ 5.47+00	MGOS	1.6830/ 1.68+00	MG	.8034/ 8.03-01
H2	.5541/ 5.54-01	H2O	.4267/ 4.27-01	CO2	.1222/ 1.22-01
MGO	.1125/ 1.12-01	HCL	.1050/ 1.05-01	HO	.0440/ 4.40-02
CL	.0293/ 2.93-02	MGCL	.0232/ 2.32-02	O	.0113/ 1.13-02
MGCL2	.0063/ 6.32-03	O2	.0036/ 3.57-03	MGHO	.0004/ 3.87-04
MGN	.0001/ 6.55-05	N	.0000/ 2.13-05	CHO	.0000/ 1.12-06
CHO	.0000/ 1.01-06	N2O	.0000/ 7.93-07	CL2	.0000/ 3.45-07
CNH	.0000/ 2.26-07	CH2O	.0000/ 1.38-08	NH3	.0000/ 6.02-07
CH	.0000/ 6.41-12	CH2	.0000/ 1.68-12	O3	.0000/ 2.28-11

HYPOTHESIS	IMPULSE	IS EXP	THR. T	THR. P	CF	ISP*	OPT EX	EXH V	RHO-ISP	ELLIS PARA.	A*/M	EX T
FROZEN	92.3	1.2220	2544.	.38	.695	169.2	1.00	2708.	.0	.0	13.2778	2536.
SHIFTING	93.4	1.1041	2728.	.40	.679	169.2	1.00	3006.	.0	.0	13.7750	2717.

NADLER

```
INGREDIENTS                        H    C    N    O    MG   CL   AR                          WEIGHT   CAL./G.  DENSITY
MAGNESIUM (PURE CRYSTALINE)      .000 .000 .000 .000 .001 .000 .000  .000 .000 .000 .000     64.000     0.     .0628
AMMONIUM PERCHLORATE (AP)        .004 .000 .001 .004 .000 .001 .000  .000 .000 .000 .000     20.000   -602.    .0704
HTPB (SINCLAIR)                  .103 .073 .000 .001 .000 .000 .000  .000 .000 .000 .000     16.000    13.     .0332
AIR (DRY AT SEA LEVEL)           .000 .000 .835 .224 .000 .000 .005  .000 .000 .000 .000    500.000     0.     .0000

SYSTEM WT. IS 600.0000GRAMS

  (H )       (C )        (N )         (O )       (MG)       (CL)     (AR)
2.334446   1.171953   27.139805   7.931878   2.631579   .170217   .161495
```

NADLER

```
CHAMBER   TEMP.(K)  TEMP.(F)   PRESS.(ATM)  PRESS.(PSI)  ENTHALPY  ENTROPY   CP/CV   MOLS GAS   RT/V
RESULTS    2731.     4457.        .68        10.0000      -11.83   1262.15   1.2187   17.845    .0381

N2    13.4197/ 1.34+01    MGO$  2.4192/ 2.42+00    O2   .9166/ 9.17-01    H2O  .8668/ 8.67-01
CO2    .7349/ 7.35-01     CO     .4370/ 4.37-01    NO   .3003/ 3.00-01    HO   .2650/ 2.66-01
O      .2003/ 2.00-01     AR     .1615/ 1.61-01    MGO  .1390/ 1.39-01    H    .0907/ 9.07-02
HCL    .0889/ 8.89-02     H2     .0775/ 7.75-02    CL   .0727/ 7.27-02    MG   .0667/ 6.67-02
MGCL   .0041/ 4.10-03     MGCL2  .0023/ 2.28-03    MGHO .0002/ 1.69-04    MGH  .0001/ 8.09-05
HO2    .0001/ 5.57-05     N      .0000/ 3.87-05    MGN  .0000/ 8.46-06    NHO  .0000/ 7.37-06
CL2    .0000/ 6.00-06     NH     .0000/ 3.73-06    CHO  .0000/ 1.57-07    O3   .0000/ 9.31-08
NH3    .0000/ 2.58-08     CNH    .0000/ 3.51-09    CH2O .0000/ 7.43-10    C    .0000/ 1.82-12

EXHAUST   TEMP.(K)  TEMP.(F)   PRESS.(ATM)  PRESS.(PSI)  ENTHALPY  ENTROPY   CP/CV   MOLS GAS   RT/V
RESULTS    2599.     4219.        .37         5.5000      -67.98   1262.15   1.2159   17.619    .0212

N2    13.4475/ 1.34+01    MGO$  2.5249/ 2.52+00    O2   .9149/ 9.15-01    H2O  .9088/ 9.09-01
CO2    .8174/ 8.17-01     CO     .3545/ 3.55-01    NO   .2448/ 2.45-01    HO   .2194/ 2.19-01
AR     .1615/ 1.61-01     O      .1507/ 1.51-01    MGO  .0944/ 9.44-02    MGO  .0700/ 7.00-02
CL     .0633/ 6.93-02     H      .0655/ 6.55-02    CL   .0526/ 6.26-02    MG   .0325/ 3.25-02
MGCL   .0022/ 2.20-03     MGCL2  .0019/ 1.93-03    MGHO .0001/ 6.57-05    HO2  .0000/ 3.58-05
MGH    .0000/ 2.53-05     N      .0000/ 1.77-05    MGN  .0000/ 5.45-06    NHO  .0000/ 3.97-06
MGN    .0000/ 2.25-06     NH     .0000/ 1.58-06    CHO  .0000/ 6.05-08    O3   .0000/ 4.94-08
NH3    .0000/ 1.17-08     CNH    .0000/ 1.09-09    CH2O .0000/ 2.75-10    O3
```

```
HYPOTHESIS  IMPULSE  IS EXP  IS EXP  THR. T  THR. P   CF    ISP*  OPT EX  EXH V  RHO-ISP  ELLIS P/RA.   A*/M.    EX T
FROZEN       89.2    1.2202  1.1178   2460.    .38    .695  163.2   1.00   2871.    .0        .0        12.8477   2452.
SHIFTING     90.2    1.1178           2611.    .40    .680  163.2   1.00   2904.    .0        .0        13.2679   2599.
```

NADLER

INGREDIENTS		WEIGHT	CAL./G.	DENSITY
MAGNESIUM (PURE CRYSTALINE)		64.000	0.	.0628
AMMONIUM PERCHLORATE (AP)		20.000	-602.	.0704
HTPB (SINCLAIR)		16.000	13.	.0332
AIR (DRY AT SEA LEVEL)		1000.000	0.	.0000

	H	C	N	O	MG	CL	AR
	.000	.000	.000	.000	.001	.000	.000
	.004	.000	.001	.004	.000	.001	.000
	.103	.073	.000	.001	.000	.000	.000
	.000	.000	.835	.224	.000	.005	.000

SYSTEM WT. 151100.000GRAMS

(H)	(C)	(N)	(O)	(MG)	(CL)	(AR)
2.334445	1.171353	54.109392	15.166833	2.631579	.170217	.222989

CHAMBER RESULTS	TEMP.(K) 2013.	TEMP.(F) 3164.	PRESS.(ATM) .68	PRESS.(PSI) 10.0000	ENTHALPY -11.83	ENTROPY 2251.87	CP/CV 1.2501	MOLS GAS 34.385	RT/V .0198
N2	26.9416/ 2.69+01		O2	4.4204/ 4.42+00	MGO$	2.6308/ 2.63+00		CO2	1.1662/ 1.17+00
H2O	1.0793/ 1.08+00		AR	.3230/ 3.23-01	NO	.2261/ 2.26-01		HCL	.1320/ 1.32-01
HO	.0393/ 3.93-02		CL	.0367/ 3.67-02	O	.0110/ 1.10-02		CO	.0057/ 5.74-03
H2	.0012/ 1.16-03		MGCL2	.0007/ 7.07-04	H	.0004/ 4.28-04		CL2	.0000/ 4.36-05
MGO	.0000/ 3.17-05		HO2	.0000/ 1.85-05	MGCL	.0000/ 2.44-06		MG	.0000/ 9.58-07
NHO	.0000/ 4.33-07		O3	.0000/ 7.15-08	MGH	.0000/ 3.98-08		MGHO	.0000/ 8.97-09
NH	.0000/ 3.14-09		NH3	.0000/ 8.09-11		.0000/ 7.47-11		CHO	.0000/ 1.64-11
MGN	.0000/ 1.36-11								

EXHAUST RESULTS	TEMP.(K) 1797.	TEMP.(F) 2775.	PRESS.(ATM) .37	PRESS.(PSI) 5.5000	ENTHALPY -89.58	ENTROPY 2251.87	CP/CV 1.2547	MOLS GAS 34.368	RT/V .0109
N2	26.9952/ 2.70+01		O2	4.4850/ 4.49+00	MGO$	2.6312/ 2.63+00		CO2	1.1709/ 1.17+00
H2O	1.0868/ 1.09+00		AR	.3230/ 3.23-01	HCL	.1453/ 1.46-01		NO	.1191/ 1.19-01
CL	.0235/ 2.35-02		HO	.0144/ 1.44-02	O	.0024/ 2.38-03		CO	.0010/ 1.05-03
MGCL2	.0004/ 3.66-04		H2	.0003/ 2.56-04	CL2	.0001/ 6.09-05		H	.0001/ 5.33-05
HO2	.0000/ 5.83-06		MGO	.0000/ 8.75-07	MGCL	.0000/ 1.12-07		NHO	.0000/ 7.71-08
O3	.0000/ 1.91-08		MG	.0000/ 1.24-08	N	.0000/ 1.71-09		MGHO	.0000/ 1.34-10
NH	.0000/ 1.30-10		NH3	.0000/ 6.91-12					

HYPOTHESIS	IMPULSE	IS EXP	THR. T	THR. P	CF	ISP*	OPT EX	EXH V	RHO-ISP	ELLIS PARA.	A*/M	EX T
FROZEN	78.3	1.2526	1787.	.38	.699		1.00	2519.	.0	.0	11.2018	1784.
SHIFTING	78.4	1.2389	1801.	.38	.697	140.3	1.00	2524.	.0	.0	11.2554	1797.

NADLER

INGREDIENTS

INGREDIENTS	H	C	N	O	MG	CL	AR	WEIGHT	CAL./G.	DENSITY
MAGNESIUM (PURE CRYSTALINE)	.000	.000	.000	.000	.001	.000	.000	64.000	0.	.0628
AMMONIUM PERCHLORATE (AP)	.004	.000	.001	.004	.000	.001	.000	20.000	-602.	.0704
HTFB (SINCLAIR)	.103	.073	.000	.001	.000	.000	.000	16.000	13.	.0332
AIR (DRY AT SEA LEVEL)	.000	.000	.835	.224	.000	.005	.005	,500.000	0.	.0000

SYSTEM WT. IS 2500.000 GRAMS

(H)	(C)	(N)	(O)	(MG)	(CL)	(AR)
2.534446	1.171963	15.018152	35.871698	2.631579	.170217	.807473

CHAMBER RESULTS

TEMP.(K) 1098. TEMP.(F) 1517. PRESS.(ATM) .68 PRESS.(PSI) 10.0000 ENTHALPY -11.83 ENTROPY 5035.20 CP/CV 1.3000 MOLS GAS 86.147 RT/V .0079

N2	67.5054/ 6.75+01	O2	15.4024/ 1.54+01	MGO$	2.6316/ 2.63+00	CO2	1.1720/ 1.17+00
H2O	1.0840/ 1.08+00	AR	.8075/ 8.07-01	HCL	.1663/ 1.66-01	NO	.0074/ 7.37-03
CL2	.0016/ 1.60-03	CL	.0007/ 6.81-04	HO	.0000/ 2.03-05	MGCL2	.0000/ 2.13-06
O	.0000/ 1.03-07	HO2	.0000/ 3.24-08	CO	.0000/ 4.20-09	H2	.0000/ 3.85-09
O3	.0000/ 2.19-10	H	.0000/ 1.72-11	NHO	.0000/ 1.22-11		

EXHAUST RESULTS

TEMP.(K) 952. TEMP.(F) 1255. PRESS.(ATM) .37 PRESS.(PSI) 5.5000 ENTHALPY -116.59 ENTROPY 5035.20 CP/CV 1.3172 MOLS GAS 86.146 RT/V .0043

N2	67.5082/ 6.75+01	O2	15.4046/ 1.54+01	MGO$	2.6316/ 2.63+00	CO2	1.1720/ 1.17+00
H2O	1.0853/ 1.09+00	AR	.8075/ 8.07-01	HCL	.1639/ 1.64-01	CL2	.0031/ 3.09-03
HO	.0016/ 1.62-03	CL	.0002/ 1.61-04	NO2	.0001/ 6.85-05	HO	.0000/ 1.54-06
MGCL2	.0000/ 2.24-07	HO2	.0000/ 2.62-09	O	.0000/ 2.04-09	H2	.0000/ 8.24-11
CO	.0000/ 5.01-11	O3	.0000/ 1.48-11				

HYPOTHESIS

HYPOTHESIS	IMPULSE	IS EXP	THR. T	THR. P	CF	ISP*	OPT EX	EXH V	RHO-ISP	ELLIS PARA.	A*/M.	EX T
FROZEN	59.2	1.3131	949.	.37	.707		1.00	1905.	.0	.0	8.3762	952.
SHIFTING	59.2	1.3146	949.	.37	.707	105.3	1.00	1905.	.0	.0	8.3774	952.

INGREDIENTS

	H	C	N	O	MG	CL	AR	WEIGHT	CAL./G.	DENSITY
MAGNESIUM (PURE CRYSTALINE)	.000	.000	.000	.000	.001	.000	.000	64.000	0.	.0628
AMMONIUM PERCHLORATE (AP)	.004	.000	.001	.004	.000	.001	.000	20.000	-602.	.0704
HTPB (SINCLAIR)	.103	.073	.000	.001	.000	.000	.000	16.000	13.	.0332
AIR (DRY AT SEA LEVEL)	.000	.000	.835	.224	.000	.005	.000	5000.000	0.	.0000

SYSTEM WT. 155100.000GRAMS

(H)	(C)	(N)	(O)	(MG)	(CL)	(AR)
2.331446	1.171953219.885039	73.04E+74	2.631579	.170217	1.614945	

CHAMBER RESULTS

	TEMP.(K)	TEMP.(F)		PRESS.(ATM)	PRESS.(PSI)	ENTHALPY	ENTROPY	CP/CV	MOLS GAS	RT/V
	723.	843.		.68	10.0000	-11.83	9434.66	1.3453	172.454	.0039

N2	134.9329/ 1.35+02	O2	33.4821/ 3.35+01	MGO$	2.6316/ 2.63+00	AR	1.6149/ 1.61+00
CO2	1.1720/ 1.17+00	H2O	1.1026/ 1.11+00	HCL	.1212/ 1.21-01	CL2	.0245/ 2.45-02
NO	.0001/ 9.10-05	NO2	.0001/ 5.64-05	CL	.0000/ 3.42-06	HO	.0000/ 2.92-09
MGCL2	.0000/ 5.25-10	HO2	.0000/ 1.62-11				

EXHAUST RESULTS

	TEMP.(K)	TEMP.(F)		PRESS.(ATM)	PRESS.(PSI)	ENTHALPY	ENTROPY	CP/CV	MOLS GAS	RT/V
	620.	656.		.37	5.5000	-149.18	9434.66	1.3541	172.445	.0022

N2	134.9330/ 1.35+02	O2	33.4728/ 3.35+01	MGO$	2.6316/ 2.63+00	AR	1.6149/ 1.61+00
CO2	1.1720/ 1.17+00	H2O	1.1254/ 1.13+00	HCL	.0837/ 8.37-02	CL2	.0432/ 4.32-02
NO	.0000/ 1.73-05	NO	.0000/ 7.40-06	CL	.0000/ 2.03-07	HO	.0000/ 3.79-11
MGCL2	.0000/ 5.33-12						

HYPOTHESIS

	IMPULSE	IS EXP	THR. T	THR. P	CF	ISP*	OPT EX	EXH V	RHO-ISP	ELLIS PARA.	A*/M.	EX T
FROZEN	48.4	1.3498	616.	.37	.712	85.8	1.00	1558.		.0	6.8028	620.
SHIFTING	48.4	1.3510	616.	.37	.712		1.00	1558.		.0	6.8040	620.

INGREDIENTS

	H	C	N	O	MG	CL	AR							WEIGHT	CAL./G.	DENSITY
MAGNESIUM (PURE CRYSTALINE)	.000	.000	.000	.000	.001	.000	.000	.000	.000	.000	.000	.000	54.000	0.	.0628
AMMONIUM PERCHLORATE (AP)	.004	.000	.001	.004	.000	.001	.000	.000	.000	.000	.000	.000	30.000	-602.	.0704
HTPB (SINCLAIR)	.103	.073	.000	.001	.000	.000	.000	.000	.000	.000	.000	.000	16.000	13.	.0332
AIR (DRY AT SEA LEVEL)	.000	.000	.835	.224	.000	.000	.005	.000	.000	.000	.000	.000	.000	0.	.0000

SYSTEM WT. IS 100.000GRAMS

(H)	(C)	(N)	(O)	(MG)	(CL)	(AR)
2.674930	1.171953	.265326	1.037357	2.220395	.265326	.000000

CHAMBER RESULTS	TEMP.(K) 1902.	TEMP.(F) 2963.	PRESS.(ATM) .68	PRESS.(PSI) 10.0000	ENTHALPY -17.85	ENTROPY 199.17	CP/CV 1.2120	MOLS GAS 3.305	RT/V .2058
MG	1.3571/ 1.36+00		H2	1.3234/ 1.32+00	C$	.8426/ 8.43-01		MGO$	.7150/ 7.15-01
CO	.3224/ 3.22-01		N2	.1248/ 1.25-01	MGCL2	.1101/ 1.10-01		MGCL	.0274/ 2.74-02
MGH	.0108/ 1.08-02		HCL	.0077/ 7.72-03	CNH	.0056/ 5.63-03		H	.0020/ 2.02-03
C2H2	.0006/ 5.83-04		CH4	.0002/ 1.89-04	H2O	.0000/ 1.57-05		CL	.0000/ 9.01-06
NH3	.0000/ 2.70-06		MGN	.0000/ 2.60-06	CO2	.0000/ 9.15-07		MGO	.0000/ 3.95-07
CH2O	.0000/ 5.94-08		CHO	.0000/ 5.89-08	MGHO	.0000/ 5.91-08		CH2	.0000/ 3.70-09
AR	.0000/ 3.23-09		NH	.0000/ 2.21-09	HO	.0000/ 1.51-08		N	.0000/ 1.56-10
CH	.0000/ 7.86-11		CL2	.0000/ 6.67-11	NO	.0000/ 1.93-09		C	.0000/ 1.74-11
O	.0000/ 2.26-12					.0000/ 1.83-11			

EXHAUST RESULTS	TEMP.(K) 1840.	TEMP.(F) 2853.	PRESS.(ATM) .37	PRESS.(PSI) 5.5000	ENTHALPY -25.10	ENTROPY 193.17	CP/CV 1.2057	MOLS GAS 3.230	RT/V .1158
MG	1.3296/ 1.33+00		H2	1.3284/ 1.33+00	C$	.8770/ 8.77-01		MGO$	.7475/ 7.48-01
CO	.2898/ 2.90-01		N2	.1255/ 1.25-01	MGCL2	.1125/ 1.12-01		MGCL	.0231/ 2.31-02
MGH	.0076/ 7.61-03		HCL	.0072/ 7.23-03	CNH	.0043/ 4.32-03		H	.0017/ 1.68-03
C2H2	.0004/ 3.72-04		CH4	.0001/ 1.29-04	H2O	.0000/ 1.05-05		CL	.0000/ 7.06-06
NH3	.0000/ 1.71-06		MGN	.0000/ 1.42-06	CO2	.0000/ 5.81-07		MGO	.0000/ 2.07-07
CH2O	.0000/ 3.07-08		CHO	.0000/ 2.69-08	MGHO	.0000/ 6.77-09		AR	.0000/ 3.23-09
CH2	.0000/ 1.63-09		NH	.0000/ 1.09-09	HO	.0000/ 3.40-10		N	.0000/ 7.65-11
CL2	.0000/ 3.91-11		CH	.0000/ 3.06-11	NO	.0000/ 7.93-12		C	.0000/ 6.91-12

HYPOTHESIS	IMPULSE	IS EXP	THR. T	THR. P	CF	ISP*	OPT EX	EXH V	RHO-ISP	ELLIS PARA.	A*/M.	EX T
FROZEN	78.4	1.2217	1718.	.38	.694			2522.	.0	.0	11.3060	1713.
SHIFTING	78.4	1.0357	1847.	.40	.677	143.9	1.00	2455.	.0	.0	11.7312	1840.
							1.00					

NADLER

NADLER

INGREDIENTS

	H	C	N	O	MG	CL	AR							WEIGHT	CAL./G.	DENSITY
MAGNESIUM (FUSE CRYSTALINE)	.000	.000	.000	.000	.001	.000	.000	.000	.000	.000	.000		54.000	0.	.0628
AMMONIUM PERCHLORATE (AP)	.004	.000	.001	.004	.000	.001	.000	.000	.000	.000	.000		30.000	-502.	.0704
HTPB (BINDER)	.103	.073	.000	.001	.000	.000	.005	.000	.000	.000	.000		16.000	13.	.0332
AIR (DRY AT SEA LEVEL)	.000	.000	.005	.224	.000	.000	.005	.000	.000	.000	.000		25.000	0.	.0000

SYSTEM WT. IS 125.000GRAMS

(H)	(C)	(N)	(O)	(MG)	(CL)	(AR)	
2.654330	1.171763	1.523305	1.563105	2.220855	.245225	.008075	

CHAMBER RESULTS — TEMP.(K) 1911. TEMP.(F) 2930. ENTHALPY -17.85 ENTROPY 263.41 CP/CV 1.2356 MOLS GAS 4.288 RT/V .1585

	PRESS.(ATM) .68	PRESS.(PSI) 10.0000		
MG	1.3185/ 1.32+00	H2	.7252/ 7.25-01	MGO$
CO	.6739/ 6.74-01	MGCL2	.0278/ 2.78-02	MGCL
C2H	.0147/ 1.47-02	HCL	.0081/ 8.07-03	AR
H	.0025/ 2.48-03	CH	.0000/ 2.40-05	H2O
CL	.0000/ 1.34-05	MGN	.0000/ 2.90-06	CO2
MGO	.0000/ 6.21-07	CH2O	.0000/ 2.03-08	MGHO
NH	.0000/ 6.17-09	HO	.0000/ 5.24-10	N
CH	.0000/ 1.08-10	CH2	.0000/ 2.84-11	C
O	.0000/ 5.31-12	CL2		

EXHAUST RESULTS — TEMP.(K) 1851. TEMP.(F) 2872. ENTHALPY -27.40 ENTROPY 263.41 CP/CV 1.2315 MOLS GAS 4.216 RT/V .0887

	PRESS.(ATM) .37	PRESS.(PSI) 5.5000		
H2	1.3224/ 1.32+00	MG	1.3094/ 1.31+00	MGO$
CO	.6286/ 6.29-01	C$	.5310/ 5.31-01	MGCL
C2H	.0114/ 1.14-02	HCL	.0039/ 8.64-03	MGH
H	.0021/ 2.08-03	C2H2	.0000/ 4.01-04	H2O
CL	.0000/ 1.07-05	MGN	.0000/ 3.24-06	CO2
MGO	.0000/ 3.34-07	CHO	.0000/ 5.77-08	MGHO
NH	.0000/ 3.09-09	CH2	.0000/ 1.91-09	N
CL2	.0000/ 6.28-11	CH	.0000/ 4.31-11	C
O	.0000/ 2.31-12			

HYPOTHESIS

	IMPULSE	IS EXP	IS EXP	TIR. T	THR. P	CF	ISP*	OPT EX	EXH V	RTO-ISP	ELLIS PARA.	A*/M.	EX T
FROZEN	80.3	1.2235	7.7047	1707.	.38	.698	147.6	1.00	2583.	.0	.0	11.5087	1701.
SHIFTING	81.5	1.1066	12.0111	1857.	.40	.673		1.00	2623.	.0	.0	12.0111	1851.

INGREDIENTS

	HEIGHT	CAL./G.	DENSITY
MAGNESIUM (PURE CRYSTALINE)	54.000	0.	.0628
AMMONIUM PERCHLORATE (AP)	30.000	-602.	.0704
HTPB (SINCLAIR)	16.000	13.	.0332
AIR (DRY AT SEA LEVEL)	50.000	0.	.0000

	H	C	N	O	MG	CL	AR			
	.000	.000	.000	.000	.001	.000	.000	.000	.000	.000
	.004	.000	.001	.004	.000	.001	.000	.000	.000	.000
	.103	.073	.000	.001	.000	.000	.000	.000	.000	.000
	.000	.000	.935	.224	.000	.005	.005	.000	.000	.000

SYSTEM WT. IS 150.000GRAMS

(H)	(C)	(N)	(O)	(MG)	(CL)	(AR)
2.674380	1.171353	2.962234	1.760852	2.220395	.255326	.016149

CHAMBER RESULTS TEMP.(K) 1910. TEMP.(F) 2979. PRESS.(ATM) .68 PRESS.(PSI) 10.0000 ENTHALPY -17.85 ENTROPY 305.39 CP/CV 1.2596 MOLS GAS 5.312 RT/V .1281

N2	1.4662/ 1.47+00	MG	1.3439/ 1.34+00	CO	1.0291/ 1.03+00
MGO	.7317/ 7.32-01	CS	.1216/ 1.22-01	MGCL	.0277/ 2.77-02
CNH	.0200/ 2.00-02	AR	.0161/ 1.61-02	MGH	.0084/ 8.41-03
H	.0027/ 2.75-03	C2H2	.0005/ 6.25-04	H2O	.0000/ 2.95-05
CL	.0000/ 1.65-05	MGN	.0000/ 7.20-06	CO2	.0000/ 5.47-06
MGO	.0000/ 7.62-07	CHO	.0000/ 1.54-07	MGHO	.0000/ 2.25-08
NH	.0000/ 8.33-09	HO	.0000/ 5.05-09	N	.0000/ 7.87-10
NO	.0000/ 1.67-10	CL2	.0000/ 1.27-10	C	.0000/ 3.49-11
O	.0000/ 8.07-12				

EXHAUST RESULTS TEMP.(K) 1850. TEMP.(F) 2871. PRESS.(ATM) .37 PRESS.(PSI) 5.5000 ENTHALPY -29.67 ENTROPY 326.39 CP/CV 1.2538 MOLS GAS 5.235 RT/V .0715

N2	1.4694/ 1.47+00	N2	1.2202/ 1.32+00	CO	.9715/ 9.72-01
MGO	.7633/ 7.89-01	CS	.1811/ 1.84-01	MGCL	.0233/ 2.33-02
AR	.0161/ 1.61-02	CNH	.0154/ 1.54-02	MGH	.0058/ 5.83-03
H	.0123/ 2.31-03	C2H2	.0004/ 4.00-04	H2O	.0000/ 2.07-05
CL	.0000/ 1.33-05	MGN	.0000/ 3.83-06	NH3	.0000/ 3.52-06
MGO	.0000/ 4.12-07	CHO	.0000/ 7.99-08	MGHO	.0000/ 1.03-08
NH	.0000/ 4.18-09	HO	.0000/ 2.61-09	N	.0000/ 3.94-10
CL2	.0000/ 7.81-11	NO	.0000/ 7.72-11	C	.0000/ 1.44-11
O	.0000/ 3.55-12				

	IMPULSE	IS EXP	THR. T	THR. P	CF	ISP*	OPT EX	EXH V	RHO-ISP	ELLIS PARA.	A*/M.	EX T
FROZEN	81.4	1.6460	1990.	.88	.701	150.0	1.00	2619.	.0	.0	11.6185	1696.
SHIFTING	82.8	1.6475	1946.	.40	.673	150.0	1.00	2745.	.0	.0	12.2248	1850.

INGREDIENTS

		H	C	N	O	MG	CL	AR			WEIGHT	CAL./G.	DENSITY
MAGNESIUM (FINE CRYSTALINE)		.000	.000	.000	.000	.001	.000	.000			54.000	0.	.0628
ANTRIUM PERHCLORATE (AP)		.004	.000	.001	.004	.000	.001	.000			30.000	-602.	.0704
HTPB (BINDER)		.103	.073	.000	.001	.000	.000	.005			16.000	13.	.0332
AIR (DRY AT SEA LEVEL)		.000	.000	.835	.224	.000	.000	.005			75.000	0.	.0000

SYSTEM WT. IS 175.000 GRAMS

(H)	(C)	(N)	(O)	(MG)	(CL)	(AR)
2.67.920	1.17123	4.75704	2.122300	2.220395	.245526	.024224

CHAMBER RESULTS

	TEMP.(K) 2235.	TEMP.(F) 3574.	PRESS.(ATM) .68	PRESS.(PSI) 10.0000	ENTHALPY -17.85	ENTROPY 387.07	CP/CV 1.2456	MOLS GAS 6.016	RT/V .1131
N2	2.1503/ 2.15+00			H2	1.2639/ 1.27+00	CO	1.1705/ 1.15+00	MG	1.1545/ 1.15+00
MGO%	.9401/ 9.40-01			HCL	.0709/ 7.09-02	MGCL2	.0662/ 6.62-02	MGCL	.0505/ 5.05-02
H	.0387/ 3.87-02			AR	.0242/ 2.42-02	H2O	.0085/ 8.51-03	MGH	.0084/ 8.40-03
CL	.0016/ 1.57-03			CO2	.0014/ 1.39-03	MGO	.0007/ 6.56-04	CNH	.0001/ 7.64-05
HO	.0000/ 4.32-05			MGN	.0000/ 3.54-05	MGHO	.0000/ 8.84-06	NO	.0000/ 3.24-06
NH3	.0000/ 3.02-06			CHO	.0000/ 9.33-07	O	.0000/ 9.08-07	NH	.0000/ 4.82-07
N	.0000/ 2.48-07			CH2O	.0000/ 1.02-07	CL2	.0000/ 5.56-08	CH	.0000/ 2.39-08
C2H2	.0000/ 4.14-09			O2	.0000/ 2.56-09	NHO	.0000/ 5.27-10	CH2	.0000/ 2.25-10
C	.0000/ 1.05-10			CH	.0000/ 7.68-11				

EXHAUST RESULTS

	TEMP.(K) 2132.	TEMP.(F) 3378.	PRESS.(ATM) .37	PRESS.(PSI) 5.5000	ENTHALPY -33.77	ENTROPY 387.07	CP/CV 1.2470	MOLS GAS 5.984	RT/V .0625
N2	2.1503/ 2.15+00			H2	1.3016/ 1.30+00	CO	1.1714/ 1.14+00	MG	1.1418/ 1.14+00
MGO%	.9490/ 9.49-01			MGCL2	.0855/ 8.55-02	HCL	.0456/ 4.56-02	MGCL	.0394/ 3.84-02
AR	.0242/ 2.42-02			H	.0172/ 1.72-02	MGH	.0057/ 5.67-03	H2O	.0016/ 1.56-03
CL	.0004/ 4.45-04			CO2	.0003/ 2.82-04	CNH	.0002/ 2.44-04	MGO	.0001/ 6.90-05
MGN	.0000/ 1.30-05			HO	.0000/ 2.54-06	NH3	.0000/ 2.27-06	MGHO	.0000/ 9.49-07
CHO	.0000/ 3.31-07			NO	.0000/ 1.44-07	CH4	.0000/ 1.23-07	NH	.0000/ 9.19-08
CH2O	.0000/ 6.02-08			C2H2	.0000/ 5.02-08	N	.0000/ 3.13-08	O	.0000/ 2.41-08
CL2	.0000/ 8.71-09			CH2	.0000/ 2.12-10	CH	.0000/ 3.44-11	C	.0000/ 3.33-11
NHO	.0000/ 1.71-11			O2	.0000/ 1.24-11				

HYPOTHESIS

	IMPULSE	IS EXP	THR. T	THR. P	CF	ISP*	OPT EX	EXH V	RHO-ISP	ELLIS PARA.	A*/M.	EX T
FROZEN	88.5	1.2477	2073.	.79	.698		1.00	2847.	.0	.0	12.6716	2074.
SHIFTING	89.0	1.1544	2140.	.79	.691	159.8	1.00	2863.	.0	.0	12.8738	2132.

```
INGREDIENTS                              H     C     N     O     MG    CL    AR          WEIGHT   CAL./G.  DENSITY
MAGNESIUM (PURE CRYSTALINE)            .000  .000  .000  .000  .001  .000  .000          54.000     0.      .0628
AMMONIUM PERCHLORATE (AP)              .004  .000  .001  .004  .000  .001  .000          30.000   -602.     .0704
HTB (SINCLAIR)                         .103  .073  .000  .001  .000  .000  .000          16.000    13.      .0332
AIR (DRY AT SEA LEVEL)                 .000  .000  .035  .234  .000  .000  .005         100.000     0.      .0000

SYSTEM WT. IS 200.000 GRAMS

   (H)        (C)        (N)        (O)        (MG)       (CL)      (AR)
2.674580   1.171693   5.642243   2.491248   2.2.0395   25.526   .032299
```

```
CHAMBER    TEMP.(K)  TEMP.(F)   PRESS.(ATM)  PRESS.(PSI)   ENTHALPY   ENTROPY   CP/CV    MOLS GAS   RT/V
RESULTS    2624.     4264.      .68          10.0000       -17.85     442.80    1.2306   6.596      .1031

N2   2.3243/ 2.32+00    CO   1.1500/ 1.15+00    H2   1.0662/ 1.07+00
MG    .9797/ 9.80-01    HCL   .1357/ 1.35-01    H2O   .1302/ 1.30-01
MGCL  .0488/ 4.83-02    AR    .0223/ 3.23-02    CO2   .0219/ 2.19-02
MGO   .0134/ 1.34-02    CL    .0122/ 1.22-02    HO    .0039/ 3.89-03
NO    .0005/ 4.93-04    O     .0003/ 3.23-04    MGN   .0001/ 7.28-05
O2    .0000/ 1.63-05    N     .0000/ 4.54-05    NH    .0000/ 3.45-06
CHO   .0000/ 1.91-06    NH3   .0000/ 1.79-06    CH2O  .0000/ 7.35-08
N2O   .0000/ 7.29-08    HO2   .0000/ 5.86-09    C     .0000/ 1.54-10
CH    .0000/ 4.76-11    CH2   .0000/ 3.78-11
```

```
EXHAUST    TEMP.(K)  TEMP.(F)   PRESS.(ATM)  PRESS.(PSI)   ENTHALPY   ENTROPY   CP/CV    MOLS GAS   RT/V
RESULTS    2458.     4019.      .37          5.5000        -37.75     442.80    1.2274   6.507      .0575

N2   2.8245/ 2.82+00    MGO  1.2070/ 1.21+00    H2   1.1581/ 1.16+00
MG    .9235/ 9.23-01    HCL   .1343/ 1.34-01    H2O   .1053/ 1.05-01
MGCL  .0423/ 4.25-02    MGCL2 .0349/ 3.49-02    CO2   .0323/ 3.23-02
CL    .0043/ 8.92-03    MGO   .0079/ 7.89-03    HO    .0043/ 4.82-03
NO    .0002/ 1.66-04    O     .0001/ 9.53-05    MGN   .0001/ 5.90-05
CNH   .0000/ 3.82-06    O2    .0000/ 2.83-06    NH    .0000/ 1.82-06
NH3   .0000/ 1.25-06    CHO   .0000/ 1.01-06    CH2O  .0000/ 4.10-07
N2O   .0000/ 1.65-08    HO2   .0000/ 7.69-10    C     .0000/ 2.23-10
CH2   .0000/ 2.05-11    CH    .0000/ 1.99-11    C2H2  .0000/ 7.03-12
```

```
HYPOTHESIS   IMPULSE  IS EXP    THR.T   THR.P   CF     ISP*    OPT EX  EXH V    RHO-ISP  ELLIS PARA.   A*/M.     EX T
FROZEN       92.0     1.2624    2551.   .58     .606           1.00    2960.    .0                     13.2155   2344.
SHIFTING     93.0     1.1874    2429.   .59     .632   168.1   1.00    2934.    .0                     13.6515   2488.
```

INGREDIENTS

	H	C	N	O	MG	CL	AR		WEIGHT	CAL./G.	DENSITY
MAGNESIUM (PURE CRYSTALINE)	.000	.000	.000	.000	.001	.000	.000		54.000	0.	.0628
AMMONIUM PERCHLORATE (AP)	.004	.000	.001	.004	.000	.031	.000		30.000	-602.	.0704
HTFB (BINDAIR)	.103	.073	.000	.001	.000	.000	.005		16.000	13.	.0332
AIR (DRY AT SEA LEVEL)	.000	.000	.835	.224	.000	.000	.005		200.000	0.	.0000

SYSTEM WT. IS 300.000GRAMS

(H)	(C)	(N)	(O)	(MG)	(CL)	(AR)
2.64390	1.171763	11.043161	3.951339	2.220395	.245326	.064598

CHAMBER RESULTS

TEMP.(K) 2848.	TEMP.(F) 4667.	PRESS.(ATM) .68	PRESS.(PSI) 10.0000	ENTHALPY -17.85	ENTROPY 655.56	CP/CV 1.2185	MOLS GAS 9.271	RT/V .0734

N2	5.5029/ 5.50+00	MG%	1.4230/ 1.43+00	CO	.9493/ 9.49-01	H2O	.6751/ 6.75-01
MG	.5516/ 5.52 01	H2	.4171/ 4.17-01	CO2	.2294/ 2.29-01	CO2	.2227/ 2.23-01
MGO	.2013/ 2.01 01	HCL	.1497/ 1.50-01	HO	.1086/ 1.09-01	AR	.0646/ 6.46-02
CL	.0571/ 5.71-02	O	.0573/ 3.78-02	NO	.0373/ 3.73-02	MGCL	.0285/ 2.85-02
O2	.0249/ 2.49 02	MGCL2	.0100/ 1.00-02	MGH	.0022/ 2.23-03	MGHO	.0007/ 7.05-04
MGN	.0001/ 8.01-05	N	.0000/ 2.98-06	NH	.0000/ 1.02-05	HO2	.0000/ 5.01-06
CL2	.0000/ 4.48-06	N2O	.0000/ 1.65-08	CHO	.0000/ 1.45-06	NH3	.0000/ 3.61-07
CNH	.0000/ 1.50-07	CH2	.0000/ 1.61-12	O3	.0000/ 7.54-10	C	.0000/ 7.86-11
CH	.0000/ 8.07-12						

EXHAUST RESULTS

TEMP.(K) 2743.	TEMP.(F) 4479.	PRESS.(ATM) .37	PRESS.(PSI) 5.5000	ENTHALPY -48.38	ENTROPY 655.56	CP/CV 1.2136	MOLS GAS 9.113	RT/V .0411

N2	5.5079/ 5.51+00	MG%	1.5475/ 1.55+00	CO	.9528/ 9.53-01	H2O	.6690/ 6.69-01
MG	.4940/ 4.94-01	H2	.4350/ 4.35-01	CO2	.2191/ 2.19-01	H	.2166/ 2.17-01
HCL	.1581/ 1.58-01	MGO	.1442/ 1.44-01	HO	.0883/ 8.83-02	AR	.0646/ 6.46-02
CL	.0543/ 5.49-02	O	.0282/ 2.82-02	NO	.0272/ 2.72-02	MGCL	.0232/ 2.32-02
O2	.0177/ 1.77-02	MGCL2	.0095/ 9.54-03	MGH	.0015/ 1.48-03	MGHO	.0004/ 4.27-04
MGN	.0000/ 4.28-05	N	.0000/ 2.63-05	NH	.0000/ 6.06-06	CL2	.0000/ 3.51-06
HO2	.0000/ 2.66-06	N2O	.0000/ 1.65-06	CHO	.0000/ 8.67-07	NH3	.0000/ 2.35-07
CNH	.0000/ 9.11-08	CH2O	.0000/ 9.73-09	O3	.0000/ 2.67-10	C	.0000/ 3.25-11
CH	.0000/ 3.14-12						

HYPOTHESIS	IMPULSE	IS EXP	THR. T	THR. P	CF	ISP*	OPT EX	EXH V	RHO-ISP	ELLIS PARA.	A*/M	EX T
FROZEN	92.9	1.2199	2566.	.38	.695		1.00	2549.	.0	.0	13.3742	2557.
SHIFTING	94.1	1.1003	2754.	.40	.678	170.4	1.00	3028.	.0	.0	13.8839	2743.

NADLER

NADLER

INGREDIENTS

	H	C	N	O	MG	CL	AR	WEIGHT	CAL./G.	DENSITY
MAGNESIUM (PURE CRYSTALINE)	.000	.000	.000	.000	.001	.000	.000	54.000	0.	.0628
AMMONIUM PERCHLORATE (AP)	.004	.000	.001	.004	.000	.001	.000	30.000	-602.	.0704
HTPB (SINCLAIR)	.103	.073	.000	.001	.000	.000	.000	16.000	13.	.0332
AIR (DRY AT SEA LEVEL)	.000	.000	.835	.224	.000	.000	.005	500.000	0.	.0000

SYSTEM WT. IS 600.000GRAMS

(H)	(C)	(N)	(O)	(MG)	(CL)	(AR)
2.674880	1.171953	27.224913	8.272312	2.220395	.255326	.161495

CHAMBER RESULTS	TEMP.(K) 2635.	TEMP.(F) 4283.	PRESS.(ATM) .68	PRESS.(PSI) 10.0000	ENTHALPY -17.85	ENTROPY 1269.23	CP/CV 1.2228	MOLS GAS 18.125	RT/V .0375
N2	13.4670/ 1.35+01	MGO$	2.1380/ 2.14+00	O2	1.1467/ 1.15+00	H2O	1.0604/ 1.06+00		
CO2	.8720/ 8.72-01	CO	.3000/ 3.00-01	NO	.2909/ 2.91-01	HO	.2401/ 2.40-01		
AR	.1615/ 1.61-01	O	.1492/ 1.49-01	HCL	.1461/ 1.46-01	CL	.0980/ 9.80-02		
H2	.0568/ 5.68-02	MGO	.0563/ 5.63-02	H	.0540/ 5.40-02	MG	.0192/ 1.92-02		
MGCL2	.0043/ 4.26-03	MGCL	.0026/ 2.64-03	M3HO	.0001/ 6.44-05	HO2	.0001/ 5.77-05		
MGH	.0000/ 1.91-05	NH	.0000/ 1.80-05	CL2	.0000/ 1.62-05	NHO	.0000/ 6.00-06		
MGN	.0000/ 1.93-06	CNH	.0000/ 1.22-09	O3	.0000/ 1.02-07	CHO	.0000/ 7.13-08		
NH3	.0000/ 1.74-08			CH2O	.0000/ 3.71-10				

EXHAUST RESULTS	TEMP.(K) 2479.	TEMP.(F) 4003.	PRESS.(ATM) .37	PRESS.(PSI) 5.5000	ENTHALPY -72.65	ENTROPY 1269.23	CP/CV 1.2214	MOLS GAS 17.948	RT/V .0208
N2	13.4938/ 1.35+01	MGO$	2.1905/ 2.19+00	O2	1.1527/ 1.15+00	H2O	1.1153/ 1.12+00		
CO2	.9695/ 9.69-01	NO	.2253/ 2.25-01	CO	.2025/ 2.02-01	HO	.1787/ 1.79-01		
AR	.1615/ 1.61-01	HCL	.1573/ 1.57-01	O	.0961/ 9.61-02	CL	.0901/ 9.01-02		
H2	.0387/ 3.87-02	H	.0310/ 3.10-02	MGO	.0136/ 1.96-02	MS	.0059/ 5.85-03		
MGCL2	.0034/ 3.45-03	MGCL	.0010/ 1.04-03	HO2	.0000/ 3.42-05	MGHO	.0000/ 1.65-05		
CL2	.0000/ 1.59-05	N	.0000/ 6.04-06	MGH	.0000/ 3.39-06	NHO	.0000/ 2.80-06		
NH	.0000/ 5.76-07	MGN	.0000/ 2.93-07	O3	.0000/ 5.03-08	CHO	.0000/ 1.91-08		
NH3	.0000/ 6.32-09	CNH	.0000/ 2.45-10	CH2O	.0000/ 9.66-11				

HYPOTHESIS	IMPULSE	IS EXP	THR.T	THR.P	THR.T	CF	ISP*	ISP	OPT EX	EXH V	RHO-ISP	ELLIS PARA.	A*/M.	EX T
FROZEN	183.3	1.2244	2469.	.38		.695		160.9	1.00	2841.	.0	.0	12.7012	2361.
SHIFTING	189.2	1.1373	2491.	.39		.633		160.9	1.00	2969.	.0	.0	13.0562	2479.

INGREDIENTS

	H	C	N	O	MG	CL	AR					WEIGHT	CAL./G.	DENSITY
AMMONIUM PERCHLORATE (AP)	.000	.000	.000	.000	.001	.000	.000	.000	.000	.000		54.000	0.	.0628
AMMONIUM PERCHLORATE (AP)	.004	.000	.001	.004	.000	.001	.000	.000	.000	.000		30.000	-602.	.0704
HTPB (BINDER/AIR)	.103	.073	.000	.001	.000	.000	.005	.000	.000	.000		16.000	13.	.0332
AIR (DRY AT SEA LEVEL)	.000	.000	.000	.224	.000	.000	.005	.000	.000	.000		1000.000	0.	.0000

(H)	(C)	(N)	(O)	(MG)	(CL)	(AR)	

SYSTEM WT. 151100.000GRAMS

CHAMBER RESULTS

	TEMP.(K)	TEMP.(F)		PRESS.(ATM)	PRESS.(PSI)	ENTHALPY	ENTROPY	CP/CV	MOLS GAS	RT/V
	1649.	2986.		.68	10.0000	-17.65	2250.54	1.2586	34.940	.0195
N2	27.0221/	2.70+01	O2	4.7768/ 4.78+00	MGO	2.2194/ 2.22+00	H2O	1.2188/ 1.22+00
CO2	1.1705/ 1.17+00	AR	.3230/ 3.23-01	HCL	.2171/ 2.17-01	NO	.1503/ 1.50-01
CL	.0260/ 3.60-02	HO	.0193/ 1.93-02	O	.0032/ 3.24-03	CO	.0014/ 1.41-03
MCL2	.0003/ 9.45-04	H2	.0004/ 3.64-04	CL2	.0001/ 1.45-04	H	.0001/ 7.86-05
HO2	.0000/ 1.03-05	MGO	.0000/ 1.79-06	MGCL	.0000/ 2.55-08	NHO	.0000/ 1.58-07
O3	.0000/ 3.87-08	MG	.0000/ 2.55-08	N	.0000/ 3.09-07	MGHO	.0000/ 3.83-10
NH	.0000/ 3.29-10	NH3	.0000/ 1.85-11	CHO	.0000/ 1.05-12	MGH	.0000/ 1.00-12

EXHAUST RESULTS

	TEMP.(K)	TEMP.(F)		PRESS.(ATM)	PRESS.(PSI)	ENTHALPY	ENTROPY	CP/CV	MOLS GAS	RT/V
	1650.	2511.		.37	5.5000	-90.61	2250.54	1.2639	34.931	.0107
N2	27.0612/ 2.71+01	O2	4.8237/ 4.82+00	MGO	2.2200/ 2.22+00	H2O	1.2176/ 1.22+00
CO2	1.1718/ 1.17+00	AR	.3230/ 3.23-01	HCL	.2335/ 2.34-01	NO	.0721/ 7.21-02
CL	.0206/ 2.06-02	HO	.0059/ 5.91-03	O	.0005/ 5.46-04	MGCL2	.0004/ 4.07-04
CL2	.0002/ 2.05-04	CO	.0002/ 1.93-04	H2	.0001/ 6.26-05	H	.0000/ 6.93-06
MO2	.0000/ 2.79-06	MGO	.0000/ 2.72-08	N2O	.0000/ 2.21-08	O3	.0000/ 8.89-09
MGCL	.0000/ 8.20-09	MG	.0000/ 1.57-10	N	.0000/ 9.99-11	NH	.0000/ 8.54-12
MGHO	.0000/ 2.93-12	NH3	.0000/ 1.15-12				

HYPOTHESIS

	IMPULSE	IS EXP	THR. T	THR. P	CF	ISP	OPT EX	EXH V	RHO-ISP	ELLIS PARA.	A*M.	EX T
FROZEN	75.8	1.2614	1644.	.38	.700		1.00	2438.	.0	.0	10.8239	1642.
SHIFTING	75.9	1.2521	1653.	.38	.639	135.6	1.00	2441.	.0	.0	10.8604	1650.

NADLER

INGREDIENTS							WEIGHT	CAL./G.	DENSITY
MAGNESIUM (PURE CRYSTALINE)							54.000	0.	.0628
AMMONIUM PERCHLORATE (AP)							30.000	-602.	.0704
HTPB (SINCLAIR)							16.000	13.	.0332
AIR (DRY AT SEA LEVEL)							2500.000	0.	.0000

	H	C	N	O	MG	CL	AR
	.000	.000	.000	.000	.001	.000	.000
	.004	.000	.001	.004	.000	.001	.000
	.103	.073	.000	.001	.000	.000	.000
	.000	.000	.835	.224	.000	.005	.005

SYSTEM WT. 152600.000GRAMS

(H)	(C)	(N)	(O)	(MG)	(CL)	(AR)
2.674980	1.171945	35.103262	37.212132	2.220395	.245326	.807473

CHAMBER RESULTS	TEMP.(K) 1021.	TEMP.(F) 1378.	PRESS.(ATM) .68	PRESS.(PSI) 10.0000	ENTHALPY -17.85	ENTROPY 5010.22	CP/CV 1.3160	MOLS GAS 86.713	RT/V .0078
N2	67.5499/ 6.75+01		O2	15.7146/ 1.57+01	MGO6	2.2204/ 2.22+00		H2O	1.2151/ 1.22+00
CO2	1.1720/ 1.17+00		AR	.8075/ 8.07-01	HCL	.2447/ 2.45-01		CL2	.0051/ 5.08-03
NO	.0055/ 3.53-03		CL	.0004/ 4.36-04	HO	.0000/ 5.61-06		MGCL2	.0000/ 1.38-06
O	.0000/ 1.29-08		HO2	.0000/ 1.08-08	H2	.0000/ 5.51-10		CO	.0000/ 4.03-10
O3	.0000/ 6.95-11		NHO	.0000/ 2.09-12	H	.0000/ 1.03-12			

EXHAUST RESULTS	TEMP.(K) 883.	TEMP.(F) 1130.	PRESS.(ATM) .37	PRESS.(PSI) 5.5000	ENTHALPY -115.77	ENTROPY 5010.22	CP/CV 1.3245	MOLS GAS 86.710	RT/V .0043
N2	67.5513/ 6.75+01		O2	15.7135/ 1.57+01	MGO6	2.2204/ 2.22+00		H2O	1.2200/ 1.22+00
CO2	1.1720/ 1.17+00		AR	.8075/ 8.07-01	HCL	.2399/ 2.35-01		CL2	.0102/ 1.02-02
NO	.0007/ 6.72-04		CL	.0001/ 8.62-05	NO2	.0001/ 5.09-05		HO	.0000/ 3.31-07
MGCL2	.0000/ 1.09-07		HO2	.0000/ 6.97-10	O	.0000/ 1.71-10		H2	.0000/ 8.00-12
O3	.0000/ 3.68-12		CO	.0000/ 3.04-12					

HYPOTHESIS	IMPULSE	IS EXP	THR. T	THR. P	CF	ISP*	OPT EX	EXH V	RHO-ISP	A*/M.	EX T
FROZEN	57.3	1.2203	880.	.37	.708		1.00	1842.	.0	8.0878	883.
SHIFTING	57.3	1.2218	880.	.37	.708	101.7	1.00	1842.	.0	8.0899	883.

INGREDIENTS	H	C	N	O	MG	CL	AR					WEIGHT	CAL./G.	DENSITY
MAGNESIUM (PURE CRYSTALINE)	.000	.000	.000	.000	.001	.000	.000	.000	.000	.000	.000	54.000	0.	.0628
AMMONIUM PERCHLORATE (AP)	.004	.000	.001	.004	.000	.001	.000	.000	.000	.000	.000	30.000	-602.	.0704
HTPB (SINCLAIR)	.103	.073	.000	.001	.000	.000	.000	.000	.000	.000	.000	16.000	13.	.0332
AIR (DRY AT SEA LEVEL)	.000	.000	.835	.224	.000	.005	.005	.000	.000	.000	.000	5000.000	0.	.0000

SYSTEM WT. 155100.000GRAMS

(H)	(C)	(N)	(O)	(MG)	(CL)	(AR)
2.674880	1.171957	69.951199	73.336908	2.220395	.455326	1.614345

CHAMBER RESULTS	TEMP.(K)	TEMP.(F)		PRESS.(ATM)	PRESS.(PSI)		ENTHALPY	ENTROPY	CP/CV	MOLS GAS	RT/V
	682.	768.		.68	10.0000		-17.85	9383.25	1.3503	173.006	.0039
N2	134.9755/	1.35+02	O2	33.7787/	3.38+01	MCO$	2.2204/	2.22+00	AR	1.6149/	1.61+00
H2O	1.2652/	1.27+00	CO2	1.1720/	1.17+00	HCL	.1445/	1.45-01	CL2	.0554/	5.54-02
NO2	.0000/	4.12-05	NO	.0000/	3.65-05	CL	.0000/	1.48-06	HO	.0000/	6.03-10
MXCL2	.0000/	1.62-10	HO2	.0000/	4.15-12						

EXHAUST RESULTS	TEMP.(K)	TEMP.(F)		PRESS.(ATM)	PRESS.(PSI)		ENTHALPY	ENTROPY	CP/CV	MOLS GAS	RT/V
	583.	590.		.37	5.5000		-147.61	9383.25	1.3592	172.992	.0022
N2	134.9755/	1.35+02	O2	33.7645/	3.38+01	MCO$	2.2204/	2.22+00	AR	1.6149/	1.61+00
H2O	1.2935/	1.29+00	CO2	1.1720/	1.17+00	HCL	.0876/	8.76-02	CL2	.0839/	8.39-02
NO2	.0000/	1.18-05	NO	.0000/	2.47-06	CL	.0000/	6.37-08	HO	.0000/	5.68-12

HYPOTHESIS	IMPULSE	IS EXP	THR. T	THR. P	CF	ISP*	OPT EX	EXH V	RHO-ISP	ELLIS PARA.	A*/M.	EX T
FROZEN	47.1	1.3548	579.	.36	.712		1.00	1514.	.0	.0	6.6061	583.
SHIFTING	47.1	1.3556	579.	.35	.712	83.4	1.00	1514.	.0	.0	6.6081	583.

NADLER

THERMODYNAMICS OF INITIATION OF THE
TiH$_x$-KClO$_4$ PYROTECHNIC COMPOSITION

J. W. Reed, J. L. Ivey,
and R. H. Steinmeyer, Mound Laboratory*

ABSTRACT

A combined experimental and theoretical study of the system
TiH$_x$-KClO$_4$ was performed to investigate the thermodynamic aspects
of initiation and to obtain data of interest in mathematical
modeling of initiation and propagation from a hot bridgewire
source. Experimental results along with equilibrium thermodynamic
computations are of interest in understanding the chemical pro-
cesses involved. Reaction temperatures, obtained from equilibrium
thermodynamic computations, range from 2800 to over 5000 K depend-
ing on hydride composition, mixture ratio and equilibrium pressure.
Lower temperature computations of the product composition matrix
were used along with simultaneous differential thermal-differential
thermogravimetric analysis to determine if the initiation reactions
were likely to be equilibrium controlled.

INTRODUCTION

This paper describes an experimental and computational study undertaken to obtain information on initiation characteristics and combustion properties of the pyrotechnic system TiH_x-$KClO_4$. The pyrotechnic has been developed as a static insensitive material to be initiated by a hot wire. The applications of interest include devices which are energy limited; that is the electrical energy available for heating the initiator wire is rather small.

The information obtained includes data of interest in modeling the initiation and combustion processes in a pyrotechnic device utilizing the TiH-$KClO_4$ pyrotechnic material.

EXPERIMENTAL

The experimental work was carried out using a Mettler TGA-DTA thermobalance system and a Perkins-Elmer differential scanning calorimeter. Differential scanning calorimetry was carried out primarily as a survey technique on many samples of the pyrotechnic mixture (TiH_x-$KClO_4$) to determine initiation temperature and to obtain an indication of relative reaction rate. The initiation temperature was found to vary over the range 750-800 K with a few as low as 725 K. Some of the samples exhibit pre-initiation exothermic peaks as low as 650 K. The heating rate for differential scanning calorimetry was much higher than for DTA-TGA, on the order of 40-80 K/min as opposed to 6-10 K/min. The positions of peaks are thus shifted considerably because of kinetic considerations.

The prime feature observed by differential scanning calorimetry is the difference in peak shape as the TiH_x composition varies from the metal (x = 0.1) to TiH_2 (x $\cong$ 1.93). The DSC exotherms

are shown in Figure 1. The pyrotechnic mixes are all (fuel/oxidizer) - 33/67 in this series. The mix containing TiH_2 has a rapid increase in dQ/dt and a sharp peak. As the TiH_x composition is reduced in hydrogen the dQ/dt rise becomes less steep and the exotherm peak becomes broader. For the composition $Ti-KClO_4$ (33/67) the rate of increase in dQ/dt is relatively slow and the peak is broad with a number of individual peaks appearing. Thus it appears from these considerations that the reaction rate is greatest for the TiH_x with the highest hydrogen composition in a TiH_x-KClO_4 mixture F/O = 33/67 by weight.

DIFFERENTIAL THERMO-GRAVIMETRIC WORK

Differential thermo-gravimetric thermograms indicate an initiation temperature of approximately 725-740 K for the materials shown in Figures 2-4. These materials are $KClO_4-TiH_{0.66}$ with fuel-to-oxidizer ratios 33/67, 39/61, and 45/55. The exotherm peaks occur at about 820-835 K. The maximum rate of weight loss occurs at the maximum in the exotherm for the 39/61 and 45/66 F/O ratios, while the maximum weight change occurs slightly later than the maximum in the exotherm for 33/67 F/O ratio. The difference is however not general.

The DTA/DTG samples were run in argon flowing at about 140 ml/min (2.36 ml/sec) at a heating rate of 6°/min. The weight loss corresponding to the reaction exotherm can be assumed to be essentially oxygen since the amount of hydrogen in the system is less than 5.4% of this weight loss and the KCl has no significant volality until about 1000 K. The ratios of O/Ti calculated from the weight loss during the reaction exotherm and corrected for hydrogen are 0.94, 1.11 and 1.19 for F/O ratios 45/55, 39/61, and 33/67 respectively.
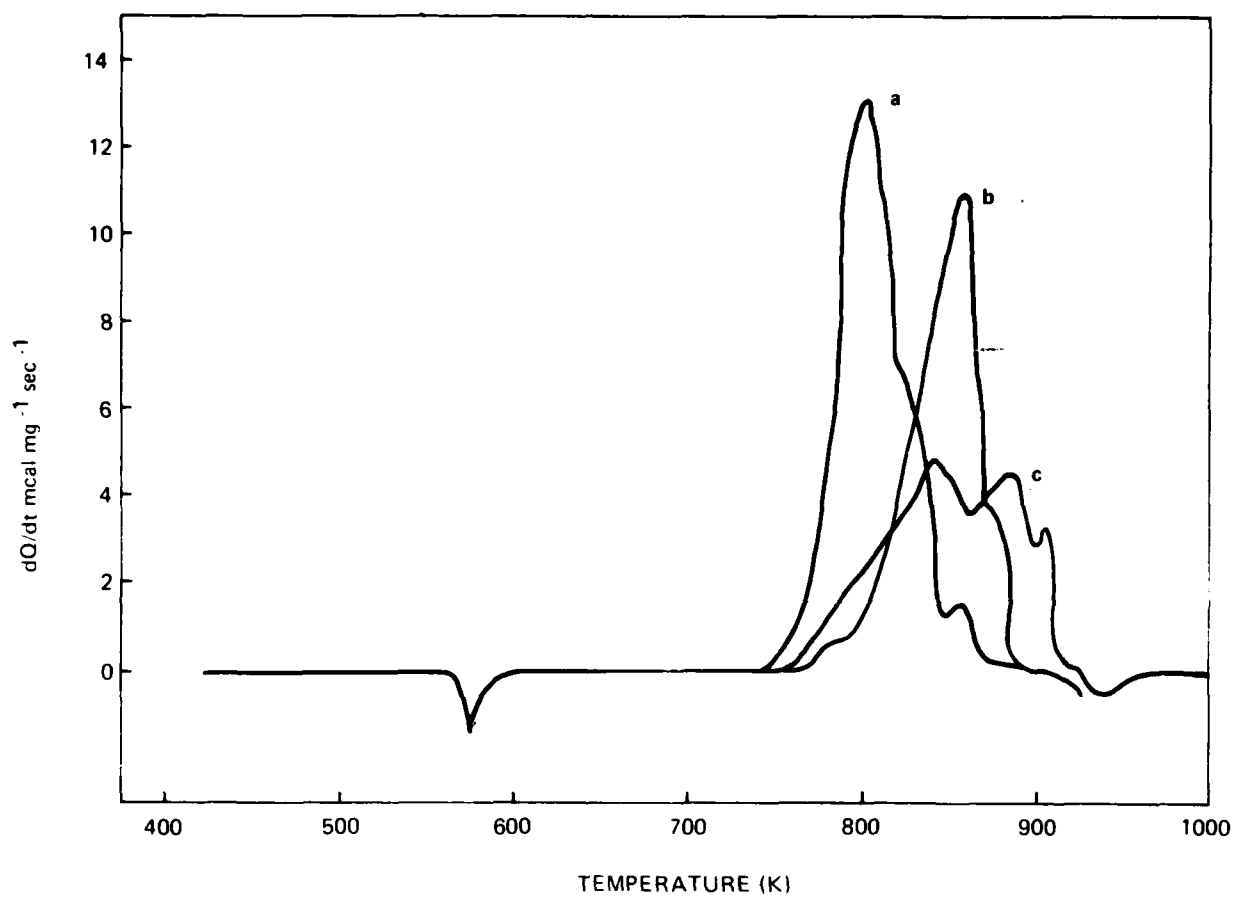
Figure 1 Differential scanning calorimeter thermograms of $TiH_x/KClO_4$ pyrotechnic compositions in weight ratio 33/67.

(a) x = 1.97
(b) x = 0.65
(c) x = 0.1
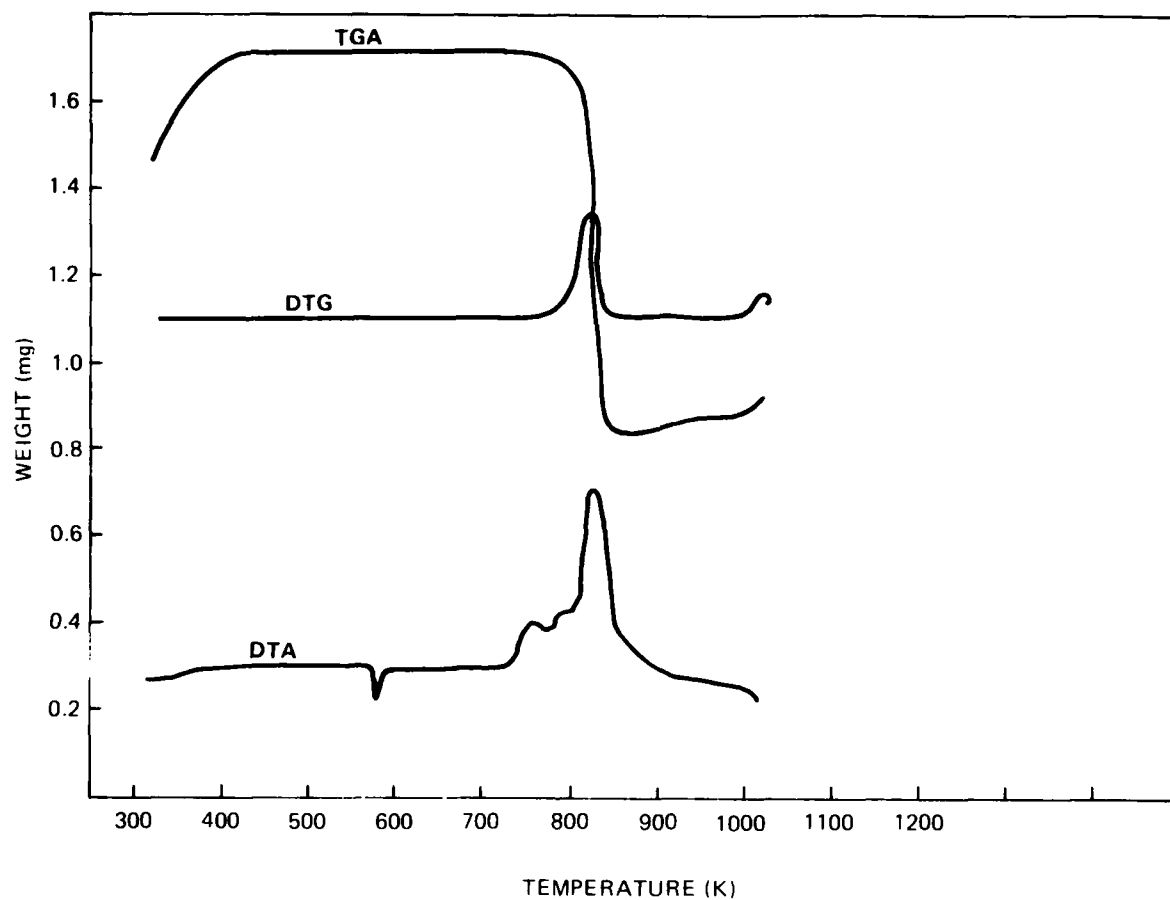
Figure 2 Differential thermogravimetric curves for $TiH_{0.66}/KClO_4$ in a weight ratio 45/55.

448
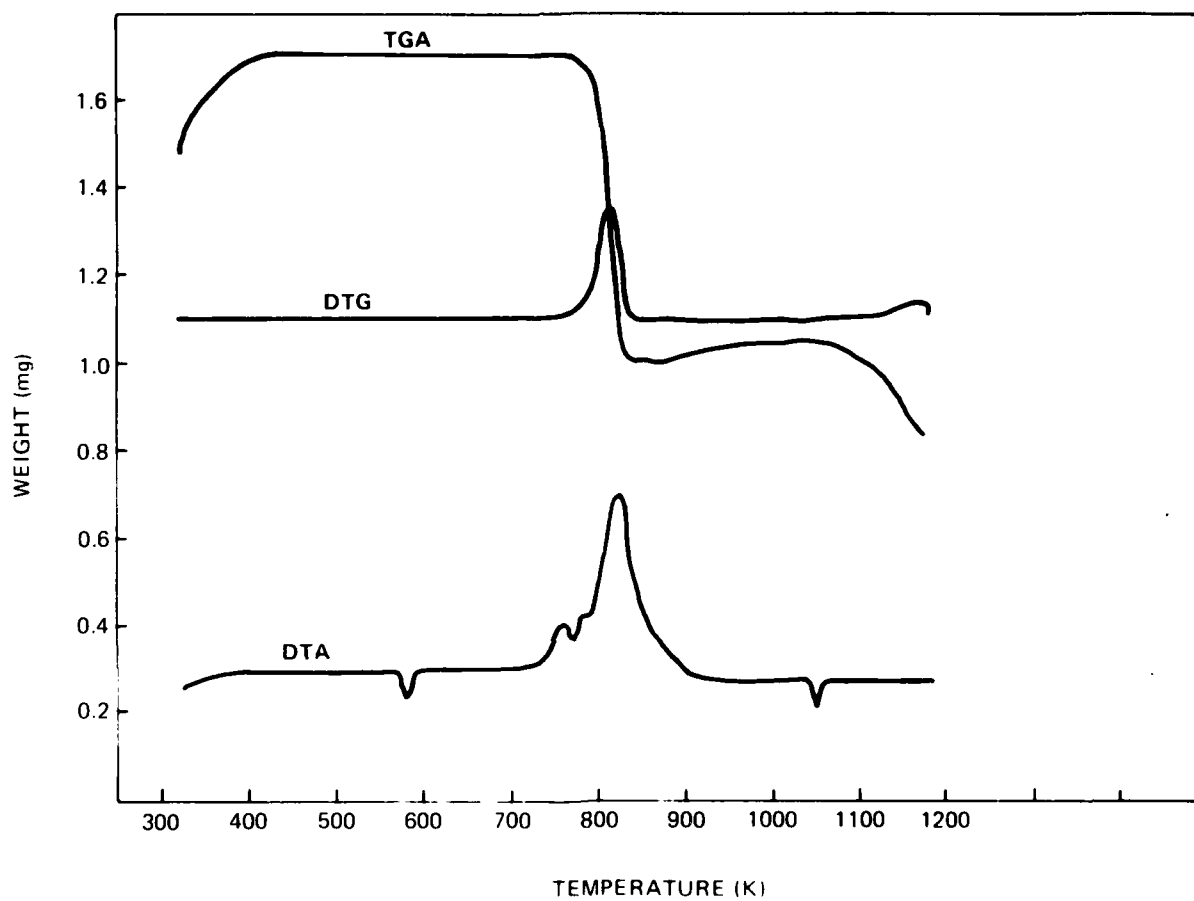
Figure 3 Differential thermogravimetric curves for $TiH_{0.66}/KClO_4$ in a weight ratio 39/61.
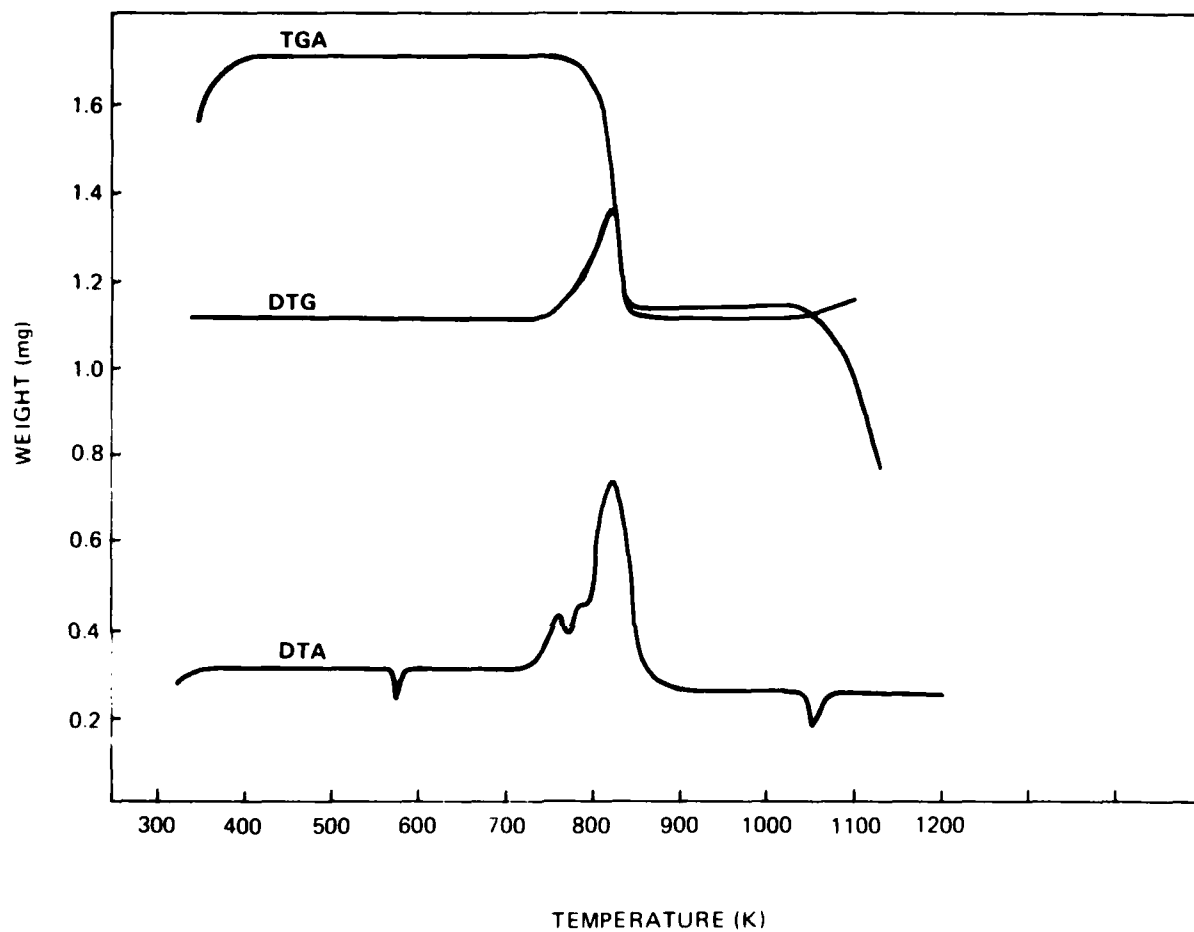
Figure 4 Differential thermogravimetric curves for $TiH_{0.66}/KClO_4$ in a weight ratio 33/67.

A thermogram for a low hydrogen ($TiH_{0.19}$) pyrotechnic, with a high surface area (8.2 m^2/g), Figure 5, again shows an initiation temperature of about 730; however the exotherm covers a rather broad temperature region. The maximum rate of weight loss does not occur until near the end of the exotherm and not until the exotherm is considerably reduced. The O-Ti ratio from weight loss during the reaction exotherm is 1.22.

A thermogram for a sample of pyrotechnic prepared from a $TiH_{0.78}$ ground to a higher surface area (2.49 m^2/g as compared to 1.06 m^2/g) is shown in Figure 6. The F/O ratio is 33/67. The initiation temperature is about 725 K with an exotherm peak at 800 K. The maximum rate of weight loss occurs approximately at the peak in the exotherm but the rate of weight loss does not fall off as rapidly as other materials with a lower surface area. The O/Ti ratio from weight loss during the exotherm is 1.3. It appears that the initiation temperature and the peak reaction temperature are not much affected by the O/F ratio or the surface area of the TiH_x. The extent of the reaction is apparently increased with surface area as seen from the O/Ti ratios. Since the weight loss occurred over a fairly long period of time the residence time of the released gas is very short. Therefore in the temperature, pressure, and heating rate regime investigated by DTA/TGA, the TiH_x-$KClO_4$ reaction probably progresses primarily as a surface reaction. From thermodynamic considerations at the initiation temperature and low pressure the equilibrium composition should be TiO_2 in a F/O = 33/67 mix. For a F/O of 45/55 the O/Ti ratio is 1.7 at equilibrium at 800 K and 0.005 atmosphere from equilibrium thermodynamics.
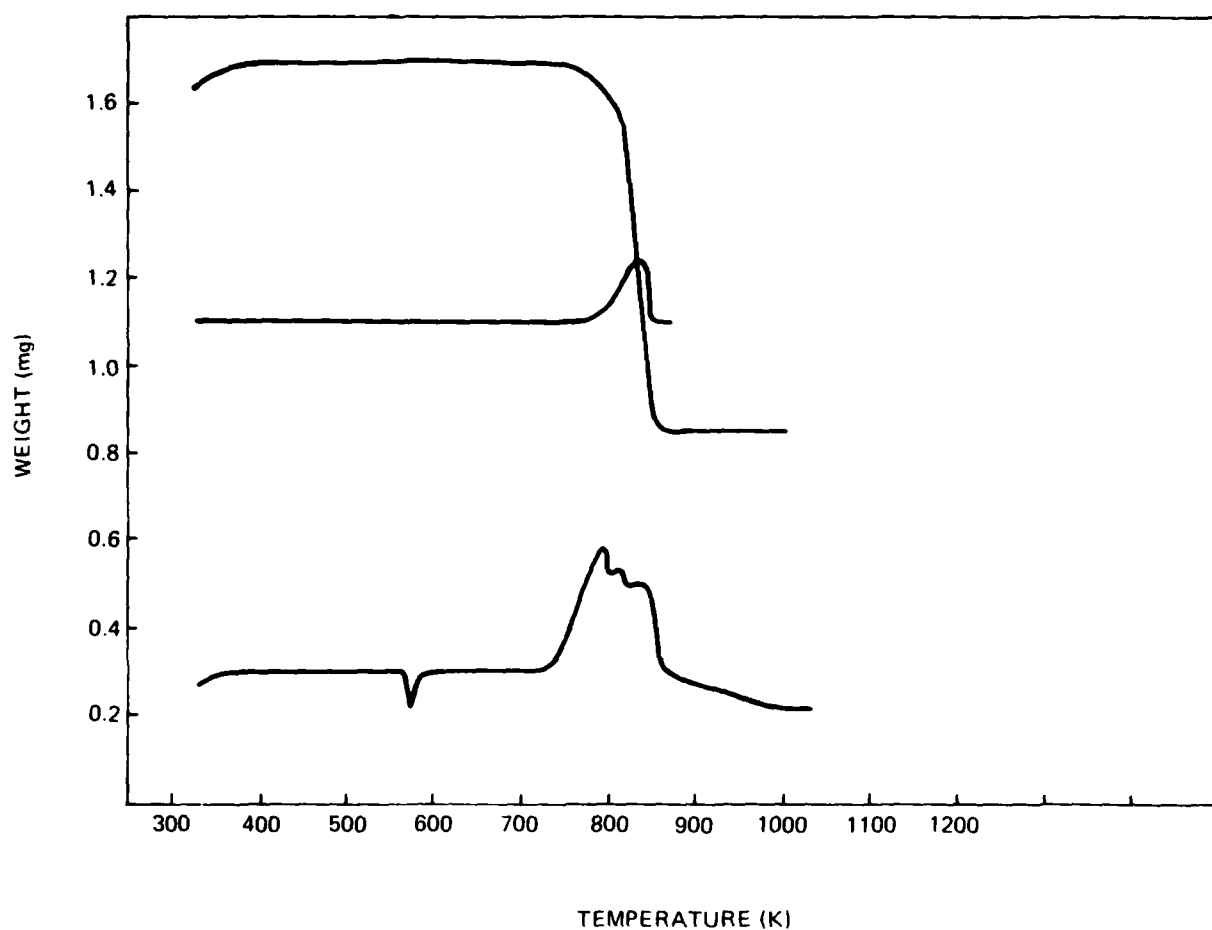
Figure 5 Differential thermogravimetric curves for $TiH_{0.19}/KClO_4$ in a weight ratio 33/67. The $TiH_{0.19}$ is a high surface area material.

452
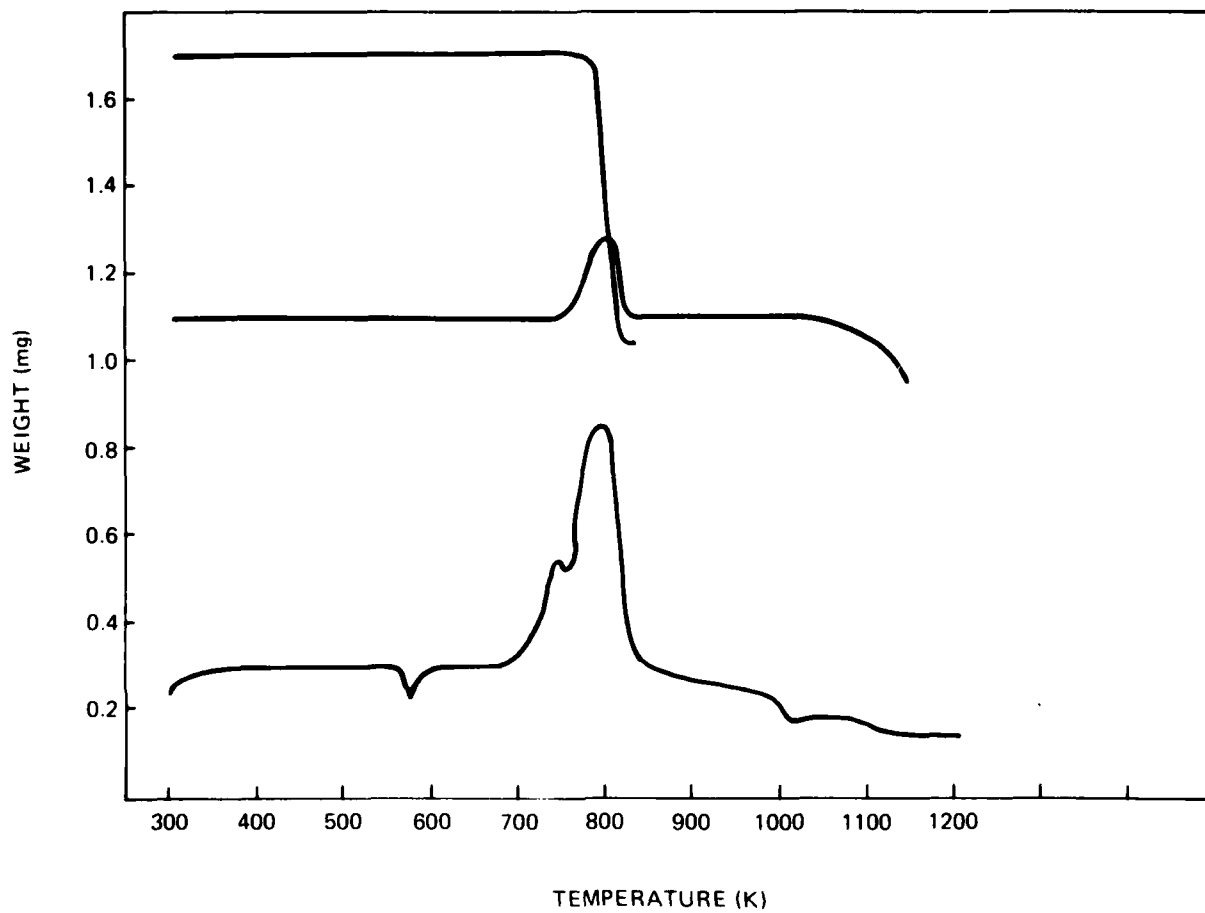
Figure 6 Differential thermogravimetric curves for $TiH_{0.78}/KClO_4$ in a weight ratio 33/67. The $TiH_{0.78}$ is a high surface area material.

The work indicates that the rate of reaction in the system TiH_x-$KClO_4$ (33/67) increases as the hydrogen content of the TiH_x is increased. The extent of reaction, as determined by the O/Ti ratio in the product appears to be a function of the surface area of the TiH_x fuel.

EQUILIBRIUM THERMODYNAMIC CALCULATIONS

A computer program[1] was used to calculate equilibrium reaction temperatures and compositions of pyrotechnics as well as equilibrium compositions and enthalpies at the initiation temperature and at intermediate temperatures.

The method of computation is by a Newton Raphson decent solution of a non-linear matrix of compositions including minimization of free energy, mass balance, and energy balance. The computation method assumes the ideal gas law and equilibrium between gaseous and condensed species.

The data required as input for these chemical equilibrium calculations are heats of formation of the reactant and the product species along with specific heat data for the product species. The thermodynamic data must be consistent for all species for heat capacity, enthalpy, free energy function, and heat of formation. The specie enthalpy at 298.15 K has arbitrarily been assigned to be the heat of formation of the specie at 298.15 K. Therefore at any temperature T the assigned molar enthalphy is

$$\overline{H}^o_T = \Delta H^o_{f\ 298.15} + H^o_T - H^o_{298.15} \tag{1}$$

and the assigned enthalphy of the total reaction products is the sum of the individual enthalpies

$$\sum_{i}^{n} \bar{H}_{T\ i}^{\circ} = \sum_{i}^{n} \left\{ \left[\Delta H_{f\ 298.15}^{\circ} \right]_{i} + \left[H_{T} - H_{298.15}^{\circ} \right]_{i} \right\} \qquad (2)$$

where $H_{T}^{\circ} - H_{298.15}^{\circ}$ is the molor enthalpy referred to 298.15 K.

The source of the data is primarily the JANAF Tables.[2] Tabulated data are, however, not used in the program; therefore any data required must be fitted to an appropriate set of equations for C_{p}°, H_{T}°, and S_{T}° or F_{T}°. The fitting involves determining seven least squares coefficients which include integration constants relating H_{T}° and S_{T}° or F_{T}° to C_{p}°.[3] To our knowledge the thermodynamic data for none of the compounds of interest containing titanium have been previously fitted to these equations. The titanium compounds have been calculated for this work and are contained on a magnetic tape of coefficients of thermal functions. The thermodynamic data were conveniently available for all compounds of interest in the JANAF Tables except for the substoichiometric titanium hydrides. Since the sub-stoichiometric hydrides of titanium are not produced as equilibrium reaction products in any significant quantity, only the heat of formation is required. The heats of formation of the substoichiometric hydrides were obtained by using the heat of a formation from JANAF Tables for $TiH_{1.73}$[4] and correcting by the heat of dissociation from Gibb, McSharry, and Bragdon[5] to obtain a linear plot of heat of formation from $TiH_{1.73}$ to $TiH_{2.0}$ and a second linear plot connecting the $\Delta H_{f_{298}}^{\circ}$ for $TiH_{1.73}$ and $\Delta H_{f_{298}}^{\circ} = 0$ for Ti metal. Other data in the region $TiH_{1.6}$ to TiH_{2}[6] indicate a somewhat lower $\Delta H_{f_{298.15}}^{\circ}$ for TiH_{2}. The value $\Delta H_{f\ 298.15}^{\circ} = 31.99$ calculated from Gibb et al for TiH_{2} was used in these calculations. The values of $\Delta H_{f_{298.15}}^{\circ}$ for the TiH_{2} and subhydrides are shown in Figure 7 as a plot of heat of formation against atoms of hydrogen (X) in TiH_{x}.
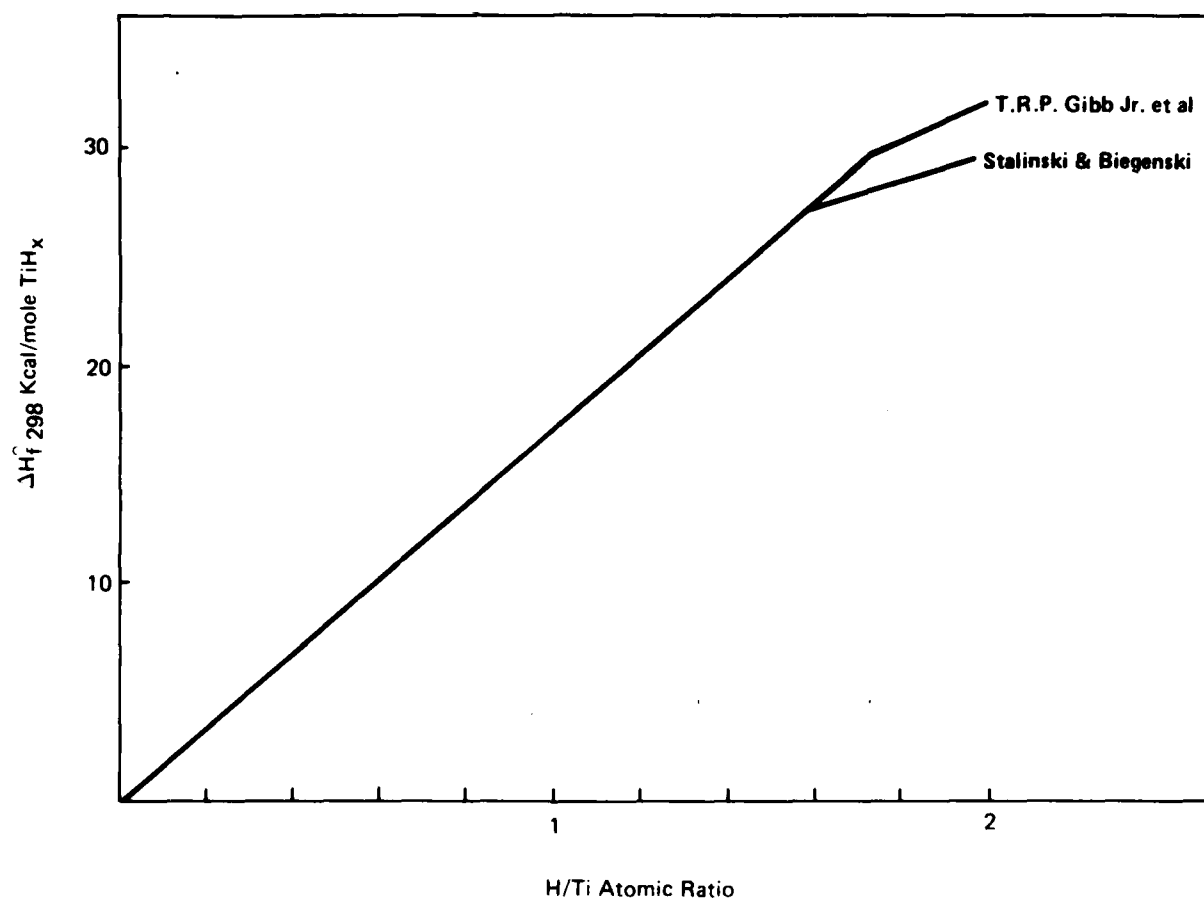
Figure 7 Heart of formation of TiH$_x$ as a function of Hydrogen content.

The computed reaction temperatures as a function of composition of the pyrotechnic mix are displayed in Figure 8. Each series of computations is for a single hydride stoichiometry and a specific reaction pressure. As the degree of confinement is increased, the reaction temperature increases and the effect of mixture ratios becomes more noticeable. The series of computations at higher pressures show inflected curves with maxima around 40-42% TiH_x.

The higher hydrides, as x approaches 2, are simple curves. The maximum in temperature occurs at about 36% TiH_2 at 200 atm. In general the reaction temperature maximum shifts in the direction of higher ratios of fuel to oxidizer as the reaction pressure decreases. The position of the maximum is an indication of the most efficient mixture ratio for the specific hydride stoichiometry and pressure of interest. The lower pressure curves display a broad maximum and the mixture ratios appear to be not very critical over rather broad composition regions. Because of this small effect over a wide range of mixture ratios for low pressure reaction conditions the higher pressure maxima may be used to determine the mixture ratio for maximum reaction efficiency.

In these computations of chemical equilibrium reaction products and temperatures, the sum of the enthalpies of the equilibrium reaction products is equated to the total enthalpy of the reactant pyrotechnic mixture. For any temperature other than the equilibrium reaction temperature, the enthalpies of the reactants and products are not balanced. At any temperature lower than the equilibrium reaction temperature, the enthalpy difference between products and reactants is the energy which is available to heat the products to reaction temperature. This includes the heat of dissociation
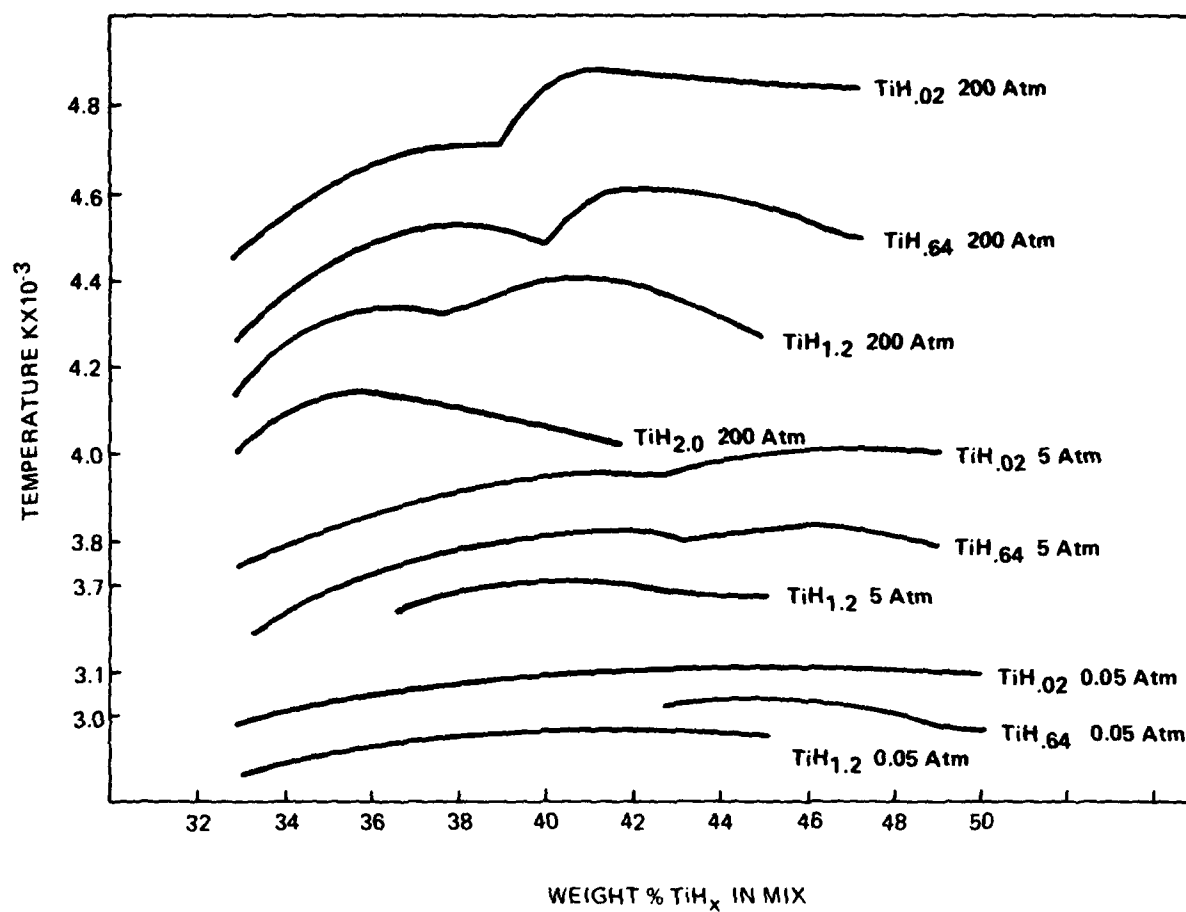
Figure 8 Equilibrium reaction temperature as a function of composition

which is usually involved in limiting the equilibrium reaction
temperature. In developing a mathematical model of initiation
of a device using a particular pyrotechnic material, various energy
dissipating modes are included. Some processes contributing to
energy loss might be dissipation of heat by thermal conduction
away from the reaction zone by the device housing or by unreacted
pyrotechnic, or energy loss by radiation or by thermal dissociation
of some of the pyrotechnic. This heat loss will be supplied by
the pyrotechnic reaction and will cause a lowering of the reaction
temperature.

A number of computations were carried out to obtain equilibrium
chemical compositions and enthalpies of reaction products at tem-
peratures lower than the equilibrium reaction temperature. The
results of these computations are the equilibrium reaction tem-
peratures and compositions of the pyrotechnic reaction products
in which part of the energy of reaction was dissipated external
to the reaction. The energy dissipated is the difference between
the computed enthalpy of the equilibrium reaction products at the
assigned temperature and pressure and the enthalpy of the unreacted
pyrotechnic mixture as described in Equation (2).

Figures 9 through 13 display enthalpy curves as a function of
temperature. Each figure contains curves for several F/O ratios
at a specific pressure for a single hydride composition TiH_x.

The heat loss per gram of pyrotechnic producing a specific reaction
temperature is the difference between the enthalpy for that tem-
perature on the proper composition curve and the enthalpy of the
pyrotechnic mix from Equation (2).
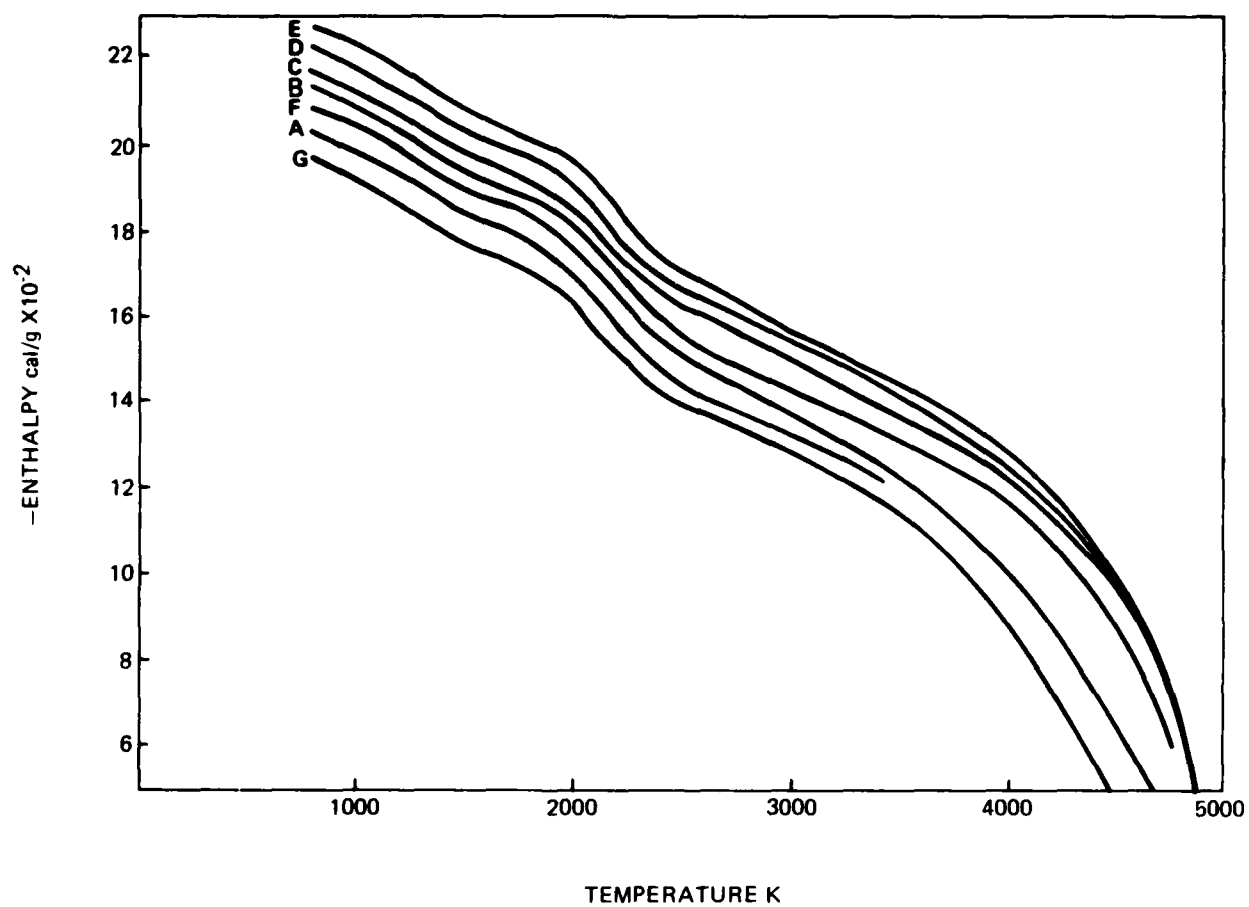
Figure 9 Excess enthalpy of equilibrium reaction products with temperature for the system $TiH_{0.02} \cdot KClO_4$. Pressure = 200 Atm. A 50% $TiH_{0.02}$, B 47%, C 45%, D 43%, E 41%, F 36%, G 33%.
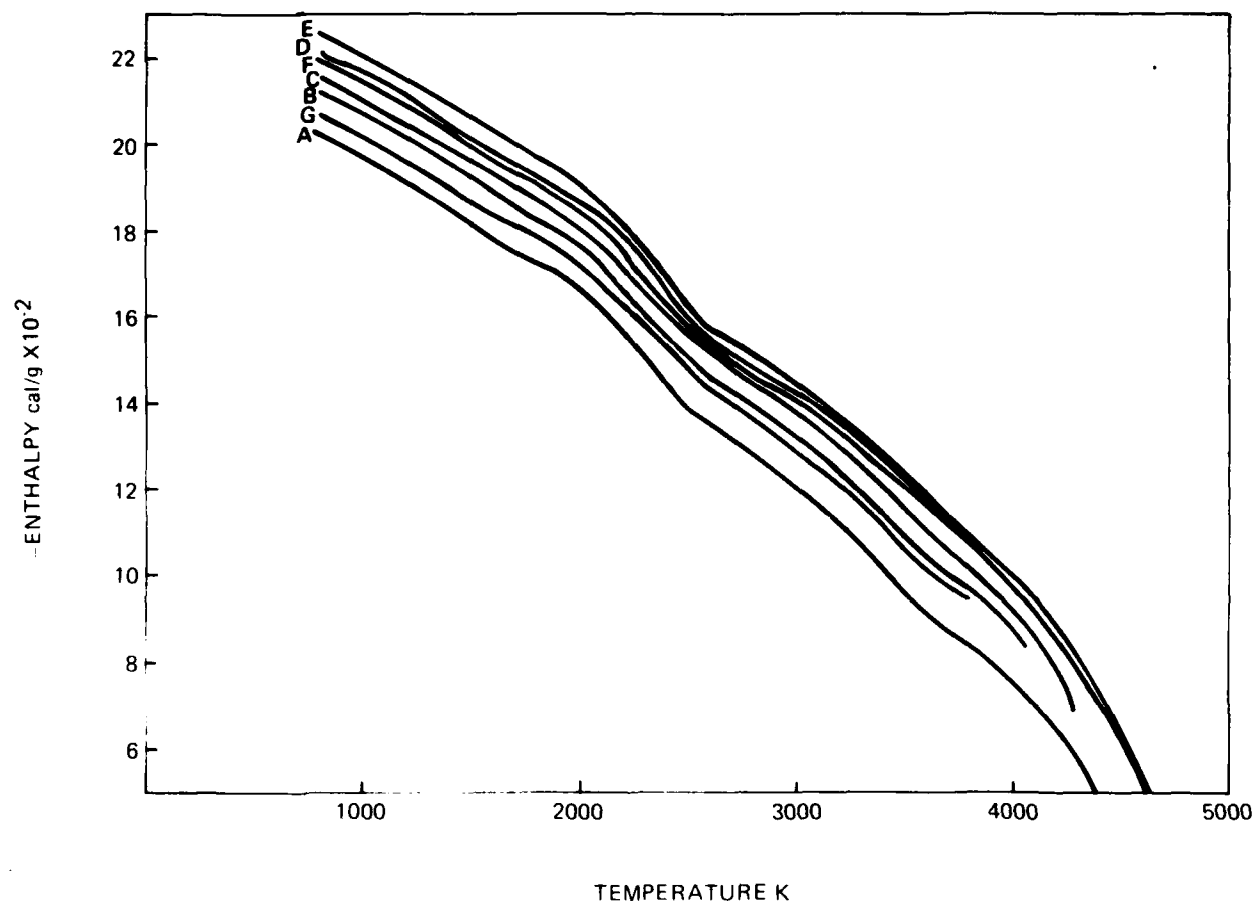
Figure 10 Excess enthalpy of equilibrium reaction products with temperature for the system $TiH_{0.64}$ $KClO_4$. Pressure = 200 Atm. A 50% $TiH_{0.64}$, B 47%, C 45%, D 43%, E 41%, F 36%, G 33%.
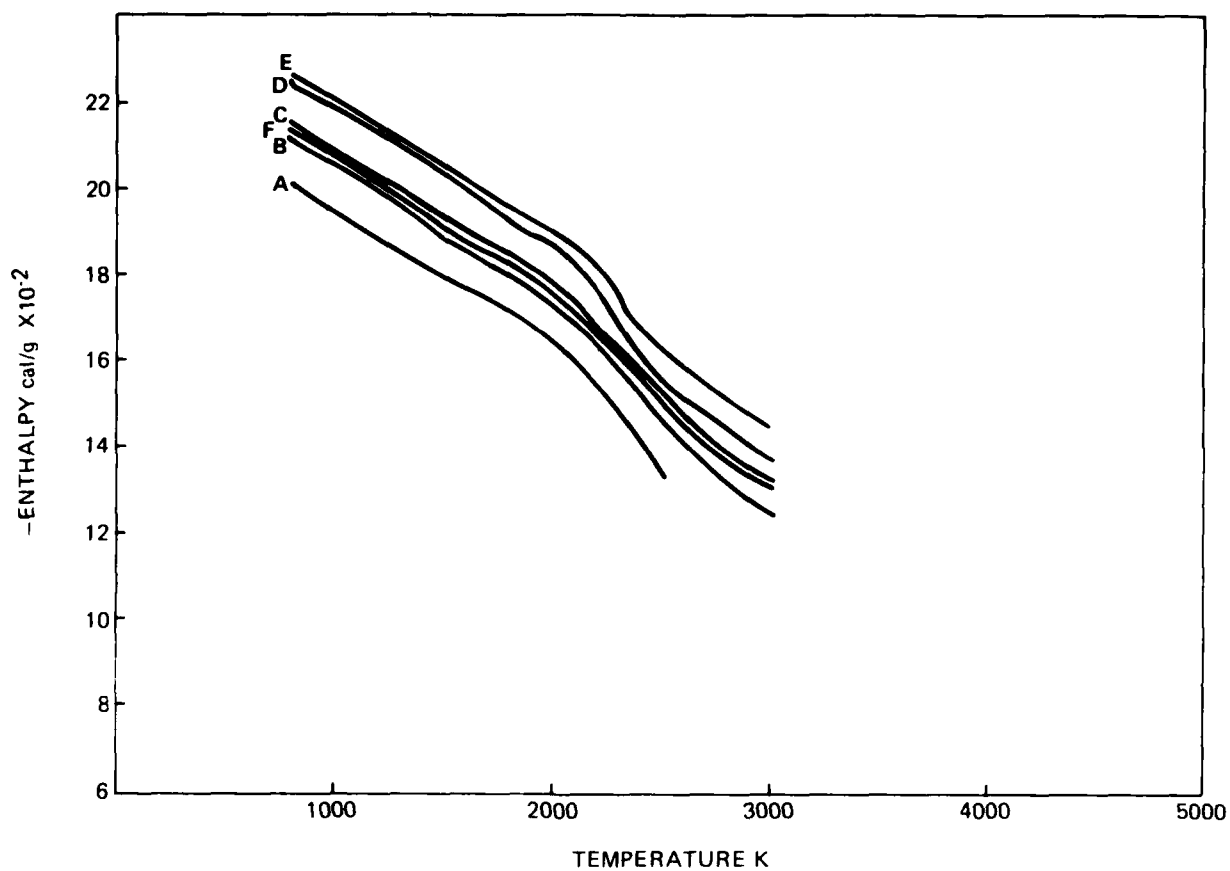
Figure 11 Excess enthalpy of equilibrium reaction products with temperature for the sy
tem $TiH_{1.0} \cdot KClO_4$. Pressure = 200 Atm. A 50% $TiH_{1.0}$, B 47%, C 45%, D 41%, E 36%,
F 33%.
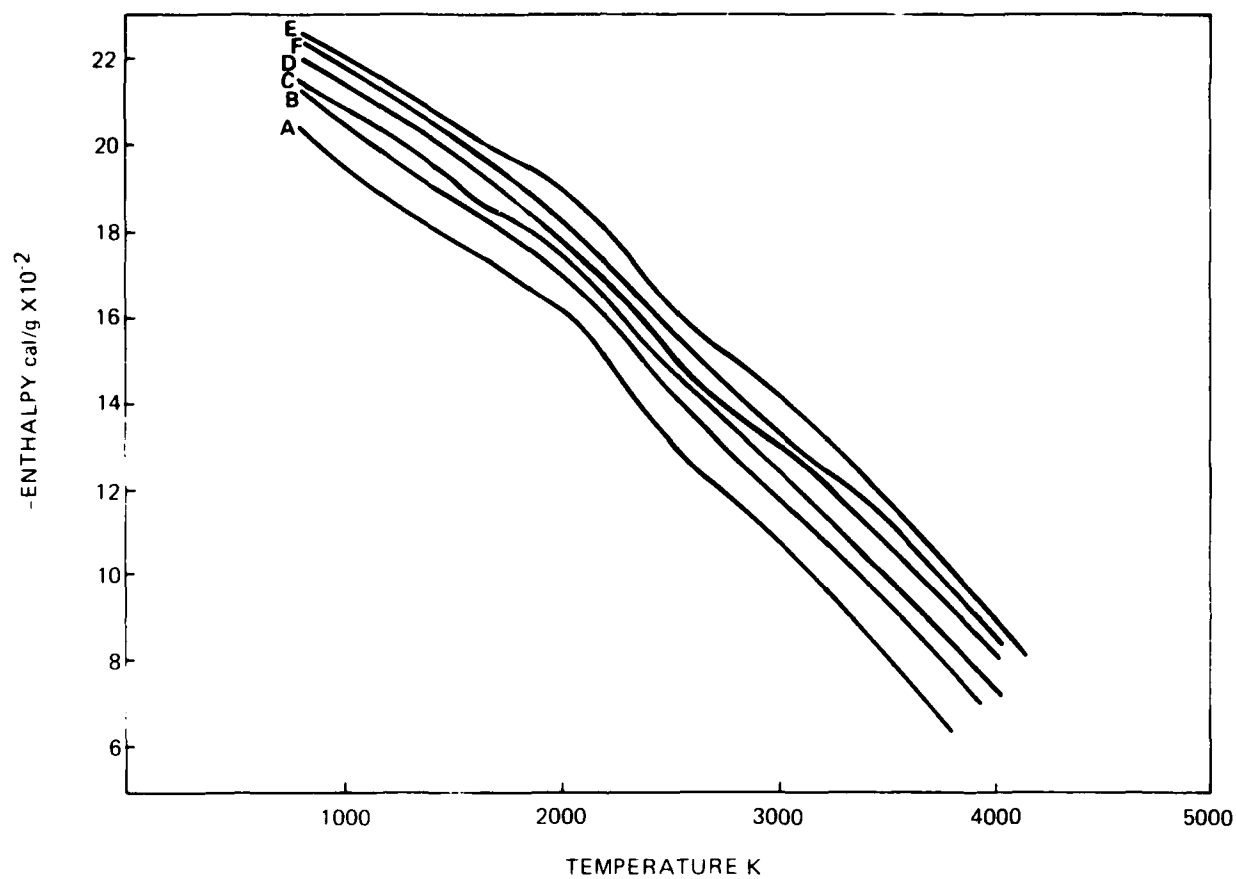
Figure 12 Excess enthalpy of equilibrium reaction products with temperature for the system $TiH_{1.4}$ - $KClO_4$. Pressure = 200 Atm. A 50% $TiH_{1.4}$, B 47%, C 45%, D 43%, E 41%, F 36%.
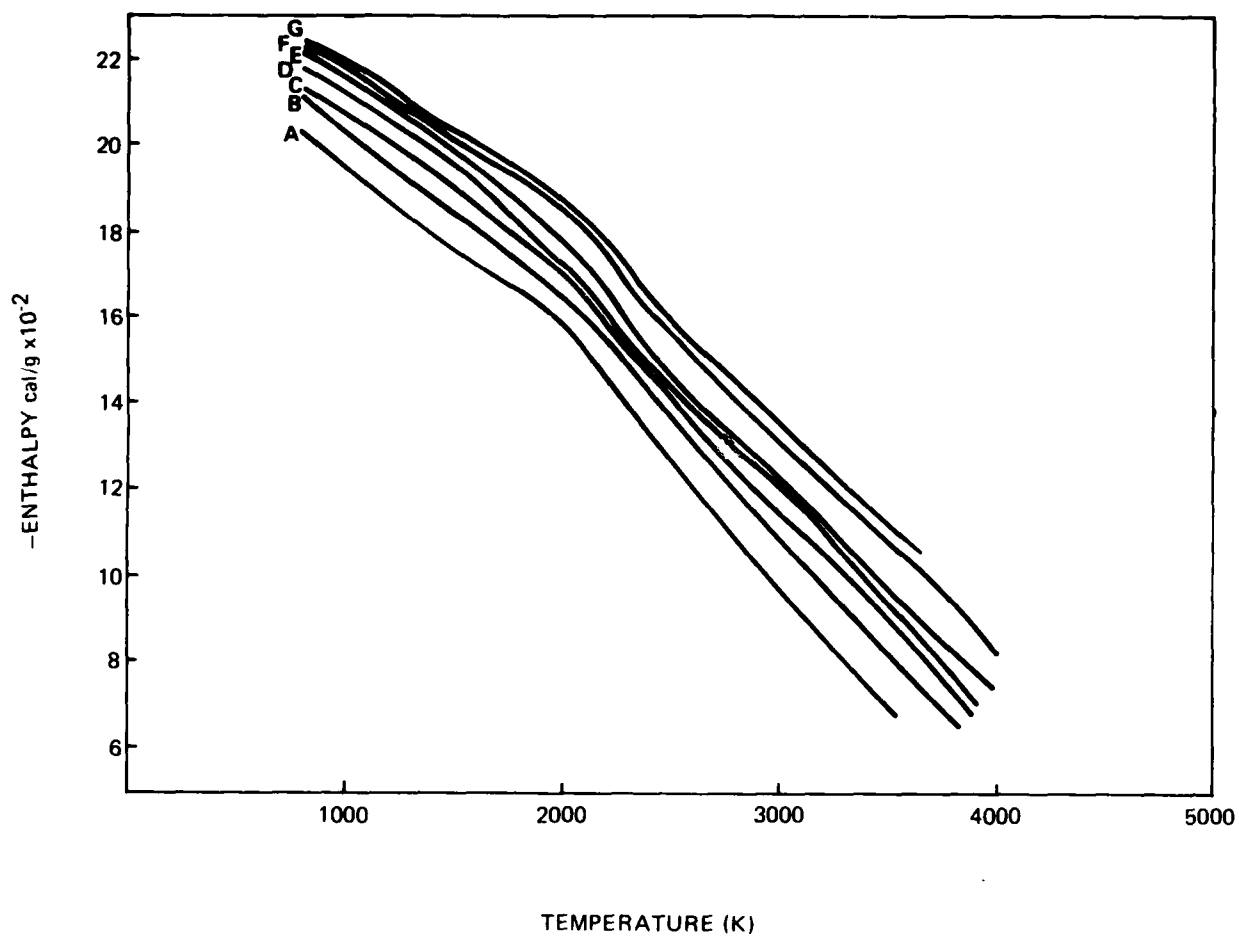
Figure 13 Excess enthalpy of equilibrium reaction products with temperature for the system TiH$_2$ · KClO$_4$. Pressure = 200 Atm. A 50% TiH$_2$, B 47%, C 45%, D 43%, E 41%, F 36%, G 33%.

The effect of hydride stoichiometry and fuel/oxidizer ratio on equilibrium reaction product composition is shown in Figures 14 through 25. In all cases at lower temperatures near the initiation temperature the primary product is TiO_2 and H_2O when the F/O ratio is low enough to contain sufficient oxidizer. As the F/O ratio increases the H_2O is reduced and H_2 increases. As might be expected at the initiation temperature, the equilibrium products are oxidized to the extent of the available oxygen. TiO_2 is the primary titanium specie until oxygen is depleted, then Ti_3O_5 rapidly increases as F/O increases and with further oxygen depletion Ti_2O_3 becomes the predominate titanium specie.

As the temperature increases there is some shift in equilibrium in favor of H_2O at the expense of TiO_2 in those systems with hydrogen available.

The most significant composition changes occur as the temperature approaches the pyrotechnic equilibrium reaction temperature. The reaction temperature is limited by dissociation of the lower temperature product species. Dissociation is relatively easily accomplished at lower pressure. At high pressure dissociation is reta ded and the equilibrium reaction temperature becomes proportionally higher.

SUMMARY AND CONCLUSIONS

From differential scanning calorimetry and differential thermal analysis initiation temperatures on the order of 725 - 740 K are observed at slow heating rates and higher temperatures for faster heating rates. Reaction rates for the system $TiH_x/KClO_4$ (33/67) are highest with large x. Reaction rate apparently increases with x, other considerations the same.
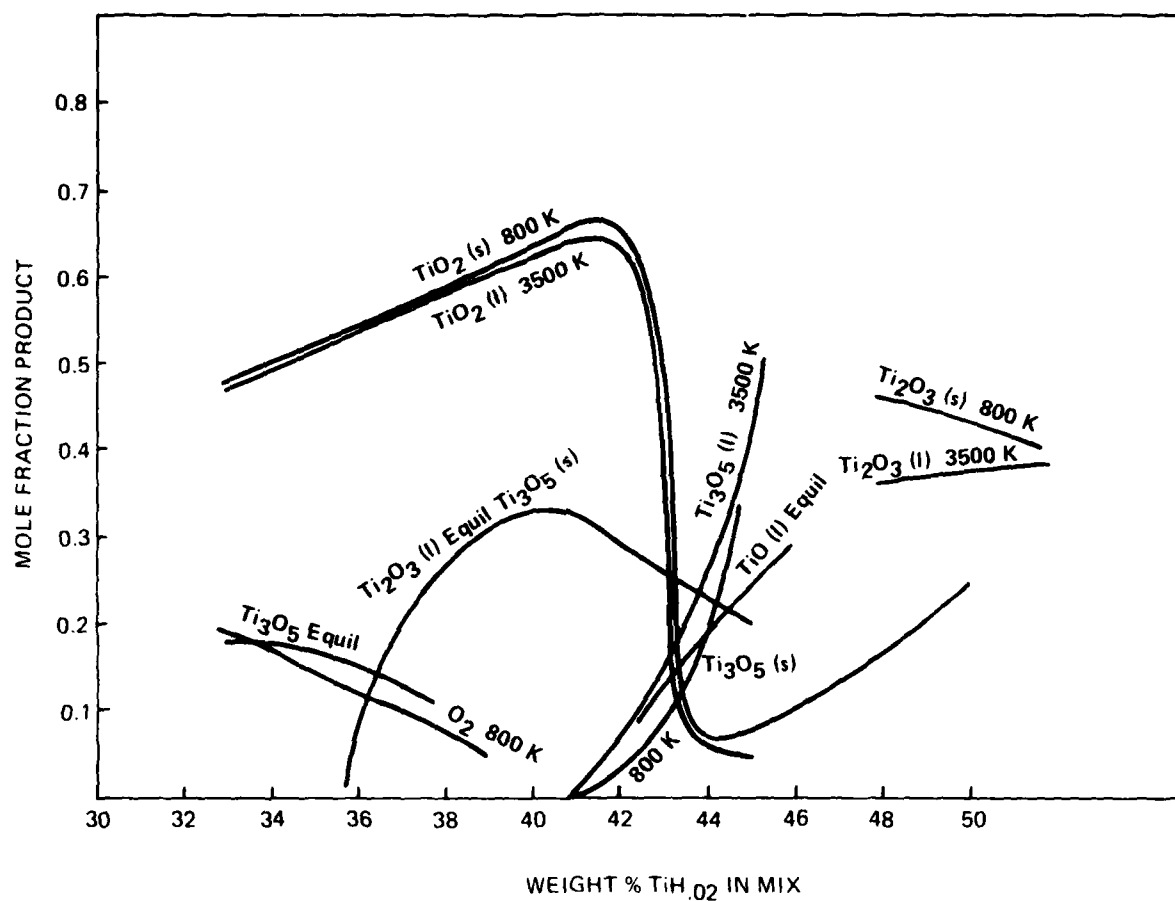
Figure 14 Equilibrium composition of reaction products as a function of pyrotechnic composition. Pressure 200 Atm.
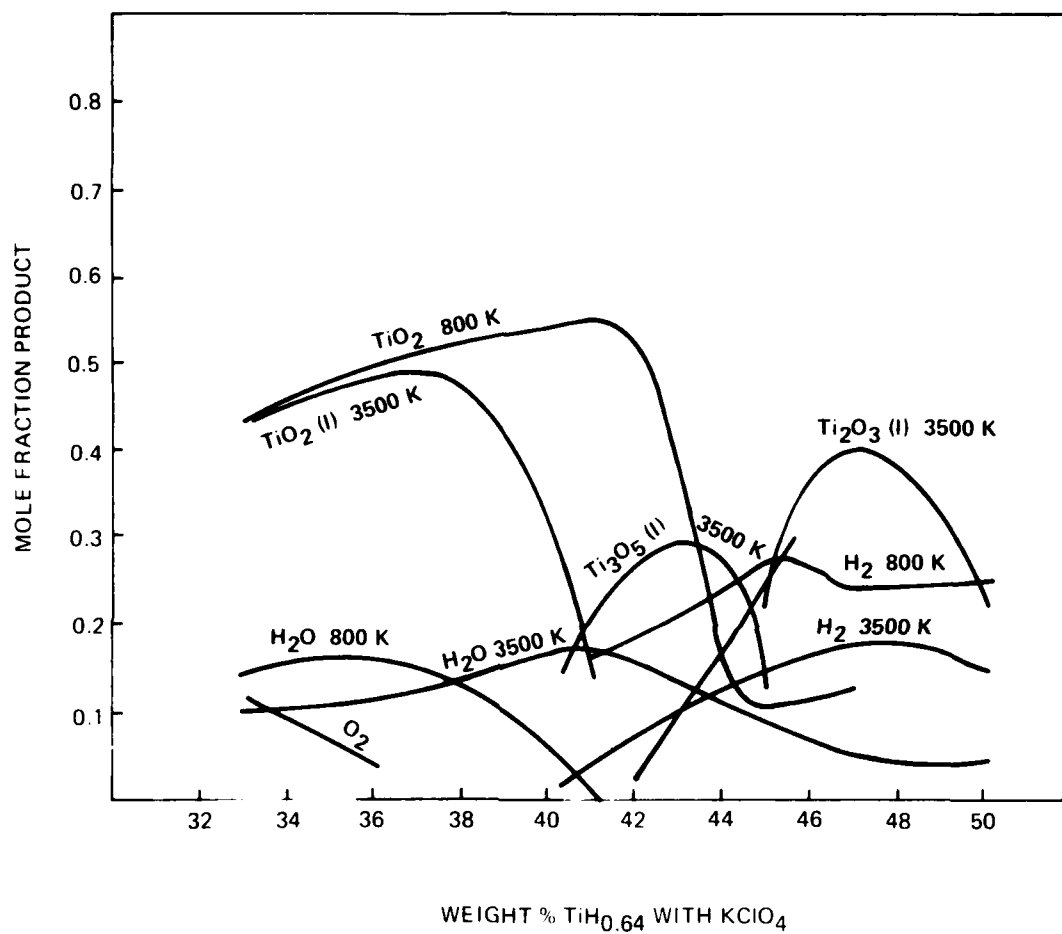
Figure 15 Equilibrium composition of reaction products as a function of pyrotechnic composition. Pressure 200 Atm.
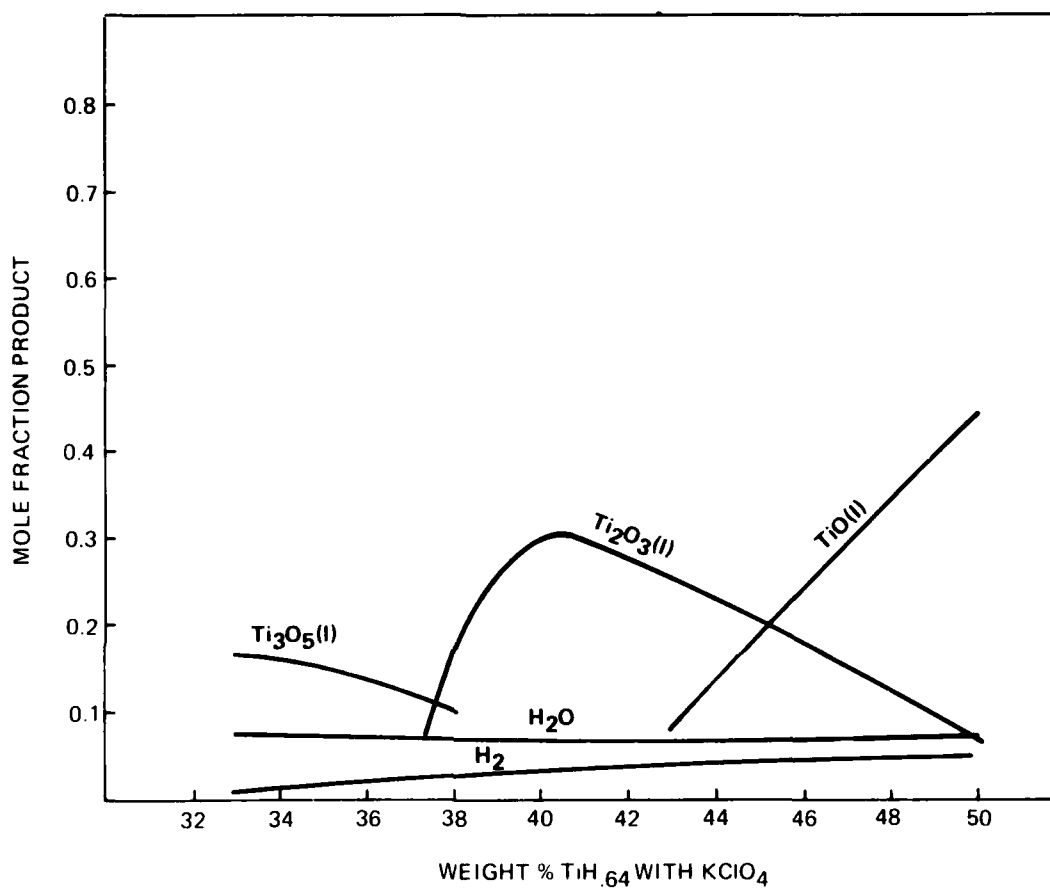
Figure 16 Equilibrium composition of reaction products as a function of
Pyrotechnic composition at equilibrium reaction temperature. Pressure 200 Atm.
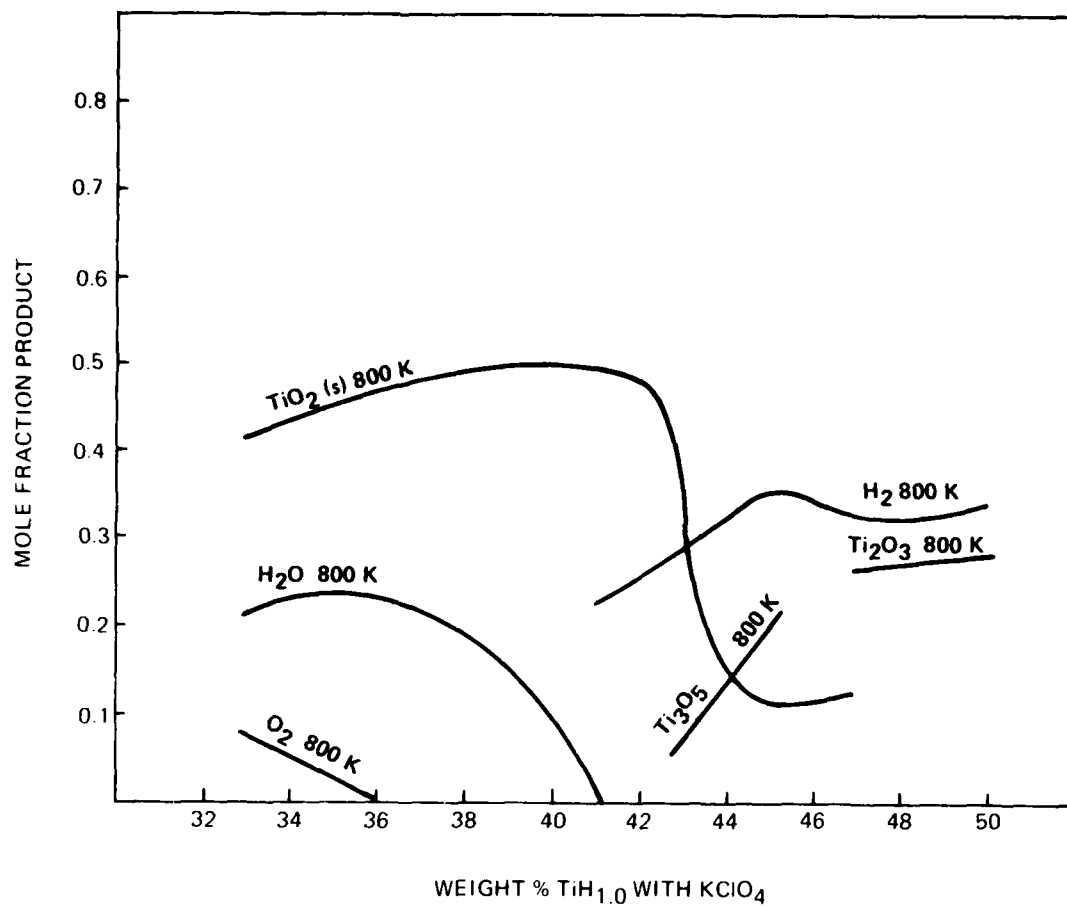
Figure 17 Equilibrium composition of reaction products as a function of Pyrotechnic composition. Pressure 200 Atm.
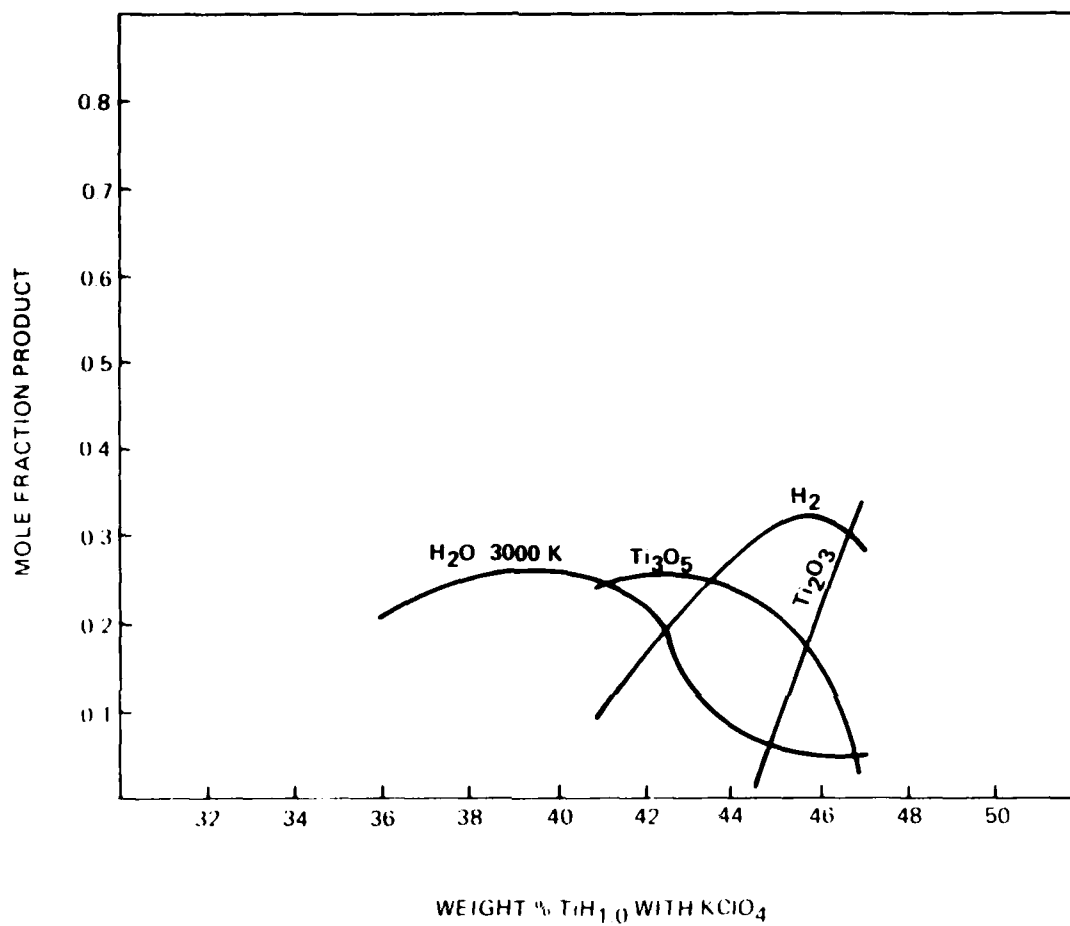
Figure 18 Equilibrium composition of reaction products as a function of Pyrotechnic composition at 3000K Pressure 200 Atm.
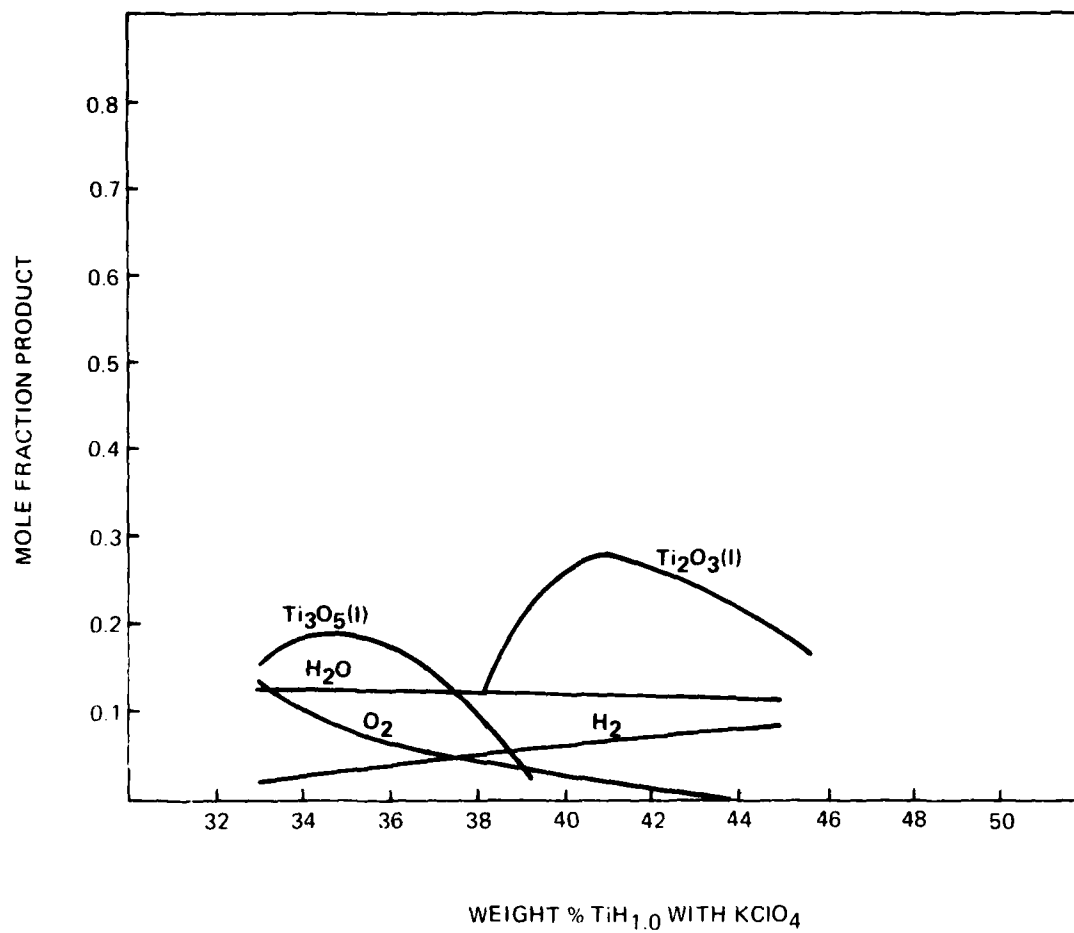
Figure 19 Equilibrium composition of reaction products at equilibrium reaction temperature as a function of pyrotechnic composition. Pressure 200 Atm.
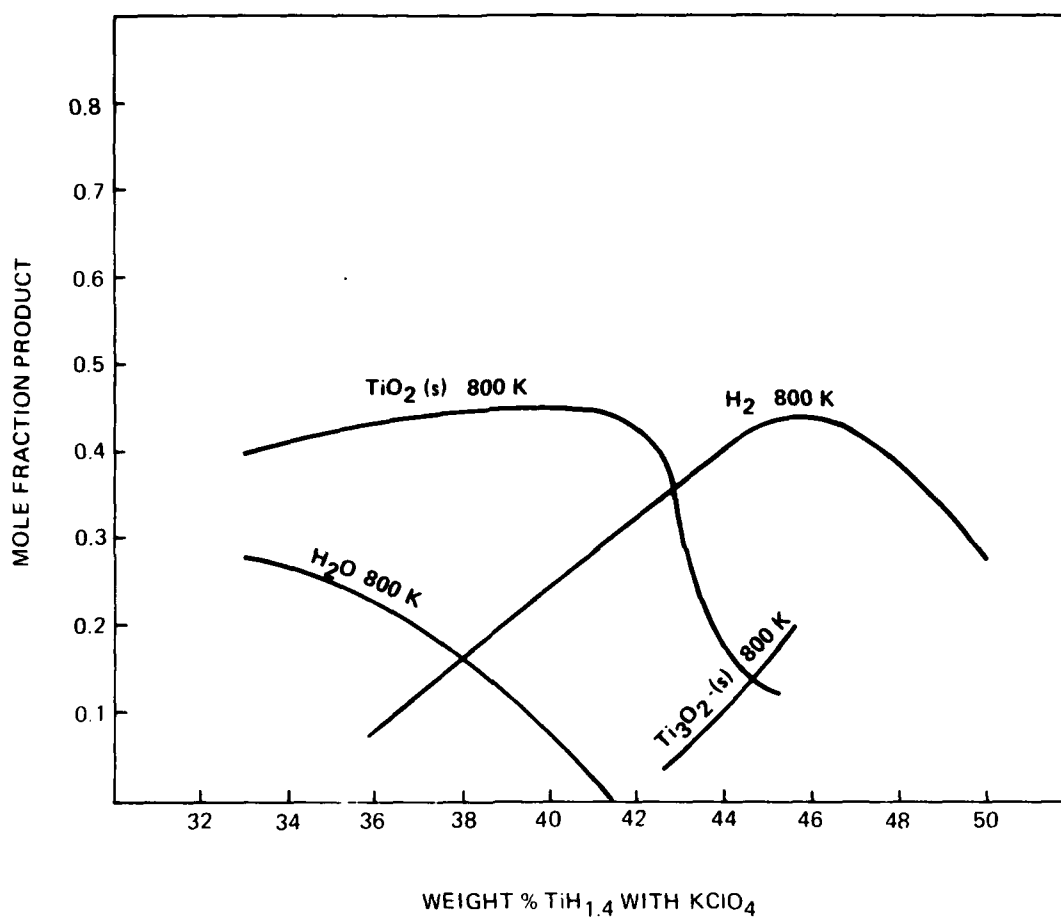
Figure 20 Equilibrium composition of reaction products as a function of pyrotechnic composition. Pressure 200 Atm
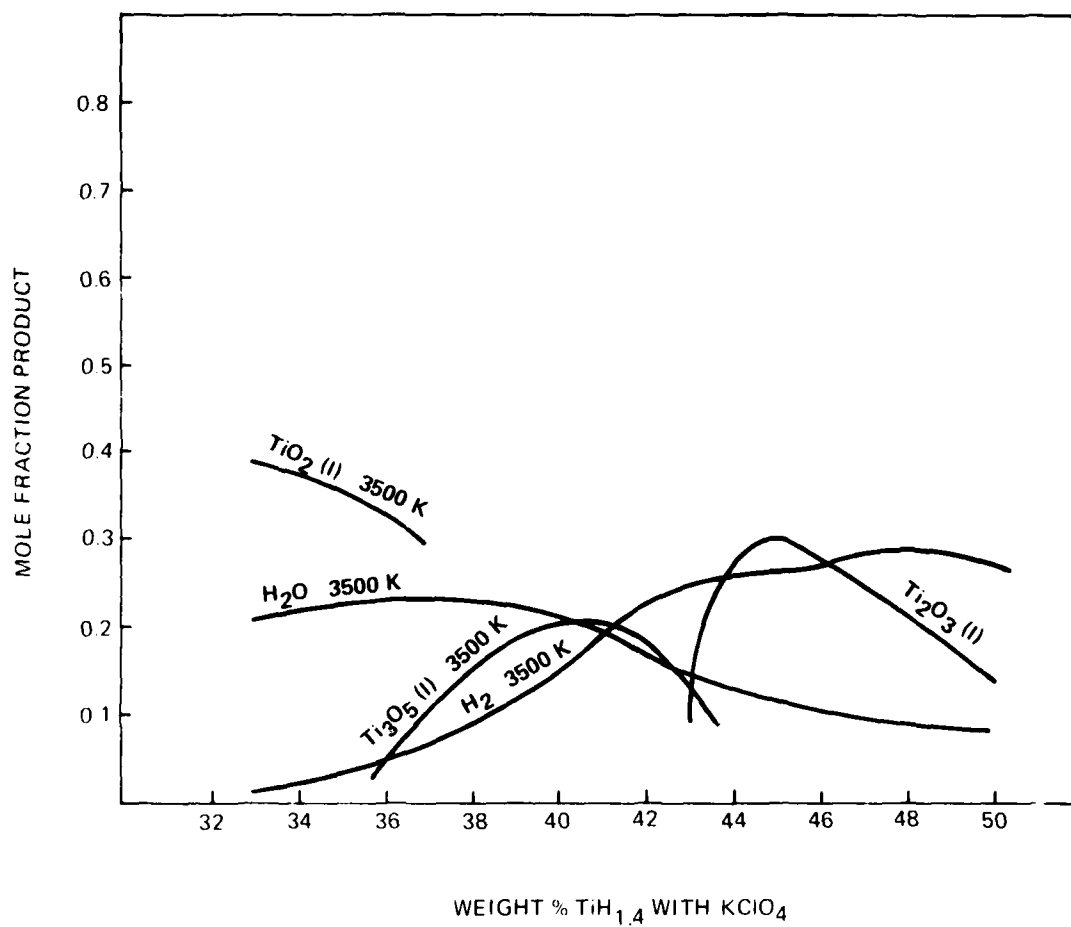
Figure 21   Equilibrium composition of reaction products as a function of pyrotechnic composition. Pressure 200 Atm
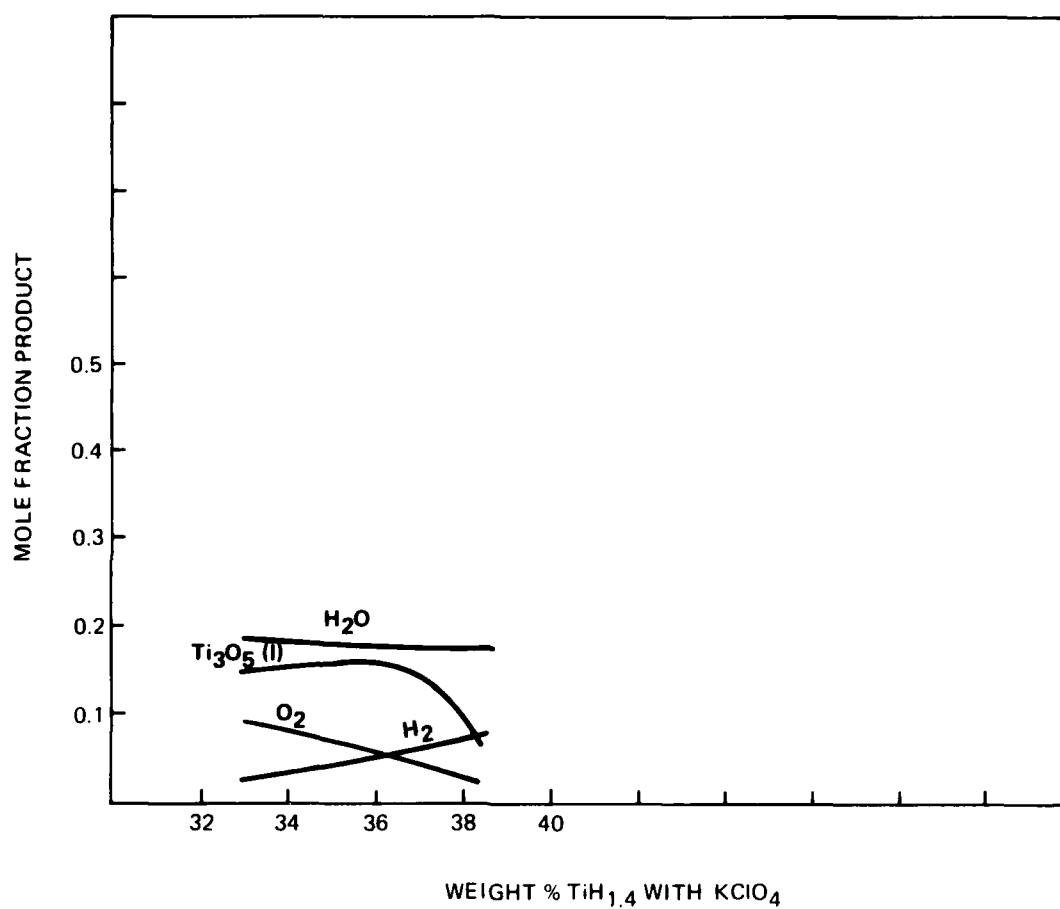
Figure 22 Equilibrium composition of reaction products at equilibrium reaction temperature as a function of pyrotechnic composition. Pressure 200 Atm.
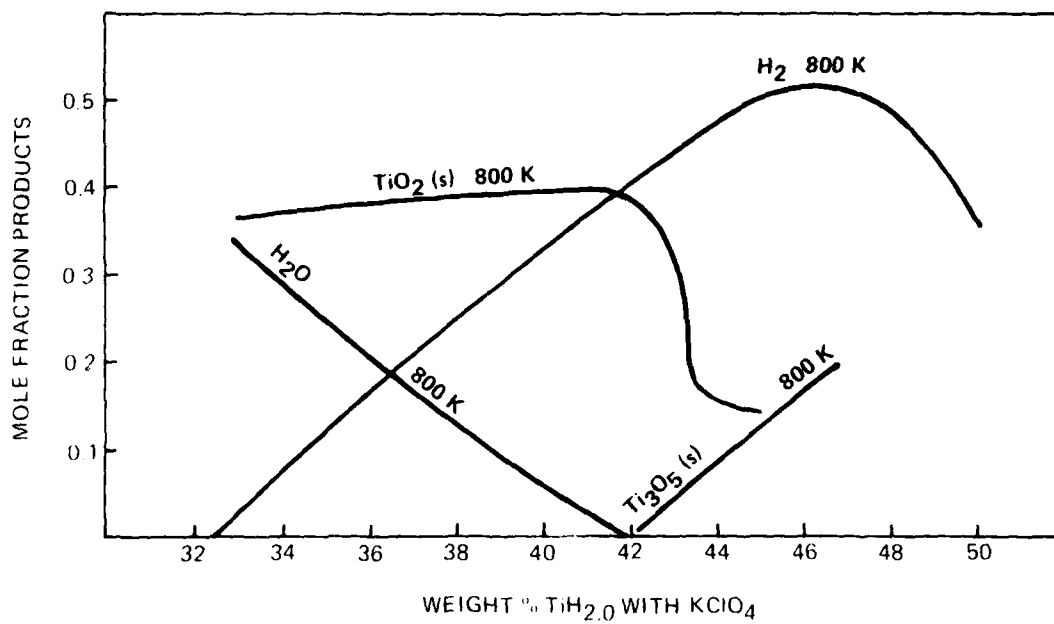
Figure 23 Equilibrium composition of reaction products as a function of pyrotechnic composition Pressure 200 Atm.
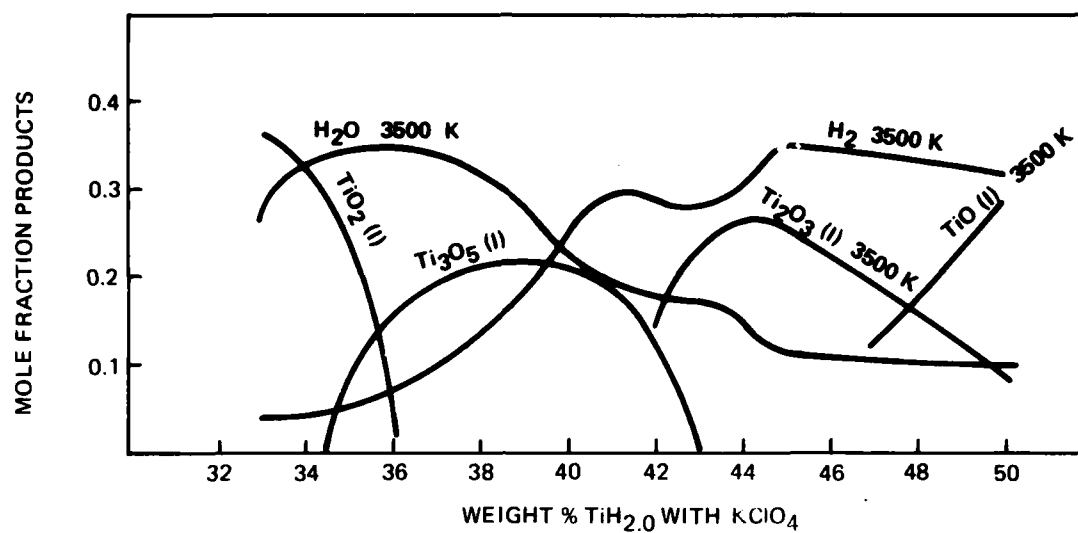
Figure 24 Equilibrium composition of reaction products as a function of pyrotechnic composition Pressure 200 Atm.
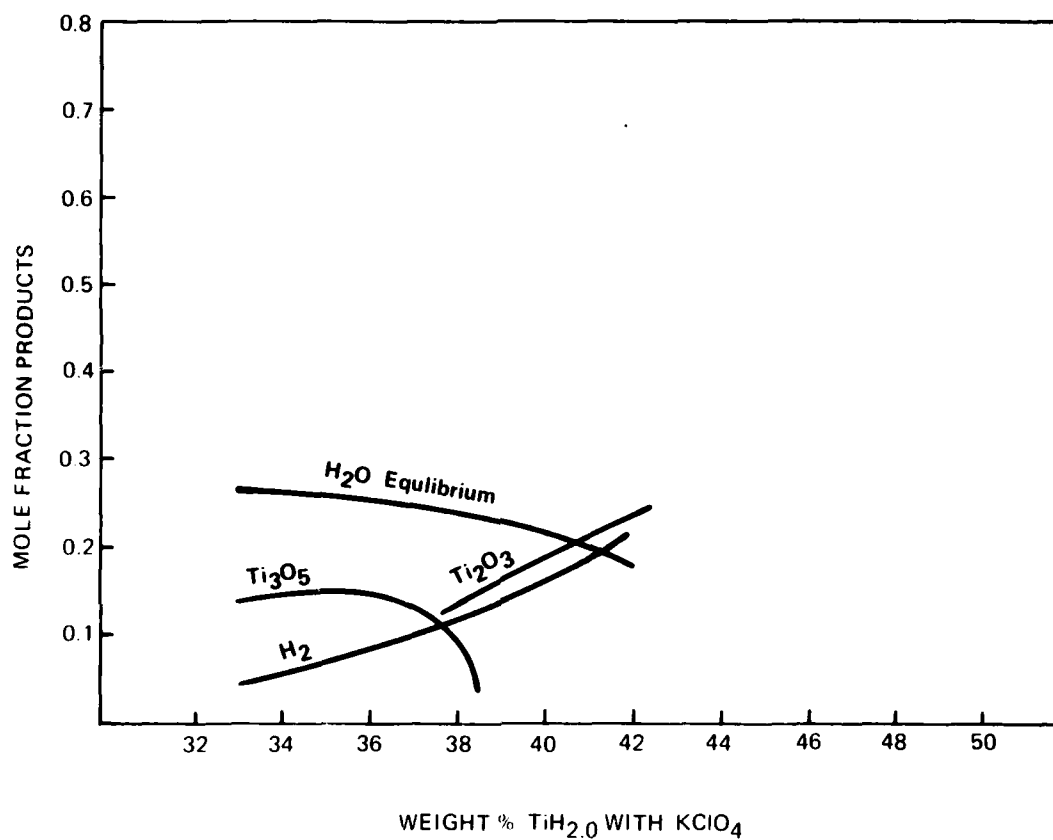
Figure 25 Equilibrium composition of reaction products at equilibrium reaction temperature as a function of pyrotechnic composition. Pressure 200 Atm.

The extent of the reaction as determined by the O/Ti ratio in the product appears to be a function of the surface area of the TiH_x fuel. No study was done relative to the surface area of the oxidizer.

The pyrotechnic equilibrium reaction temperature, as calculated from thermodynamic considerations, maximizes about 36% TiH_2 and shifts to higher fuel/oxidizer ratios as the amount of hydrogen decreases. The maximum in temperature shifts toward higher F/O ratios also as the equilibrium pressure decreases.

Reaction product compositions and enthalpies were calculated at both equilibrium reaction temperatures and at lower temperatures. The reaction product enthalpy may be used to estimate heat loss.

Equilibrium calculations indicate complete oxidation of fuel species to the full extent of available oxygen. For fuel rich systems there is a shift in equilibrium in favor of H_2O at the expense of TiO_2 as temperature increases.

The DTA-TGA work indicates a loss of oxygen and O/Ti ratios for the Ti-O species considerably less than the theoretical value of 2 for complete oxidation of titanium to TiO_2. At low temperatures, near the initiation temperature, equilibrium conditions do not hold for conditions encountered in these thermo-analysis experiments.

APPENDIX A

Theory of Computational Method

The equations describing chemical equilibrium can take either of
two forms.[1] The two formulations, equilibrium constants or minimi-
zation of free energy, are equivalent. Fewer difficulties are,
however, encountered with the minimization of free energy. In
this method the condition of equilibrium may be stated in terms
of Gibbs free energy or Helmholtz free energy or maximization of
entropy. Normally Gibbs free energy is minimized because it is
normally described in terms of temperature and pressure, the
variables usually under consideration.

In these computations the ideal gas equation is the equation of
state

$$PV = P/\rho = nRT \tag{3}$$

where P is pressure; V specific volume, ρ is density, n moles of
gas, T temperature (K) and R is the gas constant.

This equation (3) is assumed to be correct including small amounts
of condensed species. The condensed species are assumed to
occupy negligible volume. The mass includes condensed phases
while n includes only gas. Therefore molecular weight, $M = 1/n$,
is the total mass including condensed species divided by the
number of moles of gas where

$$n = \sum_{j=1}^{m} n_j \tag{4}$$

with n_j the number of kilograms-moles of species j per kilogram
of mixture.

For a mixture, the Gibbs free energy is

$$g = \sum_{j=1}^{n} \mu_j n_j \tag{5}$$

with

$$\mu_j = \left(\frac{\partial g}{\partial n_j}\right)_{T,P} \tag{6}$$

the chemical potential per kilogram-mole of species j.

The condition of equilibrium is the minimization of free energy. The minimization is subject to the following mass balance constraints.

$$\sum_{j=1}^{n} a_{ji} n_j - b_i^o = 0 \qquad i = 1, \ldots, \ell \tag{7}$$

or

$$b_i - b_i^o = 0 \qquad c = 1, \ldots, \ell \tag{7a}$$

where the stoichiometric coefficients a_{ij} are the number of kilogram-atoms of element i per kilogram-mole of species j, b_i^o is the assigned number of kilogram atoms of element i per kilogram of total reactants and

$$b_i = \sum_{j=1}^{n} a_{ij} n_j \qquad c = 1, \ldots, \ell \tag{7b}$$

is the number of kilogram atoms of element i per kilogram of mixture.

Defining a term G to be

$$G = g + \sum_{i=1}^{\ell} \lambda_i (b_i - b_i^o) \tag{8}$$

where λ_i are Lagrangian multipliers, the condition for equilibrium becomes

480

$$S G = \sum_{j=1}^{n} \mu_j + \sum_{J=1}^{n} \lambda_i a_{ij} \ Sn_j + \sum_{i=1}^{\ell} (b_i - b_i^o)$$

$$\delta\lambda_i = 0 \tag{9}$$

Treating the variations δn, and $\delta\lambda_i$ as independent gives

$$\mu_j + \sum_{i=1}^{\ell} \lambda_i a_{ij} = 0 \qquad j = 1,\ldots, n \tag{10}$$

along with the mass balance Equation (7a).

Based on the assumptions covering the Equation of State the chemical potential is

$$\mu_j = \begin{cases} \mu_j^\bullet + RT \ln \dfrac{n_j}{n} + RT \ln Patm & (j = 1_j\circ\ldots m) \\ \mu_j^\bullet & (j = m + 1,\ldots,n) \end{cases} \tag{11}$$

where μ_j^o for gases $(j = 1,m)$ and condensed phases $(j > m)$ is the chemical potential in the standard state. For a gas, the standard state is the hypothetical ideal gas at unit fugacity. For a pure solid or liquid, the standard state is the substance in the condensed phase under pressure of one atmosphere.

Equations (7) and (10) permit determination of equilibrium compositions for thermodynamic states specified by an assigned temperature T_o and pressure P_o. That is in addition to Equations (7) and (10)

$$T = T_o \tag{12a}$$

$$P = P_o \tag{12b}$$

The thermodynamic state may also be specified by assigning any two state functions. The thermodynamic state corresponding to

a constant pressure combustion is specified, instead of by (12) by

$$h = h_o \tag{13a}$$

$$P = P_o \tag{13b}$$

where h_o is a constant equal to the enthalpy of the reactants and h is the enthalpy of the mixture

$$h = \sum_{j=1}^{n} n_j (H_T^o)_j \tag{14}$$

where $(H_T^o)j$ is the standard state enthalpy for species j.

The equations required to obtain composition are not all linear in composition and an interation technique is required. A descent Newton-Raphson method is used to solve for corrections to initial estimates of compositions n_j, Lagrangian multipliers λ_i, moles n and temperature t. The method involves a Taylor series expansion of the appropriate equations with terms containing derivatives higher than the first truncated. The correction variables are $\Delta\ln n_j$ (j = 1,...,m), Δn_j (j = m + 1,...,n), $\Delta\ln n$, $\pi_j = \lambda_i/RT$ and $\Delta\ln T$. After reduction of those equations containing thermodynamic functions to a dimensionless form, the Newton-Raphson equations are

$$\Delta\ln n_j - \sum_{i=1}^{\ell} a_{ij} \pi_i - \Delta\ln n - \left[\frac{(H_T^o)_j}{RT}\right] \Delta\ln T = \frac{\mu_i}{RT}$$

$$j = 1,...,m \tag{15}$$

$$-\sum_{i=1}^{\ell} a_{ij}\,\pi_i - \left[\frac{(H_T^\circ)_j}{RT}\right]\,\Delta\ln T = -\frac{\mu_i}{RT} \quad j = m+1,\ldots,n \qquad (16)$$

$$\sum_{j=1}^{m} a_{kj}n_j\,\Delta\ln n_j + \sum_{j=m+1}^{n} a_{kj}\,\Delta n_j = b_R^\circ - b_R$$

$$k = 1,\ldots,\ell \qquad (17)$$

$$\sum_{j=1}^{m} n_j\,\Delta\ln n_j - n\,\Delta\ln n = n - \sum_{j=1}^{m} n_j \qquad (18)$$

$$\sum_{j=1}^{m}\left[\frac{n_j\,(H_T^\circ)_j}{RT}\right]\,\Delta\ln R_j + \sum_{j=m+1}^{n}\left[\frac{(H_T^\circ)_j}{RT}\right]\,\Delta n_j +$$

$$\left[\sum_{j=1}^{n}\frac{n_j\,(C_p^\circ)_j}{R}\right]\,\Delta\ln T = \frac{h_o - h}{RT} \qquad (19)$$

For large systems it is necessary to solve a large number of simultaneous equations. The number of equations can be reduced to a much smaller number by substitution of the expression for $\Delta\ln n_j$ into Equations (17) to (19).

The resulting equations are:

$$\sum_{i=1}^{\ell}\sum_{j=1}^{m} a_{kj}\,a_{ij}\,n_j\,\pi_i + \sum_{j=+1}^{n} a_{kj}\,\Delta n_j + \sum_{j=1}^{m} a_{kj}\,n_j$$

$$\Delta\ln n + \sum_{j=1}^{n}\frac{a_{kj}\,n_j\,(H_T^\circ)}{RT}\,\Delta\ln T = (b_R^\circ - b_R) + \sum_{n=1}^{m}$$

$$\frac{a_{kj}\,n_j\mu}{RT}; \qquad (k = 1,\ldots,1) \qquad (20)$$

$$\sum_{j=1}^{\ell} a_{ij}\pi_i + \frac{(H_T^o)_j}{RT} \Delta \ln T = \frac{\mu_j}{RT} \quad (j = m+1,\ldots,n) \qquad (21)$$

$$\sum_{i=1}^{\ell} \left[\sum_{j=1}^{m} a_{ij}n_j\pi_j\right] + \left[\sum_{j=1}^{m} n_j - n\right] \Delta \ln n + \sum_{j=1}^{m} \frac{n_j(H_T^o)_j}{RT} \Delta \ln T$$

$$\sum_{i=1}^{\ell} \left[\sum_{j=1}^{n} \frac{a_{ij}n_j(H_T^o)_j}{RT}\right] \pi_i + \sum_{j=m+1}^{n} \frac{(H_T)_j}{RT} \Delta n_j +$$

$$\sum_{j=1}^{m} \frac{n_j(H_T^o)_j}{RT} \Delta \ln n + \sum_{j=1}^{n} \frac{n_j(H_T^o)_j^2}{R^2 T^2} \Delta \ln T = \frac{h_o - h}{RT} +$$

$$\sum_{j=1}^{m} \frac{n_j(H_T^o)_j}{R^2 T^2} \mu_j \qquad (23)$$

A summary of correction equations required for several types of constant pressure problems are as follows along with the required correction variables:

TABLE I: Correction Equations

Problem	Equations	Correction Variables
Assigned temperature and pressure	(20), (21), (22)	π_i, Δn_j, $\Delta \ln n$
Assigned Enthalpy and pressure	(20), (21), (22), (23)	π_i, Δn_j, $\Delta \ln n$, ΔT

After the required correction variables are obtained, the corrections for gaseous species Δn_j $(j = 1,\ldots,m)$ are obtained from Equation (15).

REFERENCES

[1] Gordon, Sanford, and McBride, Bonnie J.; Computer Program for Calculation of Complex Chemical Equilibrium Compositions, Rocket Performance, Incident and Reflected Shocks, and Chapman-Jouguet Detonations, NASA SP-273.

[2] Stull, D. R., Prophet, J.; JANAF Thermochemical Tables, Second Edition, NSRDS-NBS37, June 1971.

[3] McBride, Bonnie J., and Gordon, Sanford; Fortran IV Program for Calculation of Thermodynamic Data, NASA TN D4097, 1967.

[4] Sieverts, A., and Gotta, A.; Z. anorg. allgem. Chem. 199, 384 (1931).

[5] Gibb, T. R. P., Jr.; McSharry, J. J., and Bragdon, R. W., J. Am. Chem. Soc. 73, 1751 (1951).

[6] Stalimski, B. and Bieganski, Z., Bull. Acad. Polon. Sic., Ser. Sci. Chim. 8, No. 5, 243 (1960) and 10, 247 (1962).

High Speed Optical Studies of
Pyrotechnic Initiation Phenomena*

M. M. Robertson and E. A. Igel
Optical Division of the
Exploratory Measurements Department
Sandia Laboratories, Albuquerque, N. M.   87115

Abstract

Techniques and instrumentation have been developed to monitor opti-
cally the interface between igniter headers and pyrotechnic charges during
ignition. The headers are optical quality sapphire which transmit visible
and infrared radiation. The instrumentation includes an infrared radio-
metric microscope modified to provide a visible channel. The visible
channel records the birth and growth of initiation with a high speed
electronic framing camera while infrared radiance measurements are simul-
taneously made by the radiometer from a selected portion of the reacting
interface. The infrared radiation is compared to that from a calibrated
black body and minimum temperatures are determined as a function of time.
The framing camera data show ignition and burn phenomena. Hot wire igni-
tion of $TiH_x/KC\ell O_4$ and $B/CaCrO_4$ has been studied for the unconfined case.
The interface burn rate of $TiH_{0.68}/KC\ell O_4$ (33/67) is about 220 mm/ms and
the interface burn rate of $B/CaCrO_4$ (20/80) is about 0.15 mm/ms. The in-
strumentation, experimental techniques, and data are discussed.

Introduction

Igniter use in weapons, space, and other specialized applications impose requirements not encountered in systems with lower reliability demands or in systems with less stringent weight restrictions. A better understanding of ignition and burn phenomena as a function of pyrotechnic materials properties and igniter design is needed. The resistance after fire, the jitter and the reliability continue to be problem areas. In an effort to gain knowledge of the factors that affect igniter performance, experiments have been conducted on some igniter mixtures in specific configurations to determine their burn rates, ignition times, back surface temperature profiles, and various electrical signatures. Unique instrumentation has been developed to accomplish these objectives. The basic approach has involved using an optical quality sapphire header in a special igniter body. The visible and infrared (IR) radiation intensity and/or distribution at the interface of the header and pyrotechnic mixture were studied during firing with an IR radiometric microscope, high speed electronic framing camera, and visible light photometer. The current through and the voltage across the bridgewire were monitored during the firing sequence. The experiments to be reported in this paper utilized $TiH_{0.68}/KClO_4$ (33/67) and $B/CaCrO_4$ (20/80) as the pyrotechnic mixtures.

Instrumentation

One design of the experimental igniter is shown in Figure 1. The housing is made of stainless steel to facilitate cleanup and reuse. The bridgewires are made of Tophet-C and are resistance welded to the Kovar pins. These are sealed into the sapphire header with a "glassing" process

using a mixture of the oxides of manganese (50%), silicon (30%), and aluminum (20%), fired in a reducing atmosphere, to approximate the coefficients of thermal expansion of the Kovar and sapphire. The pins are 0.5 mm in diameter and have their centers spaced 1.88 mm apart. The Tophet C bridgewire is .047 mm in diameter and the bridges were intended to be one ohm although in practice most of them measured slightly higher.

The schematic of the optical system is shown in Figure 2. The 2X reflecting objective lens indicated by "mirrors" on the schematic forms an image in the IR (2-5 μm) on the liquid nitrogen cooled InSb detector and in the visible on the fiducial cross hair. This visible image is relayed to the photocathode of the camera along with an image of the cross hair. At the 2X magnification used, the detector v   a 0.25 mm diameter area and the framing camera views the 3.2 mm clear aperture of the headers. The center of the cross hair is aligned to indicate the center of the area viewed by the detector.

Although not shown on the schematic, a beam splitter is sometimes inserted into the visible beam and a photodiode, sensitive to the visible and very near IR, views the clear aperture of the header. Others[1] have used optical light pipes to monitor the bridgewire surface of explosives or pyrotechnic mixtures which delivered similar information to that from the photodiode. The infrared radiometer (an extensively modified Barnes model RM-2A) was calibrated by use of standard black bodies so all temperature measurements could be expressed as black body equivalents. The electronic camera is a TRW model 1D framing-streak camera and the image intensifier is a four stage EMI unit. The film camera uses standard Polaroid film.

The electrical block diagram is shown in Figure 3. When the switch to the power supply is closed the shutters on all the oscilloscope cameras are opened and the firing sequence is initiated. The fireset provides the power to the bridgewire to provide hot wire ignition. The current is pre-selected and currents in the 3 to 5 ampere range are used. The blocks labeled "oscilloscope" each represent one or more oscilloscopes. The voltage across the bridgewire, current through the bridgewire, camera monitor pulses, infrared signals, and visible light signals are simultaneously recorded on different time bases and sensitivity levels. The IR detector views a portion (0.25 mm diameter) of the bridgewire and the pyrotechnic material immediately adjacent to it. The IR detector output resulting from bridgewire heating and pyrotechnic initiation is amplified and presented to the oscilloscopes. The jitter in bridgewire burnout and in ignition of the units precluded using preset delays so the ignition it-self activates the camera recording sequence. In some instances the IR de-tector output was used as a camera trigger and in other instances the photodiode output or the falling current associated with bridgewire burnout was used.

Pyrotechnic Materials

The materials studied were $TiH_{0.68}/KClO_4$ (33/67) and $B/CaCrO_4$ (20/80). The $TiH_{0.68}$ was prepared by Mound Laboratories to Sandia Laboratories spec-ifications. It was made from 2 μm TiH_2 with the resultant $TiH_{0.68}$ particles being somewhat larger due to sintering during the dehydriding process. The $KClO_4$ was supplied by Barium and Chemicals Co. and passed a 400 mesh screen (particles averaged about 9 μm). The B and $CaCrO_4$ were supplied by

Unidynamics and were composed of 1 μm and 2 μm particles respectively. The charges loaded into the igniters were about 25 mg and the $TiH_{0.68}/KC\ell O_4$ (33/67) was pressed at 68.9 MPa (10 K psi) and the $B/CaCrO_4$ (20/80) was pressed at 103.4 MPa (15 K psi). In the experiments performed to date the igniters have been fired in an unconfined state.

Results

We will discuss the $TiH_{0.68}/KC\ell O_4$ (Ti mixture) data first. Table I documents some of the parameters for a series of Ti shots. The bridge burst time is defined as the time from current application to the time the current drops to the half-value point from its preset level. The bridge resistance is the resistance measured before loading. The charge weight shows the weight of the charge loaded and, for comparison purposes, the weight of the residue after firing. The amount of the residue is of interest because it undoubtedly affects the resistance after firing (RAF). The variations shown in density of the pressed pyrotechnic mixture probably arise from thickness measurement errors. The thicknesses of charges were approximately 0.6 mm so a slight error in measurement made a significant difference in the calculated density. The firing energies were calculated from the current and voltage measured during firing and from the current during firing and the resistance measured for the bare bridgewire prior to loading the igniters. Within experimental error the magnitudes were the same for both cases. It was initially thought that resistance changes, during firing, by conduction through the pyrotechnic mixture would make the current voltage relationship the only valid power value. Apparently there was minimal conduction through the pyrotechnic mixture.

Figure 4 gives an example of the data collected on a shot of $TiH_{0.68}$/ $KClO_4$ (33/67). Figure 4a shows the bridgewire current which dropped quickly at 2.25 ms into the pulse. The lower trace shows the IR signal starting to increase as soon as current was applied, then shows a plateau before the rapid increase close to bridgewire burnout. This rapid increase is apparently associated with the exothermic reaction of the pyrotechnic mixture at ignition. This trace goes off scale so the temperature maximum cannot be determined. Figure 4b shows the current through the bridgewire with the TRW camera monitor pulses superposed in the upper trace which is at a faster sweep rate than in Figure 4a. The lower trace shows the IR readout which quickly saturates and that the IR excursion occurred at very close to the same time Frame 1 was taken. The exposures shown in Figure 4c were taken at the times indicated in Figure 4b which means ignition apparently occurred before bridgewire burnout which has been defined as the drop in bridgewire current to the half value point. Each of the frames show the cross hair whose intersection coincides with the center of the area viewed by the IR detector. In Frame 1 the initiation of ignition is barely visible. The burn then expands to fill the back face of the header by the fourth frame and starts dimming by Frame 5. The brightness of the reaction zone was great enough so these data were taken without using the image intensifier. The visible burn velocity at the pyrotechnic mixture header interface measured on this and other shots is 220 ± 50 mm/ms for $TiH_{0.68}$/$KClO_4$ (33/67). The notches in the image are caused by the bridge-wire pin leads obscuring part of the interface.

Some of the data collected on a series of $B/CaCrO_4$ (20/80) shots are summarized in Table II. The parameters are as defined for Table I. The

omitted density numbers are for igniters that showed obvious loss of pyrotechnic mixture prior to firing; e.g., shots 29 and 30 had lost about one third of their total charge from around the edges. The density of the remaining material was probably consistent with the calculated densities for other shots since it was all pressed to the same pressure.

Figure 5 shows some of the data collected on a $B/CaCrO_4$ shot. The upper trace in Figure 5a shows a typical current flow through the bridge. The 3.6 ampere current flows for about 2.25 ms, drops to zero at what we call bridgewire burst and then ramps back up for 2 to 3 ms until it is close to its maximum value and then again drops to near zero. It then becomes erratic for the duration of the burn but does not reach the levels attained earlier. The infrared signal tends to increase methodically up until bridgewire burst and then sits on a plateau until the end of the current ramp which correlates with the infrared excursion interpreted as ignition. The three dots are the monitor pulses from the framing camera and indicate when the photographic exposures were made. The camera was operated with 400 µs between frames and this was near the maximum delay possible. The B mixture burns so slowly that a longer time coverage would be desirable. Figure 5b shows the voltage across the bridge.

Figure 5c shows three exposures taken at the times indicated on Figure 5a. Since the brightness of the burn was much dimmer than for the Ti mixes the use of the image intensifier at high gain was mandatory. The ignition appears to have occurred along the length of the bridgewire and then propagated at an average velocity of 0.15 mm/ms to form a rectangular pattern. The velocity was determined from measurements of the luminous area as a function of frame times. A photodiode record of the back surface burn shows a linear increase in signal with time. This would be consistent with

the signal being proportional to the perimeter rather than the area of the burn region; i.e., that the burn front moves out from the bridgewire leaving a non-luminous region behind. This dark area can, in fact, be seen in Figure 5c.

Discussion

The resistance of all the igniters fired by the authors to date has remained greater than 1 Ω during and after firing. The $TiH_{0.68}/KClO_4$ mixture burns rapidly and has high RAF. There is a film of KCl on the sapphire header after firing and this is, of course, a good conductor while hot or molten; however, it doesn't seem to create a real problem in these unconfined firings. In general the total residue after firing the Ti mixture is minimal. The $B/CaCrO_4$ mixture burns slowly and leaves extensive residue. Variance of residue weights in Table II are due to loss of material from the igniter after firing but before final weighing. The resistance during firing is erratic and approaches 1 Ω at times during a burn. One of the drops in resistance is associated with the current ramp after bridgewire burst.

The average temperature of the back surface of the pyrotechnic mixture during the plateau period close to bridgewire burst time is measured at about 630 ± 50 K for the Ti mixture, assuming an emissivity $(\epsilon) = 1$. There is an exotherm occurring at 673 to 723 K according to differential thermal analysis $(DTA)^2$ in Ti and TiH_2 (33/67) mixtures with $KClO_4$. If, as we believe, this exotherm occurs at the same temperature for the $TiH_{0.68}$ mixture as for the Ti and TiH_2 mixtures then an emissivity of 0.69 to 0.45 is required for the 673 and 723 K temperatures respectively in the 2 to 5

μm wavelength bandpass of the radiometer. As mentioned earlier the rapidly rising infrared signal at the end of the temperature plateau is considered to constitute ignition. No maximum burn temperatures were determined for the Ti mixtures since all records went off scale. The adiabatic burn temperature[3] would be 2773 to 3273 K based on the boiling temperature of TiO_2.[4]

The backsurface temperature recorded during the plateau for the B mixture was 1043 ± 50 K, assuming $\varepsilon = 1$. The DTA data show an exotherm in the 773 to 1023 K region[2]. The plateau may be due to some endothermic reaction but must be partially due to the reduced power input immediately after bridgewire burst. It may also be partially due (in this case and for other materials also) to where the IR detector is looking with respect to the point where ignition actually initiates. The adiabatic flame temperature of $B/CaCrO_4$ is 2133 K based on the boiling temperature of B_2O_3.[5] We measure 1993 K assuming $\varepsilon = 1$. This requires $\varepsilon = 0.83$ at this temperature across the 2 to 5 μm passband in order to agree with the adiabatic flame temperature. Since the heat values of $B/CaCrO_4$ mixtures peak at the 20/80 ratio[6] this ratio has often been used in component design. Changes in ratios are expected to alter exotherm positions somewhat and have been reported to significantly change RAF[7] - the higher the boron content the lower the RAF.

Ignition appears to start at a localized point for both the Ti and B mixtures. The Ti mixture burns out from this ignition point in a semisymmetric fashion with velocities varying slightly in random directions. The B mixture seems to propagate first along a line in the mixture that was preheated by the bridgewire and then it burns outward from this line

494

at a reasonably uniform rate. The burn velocity measured at the header pyrotechnic mixture interface under our conditions was 220 ± 50 mm/ms for the $TiH_{0.68}/KC\ell O_4$. The velocity measured for the $B/CaCrO_4$ mixture was 0.15 mm/ms. All the burn rates reported here fall in the range reported for delay mixtures.[8]

Acknowledgements

References

1. Howard S. Leopold, Effects of Loading Density on the Hot Wire Initiation of Normal Lead Styphanate and Barium Styphanate, NOLTR-70-96, (United States Naval Ordnance Laboratory, White Oak, Maryland, August 1970).

2. T. M. Massis, Sandia Laboratories, Albuquerque, New Mexico. Private communication, April 1976.

3. Headquarters, U. S. Army Materiel Command, "Engineering Design Handbook Military Pyrotechnics Series, Part One, Theory and Applications" AMCP 706-185 April 1967, p. 3-19.

4. Robert C. Weast, editor, "Handbook of Chemistry and Physics", (Chemical Publishing Co., Inc., 55th Edition, New York, 1974) p. B-150.

5. Robert C. Weast, editor, "Handbook of Chemistry and Physics", Chemical Publishing Co., Inc., 55th Edition, 1974), p. B-74.

6. Herbert Ellern, "Military and Civilian Pyrotechnics", (Chemical Publishing Co. Inc., New York, 1968), p. 283.

7. N. E. Brown and P. K. Morenus, Ignition Characteristics of Boron/ Calcium Chromate, Fifth International Pyrotechnics Seminar, 12-16 July, 1976.

8. Herbert Ellern, "Military and Civilian Pyrotechnics," (Chemical Publishing Co. Inc., New York, 1968), p. 198.

3.2 MM

15.9 MM

0.5 MM DIA. KOVAR PINS

RETAINER PLATE

SAPPHIRE HEADER
(6.35 MM DIA.)

3.2 MM

2.0 MM

11.1 MM

O-RING

PYROTECHNIC
MATERIAL

4.4 MM

BRIDGEWIRE

HOUSING
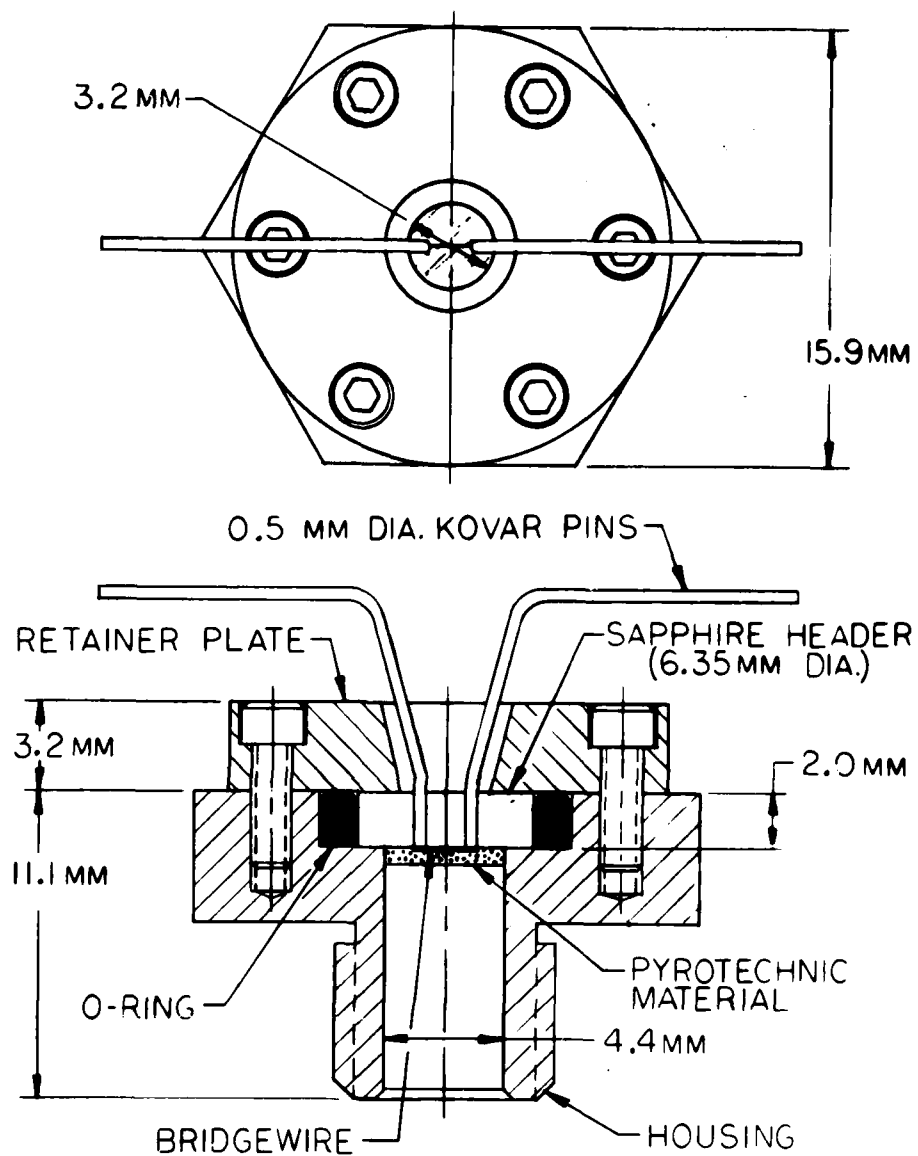
Figure 1. Experimental Igniter

SIGNAL → TO RECORDING SYSTEM AND CAMERA TRIGGER

InSb DETECTOR

IR RADIATION

FIDUCIAL CROSSHAIR

LENSES

Ge BEAMSPLITTER

ELECTRONIC CAMERA

IMAGE INTENSIFIER

VISIBLE RADIATION

FILM CAMERA

MIRRORS

TO FIRESET AND MEASURING CIRCUITS

TRANSPARENT Al_2O_3 HEADER

BRIDGEWIRE

PYROTECHNIC MATERIAL

BOOMBOX

EXHAUST
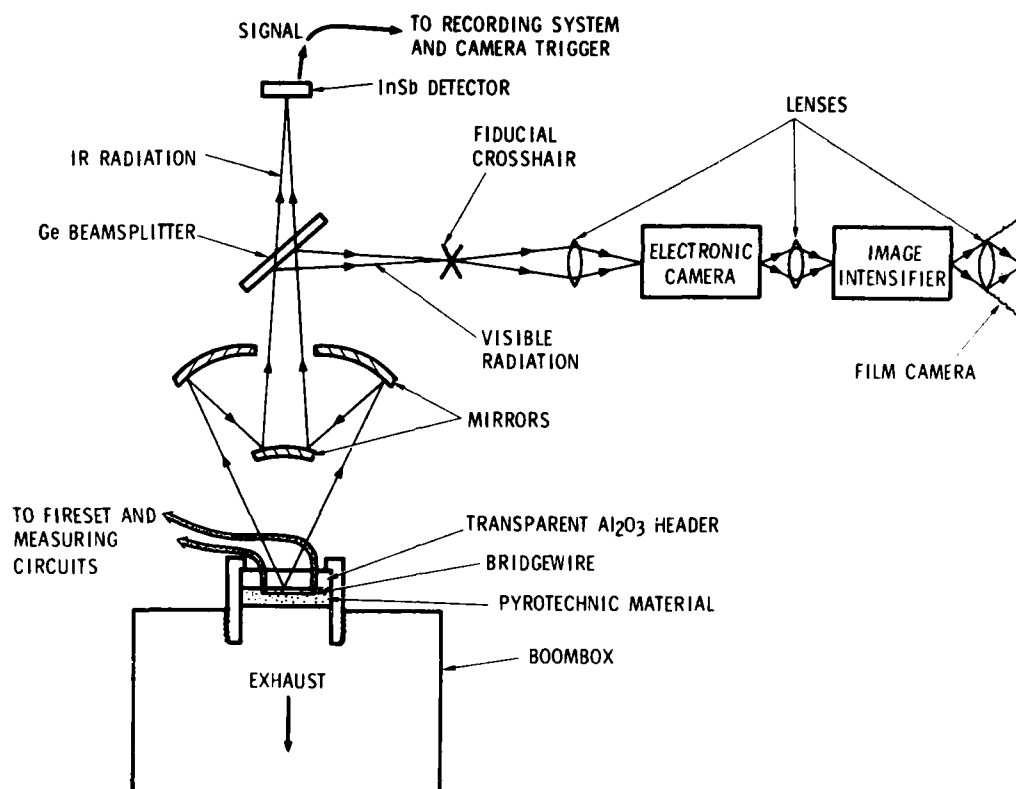
Figure 2. Optical System Schematic

TRIGGER CIRCUIT

ELECTRONIC CAMERA

IMAGE INTENSIFIER

IR DETECTOR

PREAMPLIFIER

OSCILLOSCOPE

POWER SUPPLY

CURRENT VIEWING RESISTOR

BRIDGEWIRE

FIRESET

DELAY

POWER SUPPLY

OSCILLOSCOPE (CURRENT THROUGH BRIDGEWIRE)

OSCILLOSCOPE (VOLTAGE ACROSS BRIDGEWIRE)

ELECTROMECHANICAL SHUTTERS ON OSCILLOSCOPE CAMERAS
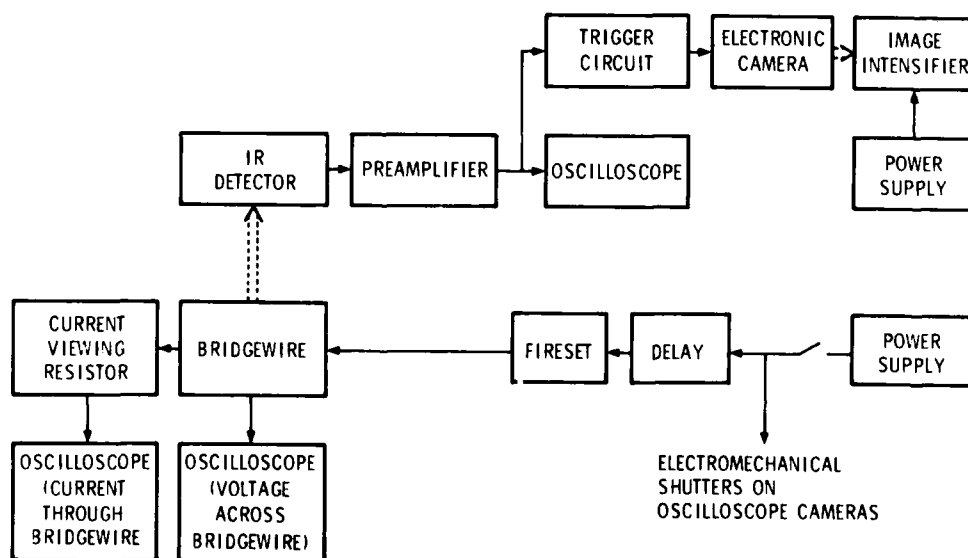
Figure 3. Electrical Block Diagram

498
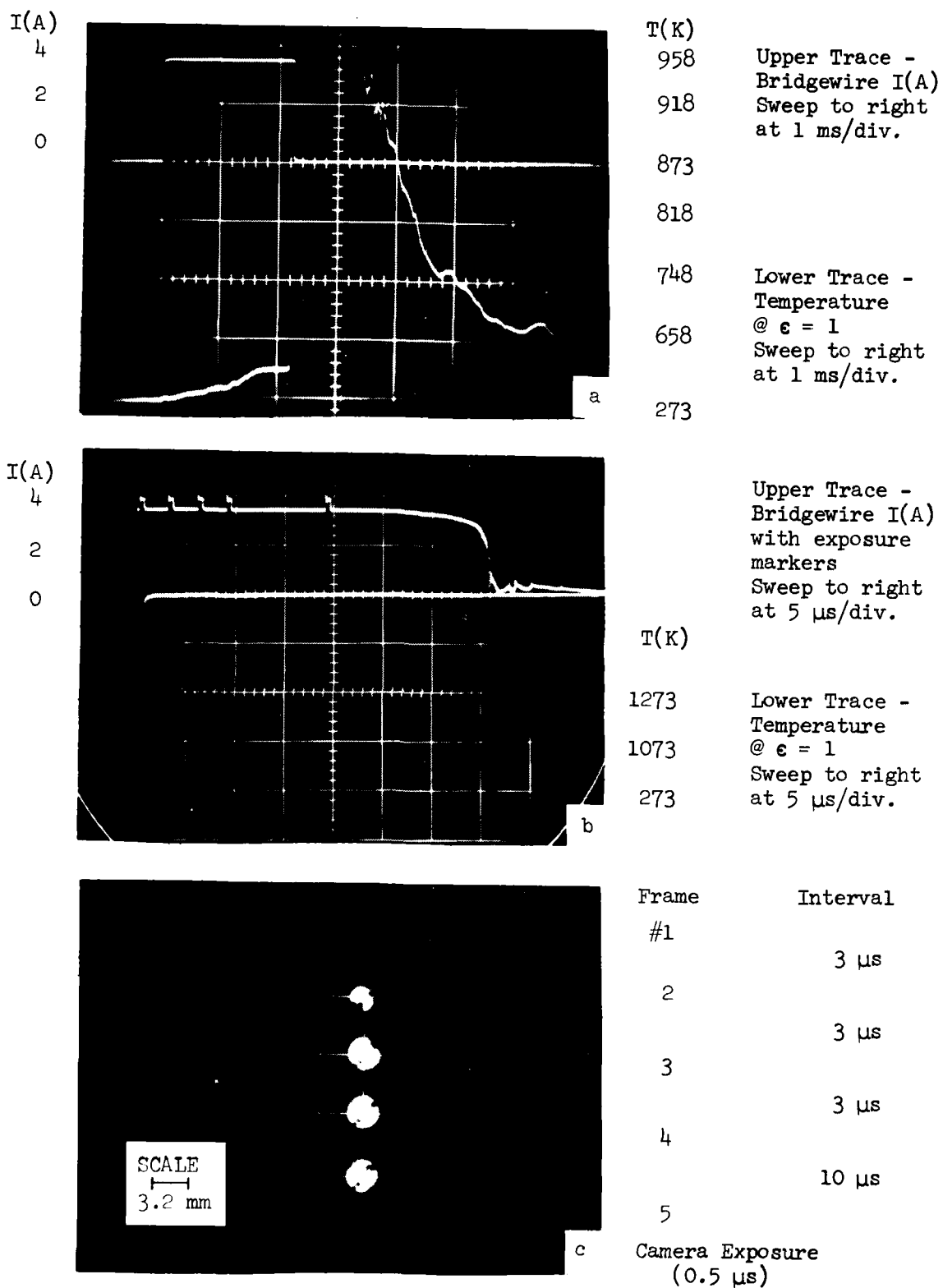
Figure 4. $TiH_{0.68}/KClO_4$ (33/67) Firing Data

I(A)

	T(K)	
	1413	Upper Trace - Bridgewire I(A) with exposure markers Sweep to right at 1 ms/div.
	1343	
	1273	
	1188	(Markers)
	1073	Lower Trace - Temperature
	918	@ ε = 1 Sweep to right
	273	at 1 ms/div.

a

V

Volts Across Bridgewire Sweep to right at 0.5 ms/div.

b

Frame	Interval
1	
	400 µs
2	
	400 µs
3	

SCALE
3.2 mm

c   Camera Exposures
(10 µs)
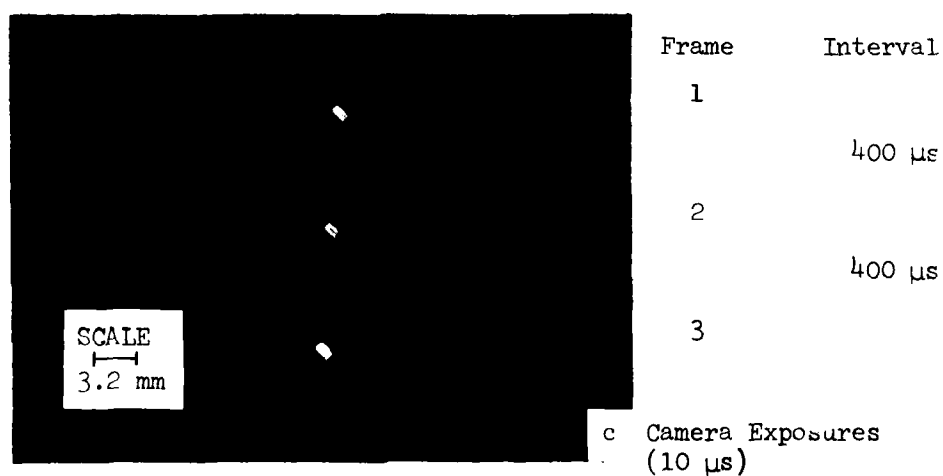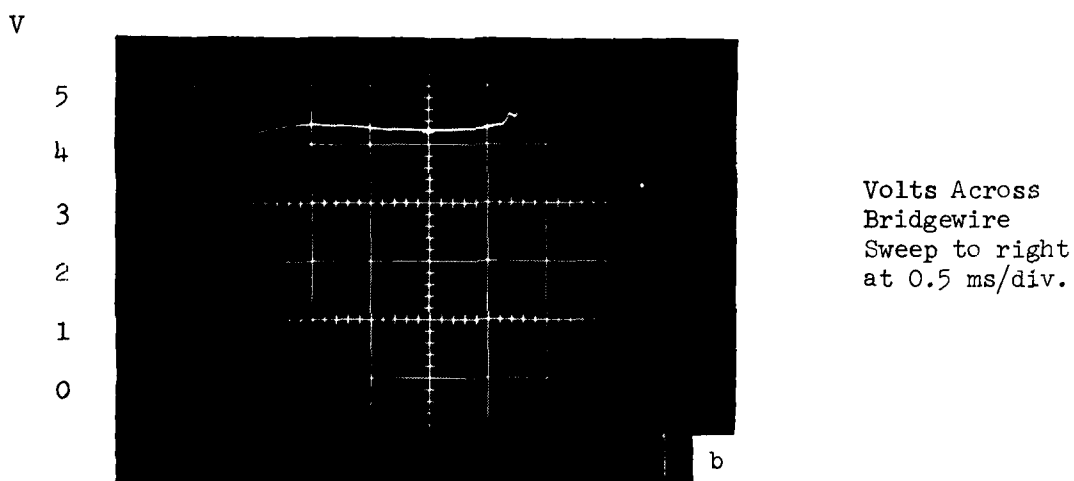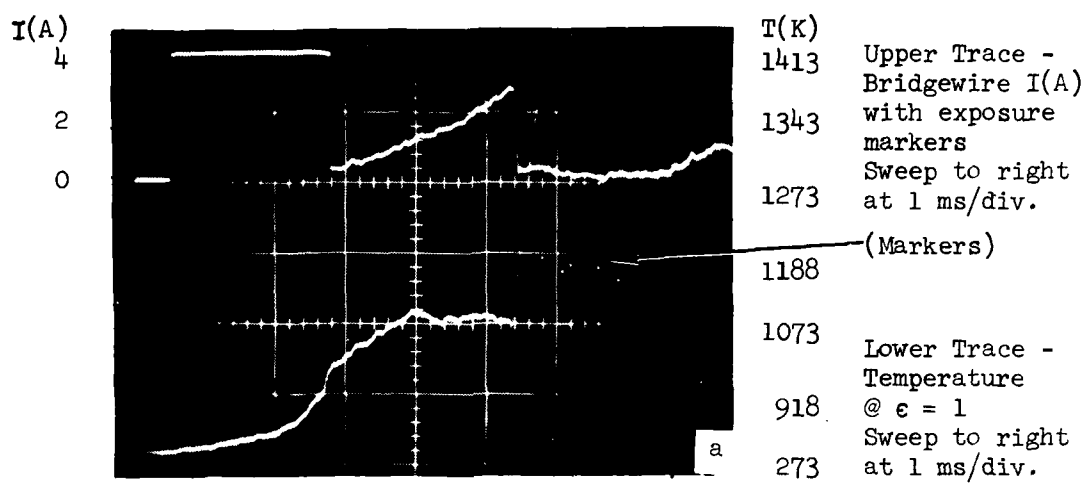
Figure 5.   B/CaCrO$_4$ (20/80) Firing Data

Table I

$TiH_{0.68}/KClO_4$ (33/67)

Shot #	Bridge Burst Time ms	Bridge Resistance Ω	Charge Weight Residue/Original mg	Pellet Density g/cm³	Current A	Firing Energy mJ
2	1.60	1.16	0.3/23	2.36		
3	1.75	1.42	0.9/23.1	2.19	3.6	32.2
4	1.65	1.22	0.8/23.5	2.36	3.8	29.1
5	1.80	1.19	2.0/25.0	2.16	3.5	26.2
6	1.75	1.19	2.1/24.7	2.21	3.5	25.5
7	2.40	1.13	1.0/25	2.22	3.5	33.2
8	2.30	1.16	1.4/25	2.32	3.5	32.7
9	2.25	1.26	1.2/25	2.29	3.5	34.7

Table II

B/CaCrO$_4$ (20/80)

Shot #	Bridge Burst Time ms	Bridge Resistance Ω	Charge Weight Residue/Original mg	Pellet Density g/cm^3	Current A	Firing Energy mJ
16	1.80	1.20	17.6/22.4	1.82	3.5	26.5
17	2.10	1.24	18.2/23.6	1.87	3.6	33.7
23	1.85	1.22	4.0/22.5	1.87	3.6	29.3
24	2.30	1.29	21.1/22.7		3.6	38.5
25	2.10	1.35	4.1/22.5	1.87	3.6	36.7
26	2.25	1.27	20.9/22.6	1.78	3.6	37.0
27	2.10	1.32	5.5/22.6	1.85	3.6	35.9
28	2.15	1.18	5.3/20.6		3.6	32.9
29	2.10	1.37	4.8/16.7		3.6	37.3
30	2.25	1.30	3.8/14.2		3.6	37.9
31	2.00	1.38	6.3/19.8		3.6	35.8

Acknowledgement

PYROTECHNIC SYSTEMS AND DEVICES
USED IN THE NASA SPACE SHUTTLE

Ed A. Timmons
National Aeronautics and Space Administration
Kennedy Space Center, Florida

PYROTECHNIC SYSTEM & DEVICES
USED IN THE NASA SPACE SHUTTLE

Introduction

The Space Shuttle vehicle presently under development by the National Aeronautics and Space Administration, is a new concept in the Space Transportation System. The primary design and operational goal for the Space Shuttle Program is to provide a low cost, reusable vehicle capable of delivering payloads into earth orbit and returning for reuse with a minimum amount of refurbishment.

The Space Shuttle flight system is composed of an Orbiter, an external tank (ET) and two solid rocket boosters (SRB). The Orbiter and solid rocket boosters (SRB) are reusable; the external tank is expended on each launch.

122.3 FT

SHUTTLE VEHICLE

- DESIGN LAUNCH
  WEIGHT (LB)   4369K *
- PAYLOAD (LB)
  DUE EAST   65K
  DESIGN (104°)   32K

* PRELIMINARY
  VALUES

ORBITER

- PAYLOAD BAY
  15 FT DIA X 60 FT LG
- 3 MAIN ENGINES
  470K LB VAC THRUST, EA
- 2 OMS ENGINES
  6000 LB VAC THRUST, EA
- 38 RCS ENGINES
  900 LB VAC THRUST, EA
- 6 RCS VERNIER ENGINES
  25 LB VAC THRUST, EA
- WEIGHT (LB)
  DRY   150K
  DESIGN LANDING   187K

EXTERNAL TANK

- LENGTH (FT)   154
- DIAMETER (IN.)   331
- WEIGHT (LB)
  LAUNCH   1631K
  USABLE PROP   1553K

Space Shuttle Vehicle

The Orbiter carries a crew of four plus up to three scientific or technical personnel. It will normally remain in orbit for seven days, but with special payloads can remain in orbit up to 30 days. The Orbiter main rocket engines used during ascent obtain their propellants from the external tank. Smaller orbiter rocket engines provide maneuvering and control capability during space flight. Aerodynamic surfaces on the wings and vertical stabilizer control the orbiter during atmospheric flight.

The crew and passengers occupy a two-level cabin in the forward end of the vehicle. The crew controls the launch, orbital maneuvering, atmospheric entry and landing phases of the mission from the upper level flight deck. Aft of the crew compartment is the payload bay, which is approximately 15 feet in diameter and 60 feet long, and can accommodate payloads weighing up to 65,000 pounds.

One important Space Shuttle mission will be the placement of satellites in earth orbit. A satellite launched on a previous mission can be retrieved and returned to earth for refurbishment and reuse. As many as five individual satellites may be delivered on a single mission. Upon reaching the desired orbit, the mission and payloads specialist will conduct predeployment checks and operations. After determining that the satellite is ready, the crew will operate the payload deployment system, which lifts the satellite from the payload bay, extend it away from the Orbiter, and releases it. The Orbiter will stand by until the satellite is performing satisfactorily before proceeding with the remainder of the mission.

The external tank contains 1.55 million pounds of usable propellant at liftoff for use by the Orbiter main engines. The LH_2 tank volume is 53,800 cubic feet, and the LO_2 tank volume is 19,500 cubic feet. The external tank is the only part of the Space Shuttle which is expended on each launch.

Two solid rocket boosters (SRB's) burn in parallel with the Orbiter main propulsion system to provide initial ascent thrust. Each SRB is approximately 150 feet long and 12 feet in diameter and produces 2.65 million pounds of thrust at sea level. The SRB's will be retrieved from the ocean after each flight and returned to the Kennedy Space Center where they will be disassembled. The motor case segments will be disassembled, placed on rail cars, and returned to the Thiokol Corporation, Wasatch, Utah, for refurbishment, recasting, and then returned again for another flight.

Pyrotechnics, because of their desirable characteristics, such as high energy-to-weight ratio, quick action, high reliability, small size, and low cost, play an important role in the Space Shuttle Program. Past spacecraft programs have used explosive devices and systems in many applications. The Mercury spacecraft used approximately 50 devices, the Gemini spacecraft 90 devices, and the combined Apollo spacecraft and Saturn V launch vehicle utilized over 450 explosive actuated devices. The types of application have also evolved into more and more complex systems. As in previous programs, the majority of the Shuttle pyrotechnics functions are crew-critical, i.e., crew safety depends on safety from inadevertent operations and realiability of operations upon command.

The Story of a Normal Shuttle Mission

As the countdown clock continues to tick away the last few minutes of the countdown sequences, the test conductor makes his final systems status checks. The Range Safety Officer has completed his pre-launch test and has given his "go." The external tank has been filled with LO_2 and LH_2 and white clouds of vapor float out of the overflow vents. The signal is sent to each Solid Rocket Booster safe and arm device, moving the internal rotor 90°, allowing the two NASA Standard Initiators (NSI's) to line up with the propellant basket of the motor igniter. (Figure 1) Only three more commands are needed to ignite the 2.65 million pound thrust solid rocket motors.

The sight of the Shuttle vehicle perched on Launch Complex 39 is unfamiliar to the long time missile watchers around Cape Canaveral. Usually on Launch Complex 39 one would expect to see the mighty Saturn rocket with the Apollo spacecraft atop it. Now, instead of one tall cylinderical projectile you see one large cylinder, two smaller cylinderical objects attached to it, and an aircraft looking vehicle about the size of a Douglas DC-9 standing on its tail. This cluster is held to the launch complex by eight 3½" bolts, 4 of which attach the aft skirt of each solid rocket booster (SRB) to the launch pedestal.

As the countdown appraoches T-3.5 seconds the Orbiter's three main propulsion engines ignite and each quickly builds up to 375,000 pounds of thrust. These engines are throttleable and are capable of being gimbaled for flight control during the Orbiter boost phase. At T-0 the two NASA Standard Initiators in each SRB ignition system fire and the SRBs are ignited. As their thrust starts to build, the umbilicals which have connected the Shuttle vehicle to the ground systems are separated by means of explosive bolts. With the Orbiter engines and both SRBs thrusting the signal is sent to the sixteen detonators, two in each of the eight 3½" frangible nuts which hold the SRBs to the launch pedestal. The force of the detonator plus an additional base change fracture the holddown nuts. (Figure 2)
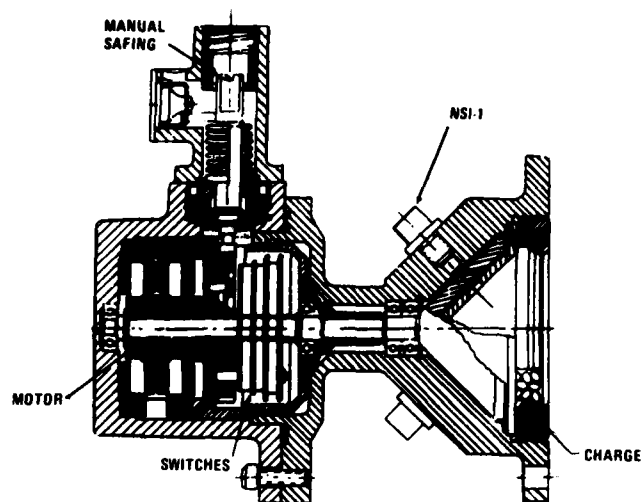
Figure 1 SRM Safety & Arming Device
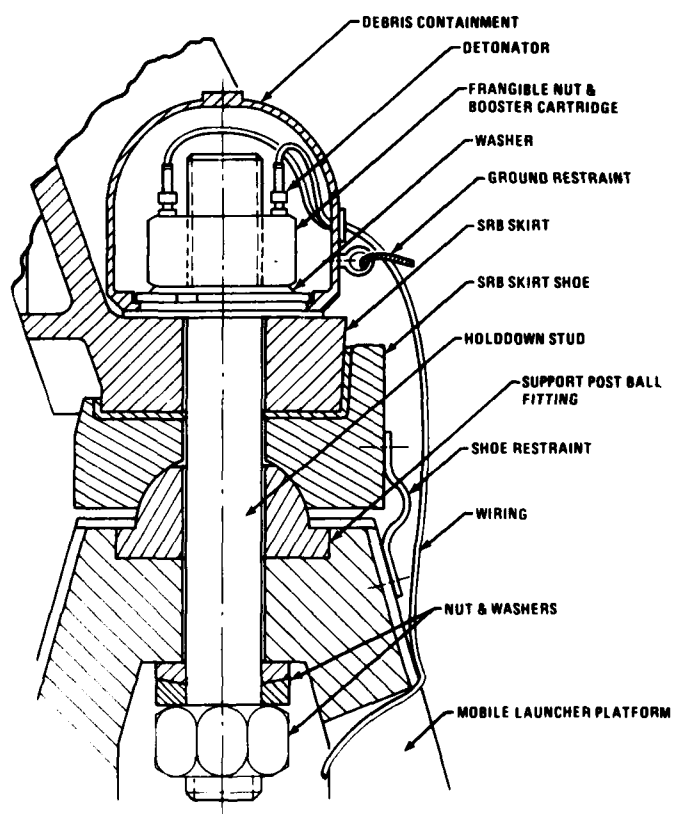
Figure 2 Solid Rocket Holddown

506

The thrusting vehicle, now completely disconnects from the launch complex, raises slowly and climbs upward in a thundering roar. The vehicle continues to climb and increases in speed. The SRB and Orbiter main engines continue to thrust for 110 seconds, at this time the SRBs start a rapid thrust decay and at 122 seconds in the flight and 27 nautical miles above the earth, the SRBs are separated from the external tank.

The SRB and ET are held together at the forward end by one separation bolt, with a NSI pressure cartridge installed in each end of the bolt. (Figure 3) The pressure produced by each cartridge acts against a primary piston and the force of the primary piston, amplified through compression of a silicone rubber disc, is applied to a secondary piston. The force generated by the secondary piston reacting against the secondary piston of the redundant side of the bolt causes the bolt housing to fail in tension.
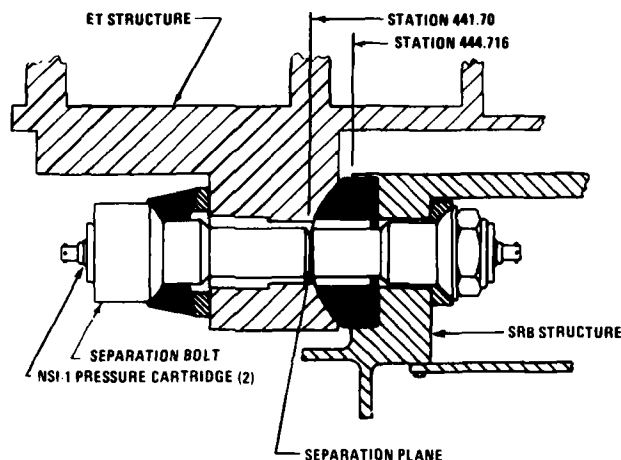
Figure 3 SRB/ET Forward Attach Point

The aft attach point is composed of three structs which hold the SRB to the external tank. (Figure 4) On the inside of each struct is a tandom piston type bolt, much like the one used at the forward attach point. Initiation of the six pressure cartridges will complete the separation of the SRB from the external tank.
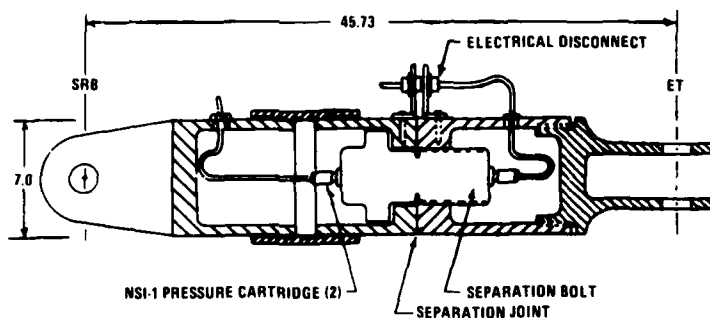
Figure 4 SRB/ET Aft Strut

At the same time the attach points are separated another series of signals are sent to four detonators, which in turn initiate 38 other explosive devices and eight solid rocket motors on each SRB. This system is designed to push the expended SRB away from the still thrusting Orbiter and the External Tank. Identical separation motor systems are located in the forward and aft skirt of each SRB to produce a positive, uniform, force away from the external tank. (Figure 5) Each system consists of nine confined detonating fuse (CDF) assemblies, two NSI detonators, two CDF manifolds and eight CDF motor initiators. Redundant separation signals to the forward and aft separation motor systems initiate redundant NSI detonators. The detonation shock wave from the NSI detonators propagates through two CDF manifolds and eight CDF assemblies to eight CDF initiators, igniting the separation motors. The eight separation motors, each producing 22,000 pounds of thrust, propells the SRB away from the external tank. The expended SRBs having reached their highest altitude starts to descend and the SRB recovery sequence begin.
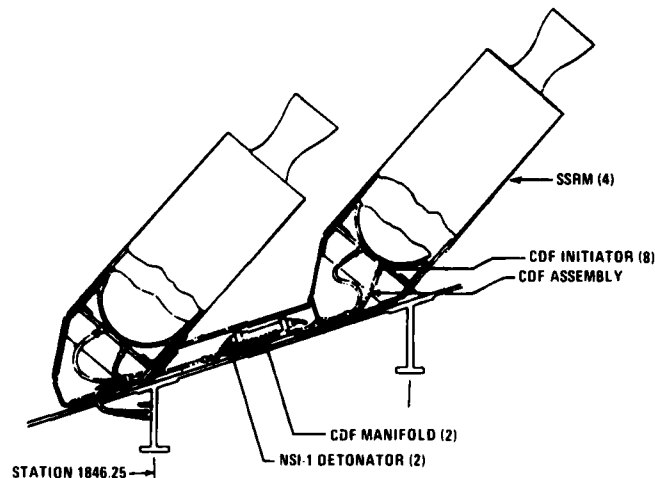
Figure 5 Separation Motor Ignition Aft

First, the Solid Rocket Motor (SRM) nozzle severance system consists of a NSI detonator, CDF assembly and linear shape charger is fired. (Figure 6) When the system is initiated the 300 gr/ft. shape charge severs the motor nozzle allowing it to fall away from the SRB. The nozzle is severed to reduce recovery weight and protect the hydraulic actuators, attached to the forward nozzle, from damage upon ocean impact.
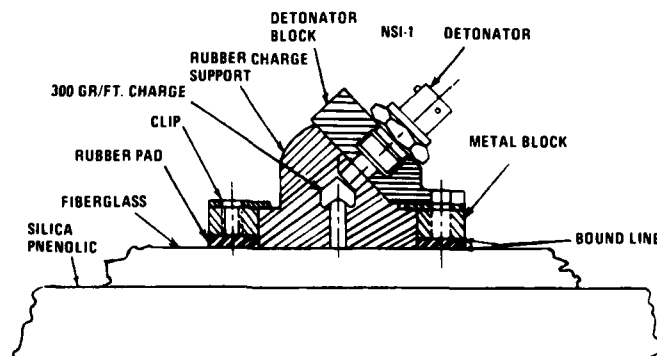
Figure 6 SRM - Nozzle Severance

SPACE SHUTTLE from Launch to Landing

ENTRY INTO ORBIT

FUEL TANK DROPPED

ORBIT-FLIGHT TASKS ACCOMPLISHED

SOLID MOTORS DROPPED

REENTRY

LAUNCH

BOOSTER SPLASHDOWN

LANDING
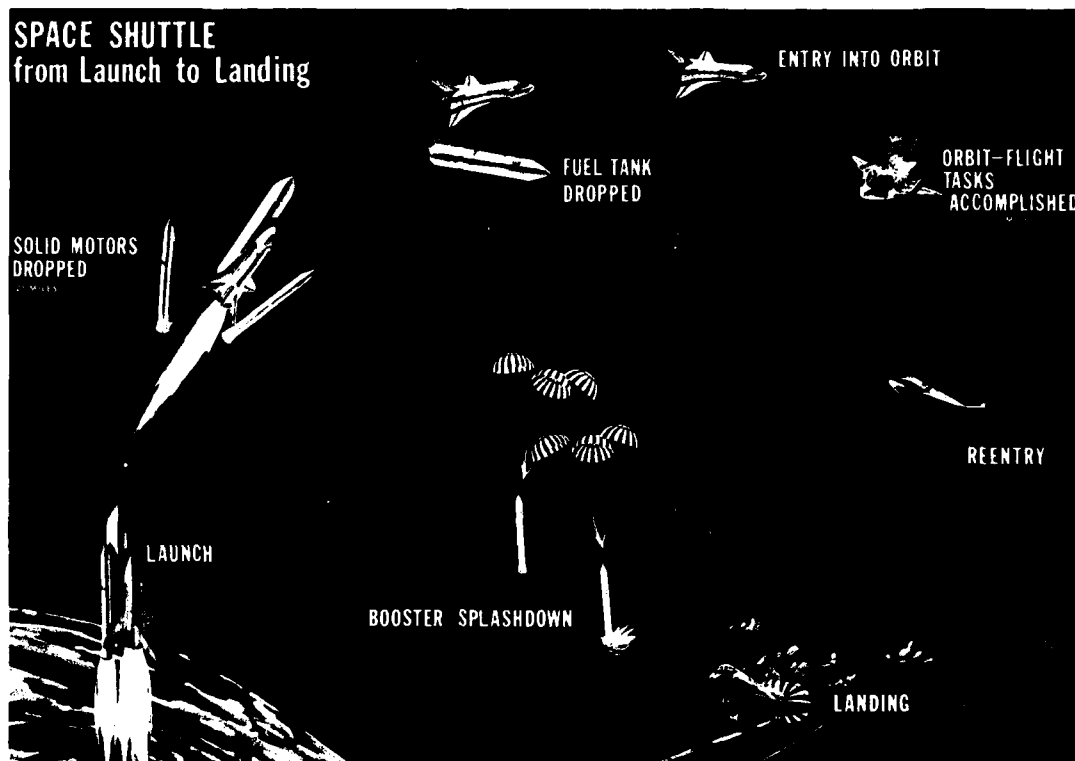
The next recovery event is the jettisoning of the nose cone which contains the pilot and drogue parachutes. The nose cone separation system consists of a NSI detonator, CDF manifold, three CDF assemblies and three thruster pressure cartridges. The SRB free falls to a predetermined altitude, where barometric switches are actuated, sending fire commands to the NSI detonator.

The output of the detonator is propagated through the CDF manifold and CDF assemblies to the three thrusters spaced 120° apart on the top ring of the frustum. (Figure 7) Upon initiation the pressure cartridges produce pressure against the thruster piston, causing the thruster to release and the piston rod to begin producing a 30,000 pound thrust over a six inch stroke. At the end of the six inch stroke the piston rod separates from the piston and is ejected with the nose cap. The nose cap is accelerated to a velocity of 80 ft/second as it leaves the SRB.

CDF ASSY

NOSE CAP

STATION 286

PRESSURE CARTRIDGE

THRUSTER (3)

FRUSTUM
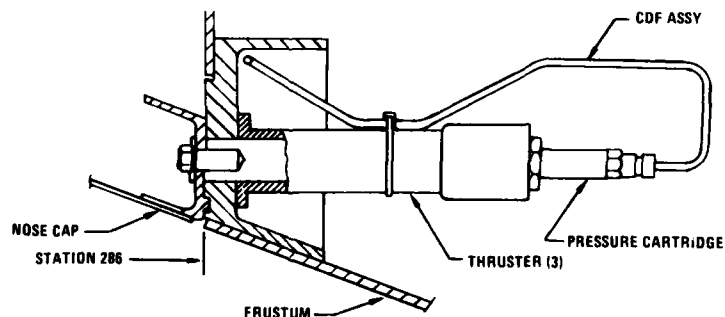
Figure 7 Nose Cap Separation

As the nose cone moves away from the SRB, the pilot and the drogue parachutes, which are packed inside the nose cone, are pulled out. The 54' diameter drogue parachute incorporates a reefing line which prevents the parachute from being fully deployed for eight seconds. This reefing is necessary to stabilize the SRB attitude, and to prevent the parachute from damage as a result of excessive shock deployment. The reefing line is cut after eight seconds by means of pyrotechnic reefing line cutters which are percussion initiated. (Figure 8) When the reefing lines are severed the drogue parachute is allowed to inflate fully at an altitude of approximately 12,500 feet. The drogue parachute continues to stabilize and deaccelorate the expended SRB until another barometric switch is activated at approximately 9,000 feet. This switch sends a fire signal to a NSI detonator which in turn detonates a 360° shape charge around the frustum separation ring. The severed frustum section is pulled away by the force of the drogue parachute deploying the three main 104-foot diameter parachutes, which were packed inside the frustum section. The three main parachutes undergo a double reefing like the drogue parachute. After the second reefing the parachutes fully deploy at an altitude of 3,500 feet and descend gently into the sea, at a point about 150 miles from the launch site. Upon sea impact a fire command is sent to a NSI detonator, which in turn initiates a CDF manifold, six CDF assemblies and six CDF initiators. Pressure produced by the initiator cause the segmented nuts to release and eject the main parachute attach fitting bolts, thereby releasing the three main parachutes.
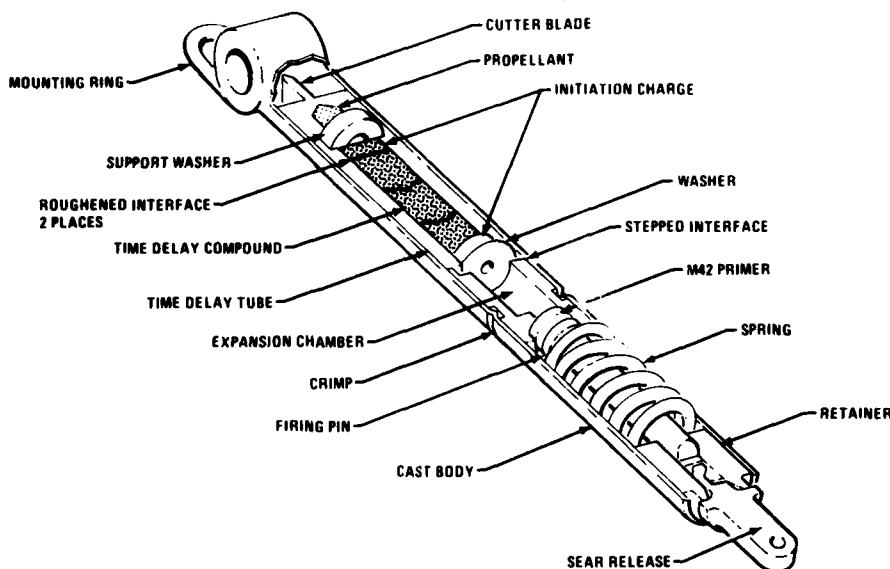
Figure 8 Reefing Line Cutter

Retrieval vessels will be directed to the SRB splashdown area by data provided by the Launch Control Center and on-board tracking aids. The hardware to be recovered from the water consists of the two SRB casing, six main parachutes, and two frustums with drogue parachutes attached. These recovered items will be returned to the Kennedy Space Center. The case will be washed, disassemblied, placed on rail cars and returned to the Thiokol plant for recasting. The recovered parachutes will be washed, dried, repaired if necessary, repacked, and cycled back into the normal hardware flow.

After the SRBs separate from the thrusting Shuttle vehicle, the Orbiter's three main propulsion engines continue their eight minute burn. When the Orbiter's main engines have reached zero thrust, Orbiter/ET separation occurs. The ET, which has played a total passive role in the operation, falls away and begins its 375,000 feet decent into the ocean to a predicted impact area. Eighteen explosive devices are required to perform Orbiter/ET separation. The two 17-inch fuel and oxidizer lines, which have been feeding propellant to the Orbiter, are separated after six frangible nuts with two detonators in each nut are fractured. The two Orbiter umbilical halves (LH_2 and LO_2) are then pneumatically retracted into the Orbiter separating all fluid and electrical disconnects.

Structural attachments are pyrotechnically separated by simultaneous signals. The Orbiter had been attached at the forward end by a tandom piston explosive bolt. (Figure 9) Two large pressure cartridges are installed in the bolt either of the cartridges will produce sufficient energy to fracture the bolt. The two Orbiter/ET aft attachments are held in place by two frangible nuts. (Figure 10) When the two detonators in each nut are detonated, the frangible nut breaks in half and the Orbiter is then completely separated from the external tank.
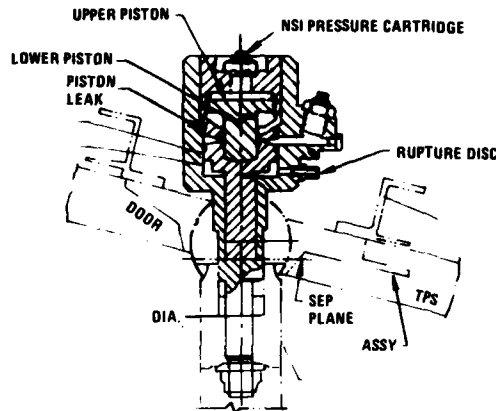
Figure 9 Orbiter/ET Forward Attachment
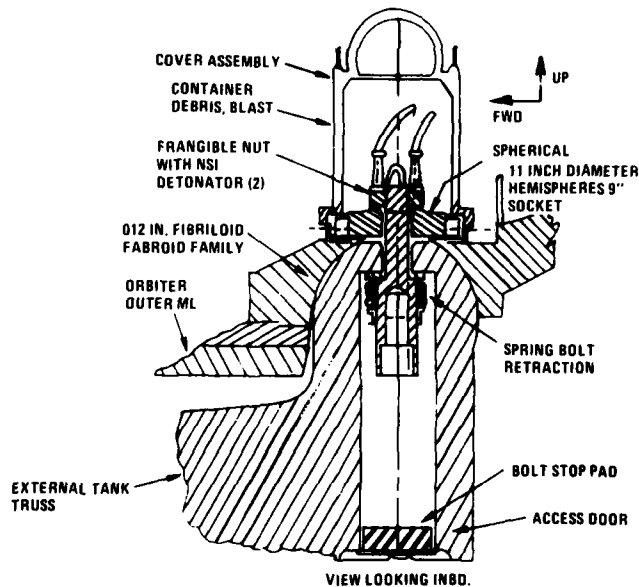
Figure 10 Orbiter/ET Aft Separation

The Orbiter's Orbital Maneuvering Subsystem (OMS), which is contained in two external pods on the aft fuselage, now fires and provides the thrust necessary to place the crew in orbit. The OMS is also used for orbit change, rendezvous, and return to earth. The Reaction Control Subsystem (RCS) is contained in the two OMS pods and in a module in the nose section of the forward fuselage. These units provide altitude control in space and precision velocity changes for the final phases of rendezvous and docking or orbit modification.
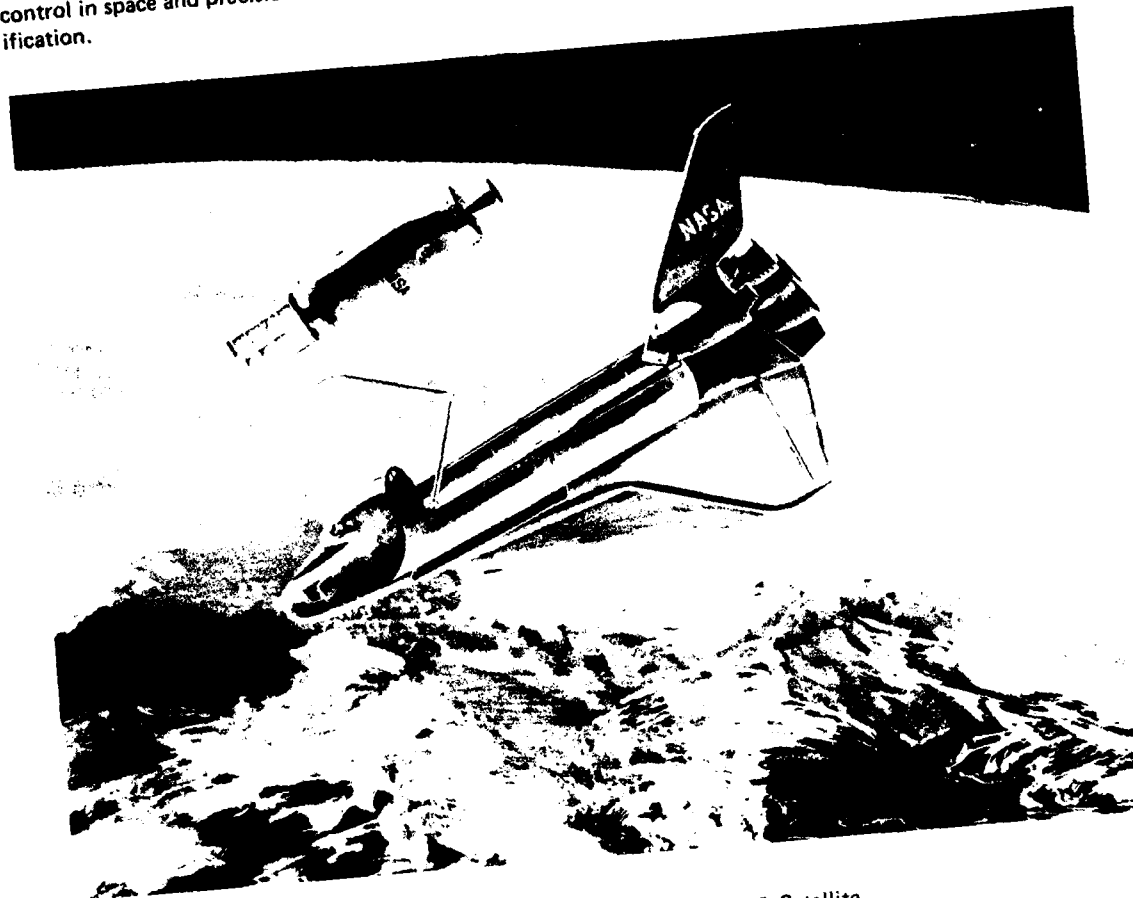
Delivery & Return of Propulsion Stage & Satellite

In orbit the crew will maneuver the Orbiter as necessary to perform mission objectives. The Orbiter has the capability to carry out missions unique to the space program; retrieve payloads from orbit for reuse, service or refurbish satellites in space, and operate space laboratories in orbit.

Inside the payload bay is a 50-foot manipulator arm used to pickup, extend, and release payloads. (Figure 11) If problems should arise with retracting the arm to its stored position, it can be jettisoned by means of explosive devices. This system has not been fully designed, and will be used for emergency situations only.
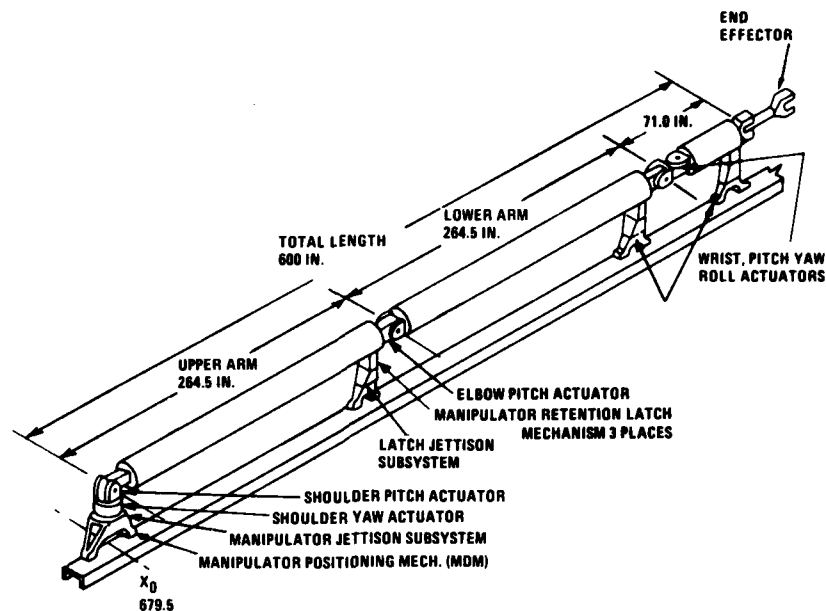
Figure 11 Manipulator Arm

After mission objectives are accomplished the crew will use the reaction control system in conjunction with the Orbiter's aerodynamic control surfaces to achieve reentry. During reentry two more pyrotechnic systems are available if necessary. Normally the nose and main landing gears are released by a hydraulic actuator. In case of a hydraulic system failure, dual pressure cartridges in each uplock can be fired which will release the landing gears. (Figure 12).
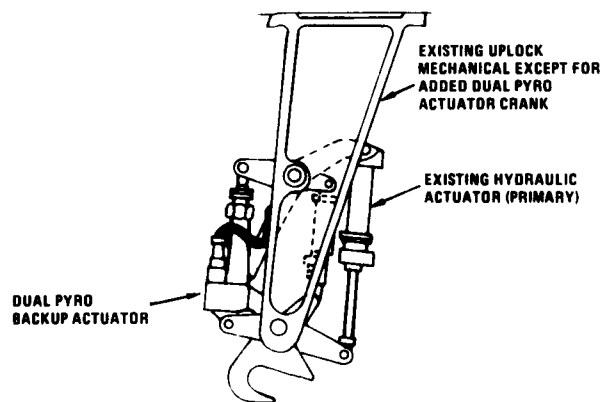
Figure 12 Nose Gear Uplock

Reentry is made into the Earth atmosphere at a high angle of attach. At low altitude, the Orbiter goes into horizontal flight for an aircraft-type approach and lands at a speed of 185 knots, similar to current high performance aircraft. After landing the Orbiter will be safed, deserviced, refurbished, and payloads removed. In fourteen days this same Orbiter will be back on Pad 39, awaiting that liftoff signal to begin another voyage into outer space.
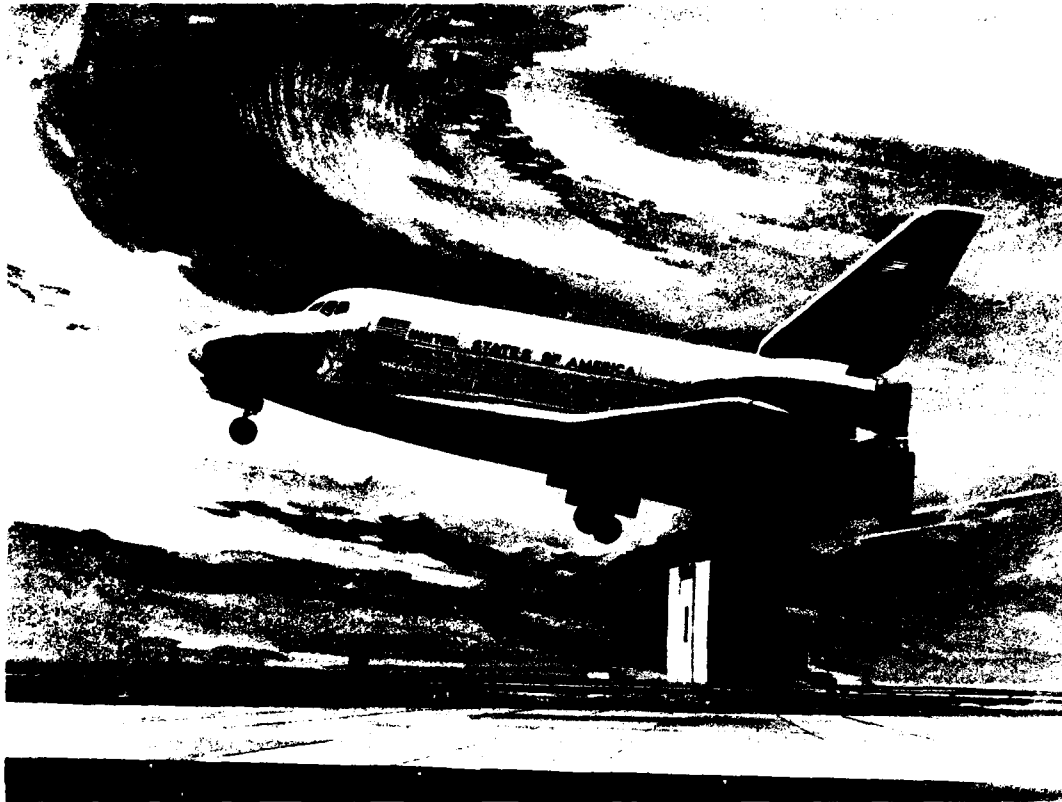
Orbiter Landing

The NASA Standard Initiator

CONCEPT AND FIRST GENERATION — The heart of the Shuttle pyrotechnic systems is the electro-explosive device that receives the electrical firing signal and produces usable explosive energy. Early in the Apollo Program, NASA made the decision to use a single, separable, general-purpose initiator of minimal size and weight and to adapt its output to specialized functions by means of cartridge modules containing appropriate booster charges. This concept permitted the exhaustive testing of the most critical region, the electroexplosive interface, independently and prior to installation into cartridge modules. Since the interface would be common to all devices, its demonstrated reliability would be enhanced by the multiple use. Hence, the firing of the rocket motor, valves, and all other devices would contribute to the demonstration of the reliability of each other. Furthermore, since development and qualification of only one initiator would be necessary, it would be possible to test and more thoroughly understand the characteristics of that device than would have been possible with a number of different initiators. This concept, and the initial hardware embodiment of the concept, was known as the Apollo Standard Initiator (ASI). Since redundance requirements for all pyrotechnic systems could not be predicted at the time the development of the ASI was initiated, dual bridgewires were incorporated into the design-one bridgewire for firing circuit A and the other for firing Circuit B. Since the initiator would be exposed to various environments in its applications, the unit was developed and qualified for the "worse case," that is, exposed to deep-space environments with no external protection. The ASI was qualified as an independent unit and then, serially, as an integral component of all the assemblies, devices, and systems. It was also flight tested on the unmanned missions and in the parachute drop-test program.

SECOND GENERATION — As the Apollo Program progressed and the pyrotechnic applications became more clearly defined, it became apparent that the dual-bridgewire feature would not be needed, since the required reliability and redundancy could be better achieved at higher levels of assembly. For this reason and because certain characteristics of the ASI imposed undesirable constrains on the systems design, it was decided to develop and qualify a second-generation device which would retain the performance and desirable characteristics of the ASI and remove the system constraints. The resulting second-generator device is the Single-Bridgewire Apollo Standard Initiator (SBASI) into which the following improvements were incorporated:

1. The body material was changed from type 17-4 PH stainless steel to Inconel 718 to improve impact resistance in cryogenic temperature applications.
2. The body wall thickness was increased to provide a higher internal pressure capability.
3. The pin-to-case electrostatic discharge survival capability was increased from 9,000 to 25,000 V, and the spark gap providing this protection was moved to the interior of the unit where the gap is immune to environmental effects and handling contamination.
4. A stepped Inconel 718 header was incorporated, with the contact pins glassed to the header and the header welded to the body.
5. The undesirably low interbridgewire electrical resistance, which is characteristic of all conductive explosive mixes, and the high sensitivity to electrostatic discharge in the circuit-to-circuit mode where automatically eliminated by removal of the second bridgewire circuit.
6. A technique for indexing, or clocking the electrical connector after manufacture and acceptance of production parts was incorporated.

In development of the SBASI, the header-body assembly was subjected to repeated thermal shocks from -320 to +500°F and then to hydrostatic testing to over 100,000 psi without failure, demonstrating adequate strength against the pin blowout which frequently occurred in high-pressure cartridges when using the ASI. The internal pressure capability of the header-body assembly to over 70,000 psi was demonstrated. All production units are electrostatically tested at 25,000 V; the header-body assemblies are gas-leak tested to 6,000 psi; the complete assemblies are helium-leak tested at 10^{-6} Torr for hermetic seal integrity; and on a sample basis, the header-pin assemblies are tested at 40,000 psi. Additional nondestructive tests are also conducted on all units in every production.

Connector Indexing

The capability to index the connector of the initiator after its manufacture is a unique and important feature which permits manufacturing and stocking of the initiator in a general-use configuration and subsequent configuring of the connector to any of nine special keyway combinations for special-purpose applications. Reconfiguration to combination restricted to nonflight use assures that rejected parts will not mate with spacecraft wire harnesses. The indexing technique is covered by NASA-owned U.S. Patent 3,287,031 and is available on a royalty-free, nonexclusive license basis for commerical use. The technique can also be used on other nonpyrotechnic electrical connectors.

Two additional keyways are broached in the initiator connector at the time of manufacture; with the master keyway at 12 o'clock; these numbers 1 and 6. (Figure 13) The units are procured and stocked in bonded storage in the "all open" configuration; however, none may be shipped in that configuration without special NASA authorization because such a unit will mate with any electrical connector. Prior to shipment to a cartridge manufacturer two of the keyways are blocked by being staked inwardly to within 0.001 in. of being flush with the inner surface of the connector. Configuration XX5 is also prohibited from Shuttle use. This configuration is reserved for rejected flight hardware and devices that become discrepant are restaked to XX5. The special indexing combination used for Shuttle flight pyrotechnic circuits are prohibited from use in nonpyrotechnic circuits. The family of shielded connectors mating with the various initiator keyway configurations provides complete radio-frequency shield continuity.
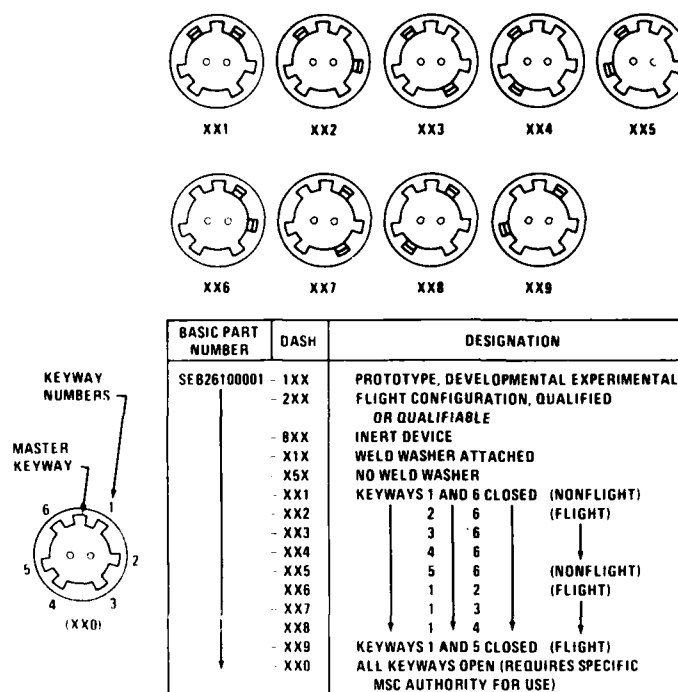
XX1 XX2 XX3 XX4 XX5

XX6 XX7 XX8 XX9

KEYWAY
NUMBERS

MASTER
KEYWAY

6 1
5 2
4 3
(XX0)

BASIC PART NUMBER	DASH	DESIGNATION
SE826100001	-1XX	PROTOTYPE, DEVELOPMENTAL EXPERIMENTAL
	-2XX	FLIGHT CONFIGURATION, QUALIFIED OR QUALIFIABLE
	-8XX	INERT DEVICE
	-X1X	WELD WASHER ATTACHED
	X5X	NO WELD WASHER
	-XX1	KEYWAYS 1 AND 6 CLOSED (NONFLIGHT)
	-XX2	2 6 (FLIGHT)
	-XX3	3 6
	-XX4	4 6
	-XX5	5 6 (NONFLIGHT)
	XX6	1 2 (FLIGHT)
	-XX7	1 3
	XX8	1 4
	-XX9	KEYWAYS 1 AND 5 CLOSED (FLIGHT)
	XX0	ALL KEYWAYS OPEN (REQUIRES SPECIFIC MSC AUTHORITY FOR USE)

Figure 13 Initiator Indexing and Dash Numbering

Wrench Section

A particular spanner-type section is provided for installing the initiator in a higher level of assembly instead of the normal hexagonal section. This feature prevents application of torque to the initiator with attendant damage to the hermetic seal, when a cartridge assembly is installed in the spacecraft. Because a special tool is required to install or to remove an initiator, only authorized personnel possessing this tool can perform this operation.

Provisions for Hermetic Sealing

A thin metal washer is welded to the underside of the initiator torquing section during preshipment configuration operations. After installation into a cartridge body, this washer is welded around the outer edge to the top of the cartridge body, providing a hermetic seal between the two components.

Dash Numbering System

The complete NSI part numbering system is shown in Figure 13. The first digit of the dash number indicates the flight status of the part; the second digit shows whether a weld washer has been installed; and the third digit indicates the keyway combination.

Preshipment Operations

The initiator is Government-furnished equipment for the Shuttle Program and is supplied from NASA stock as required for the manufacture of cartridges and for other use. The units are stocked in configuration XX0, with the basic part number, lot designator, serial number, etc., marked on the unit. Prior to each shipment, the required quantity is indexed, fitted with washers if required, marked with the appropriate dash number, and nondestructively tested. Units which fail the shipping test are reconfigured to the XX5 indexing, are color coded (blue band) as rejected parts, and are shipped to NASA to be removed from the flight worthy stock. Any initiator based cartridge which is rejected at any time is also restaked to configuration XX5 and removed from flight stock.

NASA Standard Initiator

Recently the SBASI was redesignated as the NASA Standard Initiator (NSI) and has been baselined for use on the Shuttle Program. A Space Shuttle pyrotechnic specification, JSC 08060, has also been written based on the experience and lessons of past programs. The specification applies to all pyrotechnics in the Space Shuttle and all NASA centers having hardware responsibilities as well as their contractors. It contains requirements, policies and guidance from the lowest level of piece-parts to the major pyrotechnic function level. The Shuttle preferred Pyrotechnic Items List is located in Appendix A, and specifies devices that have been proven in past programs, conform to the requirements and intent of JSC 08060, and may be applicable to the Shuttle.
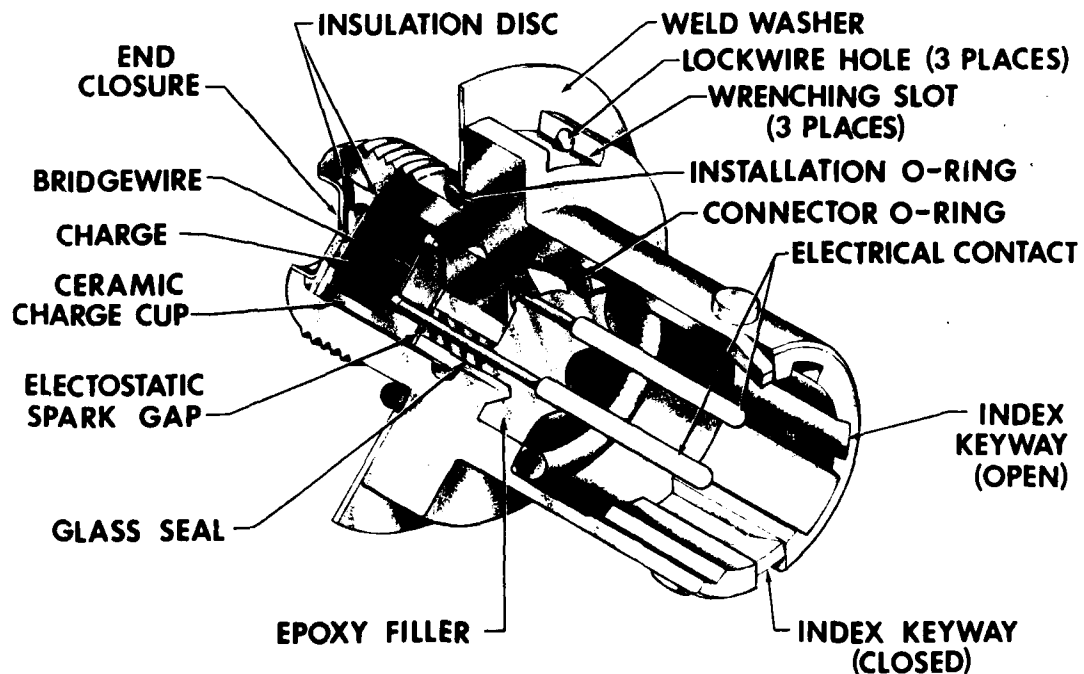
NASA Standard Initiator, Type 1 (NSI-1)

Reliability

The NSI has a perfect reliability record; neither the SBASI nor the predecessor ASI has been known to have failed to fire when subjected to the proper minimum all-fire firing pulse. The only premature firing occurred when the temperature control on a high-temperature conditioning chamber failed; the temperature record proved that the units were heated well above the "cook-off" temperature of the explosive mix. The units have undoubtedly undergone more exhaustive and extensive testing than any other initiators in any single space program; over 25,000 ASI units were used in development of the Apollo spacecraft, followed by well over 8,000 SBASI units. The extent of use of these units in non-Apollo programs is not known exactly; however, it is known that they were used in the Scout, Mariner and Viking Programs. It is expected that the Shuttle vehicle will require 12,000 to 15,000 initiators annually.

Modular Cartridge

Adoption of the standard initiator concept resulted in development of a family of special purpose cartridges. During the Apollo program three types of cartridge assemblies were used: an igniter cartridge for rocket motor ignition, a pressure cartridge for operating mechanical devices, and a detonator cartridge for initiating high explosive systems. Not only has this modular concept been extended to include the Shuttle program, but the actual devices, techniques, and experience will be carried over. The carry over of manufacturing processes, quality control techniques, test procedures, and experience are cost effective and offer benefits in quality and reliability. The family of cartridges used on the Apollo program are shown in Figure 14. Cartridges which had the same output and were located close to each other and were fired at different times were indexed to prevent misconnection of the spacecraft firing wires. Cartridges which had different outputs had different threads to prevent misinstallation.

Each cartridge assembly will consist of one or two NSI units and a cartridge module hermetically sealed together by a weld washer. Right and left hand threads will be used on various of these and other cartridges where installation near other cartridges whose devices have different functions or where different firing times could present a problem.
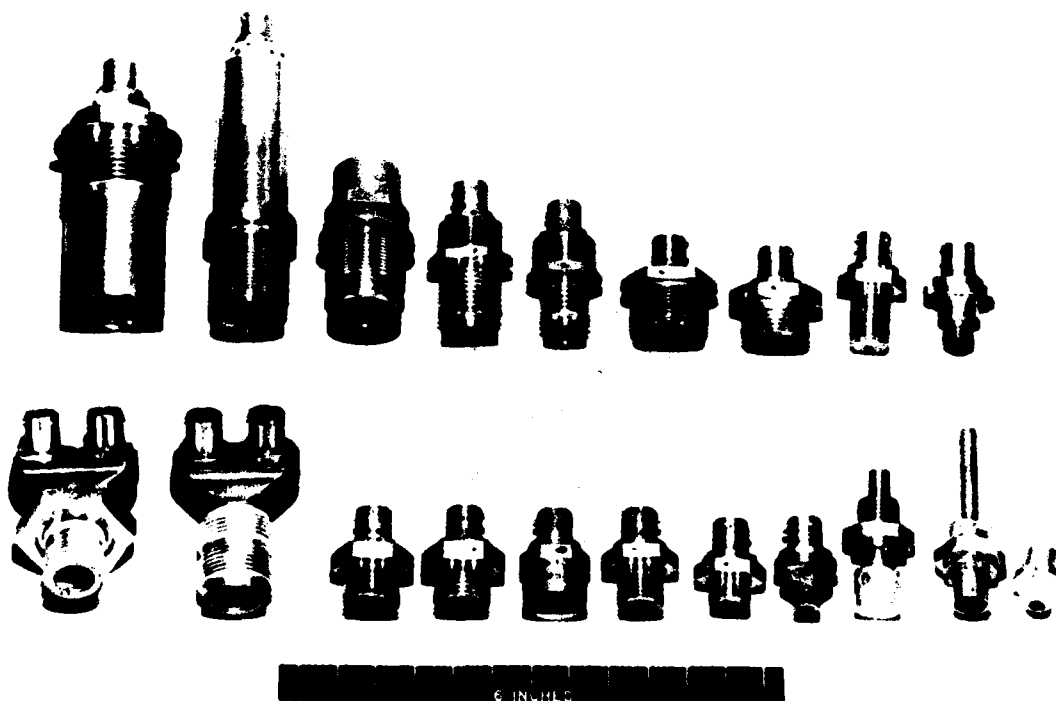
Figure 14 Spacecraft Cartridge Family

Pyrotechnic Electrical System

Reliability of the electrical firing system is essential to the overall functional reliability of the pyrotechnic system. It is not enough to provide a reliable ignition system to assure firing, it is imparative that a premature firing does not occur. The heart of the Shuttle electrical system is the Pyrotechnic Initiator Controller (PIC). Each initiator will have a dedicated PIC. The PIC is a capacitor energy storage/discharge device that requires three separate signals in the proper sequence and timing to initiate a Pyro. It functions as follows:

The ARM signal is a nominal 28 volts DC and supplies power through a current limiter and voltage regulator to a DC to DC converter which then provides a charge voltage of 41 volts DC to the firing capacitor.

Two separate fire signals close two series redundant transistor switches allowing the capacitor to discharge through the initiator with a minimum of 100 millijoules of energyy with 5 milliseconds.

In addition to its functional operation, the PIC houses the following built-in test circuitry:

A lead test circuit which analyzes the capacitor discharge curve to determine if enough energy is delivered to the initiator and providing a go/no-go output. This circuit is utilized during ground testing with initiator simulators and actual firelines providing a functional check of the PIC operation.

A resistance test circuit capable of measuring the total firing circuit resistance of the PIC and providing a go/no-go output. This circuit is utilized during ground check out after live initiators are electrical mated to verify proper connection of initiator to firelines.

Crew Escape System

A crew escape system is being provided for the astronauts during the Orbiter flight test phase. The system is composed of a pair of off-the-shelf ejection seats, which are currently being used on the SR-71 aircraft and a panel severance system to provide an escape route through the Orbiter overhead structure. The crew escape system can be used successfully from zero velocity, zero altitude to Mach 3 velocity and an altitude of 75,000 feet. The panel severance and ejection seat system utilizes approximately 140 explosive devices. Some of these devices are expandable tubes, mild detonating fuses, guillotines, percussion initiators, delay trains, thrusters, one-way transfers, gas generators, shielded mild detonating fuses, and rocket catapults.

The escape system is astronaut controlled, has no electrical interfaces, and is basically a series of pyrotechnic devices functioning to provide the crew emergency egress capability.

Ejection Sequence

The Crew Escape System can be initiated by either astronaut. Both systems are connected so if either crewman pulls the "D" ring both men are ejected. When the "D" ring is pulled a percussion initiator is fired and a Shielded Mild Detonating Cord (SMDC) is detonated, which in turn initiates the hatch severance system. The Orbiter's outer panel is separated by double strands of mild detonating fuse, and the inner panel is separated by an expandable tube assembly (Figure 15). A wire bundle, which runs over the panel interface is severed by a guillotine and a thruster pushes the separated panel away from the Orbiter. A rocket catapult is then ignited and propels the astronaut and seat out of the Orbiter. The time from "D" ring pull to catapult firing is .240 seconds, .225 seconds later the seat drogue parachute deployment is initiated. If the crew ejects at high altitude, they must remain in the seat until they descend to 15,000 feet. At this altitude an aneroid-actuated initiator will fire, and the crewmen will be propelled from their seats by means of a seat-man separator system. A personal parachute on the astronaut is then deployed enabling him to descend to a safe landing.
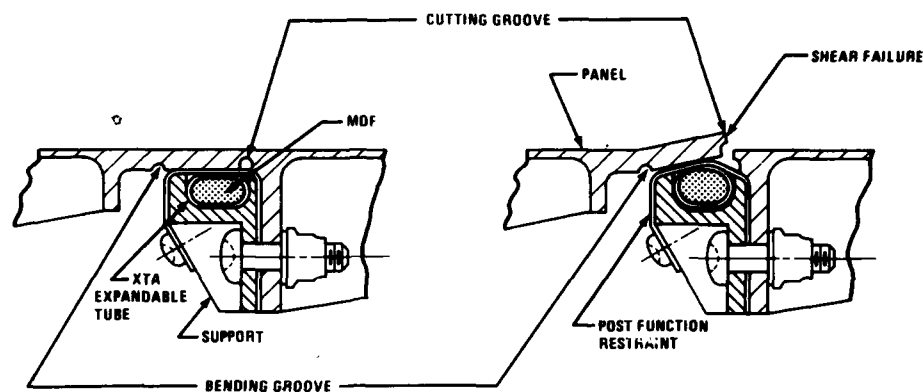
Figure 15 Expanding Tube Assembly (XTA)

Other functions accomplished by explosive devices are:

"D" ring cable cutter
Foot retractor actuator
Bridle line cutters
Lap belt release mechanism
Shoulder harness reel
Shoulder harness cutter
Foot Restraint cable cutter
Emergency face heat system

Range Safety System

In order to comply with Range Safety Regulation AFETRM 127-1 a flight termination system has been designed for the Shuttle program.

The SRB system will consist of a safe and arm device, detonators, CDF assemblies, and linear shape charge of sufficient size to completely cut through the motor case. The safe and arm device, antenna system, receiver/decoders, controls, and relays will be located in the water tight forward skirt o₁ each SRB. CDF will connect the S&A device to the linear shape charge which will have the capability to cut 70% of the total SRB length.

The flight termination system will be armed just prior to launch and will remain in that mode until just prior to SRB/ET separation. The astronaut will send the safe command to the safe and arm device prior to separation and will receive conformation that the system has been safed. Most parts of the flight termination will be removed from the recovered SRB, inspected, and if not damaged will be reused.

The design of the External Tank flight termination is still in the preliminary stages, but will probably utilize a double ended conical shape. The charge will be mounted in the inner stage area between the LO_2 and LH_2 tanks. These charges will have the capability of demolishing the bottom of the LO_2 tank and the top of the LH_2 tank, and the mixing of these two components will destroy the external tank.

Kennedy Space Center Operations

Pyrotechnics for the Shuttle program will be shipped directly from the manufacturer's facility to the Kennedy Space Center (KSC). Soon after arrival all devices will undergo a receiving inspection. All electro-explosive devices are given a bridgewire resistance test (.95-1.15 ohms for the NASA Standard Initiator) and

an insulation resistance test (2 megohms at 250 volts). A very thorough visual inspection is performed on each device and also thread checks are made on all units. Acceptable components are then placed in storage until required for flight. All lots of devices arriving must be accompanied by a lot certification statement. Certification means that not only has the manufacturer and Government quality personnel witnessed the in-process operations, but the quality and engineering personnel of the prime contractor and NASA design agency have reviewed the following information:

Test requirements
Parts lists and drawings
Explosive mix
Failure data
Operational data
Traceability
Corrective action records
Waivers or deviation records
Material review board action
Lot acceptance test data
X-rays and N-rays
Bridgewire and insulation resistance tests
Hermetic seal test
Electrostatic sensitivity

Lot Verification Testing

The last Mercury spacecraft flight (May 1963) experienced multiple in-flight pyrotechnic failures. A post flight failure analysis revealed that some pressure cartridges, which had the correct part number, size, threads, electrical connection, etc., but insufficient explosive charge, had been installed in the spacecraft retro-rocket umbilical separation system. The results were that the retro rocket pack burned off in flight rather than being separated. This failure initiated test program called "Lot Verification" which has been performed on all Gemini, Apollo, and Skylab pyrotechnic lots. The purpose of the program is to test a device from each lot of explosive devices just prior (30 days) to flight. The test method and acceptance criteria is the same as the manufacturer used during lot acceptance tests. As in the case of a pressure cartridge, KSC uses the same size and configuration of closed bomb and same pressure transducer.

Shape charge assemblies are required to cut a sample of material the same thickness (plus 20%) and hardness as the actual flight material. Detonators are plate dent tested and results compared to the specification. Reefing line cutters are tested for pull forces, delay time, and line cutting ability. Confined detonating cords are tested by plate dent and detonation velocity tests. So far approximately 500 explosive devices have been destructively tested at the pyro test lab at KSC.

Lot verification test of Gemini devices discovered one lot of detonators which had become"dubbed" because of a contaminment accidently introduced during manufacturing and one lot of pressure cartridges which did not have sufficient output. Testing of Apollo devices produced one failure. The failure was not a pyrotechnic failure, but was caused by a sealent material used in conjunction with the device. Both the Gemini and Apollo failures if not found could have caused castopheric results. The Gemini failure would have prevented the spacecraft from separating from the Titan launch vehicle.

Lot verification testing has not been defined for the Shuttle program but will probably be performed on a yearly basis and only crew critical components will be tested. This reduction in testing is a result of better quality control, lot certification, and more advanced test and inspection techniques.

Pyrotechnic Installations

The installation of explosive devices at KSC is determined by access, safety restrictions, and completion of major electrical tests. Normally most electro-explosive devices are installed late in the launch flow, however, this is not always true. The complete recovery system of the Apollo spacecraft which utilized approximately 38 explosive devices was installed at Downey, California prior to shipping the spacecraft to KSC.

The Solid Rocket Booster and External Tank explosive devices will be installed in the Vehicle Assembly Building (VAB). Some Orbiter devices will also be installed in the VAB but most will be installed in the Orbiter Processing Facility. Many of the SRB non-electrical components will be installed early in the build-up flow and the initiator or detonator which activates these systems will be installed just prior to moving out of the VAB. Immediately prior to connecting a firing circuit to an electro-explosive device a no-voltage test is performed. A grounding check of the fire line shield is also done at this time. After all initiators are connected a complete circuit resistance test is performed. In past programs this was done with special ohm meters and took several hours to perform. The Shuttle pyrotechnic devices and circuits will be tested in a matter of seconds using the Orbiter computer in conjunction with the buildin test circuit of each pyrotechnic Initiator Controller (PIC).

Safety

NASA safety regulations control all phases of pyrotechnic testing and installation. All hazardous procedures are reviewed and approved by the Safety Officer. Special non sparking safety tools are not required for the Shuttle program. Safety has also removed the requirement for personnel grounding devices when handling the NASA Standard Initiators (NSI). This personnel grounding requirement was removed because after manufacturing each NSI is subjected to a 25,000 volt static discharge test from a 500 micromicrofarad capacitor between both pins shorted together and the initiator body. Personnel handling explosive devices do, however, wear clean, non static producing, flame retardant, lint free coveralls.

The Kennedy Space Center has a perfect safety record involving pyrotechnic, and with no inadvertent firing, no injuries, and no fatalities.

Summary

Pyrotechnics have been and will continue to be used extensively in aerospace vehicles to perform a variety of functions. They provide instantaneous energy upon demand, and are small in comparison to the functions they perform. Some devices are crew critical and must perform as designed or there will be loss of life. The Solid Rocket Booster (SRB) explosive devices must function in order to recover the expended SRB. Many of the Orbiter pyrotechnic devices are designated as contingency items and may never be used. A perfect example of a contingency system has been the Mercury, Gemini, and Apollo Crew Escape System. Thus far these complex launch escape and ejection systems have never been needed. The Shuttle program, with its Orbiter that lands like an aircraft, can be serviced and readied for another mission in 14 days. For the first time in manned spacecraft history explosive devices will be flown in more than one mission. Due to the short turnaround time many of the Orbiter's electro-explosive devices will remain electrically connected and a circuit confidence test performed just prior to flight. Another first is the recoverable, refurbishable booster. The recovered SRB will be disassembled, washed, and segments returned to Utah (vendor) for recasting.

The Shuttle program begins a new era in space transportation that will become operational in the 1980s. With its versatility and reusability, the Space Shuttle will truly open the door to an economical and routine use of space. Pyrotechnics, as always, will play a major role in this NASA space venture.

ON INTERMEDIATE EXPLOSIVE COMPOSITIONS

Allen J. Tulis

IIT Research Institute
10 West 35th Street
Chicago, Illinois 60616

ABSTRACT

There exist many and unique applications for the intermediate explosives; i.e., explosives that have detonation velocities in the 1 to 2 mm/μsec range and detonation pressures in the 1 to 10 kbar range. We have previously presented work involving very-low-density foamed explosives and foamed and extruded pyrotechnic compositions that were suitable for applications requiring non-contained propulsion of items that would be damaged or destroyed using conventional explosives. One major drawback was that the critical diameter was excessive for many applications and initiation was difficult under desirable conditions.

In this paper work involving composite-type explosive formulations is discussed. The purpose of investigating composite explosive formulations was with the objective of realizing low detonation velocities with attendant low detonation pressures, based on reduction of the loading density of the active explosive component. Dilution with reactive and inert compositions was conducted, both separate and combined. An example was the development of a nitroguanidine-ammonium perchlorate composition. The effective explosive density was reduced to below 0.1 gm/cc in an explosive composition that had an overall density greater than 1.0 gm/cc but still detonated at near-ideal velocity. Intitiation was readily achieved with nominal boostering and the critical diameter was below 1 inch.

INTRODUCTION

Thermodynamically unstable materials or systems that can react rapidly releasing sudden bursts of energy are termed explosives. This discussion will be limited to chemical materials or systems. For these, fundamental thermohydrodynamic theory defines two distinct, stable reaction mechanisms termed deflagration and detonation. Deflagration reactions depend on transport processes such as conduction and convection and are therefore necessarily subsonic. Detonation reactions are shock-initiated at the wave front and propagate at supersonic velocity.

Figure 1[1] illustrates the typical ranges of propagating rates and reaction pressures associated with conventional detonating and deflagating explosive materials. It is apparent that there exists a rather broad region between these two mechanisms which is designated the "intermediate" explosive range. There exist many and unique applications for intermediate explosives; i.e., explosives that have reaction rates in the 1 to 2 mm/μsec range and reaction pressures as low as several kbar.

The IIT Research Institute (IITRI) has been actively investigating explosive systems that fall in this range for the last 10 years, actually dating back to 1964 when Sadwin[2] investigated low-density nitroguanidine for explosive welding of metals. We have previously reported work involving very-low-density foamed explosives[3] and extruded pyrotechnic compositions[4] that were suitable for applications requiring non-contained propulsion of items that would be damaged or destroyed using conventional explosives. This paper will be confined to investigations involving composite-type explosive formulations.

524

THEORETICAL CONSIDERATIONS

The thermohydrodynamic theory is quite specific for conventional explosives. Utilizing the common calculation for detonation pressure:

$$p = 2.5 \rho D^2 \text{ kbar} \tag{1}$$

where: ρ = density in gm/cc and

D = detonation velocity in mm/μsec,

it is apparent that detonation velocity is highly critical for determining detonation pressure. However, detonation velocities are constant for ideal detonations, being dependent only on bulk explosive density; e.g., for nitroguanidine the typical empirical detonation velocity relationship is:[5]

$$D = 1.440 + 4.015 \rho \text{ mm/μsec} \tag{2}$$

In a review on explosion phenomena intermediate between deflagration and detonation[1] four categories are specified for obtaining the intermediate ranges of explosive materials:

- Ideal detonation on low density media

- Nonideal detonation

- Low-Velocity-Detonation (LVD)

- Convective deflagration

We will limit this discussion to ideal detonation. Information on the other approaches is available in the above review and elsewhere.

Considering nitroguanidine as an example, this explosive has been reported to be detonable at bulk densities from 1.7 down to 0.11 gm/cc[1] although work reported elsewhere[2,6] has not evaluated densities below about 0.4 gm/cc. The main reason for this is that it is very difficult to obtain bulk densities of nitroguanidine, as well as other explosives, at lower bulk densities. Even at the low densities reported

practical considerations are precluded because of settling, separation, and other adverse effects of low-bulk powder systems.

At any rate, the lower limit for detonation velocity is the sonic velocity in the unreacted explosive system since by definition detonation is a shock initiated mechanism. Sonic velocities for condensed-phase explosive materials generally range from 1.5 to 3 mm/μsec[1]. Figure 2 illustrates the empirical detonation velocity vs loading density relationship of Hurowitz[5]. Note that the cut-off velocity would be about 1.5 mm/μsec. Thus, using this lower detonation velocity limit and the lowest practical bulk density of about 0.4 gm/cc, the detonation pressure for nitroguanidine would be just over 2 kbar.

In the Fourth Pyrotechnics Seminar we reported the detonation of an explosive dust in air.[7] The measured detonation velocities were about 1.8 mm/μsec and the explosive dust concentration was estimated at about 0.002 gm/cc. Using equation 1 we can calculate a detonation pressure of less than .02 kbar. This is two orders of magnitude lower than the pressure for the low-bulk density nitroguanidine. Therefore we advance the following rather interesting conclusions:

(1) The lower limit for detonating explosives is the sonic velocity in the unreacted explosive.

(2) Explosives may be made to detonate at several orders of magnitude below their bulk density.

Thus, if an explosive powder could be "frozen" in a non-interfering matrix at extremely low densities it could still detonate, ideally, and conform to the thermohydrodynamic laws of conventional explosives.

An explosive dust system is in fact a composite system; the other component just happens to be air (as in low-bulk explosives also). For practical considerations, a solid matrix is required. This is the basis for explosive foams

such as we reported upon in the third Pyrotechnics Seminar.[8]
However, in these explosive foams the explosive component is
bound in the polyurethane. The gas-filled cells are closed.
These are adverse conditions for the continuity of detonation
propagation between the explosive particles necessitating
high explosive loadings in the polyurethane. A powdered
composite system or an open-celled matrix structure would
not isolate the explosive particles to this extent. In
particular, in an open-celled structure the explosive component
should be deposited upon the surface of the matrix rather
than embedded within the matrix.

COMPOSITE EXPLOSIVES

IITRI has been investigating various approaches to
obtain ideal detonation (not dependent on particle size,
confinement, excessive critical diameter, etc) of which composite
explosive systems were prime candidates. For this purpose
we utilized nitroguanidine in combination with various
reactive and inert components. The theoretical aspects of
this concept are being reported elsewhere[9,10] but the practical
aspects can be summarized in the following table of experi-
mental results.

Table 1

DETONATION VELOCITIES OF NQ/AP COMPOSITE EXPLOSIVE

Density, gm/cc			Detonation Velocity, mm/μsec	
NQ	AP	% NQ	Ideal	Measured
0.060	1.130	5	1.68	2.03
0.030	1.180	2.5	1.56	1.69
0.015	1.195	1.25	1.50	1.34
0.008	1.242	0.625	1.47	1.27 (unstable)
0.000	1.310	0	0.00	0.00

In these experiments the size of the test apparatus was
4 cm diameter by 15 cm long, under plexiglass confinement.
As can be seen, we were approaching the explosive density of
0.002 gm/cc estimated in our explosive-dust detonation
experiments. However, in these composite systems an explosive
density below about 0.01 gm/cc, surrounded by over 99 percent
of another component which is a solid evidently abstracts
too much energy from the reaction to allow support of the
shock front and the detonation decays. In these experiments
the other component was a reactant and entered into the
detonative reaction, but that does not alter the fact that
detonation of composites is feasible and that this approach
is practical to reduce the explosive density well below
the minimum bulk density.

SUMMARY

We have shown that explosive composites can be devised
to obtain the low explosive densities needed to achieve
ideal detonation velocities of explosives well below their
minimum bulk densities. The other component or components
of the composite, whether reactive or inert, are important
in that they can contribute to the energy output
(as in the case of ammonium perchlorate or ammonium nitrate)
or can further attenuate the shock output of the detonation
(as in the case of ethyl cellulose). Furthermore, IITRI
is presently investigating explosive composite matrices in
which open-cell structures are utilized to diminish the
loading density of the other component. In this manner we
expect to attain detonation of explosives at densities down
to the range of the explosive-dust densities.

528

REFERENCES

1. Brown, J.A. and Collins, M., "Explosion Phenomena Intermediate Between Deflagration and Detonation," Esso, Army Research Office STAF, Contract No. DA-49-092-ARO-140, October 1967.

2. Sadwin, L.D., "Explosive Metal Welding," Science, 14, 1164, (1964).

3. Austing, J.L., Tulis, A.J. and Johnson, C.D., "Detonation Characteristics of Very Low Density Explosive Systems", Fifth Symposium on Detonation, Office of Naval Research, ACR-184, 47, (1970).

4. Tulis, A.J., "Foamed and Extruded Pyrotechnic Compositions," Eight Symposium on Explosives and Pyrotechnics, Proceedings, February 1974.

5. Hurwitz, M.D., OSRD 5611, 1945. (See also Ref. 6).

6. Price, D. and Clairmont Jr., A.R., "Explosion Behavior of Nitroguanidine", Twelfth (Int) Symposium on Combustion, The Combustion Institute, 761, (1969).

7. Tulis, A.J. and Remaly, R.F., "Dispersion and Detonation of Explosive Dusts," Fourth (Int) Pyrotechnics Seminar, Proceedings, July 1974.

8. Tulis, A.J., Austing, J.L. and Remaly, R.F., "Development and Evaluation of Explosive Materials for the Task of Explosive Dispersion of Projectiles," Third (Int) Pyrotechnics Seminar, Proceedings, August 1972.

9. Tulis, A.J., "Sympathetic Detonation of Ammonium Perchlorate by Small Amounts of Nitroguanidine," Sixth Symposium (Int) on Detonation, August 1976.

10. Tulis, A.J., "Detonation of Very Low Density Explosives on the Surface of Low Density Open-Called Matrices," Invention Disclosure, 1976.

Reference 1
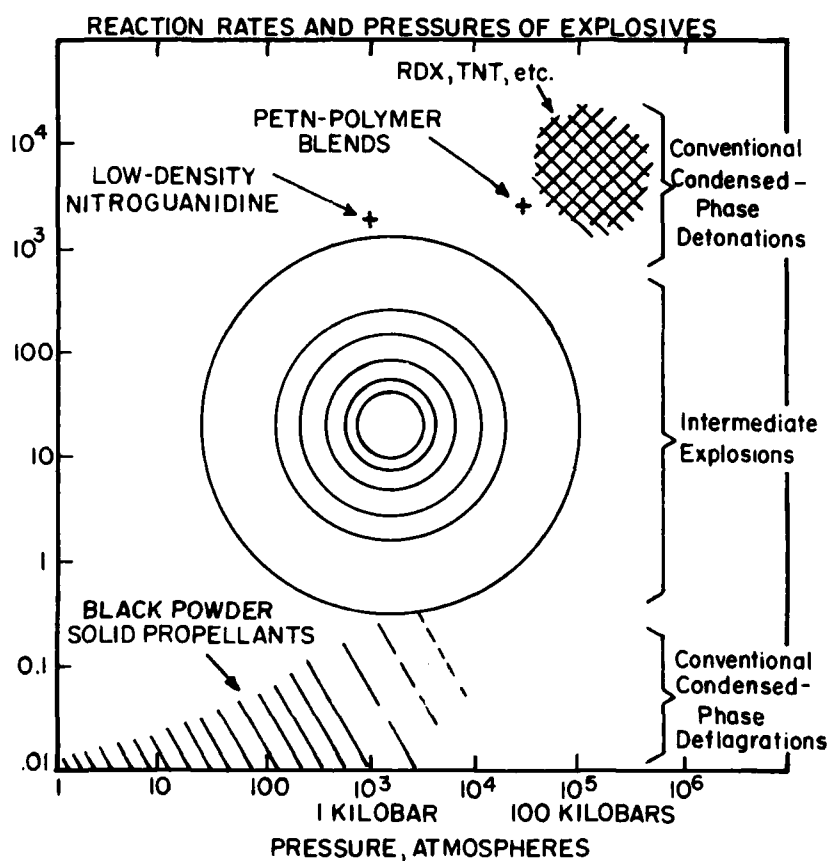
Figure 1: Reaction Rates vs Reaction Pressures for Conventional Condensed Phase Detonations and Deflagrations, Showing the Large Gap that Constitutes the Regime of Intermediate Explosions.
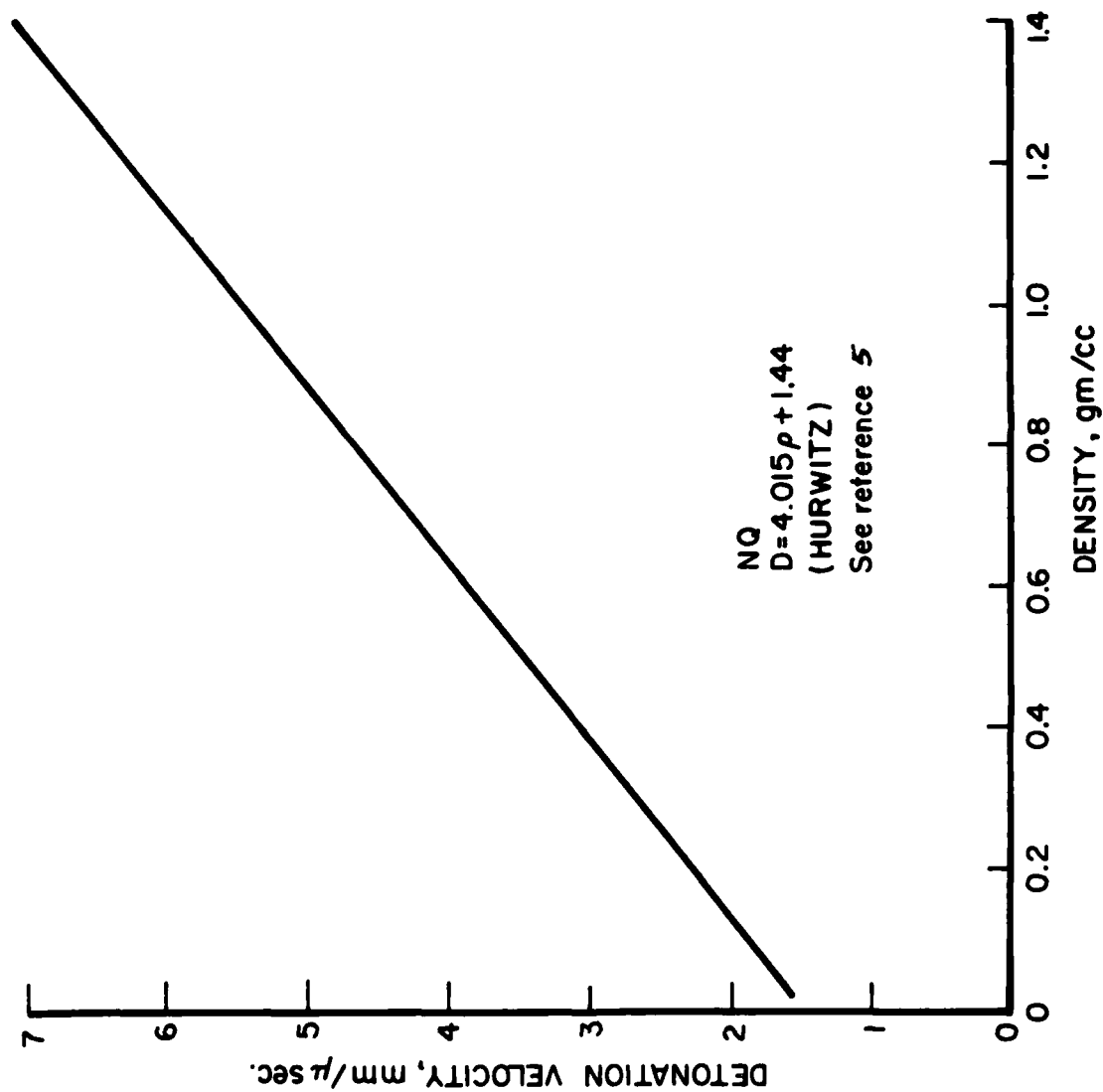
Figure 2: Detonation Velocity as a Function of Density for Nitroguanidine

NQ
D=4.015ρ+1.44
(HURWITZ)
See reference 5

DENSITY, gm/cc

DETONATION VELOCITY, mm/μsec.

New Smoke Concepts

Abraham Turetsky

Edgewood Arsenal
Aberdeen Proving Ground, Maryland

ABSTRACT

Studies have shown the feasibility of imbibing a non-
toxic, non-corrosive fog oil and disseminating it as an
aerosol from an intimate pyrotechnic mixture. Further
exploration suggests that the concept may be extended to
other liquids. The investigation evaluates an imbibed
fog oil pyromix in several canisters and in terms of
vaporization efficiency, sensitivity, and storage stability.

INTRODUCTION

The major goal of this program was to develop an intimate pyrotechnic composition which when functioned would yield a non-toxic, non-corrosive, visual screening smoke. Such an innocuous smoke would also fullfill some military training needs.

Currently available military visual smoke screens whether disseminated pyrotechnically or by other means yield a hydrolized phosphoric acid, sulfuric acid, metallic oxychloride, or fog oil aerosol. Based on medical guidance and because of its non-corrosive characteristic, fog oil is the material of choice in the above inventory of smokes.

RESULTS AND DISCUSSION

Imbiber beads are commercially produced for use in soaking up hydrocarbon spills which pose an ecological hazard. We have exploited this solvation property and found it possible to thermally reverse the process thereby producing liquid aerosol smoke. Table 1 lists the physical properties of imbiber beads which we have determined to date. Of particular interest are the hydrophobic and high thermal stability values shown in Table 1.

The major thrust of our investigation has been with imbibed fog oil. However, other liquids have successfully been imbibed. Table 2 shows the liquids surveyed to date and indicates bead capacity for these liquids. Two general observations may be inferred from this data: 1. Imbibed

TABLE 1
PHYSICAL PROPERTIES
IMBIBER BEADS

PROPERTY	VALUE
WATER SOLUBILITY	0
DENSITY @ 26°C	0.96 G/CC
PARTICLE SIZE	MMD = 300 uM NMD = 150 uM
THERMAL STABILITY (DTA)	NO DECOMPOSITION BELOW 300°C

534

TABLE 2
IMBIBITION SURVEY

LIQUID	PERCENT* IMBIBED
TITANIUM TETRACHLORIDE	> 90**
TRIETHYL ALUMINUM	> 50
EUTECTIC WHITE PHOSPHORUS	66
FOG OIL	94
DIESEL OIL	90
MINERAL OIL	89
ROSIN OIL	> 91
COD LIVER OIL	> 86
LINSEED OIL	> 85
CORN OIL	> 80

*(WEIGHT OF OIL/WEIGHT OF OIL + WEIGHT OF BEAD) (100)
** UNSTABLE

oxidizers are likely to induce bead instability and 2. Oils
are imbibed well. Figure 1 illustrates the capacity of
imbiber beads for suitable liquids. It shows 2 grams of
beads and 2 grams of beads fully imbibed with fog oil. Fog
oil imbibition has been followed microscopically. Time
sequential photomicrographs of this observation are shown
in figure 2, which indicates bead volume has increased
appreciably. The rate at which imbibition occurs with a
given liquid is bead size dependent. Figure 3 depicts
this relationship. Some data points are not included in
the graphs, however, they indicate maximum oil intake
is eventually reached and that this yields a stable bead
volume value.

Based on infrared spectra we have postulated that the
imbiber bead we are studying is composed of chains of
tertiary butyl styrene copolymerized with monomeric styrene
and a polymeric ester such as methyl methacrylate to form linear
chains. Figure 4 depicts one such chain. Many such chains
can be crosslinked with divinylbenzene as seen in figure 5.
The figure depicts the polymer to be made up of box-like
units, the corners of which are phenyl groups whose origin
is styrene monomer. These crosslinked sites are the likely
potential sites in the linear chains that can be crosslinked
since all other phenyl groups are blocked in the para position.
The spatial area within these corners can be varied by
altering the amount of divinyl benzene and the amount of
ester and tertiary butyl styrene utilized to build the polymer

536

FIGURE 1   IMBIBER BEADS
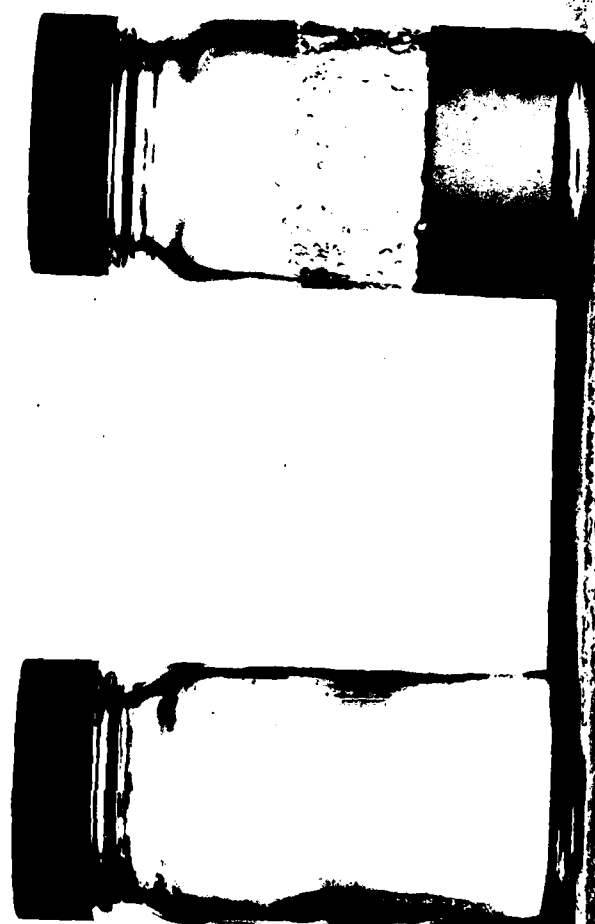
2G   2G CONTAINING 90% OIL

FIGURE 2 PHOTOMICROGRAPHS OF FOG OIL IMBIBITION
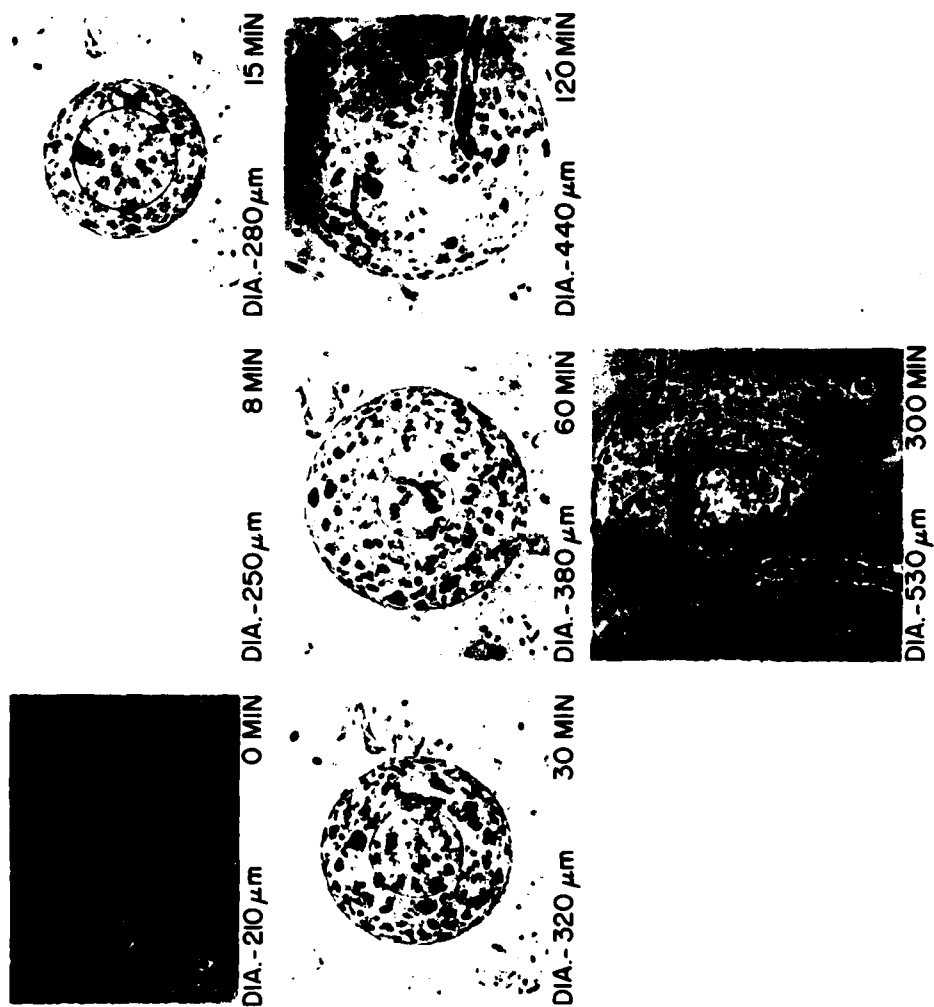
FIGURE 3. FOG OIL IMBIBITION

FIGURE 4

A STYRENE BASED LINEAR COPOLYMER

FIGURE 5

A STYRENE BASED CROSSLINKED COPOLYMER
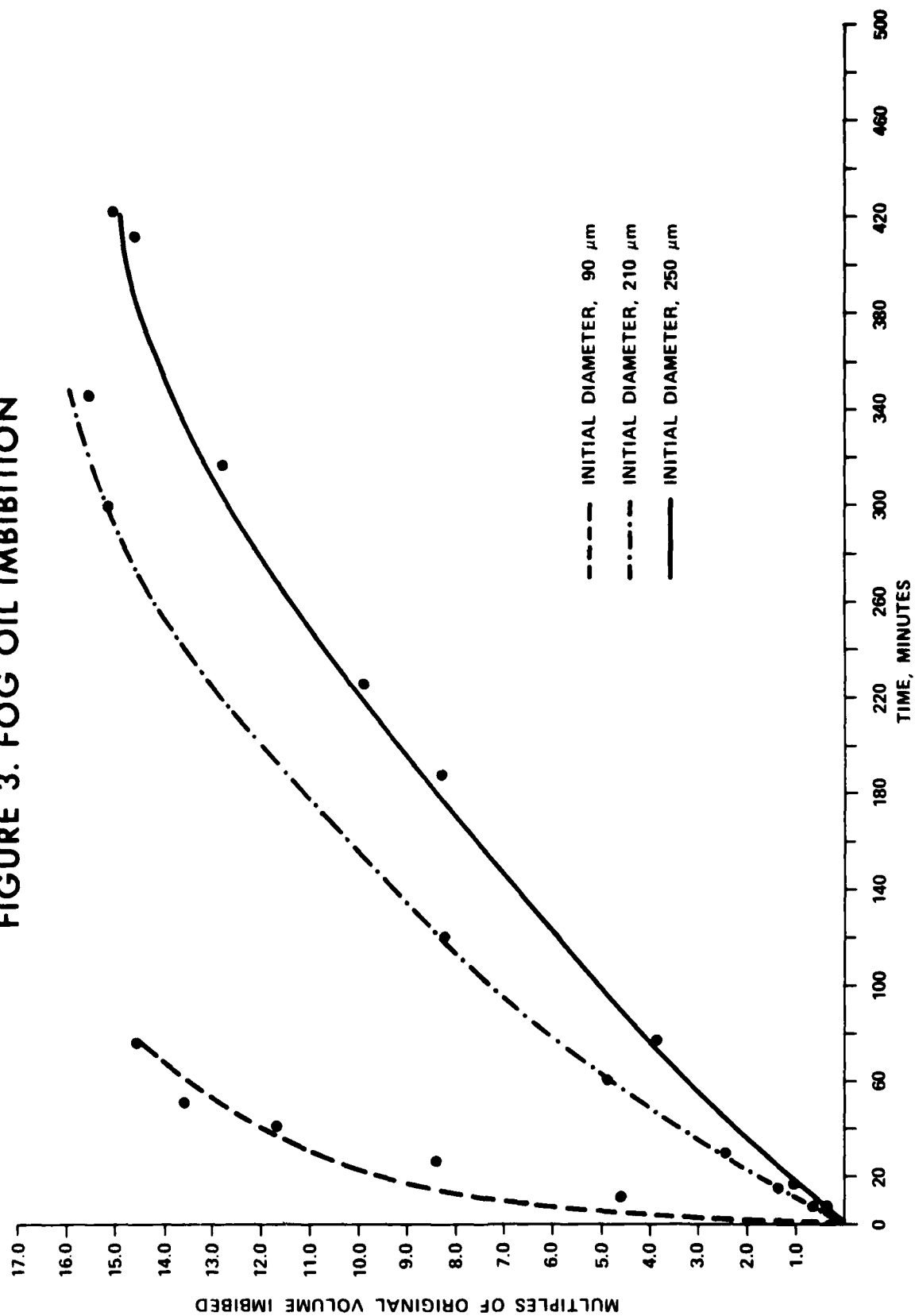
network. The polymer network is 3 dimensional. We postulate
that the size of these "chemical holes" or crosslink density
determine entrance into or imbibition of liquids by the
polymer.

The oil smoke we are disseminating is new in the sense
that it is emitted from a canister containing an intimate
pyrotechnic mixture. This mixture is composed of pyromix
granules blended with imbibed fog oil. Prior to these
studies fog oil was pyrotechnically disseminated only by
means of a more complicated two compartment generator design.
Figure 6 indicates the relative complexity of the older
design. This particular design efficiently vaporizes oil
only when the smoke pot is in an upright position.

An imbibed fog oil mixture was prepared by manufacturing
fuel pyromix composed of potassium chlorate, sugar, and
magnesium carbonate granulated with nitrocellulose. The
grains were then blended with oil and imbiber beads. The
composition of this mixture is shown in Table 3. Two
standard canisters which have been loaded and functioned
with imbibed fog oil pyromix are the M8 and M48 canisters.
Figure 7 shows an M8 grenade loaded with imbibed fog oil
pyromix. The 285 gram fill weight is comparable to that of
the standard colored smoke grenade. Figure 8 shows an M8
grenade loaded with imbibed fog oil pyromix functioning.
Almost complete obscuration of a trailer is seen produced
by an estimated 122 grams of aerosolized fog oil disseminated
over a 160 period. Figure 9 illustrates a similar
result using an M48 grenade containing 255 grams of imbibed
fog oil pyromix.

FIGURE 6
COMPARISON OF FUEL BLOCK AND INTIMATE MIX DESIGNS

STARTER MIXTURE

FILLING

M8 SMOKE GRENADE

FUZE

OIL

FUEL

M6 OIL CANDLE

PRESSURIZING ORIFACE

FEED ORIFACE
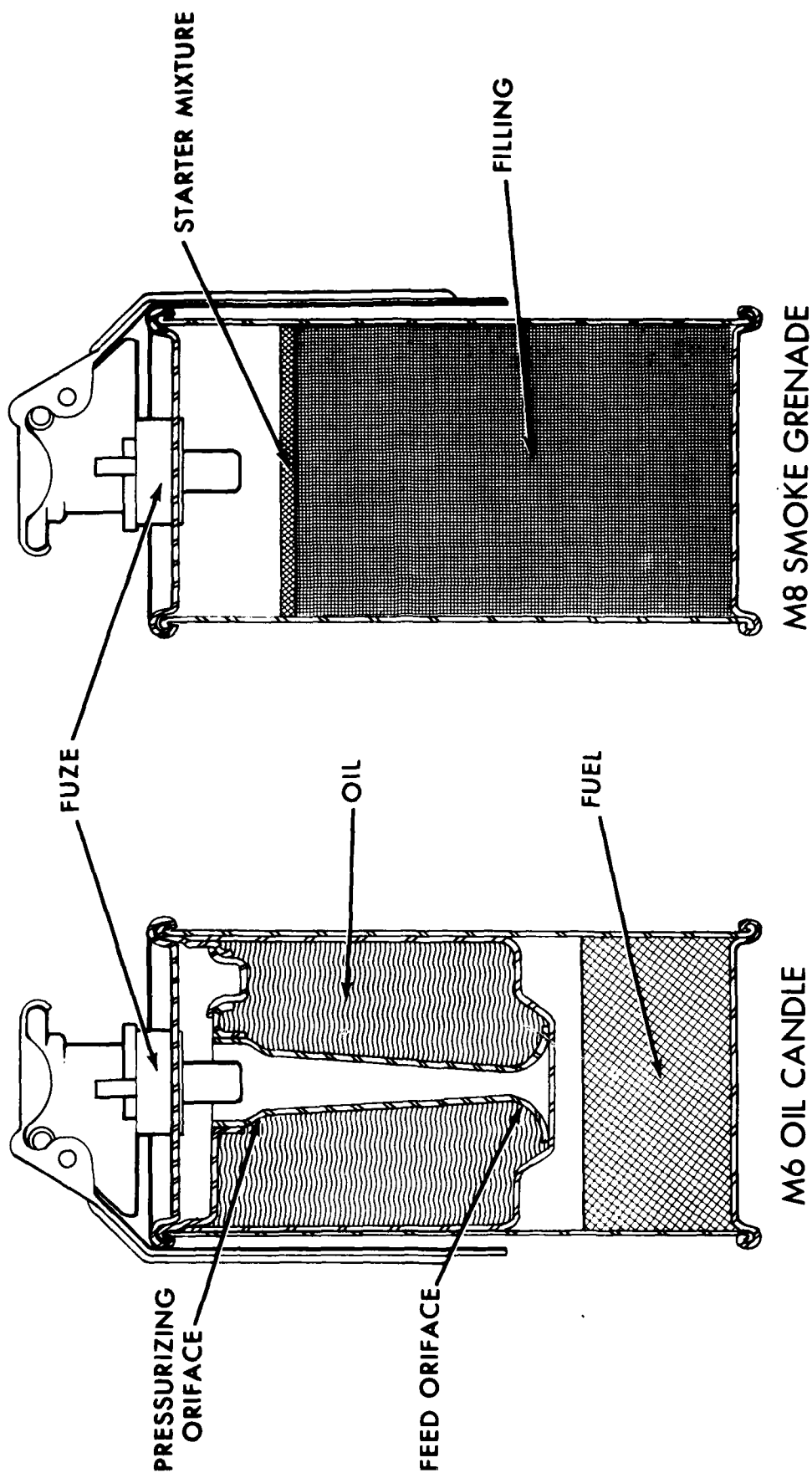
TABLE 3
IMBIBED FOG OiL PYROMIX COMPOSITION

INGREDIENT	WEIGHT PERCENT
POTASSIUM CHLORATE	22.2
MAGNESIUM CARBONATE	9.8
SUGAR	14.7
NITROCELLULOSE	5.2
FOG OIL	43.3
IMBIBER BEADS	4.8

FIGURE 7
GRENADE, M8 CONFIGURATION, 285 GRAM FILL

FIGURE 8
GRENADE, M8 CONFIGURATION, 160 SECOND BURNING TIME

FIGURE 9. GRENADE, M48 CONFIGURATION
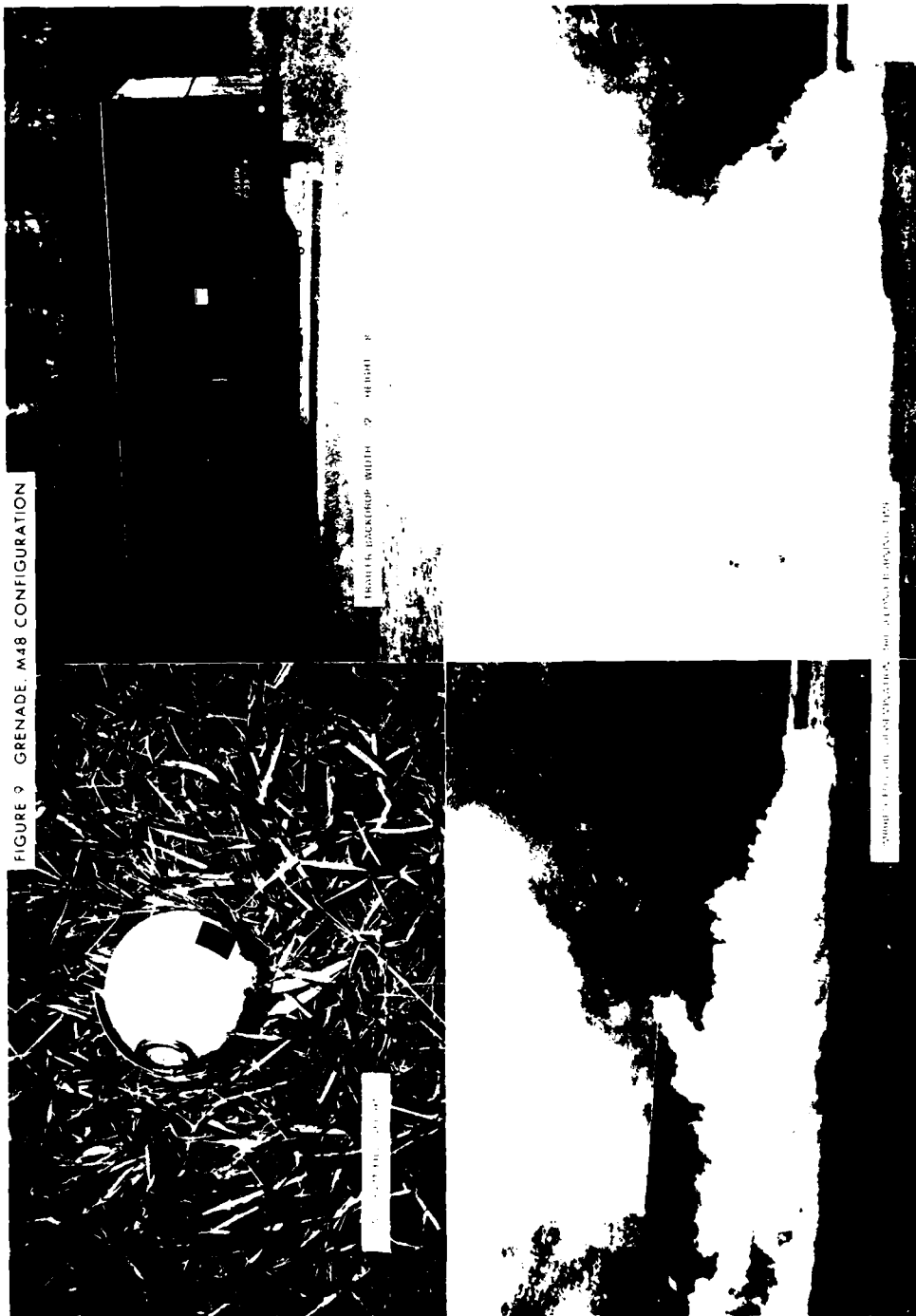
A batch of imbibed fog oil pyromix was prepared and loaded into small test vehicles. Several of these were functioned in a test chamber for oil vaporization efficiency and several as controls for a storage stability test. The chamber data indicate that the formulation is 95% efficient in vaporizing fog oil. The results of the storage tests are given in Table 4. The burning time data obtained after storage was statistically compared to the control data. At a significant level of 0.1, we concluded there was no difference in mean burning time between control canisters and canisters stored under ambient conditions or between control canisters and canisters stored at $160^{\circ}F$ for 12 weeks. The β risks were calculated to be .299 for the ambient comparison and .166 for the elevated temperature comparison.

The sensitivity of imbibed fog oil pyromix was determined using standard methods and techniques. Table 5 summarizes these studies. The values obtained are well within the range normally obtained for pyrotechnic materials. We note however, that imbibed fog oil pyromix has insensitive frictional and impact ignition threshold values.

Further studies of this concept will compare several imbibed smoke forming oils in terms of visible obscuration quality. These studies would also address pyromix optimization in terms of a maximum aerosol yield. The possibility of screening enhancement by mixing of several liquid materials is yet to be studied. This technique might

TABLE 4

IMBIBED FOG OIL PYROMIX CHARACTERISTICS

CANISTER FILL WEIGHT (G)	TEST	CHARACTERISTIC	MEAN VALUE OBTAINED
25	CONTROL	BURNING TIME	36.8 SEC.
25	AMBIENT STORAGE	BURNING TIME	40.3 SEC.
25	ELEVATED TEMPERATURE STORAGE	BURNING TIME	40.3 SEC.

TABLE 5
SENSITIVITY

PYROMIX	IGNITION TEMPERATURE (DTA), °C	50% PROBABILITY OF IGNITION ON IMPACT* KG CM	STATIC SPARK** JOULES	FRICTION SENSITIVITY (DuPONT METHOD)
IMBIBED FOG OIL	177	> 1500	0.295	0/20
RED SMOKE III	173	450	0.055	0/20

*5 KG DROP WEIGHT

** MINIMUM ENERGY AT WHICH IGNITION OCCURRED IS INDICATED

prove particularly fruitful.

Thus far we have encountered but one technical problem in this study. Imbibed fog oil pyromix is an elastic mass in contrast to other pyrotechnic compositions and therefore cannot be pressed into a canister to hold it in place. Depending on canister design, this can lead to ignition problems. Insertion of wire mesh or ignitable barriers represents a possible solution to this problem that will be investigated shortly.

EMISSION FROM MOLECULAR SPECIES IN PYROTECHNIC FLAMES

Henry A. Webster III
Applied Sciences Department
Naval Weapons Support Center, Crane, Indiana

ABSTRACT

Visible spectra of flares containing magnesium as a fuel and sodium nitrate, potassium nitrate and rubidium nitrate as oxidizers are examined for molecular emission from species such as diatomic alkali metals, alkali metal-magnesium diatomics and quasi-molecules such as Na-N_2. Atomic and molecular emissions are identified and assigned to electronic transitions. Emission characteristics of the atomic emitters are the same as those observed in other studies.

Emission bands from diatomic sodium, diatomic potassium and diatomic rubidium are identified. Emission from a sodium-magnesium interaction is also observed. Assignments are made for the electronic states and transitions which give rise to these emitters. The nature of these interactions is discussed.

INTRODUCTION

Pyrotechnic compositions used for the production of visible light, either for illumination or for signaling purposes, rely on emission from atomic and molecular species formed as reaction products from the combustion of magnesium and a solid oxidizer, usually an alkali or alkaline earth metal nitrate or perchlorate.[1] The most widely studied system is the magnesium-sodium nitrate flare which is used for illuminating purposes. It has been shown that most of the visible light produced by this flare comes from the broadened sodium resonance lines centered at 589 nm.[2-4] During the course of the studies to determine the processes occurring in the magnesium-sodium nitrate system, additional information was obtained on the visible and near-infrared spectra of pyrotechnic compositions containing barium and strontium salts and the other alkali metal nitrates; namely, lithium, potassium, cesium and rubidium.[5,6] It was determined that the use of any alkali or alkaline earth metal nitrate other than sodium nitrate for illumination purposes was unsatisfactory. The use of alkali metal nitrates for colored signals was also considered unsatisfactory in comparison to the alkaline earth compounds currently used. It was apparently for these reasons that no attempt was made to further investigate the spectra of the magnesium/ alkali metal nitrate flares in any detail.

Recently, the spectra of alkali metal nitrate/magnesium flares were re-evaluated.[7] The analyses of the spectra indicated the existence of possible diatomic alkali metal molecules and alkali metal-magnesium molecules in flares containing sodium nitrate, potassium nitrate and rubidium nitrate. The purpose of this paper is to report those results and to discuss in detail the nature of the electronic energy states involved in the transitions.

EXPERIMENTAL*

Construction of Flares

An initial series of calculations was done using the NASA thermodynamics program[8] to optimize the magnesium, alkali metal nitrate, binder formulations to give the maximum adiabatic temperature. The organic binder level was fixed at five percent and the fuel to oxidizer ratio was varied until the maximum temperature was computed. The final formulas used in this study are given in Table 1.

The chemicals used in making the formulations ranged from research grade rubidium nitrate to practical grade sodium and potassium nitrate. These oxidizers were ground and dried prior to mixing. The particle size was approximately 30 microns. The magnesium was MIL-M-382, granulation 17, which has an approximate particle size of 75 microns.

---

*In order to specify procedures adequately, it has been necessary occasionally to identify commercial materials and equipment in this report. In no case does such identification imply recommendation or endorsement by the Navy, nor does it imply that the material or equipment identified is necessarily the best available for the purpose.

The binder used was a combination of Dow Epoxy Resins[@], DER 321 and DER 732 and a polyamine CX 3482.1 in the ratio DER 321 - 61.3%, DER 732 - 26.3% and CX 3482.1 - 12.4%. This is a typical epoxy binder formulation currently in use in illuminating flares. In an effort to prevent contamination, the mixing, screening and drying apparatus was washed and dried between each formula change.

The flares were pressed into paper tubes at 10,000 pounds dead load. Fifty grams of composition were used for each candle. The finished size was 3.3 cm in diameter and 5.1 cm in length. Five grams of ignition composition were pressed on the surface of each candle.

Experimental Procedure

The flares were burned face up at a distance of 6.0 meters from the spectrographs. Visible spectra from 0.40 - 0.70 μm were recorded on a Bausch and Lomb 1.5 m grating spectrograph. This instrument has a 450 line/mm grating giving a dispersion of 15 Å/mm in the first order on the photographic film. Kodak Linagraph Shellburst[@] film was used for recording these spectra.

Earlier results indicated that flare groups 7308, 7309 and 7311, containing sodium nitrate, rubidium nitrate and potassium nitrate, respectively, appeared to have polyatomic emission features.[7] Higher resolution spectra of these compositions were taken in the second order using a one meter Spex Model 1802 grating spectrograph. The spectrograph was equipped with a 1200 line/mm grating and gave a second order dispersion of 4.0 Å/mm in the regions of interest. The spectra of the diatomic features were recorded on Kodak I-N spectroscopic plates.

Spectra of a 200 watt quartz-iodine lamp were recorded on the same plates to provide a film response correction. In these experiments, the flares were masked in such a way that the spectrographs were observing a position in the flame seven centimeters above the surface of the candle.

The spectra were scanned and digitized on an Optronics S2000 densitometer. Points were taken at approximately 0.60 nm intervals. The resulting digital output was processed by standard procedures and the film density converted to radiant and luminous power readings.

RESULTS

The visible radiant power spectra of flare groups 7308, 7309, and 7311, containing sodium nitrate, rubidium nitrate and potassium nitrate, respectively, are shown in Figures 1-3. These are the low resolution spectra obtained on the Bausch and Lomb spectrograph. Each of these spectra was selected as being representative of a large number of spectra obtained for each group. To avoid confusion and to show as much of the important structure as possible, each figure is normalized to a value of one at its maximum. The relative magnitudes of the maxima are 1:0.02:0.03 for Na, K and Rb, respectively. A detailed analysis of the atomic emission features for these flares and for the the other alkali metal nitrates has been published in an earlier report. For the

purpose of making this report as complete as possible, some of the previous work will be presented again here.

DISCUSSION

Assignment of the Spectra

Sodium

The electronic structure of sodium is $1s^2 2s^2 2p^6 3s^1$ making the ground state energy level of the sodium atom a 3s. The spectrum to be assigned is shown in Figure 1; the flare formula is 7308, high sodium-low lithium concentrations. The first peak at 460.3 nm is the lithium 4d→2p transition. The next three peaks are MgO bands, B→X transition, at 498.6, 499.7 and 500.7 nm and are assigned to the 2,2;1,1 and 0,0 transitions, respectively.[9] There is also a sodium transition, 5d→3p, superimposed on these bands at 498.3 nm. The next two lines are the sodium doublet at 514.9 and 515.4 nm and are due to the 6s→3p transition. The next three lines are the 4s→3p transition in magnesium at 516.7, 517.3 and 518.4 nm.

The major feature in the sodium spectrum is the broadened resonance line continuum which has been well described both experimentally and theoretically by Douda.[2,3] The emission is centered at 589.3 nm and is due to the 3p→3s transition. The halfwidth of the broadened lines is approximately 50 nm.

Superimposed on the short wavelength side of the continuum is a sodium doublet at 568.27 and 568.82 nm. These lines are due to the 4d→3p transition. Superimposed on the long wavelength side are lithium lines at 610.36 nm and 670.79 nm and another sodium doublet at 615.42 and 616.07 nm due to the 5s→3p transition.

At 530 nm there is an apparently continuous emission feature. Barratt[10] observed a magnesium-sodium interaction in an absorption spectrum taken through a mixture of gaseous magnesium and sodium. This band was degraded to the blue and had a band head at 529 nm. The band observed here in emission and the band observed by Barratt are probably the same. There has been no effort to determine possible electronic energy states. This band is not apparent in any of the spectra where sodium is not present, indicating that at least a high concentration of sodium is required. Spectra taken of a high pressure sodium lamp also do not show this particular emission feature, indicating that it is not a feature of high concentrations of sodium alone. The high resolution spectra taken in this region indicate that there is no structure associated with this feature.

A much more refined analysis is required to determine not only the exact identity of this species but also the possible electronic states which could give rise to this emission. Tentatively this feature is assigned to emission from a diatomic molecule formed by the interaction of magnesium and sodium.

Another interesting molecular-type emission is observed on the wing of the broadened sodium doublet at 550 nm. The high resolution spectra of this feature show that it, like the one at 530 nm, has no structure. In the past this feature has been attributed to a sodium-nitrogen interaction of the type observed by Chen and Takeo. Efforts to enhance this emission feature by the addition of nitrogen have proven unsuccessful. Preliminary experiments show that this feature is not present when sodium perchlorate rather than sodium nitrate is used as the oxidizer. Spectra taken of the high pressure sodium lamp show that this feature is present under these conditions. In spectra taken of low pressure, high temperature sodium vapor, Hamada observed similar emission at 550 nm. This emission was attributed to quasi molecules of Na_2.

Much work has been done on Na_2 and thus good estimates of diatomic potential energy surfaces are available. Figure 4 shows the potential surfaces for two states of Na_2 known to give rise to molecular spectra. The ground state, $^1\Sigma_g^+$, is the result of the interaction of two ^2S sodium atoms. The upper state, $^1\Sigma_u^+$, is the result of the interaction of a ground state ^2S sodium and an excited state ^2P sodium atom. The transition marked A in Figure 4 is probably the transition which gives rise to the emission feature at 550 nm.

The lower energy transitions which would show the vibrational-rotational structure normally associated with diatomic sodium are either not present or are masked by the high intensity of the sodium resonance lines. The work by Hamada has shown that as the temperature of the sodium vapor is increased, the bound state lower energy transition disappear. In other words, all the emission comes from quasi-molecules rather than bound state molecules. The feature at 550 nm is thus assigned to a diatomic sodium molecule emitting from the $^1\Sigma_u^+$ to the $^1\Sigma_g^+$ ground state.

Potassium

Potassium salts find heavy use in pyrotechnics as oxidizers probably because of their relative inexpensiveness and lack of emission in the visible spectra region. The fact that potassium does have significant visible emission may account in part for the current inability to obtain high purity colors in signals which incorporate it as an oxidizer.

The electronic structure of potassium is $1s^2 2s^2 2p^6 3s^2 3p^6 4s^1$ making its ground electronic state a 4s. The assignments are made for Figure 2, flare formula 7311, consisting of magnesium, potassium nitrate and binder only. In terms of specific line emission, the potassium spectrum is relatively simple. Barely distinguishable at approximately 490 nm are three potassium lines assigned as 495.08, 495.60 and 496.50 nm. These lines are a result of the transitions 8d→4p, 10s→4p and 8d→4p. The next series of lines are two doublets at 508.42, 509.92, 509.71 and 511.20 nm and are assigned to the transitions 9s→4p and 7d→4p. Two more potassium doublets are observed at 532.23, 533.97 and 534.30, 535.95 nm and are due to the 8s→4p and 6d→4p transitions. A fourth set of

potassium doublets is observed at 578.36, 580.20 and 581.25, 583.21 nm and are assigned to the $7s \rightarrow 4p$ and $5d \rightarrow 4p$ transition. The sodium doublet at 589 nm is due to an impurity in the mix. Quantitative analysis of a similar composition showed the concentration of the sodium impurity to be less than 1 ppm. This illustrates the excellent emission properties of atomic sodium. It is possible that some of this emission comes from the paper tube. Similar work using slightly different formulas showed no reduction of the sodium emission when the flares were burned without tubes so the case is probably not the origin of the emission.

In terms of diatomic or polyatomic emission characteristics, there is one region of the spectrum shown in Figure 2 that warrants further consideration. This feature is the symmetrical hump centered at 572 nm. Rebbeck and Vaughan have observed a similar feature at 572 nm in low power discharges through potassium vapor.[12] The half intensity width of the main band in the Rebbeck and Vaughan work was approximately 3.0 nm in reasonable agreement with the feature observed in this spectrum. This emission was attributed to a diatomic emission from a bound upper state to a repulsive lower state. The electronic state of the upper state was not determined but it probably results from the interaction of a ground state potassium atom $4\,^2S$ and an excited atom $5\,^2P$. Applying the Wigner-Witmer rules for possible states we find that a $^2S + ^2P$ can give rise to singlet and triplet Σ^-, Σ^+ and Π states. In addition, these states may have odd or even parity depending on the parity of the initial atoms. Thus, it is impossible to ascertain the exact nature of the upper state with the limited information available.

The lower state is either a $^1\Sigma_g^+$ or $^3\Sigma_u^+$, the only two states possible from the combination of $^2S + ^2S$. Absorption spectra of K_2 vapor have established that a bound lower state $^1\Sigma_g^+$ exists. The nature of the spectra observed by Rebbeck and Vaughan indicates that the molecular species responsible for the 572 nm emission is not a bound state thus eliminating the $^1\Sigma_g^+$ state from further consideration. It appears then that the ground state of this transition is a repulsive $^1\Sigma_u^+$ state.

The high resolution spectra of this emission feature show no vibrational-rotational structure in agreement with the spectra obtained by Rebbeck and Vaughan. This lack of structure makes it virtually impossible to say anything about the nature of the upper state.

Several different electronic states of K_2 have been observed and analyzed in absorption by various investigators.[9] The potential energy diagram for the various states is shown in Figure 5. The lowest energy transition is at 857 nm and would not have been observed in these experiments. The next transition observed in absorption is the $^1\Pi_u - ^1\Lambda_g^+$ transition at 650 nm. This transition is possibly what gives rise to the increased emission at 650 nm shown in Figure 2. The other transition which might have been observed is the $^1\Sigma_u^+ - ^1\Sigma_g^+$ at 436 nm.

The spectra in these regions are quite complex and contain hundreds of emission lines, none of which are readily associated with vibrational-rotational structure, i.e., there are *no clear band heads*. Much higher resolution spectra will be required to identify these other transitions.

Rubidium

The electronic structure of rubidium is $1s^2 2s^2 2p^6 3s^2 3p^6 3d^{10} 4s^2 4p^6 5s^1$ making the ground state a 5s. The assignments given are for Figure 3, flare formula 7309, consisting of magnesium, rubidium nitrate and binder. As can be seen from Figure 3, rubidium has a large number of emission lines in the visible. At the extreme left of the figure, centered at 420.7 nm, we see the 6p→5s transition in rubidium. Unfortunately, the sensitivity of the film was such that this feature was barely apparent. The two lines at 455.5 and 459.3 nm are due to a cesium impurity. In the region from 550-535 nm there are a series of several lines as yet unidentified. These are apparently narrow with little or no degrading indicating that this is probably atomic emission rather than molecular band emission. The exact wavelengths of the major lines are 515.3, 518.6, 526.4 and 532.6 nm. These lines are followed by another unidentified line at 539.4 nm.

The next line is a rubidium line at 543.15 nm and is due to the 8d→5p transition. The next rubidium line is seen at 557.88 nm and is the transition 9s→5p. The next line is actually two unresolved rubidium lines at 564.81 and 565.37 nm coming from the 7d→5p and 9s→5p transitions. Next is a rubidium line at 572.45 nm and is from the 7d→5p transition. The next line is the sodium doublet at 589 nm. Skipping the band emission at 600 nm the next line is a rubidium line at 615.96 nm arising from the 8s→5p transition. The next line is at 620.63 nm, a rubidium line from the 6d→5p transition followed by the rubidium transition at 629.83 nm. This transition is also the 6d→5p. The last two lines superimposed on a continuum are lithium at 670.7 and cesium at 672.3 nm.

Diatomic rubidium absorption has been previously observed at 439, 480 and 682 nm.[9] The potential energy diagram for these transitions is shown in Figure 6. The visible spectrum in Figure 3 does not show these transitions in emission.

The emission observed at 600 nm appears to be completely continuous both under high and low resolution conditions.

Walter and Barrett report bands at 599.2, 603.3 and 605.4, degraded to the red, in absorption.[13] These absorption bands and the continuous emission observed in rubidium flares are probably the same. Due to the lack of sufficiently resolved spectra, no attempt has been made to identify the molecular state associated with this emission feature.

CONCLUSIONS

The visible radiant power spectra of flares containing magnesium as the fuel and sodium nitrate, potassium nitrate and rubidium nitrate as oxidizers have been presented and analyzed for emission from diatomic molecules. In the sodium nitrate flares, emission was observed from NaMg at 530 nm and Na_2 at 550 nm. In the potassium nitrate flares, emission from K_2 was observed at 572 nm. In the rubidium nitrate flares, emission from Rb_2 was observed at 600 nm. In all cases the emission bands were continuous indicating that one or both of the electronic states involved in the transition were repulsive, except in the case of Na_2 in which both states were bound but the translational energy of the sodium atoms was so great that quasi-molecules were produced rather than bound diatomics.

REFERENCES

1. H. Ellern, *Military and Civilian Pyrotechnics* (Chemical Publishing Company, New York, 1968), p. 337.

2. B. E. Douda, *Radiative Transfer Model of a Pyrotechnic Flame*, RDTR No. 258, Naval Ammunition Depot, Crane, Indiana (1973). Available DDC-AD 769273.*

3. B. E. Douda and E. J. Bair, J. Opt. Soc. Am. 60, 1257 (1970).

4. B. E. Douda and E. J. Bair, J. Quant. Spectrosc. Radiat. Transfer, 14, 1091 (1974).

5. B. E. Douda, R. M. Blunt and E. J. Bair, J. Opt. Soc. Am. 60, 1116 (1970).

6. R. M. Blunt, *Study of Illuminating Flames from Solid Reactants*, RDTR No. 77, Naval Ammunition Depot, Crane, Indiana (1970). Available DDC-AD 707720.

7. H. A. Webster, *Alkali Metal Emitters: I. Analysis of Visible Spectra*, NWSC/CR/RDTR-16, Naval Weapons Support Center, Crane, Indiana (1975).

8. S. Gordon and B. J. McBride, *Computer Program for Calculation of Complex Chemical Equilibrium Compositions, Rocket Performance, Incident and Reflected Shocks, and Chapman-Jouguet Detonations*, NASA SP-273, Lewis Research Center (1971). Available NTIS-N71 37775.**

9. G. Herzberg, *Spectra of Diatomic Molecules* (D. Van Nostrand Co., Inc., Princeton, N. J., 1966).

10. S. Barratt, Proc. Roy. Soc. A109, 194 (1925).

11. H. Hamada, Phil. Mag. 15, 574 (1933).

12. M. M. Rebbeck and J. M. Vaughan, J. Phys. B. Atom. Molec. Phys. 4, 15 (1971).

13. J. M. Walker and S. Barratt, Proc. Roy. Soc. A119, 257 (1928).
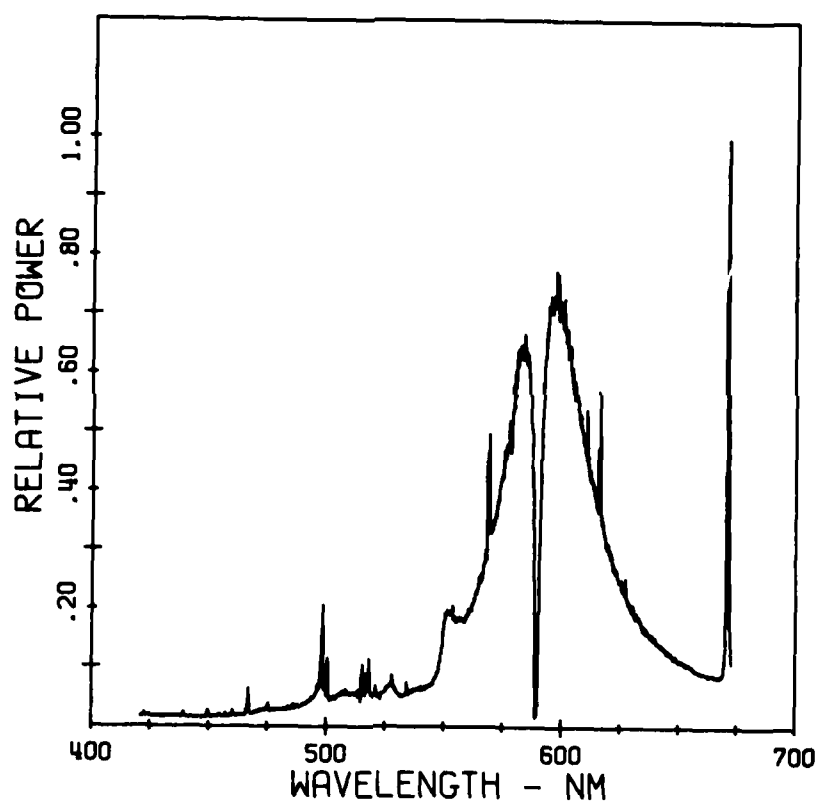
Figure 1.   Group 7308 - High [Na]/Low [Li]
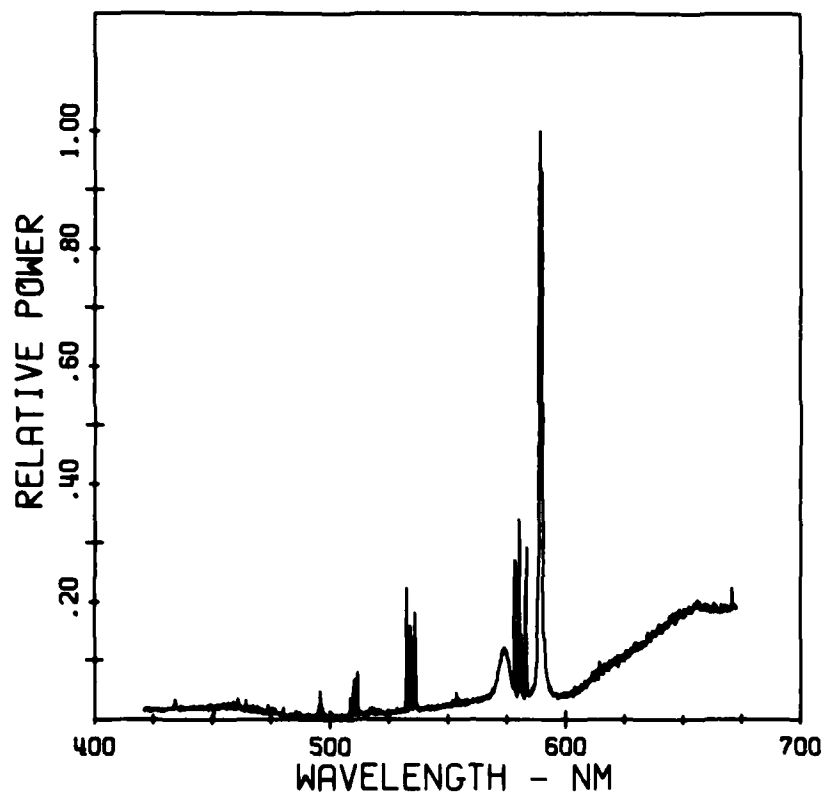
Figure 2.   Group 7311 - High [K]

562
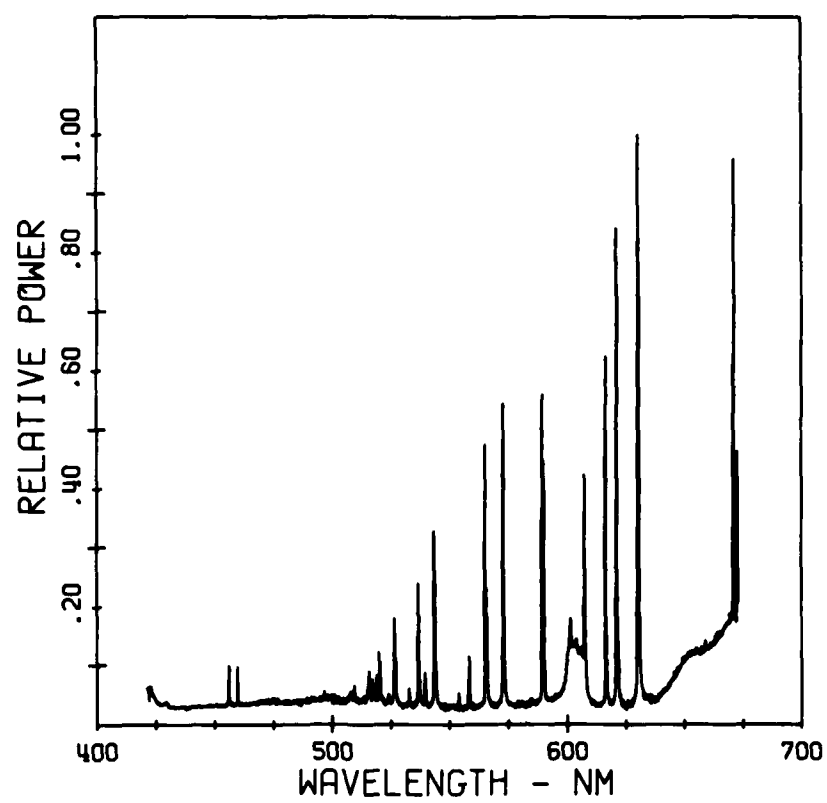
Figure 3.   Group 7309 - High [Rb]
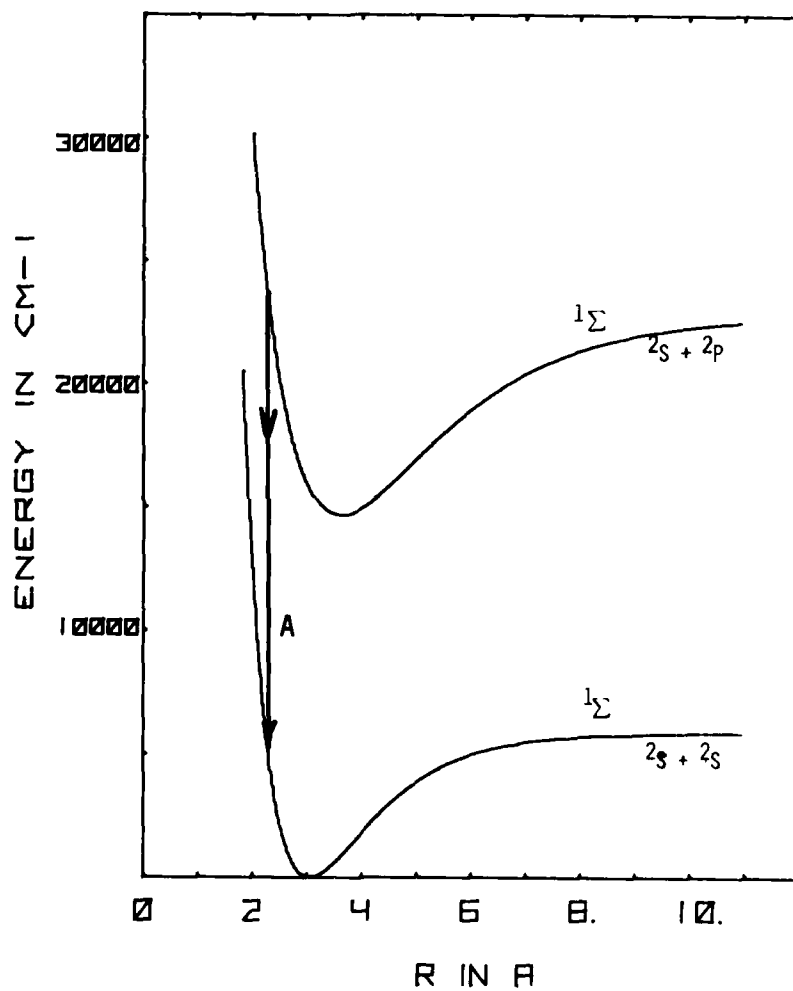
Figure 4. Potential Surfaces for Na$_2$
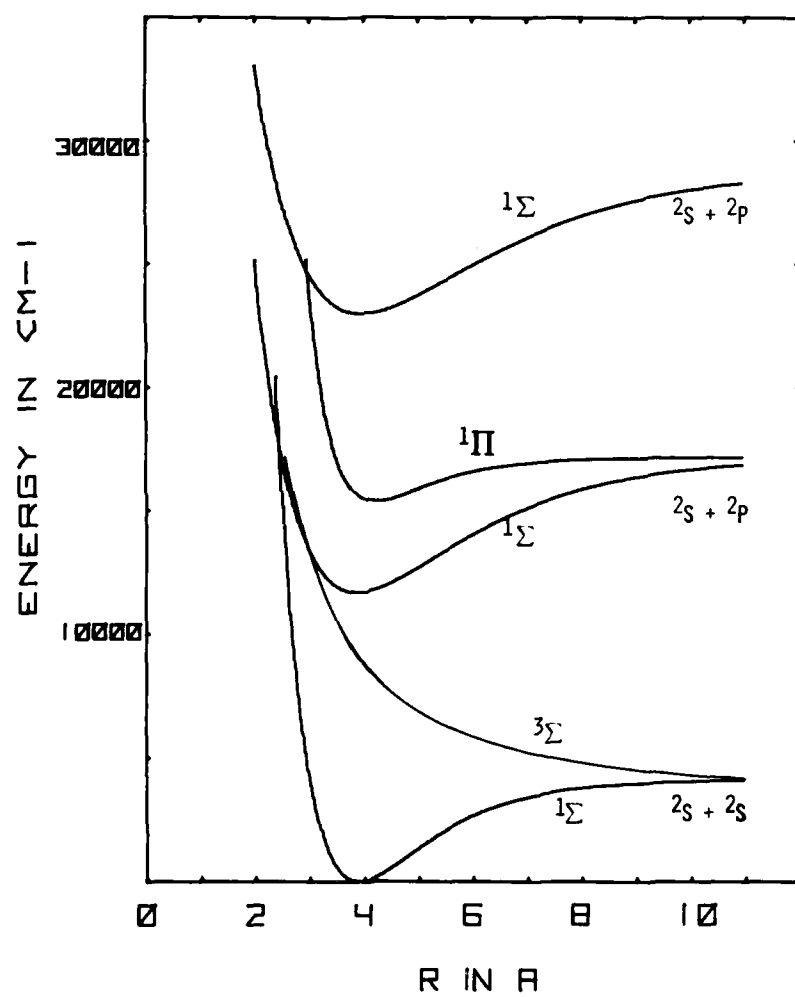
Figure 5. Potential Surfaces for K_2
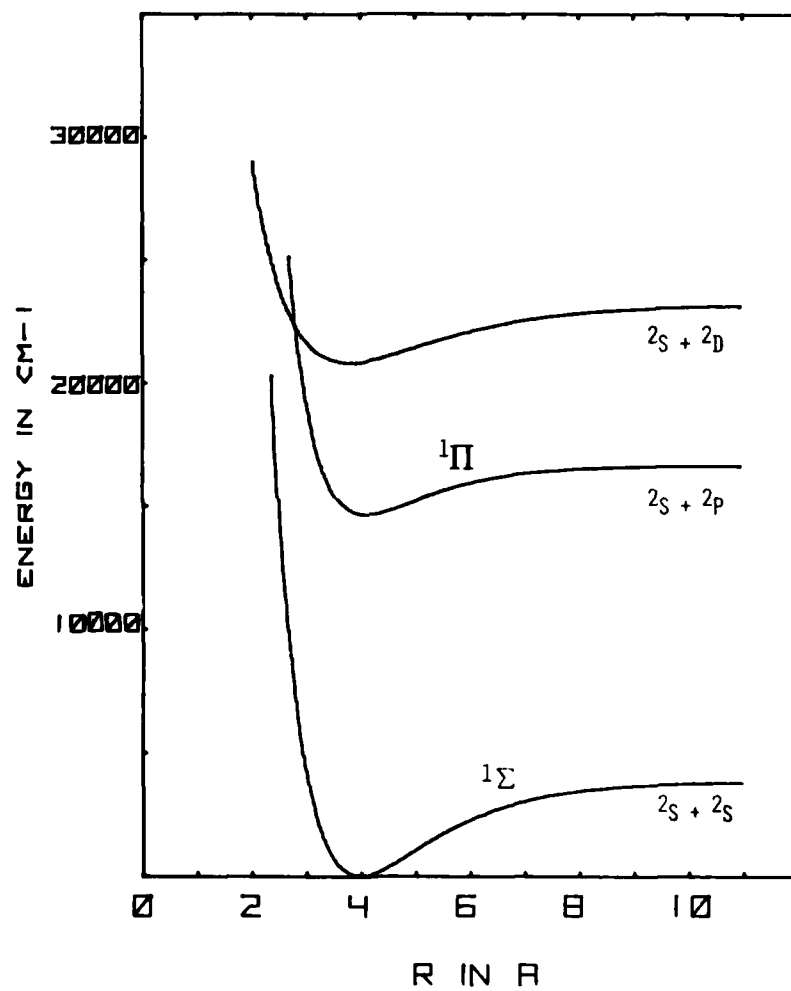
Figure 6. Potential Surfaces for Rb_2

SMOKE COLORIMETER

Henry A. Webster III
Applied Sciences Department
Naval Weapons Support Center, Crane, Indiana

ABSTRACT

A device for measuring the color, brightness and optical density of smoke displays is described. The colorimeter measures the light reflected from a smoke with three detector-filter combinations designed to match the CIE colorimetric spectral functions. Data are presented for yellow, green and orange standard smoke formulas. In addition, experiments are described in which variations of color between yellow and green were evaluated. The colorimeter performed well in all experiments. The results of this work indicate that the colorimeter can be used both as a research tool to help determine optimum parameters in the design of smoke units and as a quality control device to insure that production units meet some minimum requirements for color and optical density.

INTRODUCTION*

At the present time in the state-of-the-art of pyrotechnics there is no quantitative method for measuring the color, brightness and optical density of smoke displays in real-time. The method currently in use is a qualitative assessment by several observers of whether or not a color is good. In most cases it is probably a safe assumption that these observers have not even been tested for adequate color vision. Obviously this is not an ideal method.

A smoke color measuring device was developed by NBS[1] for the Army. In this instrument a smoke unit is functioned in a closed container. Reflected light from the cloud formed in the chamber is measured by a set of three detectors equipped with appropriate filters. The filters were chosen in such a way that the source plus detector plus filter response matched the three CIE colorimetric spectral functions.[2] The smoke in the chamber is stirred by a fan so that time resolved measurements of changes in smoke color can be made. Red and yellow smokes were measured. Due to a lack of good matching between the detector-filter-source and the CIE functions, it was necessary to calibrate the instrument with Munsell chips of approximately the same color as the smoke to be measured. From the limited data presented, it appeared that reasonable agreement with visual observations could be obtained. Later efforts to use this colorimeter for smoke measurements showed that the device was very unstable,[3] probably as a result of the problems normally associated with photomultiplier tubes, and it was not used to any great extent.

A smoke measuring device has been developed by BAI Corporation for the Army.[4] This device is a large chamber with a fan and filter system at one end and detector optics located on one side. The smoke unit to be tested is initiated at one end of the chamber and the cloud is pulled past the detectors by the fan. In this way, simulated outdoor use can be obtained. The optics consist of three photomultipliers with three variable transmission filters which are masked so that the response of the filter-detector-source combination match the CIE chromaticity functions. In the final report describing the instrument, good results were obtained. There must have been some difficulty, however, with the electronics and optics since very recently the Chromacorder, a forty element multiple detector-filter combination developed for measuring colored flares at Picatinny Arsenal, has been modified for use with the BAI colorimeter.[5] The calibration problems associated with forty simultaneous detectors will probably make its use marginal. The Chromacorder has yet to be tested with the colorimeter. It was tested against Munsell calibration papers and worked well.

---

*In order to specify procedures adequately, it has been necessary occasionally to identify commercial materials and equipment in this report. In no case does such identification imply recommendation, endorsement, or criticism by the Navy, nor does it imply that the material or equipment identified is necessarily the best available for the purpose.

In a recent report by Diener,[6] spectral reflectance measurements were made of the dyes used in standard M18 smoke grenades. In these experiments, M18 type compositions were burned and samples of the resulting dye aerosols were collected on glass fiber filter mats. The reflectance spectrum of the aerosol was taken on a Beckman DK-2 spectro-reflectometer and the chromaticity coordinates were calculated. As Diener points out, the data obtained do not necessarily indicate or refer to the actual colored smoke cloud since this is not a real-time measure-ment and the collection process changes the particle size distribution which has been shown to play an important part in the color of a smoke cloud.[3] This work, however, does provide the best first approximation to date.

The Navy has a smoke colorimeter located at the Naval Weapons Support Center, Crane, Indiana, which is a refined combination of the NBS detector and BAI smoke flow system. The basic instrument, designed to measure smoke color, brightness, and optical density in air flows up to 15 knots to simulate outdoor conditions, was described in an earlier report.[7] In this report, as in most others on smoke colorimeters, no real attempt was made to describe measurements and present data on actual smoke.

The purpose of these experiments was to evaluate the usefulness of the Navy smoke colorimeter for measuring differences in smoke colors. The color differences were not simply the difference between red, yellow and green but also variations between yellows and greens. This report will describe the experiments done and present the evaluation of the data.

EXPERIMENTAL PROCEDURES AND RESULTS

Instrumentation

Basic Colorimeter Design

Since a physical description of the colorimeter was given in an earlier report,[7] only a brief review will be given here. A schematic of the entire system is given in Figure 1. The smoke chamber is a rectangular box measuring 17x3x3 feet (about 5.2x1x1 meters). The box is made up of three smaller boxes each with a hinged lid to permit easy access for adjustment and cleaning. The first section is a mixing section where the smoke unit is fired. This section contains three vertical baffles which can be adjusted to give proper mixing. The second section is designed to restrict the smoke flow slightly and to shape the cloud for measurement. The last section is the measuring section and contains a viewing port, a port for making the color measurements, and the densitometer for measuring the smoke density.

A fan and filter unit is located at one end of the chamber to provide movement of the smoke and to exhaust the system when the experiment is completed. The fan can be controlled by a variable transformer to provide wind speeds from 0-15 knots. The filter unit consists of two inch fiberglass prefilters and a sack filter. These filters trap all but sub-micron size particles. Another filter unit is located behind these filters and traps any remaining particles. With these filters it is possible to operate the colorimeter in any area without having to worry about problems associated with discharging the smoke into the atmosphere.

Color Measuring Optics and Electronics

The color measuring optical system schematic is shown in Figure 2. The smoke cloud is illuminated by two 150 watt projection lamps. The light reflected from the smoke cloud is collected by the front lens system, focused onto a variable aperture and then to a field lens which provides uniform illumination of the detectors. The detectors for measuring the X and Y signals are planar diffused PIN-10 silicon photodiodes. The Z detector is a blue sensitive, Schottky barrier PIN-10 photodiode.

The silicon detectors are used with colored glass filters to obtain the closest possible match to the $\bar{x}$, $\bar{y}$, and $\bar{z}$ color-matching function. The bi-modal $\bar{x}$ function is generated by using electronics to add the signals from the X detector and the Z detector. The filter transmission curves and the corresponding filter plus detector curves are shown in Figures 3, 4, and 5. Due to difficulties associated with making spectroscopic measurements with the detectors in the system, the filter plus detector curves were constructed by using a typical detector response curve and multiplying it by the measured filter transmission curve. The points in Figures 3, 4, and 5 are the standard CIE chromaticity functions.

A block diagram of the electronics used in this system is given in Figure 6. The detector signals are fed to operational amplifiers which are used as current-to-voltage converters. At this stage, the X and Z signals are also added to provide the bi-modal $\bar{x}$ function. These signals are then amplified by operational amplifiers each with a variable gain control. This gain control can be used to adjust the relative magnitudes of the X, Y, and Z signals so that the instrument can be calibrated against color standards.

The X, Y, and Z signals are then displayed either on the front panel meter or a strip chart recorder. The X, Y, and Z signals are also input into an operational amplifier connected as a summing amplifier. Precision dividers take the outputs of X and Y and divide them by the sum of X, Y, and Z to give the CIE chromaticity coordinates, x and y. These values can also be displayed on the front panel meter or on strip chart recorders.

Densitometer Optics and Electronics

The densitometer optical system consists of lamp, several lenses, and a silicon PIN-10 photodiode. The pathlength for density measurements is 38 mm. The signal from the photodiode is fed to a logarithmic amplifier where the transmission signal is converted to an optical density which can then be displayed on the front panel meter or a strip chart recorder. The densitometer output is linear over three density units or three orders of transmission.

Calibration of Colorimeter

The colorimeter is calibrated at the beginning of an experiment, at several stages during the experiment, and again at the end of the experiment. Calibration is done by inserting colored papers with a known spectral reflectance in front of the lamp and measuring the light reflected from paper. The gain potentiometers on the X, Y, and Z detectors are adjusted to give the correct reading for the particular paper. In general, a white paper, Munsell notation N9.25/, can be used for calibration. It is suggested by the manufacturer that when dark colors are measured it is advisable to calibrate the instrument with a color near the one to be measured.

As a check on the accuracy and reproducibility of the color measuring device, eighteen different colored papers were checked. These papers were selected so that both dominant wavelength and purity could be varied in a specific manner. The measured and actual chromaticity coordinates, x and y, and the dominant wavelength and purity of the samples are given in Table 1.

The results given in Table 1 are the average values of different determinations taken on several different days. In addition, the values are averages taken with different range settings to improve the signal to noise ratio. The average error among all these runs was less than 0.2%.

Smoke Testing

Two experiments were done to validate the operation of the color-imeter and to obtain initial values for the chromaticity coordinates of the smoke clouds. In all experiments the colorimeter was calibrated against the white standard paper. In the first experiment, green and yellow M18 smoke grenades and orange Mk 13 distress signals were burned to determine the values of X, Y, and Z. The compositions of the smoke units are given in Table 2 and the experimental results are given in Table 3.

The second experiment in this series was designed to validate the operation of the colorimeter and to get some idea of the limits on determining different colors. In this experiment, Mk 117 and Mk 118 smoke compositions were used as green and yellow standards, respectively. In addition to these formulas, three new formulas were made by mixing Mk 117 and 50% Mk 118 compositions; 25% Mk 117 and 75% Mk 118, and Mk 117 and 25% Mk 118 compositions. These formulas were

three distinct colors between the standard green Mk 117 and the standard yellow Mk 118. The actual formulas are given in Table 4 for all five compositions. The smoke compositions were pressed in 5.0 cm paper tubes at approximately 5000 psi. The completed candles had a 0.4 cm center hole to reduce the filtering problem caused by the ash. The experimental results for these tests are given in Table 5.

DISCUSSION

An examination of Table 1 quickly points out the basic problems associated with the Navy smoke colorimeter as it now exists. In the yellow spectral region, the agreement between the measured values of x and y for the colored papers and the values determined by reflectance spectrometry is better than 1% and is excellent. In the green region, the error is between 1 and 6%. The worst region is in the red where errors up to 12% occurred. In all cases, the error was worse in the x value than in the y value. In the red region of the spectrum, $\lambda > 580$ nm, the values obtained for dominant wavelength were consistently 5 nm higher than the actual values. In the green region of the spectrum, $\lambda > 570$ nm, the values for dominant wavelength were generally about 4 nm less than the actual values. In order to account for these differences, it is necessary to discuss the colorimeter optical system as a whole and to investigate the calibration technique.

The radiant flux reflected by an object which is regarded as a color stimulus is called the object color. An object color is specified by the spectral distribution $\rho_\lambda H_\lambda \Delta\lambda$, where ρ_λ is the spectral reflectance and $H_\lambda \Delta\lambda$ is the spectral distribution of the flux irradiating the object. The tristimulus values X, Y, and Z are then given by

$$X = K \sum_\lambda \rho_\lambda H_\lambda \bar{x}_\lambda \Delta\lambda$$
$$Y = K \sum_\lambda \rho_\lambda H_\lambda \bar{y}_\lambda \Delta\lambda \qquad (1)$$
$$Z = K \sum_\lambda \rho_\lambda H_\lambda \bar{z}_\lambda \Delta\lambda \ .$$

The color-matching functions, $\bar{x}$, $\bar{y}$, and $\bar{z}$, are those of the CIE standard observer or, for the case of a color measuring device, the filter plus detector response curve. The normalizing factor K is usually given the value

$$K = 100 / \sum_\lambda H_\lambda \bar{y}_\lambda \Delta\lambda \ . \qquad (2)$$

When Eq. (2) is used as the normalizing value, the Y value of a reflecting object is its luminous reflectance or brightness expressed as a percentage.

The calibration technique suggested by the manufacturer of placing a white card with known values of X, Y, and Z in the system and adjusting the colorimeter outputs to these values was followed in all these experiments. Unfortunately, the values assigned to the calibration paper were assigned when standard source C was used for illumination. Figure 7 shows the differences in the radiant flux produced by standard source C, standard source A and the colorimeter source. This figure shows that source C has much higher output in the blue spectral region and much lower in the red than the colorimeter source. Figures 8, 9, and 10 show the quantities $\rho_\lambda H_\lambda \bar{x}_\lambda$, $\rho_\lambda H_\lambda \bar{y}_\lambda$ and $\rho_\lambda H_\lambda \bar{z}_\lambda$, respectively, for the colorimeter source, detector, filter combination and the white paper reflectance standard. The points on the curves are the values calculated for standard source C, the CIE observer response and the white paper reflectance standard. Integration of the areas under the curves gives the tristimulus values X, Y, and Z. The curves shown in Figures 8, 9, and 10 are normalized so that the areas correspond to the values of X, Y, and Z given by the paper manufacturer for the white reflectance standard illuminated with source C.

The colorimeter calibration technique simply amounts to increasing the detector gain to achieve equal areas under the curves with no regard to spectral distribution. This technique, while not fundamentally correct, produces some interesting results. Figure 5 shows the filter-detector response of the z channel. The colorimeter curve is skewed to shorter wavelengths when compared with the standard CIE curve. The colorimeter source is much less intense in the blue region of the spectrum. The overall effect, shown in Figure 10, of coupling the source with the filter and detector is to improve the fit of the curves. The peaks of the curves are now at the same wavelengths and the leading edges are more nearly correct.

The y response curve shown in Figure 4 is likewise shifted to bluer wavelengths. From 500-560 nm source C and the colorimeter source have approximately the same distribution. From 560-700 nm the colorimeter source is more intense than source C. The overall effect of coupling the filter, detector and source is to broaden the overall curve in Figure 4 and subsequently shift the peak of the curve to longer wavelengths. As is shown in Figure 9, this improves the fit between calculated and actual responses.

The x response curve shown in Figure 3 is composed of a blue lobe and a red lobe. When the source is taken into account, the red lobe behaves like the y response curve and the blue lobe behaves like the z curve as described previously in terms of the shifts in the maxima of the curves. The major problem comes because the flux from source C is much greater than from the colorimeter source in the region from 400-500 nm. In the case of the z response curve, this was compensated for by the normal gain control. In the case of the x response there is no such adjustment for each separate peak and the overall effect is that the response from 400-500 nm is a factor of at least three too low and is too high in the region from 500-700 nm. This fact accounts for the large errors observed when red standards are measured.

The tristimulus values X, Y, and Z measured for the M18 smoke grenades and Mk 13 distress signal were given in Table 3. The chromaticity coordinates for these devices are calculated using the standard equations

$$x = \frac{X}{X+Y+Z}$$

$$y = \frac{Y}{X+Y+Z}$$

and are plotted on a chromaticity diagram in Figure 11. For the green M18 the dominant wavelength is 492 nm and the purity is 17%. Diener calculates a dominant wavelength of 500 nm and a 6% purity.[6] The BAI colorimeter gave a dominant wavelength of 504 nm and a purity of 27%. These values agree reasonably well. If the smoke colorimeter is calibrated against a green calibration paper, the values x=0.241 and y=0.379 are obtained for the green M18 grenade. These values correspond to a dominant wavelength of 502 nm and a purity of 23% which makes the agreement with the two reported Edgewood values even better. It should be pointed out that the calibration against green standards is good only if green smokes are being tested.

For the yellow M18 grenade, the dominant wavelength is 568 nm and the purity is 65%. Diener obtained values of 582 nm and 86% and the BAI colorimeter gave 576 nm and 79% purity. These numbers are in reasonable agreement. Since the tests with the calibration papers showed good agreement in this region, no attempt was made to recalibrate against a yellow standard.

Standard red M18 smoke grenades were not available for testing. As a test in the red region, the Mk 13 Distress Signal which gives an orange smoke cloud was used. The value of dominant wavelength for the Mk 13 was 606 nm and the purity was 86%. Based on the results obtained from the calibration papers, the actual dominant wavelength is probably around 600 nm. No attempt was made to calibrate against a red paper and redo the experiment. Since this procedure worked for the green smoke/green paper it should work for the orange smoke/ orange paper.

The final experiment in this test of the colorimeter was to determine to some extent the range and ability of the instrument to detect changes in smoke color. Five different smoke formulations were pressed. As discussed previously, these formulations were designed to give green, yellow, and three colors in between these two. The results of this experiment are plotted in Figure 12. As in the previous experiment, the white paper was used for calibration. The dominant wavelength for the green smoke was 495 nm and the purity was 20%. This is in excellent agreement with the values obtained for the M18 smoke grenade. The dominant wavelength and purity for the yellow smoke were 573 nm and 75%. This is also in reasonable agreement with the standard M18 yellow

grenade. For Formula 2, the 75% green-25% yellow combination, the dominant wavelength was 514 nm and the purity was 15%. For Formula 3, 50% green-50% yellow, the dominant wavelength was 546 nm and the purity was 38%. For Formula 4, 25% green-75% yellow, the dominant wavelength was 560 nm and the purity was 60%. Thus, it appears that the colorimeter is capable of distinguishing object colors which differ by as little as 20 nm. Whether or not finer gradations are possible remains to be answered.

CONCLUSIONS

The Navy smoke colorimeter has been tested using both standard calibration papers and typical smoke compositions. Comparisons indicated that due to mismatches between filter-detector-source response curves low values of dominant wavelength and purity are obtained in the green region of the spectrum while high values are obtained in the red region. When the colorimeter is used to measure smoke clouds from standard compositions, reasonable agreement with previously reported results is obtained. Experiments designed to test the ability of the colorimeter to distinguish gradations in smoke color indicated that the colorimeter can determine at least 20 nm color changes and probably less. This color change results from dye concentration changes on the order of 10-15% in the composition. The reproducibility of the readings, the ease of calibration and operation, and the ability to detect small color changes resulting from small changes in dye composition should make this instrument a very useful tool for quality control and testing of colored smoke compositions.

The most needed improvement is a better match between response curves. If one wishes to remain with a three detector colorimeter, the filters in this instrument should be modified to give a better response curve fit. The ideal method for determining smoke color is to make a real-time measurement of the spectral reflectance. With the availability of optical multi-channel analyzers and rapid scanning spectrometers, this type of measurement is now within reach. If the spectral reflectance could be fed into a minicomputer where the standard $\bar{x}$, $\bar{y}$, and $\bar{z}$ color-matching functions could be applied, an essentially real-time completely accurate measurement of the chromaticity coordinates x and y could be made.

REFERENCES

1. I. Nimeroff and S. W. Wilson, J. Res. NBS 52, 195 (1954).

2. G. Wyszecki and W. S. Stiles, *Color Science: Concepts and Methods, Quantitative Data and Formulas* (John Wiley and Sons, Inc., New York, N.Y., 1967).

3. Armour Research Foundation, *Relationship Between Size and Shape of Dye Particles and the Color of Smoke*, Illinois Institute of Technology, Chicago, Illinois (1954). Available DDC-AD 84078.*

4. J. E. Moorhead, *Smoke Grenade Color and Density Meter System*, BAI Corporation, Stamford, Connecticut (1970). Available DDC-AD 882032.

5. L. R. Szabo, *The Smoke Chromacorder*, Technical Report 4671, Picatinny Arsenal, Dover, N.J. (1975). Available DDC-AD-B004826L.

6. A. Deiner, *M18 Colored Smoke Grenades. Color of Smoke and Munition Efficiency*, Technical Report ED-TR-75022, Edgewood Arsenal, Maryland (1975). Available DDC-AD-B008362L.

7. C. A. Lipscomb, *Navy Smoke Colorimeter*, RDTR No. 256, Naval Ammunition Depot, Crane, Indiana (1973). Available DDC-AD 915212L.

*Available DDC indicates that this document is available from Defense Documentation Center, Cameron Station, Alexandria, Virginia 22314

TABLE 1. CALIBRATION PAPER RESULTS

				Measured				Actual		
Color Designation		x	y	λ(nm)	Purity	x	y	λ(nm)	Purity
7.5 G	4/6	0.25	0.39	507	20	0.25	0.38	504	20
5 G	5/8	0.25	0.42	513	22	0.25	0.41	512	21
2.5 G	5/8	0.26	0.46	525	27	0.27	0.44	530	25
10 GY	6/10	0.30	0.49	547	44	0.31	0.49	551	48
2.5 GY	8/10	0.38	0.49	566	65	0.40	0.47	570	71
5 Y	7/10	0.44	0.48	575	79	0.45	0.47	576	79
2.5 Y	5/6	0.44	0.44	579	68	0.44	0.43	579	65
2.5 Y	6/8	0.45	0.45	579	74	0.45	0.44	579	71
2.5 Y	7/10	0.46	0.46	578	81	0.46	0.45	579	77
2.5 Y	8/12	0.46	0.46	578	80	0.46	0.46	579	81
7.5 YR	6/10	0.50	0.42	586	79	0.49	0.42	585	77
2.5 YR	6/6	0.44	0.37	589	50	0.42	0.36	590	41
2.5 YR	6/12	0.55	0.38	596	80	0.52	0.39	592	76
10 R	6/10	0.51	0.36	599	65	0.48	0.36	595	58
10 R	4/10	0.56	0.35	604	75	0.52	0.36	600	73
5 R	6/10	0.48	0.33	607	51	0.45	0.32	609	40
5 R	4/10	0.57	0.29	635	64	0.50	0.32	615	53
2.5 R	5/8	0.47	0.31	625	42	0.42	0.31	627	29

TABLE 2. STANDARD SMOKE COMPOSITIONS

M18 Yellow		M18 Green	
Yellow Dye	38.5	Green Dye	40.0
S	8.5	S	10.4
$NaHCO_3$	33.0	$NaHCO_3$	22.6
$KClO_3$	20.0	$KClO_3$	27.0

Mk 13 Marine Smoke and Illumination Signal

Orange Dye	60.2
$KClO_3$	18.9
Sugar	14.6
Graphite	1.5
Sil-O-Cel	4.8

TABLE 3. STANDARD SMOKE RESULTS

	x	y	λ(nm)	Purity
M18 Green	0.254	0.325	492	17
M18 Yellow	0.391	0.473	568	65
Mk 13 Orange	0.612	0.338	606	86

TABLE 4. EXPERIMENTAL SMOKE COMPOSITIONS

	Formula 1	Formula 2	Formula 3	Formula 4	Formula 5
$KClO_3$	28.0	27.5	27.0	26.5	26.0
Sugar	16.0	15.8	15.5	15.3	15.0
$NaHCO_3$	4.0	3.8	3.5	3.3	3.0
Sil-0-Cel	4.0	4.0	4.0	4.0	4.0
Indanthrene Golden Yellow	5.0	12.3	19.5	26.8	34.0
Benzanthrone	10.0	12.0	14.0	16.0	18.0
Solvent Green 3	33.0	24.6	16.5	8.1	---

TABLE 5. EXPERIMENTAL SMOKE RESULTS

Formula	x	y	λ(nm)	Purity
#1 Green	0.285	0.327	495	20
#2 75G/25Y	0.269	0.387	514	15
#3 50G/50Y	0.288	0.475	546	38
#4 25G/75Y	0.342	0.508	560	60
#5 Yellow	0.417	0.472	573	72

TO FAN

DENSITOMETER MODULE

COLOR MEASURING
MODULE

SHAPING CHAMBER

MIXING BAFFLES

SMOKE CANISTER DRAWER
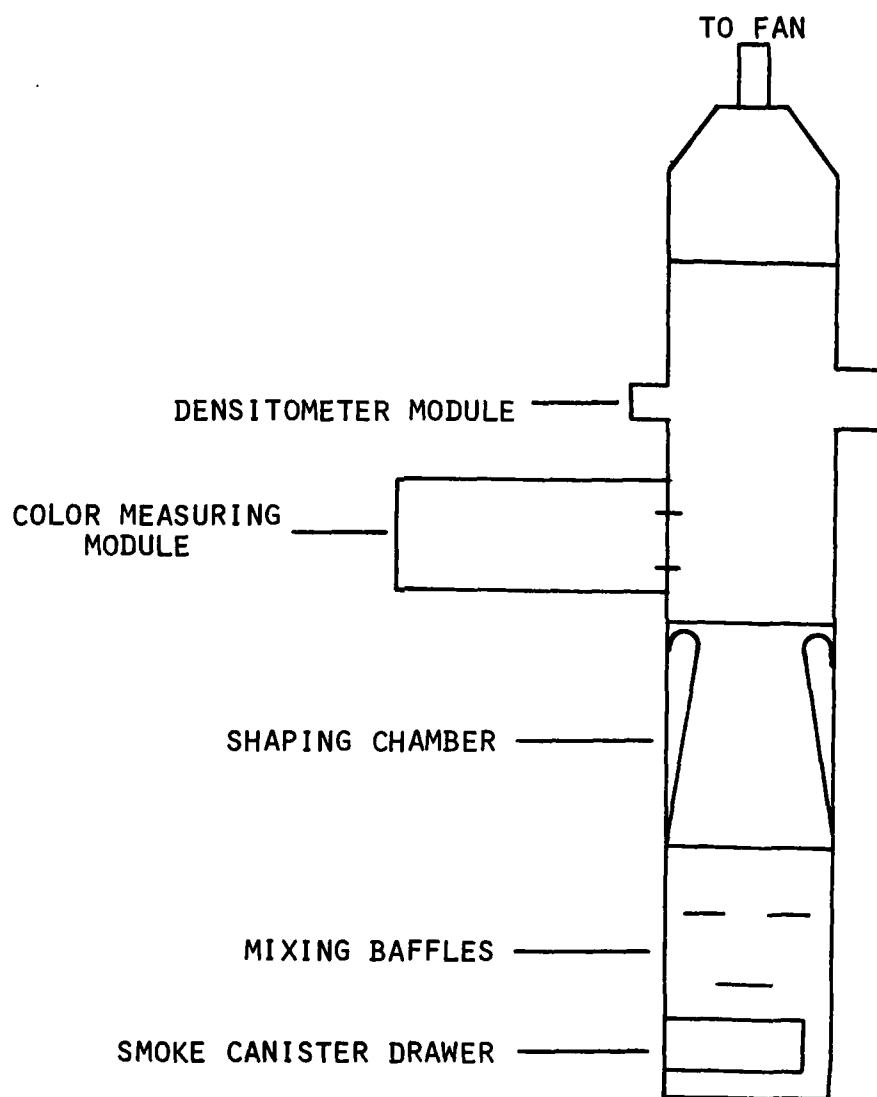
FIGURE 1. SMOKE COLORIMETER SCHEMATIC
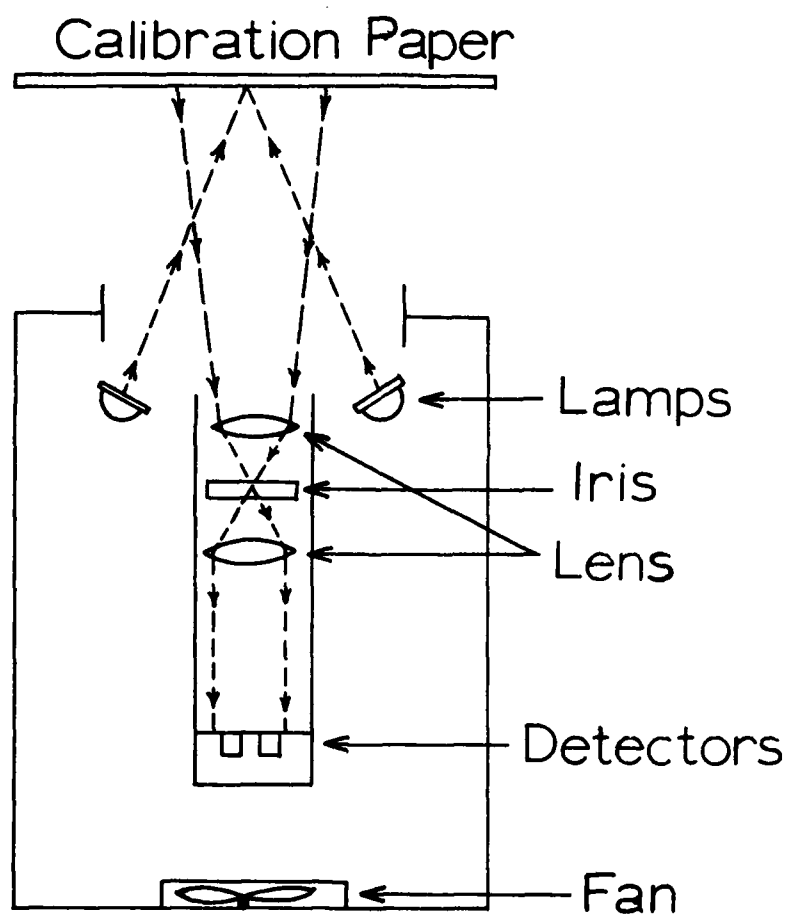
FIGURE 2. COLORIMETER OPTICAL SCHEMATIC
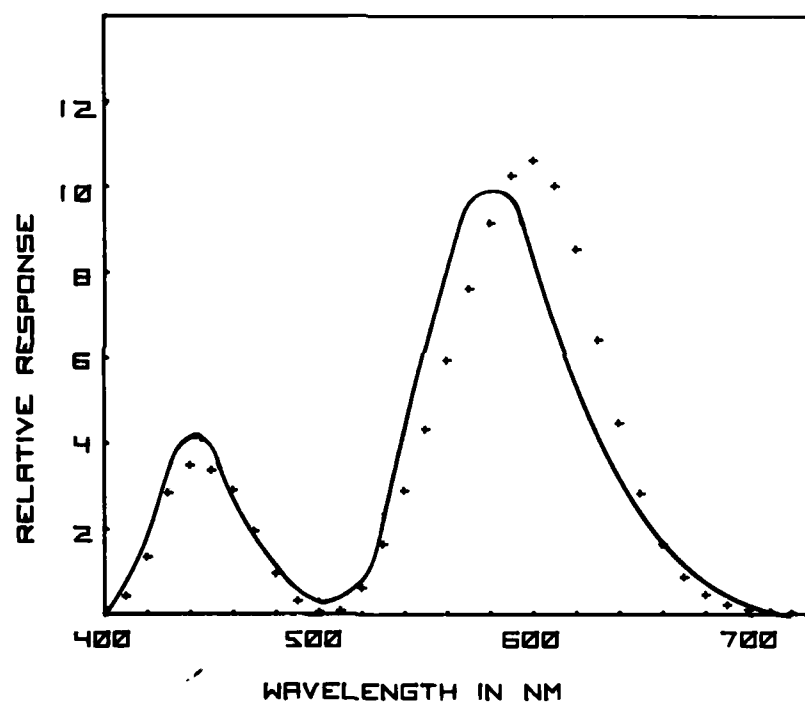
FIGURE 3. DETECTOR + FILTER RESPONSE - $\bar{x}$
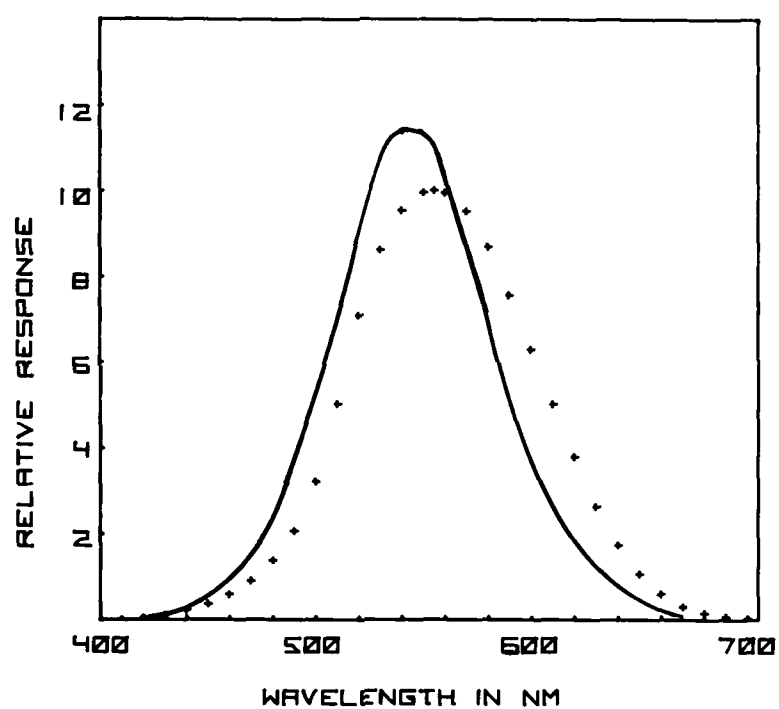
FIGURE 4. DETECTOR + FILTER RESPONSE - $\overline{Y}$
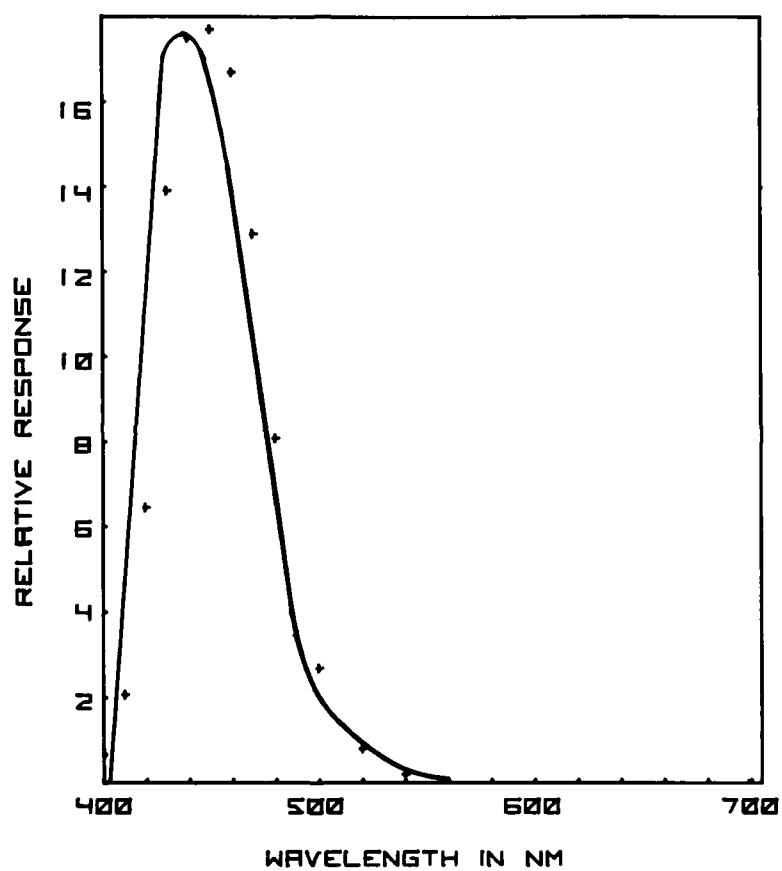
FIGURE 5. DETECTOR + FILTER RESPONSE - $\overline{z}$

584
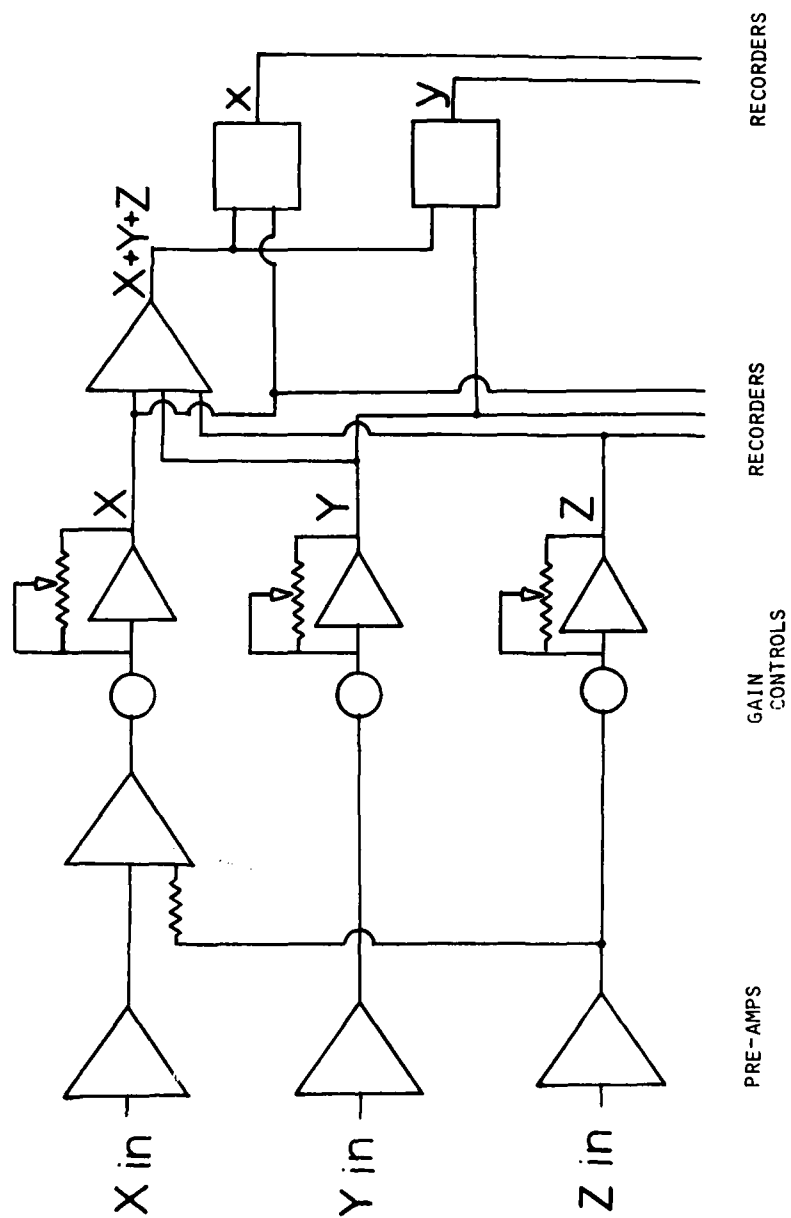
FIGURE 6. COLORIMETER ELECTRONICS
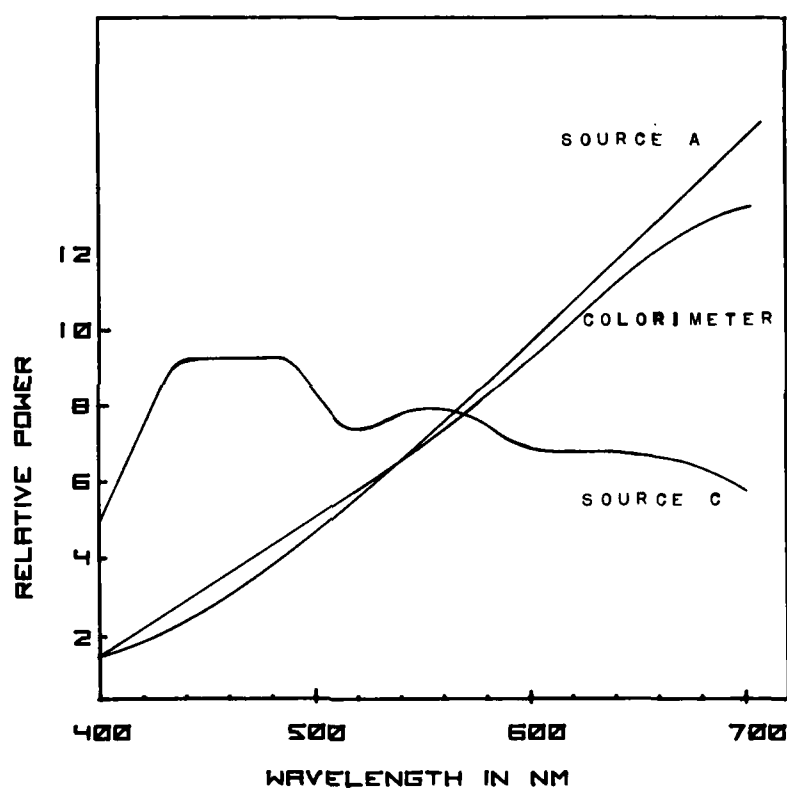
FIGURE 7. COMPARISON OF LIGHT SOURCES
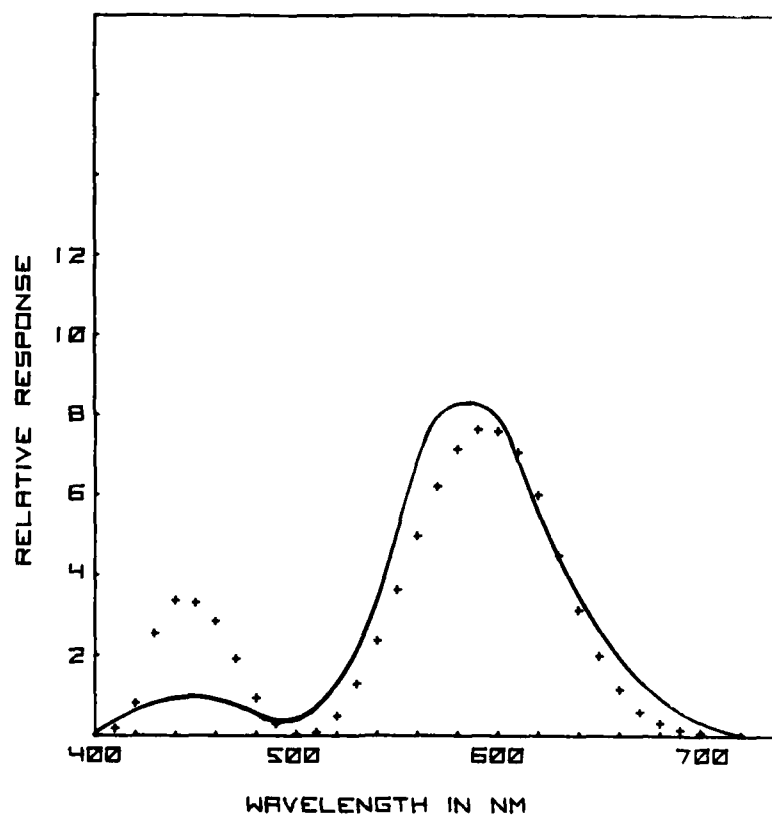
FIGURE 8. X RESPONSE TO WHITE PAPER STANDARD
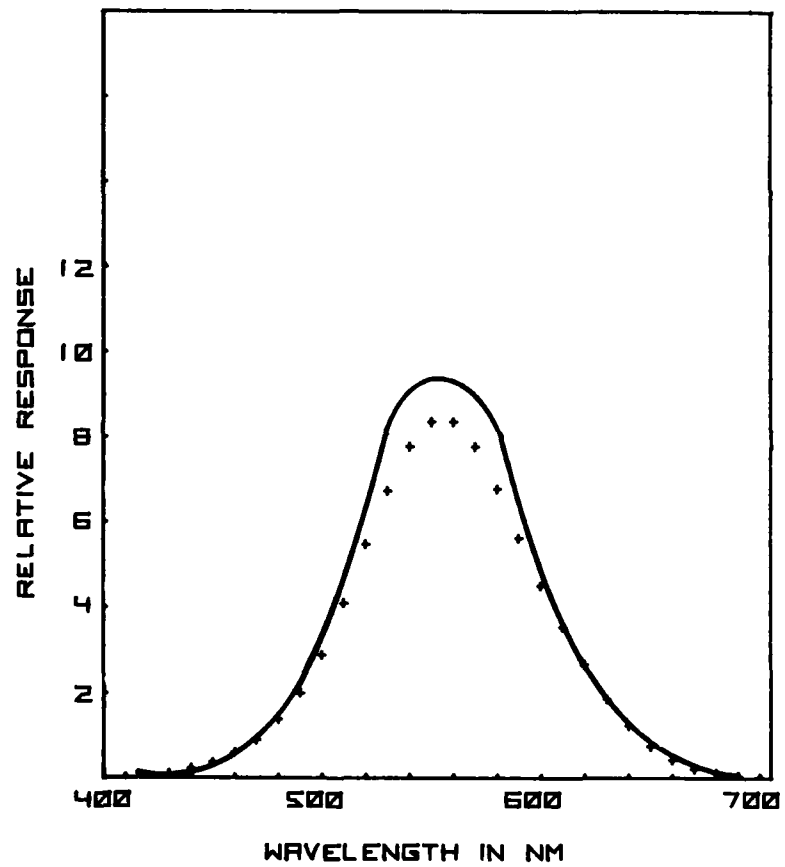
FIGURE 9. Y RESPONSE TO WHITE PAPER STANDARD
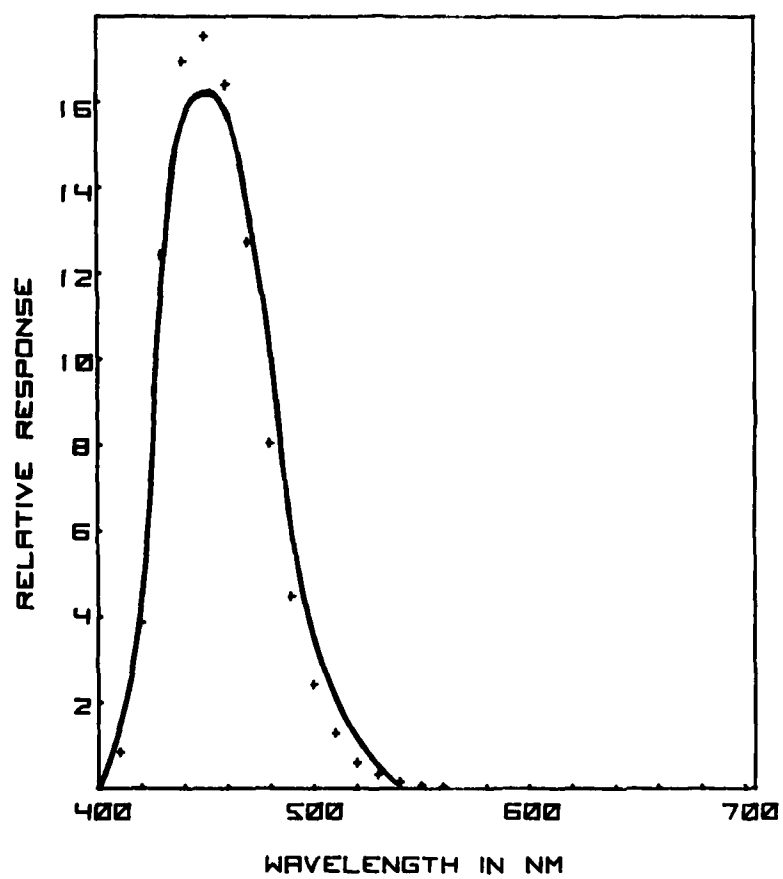
FIGURE 10. Z RESPONSE TO WHITE PAPER STANDARD
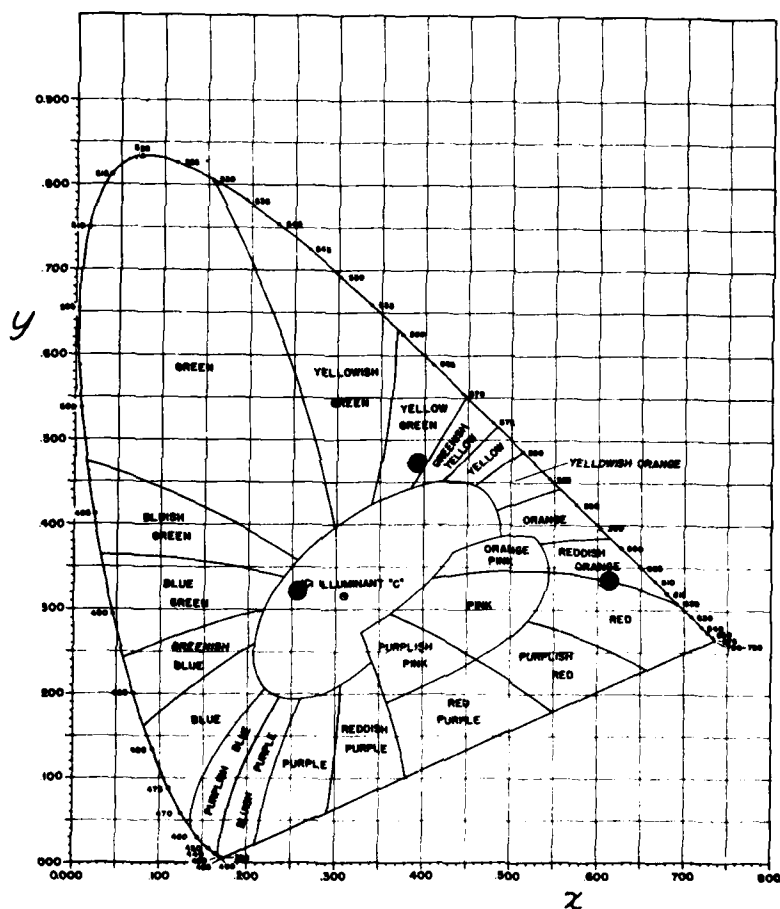
FIGURE 11. CHROMATICITY DIAGRAM - STANDARD SMOKES
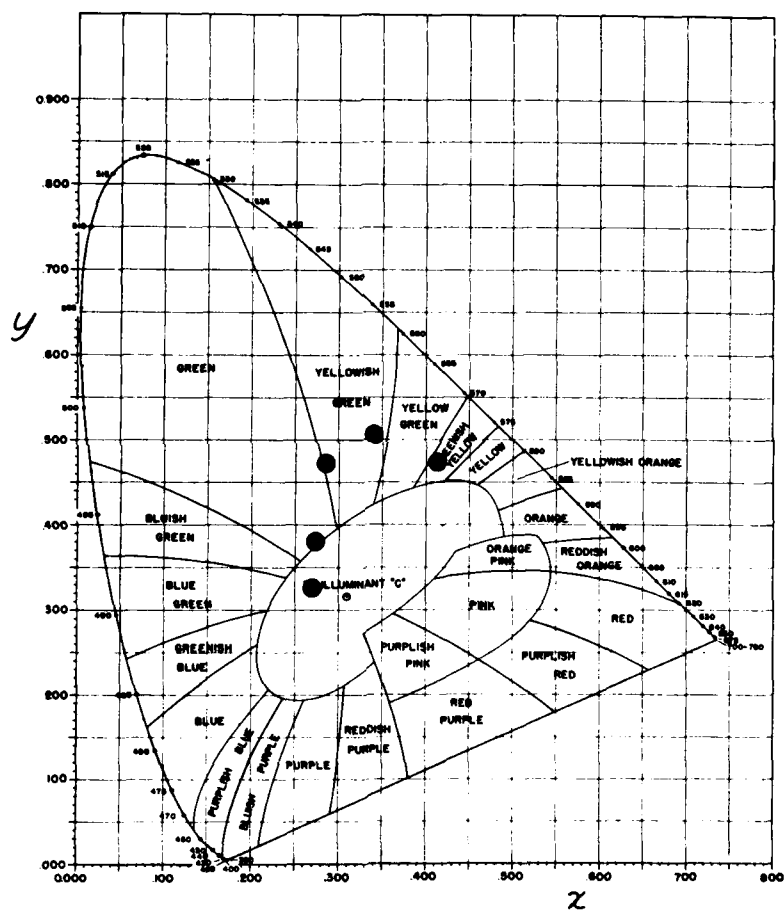
FIGURE 12. CHROMATICITY DIAGRAM - EXPERIMENTAL SMOKES

FLARES CONTAINING CALCIUM NITRATE AS AN OXIDIZER

H. A. Webster III and J. E. Tanner, Jr.
Applied Sciences Department
Naval Weapons Support Center, Crane, Indiana

ABSTRACT

Flares composed of magnesium, sodium nitrate, calcium nitrate, and boron in varying ratios were prepared and tested. Luminous efficiencies, spectral power curves, and color data are presented for various formulas. Although no improvements in luminous efficiency were observed, significantly higher luminous intensity was observed in some cases when magnesium-calcium nitrate-sodium nitrate were compared with standard magnesium-sodium nitrate formulas. The dominant wavelength and excitation purity were essentially the same in all cases except when pure calcium nitrate-magnesium formulas were used. A detailed analysis of the visible spectra from magnesium-calcium nitrate and magnesium-calcium nitrate-boron flares is given.

INTRODUCTION

During the past few years attempts have been made to produce illuminating flares whose spectral distributions were such that the resulting illumination was "white light". While many of the compositions tested produced white light, the luminous efficiencies were generally an order of magnitude less than the standard magnesium-sodium nitrate illuminating flare.[1] Preliminary results have been reported which indicate that when anhydrous calcium nitrate was partially substituted for sodium nitrate in a standard magnesium-sodium nitrate formula there was no loss in efficiency.[2] Similar results were obtained when calcium nitrate was substituted completely for sodium nitrate.[3] No attempt was made to optimize the formula or to measure the color of the emitted light. Since calcium-oxygen species, e.g. CaO, CaOH and Ca_2O_2, emit strongly in the blue, green and red regions of the spectrum, a flare with calcium nitrate as part of the oxidizer might provide a means of producing high intensity white light.[4,5]

The purpose of this report is to describe the experiments which were performed to test this hypothesis. In addition, an analysis of the visible emission spectra obtained will be presented.

EXPERIMENTAL

Flare Compositions

Based on the earlier results, the eight groups of flares listed in Table 1 were made. Flare groups WL29-WL32 were designed to test the effect of adding boron to the compositions containing calcium nitrate. Flare groups WL33-WL36 were designed to test the effect of adding calcium nitrate to a standard magnesium-sodium nitrate composition and to find the optimum calcium nitrate/sodium nitrate composition.

Except for the calcium nitrate, all the materials used in the manufacture of these flares were standard MIL-SPEC ingredients. All solid materials were dried prior to use. The calcium nitrate was obtained in the hydrated form, $Ca(NO_3)_2 \cdot 4H_2O$. The hydrated material was oven-dried under vacuum at 150°C for 24 hours. This procedure completely removes the waters of hydration without decomposing the calcium nitrate. The anhydrous calcium nitrate was then ground and sieved at -30 mesh under an inert nitrogen atmosphere.

The epoxy resin used for the binder was a mixture of Dow resins*: DER 321, 61.2 percent; DER 732, 26.3 percent and CS 3482.1, a polyamine hardener, 12.5 percent. This is a standard Mk 45 binder composition.

After mixing, the compositions were pressed into paper tubes 5.5 cm in diameter. Approximately 300 grams of composition were used in

---

*These names are trademarks of the Dow Chemical Company, Midland, Michigan.

TABLE 1. FLARE FORMULAS AND EXPERIMENTAL RESULTS

	WL29	WL30	WL31	WL32	WL33	WL34	WL35	WL36
Mg	45	35	35	45	58	58	58	58
B	10	15	15	5	--	--	--	--
$NaNO_3$	--	--	5	--	37	25	18	--
$Ba(NO_3)_2$	--	--	15	--	--	--	--	--
$Ca(NO_3)_2$	40	45	40	30	--	12	19	37
Epoxy	5	5	5	5	5	5	5	5
Candlepower (kcd)	311	269	351	166	222	265	299	210
Efficiency (cd-sec/g)	29200	33170	39850	21500	36800	33600	40500	31000
Burn Time (sec)	24.0	37.0	33.5	39.0	70.0	52.0	60.0	60.0
x	0.582	0.586	0.582	0.580	0.525	0.573	0.583	0.614
y	0.394	0.401	0.403	0.394	0.452	0.405	0.400	0.371
down λ	594	594	593	593	584	592	595	600
Purity	94	96	96	95	94	94	94	96

flare groups WL29-WL32 and 450 grams in groups WL33-WL36 for each candle. The flare compositions were consolidated at 7.03 x 10^6 kg/m^2 (10000 psi) pressing pressure.

Experimental Details

The flares were burned face down at a distance of four meters from the spectrographs. No attempt was made to isolate any specific area in the flame. Visible spectra were taken in the region from 400-700 nm with a 1.5 m grating spectrograph. This spectrograph has a 450 line/mm grating and gives a dispersion of 15 Å/mm in the first order. Kodak Linagraph Shellburst® film* was used for recording the spectra. The spectra were scanned and digitized on an Optronics S-2000 densitometer and the film density was converted to radiant and luminous power readings using the techniques described previously.[1]

Measurements of the candlepower were made with a silicon photodiode equipped with appropriate filters so that the filter plus detector response match the standard CIE eye response curve. The photodiode was calibrated prior to the experiments by measuring the known value of candlepower from an NBS traceable standard 1000 watt quartz-iodine lamp. The output signal of the photodiode was integrated with a precision integrator to obtain an average candlepower reading. Integration was started three seconds after ignition and stopped approximately three seconds before the flare burned out.

Results

The results of this work are summarized in Table 1. This table gives the average values of candlepower, burn time, luminous efficiency, color coordinates, dominant wavelength, and purity for all flares tested. The values quoted are averages of 7-10 different flares. The average experimental error in candlepower and efficiency is ±5 percent.

The values of the chromaticity coordinates, x and y, were calculated by applying the color-matching functions, $\bar{x}$, $\bar{y}$, and $\bar{z}$, to the radiant power spectra at 1.0 nm intervals and integrating the area under the curve to obtain the tristimulus values X, Y and Z. The chromaticity coordinates were then obtained using the expressions

$$x = \frac{X}{X+Y+Z}$$

and

$$y = \frac{Y}{X+Y+Z}$$

---

*Linagraph Shellburst is a registered trademark of the Eastman Kodak Co., Rochester, New York.

The values of dominant wavelength and purity are determined by the standard graphical method after plotting the chromaticity coordinates on a chromaticity diagram.[6] The average experimental error in the values of x and y is ±2 percent.

The relative radiant and luminous power spectra for each flare group are plotted in Figures 1-16. The luminous power spectrum is obtained by applying the CIE color-matching function, $\bar{y}$, to the radiant power spectrum. The area under the luminous power curve is then directly proportional to the candlepower. In order to show as much detail as possible, each spectrum is normalized to a value of one at its maximum. The spectra which are shown were selected as being representative of the flare group. The criteria used for this selection was to choose the spectrum which had chromaticity coordinates the same as the average value presented in Table 1. It should be pointed out that none of the spectra within a given flare group differed significantly from the ones presented.

DISCUSSION

General Observations

Substitution of $Ca(NO_3)_2$ for $NaNO_3$

The results of this work are in general agreement with previously reported work. A one hundred percent substitution of calcium nitrate for sodium nitrate reduces candlepower, burn time, and efficiency. The substitution of fifty percent calcium nitrate for sodium nitrate (flare group WL35) significantly increases the candlepower but the composition burns faster. The overall effect is a small increase in efficiency. The substitution of twenty-five percent calcium nitrate does not significantly affect the efficiency. Within the measurement limits of these experiments, there is no change in efficiency except when pure calcium nitrate is used as the oxidizer.

The dominant wavelength shifts to longer wavelength as calcium nitrate is substituted for sodium nitrate. The flares containing only calcium nitrate, WL36, have a dominant wavelength of 600 nm and are reddish orange in color while the sodium nitrate flares, WL33, have a dominant wavelength of 584 nm and are yellowish white. The flares containing mixtures of sodium nitrate and calcium nitrate have dominant wavelengths of 592 and 595 nm which fall between those of the flares containing only the pure oxidizer. There is no decrease in the excitation purity and these flares appear to be yellowish white and indistinguishable from the sodium nitrate flare.
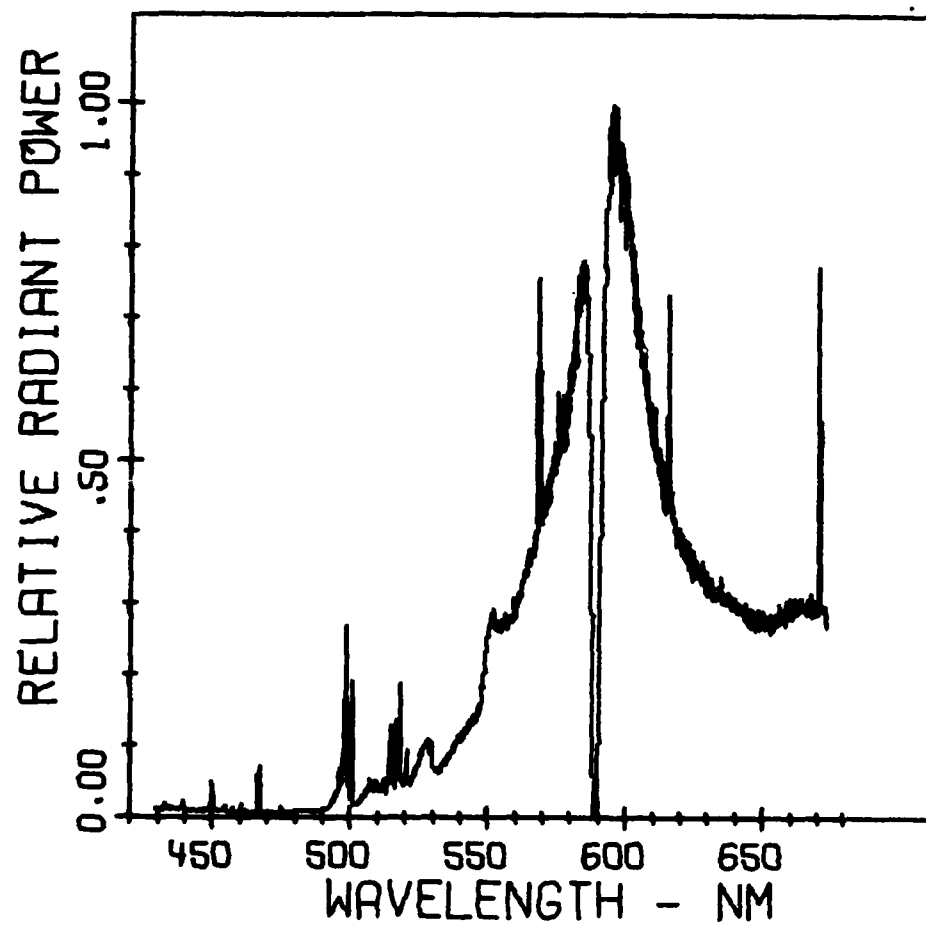
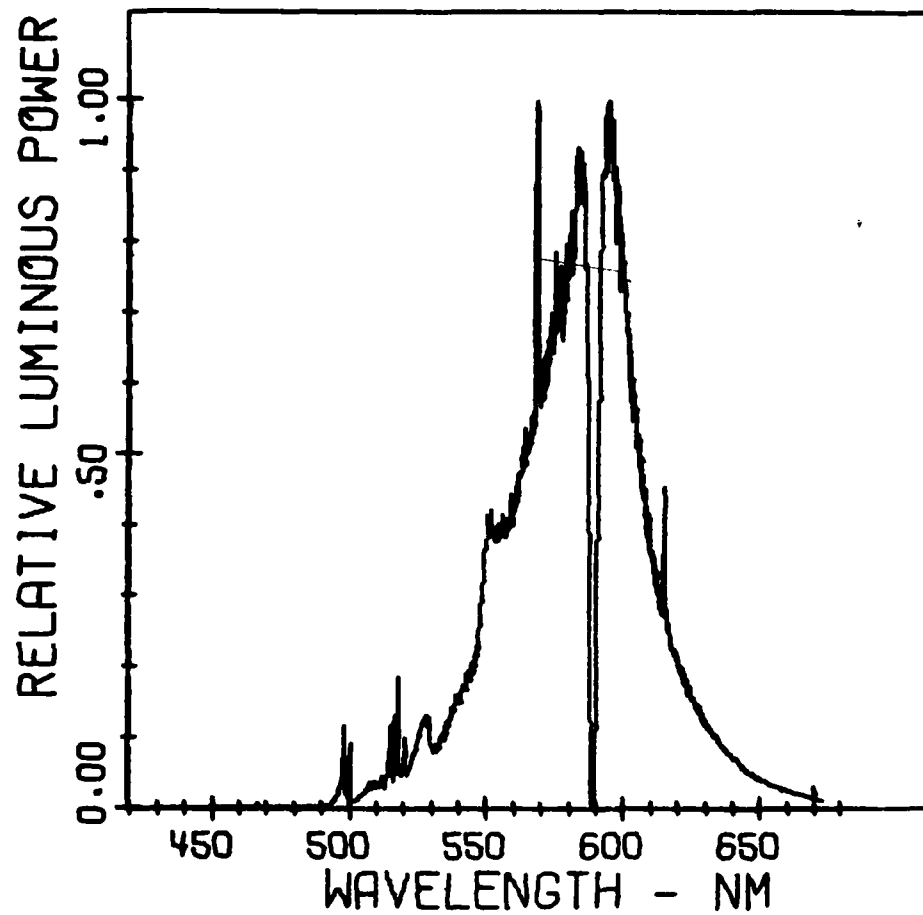Figure 1.   Radiant Power -- Group WL33

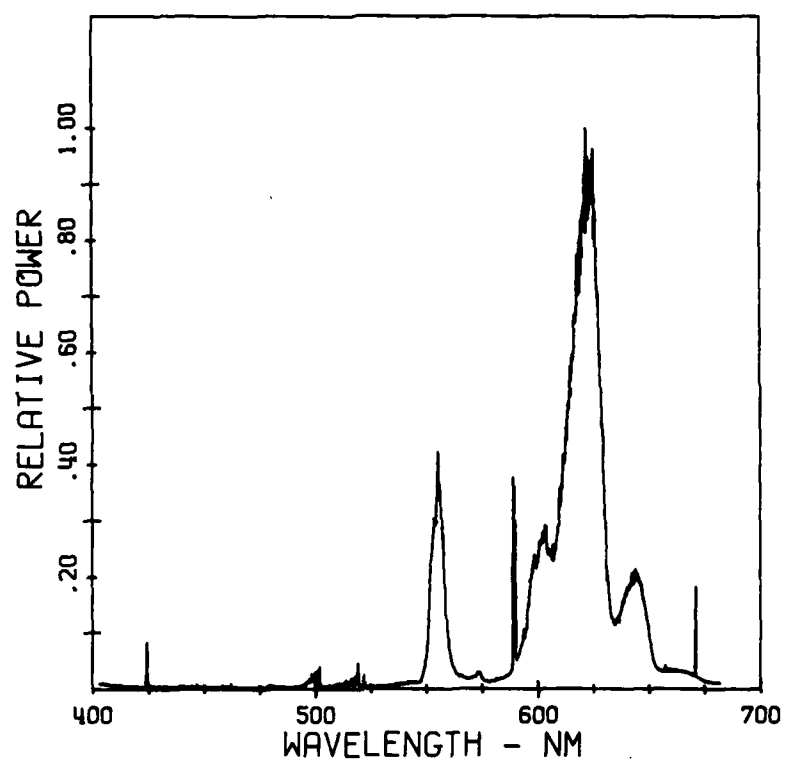Figure 2.   Luminous Power -- Group WL33
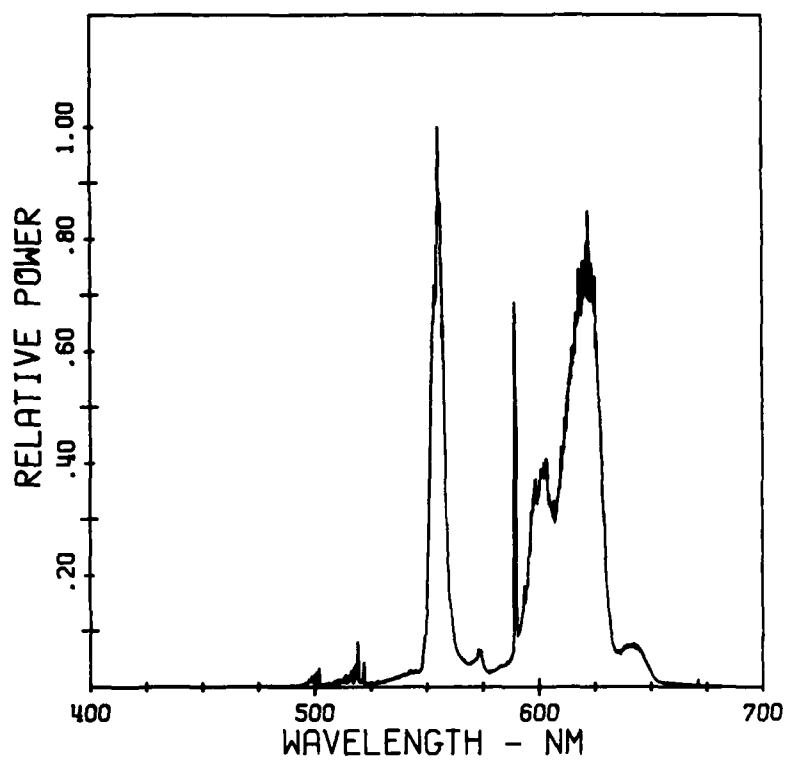
Figure 3.   Radiant Power -- Group WL36

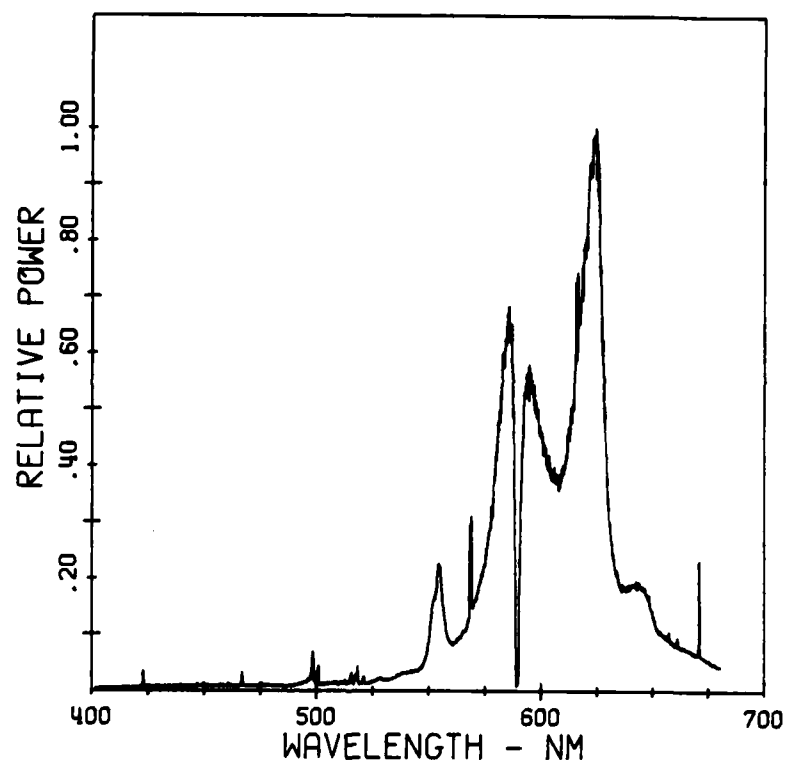Figure 4. Luminous Power -- Group WL36

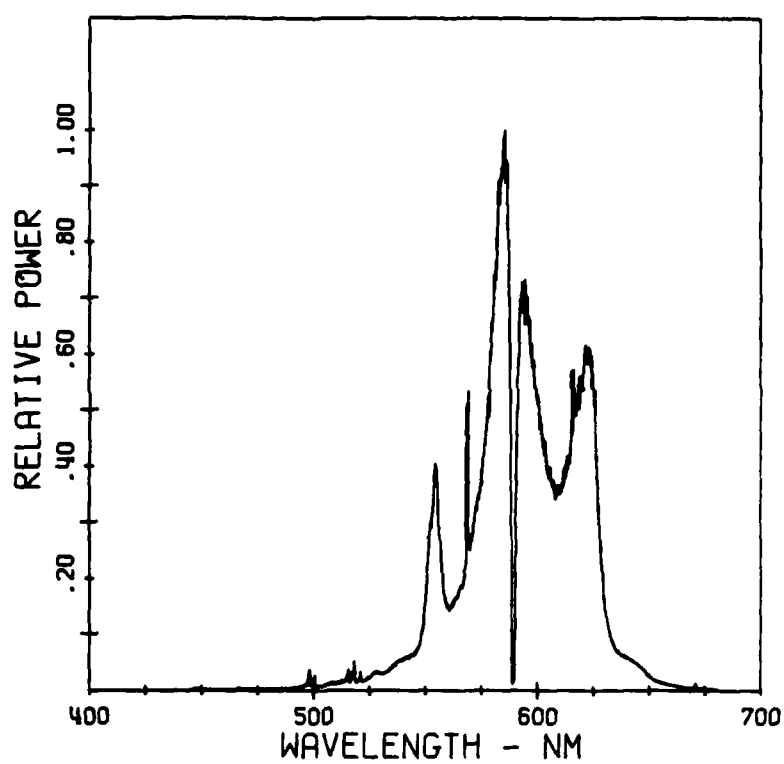Figure 5.   Radiant Power -- Group WL35
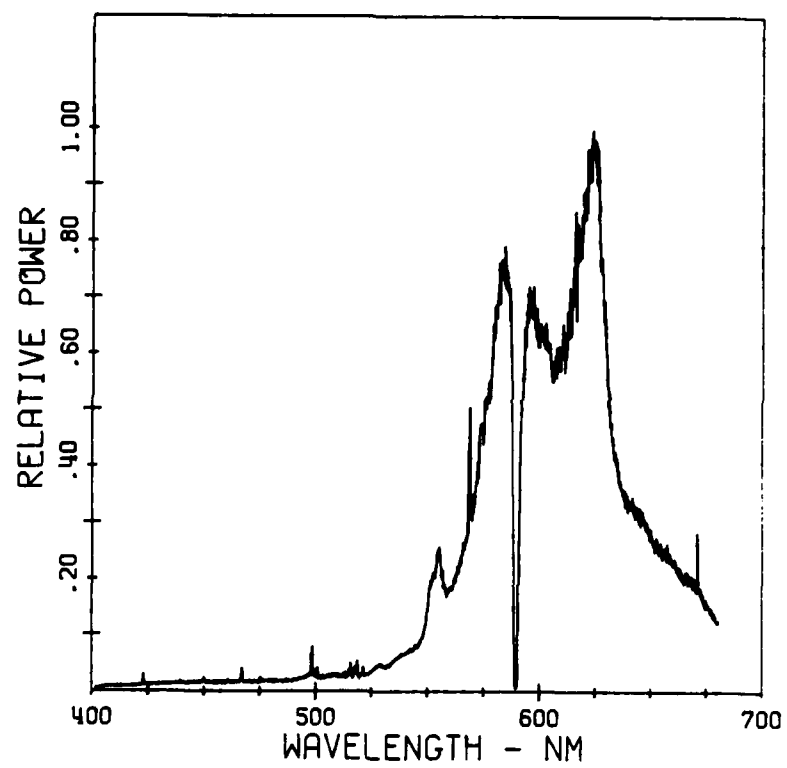
Figure 6. Luminous Power -- Group WL35
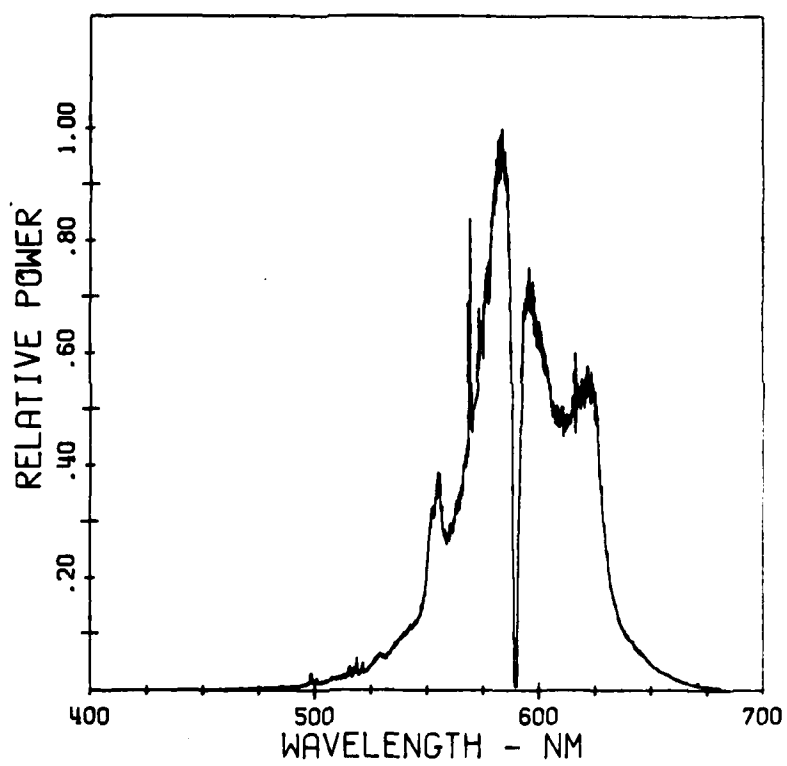
Figure 7.   Radiant Power -- Group WL34
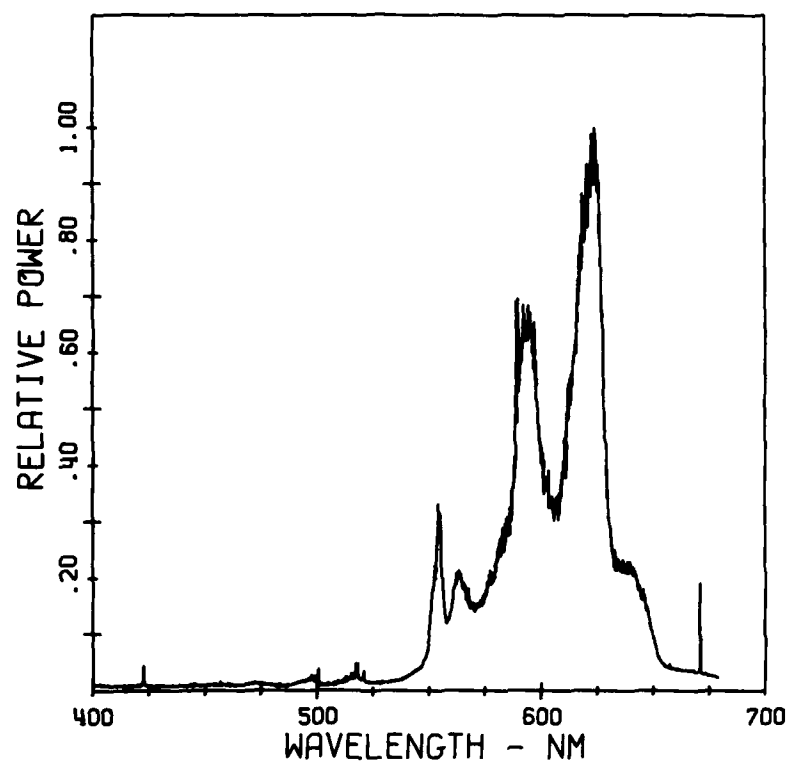
Figure 8. Luminous Power -- Group WL34

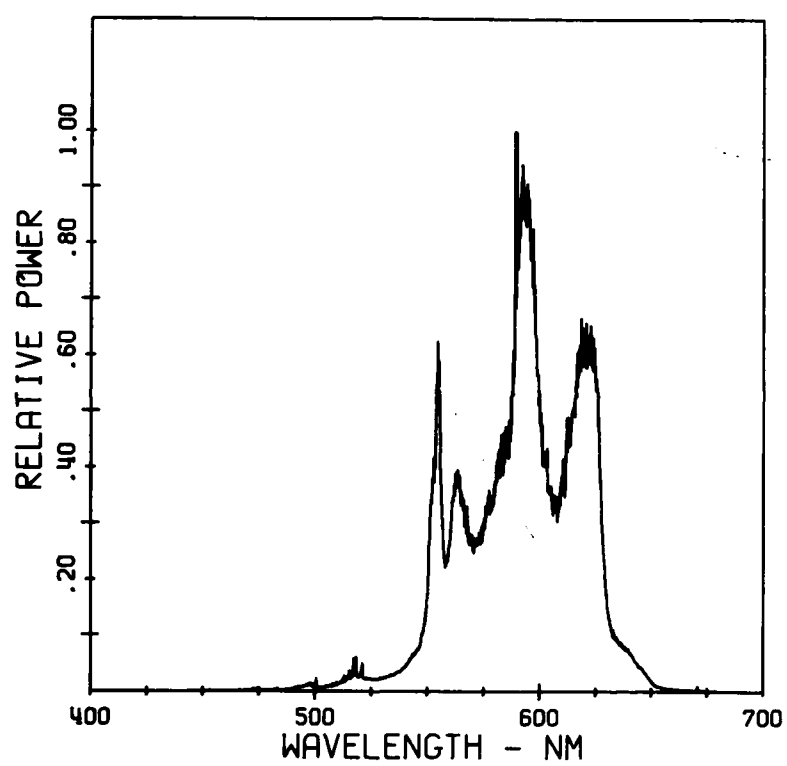Figure 9. Radiant Power -- Group WL29

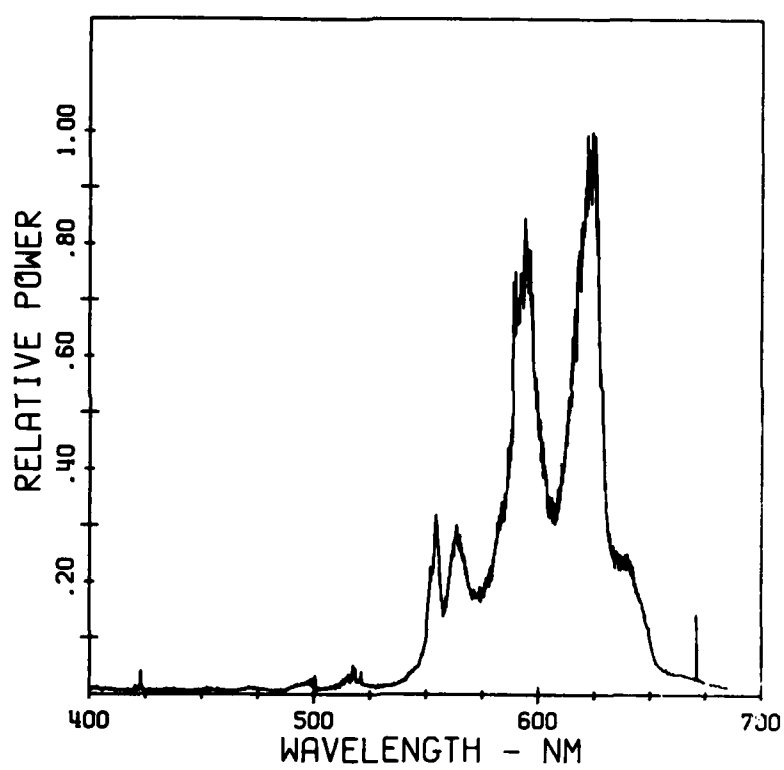Figure 10.   Luminous Power -- Group WL29

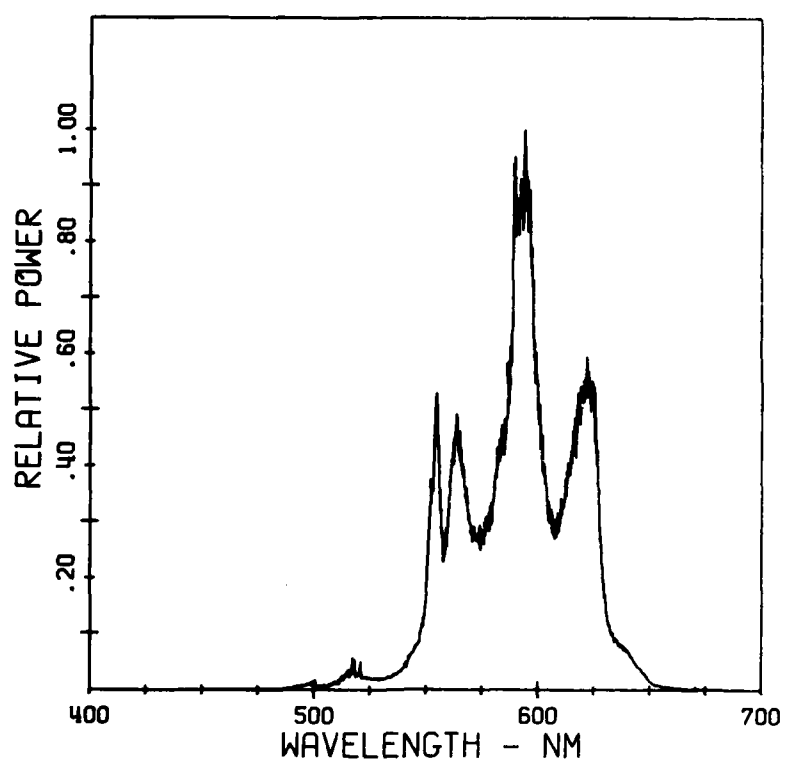Figure 11.   Radiant Power -- Group WL30
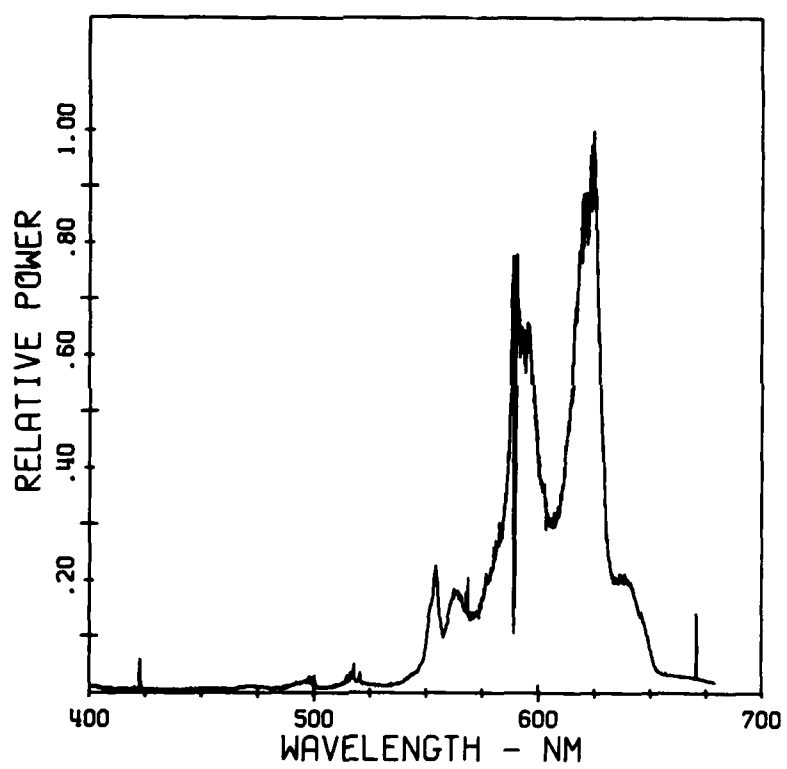
Figure 12.   Luminous Power -- Group WL30

Figure 13.   Radiant Power -- Group WL31
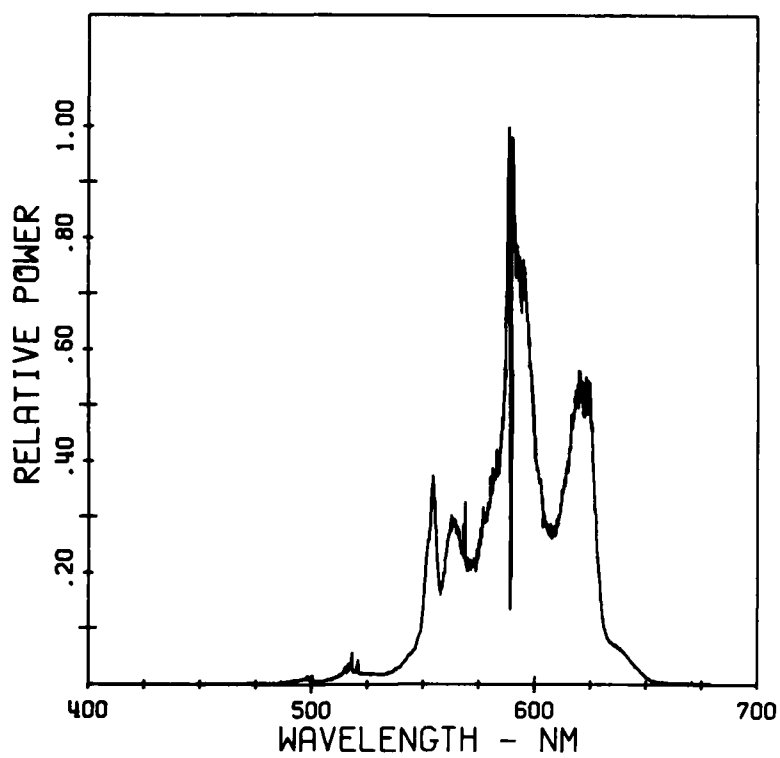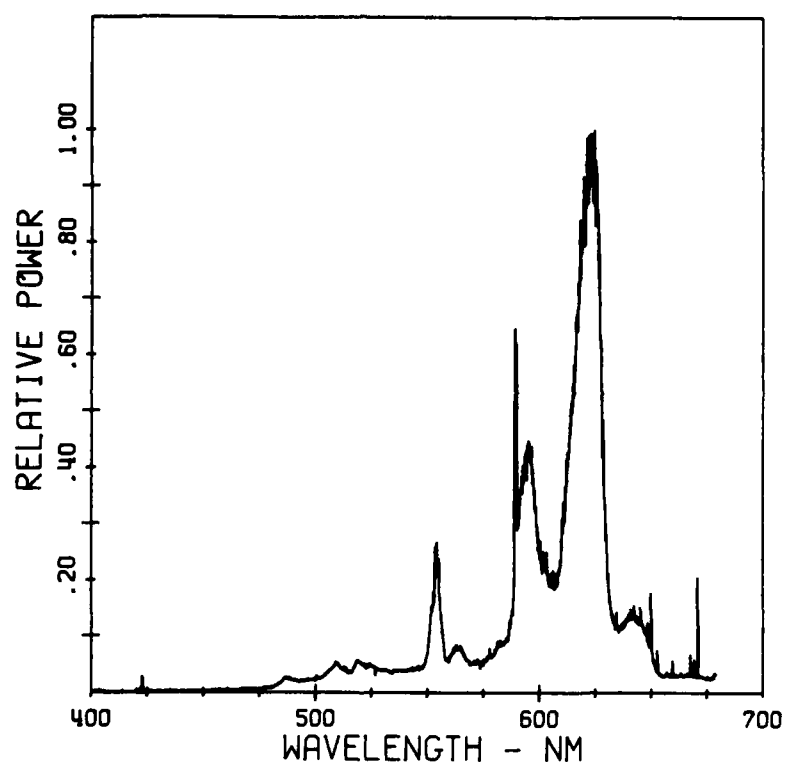
Figure 14.   Luminous Power -- Group WL31

Figure 15.   Radiant Power -- Group WL32
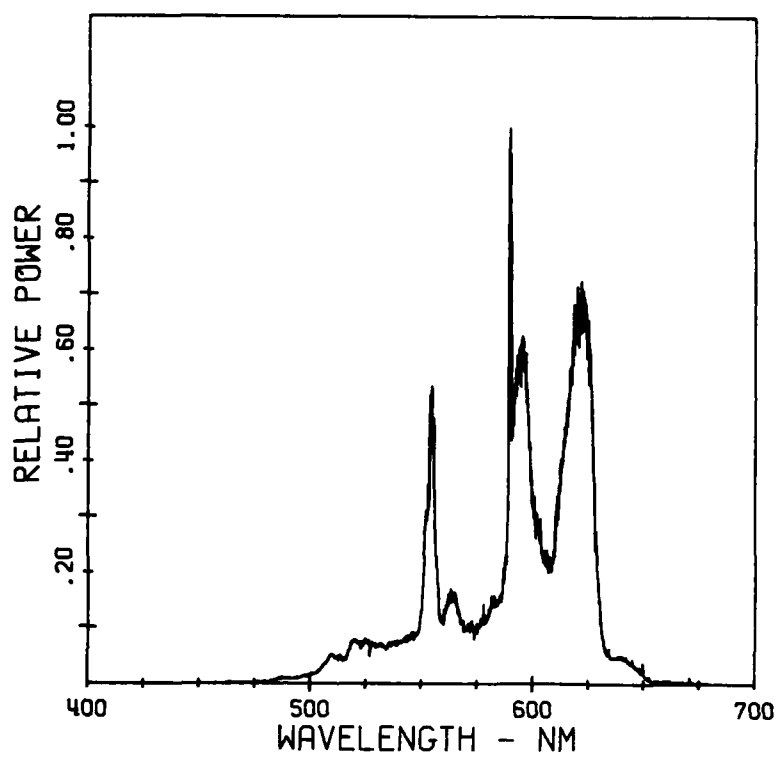
Figure 16.   Luminous Power -- Group WL32

Addition of Boron

The addition of boron at the ten and fifteen percent level in a flare containing only calcium nitrate as the oxidizer does not significantly change the efficiency. The boron-calcium nitrate-sodium nitrate flares, WL31, show significant increases in candlepower compared to standard illuminating flares while burning much faster. The overall effect is a slight increase in efficiency.

The substitution of barium nitrate for calcium nitrate in a boron-calcium nitrate flare greatly reduces the candlepower and the efficiency. The same effect is seen when barium nitrate is substituted for sodium nitrate in a standard illuminating flare. The intensity of barium oxide emission is remarkably less than that of most of the other molecular species.

The addition of boron to a calcium nitrate flare shifts the dominant wavelength to shorter wavelength as one would expect. The dominant wavelength of 594 nm obtained is the same as the dominant wavelength obtained when mixtures of calcium nitrate and sodium nitrate are used as oxidizers. The excitation purity of the boron-calcium nitrate flares is still very high and the flares appear to be yellowish white in color. The color is indistinguishable from the magnesium-sodium nitrate flares.

Analysis of the Spectra

The relative radiant and luminous power spectra for a standard magnesium-sodium flare, WL33, are shown in Figures 1 and 2. These spectra have been discussed and analyzed in great detail in earlier reports.[7,8] For this reason, no detailed discussion will be given. The prominent features are the MgO emission at 500.7 nm, the sodium doublets at 568 nm and 615 nm and the broadened resonance line emission centered at 590 nm.

The relative radiant and luminous power spectra for a magnesium-calcium nitrate flare, WL36, are shown in Figures 3 and 4. The emission features in these spectra are essentially all from molecular species. The emission at 500.7 nm is due to MgO. Emission from the CaO $B^1\Sigma \rightarrow X^1\Sigma$ is observed from 420 nm to 450 nm. This emission is much weaker than any other emission in the system and does not show in the normalized spectra. Spectra taken in the infrared region, 720 nm to 840 nm, show the CaO $A^1\Sigma \rightarrow X^1\Sigma$ system.

The most prominent features in the calcium nitrate spectra are the band emissions at 555 nm, 573 nm, 604 nm, 623 nm and 642 nm. These emission features are due primarily to CaOH.[4] The bands overlap another band system due to a diatomic calcium oxide species, Ca_2O_2. The strong emission at 623 nm is the emission primarily responsible for the reddish orange color observed in the calcium nitrate flare. Atomic emission from calcium is observed at 423 nm, from sodium at 589 nm and from lithium at 671 nm.

Figures 5 and 6 and Figures 7 and 8 show the changes which result from the addition of sodium nitrate to a magnesium-calcium nitrate flare. In Figure 5, flare group WL35, the ratio of sodium nitrate to calcium nitrate is approximately one to one and the CaOH emission at 623 nm is still the overriding feature. The broadened sodium resonance lines centered at 589 nm are the emissions which shift the dominant wavelength to a shorter wavelength.

In Figure 7, flare group WL34, the ratio of sodium nitrate to calcium nitrate is two to one and the emissions from sodium at 589 nm contribute more than the CaOH emission at 623 nm and the dominant wavelength again shifts to shorter wavelength. The absence of any emission in the blue and green regions of the spectrum accounts for the very high excitation purities which were observed.

The effect of adding boron to a magnesium-calcium nitrate flare is shown in Figures 9 and 10, flare group WL29, and Figures 11 and 12, flare group WL30. The emission features at 555 nm, 623 nm and 642 nm are again due to CaOH. Emission at 462 nm and 475 nm is very weak but present and is due to the $A^2\Pi \rightarrow X^2\Sigma$ BO $_x$ system.[4] As in the case of CaO, these emissions are too weak to be shown on the normalized spectra.

Emission from a boron species is observed at 541 nm, 565 nm and 590 nm. These bands are possibly the "boric acid fluctuation bands" at 545 nm and 580 nm which are attributed to BO_2 overlapped by some BO bands.[4] The discrepancy in wavelengths and the absence of some of the other fluctuation bands makes this assignment tentative at best. Spectra taken of flares composed of magnesium, barium nitrate, and boron do not appear to show these bands. This result could mean that the strong emissions at 565 nm and 590 nm are previously unreported emissions from a boron-calcium interaction.

Figures 13 and 14, flare group WL31, show the effect of adding a small amount of sodium nitrate, 5 percent by weight, to the magnesium-boron-calcium nitrate formula. Since the sodium concentration was low, the resonance lines at 589 nm are broadened less than in a standard magnesium-sodium nitrate flare. This behavior is in good agreement with the results predicted by the radiative transfer model.[8] All the other calcium and boron oxide features are still present.

Figures 15 and 16 show the relative radiant and luminous power spectra of flare group WL32 in which barium nitrate was added to a magnesium-boron-calcium nitrate flare. In these spectra BaO emission is observed at 480 nm, 510 nm and 520 nm. The red BaO system is probably masked by the CaOH emission. It should be noted that while the boron concentration was only 5 percent by weight in this formula, the anomalous boron bands at 565 nm and 590 nm are still reasonably strong. This observation tends to substantiate a possible boron-calcium interaction. Even though there is now increased emission in the green spectral region, it is not strong enough to override the red emission and the excitation purity does not change.

CONCLUSIONS

The addition of calcium nitrate to a standard magnesium-sodium nitrate formula does not decrease the luminous efficiency significantly. The dominant wavelength shifts to longer wavelength and the excitation purity remains constant. Molecular emission from CaOH at 555 nm and 623 nm make up the bulk of the luminous output.

The addition of boron to a magnesium-calcium nitrate composition significantly increases the candlepower output but causes the flare to burn much faster. The overall result is a slight reduction in efficiency. Molecular emission from CaOH at 555 nm and 623 nm and molecular emission from a boron species, possibly BO_2, at 565 nm and 590 nm make up the bulk of the emission. The assignment of the boron emissions at 565 nm and 590 nm to BO_2 is tentative since (1) these bands are not at the same wavelengths as those generally attributed to BO_2 and (2) these bands are not apparently present in flares containing only magnesium, boron and barium nitrate. It is possible that these bands are due to a calcium-boron interaction.

The excitation purity of magnesium-boron-calcium nitrate flares is high and the color is yellowish white. The substitution of small amounts of barium nitrate for calcium nitrate in these compositions significantly reduces both the candlepower and efficiency. The green BaO emission bands are present but weak and do not substantially change the excitation purity. None of the formulas tested produced white light.

REFERENCES

1. H. A. Webster and C. W. Gilliam, *Spectral Characteristics of Flares Containing Sodium Iodate as an Oxidizer*, RDTR No. 276, Naval Ammunition Depot, Crane, IN (April 1974). Available DDC-AD 782510.*

2. J. E. Tanner, C. E. Dinerman, and H. A. Webster, *Effect of Barium and Calcium on Illuminating Flare Performance*, RDTR No. 281, Naval Ammunition Depot, Crane, IN (September 1974). Available DDC-AD 923559.

3. D. Hart and H. J. Eppig, *Long Range Research on Pyrotechnics: Burning Characteristics of Binary Mixtures*, Technical Report No. 1669, Picatinny Arsenal, Dover, NJ (October 1947).

4. R. W. B. Pearse and A. G. Gaydon, *The Identification of Molecular Spectra, Third Edition* (Chapman and Hall, Ltd, London, 1965).

5. R. M. Blunt, *Evaluation of Processes Occurring in Pyrotechnic Flames*, RDTR No. 91, Naval Ammunition Depot, Crane, IN (March 1967). Available DDC-AD 655820.

6. G. Wyszecki and W. S. Stiles, *Color Science: Concepts and Methods, Quantitative Data and Formulas* (John Wiley and Sons, Inc., NY, 1967).

7. H. A. Webster, *Alkali Metal Emitters: I. Analysis of Visible Spectra*, NWSC/CR/RDTR-16, Naval Weapons Support Center, Crane, Indiana (1975). Available NTIS-AD-A019367.**

8. B. E. Douda, *Radiative Transfer Model of a Pyrotechnic Flame*, RDTR No. 258, Naval Ammunition Depot, Crane, Indiana (1973). Available DDC-AD 769273.

---

*Available DDC indicates that this document is available from Defense Documentation Center, Cameron Station, Alexandria, Virginia 22314.

**Available NTIS indicates that this document is available from National Technical Information Service, 5285 Port Royal Road, Springfield, Virginia 22161.

THE EFFECT OF PARTICLE SIZE-SURFACE AREA AND OXYGEN ON THE HYDROGEN CONTENT OF TITANIUM HYDRIDES

R. F. Salerno and R. S. Carlson

Monsanto Research Corporation
Mound Laboratory*
Miamisburg, Ohio 45342

ABSTRACT

Hydrogen stoichiometry of powdered titanium hydrides appears to be directly affected by the particle size-surface area distribution and oxygen associated with each particle.

Titanium hydride powders were classified into narrow particle size fractions and analyzed for oxygen and hydrogen. It was found, as suspected, that high surface area particles contained lower hydrogen-to-oxygen ratios than the lower surface area particles of the hydrides investigated.

INTRODUCTION

The study of titanium hydride in the past has usually dealt with titanium hydride prepared from magnesium-reduced titanium in the form of plate, foil, sponge, chips, and/or powders having lower oxygen content and surface area. The purpose of hydriding titanium usually is associated with the preparation of titanium powder for commercial use in alloying, as the titanium hydride is brittle and easily ground to fine powder.

In recent years titanium hydride has provoked the interest again of the pyrotechnist, and the need for a reliable titanium hydride fuel is evident. As in the past, the pyrotechnist of today has been plagued with titanium hydride fuels which are unreliable. Recently, however, some of the inherent properties of titanium hydride powder fuels are unfolding. One area of interest is the relationship of hydrogen solubility in high surface area titanium powder with high oxygen

content. A literature search showed little concerning this relationship (i.e., in high surface area titanium powders). Therefore an investigation was launched to determine whether the solubility of hydrogen in titanium powders is affected by high surface area and impurities such as oxygen.

THEORY

Investigations of titanium-hydrogen systems have obtained information of effects on the equilibrium of titanium-hydrogen systems from common impurities found in commercially available magnesium-reduced titanium. For example, Gibb and Kruschwitz[1] studies depict temperature/hydrogen concentration of high purity titanium (Van Arkel titanium) compared to commercial magnesium-reduced titanium (Figure 1). Impurities such as oxygen and nitrogen are discussed as retarding attainment of equilibrium and generally displace it in the direction of lower hydrogen content. Comparisons were difficult due to impurities stabilizing certain phases while other impurities stabilize other phases. It was shown that the system must be considered not as a binary system, but as a multicomponent system. The displacement of hydrogen in these systems would be consistent with the interstitial solution concept; i.e., occupance of interstitial sites by impurity atoms and electrons changes or reduces the solubility potential of hydrogen in the crystal lattice. From the above guidelines a study was undertaken to determine whether a correlation exists among the solubility of hydrogen, the surface area, and impurity distribution found in titanium hydride powder.

EXPERIMENTAL PROCEDURE

This paper deals specifically with the apparent hydrogen, oxygen/surface area relationship in titanium powders. The titanium hydride powder used in this study was commercially prepared by Alfa Ventron Corp. The composition and average surface area are given in Table 1.

The titanium hydride powder was classified into four particle size fractions using a Bakco Micro-particle classifier (Figure 2). This classifier is a combination air centrifuge-elutriator consisting of a brush feed system and rotor assembly driven by a 1-Hp, 220-V, 3-phase motor. The motor operates at 3500 rpm creating precisely controlled air velocities with the air spiral and sifting chamber of the centrifuge. The principle of operation is as follows: a sample is

introduced into the spiral-shaped air current flowing towards the center. The spiral current of air having tangential and radial velocities separates the particles according to size, form, and weight.

Table 1

CHEMICAL ASSAY OF TITANIUM HYDRIDE $TiH_{1.92}$ POWDER

Element	Amount (wt %)
Sn	<0.005
B	0.005
Si	0.01
Fe	0.01
Al	0.01
Mn	<0.005
Mg	<0.005
Cr	<0.005
Ni	0.01
Cu	<0.005
Zr	0.01
Pb	0.005
Cd	<0.01
Na	0.02
H	3.84
O	2.0
N	0.4

Average Surface Area 3.98 m^2/g

A list of chemical analysis performed and methods of analysis used for titanium hydride powder fractions are given in Table 2.

Table 2

CHEMICAL AND METHOD OF ANALYSIS

Type Analysis	Method of Analysis	Equipment
Hydrogen	Combustion Decomposition	Perkin-Elmer Elemental Analyzer
Oxygen	Neutron Activation	Neutron Generator
Nitrogen	Neutron Activation	Neutron Generator
Other Impurities	Emission Spectrometry	Spark Emission Spectrometer
Surface Area	Gas Adsorption	Gas Adsorbtometer

RESULTS

As previously mentioned the material used for this investigation was titanium hydride ($TiH_{1.92}$) powder purchased from Alfa Ventron Corporation. The material was blended and sampled randomly to ensure that the sample taken was representative. The sample was then blended and classified into five fractions using the Bahco particle classifier. The fractions were analyzed for impurities and surface area (Table 3).

Table 3

CHEMICAL ASSAY OF FRACTIONED TITANIUM HYDRIDE

Composition	Fraction (wt %)			
	1	2	3	4
H_2	3.53	3.72	3.80	3.83
O_2	3.98	2.53	1.42	0.97
Sn	0.009	0.007	0.006	0.006
B	<0.005	<0.005	<0.005	<0.005
Si	0.15	0.04	0.01	0.01
Fe	0.15	0.10	0.03	0.03
Al	0.15	0.05	0.02	0.01
Mn	<0.005	<0.005	<0.005	<0.005
Mg	0.01	0.005	<0.005	<0.005
Cr	0.006	<0.005	<0.005	<0.005
Ni	0.1	0.01	0.02	0.02
Cu	0.008	0.005	≤0.005	≤0.005
Zr	0.01	0.01	0.01	0.01
Pb	<0.005	<0.005	<0.005	<0.005
Cd	0.05	0.04	0.01	ND*
Na	0.05	0.03	0.02	0.02

ND = none detected

Fraction	Surface area m^2/g
1	4.27
2	2.70
3	1.40
4	0.66

In general, Table 3 shows that the concentration of impurities, in particular oxygen, increases with increasing particle surface area of the titanium hydride. Figure 3 illustrates that as the oxygen concentration increases it apparently displaces the hydrogen to lower and lower concentrations. In Figure 4 it is also evident that the hydrogen/oxygen ratio decreases as a function of surface area; that is the ratio increases as the surface area decreases and the concentration of

hydrogen in a titanium hydride powder is displaced to lower concentrations as surface area and oxygen concentration increase.

To further study the correlation between hydrogen solubility and impurity content of fines in titanium hydride powder, the above fractions 1 through 4 were dehydrided simultaneously in the same reactor. Figure 5 is representative of the temperature/pressure time plot of the dehydriding process. The reaction comes to equilibrium and the surface of the metal is then exposed to air slowly. After being dehydrided, each fraction was analyzed for hydrogen/oxygen and surface area. Table 4 shows the results of the analysis.

Table 4

CHEMICAL ANALYSIS OF SUBHYDRIDE FRACTIONS

Subhydride Fractions	H_2 (wt %)	O_2 (wt %)	Surface Area (m^2/g)
1	1.32	4.4	3.37
2	2.00	3.2	2.34
3	2.55	2.0	1.35
4	2.62	1.4	0.89

The results of the analysis show that the hydrogen content appears to be displaced proportionally with the increase in oxygen content in each fraction after dehydriding and air passification (Figure 6) and that the hydrogen-to-oxygen ratio again decreases as a function of surface area as depected in Figure 7.

DISCUSSION

If it is assumed that the interstitial solution concept is valid, then it follows that the hydrogen displacement to lower concentrations from theoretical in titanium hydride could be due to impurities present in the crystal lattice and that the impurity present in the largest quantities would probably effect the greatest change in hydrogen solubility. Then it could follow that the hydrogen displacement to lower concentrations from theoretical in titanium hydride is primarily due to oxygen contamination. From the experimental data it was shown that the impurities increased with increasing surface area in the titanium hydride powder, oxygen being the primary impurity. It was shown further that hydrogen appeared to be displaced to lower concentrations as the oxygen concentration increased. One cannot argue that the oxygen content increased due to increasing surface area, as the surface area decreased slightly after de-

hydriding. However, the increases in oxygen content could be attributed to migration of oxygen from the extremities of the crystal deeper into the crystal lattice during dehydriding. If this were the case, the extremities of the crystal would absorb more oxygen during air passification further displacing the equilibrium to lower hydrogen content, which case was observed experimentally after dehydriding. This could be questioned as there appeared to be no sign of a hydrogen overpressure in the system after air passification. If this were the case, then the argument is that the initial impurity content inherent in the crystal lattice reduced the fermi state (chemical potential) of the system, thereby reducing the solubility potential of hydrogen. In this case the hydrogen atoms would be reoriented in the crystal lattice during the dehydriding process favoring lower concentration in those particles having high concentrations of impurities. In either case the oxygen concentration could increase replacing the surface oxygen that migrated deeper into the crystal lattice. Large variations in oxide thickness after dehydriding seem to support the theory of oxygen migration into the lattice further displacing hydrogen to lower concentrations.

CONCLUSIONS

We have established that titanium hydride powders prepared by Alfa Ventron from commercial magnesium-reduced titanium contain impurities, the greatest of which is oxygen, and that the concentration of the impurities increases with increasing surface area. It was also established that the hydrogen content of those particles containing high concentrations of impurities, the greatest of which is oxygen, is lower than those particles containing low concentrations of impurities.

The attempt to prove that oxygen was the primary cause of hydrogen displacement can still be questioned. However, one cannot deny that a linear relationship between hydrogen and the impurity oxygen in titanium hydride appears to exist.

622

REFERENCES

1. T. R. P. Gibb, Jr., and H. W. Kruschevits, Jr., "The Titanium-Hydrogen System and Titanium Hydride. I. Low Pressure Studies," J. Amer. Chem. Soc., 72, 5365-5369 (1950).

2. N. C. Birla and V. Depierre, "Dehydriding of Ti-6Al-2Sn-4Zr-6Mo Hydride Powder," Powder Metallurgy, 18:35, 15 (1975).

3. H. M. Lee, "The Solubility of Hydrogen in Transition Metals," Metall. Trans. A., 7A, 431 (1976).

4. W. M. Mueller, J. P. Blackledge, and G. G. Libowitz, Metal Hydrides, Academic Press New York and London, 1968.

5. W. E. Moddemon, Oxide Thickness of TiH_x Materials Measured by ESCA, Research Institute, University of Dayton.
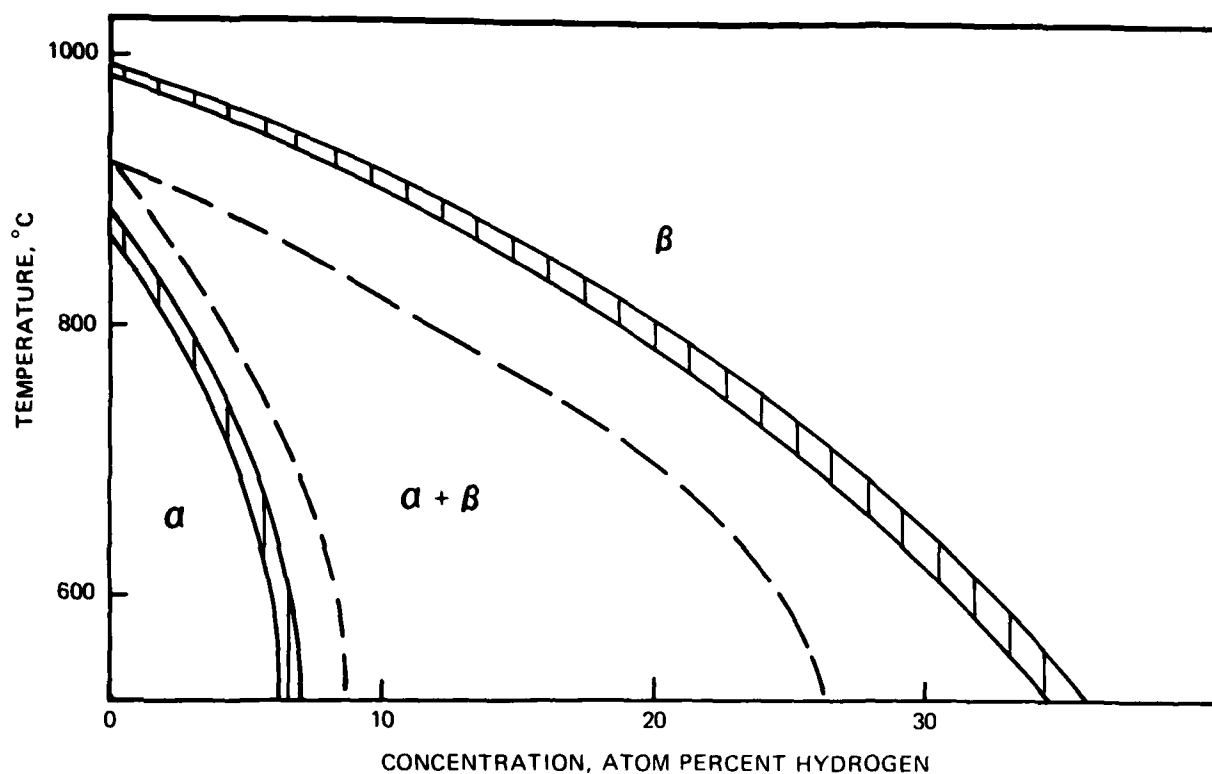
Figure 1. Diagram of Hydrogen With Magnesium Reduced Titanium. Dashed Line: Pure Titanium-Hydrogen System. Shadowed Line: Magnesium Reduced Titanium

1. Hopper	9. Rotary Duct Opening
2. Spring Plate	10. Sifting Chamber
3. Brush	11. Symmetrical Discs
4. Orifice Tube	12. Catch Basin
5. Vibrator	13. Throttle Nut
6. Feed Nozzle	14. Throttle Spacer
7. Rotor Casting	15. Motor
8. Fan Vanes	
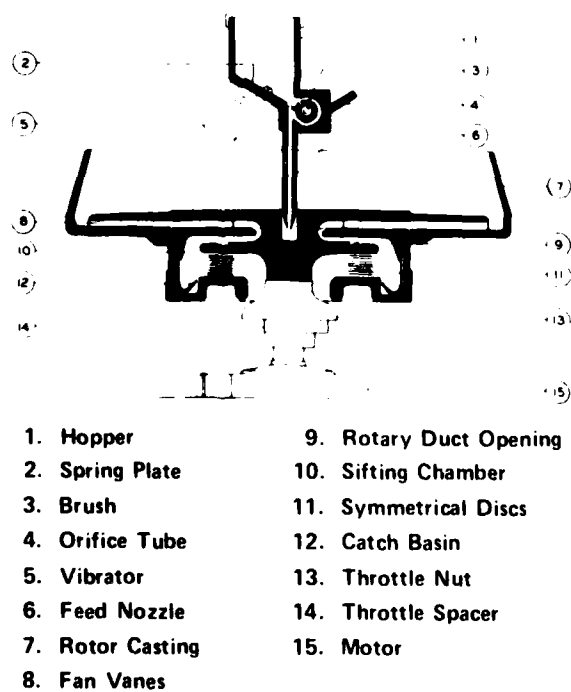
Figure 2. Schematic Diagram of Bahco Particle Classifier
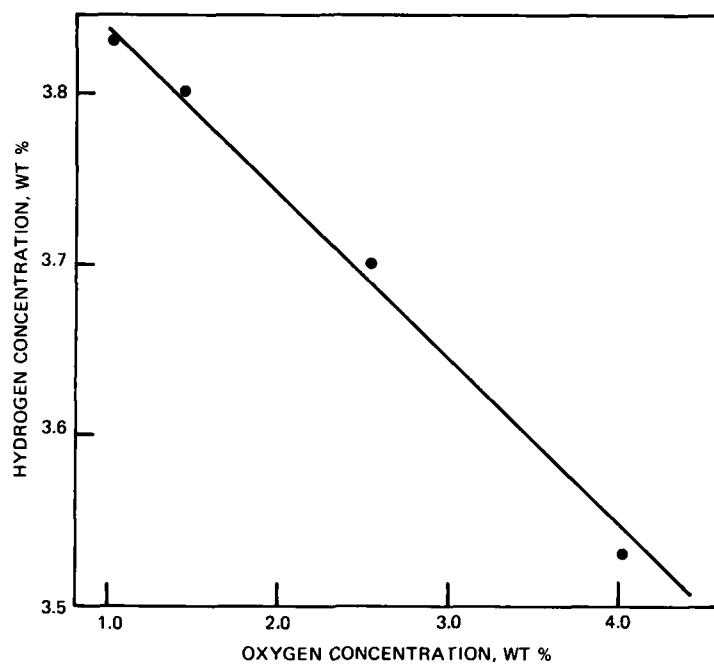
Figure 3. Hydrogen/Oxygen Concentration of TiH$_{1.92}$ Powder Fractions
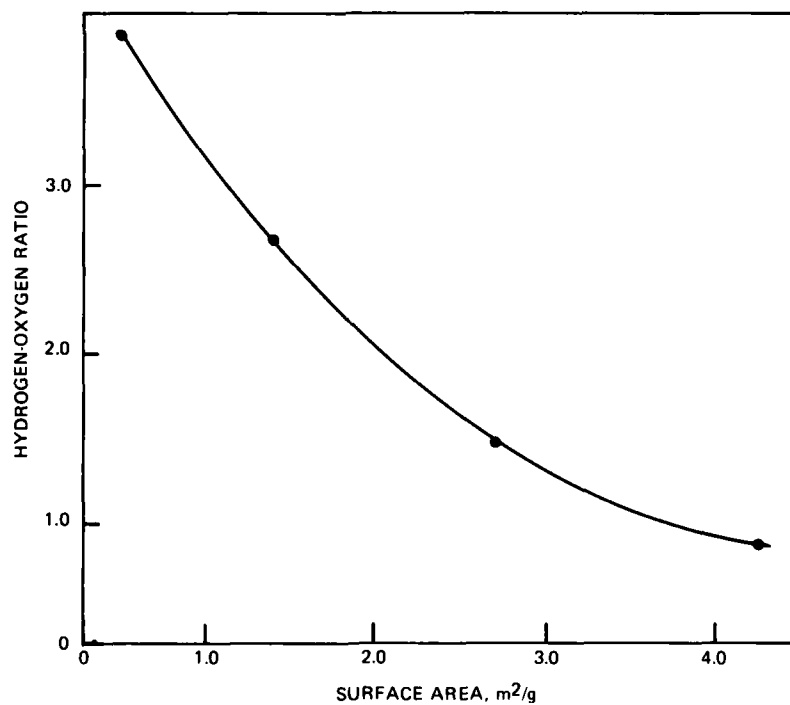
Figure 4.   Hydrogen/Oxygen Ratio as a Function of Particle Surface
Area Decreases as Surface Area Increases
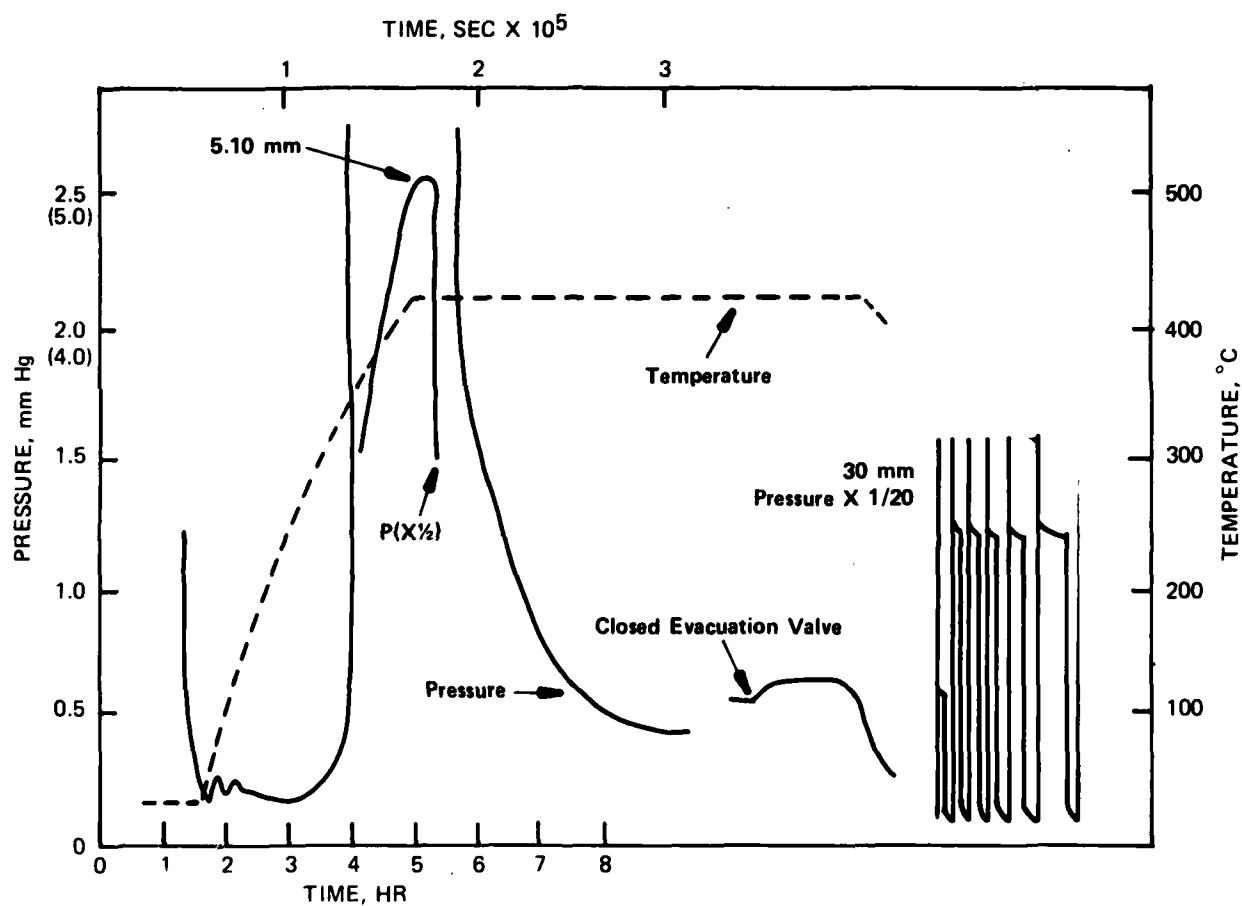
Figure 5.   Recorder Trace (typical) of T ($^\circ$C) and P(mmHg) VS Time (hrs.) for Dehydriding of TiH_2 and Passivating The Dehydride Material With Air

626
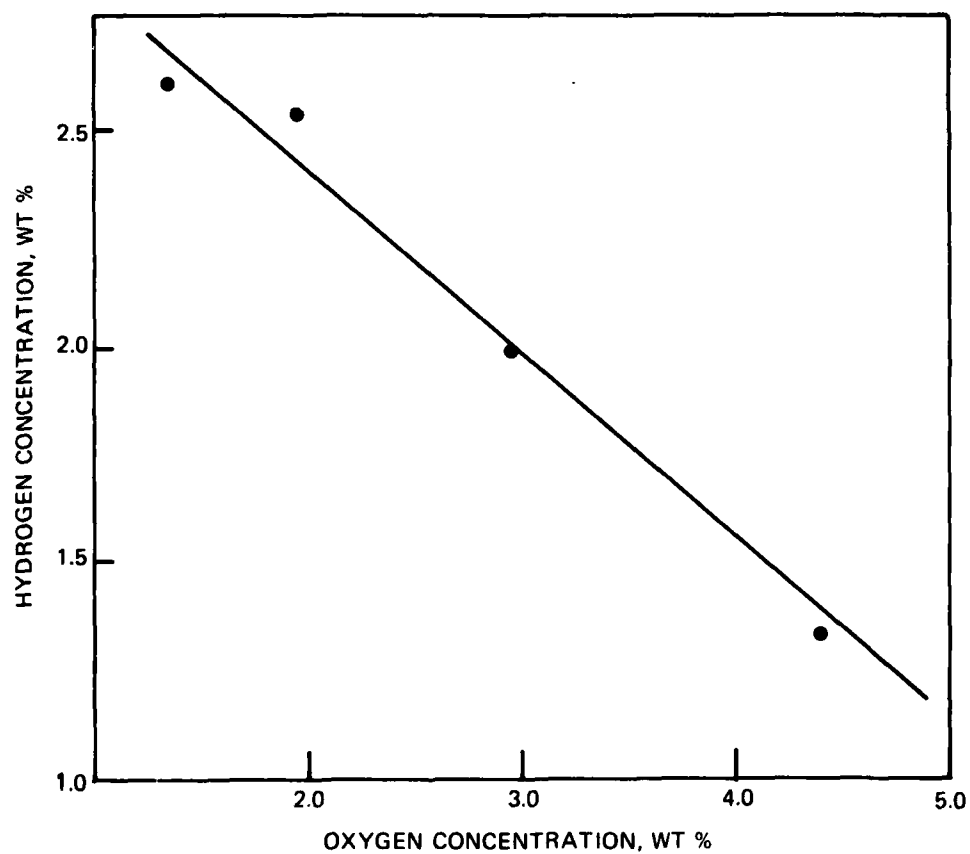
Figure 6. Hydrogen/Oxygen Concentration of Dehydrided TiH$_{1.92}$ Powder Fractions
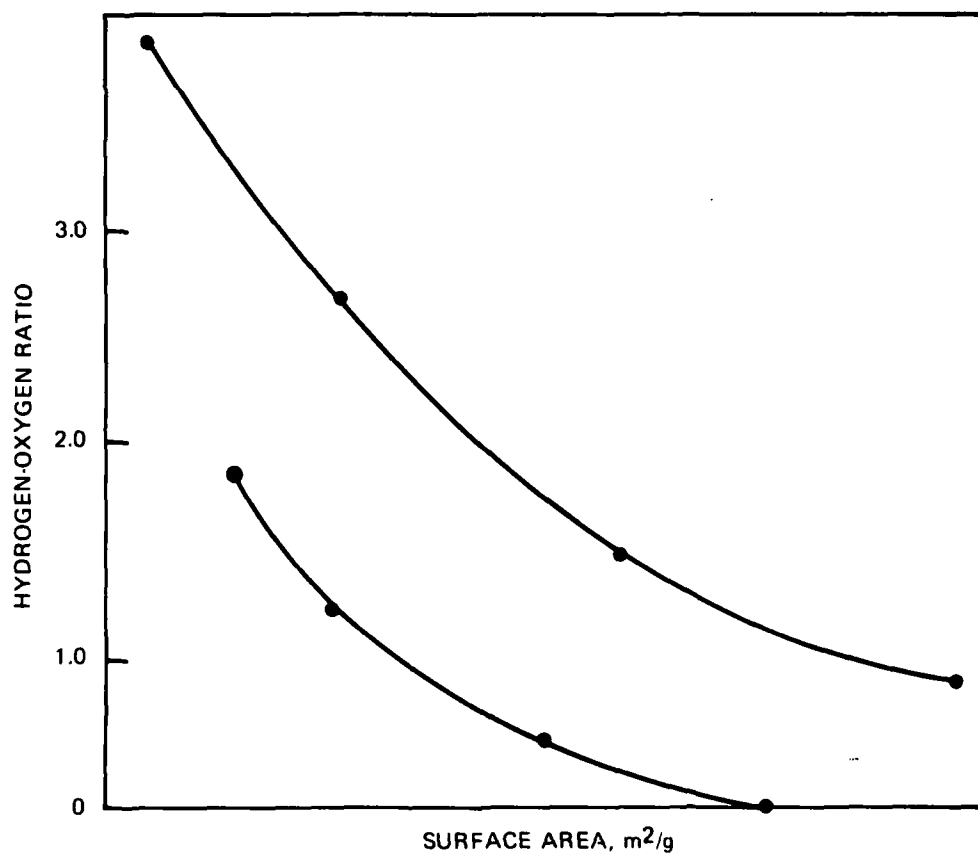
Figure 7. Comparison of Titanium Hydride TiH$_{1.92}$ and TiH$_{1.92}$ After Dehydriding. Graph Shows Relative Hydrogen Displacement Before and After Dehydriding as a Function of Particle Surface Area

RECLAMATION OF PROPELLANT
AND FLARE INGREDIENTS

by

G. C. Shaw
W. O. Munson
V. T. Dinsdale
M. J. McIntosh

THIOKOL/WASATCH DIVISION
A Division of Thiokol Corporation
P.O. Box 524, Brigham City, Utah 84302

ABSTRACT

Large quantities of propellant, flare, and other pyrotechnic compositions have been, and are being, burned in open pits. Due to increasing environmental pressure, much of the excessed and waste materials is being burned and the exhaust scrubbed, or plans are made to do so in the future. Only minor effort has been expended toward reclaiming the ingredients used in the pyrotechnic compositions. The industry-wide opinion has been that open burning is the most economical way to dispose of the various materials. Most other alternatives, such as controlled burning and scrubbing of exhaust products, involve the construction of new facilities which, in some cases, amounts to several million dollars. The results of this study indicate that at least in some cases the recovery of ingredients from waste composite propellant, for example, could be profitable.

This paper presents a study and its results which investigated the breakdown of composite solid propellant and flare compositions into oxidizer, metal fuel (either aluminum or magnesium) and binder for reuse or resale.

INTRODUCTION

Large quantities of waste propellant have been, and are being, burned in open burning pits. Due to increasing environmental pressure, many propellant producers are either now burning waste propellant and scrubbing the exhaust gases, or are planning to do so in the future.

Very little effort has been expended toward reclaiming ingredients from waste composite propellant or flare compositions. The industry-wide opinion has been that

open burning is the most economical waste propellant disposal method. The objective of the study discussed in this paper* was to investigate and evaluate as many non-burning methods for disposal of waste propellant as possible, including: (1) recovery of the AP from the waste propellant; (2) recovery of the aluminum and polymer from the residues left after the AP has been removed; (3) use of waste propellant and/or residues with additives, as a slurried explosive; and (4) direct utilization of cured and uncured waste propellant. It was observed that most of these methods could also be applied to the recovery of flare ingredients.

The technical feasibility of each of these methods has been established. A flow diagram of the methods developed is presented in Figure 1. Some of the methods make use of the waste propellant directly as in fire starters; others are interdependent. The extraction of AP from propellant leaves a residue enriched with aluminum that is amenable to further processing for separating the aluminum and binder.

AMMONIUM PERCHLORATE RECOVERY

Leaching of ammonium perchlorate from the propellant was conducted in a tank equipped with steam jacket and a variable speed laboratory stirring motor having a sharp, three-blade propeller. Chopped or sliced propellant was added to a heated water solution containing 14% AP and a friction reducing agent. In a pilot plant operation, lean AP solution would be reused in a continuous leaching operation. To simulate recycling of the leach solution, the laboratory scale leach runs were made with a 14% AP solution. The amount of propellant added was adjusted to provide the amount of ammonium perchlorate required to give a saturated solution at a desired temperature, such as 150°F.

Leaching appeared to be complete within 15 min when conducted at 180°F. The leach solution was decanted, allowing it to drain from the swollen binder-aluminum residue. The residue was then given a fresh water wash, filtered and dried. The AP was recovered from the leach solution by cooling to 50°F, filtering and drying.

AP extraction efficiencies up to 95% have been obtained from a single leaching cycle. Examples given in Table I show data and recovery results from some typical AP leach runs. Combining the leaching operation with a single residue wash increased the amount of AP extracted from the propellant to over 98%. A continuous operation in which the washings would be reused, eventually ending up in the leaching operation, will increase the AP recovery to 98% or more. Also, it has been shown that the effectiveness of AP extraction from the propellant was not adversely affected by using an AP solution instead of plain water.

---

*Part of this work was performed at Thiokol under a contract with JPL, Contract 954161
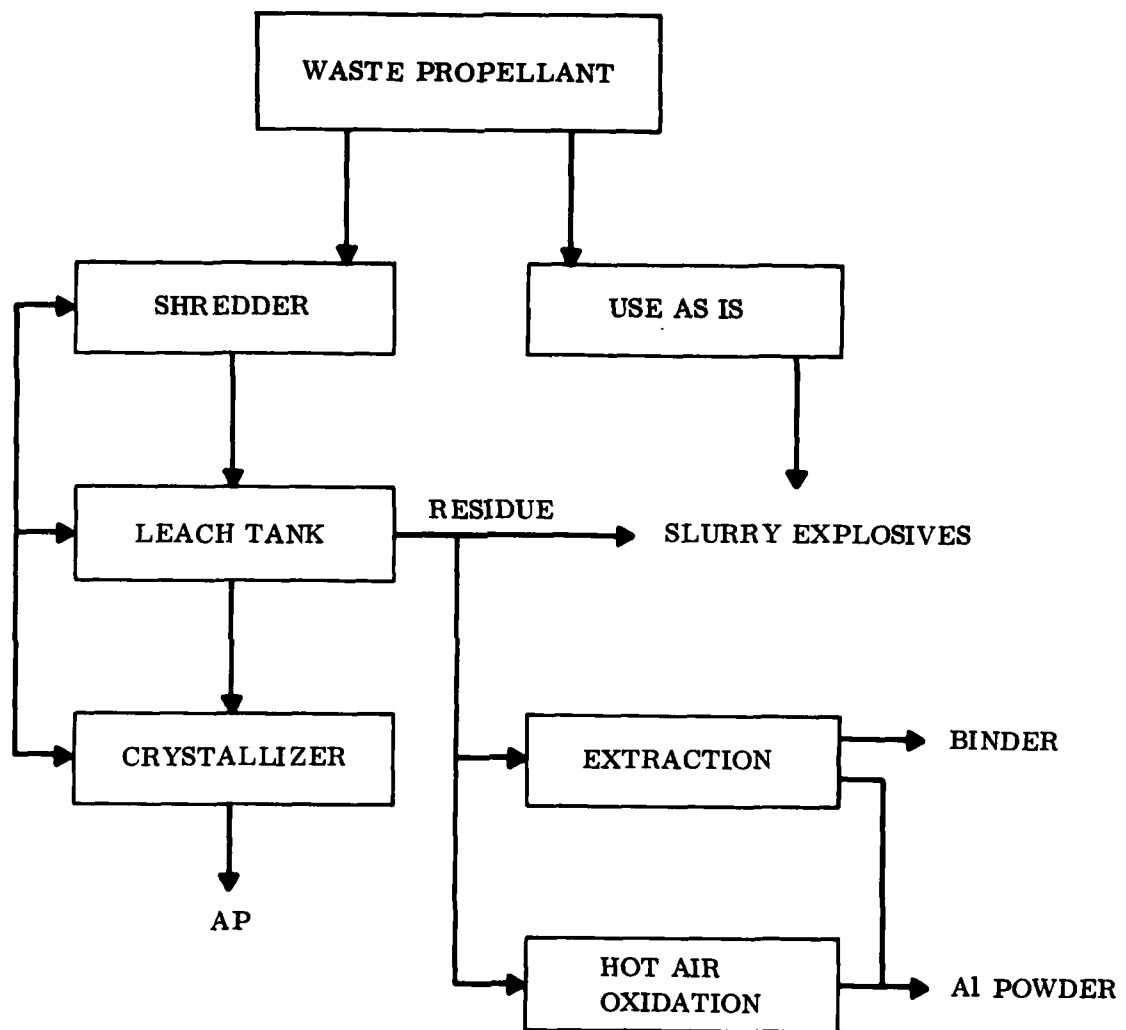
Figure 1. Propellant Disposal Methods Flow Diagram

TABLE I

AMMONIUM PERCHLORATE LEACHING FROM SCRAP PROPELLANT

Propellant Type	TP-H1011	TP-H1011	TP-H1123	ANB-3066	TP-H1123 Uncured
Leach Solution Temp (°F)	174	163	180	180	180
Leach Time (min)	30	30	30	15	10
Precipitation Temp (°F)	50	50	50	50	50
AP Recovery* (%)	92	91	83	78	96
AP Content of Residue** (%)	3.3	1.8	1.9	7.2	--
Overall AP Extraction (%)	96.7	98.2	98.1	92.8	96

*Obtained from a single leach
**After one additional fresh water wash

An analysis of the AP recovered from the leach runs is tabulated in Table II, along with a comparison with the specification for Minuteman TP-H1011 propellant. The results from other analyses such as emission spectrophotometry, for trace materials, indicate a higher than normal potassium content of 253 ppm, with other metal contents appearing typical for the AP used in propellants. From a chemical purity standpoint, the recovered AP is acceptable for reuse in propellant compositions.

TABLE II

ANALYSES OF RECLAIMED AMMONIUM PERCHLORATE

	Reclaimed From TP-H1011 Propellant**	Specifications for TP-H1011 Propellant
Sulphated Ash as MSO_4* (%)	0.114	0.90 max
Iron as Fe_2O_3 (ppm)	3.4	36.00 max
Chlorate as $NaClO_3$ (%)	0.001	0.01 max
Chloride as NH_4Cl (%)	0.003	0.155
Perchlorate as NH_4ClO_4 (%)	98.75	98.3

*Any metal sulfate
**First Stage Minuteman propellant

The AP leach and extraction rates, product purity, and recovery percentages obtained in the bench scale tests were excellent. They indicate the feasibility of recovery of high quality AP from waste composite propellant. Based on the results obtained from these bench scale tests, the design of a pilot plant was investigated.[1] The economics of reclaiming AP from this designed pilot plant were then calculated. A few of the pertinent assumptions made were:

1. Plant capacity is 7,000 lb of waste composite propellant per 8 hr shift

2. 70% of propellant is AP

3. 95% of the AP is recovered

4. Freight to Henderson, Nevada, from Brigham City, Utah is 1.635¢ per lb

From these assumptions, the cost of producing AP from waste propellant and shipping it to Henderson, Nevada, would be 8.92¢ per lb. The value of reclaimed AP, when sold to an AP vendor is expected to be 16¢ per lb. This represents a net savings of 7.08¢ per lb. The expected quantity of waste composite propellant from the Space Shuttle Solid Rocket Motor boosters, from 1976 thru 1989 is 7.9×10^6 lb. This would result in a savings in excess of $374,895, plus eliminating most of the normal costs of disposing of waste propellant by burning. At Thiokol/Wasatch Division, the cost of burning waste propellant, for the past several years, has averaged $75,000/year. The elimination of the majority of this expense, plus the savings garnered from the AP alone would amount to over $1 million on just the AP recovery over the 14 year span.

RESIDUE TREATMENT

Three treatments of the aluminum and binder residue remaining after the AP has been extracted, were investigated. Reuse in slurry explosives will be discussed in the next section. The other two treatments, air oxidation of the binder to yield aluminum, and chemical breakdown of the binder to yield both aluminum and depolymerized binder, will be discussed in this section.

Air oxidation of the residue obtained from the AP leach process, was carried out at 450° to 500°C (844° to 932°F). When the AP content of the residue is less than 10%, the binder fumes off. If the AP content is near 15%, ignition will occur, resulting in the burning of a portion of the residue. After oxidation of the binder, free flowing aluminum powder remained. Table III presents data from two oxidation runs, plus a control run. These samples were placed in an open tray in a muffle furnace at 500°C (932°F). The control sample, which had not been exposed to the leach solution, lost 0.6% active aluminum content. The R-18 residue came from a lower temperature leach operation (150°F) than did the R-12 residue (180°F). This possibly explains the fact that its loss in active aluminum content is slightly less than that of run R-12.

The aluminum obtained by this process was recovered in near quantitative amounts, and could be used in a number of less exacting applications which do not require a very high active aluminum content.

TABLE III

RECOVERED ALUMINUM FROM OXIDATION OF BINDER - Al RESIDUE

Sample No.	R-18	R-12	Control*
AP Content of Residue (%)	8.28	3.15	0
Active Al Content (%)	97.2	96.8	98.6
Loss in Active Al Content** (%)	2.0	2.4	0.6

---

*Before heating, control sample contained 99.2% active aluminum, same
    aluminum as used in TP-H1011 propellant
**Oxidation condition, 3-1/2 hr at 500°C

The economics of aluminum extraction by this technique, with a 21,000 lb per day waste propellant disposal facility, indicate that it will cost 2.2¢ per lb to separate the aluminum from the binder. The estimated value of the aluminum powder is 40¢ per lb, representing a savings of 37.8¢ per lb. This would result in a savings of $481,000 during the projected Space Shuttle lifetime (through 1989).

The second method, which showed the greatest potential for recovering high purity aluminum is transesterification, in which the binder is removed chemically, depolymerized, filtered and washed from the aluminum residue.

This method uses a solvent with an alcoholic solution of sodium methoxide to transesterify the crosslinked sites of the binder system. When moisture is excluded from the system, the highly basic alkyl oxide radical has little effect upon the aluminum present, but reacts very rapidly with the binder. Mixed solvents of either methanol and tetrahydrofuran or toluene were effective in the transesterification reactions. The products of the reaction were soluble in toluene. Washing the binder from the aluminum generally resulted in the recovery of 98.7 to 99.7% of the theoretical amounts. Analysis for active aluminum content ranged from 98.5 to 99%, which was well above the minimum specification level of 98% for propellant usage. The recovery of aluminum powder was essentially quantitative, indicating that this procedure is superior to other methods tried, or found in the literature. The results of some of the transesterification reactions are shown in Table IV.

634

TABLE IV

TRANSESTERIFICATION REACTIONS OF TP-H1011
BINDER - Al RESIDUES

Run No.	1	4	6	7
Al Content of Residue (%)	52.16	52.16	52.16	49.49
AP Content (%)	2.20	2.20	2.20	7.20
Solvents (% of Total)				
Methyl Alcohol	40.00	75.00	100.00	10.00
Tetrahydrofuran	60.00	25.00	--	--
Toluene	--	--	--	90.00
Al Recovery (% of Theoretical)	94.00	99.70	98.70	102.00*
Active Al Content (%)	98.60	97.80	99.00	93.70
Weight Loss of Al After One Hr at 500° C (%)	0.00	0.23	0.00	2.10
Active Al Content After One Hr at 500°C (%)	98.80	98.00	98.30	96.40

*The residue appeared to contain some oxidizer salts

In run No. 6 (Table IV) the methyl alcohol-sodium methoxide solution in contact with binder, heated to reflux, 60°C (140°F), was sufficient for the reaction to proceed. After 1 hr reaction time, the organic portion of the reaction residue was soluble in toluene. Filtering and washing the residue with toluene resulted in a free flowing aluminum powder when dried.

The binder portion of the residue was recovered from the transesterification reactions by neutralizing the residues and washing with water. Evaporation of the solvent resulted in a liquid resembling the starting premix used to make the propellant. The recovered binder was depolymerized to a molecular weight slightly higher than the prepolymers originally used, although much of it was in the form of a methyl ester. The HB polybutadiene prepolymer could be recovered by additional hydrolysis and extraction from the remaining epoxy derivative.

It would be suitable for disposal by several methods, ranging from landfill, mixed and used with fuel oil, or use by rubber formulators. At this point, however, its possible recovery as a reusable PBAN prepolymer could be accomplished using straightforward and established procedures to regenerate the carboxyl functional groupd in the prepolymer.

Binder depolymerization by transesterification has resulted in the recovery of the aluminum from Minuteman TP-H1011 propellant. Quantitative yields of aluminum meeting the specification requirements of purity for propellant usage were obtained. Using the same size plant, 7,000 lb of waste propellant per shift, it is

estimated that the aluminum could be separated from the residue for 4.12¢ per lb.
This aluminum would be of propellant quality, and could be reused in propellant with-
out any further treatment; therefore, its value should approach 75¢ per lb. This
would represent a savings of 70.9¢ per lb, or $903,022 during the projected Shuttle
lifetime. The total expected savings from reclaimed AP aluminum and polymer
could exceed $1.5 million through the 1976 to 1989 Space Shuttle Solid Rocket Motors
production period.

FLARE MATERIAL

It was observed that removal of the oxidizer from the flare compositions
was unnecessary, as was the case with propellant containing ammonium perchlorate.
The sodium and strontium nitrate oxidizers appeared to have little interaction with
the sodium methoxide catalyst used. The presence of large amounts of ammonium
perchlorate, for example, would interact with the catalyst, forming sodium perchlorate,
methanol and ammonia. The ammonia formed is a much poorer catalyst for the deg-
radation of the crosslinked polymer and therefore effectively diminishes the break-
down of the binder network.

The recovery of the flare ingredients has been accomplished in three types
of compositions as shown in Table V. The transesterification reaction upon the
binder using a solvent as methanol or methanol-THF mixture proceeded rapidly dis-
solving the binder, freeing the solids. Filtration and washing with solvent resulted
in a mixture of oxidizer, magnesium and other flare additives. The water soluble
nitrate salts were dissolved and rapidly washed from the magnesium to minimize
the reaction between the water and magnesium. Other methods of separating the
oxidizer and magnesium could be devised, such as flotation using a non-reactive
liquid of the proper density to separate the magnesium from the more dense oxidizer.

TABLE V

FLARE RECOVERY

Composition	1	2	3
Binder			
Witco F17-80/ERL-0510	9	--	15
Laminac	--	5	--
Magnesium	63	58	20
Sodium Nitrate	28	37	--
Strontium Nitrate	--	--	50
Dechlorane	--	--	15
Recovered Solids (% of Theoretical)			
(Solids + Mg)	96	97	96
Mg (% active content)	97.2	--	--

SLURRY EXPLOSIVES

Work accomplished in this portion of the program established that propellant, or propellant residue, after AP extraction can be successfully incorporated into slurry explosives, with resultant energy enhancement. Investigations were conducted with three different types of composite propellant, including Minuteman First Stage (TP-H1011), Minuteman Third Stage, and an advanced development high burn rate material. Tests showed there was not a discernible difference in explosive behavior as a result of changing propellants. Slurry explosive composition was investigated to determine the effect of sensitizing agent and the effect of soluble oxidizer type on explosive sensitivity and energy. Successful sensitizations were accomplished with either PETN, TNT, or HMX as an explosive additive. The latter material was investigated because it will be available as scrap from several propellant programs, while PETN and TNT can be purchased commercially. As for the soluble oxidizer portion of the slurry, the data clearly demonstrate the need to have ammonium nitrate (AN) in the formulation because of its high solubility. Explosive performance tests were conducted and relative energy levels (compared to TNT) were determined for some formulations. Some of the energy values exceeded those obtained with TNT.

The slurry explosive effort did not establish an optimum formulation with regard to processibility, energy, or cost but did lay out guidelines for any further development effort. Slurry explosive performance can be tailored over fairly wide ranges, according to the type and level of ingredients included in the formulation.

The present study was aimed at making slurries containing a minimum amount of sensitizer and a maximum amount of propellant to facilitate propellant disposal. Explosive properties for formulations containing approximately 40% propellant show relative bubble energies from 1.17 to 1.32 times that of TNT (formulations A, C, D, Table VI). The relative bubble energy is an approximation of the amount of work an explosive is capable of and is determined by a standard method in underwater tests. The highest energy formulation made, using propellant residue (B, Table VI), did not equal that of TNT. A more thorough discussion of the use of residues is given later.

Figure 2 shows a comparison of the varied explosive strength obtained from the slurried explosive compositions tested. The test sample in a 2-in. schedule 80 pipe 8-in. long. was placed on a witness plate 0.5 in. thick and 6.0 in. square. Initiation with a Pentolite booster results in damage to the witness plate according to the contribution provided by the test sample. The coded number (between 1 and 5) indicates the extent of the damage contributed by the test sample.

The roll of the sensitizer can be visualized by further examination of Table VI. The levels of explosive sensitizer in formulations A, C, and D were established by determining a minimum amount required to detonate a base solution ($AN/SN/H_2O$).

Figure 2. Witness Plate Code

On a weight basis, PETN is the most effective and TNT the least effective sensitizer; however, on the basis of cost, their relative effectiveness would be about equal. Because of its high cost, HMX would not normally be considered as a sensitizer, however, it will be available as scrap from some propellant programs and thus was included in the experimental program. It is not clear now how much HMX will be available, but the slurry formulations can effectively use whatever quantity there is as a supplement to other selected sensitizers.

TABLE VI

RESIDUE AND PROPELLANT CONTAINING SLURRIED EXPLOSIVES

	Formulation			
	A	B	C	D
Ingredients (%)				
NH4NO3(AN)	23.1	33.7	24.0	22.0
NaNO3(SN)	5.8	8.4	6.0	5.5
H2O	14.0	20.3	8.0	7.3
Propellant	41.7	--	41.0	39.8
Residue	--	15.2	--	--
Sensitizer	14.6[1]	21.3[1]	20.5[2]	24.5[2]
Gel Agent	0.8	1.1	0.5	0.5
Witness Plate Detonation Code[3]	5.0	--	3.0	1.0
Relative Bubble Energy (TNT = 1)	1.17	0.895	1.26	1.32
Relative Shock Energy (TNT = 1)	0.93	0.75	1.20	1.01
Explosive Density (gm/cc)	1.43	1.39	1.51	1.39

---

[1] PETN
[2] HMX
[3] See Figure 2 for witness plate code

The effect of adding propellant to slurry compositions was determined by establishing a baseline formulation (without propellant) and then adding propellant in increasing amounts to the base solution (Table VII). No upper limit of propellant additives was established on the basis of detonability; however, mixing became very difficult with more than 45% propellant in the mix. Thus, the upper limit was established on the basis of processing. As shown in Table VII, the oxygen balance of the system is zero at about 24% propellant. According to the Bureau of Mines Circular 8560, slurried explosives are generally designed to be slightly oxygen deficient in order to minimize the oxides of nitrogen in the detonation products. Thus, the optimum propellant level may be established on the basis of oxygen balance rather than detonability. With propellant containing AP in the formulation, HCl must also be considered a toxic product. Methods for reacting the HCl with a metal to form a

metal chloride have been successfully accomplished in the literature (British Patent 297,375). For instance, sodium nitrate (SN) can be added in stoichiometric quantities so the NaCl will be a product.

TABLE VII

EFFECT OF PROPELLANT LEVEL ON EXPLOSIVE PERFORMANCE

Base Solution   AN/SN/H_2O/TMETN/Gel Agents
Approximate Ratio   40/10/24/25/1

	Formulation (%)				
	1	2	3	4	5
Base Material	100.00	84.800	65.00	58.300	52.70
Propellant	0.00	15.200	35.00	41.700	47.30
Witness Plate Damage Code	4.00	5.000	5.00	5.000	--
Bubble Energy Results (TNT = 1.0)					
Test Series 1	--	1.097	--	1.316	--
Test Series 2	--	--	1.04	1.170	1.18
Shock Energy Results (TNT = 1.0)	--	--	0.95	0.930	0.99
Avg Charge Density (gm/cc)	1.23	1.440	1.37	1.450	1.44
Oxygen Balance	+8.50	+3.000	-4.10	-6.500	-7.60

The use of the propellant residue which remains after AP extraction in slurry explosives is an attractive option. First, less expensive and more soluble AN can be used as the oxidizer. Second, HCl as a combustion product can be eliminated. Because of this, tests were performed using the same base solution shown in Table VIII with different levels of propellant residue being added. The data from these tests are given in Table VIII. The residue was in the form of particles approximately 1/64 up to 1/8 in. diameter. The bubble energies obtained from the formulations in approximately 800 gm charges went through a maximum at about 15% residue. The results demonstrate that the residue is participating in the detonation reaction and that useful energy is being obtained from the aluminum in the residue.

Manufacture of slurry explosives from waste propellant, including purchase of all necessary additives, will cost 18.6¢ per lb. The current market value of slurry explosives ranges from 25¢ to 50¢ per lb. This represents a potential savings of between 6¢ and 31¢ per lb.

TABLE VIII

EFFECT OF RESIDUE ON SLURRY EXPLOSIVE ENERGY

	Formulation					
	43-1	43-2	46-7	43-3	43-4	43-5
Ingredients (%)						
NH_4NO_3	39.70	36.400	34.800	33.700	29.200	23.100
$NaNO_3$	9.90	9.100	8.700	8.400	7.300	5.800
H_2O	24.00	22.000	21.000	20.300	17.600	14.000
PETN	25.10	23.100	22.000	21.300	18.500	14.600
Percent Residue (Total)	0.00	8.200	12.600	15.200	26.500	41.800
Gel Agent	1.50	1.200	1.000	1.100	0.900	0.700
Density (g/cc)	1.31	1.420	1.430	1.390	1.300	1.310
Detonation Code						
Relative Energy (TNT = 1)	Lost	0.786	0.830	0.895	0.830	0.719

DIRECT USE OF WASTE PROPELLANT

Waste solid propellant could be used directly in some applications. One which was investigated was a fire starter for use by the U.S. Forest Service; another, incorporation into slurry explosives, has already been discussed. The basic criteria established for a good fire starter are:

1. Low item cost

2. Capable of igniting wet material

3. Easy to use

4. Relatively safe to handle

Waste composite propellant is able to meet these requirements.

Two sizes of fire starters were investigated, one-half and one gallon sizes. All were manufactured by placing waste propellant into a plastic bag which was then placed into an ice cream carton. A fuze was inserted and the carton was taped shut. Figure 3 presents a sketch of a fire starter. The U.S. Forest Service estimates that they could use as much as 10,000 lb of fire starters per year in the Rocky Mountain area; nationwide use would increase that number significantly. The manufacturing costs for one-half and one gallon fire starters are estimated to be $1.97 and $2.72, respectively. Their selling price would be $2.75 and $3.25 each.

641

CARTON SIZE	A	B	C	PROPELLANT (LB)
1/2 GALLON	5 IN.	3-1/2 IN.	7 IN.	8.5
1 GALLON	7 IN.	5 IN.	7 IN.	17

NOTE: FIRE STARTERS TO HAVE APPROPRIATE LABEL FOR "PROPELLANT CLASS B EXPLOSIVE"

TAPE SEAL

B

A

C

CLOSED FIRE STARTER
(FOR SHIPPING)

POLYETHELENE
BAG (CONTAINING
PROPELLANT)

STANDARD WATERPROOF
SAFETY FUSE – LENGTH
TO SUIT (END NEEDS TO BE
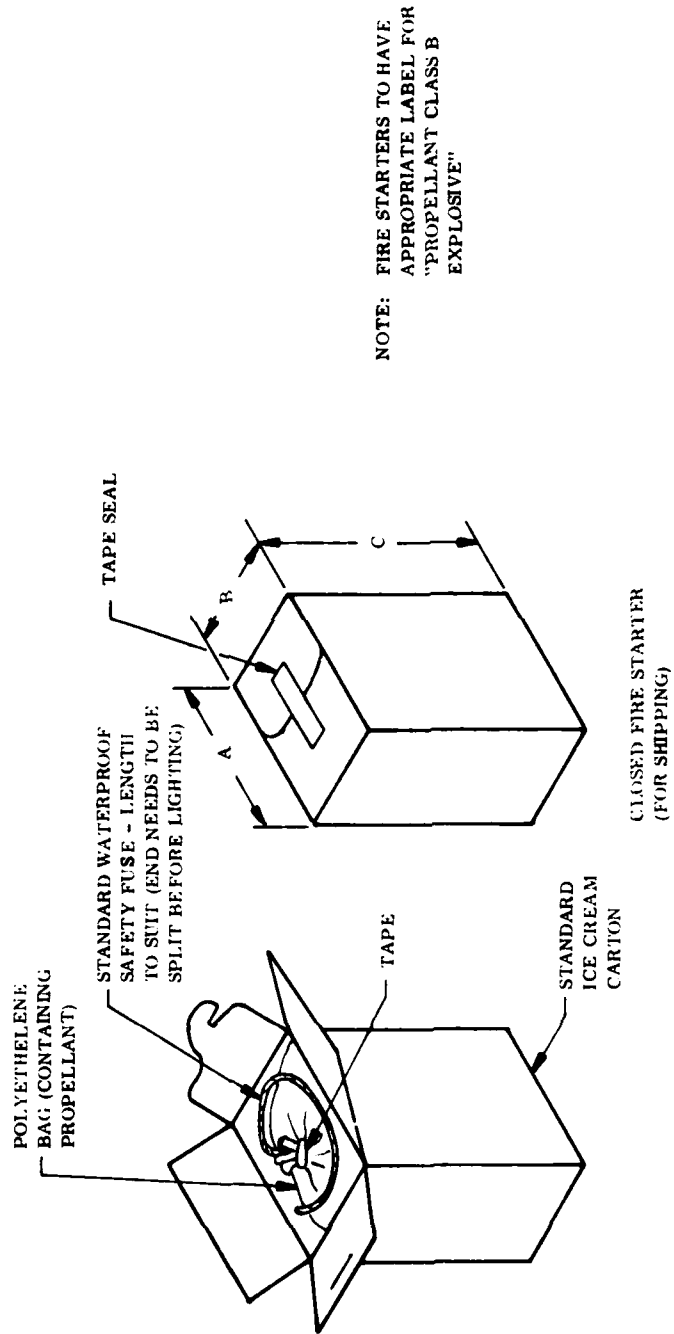SPLIT BEFORE LIGHTING)

TAPE

STANDARD
ICE CREAM
CARTON

Figure 3.   Fire Starters for Forest Service

CONCLUSIONS

The feasibility of disposal of waste composite solid propellants, by break-down of the propellant into its three basic ingredients; oxidizer, fuel, and binder has been demonstrated. Moreover, the economics of this disposal approach appear attractive. The sale of reclaimed ingredients plus elimination of the recurring costs of burning waste propellant could lead to savings of between \$1.65 and \$2.0 x 10^6 during the lifetime of the Space Shuttle (1976 thru 1989). Finally, the disposal technique is environmentally acceptable, in that no waste products will be discharged into the atmosphere or ground water.

REFERENCE

1. McIntosh, M. J., Munson, W. O., Shaw, G. C., and Dinsdale, V. T.: Solid Rocket Propellant Waste Disposal/Ingredient Recovery Study. Final Report, JPL Contract 954161; Thiokol/Wasatch Division, Brigham City, Utah, Report No. MER-1374, 28 July 1975.

THE PHENOMENON OF PULSATING BURNING IN PYROTECHNICS

Friedrich-W. Wasmann

Institut für Chemie der
Treib- u.Explosivstoffe

D-7507 Pfinztal,W.-Germany

It is expected that pyrotechnical systems burn with a
constant speed to generate light,sound, heat and smoke.
A constant speed of reaction is also expected in applications
regarding ignition and ignition delay.

A constant burning is important for most pyrotechnic systems
and considerable effort is made to suppress any irregulari-
ties in the burning rate.

It is evident that irregularities in the burning rate, for
example, cause strong variations in the brightness of a
light signal which is not desired. Irregularities in the
burning rate of solid rocket propellants can lead, in the
worst case, to destruction of the rocket motor. In most
cases these instabilities lead to decreased efficiencies.

For exact functioning of pyrotechnic igniters and delay
elements which contain pyrotechnical compositions a constant
burning rate is highly desired.

In this sense there is much endeavour to develope pyrotechnic
systems which burn with a controlled and constant rate.

In practice, however, these requirements are often not met
due to the complexity of the underlying pyrochemical
reactions. This causes considerable problems especially
for military applications.

In civilian applications the requirements imposed on the
steady burning rate are not as stringent. In contrast,steps
were undertaken to make use of irregular burning behaviour
of pyrotechnic compositions to create new effects especially
with respect to amusement fireworks. For this purpose a
periodical occurrence of the irregular burning behaviour
is desired.

Such periodically pulsating burning compositions were dis-
covered by chance and became known for example as whistling
compositions. They form a special case in the domain of
periodical pulsating burning compositions because of their
high rate of pulsation which is in the range of 2000 to
5000 cps. These compositions, however, are not subject of
this paper. Compositions with a burning frequency in the

range of 0.1 cps to 10 cps will be discussed here and
examples of possible underlying reaction mechanisms are
given.

Knowledge of an old composition - the oldest I know -
functioning in that range, was given to me by Mr.R.G.Hall,
Director of Brock's Fireworks Ltd. (1)   The composition
was found in one of the firm's old mixing books,dated
1898, under the heading "Orion Flashing Guns":

51 % Sulphur		55 % Sulphur
17 % Fine Magnesium Powder		18 % Fine Magnesium Powder
7 % Fine Aluminum Pyroflake		27 % Bariumnitrate
25 % Bariumnitrate		

Fig. 1: Pulsating Flash Compositions (Brock's Fireworks,1898)

The compositions were pressed into hard pellets and burn
periodically after ignition with white flashes. Own measure-
ments on these compositions and compositions which were
slightly varied showed pulsation frequencies in the range
of 0,5 to 5 cps. These compositions did not gain much
importance at that time due to the expensive materials used like
aluminum and magnesium powder. In addition,chemical stability
was low because of the high content in sulphur and light
metal powder. These compositions function satisfactory and,
surprisingly, were not developed further.

Similar pyrotechnic compositions called "Martinikas" were
fabricated at the same time in Germany. (2)   Fabrication
of these compositions were highly hazardous. They contained
white phosphorous and potassiumchlorate:

 4,8 %   Phosphorous white

 6,6 %   Potassiumchlorate

 9,6 %   Calciumcarbonate

34,7 %   Bole white

12,9 %   Gum arabic

31,4 %   Water

Fig. 2: Pulsating Composition (Nico-Pyrotechnik ca. 1930)

For preparation cardboard was coated with a dispersion of
this composition in water, and dried. The substance is
ignitable by friction and burns with a rattling noise. The
frequencies measured were 2 - 3 cps. These compositions
were subsequently banned due to their hazardness and
poisonousness.

Pulsating burning compositions containing red phorphorous
and metal powders like magnesium and aluminum are also
known. The pulsating properties are improved by addition
of iron powder. The frequencies observed are low and are
0,1 - 0,5 cps. The compositions show intermittent bright
light in addition to   intermittent formation of smoke.

Composition of easy ignitable and at low temperature bur-
ning fuels show also oscillating burning rates. Examples
are polyformaldehyde and hexamethylenetetramine mixed with
inorganic oxidizers like   nitrates of barium and strontium.
Various combinations with finely powdered metals do improve
the pulsating effect.

An interesting pulsating burning system are mixtures of
liquid organic nitratesters like methylnitrate and poly-
methacrylicacidmethylester. Such mixtures were described
by Gol' Binder of Mendelejev Institute, Moscow, in 1961. (3)

Pulsating frequencies of 0,6 - 0,7 cps were reported for
mixtures containing 99,9 % methylnitrate and 0,1 % poly-
methacrylicacidmethylester.

All pulsating burning systems described so far were dis-
covered by chance and were not improved for practical
purposes.

Decisive improvements were carried out around 1960 leading
to pyrotechnical systems of practical importance.

Patents of Sidorow and Kravcenko were filed 1969 (4) which
described compositions of aluminum/magnesium alloys with
nitrates of earth alkaline metals and organic resins.

Intermittent light in the colors green, red and yellow
were observed together with frequencies of 0,5 - 3 cps.
The frequency stability, however, was not satisfactory
and it was not until 1973 that new patents of the same
working group were published describing other compositions
with better stability and higher light output.

Typical examples of the compositions are:

78 - 84 % Strontiumnitrate	70 - 75 % Bariumnitrate
16 - 22 % Al/Mg-alloy	12 - 18 % Al/Mg-alloy
+ 1,5-2,5% Iditol	8 - 12 % Copperpowder
	+ 2 % Iditol

Fig. 3: Pulsating flash compositions, red an green,
         Sidorov a. Kravcenko, Moscow

At the same time pulsating burning compositions were
developed by U. Krone, Nico-Pyrotechnik, Trittau,W.-Germany.
The frequency is variable over a wide range from 0.5 to
50 cps and has a good stability. In contrast to the Russian
compositions, though using a similar basic mixture, the
frequency is adjustable by addition of certain catalysts.

Reducing agent, in these mixtures is a 50 : 50 magnesium/
aluminum alloy, oxidizing agents are nitrates of earth-
alkaline metals and perchlorates. The good frequency
stabilization was achieved by an exact separation - on a
time scale - of the dark reactions and those reactions
which are accomponied by light emission. It was necessary
to quench all undesired reactions which appeared during
the dark reaction. This was possible by the addition of
certain compounds which release large amounts of gas during
these reactions. Suitable compounds for this purpose are
ammoniumperchlorate, nitroguanidine, guanidinenitrate,
dicyandiamide and nitrocellulose.

Frequency stabilization was further improved by the use
of finely ground materials only, homogene mixtures and
pressures not below 1,5 tons/cm^2 for the pressing of tablets.

Adjustment of different frequencies by addition of certain
catalysts was best achieved using copperchromite.

There is a marked dependance of the frequency on the
concentration of the added catalysts. Concentrations in
the range of 0,03 - 0,1 % of catalysts increase the fre-
quency from 0,5 cps to 50 cps.On the same basis new com-
positions could be developed which contain mixtures of pure
aluminum and magnesium powder instead of the alloy.

Typical examples of such compositions are:

65 %	Bariumnitrate	65 %	Strontiumnitrate
20 %	Al/Mg-alloy	18 %	Al/Mg-alloy
7 %	Nitrocellulose	8 %	Dicyandiamide
5 %	Ammoniumperchlorate	6 %	Ammoniumperchlorate
3 %	Sodiumoxalate	3 %	Potassiumperchlorate

60 % Bariumnitrate

20 % Al/Mg-alloy

 7 % Ammoniumperchlorate

 5 % Potassiumperchlorate

 5 % Nitrocellulose

 3 % Bariumperchlorate

Fig. 4: Pulsating flash compositions, white, red and green
         U.Krone, Nico-Pyrotechnik, W.-Germany

As a further example which concludes the presentation of pulsating burning compositions, recent developments at our Institute are described which show in addition to intermittent emission of colored light the intermittent emission of sound. (6) (7)

In contrast to the pyrotechnic systems described before which consist essentially of mixtures of powdered materials, these new compositions consist of a copolymer of nitrate groups containing acrylicacidesters with conventional methacrylicacidesters to which soluble earth alkaline perchlorates are added as additional oxidizers.

By variation of the compositon using different components and percentages the frequency could be adjusted in the range between 0,1 and 1 000 cps.

Suitable nitrate group containing monomers are various esters of the acrylic and methacrylic acids and nitrate alcohols such like glycol mononitrate, diglycol mononitrate, glycerol mono- und dinitrates, pentaerythritol mono-, di- and trinitrates.

The copolymerization components used for these nitrate group containing monomers are the conventional liquid monomers like styrene, vinyl acetate and acrylic and methacrylic acid esters of methyl, ethyl, propyl, butyl and similar alcohols.

In addition, inorganic oxidizers are used like the perchlorates of lithium, calcium, magnesium, strontium and barium which are soluble in the monomeres described above.

Typical examples of practical compositions are:

30 % Pentaerythritoldinitratediacrylate

50 % Strontiumperchloratetetrahydrate

20 % Methacrylicacidmethylester

25 % Glyceroldinitrateacrylate

50 % Strontiumperchloratetetrahydrate

25 % Methacrylicacidethylester

20 % Meso-erythritoldiacrylate

40 % Bariumperchloratetrihydrate

40 % Acrylicacidmethylester

Fig. 5: Pulsating flash-sound compositions, red 1 cps, red 10 cps and green 2 cps

F.-W. Wasmann, ICT, W.-Germany

The dependance of the pulsating frequency on the type and percentage of the components used and on ambient pressure and temperature is discussed in detail in the paper presented at "Pyrochem International 75", Univ. of Surrey, U.K. (8) But these details are not subject of this paper.

It is of vital interest to understand the underlying reaction mechanisms of pulsating pyrochemical systems. This interest stems from the fact that pulsating burning compositions are of practical importance as signal ammunition for both military and civilian applications.

So far the following pyrotechnical effects are used to transmit signals:

1) light (white light, colored light, flash light)

2) sound (report or whistling sound)

3) smoke (white, grey or colored).

By combining these effects with pulsating burning the means of transmitting signals are considerably enhanced and thus the information content of a single shot is enlarged. It therefor seems justified to clarify the underlying reaction mechanisms in order to find new and perhaps more efficient compositions.

Further domains of application are pulsating propulsion and artificial fireworks.

Pulsating signal torches and pulsating burning parachute stars are already being manufactured by Nico Pyrotechnik, Trittau, W.-Germany. Pulsating flash-sound compositions developed in our Institute will be commercialy available in the near future. (9)

What is the cause of a pulsating burning?

From a survey of the known pulsating burning systems it is evident that the overall burning behaviour is caused by different chemical reactions which are in competition. In addition, physical effects like heat flow, heat accumulation and intermittent vaporization processes are effective.

An example where the pulsating process is controlled by two competing chemical reactions is the composition of U. Krone, Nico-Pyrotechnik, which contains a magnesium/ aluminum alloy and inorganic oxidizers.

Experiments show that most of the magnesium reacts with the oxidizer to magnesium oxide during the "dark" cycle where no light emission is observed. The oxidation of aluminum

during this cycle is comparatively slow. After magnesium
is totally consumed by the oxidation process the oxidation
of aluminum is suddenly strongly enhanced due to the
increased surface area and the action of oxidative gases
like NO_2, NO etc. which are located in the formed micro-
porous structure of the surface.
This reaction is very fast and accompanied by a short
emission of light. After this process a new cycle starts.
This example illustrates the control of the pulsating burning
by two competitive reactions.

In contrast, a pulsating burning controlled solely by
physical processes is also possible. Such a process is
described by Gol'binder (3) in the case of the combustion
of a mixture of methylnitrate and polymethacrylicacidmethyl-
ester:

"In the case of a volatile explosive (methylnitrate), which
is thickened with polymethylmethycrylate, the main process
taking place in the heated layer of the condenced phase
 is vaporisation.
If, as in the case with polymethylmethacrylate the thickening
additive is substantially less volatile than the explosive,
and cannot undergo exothermic gasification under the conditions
of burning, fractional evaporation occurs in the heated
layer, and the content of the volatile component in it
diminishes as burning proceeds. The viscosity of this layer
increases correspondingly, and its surface becomes a
comparatively firm film, preventing further escape of
bubbles of vapour. The increase in the viscosity of the
heated layer at the same time impedes the diffusion which
would bring the composition closer to that of the rest of
liquid. As a result, the rate of burning falls, the thickness
of the heated layer increases, and the latter ist converted
into a foam of vapour bubbles enclosed by the viscous film.
Then the vapour pressure in the bubbles becomes sufficiently
great, the film is ruptured, and a considerably quantity
of vapour is ejected into the combustion zone together with
entrained droplets of liquid, whose rapid combustion
appears as flashes, after which the cyle of phenomena is
repeated. "

In this system the pulsating burning is controlled by the
heat flow from the burning surface into the interior of
the system. This initiates, due to the special construction
of the system a pulsating vaporization.

An example for a pulsating burning which is controlled by
both   competing chemical reactions and physical processes
is the system being developed in our Institute. As already
discribed this system is composed of a copolymer of nitrate
group containing monomers with common monomers and inorganic
perchlorates.

Compositions prepared in this way burn according to the
following mechanism after ignition:

Initially, the nitrate group bearing acrylic and metha-
crylic acid component, respectively, burn and smolder,
respectively, generating a relatively small amount of heat
and producing a residual mixture of very finely dispersed
perchlorate and partly decomposed polymers, which mixture
has a microporous structure. Since on the one hand, the
ignition temperature of the residual mixture decreases
because of the relative increase in perchlorate content
and, on the other hand,there is a heat accumulation in
the microporous residual mixture because of the bad thermal
conductivity of that mixture, the point of ignition of
the residual mixture will soon be reached.

Because of the extremely large surface of the pourous
residual mixture and the very fine dispersion of the
perchlorate in it, the mixture will burn so quickly, that
a loud report accompanied by a colored flash will be produced.

Despite the marked pressure decrease following this rapid
burning the slow smoldering reaction is not interrupted
because it has again penetrated some way into the "protective"
copolymerisation product during this fast combustion.

This pulsating pyrochemical reaction is controlled by two
competing reactions, namely the chemical smolder reaction
of the nitrate group containing monomers and a fast
reaction which is initated by the physical process of heat
accumulation in the microporous residues.

In summary, the following control mechanisms are active in
the pulsating burning systems described in this paper:

1) Competing chemical reactions with opposite reaction
    path ways.

2) Competing physical processes, like evaporation,
    heat flow, heat accumulation etc.

3) Combinations of competing physical processes and
    chemical reactions.

However, the brief outline of the possible underlying
reaction mechanisms given in this paper can only be a rough
survey since these reactions are of a considerable complexity
and detailed studies are still at an early stage.

An understanding of the observed phenomena would facilitate
new developments of even more practical value.

LITERATURE

1) Private communication Dir. R.G. Hall, Brock's
   Fireworks Ltd. , Sanquhar Dumfriesshire,Scotland
   D 64 63 P, U.K.

2) Private communication Dr. U. Krone, Nico-Pyrotechnik KG
   Trittau b. Hamburg, W.-Germany

3) A.I.Gol'binder, V.V.Goryachev: "Pulsatory combustion
   of liquid explosives thickened with dissolved polymers"
   Russian Journ. of Physical Chemistry VOL 35, No. 8(1961),
   S. 889-891

4) Russian patents; A.I.Sidorov, I.P. Kravcenko (1969):
   SU 237 039, SU 237 041, SU 247 828

5) U. Krone: "Strahlungsemission in Intervallen -
   oscillierende Verbrennung pyrotechnischer Sätze"
   Vortrag Jahrestagung 1975, Institut für Chemie der
   Treib- und Explosivstoffe, D7507 Pfinztal,W.-Germany

6) F.-W. Wasmann: "Festtreibstoffe mit pulsierendem Abbrand"
   Explosivstoffe, Heft 1 (1973), Erwin Barth Verlag KG,
   Neustadt /Weinstraße, W.-Germany

7) F.-W. Wasmann: "Pulsierend abbrennende pyrotechnische
   Systeme"
   Vortrag Jahrestagung 1975, Institut für Chemie der
   Treib- und Explosivstoffe,D-7507 Pfinztal,W.-Germany

8) F.-W. Wasmann: "Pulsating pyrotechnic systems"
   Pyrochem International 1975, 21.-25.July,
   University of Surrey, Guildford, U.K.

9) Pyrotechnische Fabrik F. Feistel KG, D-6719 Göllheim,
   W.-Germany, Fa. Pyro-Chemie, D-5208 Eitorf/Sieg,W.-Germ.